UNIVERSITAT POLITÈCNICA DE CATALUNYA BARCELONATECH

Control contributions to AC microgrid inverters

Daniel Heredero Peris

Universitat Politècnica de Catalunya

Departament d'Enginyeria Elèctrica

PhD thesis

Control contributions to AC microgrid inverters

Autor: **Daniel Heredero Peris**

Director: **Daniel Montesinos Miracle**

Barcelona, January 2017

Universitat Politècnica de Catalunya
Departament d'Enginyeria Elèctrica
Centre d'Innovació Tecnològica en Convertidors Estàtics i Accionaments
Av. Diagonal, 647. Pl. 2
08028 Barcelona

Impressió a Barcelona per Alfambra copisteria
Primera impressió, January 2017

UNIVERSITAT POLITÈCNICA DE CATALUNYA
BARCELONATECH
Escola de Doctorat

Acta de qualificació de tesi doctoral

Curs acadèmic:

Nom i cognoms

Programa de doctorat

Unitat estructural responsable del programa

Resolució del Tribunal

Reunit el Tribunal designat a l'efecte, el doctorand / la doctoranda exposa el tema de la seva tesi doctoral titulada _____ _____.

Acabada la lectura i després de donar resposta a les qüestions formulades pels membres titulars del tribunal, aquest atorga la qualificació:

☐ NO APTE ☐ APROVAT ☐ NOTABLE ☐ EXCEL·LENT

(Nom, cognoms i signatura) President/a	(Nom, cognoms i signatura) Secretari/ària

(Nom, cognoms i signatura) Vocal	(Nom, cognoms i signatura) Vocal	(Nom, cognoms i signatura) Vocal

_____, _____ d'/de _____ de _____

El resultat de l'escrutini dels vots emesos pels membres titulars del tribunal, efectuat per l'Escola de Doctorat, a instància de la Comissió de Doctorat de la UPC, atorga la MENCIÓ CUM LAUDE:

☐ SÍ ☐ NO

(Nom, cognoms i signatura) President de la Comissió Permanent de l'Escola de Doctorat	(Nom, cognoms i signatura) Secretari de la Comissió Permanent de l'Escola de Doctorat

Barcelona, _____ d'/de _____ de _____

Agraïments

Són moltes les persones que, d'alguna manera, han aportat el seu granet de sorra en la realització d'aquesta tesi doctoral. M'agradaria expressar una mostra del meu agraïment en aquestes línies.

En primer lloc, al Daniel Montesinos, director d'aquesta tesi, per haver-me donat l'oportunitat de realitzar-la amb ell i ajudar-me quan les coses es ficaven difícils. Gràcies per tot. Amb ell i en Gabriel Gross va començar una aventura molt maca al CITCEA-UPC realitzant el projecte final de carrera vinculat al projecte IFRIT, amb els quals encara aprenc molt i espero continuar fent-ho.

A tots els meus companys de feina del CITCEA-UPC que m'han fet passar tantes bones estones i han estat sempre que he necessitat compartir inquietuts, donant-me un cop de mà, ajudant-me a resoldre els dubtes del dia a dia, i donant-me bons consells quan era necessari. Sense vosaltres no hauria estat el mateix. Sobretot m'agradaria descatar al Marc Pagès, al Cristian Chillón i la Maria Marin, companys que s'han convertit en grans amics. També, fer especial esmena al Marc Llonch i l'Enric Sánchez, als que dirigir els seus projectes finals de carrera (que després de fer-ho amb el pobre) ha sigut un honor i discutir moltes "anades d'olla" ha sigut molt enriquidor, i entretingut, molt entretingut.

Finalment, a la meva família, que ha estat al meu costat en tot moment, en especial els meus pares, que sempre m'han recolzat. I, com no, a l'Anna, per haver estat amb mi sempre i haver-me fet tirar endavant en els moments complicats, soportant moltes hores d'aïllament per poder fer realitat aquest somni.

Sense ànim de prolongar molt aquestes línies, m'agradaria dedicar aquest treball i l'esforç fet als meus familiars que no han pogut veure un anhel fet realitat, però que sempre em van encoratjar a tirar endavant en la vida.

Moltes gràcies a tots!!!

Abstract

This doctoral thesis is focused on the microgrid control framework. Specifically, it is concentrated on alternative current microgrids. As a result of the author involvement in different industrial projects concerning microgrids during the last years, the goal of the thesis is to apply and to expose the acquired experiences for exploring new control possibilities. The thesis is divided into six main chapters in order to successfully achieve the challenges that have been considered for the alternative current microgrid operation. In this sense, the followed methodology is detailed in the next lines.

Primarily, the thesis presents two chapters whose purpose is to introduce the concept of operation and to analyse the context and challenges posed by microgrids from a top to bottom approach. The first chapter is oriented in general terms while the second one devotes more efforts in the alternative current microgrids particular case. After identifying the different actors that play an important role in the alternative current microgrids it is disclosed that the inverter becomes a key element. In this sense, the first two chapters allows to pave the way introducing and addressing how an inverter installed in an alternative current microgrid can be considered and operated. In this direction, the named grid-tied operation mode reflects the most complex configuration. Considering that the scope of the thesis is focused on voltage source inverters, the grid-tied configuration may not only consider the grid-connected or grid-disconnected operation mode but also the transients between them. Thus, important challenges such as the inverter operation itself, the anti-islanding detection capability according to the behaviour of the inverter and the galvanic isolation restriction in a microgrid framework are dealt.

The control of voltage source inverters operated in an alternative microgrid results crucial. For this reason, a full chapter carries out a study proposing and delving into various type of controllers according to different possibilities exposed in the literature. It is conducted a stability analysis for stationary reference frame resonant current and voltage controllers. The chapter concludes with a new hybrid formulation based on fractional calculus and conventional resonant control. This novel formulation allows to enhance the controllable frequency bandwidth range decreasing inter-harmonic excitations and reducing the controller order in respect with other classical formulations.

The fourth and fifth chapters are involved into discussing and presenting different operation options when the inverter is considered as a current or a voltage source. The fourth chapter poses over how to tackle the problem of transients when a current source grid-tied inverter is assumed while grid-connected operated. Two situations are studied; the flying transference from current to voltage source and how to extend the maximum power point extraction when a back-up system supports the inverter operation. A set of different scenarios conducted in simulation and in a real experimental platform complements the two considered situations. The fifth chapter analyses the operation of the inverter from an opposite perspective. The considered inverter is operated by using a hybrid combination between alternative current droop control strategy when grid-connected and voltage-frequency control when grid-disconnected. In this way it is possible to preserve dynamics capabilities in both operation modes meanwhile the inverter is treated as a voltage source in any case. A predominant resistive model applying virtual resistance is considered for the concrete case of alternative current droop control. For both operation modes an LCL-type coupling filter is assumed, complementing the control strategy with an active damping mechanism to mitigate possible resonances. Then, a three-phase four-wire four-leg inverter is proposed to match better with a proper approximation to an alternative current microgrid that should be close to the end-users. In this sense, any kind of load -single or three-phase- can be connected or any power set-point -active or reactive, positive or negative- can be exchanged with the utility. A simplified space vector modulation is presented to operate this inverter optimizing the program memory required by the modulation implementation. The design, simulation, construction and validation of the inverter under real conditions is also performed considering special operation features; over-load supervisor when grid-connected and sinusoidal short-circuit proof when grid-disconnected operated.

Finally, the last chapter sums up the realized tasks, exposes the most relevant conclusions considering possible future works, and lists the publications derived from the scope of this thesis or related to it.

Resum

Aquesta tesi s'emmarca en el control de microxarxes. Específicament, es focalitza en microxarxes de corrent altern. Com a resultat de la participació de l'autor en diferents projectes industrials vinculats a microxarxes durant els darrers anys, l'objectiu de la tesi és aplicar i exposar les experiències adquirides per explorar noves possibilitats de control. La tesi es divideix en sis capítols principals que permeten afrontar amb èxit els reptes considerats per l'operació d'una microxarxa de corrent altern. En aquest sentit, la metodologia seguida es detalla en les següents línies.

En primer lloc, la tesi presenta dos capítols el propòsit dels quals és introduir el concepte d'operació i analitzar el context i els reptes que planteja una microxarxa des d'una aproximació de dalt a baix. El primer capítol està orientat als conceptes generals, mentre que en el segon es dediquen més esforços als detalls del cas particular de les microxarxes de corrent altern. Després d'identificar els diferents actors que juguen un paper important en les microxarxes de corrent altern, se'n despren que l'inversor n'esdevé un element clau. En aquest sentit, els dos primers capítols permeten obrir el camí introduint i afrontant de quina forma un inversor instal·lat en una microxarxa de corrent altern pot ser considerat i operat. En aquest sentit, el mode de funcionament anomenat *grid-tied* (lligat a la xarxa) reflexa la configuració més complexa a tenir en compte. Tenint present que l'abast de la tesi es centra en els convertidors de font de tensió, en la configuració lligada a la xarxa s'ha de considerar, no sols, el mode de funcionament connectat a la xarxa o desconnectat, sinó, també, el transitori entre ells. Per tant, es tracten importants reptes com ara poden ser la seva operació, la capacitat de detecció d'illa d'acord amb el comportament de l'inversor i la restricció d'ús d'aïllament galvànic en el marc de les microxarxes.

El control dels inversors de font de tensió utilitzats per operar una microxarxa de corrent altern resulta crucial. Per aquesta raó, un capítol complet porta a terme un estudi proposant i aprofundint en diversos tipus de controladors d'acord amb l'exposat en la literatura. En aquest capítol es porta a terme una anàlisi d'estabilitat pel cas de controladors ressonants de corrent i voltatge en el marc de la referència estacionaria. El capítol conclou amb una nova formulació híbrida basada en el càlcul fraccional i en el control ressonant convencional. Aquesta nova formulació permet millorar el rang

d'ample de banda en freqüència controlable disminuint les excitacions interharmòniques i reduint, al seu torn, l'ordre del controlador respecte d'altres formulacions clàssiques.

Els capítols quart i cinquè estan involucrats en la discussió i la presentació de diferents opcions d'operació quan l'inversor es considera com una font de corrent o de tensió. El quart capítol planteja com abordar el problema dels transitoris quan es suposa que un inversor lligat a la xarxa opera com a font de corrent mentre es troba connectat a la xarxa. S'estudien dos situacions; la transferència al vol de font de corrent a voltatge i la forma d'extendre l'operació des del punt de màxima potència quan s'admet un sistema d'emmagatzematge com a suport en l'operació de l'inversor. El cinquè capítol analitza el funcionament de l'inversor des d'una perspectiva oposada. L'inversor considerat funciona mitjançant l'ús d'una combinació híbrida entre l'estratègia de control *droop* per microxarxes de corrent altern quan es troba connectat a la xarxa i el control de voltatge-freqüència quan es troba desconnectat. D'aquesta manera, és possible preservar capacitats dinàmiques en els dos modes de funcionament mentre que l'inversor és tractat com una font de tensió en ambdós casos. Pel cas concret del *droop* aplicat a xarxes de corrent altern s'ha fet ús d'un model predominantment resistiu aplicant el concepte de resistència virtual. Els dos modes de funcionament consideren l'ús d'un filtre d'acoblament del tipus LCL el control del qual es complementa mitjançant esmorteïment actiu per mitigar possibles ressonàncies. Així, es proposa un inversor trifàsic de quatre fils i quatre branques perque coincideixi millor l'operació d'aquest amb una aproximació adequada a una microxarxa de corrent altern on la generació de tensió alterna ha d'estar a prop dels usuaris finals. D'aquesta forma, qualsevol càrrega pot ser connectada -monofàsica o trifàsica- o es pot intercanviar amb la xarxa qualsevol potència -activa o reactiva, positiva o negativa-. És presentada una modulació de vector espacial simplificada per poder operar aquest inversor optimitzant els requiriments de memoria de programa requerits per la implementació digital de la modulació. Es porta a terme el disseny, simulació, construcció i validació de l'inversor en condicions reals tenint en compte certes característiques especials d'operació; supervisor de sobrecàrrega quan l'inversor es troba connectat a la xarxa i capacitat de suportar curt-circuits sinusoidals en mode desconnectat.

Finalment, l'últim capítol resumeix les tasques realitzades, exposa les conclusions més rellevants tenint en compte possibles treballs futurs, i enumera les publicacions derivades de l'àmbit d'aplicació d'aquesta tesi o relacionades amb ella.

Contents

List of Figures

List of Tables

Nomenclature

Acronyms

CL	Close Loop
OL	Open Loop
AC	Alternative Current
CAN	Controller Area Network
CC	Current Controlled
CENER	National Renewable Energy Centre of Spain
CFE	Continued Fraction Expansion
CHP	Combined Heat and Power
CIM	Computer Integrated Manufacturing
CITCEA	Centre d'Innovació Tecnològica en Convertidors Estàtics i Accionaments
CSI	Current Source Inverter
CVCF	Constant Voltage and Constant Frequency
DC	Direct Current
DER	Distributed Energy Resource
DER	Distributed Energy Resources
DNO	Distributed Network Operator
DNO	Distribution Network Operator
DSM	Demand Side Management
DSO	Distribution Service Operator

DSP Digital Signal Processor

EC European Comission

EMI Electro-Magnetic Interference

EPS Electric Power System

EV Electric Vehicle

FFT Fast Fourier Transform

FI Fractal Integrator

FOC Factional Order Calculus

FOH First Order Hold

FOPID Fraction Order PID

FPR Fractional Proportional Resonant

GCI Grid Constitution Inverter

GHG Green House Gases

GPRS General Packet Radio Service

GPS Global Positioning System

GSCI Grid Support and Constitution Inverter

GSI Grid Supply Inverter

HC Harmonic Compensator

HVDC High Voltage DC

I/O Input/Output

IEC International Electrotechnical Commission

IEEE Institute of Electrical and Electronics Engineers

IIT Illinois Institute of Technology

IMC Internal Model Control

ITI Information Technology Industry

LC Local Controllers

LCL Filtre passiu format per una inductància, un condensador i una altra inductància disposades en cascada

LLD Low Level Devices

LQR Linear-quadratic regulator

LV Low Voltage

MGCC MicroGrid Central Controller

MGO MicroGrid Operator

MIMO Multiple Input- Multiple Output

MIMO Multiple-Input Multiple-Output

MO Market Operator

MPP Maximum Power Point

MPPT Maximum Power Point Tracking

MRI Mutiple Rotating Integrators

MS Master Slave

MV Medium Voltage

NDZ Non-Detection Zone

NZSV Non-Zero Switching Vector

PCC Point of Common Coupling

PD Protection Device

PE Protection Earth

PEAC Power Electronics Application Center

PID Proportional Integral Derivative

PLCC or PLC Power Line Carrier Communication

PLL Phase Locked Loop

PR Proportional Resonant

PSE Power Series Expansion

PV Photovoltaic

PWM Pulse Width Modulation

REBT Reglamento Electrotécnico de Baja Tensión

RGA Relative Gain Array

rms root mean square

RS Renewable Source

SFS Sandia Frequency Shift

SISO Single Input-Single Output

SISO Single-Input Single-Output

SMS Slip-Mode Shift

SoC State of Charge

SOGI Second Order Generalized Integrator

SRF Stationary Reference Frame

SRRF Synchronous Rotating Reference Frame

SVPWM Sinusoidal Pulse Width Modulation

SVPWM Space-Vector Pulse Width Modulation

SVS Sandia Voltage Shift

TC Transformer Center

TCP/IP Transmission Control Protocol/Internet Protocol

TEH Triangular Equivalent Hold

THD Total Harmonic Distortion

UDP User Datagram Protocol

UPC Universitat Politècnica de Catalunya

V2G Vehicle to Grid

V2G Vehicle to Vehicle

V2H Vehicle to Home

V2M Vehicle to Microgrid

VC Voltage Controlled

VDE Verband Deutscher Elektroingenieure

VPI Vector Proportional Integral

VSC Voltage Source Converter

VSI Voltage Source Inverter

ZOH Zero Order Hold

ZSV Zero Switching Vector

Chapter 1

Introduction

1.1 Overview

During last decades the renewable energy industry has been experiencing a high penetration and implantation with a trend to rise into the society at global level. Initiatives like the Horizon 20/20/20 (20% of energy produced by renewable, reducing a 20% the greenhouse emissions by 2020), impulsed by the European Union, pushes the introduction of Renewable Sources (RS) at a large scale. In Figure 1.1 can be seen the tendency from 1990 to 2010 in the particular case of Spain, described in the Renewable Energy Plan 2011-2020 [1].

The RS provide, in general, clean energy with almost zero cost in raw materials, except for some cases such as biomass or biogas. Some of these RS, as photovoltaics or wind, present a main drawback; production and demand are not overlapped in time or in quantity, i.e. they are intermittent RS. The concept of Distributed Energy Resources (DER) steams from the increasing awareness of an efficient use of more sustainable energies.

Microgrids [7–9] and other concepts as smartgrids, energy hubs, power routers or virtual power plants are supported by DER looking to a world with an increasing electrical energy demand. As a consequence, the electrical energy distribution scenario has to change, and big generators, utilities and regulators must adapt to a new and smart energy scheme. In this new paradigm, power electronics and communications are playing a major role. Traditional big fixed frequency rotating generators will no longer exist in medium and small disconnected microgrids.

The major interface for any DER, storage and even some loads, is power electronics based on static switches. Of course, power converters are not big rotating generators and for sure they will not behave the same, for instance, in terms of overload capability.

The transition from conventional grid to smartgrids or microgrids will go through an intermediate scenario where both grid types will coexist.

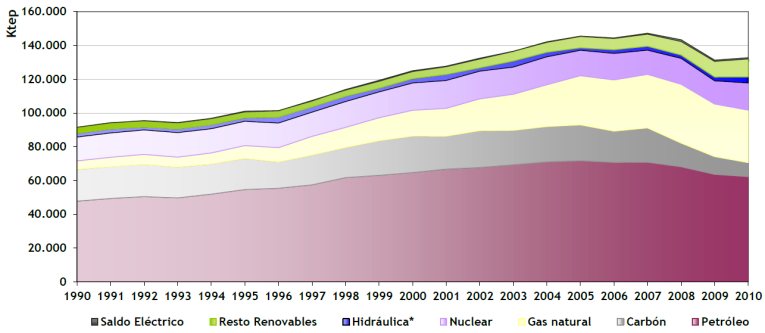

Figure 1.1: Evolution of the consumption of primary energy in Spain since 1990. Source: Renewable Energy Plan 2011-2020 [1]

All items concerning microgrids become a challenge implying technical and political (regulation) effects that will involve from DER, power converters, protections to standards, legislation or operation codes.

1.1.1 Distributed Energy Resources

DER can be defined as energy producing resources with relative low power, less than 1 MW, which are located close to the consumption points. DER are small, modular and decentralized sources. In this sense, they provide a great flexibility due to their merge capability. DER also allow to consider new actors in the electric market such as prosumers [10]. A prosumer is an entity that not only consumes but also generates energy. An active role is assumed between the consumers and the Distribution Service Operators (DSO). These new producers turn into a new challenging scenario for the conventional distribution framework.

DERs can be classified into two different groups [11]: grid feeding DER and grid forming DER. In both cases a back-to-back topology is applied, usually constituted by two Voltage Source Converters (VSC) interconnected by a common DC-link, as can be seen in Figure 1.2.

- Grid feeding DER. Usually linked with photovoltaic or wind resources, the DER is controlled by a power converter that operates it at the Maximum Power Point (MPP) thanks to the use of MPP Tracking algortihms [12]. All the available power is delivered to an intermediate DC-link. The AC-side power converter operates as an active rectifier

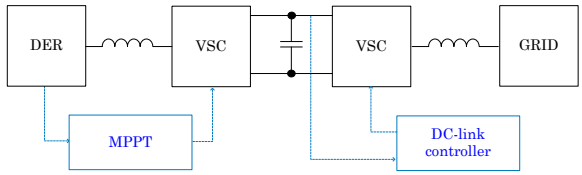

(a) Grid feeding DER

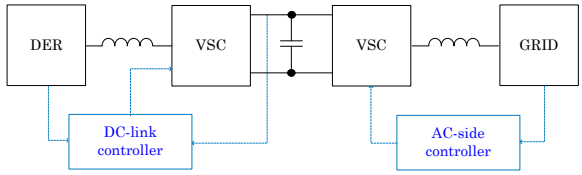

(b) Grid forming DER

Figure 1.2: Examples of grid feeding and grid forming DER integrated by a back-to-back structure

maintaining the DC-link at the proper DC voltage level. In this sense, all the power delivered by the DER is transmitted to the AC side. This mean that a grid feeding DER injects power regardless of the DSO setpoints. Other alternatives, as biomass are operated according to DSO targets becasue the energy can be stored.

- Grid forming DER. The DERs is controlled by a power converter that operates the system managing the DC voltage of the intermediate DC-link. According to the DSO setpoints, the AC-side converter delivers the requested apparent power. In case of operating without an electrical network, a grid forming DER can also be used to form the grid for isolated situations.

Then, DER can be classified, apart from into feeding DER or forming DER, into those in which energy can be stored by using storage system or assuming an energy vector in the system, and those in which energy cannot be stored. In the storable ones, the energy resource is available at any time for use. It is consumed at the time that the microgrid requests more energy in order to be self-sufficient. Thus, a third actor appears into the DER integration and allows to have a hybrid feeding-forming DER, as depicted in Figure 1.3. In that way, each converter has a stipulated role and the available DER power can be distributed into the storage system or/and the grid.

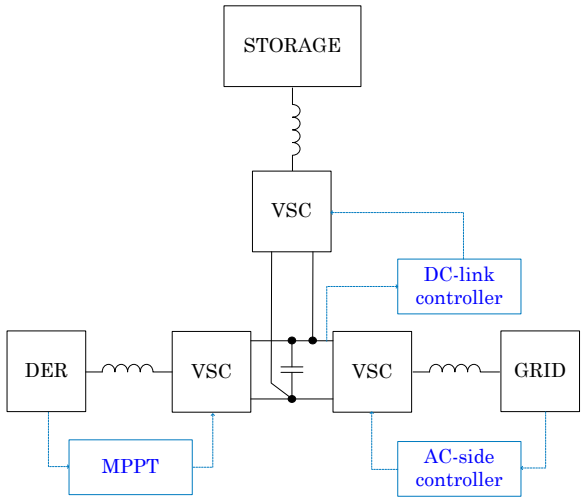

Figure 1.3: Examples of grid feeding-forming DER

1.1.2 Microgrid general operation aspects

A microgrid, as the one shown in Figure 1.4, can be seen as a natural evolution of the current distribution grid. The classical concept is based on the unidirectional distribution model. It is used to assume unidirectional high voltage transmission lines over long distances from the source to the end-users. The direct effect of this consideration derives into important associated losses. Otherwise, microgrids are dynamic active controlled and coordinated bidirectional grids, where production and consumption must be equal. Usually, a microgrid allows to manage up to few hundreds of kVA. They have to operate as part of a distribution grid (grid-connected) but also being able to be operated electrically disconnected from the grid (grid-disconnected). A main switch element allows operating the system under both modes. Then, a microgrid has also to include not only micro-energy generation with sufficient DER "credits", but also monitoring systems and hierarchical control layers.

In general terms, the literature usually talks about three hierarchical levels that will be in any type of microgrid [13]:

- Distribution Network Operator (DNO) and Market Operator (MO)
- MicroGrid Central Controller (MGCC)
- Local Controllers (LC)

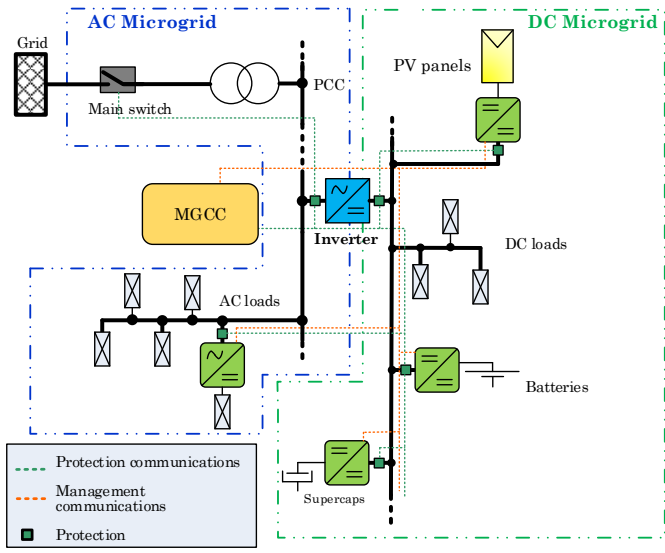

Figure 1.4: Scheme of a hybrid microgrid (including AC and DC microgrid)

These three levels have more or less intelligence and relevance depending on the used strategy. Figure 1.5 depicts the different agent interactions.

The DNO and the MO are the managers of the grid. Although they are not an explicit part of the microgrid they have to be considered as an implicit part of it. Between the DNO-MO pair and the microgrid appears the MGCC. This element is important in order to have an optimized system for a "super"-microgrid or aggregated microgrid consideration. In these aggregated microgrids an interaction with much single-elements will suppose a more complicated system to manage; each microgrid can have its own communication protocol with its own operation objects. The LC controls the DER and its power electronics converters in a lower level. Each LC can take decisions locally in order to ensure the integrity of itself, its sources and any local loads. The LC does not require commands for the proper operation of voltage, frequency or current, but requires active/reactive dispatching set-points from the MGCC. These set-points will come from the DNO. The MGCC will share the set-points in function of the availability of the resources, the storage system, the operation mode of the connected microgrids (grid-connected/grid-disconnected), weather forecast and production/consumption predictions.

The LC will have a certain level of intelligence depending on the type of the

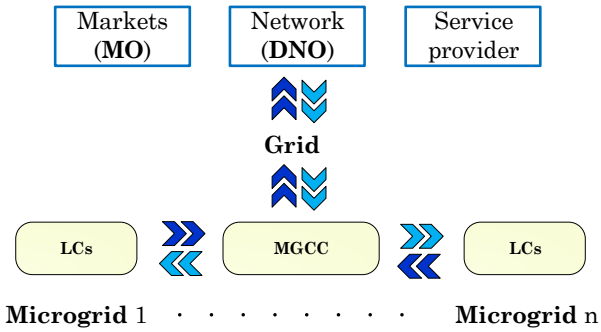

Figure 1.5: Microgrid system interaction

chosen managing approach: centralized or distributed. However, there are some decisions, for instance over-current protection, that are done locally independently of the manager centralized manage level [13]. Then, this situation is informed to the high level devices; protections, LC or the MGCC.

The high-level managing agents offer a degree of intelligence to the whole system but requires different strategies for coordination. This is achieved by the participation of industrial communication buses such as CAN, Modbus, Ethernet and communication services such as Internet or GPRS.

On the other hand, one of the most common ways to classify microgrids is according the voltage link; DC microgrids, AC microgrids or the combination of both, the hybrid microgrids. In this sense, the applications where the energy of a microgrid can be used are many and diverse. They move from such different situations as the need to provide electricity to difficult access areas, to generate power obtaining an economic benefit or to provide grid support. This imply to consider the establishment of market mechanisms to enable third party provision microgrid's services. The microgrids can also be used to improve the specifications and quality of the received energy by optimizing parameters such as distance and losses. Additionally, they can contribute with extra functionalities as harmonic current reduction, power factor correction, voltage or current balancing and interruption time minimization. Then, a microgrid is operated bidirectionally.

The fact that an AC microgrid can operate in grid-connected or in grid-disconnected mode implies to be consequent with the right decisions about protection, monitoring and neutral-scheme requirements. The main aspects regarding microgrid protections can be summarized into two items:

- Isolation detection. The system must decide at what point it should isolate the microgrid from the utility, either by a scheduled shut-down or a non-intended failure. The control mechanisms that permit to detect these situations are known as anti-islanding algorithms [14]. Their aim is to detect that the grid is not connected to the AC microgrid side in order to avoid partial energizations. For this reason, it is necessary to consider some regulations as VDE-016, VDE-AR-N-4105, IEC-61727 or IEEE-1547 [15–18] to attend dangerous situations.

- Segregation capability and reconfiguration. A microgrid should provide self-segregate capability and provide coordination in a fault situation. Although the protections of an AC microgrid are similar to those of a conventional grid, they differ in some specific points. The short-circuit power of the protections and the bidirectionality in power have to be taken into account. Moreover, when the inverter is operating in grid-connected mode the utility imposes the neutral-scheme, but when operates in grid-disconnected mode the MGCC has to decide what to do with the neutral-scheme, where, how and when connect it to the ground. Thus, the microgrid in grid-disconnected should provide a suitable ground system for the safety of people and equipment.

Continuing with the protections topic it should be clarified that a microgrid must dispose of a monitoring system and protections to minimize risks to people and to the electric network itself. However, it should be reminded that the energy flow in a microgrid is bidirectional. In this point could be also included bidirectional energy active and reactive counters. All these devices will necessarily have to communicate with the MGCC to take decisions or to be reconfigured.

1.1.3 Role and impact of a microgrid

A microgrid needs to behave as something more than a reduced scale grid that follows the prosumer idea. A fundamental consideration is to use microgrids in order to minimize operating costs combining participation, technologies and regulations. In this sense, for instance, European energy policy has done an important effort promoting low-carbon generation methods. A microgrid can occupy this parcel to achieve the mentioned 20/20/20 objective. As a microgrid integrates management, energy, industrial communications and storage it could be linked with expanding, managing and transforming the existing infrastructure into a more efficient system. A microgrid can help to increase and to enhance the following items [19–21]:

- Autonomy. The energy allowable in grid-disconnected mode is finite. A microgrid allows to integrate a wide variety of primary energy resources with storage and controlled loads. These loads have to be discriminated into different levels of criticism. For example, an air conditioner can be disconnected if the microgrid manager detects an overload situation while other ones, as the fridge, can be connected permanently. End-users will have to be more sensible with the consume under this operation mode.

- Stability. A microgrid permits to control the voltage and the frequency at the AC side. As microgrids are managed by static power converters, the obtained dynamics can be specified in the order of few milliseconds.

- Compatibility and flexibility. Various microgrids can be inter-connected in order to have a meshed microgrid structure. This idea can improve the resources thanks to the possibility of send and receive energy-packages, negotiate with the utility and optimize the system. This same concept can be applied between the active phases in case of four-wire systems. Then, the concept of power or energy routers is followed [22]. Although a microgrid needs to be as much as possible neutral in terms of technology, the number of active wires is determinant depending on the final application.

- Restoration and reliability. Microgrids are gaining importance in such places affected by atmospheric phenomena such as hurricanes or earthquakes. When a region is affected by this type of situations, usually, a black-out occurs. After a black-out it is not easy a full system restoration. Microgrids allow to move to a more meshed electric system that facilitates grid restoration by sections. As microgrids are expected to be aggregately operated and they are close to the end-users, the system restoration becomes easier. Furthermore, depending on the rate power of each microgrid, the allowable power of one microgrid can be shared with other ones less powerful.

- Modularity. As a microgrid will use bus-links (AC or DC) to interconnect the different elements it is possible to scale the system if the microgrid requires more power. If various microgrids are interconnected, the concept of aggregated microgrid can be considered. An aggregated microgrid becomes a smartgrid [23, 24] in order to take profit of all its resources and capabilities. Examples of an aggregated

DC microgrid, integrated by multiple Vehivle-to-Grid (V2G) power conditioners, can be found in the literature [25, 26].

- Economics. The microgrid, when it is operating in grid-connected operation mode can be used in order to enhance the quality of the consumed grid currents, balance the phases and dispatch reactive. This fact can derive in a retribution from the DSO. In grid-disconnected mode other ideas as Vehicle-to-Vehicle (V2V) (dis)charging strategies can be also considered [27]. New business cases will appear becoming a challenge to define ownings, operation and revenues from the exploitation of a microgrid.

- Efficiency. As a microgrid can be considered by the utility as an active load, the direction of the power flow can be managed to the loads, to the storage systems and to the grid enhancing the performance of the network depending on the particular boundary conditions.

Microgrids dispose of the potential to make the electricity market more dynamic and flexible. However, it is also necessary to take into consideration that the operation of a microgrid in a real system, under government legislation, has some barriers to overcome. Usually the regulatory, economics or exploitation barriers are more restrictive than the technical ones. In fact, it is used to observe that the higher a technology is mature the higher and complex are the rules determined by the different institutions to operate them. It should be also considered the point that each country will apply its own legislation.

New business models and new services to offer will appear determining different ways to operate a microgrid. This fact implies to consider the most optimal and efficient configuration of the microgrid to obtain the maximum benefit or assure the maximum resilience for critical loads, as can be hospitals. These business cases born from the determination of optimal locations for the microgrid exploitation according to preferred location that depends, essentially, on existing infrastructure and proximity to the end-users. The different business models that follows a microgrid, how to manage the interconnection between different microgrids, and the grid and the reconnection procedures are not clear enough. Current regulatory structure is built around a historical model of the electric utility vertically integrated by generation, transmission and distribution systems that serve to the electric customers in a territory. A microgrid structure modifies this vertical conventions structure because generation, transmission and distribution becomes a block unit, usually, concentrated close to the end-users.

Some of the main reasons of why the conventional system behaves inertially against the new framework are:

- Revenues. The lost of utility revenues if a user consumes its own energy of its own microgrid will affect the cost of the energy and the promotion of renewables. The participation in overall grid costs implies to consider all grid reinforcements moving to an unbundling scenario where grid and energy are clear separated.

- Ownership of the microgrid. Which elements of a microgrid owns to the DSO or the producer (or prosumer) have a relevance on how the microgrid can be operated (cooperative, corporation, non-profit association, community microgrids or virtual plants).

- Customer rights. Depending on the physical location of the microgrid the regulation can be slightly different producing that a same microgrid has to be customized to fulfil concrete aspects of a particular regulation.

- Interconnection. In case of aggregated microgrids, the applied regulations to the single entities that conforms the microgrid or to the full system can be, in some case, almost incompatible.

1.1.4 Standards

The use of regulations is crucial to be prone to the standardization. To facilitate the natural evolution of the existing electrical power system into smartgrids or microgrids it is needed the development of standards to promote and support real functional infrastructures, and have good practice guides. In this sense, there is an emerging role of the society to establish a regulation for the microgrid development. Some of the most relevant ones in Europe are VDE-AR-N 4105:2011-08 [16], IEEE 1547 [18] and IEEE 2030 [28].

- VDE-AR-N 4105:2011-08: *Power generation systems connected to the low-voltage distribution network*. This regulation summarises the key aspects for the integration of decentralized generators that operates in parallel with the network. It is focused in network-supporting functionalities to ensure safe and reliable grid operation for maximum integration of generating capacity in low voltage utilities. This VDE application guide substitutes the 4^{th} edition of the VDEW guideline on "Generating Plants Connected to the Low-Voltage Network" [29].

- IEEE 1547: *Interconnecting Distributed Resources with Electric Power Systems.* It is an American standard that has been updated since 2003 until 2008 in order to incorporate more considerations to define properly the full operation of interconnected electric networks. It is basically a technical standard that defines functional requirements for the interconnection itself and its tests. It is technology neutral and does not address distributed resources protection. IEEE 1547 is currently divided into nine documents:

  - IEEE 1547-2003. *Standard for interconnecting distributed resources with electric power systems.* Reaffirmed in 2008.
  - IEEE 1547.1-2005. *Conformance test procedures for equipment interconnecting distributed resources with electric power systems.* Reaffirmed in 2011.
  - IEEE 1547.2-2008. *Application guide for IEEE Std 1547 standard for interconnecting DRs with electric power systems.*
  - IEEE 1547.3-2007. *Guide for monitoring, information exchange and control of DR.*
  - IEEE 1547.4-2011. *Guide for design, operation, and integration of distributed resources island systems with electric power systems.*
  - IEEE P1547.5 (Draft). *Guidelines for interconnection of Electric Power sources greater than 10 MVA to the power transmission grid.*
  - IEEE 1547.6-2011. *Recommended Practice for Interconnecting Distributed resources with electric Power Systems Distribution Secondary Networks.*
  - IEEE P1547.7 (Draft). *Guide to conducting distribution impact studies for distributed resources interconnection.*
  - IEEE P1547.8 (Draft). *Recommended practice for establishing methods and procedures that provide supplemental support for implementation strategies for expanded use of IEEE Std 1547.*

- Standard IEEE 2030: *Smart-Grid interoperability.* It provides guidelines in understanding and defining terminology for smartgrid interoperability of the electric power system considering end-use applications and loads, see Figure 1.6. It has into account the technology

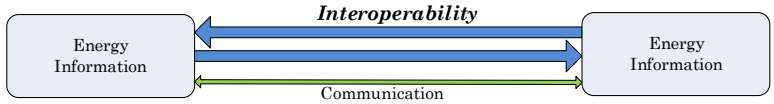

Figure 1.6: IEEE 2030 concept

and information interchanged to achieve seamless operation for electric generation-dispatch and end-use benefits. This permits a bidirectional power flow with communication and control. Finally, makes an effort to expand knowledge in grid architectural designs and operation to promote a more reliable and flexible future electric system. IEEE 2030 is currently divided into 3 documents:

- IEEE P2030.1. *Draft Guide for Electric-Sourced Transportation Infrastructure.*
- IEEE 2030.2. *Guide for the Interoperability of Energy Storage Systems Integrated with the Electric Power Infrastructure.*
- *Draft Standard for Test Procedures for Electric Energy Storage Equipment and Systems for Electric Power Systems Applications.*

1.1.5 General types of classification

A microgrid can be classified according to many criteria, but the most common in the literature implies the type of management, type of architecture or the type of bus-link [13, 30].

Type of management

A microgrid usually has some specification that permits an interaction with the utility. The control of a microgrid needs to be conceived from a manager that administrates the energy, the storage of the excess of renewable production and concentrates data from the electricity market and other parts of the system, as well as provides proper black-start and isolation procedures and decides how to operate other ancillary services. To achieve all this objectives the management of a microgrid needs to be quite smart. This intelligence can be centralized (MGCC) or distributed (LC). The centralized and distributed concept can be analysed in a similar way as in the case of communications. For this reason, it should be considered the different communication network topologies applied to microgrids:

- Star. A central element (MGCC) establishes connections between each LC that constitutes a node. The central node may be "smart" adapting communication speeds, frequency or voltage between nodes. It also allows to detect errors or connect two nodes with different communication protocols. Simple detection of faults can be achieved but all the operation depends on the central node. Figure 1.7 shows the aspect of a microgrid based on a star topology.

- Ring. Any required data to exchange is transmitted by each node before reaching its destination. It can be used different communication medias. The network continues operating if one LC fails and this role can be assumed by other LC. However, the normal operation should be discontinued to include a new LC. Figure 1.8 depicts two possibilities of a microgrid based on a ring topology. Figure 1.8(a) shows the possibility to integrate the MGCC as one more LC in the ring and Figure 1.8(b) considers that the MGCC belongs to a higher management level. This last option is usually applied when computational requirements of the MGCC are higher than for the LC.

- Tree or Bus. In the tree or bus networks all exchanged data are received by all LC. As the communication and power media is shared, the communication specifications and voltage, current and frequency must be shared, too. The addition of a new LC does not require a stop in the operation. Figure 1.9 depicts two possibilities of a microgrid based on a bus topology. In Figure 1.9(a) it is considered a branching in some LC connected to other minor LC. On the other hand, Figure 1.9(b) does not consider any difference between LC, and all of them are connected directly to the same bus-link.

Once exposed the different physical communication network topologies, the use of a centralized or distributed control strategy will influence the behaviour and operation of the microgrid:

- Centralized control strategy. Using a centralized approach, the MGCC plays the role of a gateway between the DSO-MO pair. However, the MGCC can aggregate data from more than one LC allowing "little" microgrids to be seen for the utility as a much important microgrid in terms of power. The communication between the DSO-MO and the MGCC can be of a completely different media that the one used between MGCC and LC. The first one is not as critical as the second one, so Power Line Carrier Communication (PLCC) or wireless could be a

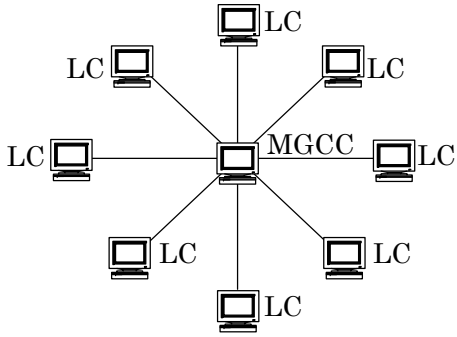

Figure 1.7: Star microgrid network topology

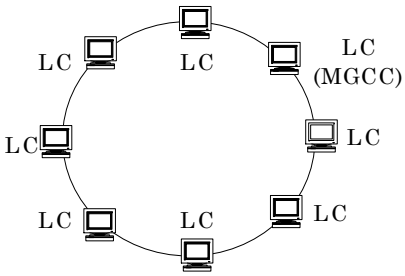

(a) Joined MGCC in the ring network

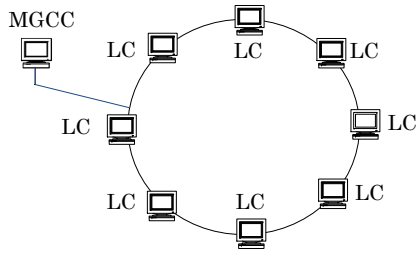

(b) Disjoined MGCC in the ring network

Figure 1.8: Ring microgrid network topologies

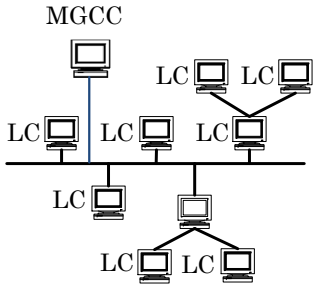

(a) MGCC in a tree network

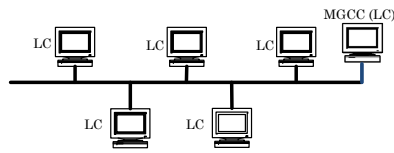

(b) MGCC in a bus network

Figure 1.9: Bus microgrid network topologies

good option with a refreshing time of the order of minutes. During this time interval different variables like market prices, bids, network security and medium-term predictions can be updated and send to/from the DSO-MO and the MGCC.

On the other hand, the high dynamics of the power converters, the variability of the natural resources and the volatility of the loads makes that a more robust and fast communication bus has to be used at this level, i.e. real-time or almost real-time. Depending on the bus network topology used, one or various physical layers can be applied in a same system. In this case, targets and feedbacks of the relevant parameters have to be refreshed in the order of few milliseconds up to seconds.

The main goal of a centralized strategy is focused on the grid-connected mode and it is related to follow the set-points from the DSO-MO in order to serve the load requirements under market prices to take the maximum economical benefits.

In grid-disconnected mode, the DSO-MO can send the availability of the grid due to maintenance or other causes, and the MGCC has to decide which will be the best instant to reconnect the system, for instance, based on the price of energy. The LC will interchange the information with the MGCC when the reconnection with the utility can be technically done with the smoothest transient. Also, the DSO-MO can operate the system with a different frequency of the rated one to inform other devices, in an indirect way, that the microgrid is operating in grid-disconnected mode.

- Distributed control strategy. In a decentralized strategy the main goal is to take decisions locally in order to optimize the performance of the power interchanged between the DER and the local loads. In other words, try to supply the critical loads during the maximum possible time using the available instantaneous energy produced by the DER and the storage systems. So, the revenue in this manage strategy is a secondary objective. Thus, the LC could also incorporate economic restrictions but conditioned by the aforementioned priority. It is possible to say that the system is rule based due to the absence of the utility.

  The inputs with a higher weight will be the forecast, the prediction of the load consumptions and the State of Charge (SoC) of the storage systems.

Type of architecture/hierarchy

A microgrid will be, partially or completely, part of a low voltage or medium voltage distribution line with its local loads. The point of interconnection is known as Point of Common Coupling (PCC). In this sense, depending on the type of loads connected, the location of the microgrid, the available electrical infrastructure and the ownership of the land or the electrical system, three subtypes of architectures can be defined: utility microgrids, industrial/commercial microgrids and remote microgrids as:

- Utility microgrids. The microgrid can be conceived as a way to integrate different DER and obtain large-scale deployments. An utility microgrid allows to a DNO to manage which portion of the required energy is supplied by the grid and which by the microgrid. The DNO controls all the process and it is optimized as a function of the renewable availability. During maintenance of the grid, an utility microgrid can continue supporting the end-users or, at least, their critical loads. Also, this type of microgrid can offer ancillary services as reactive power compensation or improve the harmonics content.

  In this way, an utility microgrid can operate in grid-connected and grid-disconnected mode.

  The benefits of this type of microgrids are:

  - Greenhouse reduction
  - DER mix integration
  - Congestion management
  - Upgrade deferral
  - Ancillary services

- Industrial/commercial microgrid. The industrial or commercial microgrids can be divided into a multi-facility (industrials parks, shopping centers) or single-facility (commercial or residential) system. So, multiple single-facilities can be aggregated to conform a multi-facility structure.

  In this case, the loads that need to be supplied in an industrial framework are classified as critical and sensitive to power quality and interruptibility. In the case of industrial loads, if them are related with cooling or heating systems, this can be considered as non-fast critical

loads. The temperature usually have enough inertia to be a controllable load. In contrast, motors and transformers units have important inrush currents to consider.

Critical loads do not tolerate transient voltage peaks/sags or high harmonic content. The different elements that integrate a microgrid can be used to mitigate this effect.

The expected behaviour of an industrial or commercial microgrid is to disconnect if in grid-connected operation mode is not possible to meet the pre-specified quality requirements and start working in grid-disconnected. An industrial or commercial microgrid can operate in grid-connected, grid-disconnected mode and grid-isolated. To go from grid-connected to grid-disconnected mode, the transition can be due to signal prices, maintenance, power quality issues or grid failure.

The benefits of this type of microgrids are:

- Premium power quality
- Reliability and efficiency
- Demand response management

- Remote microgrid. A remote microgrid is the conventional concept of geographical areas or communities with absence of electrical infrastructure. Talking about grid-connected to grid-disconnected mode, or vice versa, does not have sense in this case.

  Usually, these are the smaller microgrids considering the aforementioned architectures. Mainly, due to the capability of a single end-user to manage high power (no more than 10-20 kW).

  The benefits of a remote microgrids are:

  - Supply availability
  - Fuel reduction and supply DER mix integration
  - Greenhouse reduction
  - Increase power quality and robustness

Bus-link

It is possible to classify microgrids according to the voltage link; DC microgrids, AC microgrids or the combination of both options.

It can be assumed that DC energy will start to be an attractive way to distribute energy in next years due to the high penetration of DER and

considering DC loads or directly DER production in DC. This option could be interesting depending on the distance from the DER to the final consumption as occurs in High Voltage Direct Current (HVDC) off-shore wind farms. DC microgrids allow to cluster in a common DC-link different DER such as photovoltaics, small wind-turbines, mini-hydro or other generators such as gas turbines. This DC-link would also include some storage systems and local controllable loads to ensure the stability of the DC voltage. The used technology will influence in the time-life, the tolerable ripples, the size and price of the DC-link. In [31] a review based on different capacitor technologies is developed.

It should be remarked that the incorporation of Electric Vehicles (EV) as an alternative to fossil fuels for mobility begins to correlate with the concept of microgrid [32], resulting into interesting concepts like Vehicle to Grid (V2G) [33], Vehicle to Home (V2H) [34] or even Vehicle to microgrid (V2M) [35].

On the other hand, AC microgrids are intended to provide electricity for common residential or industrial consumptions. The MGCC manages the interoperability of the whole infrastructure for an active management of the power when the microgrid is grid-connected or the local requirements when grid-disconnected.

The advantages of DC distribution when compared to its AC counterpart can be summarised in [36]:

- Higher efficiency and reduced losses due to the reduction of multiple converters used.

- Easier integration of various DC DER, such as energy storage, solar photovoltaic.

- Most efficient supply of DC loads (EVs, industrial DC loads).

- Easier manage of electric parameters. The frequency has not to be controlled.

- Allow to dispose of a robust system against seasonal phenomena when storage systems are considered

On the other hand, DC protections are more expensive than AC equivalent ones and usually more voluminous. However, due to the penetration of EV more efforts on new protections based on static semiconductors are being developed. It should be also remarked that when a DC microgrid does not

dispose of any storage system, the energy must be consumed when it is produced, as in AC systems.

Storage systems are, usually, a cost-sensitive part of a microgrid or DER installation. For this reason, hybrid microgrids supposes an alternative when the microgrid side is operating in grid-connected mode. In hybrid microgrids, the different DC DER will be connected to a DC-link with enough voltage to have a proper relationship between the adequate level to inject to AC systems and produce the minimum losses that can be achieved via a transformer or power electronics. Then, the utility is considered as a pseudo-infinite energy buffer.

1.1.6 Some ongoing microgrids

Microgrids projects have been present in research, mainly, since the decade of the nineties. From this start-point, more and more effort at global level has been done in order to produce new control strategies, architectures, nomenclature, communications protocols and objects to evaluate the microgrid operation, capabilities and performances. Due to the last catastrophes, as can be the hurricanes in the United States or the tsunami in Japan, microgrids were established as an alternative to produce and supply energy to many end-users. The following lines summarises some of the last microgrids projects funded, partially or totally, by public money [37–41].

Activities in Europe

The following lines summarises some of the most important activities on microgrids in Europe:

- *Microgrids: Large-Scale Integration of Micro-Generation to Low Voltage Grids.* This is a $4.5 million funded project by the EC within the 5th Framework Programme. The project investigates, develops and demonstrates the operation, control, protection, safety and telecommunication infrastructure of microgrids, determining and quantifying their economic benefits, too. It is constituted by a consortium that includes fourteen partners from seven countries including utilities, manufacturers and research institutions or universities : EdF, PPC, SMA, GERNANOS, INESC. Porto, among others.

  The RD&D goals are:

  - To increase the penetration of RES and other micro-sources in order to contribute for the reduction of GHG emissions.

  - To study the main issues regarding the operation of microgrids in parallel with the mains and in islanding conditions that may follow faults.
  - To define, develop and demonstrate control strategies that will ensure the most efficient, reliable and economic operation and management of MicroGrids.
  - To define appropriate protection and grounding policies that will assure safety of operation and capability of fault detection, isolation and islanded operation.
  - To identify the needs and develop the telecommunication infrastructures and communication protocols.
  - To determine the economic benefits of the microgrid operation and to propose systematic methods and tools to quantify these benefits proposing appropriate regulatory measures.

- *More microgrids. Advanced Architectures and Control Concepts for More microgrids.* This is a $8.5 million funded project by the EC within the 6th Framework Programme. The proposed project extends *Microgrids: Large-Scale Integration of Micro-Generation to Low Voltage Grids* significantly with the following work-packages:
  - Design of micro source and load controllers for efficient integration.
  - Development of Alternative Control Strategies (hierarchical versus distributed).
  - Alternative nicrogrids designs.
  - Technical and Commercial Integration of Multi-Microgrids.
  - Standardization of Technical and Commercial Protocols and Hardware.
  - Field trials on actual Microgrids.
  - Evaluation of the system performance on power system operation.
  - Impact on the Development of Electricity Infrastructures (expansion Planning).

- Pilot Microgrid in Kythnos. On the Greek island of Kythnos a single phase microgrid is installed. Twelve houses are supplied by 10 kWp of photovoltaic, a 53 kWh battery bank and a diesel genset with a rated

power of 5 kVA. The system house is supplied by 2 kWp photovoltaic and a 32 kWh battery bank. The different elements are connected over a communication cable and controlled from the system house. It is under consideration to add a 2 to 3 kW wind turbine to minimise the use of diesel fuel in islanded operation and to obtain a better renewable production along a day.

- *ATENEA Microgrid.* The Renewable Energy Grid Integration Department in CENER (National Renewable Energy Centre of Spain) has designed, installed and developed a microgrid (ATENEA) located in the industrial area of Rocaforte (town of Sangüesa, Navarra, Spain).

  ATENEA Microgrid aimed at industrial application. It consists of AC architecture with total installed power of 120 kW approximately. The facility can supply part of Wind Turbine Test Laboratory-LEA, electric loads and Rocaforte industrial area lighting. It can be also used as a test bench for different generation and storage technologies and control strategies testing.

  The generation equipments that compose the facility are: photovoltaic system (25 kWp), small wind turbine, full converter (20 kW), diesel generator (55 kVA) and gas microturbine (30 kW). Furthermore, the different storage systems technologies located in the microgrid are: flow battery (50 kW, 4 hours); lead-acid batteries (50 kW, 2 hours) and ion-lithium batteries (50 kW, 30 minutes).

  The ATENEA microgrid structure is based on a low voltage three-phase, four-wire bus (400 V, 50 Hz) where all the different equipments are connected to.

  The control strategies allow the different elements optimization adding new functionalities, assuring load supply in grid-disconnected operation, attenuating disturbances in grid-connected operation and collaborating with the grid stability maintenance.

  ATENEA microgrid adopts the master-slave control in grid-disconnected configuration. The master role may be taken either by a diesel generator or by a storage system. In grid-connected mode there are devices operating under droop control strategy or as current sources, i.e. as conventional grid-feeding DER.

- *Smart Rural Grid.* This is a $2 million funded project by the EC within the 7th Framework Programme. It will focus on bringing the Smart Grid in the Rural Areas, because it is in this area where it has

been seen social and technological challenges to overcome with. Figure 1.10 shows the hierarchical communication proposed to operate all the different elements that will be considered in the rural framework.

Given the magnitude of this challenge, it will be considered that it is essential to seek the participation of Universities and research centers of Europe: CITEA-UPC, ZIV, CGA, KISTERs, among others.

At the end of the project it should have tested and validated new information and communications technologies and devices, aimed at providing active network management, demand response with the participation of end users, load balancing and forecasting, congestion management and easy DER integration in the network.

Also, improve the robustness and reliability of the existing telecommunication infrastructure in order to cope with critical services that require response times in the order of milliseconds developing specific telecommunications services and platforms for energy distribution, taking into account control of access to customer information and consumer data, in particular smart metering data.

Thus, the expected impact:

- Minimization of the energy losses in the distribution network.
- Reduction of the gap between power supply and demand.
- Increase of Distributed Energy Resources connected to the distribution network.
- Reduction and shifting of peak load.

- *NiceGrid.* A Utility Microgrid. The NiceGrid Microgrid project is one of the six smart grid projects of the European Union Grid4EU program with a team of partners including ERDF, EDF or Alstom. The microgrid is located in the south-east region of France. The project is designed to evaluate an innovative architecture for medium and low voltage distribution microgrids with high concentration of photovoltaic generators together with smart houses. More than 1500 residential, commercial and industrial end-users are participating in this microgrid project. Specific objectives of the NiceGrid project are as follows:

  - Optimize the operation of a medium and low voltage electrical network with a major integration of photovoltaics and electricity storage capacities in both grid-connected mode and grid-disconnected mode.

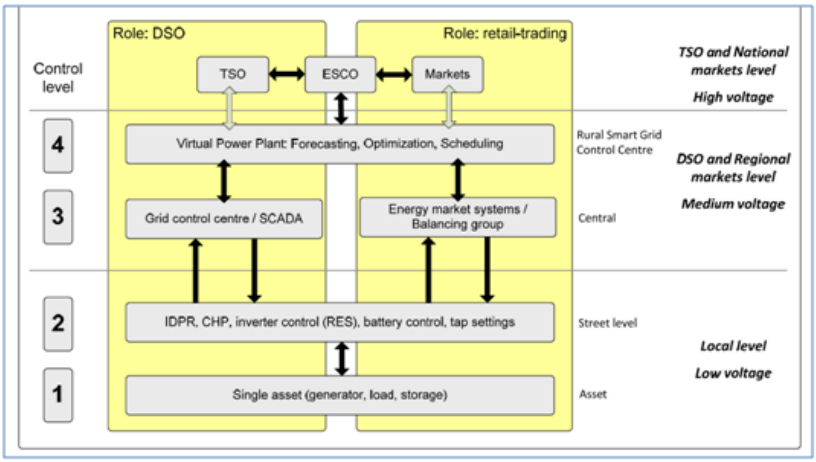

Figure 1.10: Hierarchical communication level between different assets proposed in the Smart Rural Grid project

- Test the islanding of a microgrid based on photovoltaics and electricity storage.
- Increase supply resilience and reduce potential constraints on the high-voltage transmission lines of the area.
- Encourage the customer to be proactive in managing his/her production, consumption and storage of electricity. Move to the prosumer concept.

Activities in United States

The following lines summarises some of the most important activities on microgrids in United States:

- *U.S. Army Fort Bragg.* To enhance power reliability while reducing costs, Fort Bragg, a U.S. Army base near Fayetteville, N.C., has build one of the world's largest microgrids. With guidance from Honeywell, Fort Bragg integrated a variety of distributed generation technologies that operate in conjunction with the military bases utility infrastructure about 5.2 MW.

  The base incorporates the use of several DER that are fully incorporated into the utility, information technology and communications infrastructure. It has an aggregate on-site power generating system

that includes 15 diesel gensets, one 5 kW fuel cell, and a 5 MW base-loaded gas turbine.

As Fort Bragg uses a time-of-use tariff provided by the local energy utility, when market prices exceed a certain threshold, the base automatically goes into self-generating mode enhancing, in this way, its energy reliability and reducing overall energy costs.

- *Beach Cities Microgrid Project.* The Beach Cities Microgrid Project in San Diego aim is to learn more about how the smart microgrid concept can be applied in the San Diego area providing peak shaving capacity. The goals of this microgrid are:

  - Achieve more than a 15% of reduction in feeder peak load through the integration of multiple, integrated DER, energy storage, price-driven load and demand response management.
  - Demonstrate capability of dispatching reactive power.
  - Develop a strategy and demonstration of information integration focused on security and system architecture, smart metering and apply self-healing networks strategies.

- *Perfect Power.* The Illinois Institute of Technology (IIT) has partnered with the Galvin Electricity Initiative and the United States Department of Energy (DOE) to develop a Perfect Power System-a smart microgrid for the IIT main campus at Chicago, Illinois. In collaboration with S&C Electric, Endurant Energy and ComEd, the university is building an electricity system of interconnected smart microgrids in a loop configuration with a redundant electricity supply.

  The $14 million project has equipped IIT's microgrid with a high-reliability distribution system for enhancing reliability, new sustainable energy sources (roof-top solar panels, wind generation units, flow batteries and charging stations for electric vehicles) and smart building automation technologies (building controllers, Zigbee sensors, controllable loads).

  This microgrid will offer to IIT the opportunity to eliminate costly outages, minimize power disturbances, moderate an ever-growing demand and reduce greenhouse gas emissions.

Activities in Japan

The following lines summarises some of the most important activities on microgrids in United States:

- *The Aomori Project.* In this microgrid only renewable energy sources are used to supply the total demand of electricity around 610 kW (photovoltaics, wind turbines and biomass) and heat. Thereof 150 kW are weather-dependent generation and 510 kW are controllable digester gas engines. Furthermore, a lead-acid battery system with a capacity of 100 kW is installed. The microgrid serve seven City of Hachinohe buildings.

  The main objective of this microgrid is the stabilization of weather-dependent energy because this is one of the main driving factor in Japan. To satisfy both of economical (or environmental) optimization and electric power quality, the microgrid has to control the system by four functions to handle enormous dimensions of the problems: weekly operation planing, economic dispatching control, flat tie-line control and local frequency control (grid-disconnected mode) and implement a local control system considering grid-disconnected operation.

- *Sendai's microgrid.* This microgrid operates as back-up generator in the outage by earthquake on 2011. The microgrid is constituted by two gas engines of 350 kW, photovoltaic generators of 50 kWp. The mains of this microgrid is guarantee a non interrupted service, compensating voltage at a wave level. To achieve this goal, the control strategy defines four type of loads: High quality type A (no interruption with voltage compensation), high quality type B (removing interruption within 15 microseconds), Standard quality type C (interruption allowed but removed in 1 minute) and DC load (DC supply no interruption).

- *The Kyoto Project* at Kyotango. The municipal government of Kyotango City, north of Kyoto, leads this first virtual microgrid demonstration project covering a 40 km span called the Kyoto Eco Energy Project, which started operation in December 2005. It incorporates the following generation capacities: 50 kWp of photovoltaics, 50 kW from wind-turbines, five units of 80 kW bio-gas gensets, a 250 kW from molten carbonate fuel cells and a 100 kW battery lead-acid bank. The communication is done by internet protocol over the legacy telecom-

municate network to balance demand and supply. Imbalances can be rectified over five minute time-steps.

1.2 Motivation research for microgrid control strategies

Analysing a future scenario where a massive integration of DER and microgrids will be possible, the use of such amount of power electronics, inverters for AC microgrids and AC/DC or DC/DC converters for DC microgrids, needs to be taken into account.

The growth in demand for cleaner, more reliable and affordable energies is changing the energy mix scenario. In addition, the ageing of existing infrastructures and the increasing demand requires innovative solutions at competitive costs within the current economic framework. Furthermore, the construction of new transmission facilities is limited to environmental considerations.

Microgrids can help to delay investments on new electric infrastructures becoming a new entity where it is possible to find new challenges thanks to coordination tasks. Some of these opportunities can be peak shaving capacity, energy optimization, voltage regulation, Green House Gases (GHG) reduction, local market values, aggregation energy exchanges, smart-metering, smart-pricing [42], among others. The further implementation of microgrids supposes the evolution from classical electrical grids, based on the unidirectional distribution model to an active decentralized concept with a bidirectional energy distribution. Microgrids, fundamentally, trust on integrated control systems to coordinate DER and storage systems.

A microgrid has to be able to operate efficiently in two operation modes; grid-connected mode and grid-disconnected but also smooth transients between them have to be guaranteed. In this sense, the resilience and reliability properties of conventional grids can be enhanced.

Due to the aforementioned challenges, a direct impact on the need for conduct research in order to reach improvements on current technologies, obtaining new and optimized control techniques and devices, can be done. As important is the technology as the managing criteria to handle them.

1.3 PhD related work and activities

This thesis has been developed from 2010 to 2016. During this period, the author has been involved in different technology transfer projects as project

engineer at CITCEA-UPC (Centre d'Innovació Tècnologica en Convertidors i Accionaments Estàtics de la Universitats Politècnica de Catalunya). Some of the most relevant projects are summarised in the following lines, ordered from more older to most recent ones:

- *IFRIT project* (Non competitive -2009/2011-). Development of a range of photovoltaic inverters with back-up capacity under grid-connected and grid-disconnected operation.

- *Vehicle2microgrid* (Non competitive -2009/2011-). Novare project by Endesa. Intelligent system development for the integration of electric vehicles to the utility with DER.

- *MHITO project* (Non competitive -20011/2013-). Development of the power converters, implementation of the industrial communications, protections, control and management of a hybrid DC-AC microgrid.

- *LISI project* (Non competitive -2012/2013-). Development of a four-wire three phase 135 kVA bidirectional inverter for ATENEA micro-grid.

- *6-points project* (Non competitive -2013/2014-). Development of six bidirectional and isolated 5 kVA chargers for electrical vehicles under CHAdeMO fast-charge protocol.

- *Smart Rural Grid project* (Competitive -2014/2017-). It is an FP7 European project. Development of a power router for the smart rural areas.

The realised tasks of the exposed projects have supported an important part of the development of the present thesis content.

1.4 Objectives, methodology and thesis outline

1.4.1 Objectives

As has been exposed along this chapter, it is clear that microgrids suppose to be good candidates to improve the existing electrical systems. However, the implications of including this kind of systems are complex. The main objectives of the thesis are study and comprehend them, but also provide new control alternatives for the operation of AC microgrids in grid-tied systems. In this sense, the most relevant objectives are listed (from more broad to detailed ones):

- Understanding of the different connotations that surround the "microgrid" concept.

- Listing and consideration of the correlations and control challenges of AC microgrids, specially those concerning AC microgrid inverters:
  - Elements
  - Control loops
  - Transference between operation modes
  - Galvanic isolation

- Analysis of the different inferences when a three or four-wire inverters are considered to be installed in AC microgrids.

- Analysis of the control limitations for the inner magnitudes of an inverter (voltage and current) when the existing rotatory formulations (resonant controllers) are assumed. Also, study the possibility to extend or improve them.

- As one of the most critical challenge for grid-tied inverters is the transference between modes (grid-connected or grid-disconnected), specially from grid-connected to grid-disconnected, explore:
  - The anti-islanding effect on the clearing time of droop-control based inverters.
  - Control strategies to achieve a flying transference (non zero voltage crossing) from grid-connected to grid-disconnected when conventional three-wire grid-feeding inverters are considered. This means to understand the implications when an inverter is moved from current source to a voltage source behaviour and vice-versa.
  - Control strategies to improve the time in which the maximum power point of a DER can be operated in grid-disconnected mode if a back-up system is assumed.
  - Hybridation between droop control-based inverters (during grid-connected) and voltage-frequency (during grid-disconnected) in grid-tied inverters. Thus, the dynamics in grid-disconnected mode could be improved maintaining the voltage source behaviour.
  - Study the existing Space Vector Pulse Width Modulation techniques for four-wire inverters and look for an implementation approach from the usually used three-wire systems.

- Study new control strategies to consider special features of AC microgrid inverters as can be: limited overload capability during grid-connected mode, autonomous adaptation of the inverter DC-link according to unbalance AC side needs or sinusoidal short-circuit proof capability to maintain the correct behaviour of the protective devices.

1.4.2 Methodology

The underlying idea behind the thesis is to apply a top to bottom approach for the different AC microgrid challenges that follows the motivations introduced in Section 1.2. In this sense, five chapters (including the present one) are considered to support this scope. These chapters help to provide answers for different question marks that surround the operation of AC microgrids, specially those regarding the inverter control. One more chapter adds the thesis conclusions, proposes new research and shows the publications list and results presented.

Figure 1.11 shows the content layout for the present thesis (without considering the conclusions chapter), also indicating the related projects detailed in Section 1.3.

The present chapter provides a general overview about microgrids while Chapter 2 is the core of the thesis. From Chapter 2 not only the different actors of AC microgrids are presented but also the possible operation modes and control particulates are discussed. In this sense, three more chapters are spread-out from these three key points. These relevant points and their interrelations derives into the Inner control loops analysis for AC systems (Chapter 3), Grid Supply Inverters proposals for AC microgrid (Chapter 4) and Four-wire three-phase AC inverter proposal for AC microgrids (Chapter 5).

1.4.3 Thesis outline

According to the previous Sections 1.4.1 and 1.4.2, the outline of the thesis remains as follows:

- Chapter 1: *Microgrids overview.* General concepts of microgrids are detailed to constitute the fundamentals for Chapter 2, that is focused in the AC case study.

- Chapter 2: *AC microgrids control and operation.* This chapter exposes a general background about AC microgrids and particularities on their

operation, becoming the backbone to develop the whole content of the present thesis. Thus, the different operation modes, type of inverters and different kind of ancillary and supporting elements are presented. Also, the different control layers at the Voltage Source Inverters (VSI) are detailed exposing the transference challenge according to the VSI operation criterion. Finally, the galvanic isolation topic is faced from the perspective of AC microgrids.

- Chapter 3: *Inner control loops analysis for AC systems.* As the main goal of the present thesis is the control of AC inverters or systems, this chapter is specially dedicated for this purpose. Different voltage and current control strategies are studied. This chapter contributes with a stability analysis for stationary reference frame resonant controllers and proposes a novel resonant-type controller to enhance the conventional formulation that can be found in the control literature.

- Chapter 4: *Grid Supply Inverters proposals for AC microgrid.* This chapter is focused on a conventional photovoltaic grid feeding DER (after named GSI) and proposes new control strategies for their operation when they are installed in an AC microgrid. These strategies bring the flying transference capability from grid-connected (GSI) to grid-disconnected operation. In the grid-disconnected operation, the inverter operates as a grid-forming DER (after named GCI). The chapter also extends the execution of the MPPT algorithm when a back-up system is assumed. Different simulations and experimental results support the suggested control strategies.

- Chapter 5: *Four-wire three-phase AC inverter proposal for AC microgrids.* This chapter, unlike Chapter 4, proposes the use of a four-wire VSI for AC microgrids. In this case, the inverter is based on droop control methods when grid-connected (after named GSCI) and voltage-frequency control when grid-disconnected (GCI). As in Chapter 4, the flying transference from grid-connected to grid-disconnected is also considered. The chapter also exposes a new space vector modulation technique for four-wire four-leg inverters based on the conventional three-wire three-leg SVPWM technique. The design and control of the full converter is exposed and validated on a 135 kVA prototype, proposing particular operation control strategies; short-circuit proof capability, over-load supervisor, and self-adaptation of the DC-link voltage level.

- Chapter 6: *Conclusions and further work*. This chapter presents the conclusions derived from the present study and suggests future research in the AC microgrid area.

As has been said in the previous sections, thanks to the related works and activities presented in Section 1.3, an important part of the experimental results presented along this thesis have been made possible. These related works and activities mainly involve Chapter 3 to 5. Due to the involvement of the author in all those different projects, it has not been possible to use a common set-up for all the thesis. However, this fact does not decline the obtained results ot the proposed strategies.

1.5 Main contributions

The main required element to link DC microgrids with AC microgrids becomes the inverter. The objective of this thesis is to investigate advanced control solutions to face with the microgrid VSI integration challenges. Following, there is a list of the relevant contributions of this thesis:

- Analysis on the anti-islanding clearing time when the microgrid VSI is operated under droop control strategies. Detection of the mains loss when an unintentional utility disconnection is produced results crucial. Conventionally, anti-islanding mechanisms are thought for grid-feeding DER. The effect of droop control strategies makes more difficult the application of some anti-islanding mechanisms, specially those bases on positive feedback strategies.

- Analysis on the galvanic isolation challenge in AC microgrids. When the VSI requires galvanic isolation it should be considered that a microgrid VSI implies to take into account three and four-wire distribution systems, any set of positive-negative-homopolar voltage or current application, non-linear loads and frequency or voltage variation applied at the VSI side.

- Continuous and discrete-time stability analysis for current and voltage control loops in the stationary reference frame when conventional resonant controller are used.

- Development of a new formulation of resonant controllers based on a hybrid transfer function between fractional calculus and conventional resonant controllers.

- Proposal of a transference strategy to move from a grid-connected current-controlled VSI to a grid-disconnected voltage-controlled VSI when back-up systems are considered.

- Study of a control strategy to extend the execution of MPPT in grid-feeding DER when grid-disconnected.

- Proposal of a novel Space-Vector Pulse Width Modulation (SVPWM) strategy for four-leg inverter without application of 3-D SVPWM conventional techniques. It also considers the limitations of the methodology.

- Design of a three-phase four-wire inverter based on hybrid control strategy for a real microgrid (ATENEA microgrid). When the inverter is grid-connected, the droop control strategy considers dynamic droop (close-loop approach), dynamic virtual impedance and virtual inertia emulation. When it is grid-disconnected, adaptive resonant controllers are used. The tuning procedure for the voltage loop has been extended from [43] to the voltage loop. The size of the different coupling filter elements are based on a new proposed SVPWM strategy. Some particular control strategies are proposed and validated to enhance the integration of an inverter into an AC microgrid; short-circuit proof capability during grid-disconnected operation, over-load supervisor and self-adaptation of the DC-link voltage level for grid-connected operation.

It should be noted, once more, that to demonstrate the applicability and validation of the proposed control strategies, some of these contributions have been experimentally validated in different laboratory test-bench. These different set-ups are according to different projects in which the author has been involved, see Section 1.3.

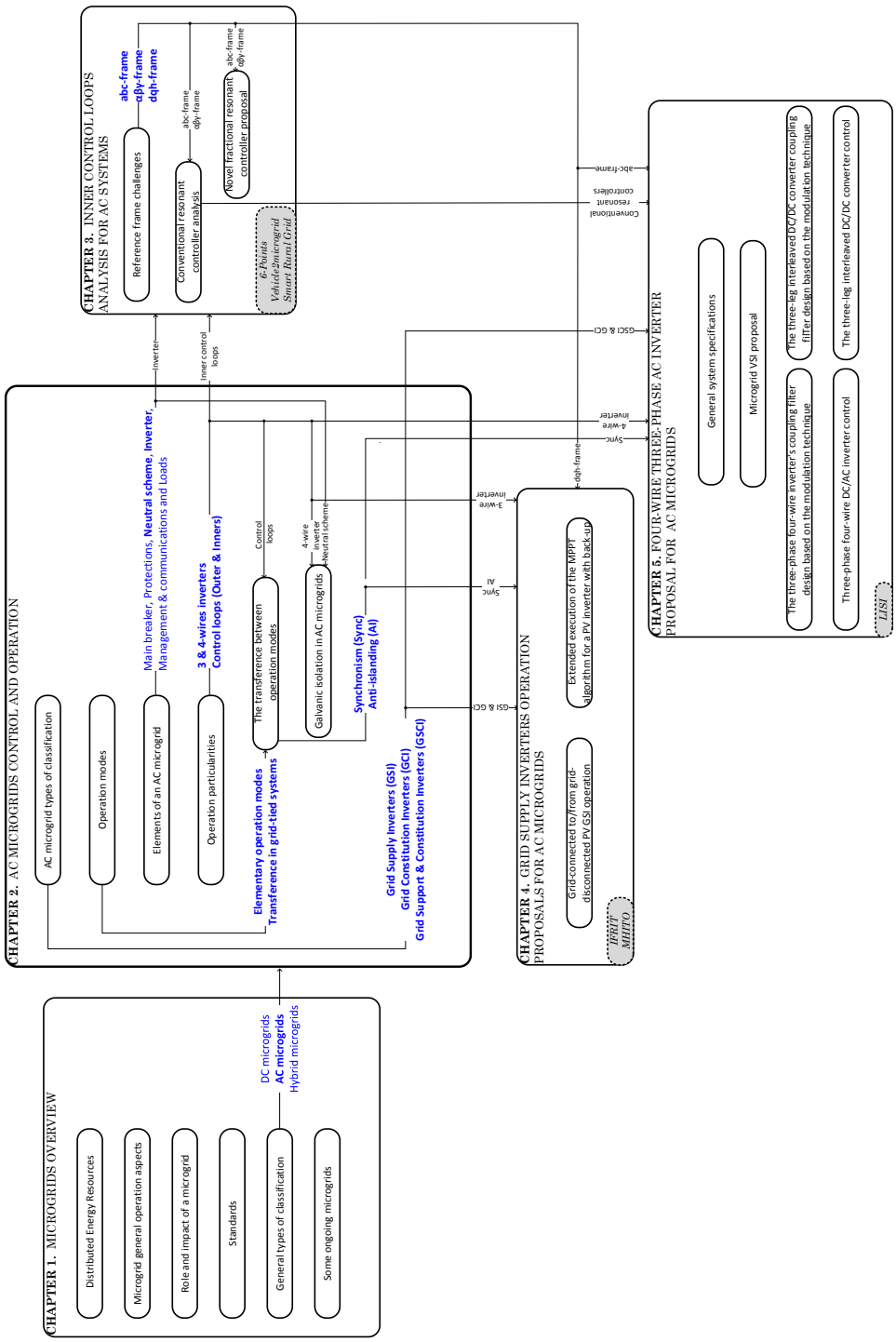

Figure 1.11: Layout of the chapters involved in the present thesis and the considered interrelations

Chapter 2

AC microgrids control and operation

2.1 Introduction

Since the late of 19th century AC power grids have been the standard choice for commercial or industrial energy systems to power the major part of loads. The easy to transform AC voltage into different levels for various applications using transformers and its inherent characteristic when rotating machines are used made the AC power to become an interesting option [44].

All Distributed Energy Resource (DER) units with AC power output are directly connected to an AC bus-link and then to the main system using power converters for their stable and controllable coupling. Examples of DER units that produce the AC output power include wind turbines, micro/mini-hydro, bio-gas or bio-mass. Essentially, those based on rotating machines.

A microgrid is a complex system where several devices coexist, motivating transversal competences as control, operation, communications or security, as has been explained in Chapter 1. The integration of all these elements can be done in AC or DC. The scope of this thesis is focused on the AC side.

As an AC microgrid can or cannot be related with the utility, hereinafter, the following nomenclature to refer to different types of AC or hybrid microgrids will be used:

- Grid-isolated. A microgrid that is never connected to the grid and it is operated independently from the grid.
- Grid-tied. A microgrid that is connected to the grid and it is operated in parallel with the grid.
    - Grid-connected. Operation mode of this microgrid when it is electrically connected from the grid
    - Grid-disconnected. Operation mode of this microgrid when it is electrically disconnected from the grid

The inverter can be considered as the gateway between DC and AC microgrids. Then, when a microgrid Voltage Source Inverter (VSI) is under study it is important to identify certain challenges to face them properly, for example:

- Intermittent DER. The consideration of intermittent DER implies the use of different storage systems and the need to study systems that are able to supply high energy inertias to the system to guarantee the microgrid stability. Note that some authors point to storage system as the solution to the lack of inertia [45]. In [46] a classification of energy storage equipment according to the response speed and power or energy density is presented.

  On the other hand, the main grid can be used as a pseudo-infinite energy buffer. The inverter constitutes the main element of interaction with the utility. However, an AC microgrid can include a single inverter or multiple inverters. The natural inclination of microgrids tends to the decentralization of resources implying that more than one inverter will be present in the system. This last option involves some implications on how an inverter can be operated, mainly, regarding synchronization challenges.

- Transferences. How to respond ahead the transferences when the converter must change from grid-connected to grid-disconnected or viceversa results crucial [47, 48]. The different operation modes require correct control strategies for proper operation and exploitation of the DER.

Then, this chapter is divided as follows:

- Section 2.2. *AC microgrid types of classification.* This section defines particular ways to classify AC microgrids.

- Section 2.3 *Operation modes.* This sections presents the elementary operation modes of the AC microgrids and which type of transferences can occur.

- Section 2.4. *Elements of an AC microgrid.* This section considers not only which type of inverters but also which other elements are present in an AC microgrid.

- Section 2.5. *Operation particularities.* This section describes how the power is distributed in an AC microgrid, i.e. the number of service

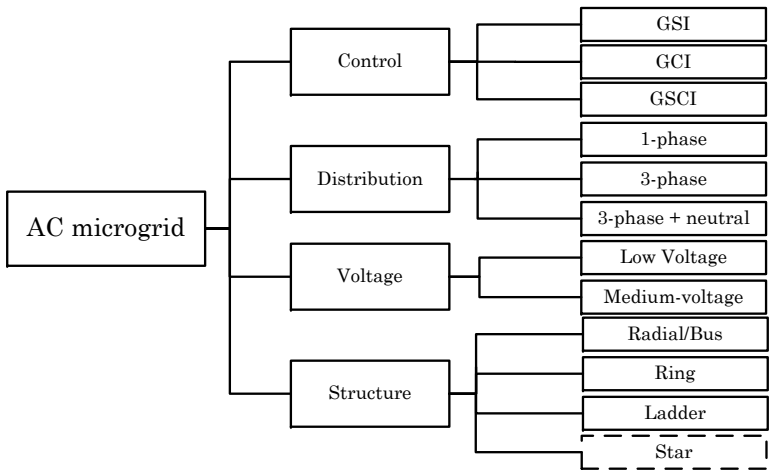

Figure 2.1: AC microgrid typologies

cables used and defines different control models. Also, different control layers are presented.

- Section 2.6 *The transference between operation modes.* This section introduces the challenge of mains loss detection when the different VSI control strategies presented in Section 2.3 are considered. The results of this section have been published in [49, 50] at EPE'15 and IEEE transactions on smart grids.

- Section 2.7 *Galvanic isolation in AC microgrids.* This section takes into account that some DER considers transformers to dispose of galvanic isolation. This galvanic isolation could be also required for security reasons or for neutral schemes compatibility.

2.2 AC microgrid types of classification

The AC microgrids can be classified into different types according to several criteria. The control strategies, the number of distributed wires, the voltage used for distribution or the chosen structure define the four more relevant ways to classify an AC microgrid. Figure 2.1 presents a summarized diagram of possible classification for AC microgrids [51–53].

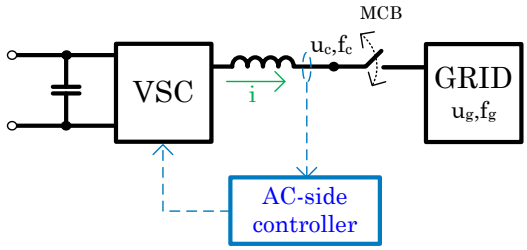

(a) Grid Supply (GSI)

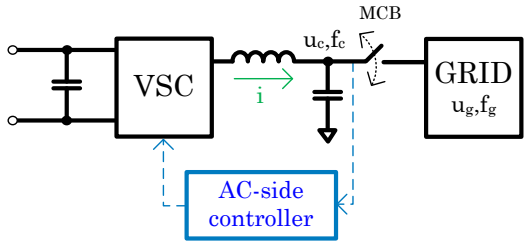

(b) Grid Constitution (GCI) and Grid Support and Constitution (GSCI)

Figure 2.2: Conceptual schemes of control alternatives for an inverter

Control classification

AC microgrids are usually controlled in terms of power. This power is then translated into a current or voltage reference that a VSI follows. This voltage or current is controlled according to the coupling filter, i.e. an inductance for current or a capacitor for voltage. Figure 2.2 shows the three categories in which a VSI can be set according to control considerations [54]. Figure 2.2(a) shows the Grid Supply Inverter (GSI) category and Figure 2.2(b) shows the Grid Constitution (GCI) or Grid Support Inverter and Constitution Inverter (GSCI) categories. In these figures, u_g and f_g indicates the voltage and frequency of the grid, u_c and f_c the voltage and frequency controlled by the VSI and i the current that the converter exchanges with the utility. It should be remarked that this control sub-classification is similar to the feeding or forming DER presented in Chapter 1.

- Grid Supply Inverters (GSI). Are the most common VSI and widely extended during last years due to the renewable penetration. They operate as Current Controlled-VSI (CC-VSI) in grid-connected mode. The controlled magnitude is the output current i depicted in Fig-

ure 2.2(a). Thus, GSI delivers minimal harmonic content and maximum power [55]. A GSI injects the maximum power available on its connected DER thanks to MPPT (Maximum Power Point Tracking) algorithms [12, 56, 57]. The GSI units require an external voltage reference for power injection when are grid-disconnected or grid-isolated operated. In some technologies and depending on the installed power, a GSI has to supply reactive power to support grid stability. The generation of the most adequate set-points in case of grid failure are a consequence of the detected grid fault type, as indicated in [58].

- Grid constitution inverters (GCI). Basically are Voltage Controlled-VSI (VC-VSI), see Figure 2.2(b), that when grid-connected they act as a mirror of the utility, $u_c^* = u_g$ and $f_c^* = f_g$, being u_c^* and f_c^* the voltage and frequency control references, respectively. Practically there is no power exchange apart from internal losses. On the other hand, when grid-disconnected or grid-isolated operated, they are GCI units continue with the last grid connected reference. From this time instant, a GCI self-generates the voltage reference (u_c^*, f_c^*) for other converters. A GCI plays the role of the master of the electrical island under the grid-disconnected or grid-isolated modes. Consequently, the GCI becomes the voltage reference for other inverters. It should be highlighted that GCI is in stand-by mode in normal operation (grid-connected). On the other hand, in the grid-disconnected mode they could need huge storage systems to interact with other GSI units.

  In GCI the short-circuit power is much lower than the grid one. This fact implies that usually it generates a weak-grid. If there are other converters, as can be GSI, injecting a certain amount of harmonic content perhaps the GCI should be disconnected producing a black-out. In order to strengthen the system it is possible to consider the use of active filters. These active filters will allow to compensate or correct several problems as voltage and current unbalances, reduce harmonic content or correct the power factor. Basically, serial and parallel active filters can be considered [59–61]. It should be noted that to compensate the harmonic content, the combination of an active filter with a passive one may be the best option, using hybrid active filters [62, 63].

  On the other hand, last years, the concept of Constant Voltage and Constant Frequency (CVCF) control [64, 65] is gaining strength. This idea can be extrapolated to a multi-inverter microgrid with the aim of use GCI directly operated in parallel thanks to an accurate global syn-

chronization signal, as for example applying Global Positioning System (GPS).

- Grid support and constitution inverters (GSCI). Are non-ideal VC-VSIs when grid-connected, $u_c = u_g + \Delta u_g$ and $f_c = f_g + \Delta f_g$ and can be also represented by Figure 2.2(b). Are based on the AC droop control or power control strategies that handles two degrees of freedom; voltage amplitude and frequency [66–69]. Droop control allows operating as a parallel source when grid-connected, being able to inject or consume requested active or reactive power if higher hierarchy levels are applied, the called tertiary control, as will be described in Section 2.5. When grid-disconnected or grid-isolated operated the GSCI continues operating as VC-VSI self-generating the voltage and frequency with also high hierarchy levels, the called secondary control, also described in Section 2.5. The idea behind the operation of a GSCI under the AC droop strategy is to behave as the utility with its regulation mechanisms to ensure the power balance between generation and consumption.

Distribution classification

An AC microgrid can be performed by single [70], three-phase with or without neutral distribution [71, 72] or hybrid options [73].

Typical configurations for low voltage installations, that corresponds to the most common cases in Europe are:

- Three-phase systems with four wires and 400 V phase to phase. It is the typical case used in supply lines of low voltage installations, residential and industrial zones.

- Three-phase systems with three wires and 230 V phase to phase. Used in some distribution low voltage lines.

- Single-phase of 230 V. Used for domestic supplies.

Focusing in the three-phase VSI units, the possible configurations are:

- Three-wire three-leg VSI. See Figure 2.3(a).

- Four-wire three-leg with split capacitor VSI. See Figure 2.3(b).

- Four-wire four-leg VSI. See Figure 2.3(c).

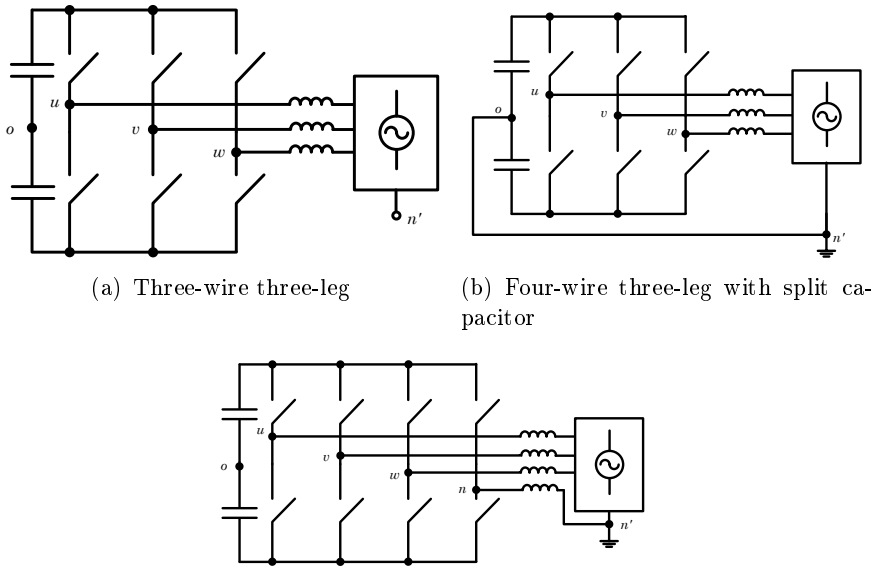

(a) Three-wire three-leg

(b) Four-wire three-leg with split capacitor

(c) Four-wire four-leg

Figure 2.3: Three-phase VSI topologies

The three-wire three-leg configuration is widely applied in feeding DER, i.e. the inverter operates in grid-connected mode behaving as a GSI. A system with three-wires is not able to control zero sequence current components. This fact reduces the number of degrees of freedom to two that are tied to a plane Π where the currents follows

$$i_u + i_v + i_w = 0 \tag{2.1}$$

being u, v and w each one of the three available active phases. The operation of a feeding DER or a GSI assumes that the injection of power will be balanced.

For a microgrid, a three-wire three-leg system supposes that there is no chance to supply zero sequence currents for non-linear loads. The increasing use of non-linear loads concerns both DSO and utility customers [74]. In this sense, a microgrid VSI can supply voltages or inject active power but also can contribute with some extra features as active filtering and current or reactive balancing requiring to distribute energy in a four-wire topology. In [75, 76] it is also concluded that three-wire three-phase systems cannot be applied for zero sequence harmonic cancellation. In this sense, the four-wire three-phase shunt active filters have shown to be a good solution to

compensate reactive power, harmonic distortion and unbalance currents in non-linear loads [77].

For all the aforementioned reasons, a four-wire topology is required in AC microgrids from a certain rated power, usually, more than 5 kW. Four-wire topologies are commonly used when a three-phase plus neutral distribution line is connected to the inverter or the inverter needs to exchange energy to a four-wire grid or even a microgrid. Thus, some typical applications for four wire inverters are [3]:

- Distributed power generation to deregulate utilities.
- Active power filters with neutral current capabilities.
- Common mode reduction.

Electrical magnitudes classification

An AC microgrid can distribute electricity in low frequency and even in high-frequency depending on the implementation and uses of the microgrid. Usually, it is essential to deal with high frequency when the available space and weight is a limiting factor, as in aviation.

In addition, regardless of the type of distribution it should be reminded that microgrids are usually in low voltage or medium voltage [78]. High voltage is reserved for conventional power plants.

Structure classification

Depending on the type of microgrid, the integration of the different components may vary substantially, affecting the control strategy and the type of protections installed into the microgrid. Significant connection devices or nodes affects how a possible fault can be managed. Each node can be considered either a DER or a load, always taking into account that at least one node must ensure the stability of the microgrid. Focusing on the possible structures it is possible to consider [53, 79]:

- Radial-type. Also known as bus-type, see Figure 2.4. These structures are the most common approach for power distribution grids and, consequently, can be applied to microgrids. This structure is characterized by a load supply from only one microgrid side. They have the advantage of being simple and cheap to build and selective protection devices are simple to design and are installed upstream of all nodes. On the other hand, are less robust in maintaining service to failures because a microgrid reconfiguration is not possible.

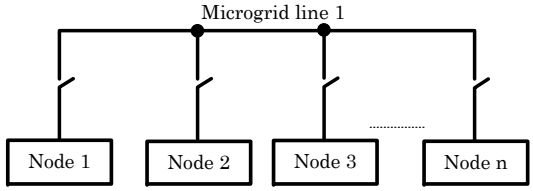

Figure 2.4: AC radial-type microgrid

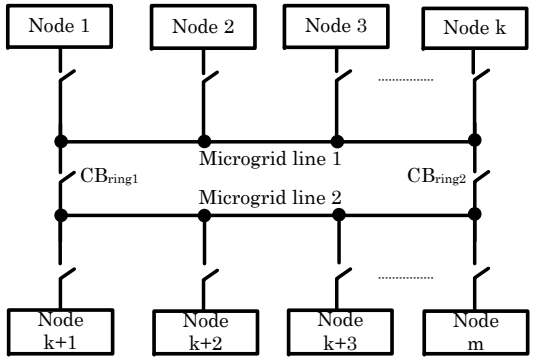

Figure 2.5: AC ring-type microgrid

- Ring-type. In this topology the nodes can be powered by two different microgrids lines. These microgrids are associated with more high installation costs and can be physically interconnected with two circuit breakers that permit the interconnection between the microgrid lines, depicted as CB_{ring1} and CB_{ring2} in Figure 2.5. If both circuit breakers are closed, a ring is constituted and both microgrids lines have to be operated in parallel. It is also possible to decide when to supply load nodes closing only one of them. Essentially, a ring constitutes a redundant system.

  The protections are technically more complex than in a radial structure but have greater operational reliability and maintainability.

- Ladder-type. This is the most complex structure. This structure permits the system to maintain various power routes from the source nodes to the critical load distribution nodes, as is shown in Figure 2.6. The result is a system that can match any power source, i.e. a DER or a distribution line, with any load.

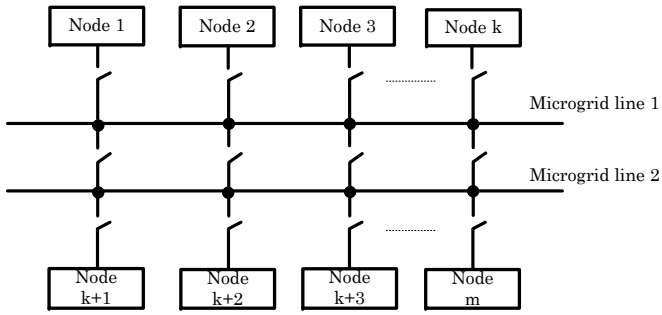

Figure 2.6: AC ladder-type microgrid

- Star-type. These structures are commonly not considered in AC microgrids due to its inherent fault of robustness in case that the central node fails.

The use a specific structure will evolute to meshed distribution architectures in the future. It should be considered the higher the complexity of the architecture the higher the complexity on protection and neutral compatibility arrangement. However, meshed structures permit to prioritize fault tolerance and availability.

2.3 Operation modes

2.3.1 Elementary operation modes

According to the exposed in the previous sections, it can be considered two possible operation modes:

- Grid-connected mode. It is the main operation mode. The microgrid operates in conjunction with the utility grid, exporting or importing energy according to the system needs. Thus, the MicroGrid Central Controller (MGCC) system controls the flow of active and reactive power through the operation of DER and the main grid.

- Grid-disconnected mode. The microgrid is disconnected from the grid. The system operates stand-alone, feeding by itself the distributed loads until the return of the grid. Once the grid is stable again, the microgrid will start a resynchronization and reconnection procedure.

The compatibility of operation between both modes will determine the degree of flexibility contributed by the AC microgrid. Both configurations

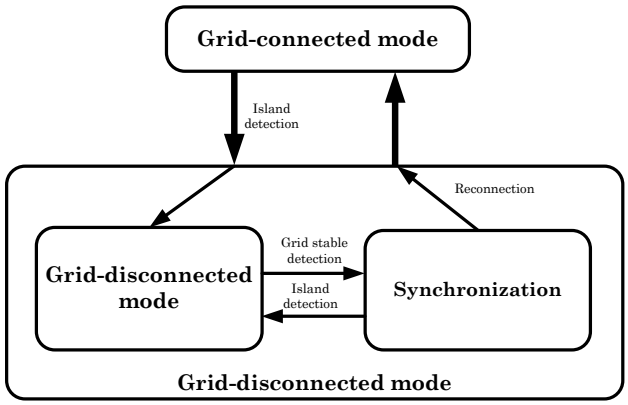

Figure 2.7: Microgrid modes and transitions states

implies sub-operation procedures, as can be seen Figure 2.7. Grid monitoring techniques will determine the loss (island detection) and recovery of the utility (grid stable detection and reconnection).

2.3.2 The transference in grid-tied AC microgrids

There exists two possible transitions in a microgrid; the reconnection to the grid and the disconnection from the grid. The most critical transition in a microgrid is the disconnection because it is asynchronous and can be caused by external non-controlled conditions. The disconnection transition is managed by a main breaker and can be provoked by several circumstances:

- Intentional. The converter receives from the MGCC a signal forcing the converter to disconnect the microgrid from the utility. Then, the VSI will act as the master of the microgrid, setting the voltage and the frequency. An intentional transition can be due to load sharing, system reconfiguration, maintenance or system status broadcasting [80].

- Non-Intentional. In this case, the event that causes the microgrid disconnection is the utility condition. The converter has to monitor continuously the utility state and when it is in bad condition, the converter must disconnect the microgrid from the utility. This is performed by an anti-islanding algorithm. Then, the VSI will act as the master of the microgrid, setting the voltage and the frequency of the microgrid.

The anti-islanding algorithm

The anti-islanding system aims to detect when an inverter energizes a portion of the network that is not connected to the grid creating what is called an electrical island. It is always considered a three port node; the inverter is connected to the utility and also to any possible local loads. This node is known as Point of Common Coupling (PCC). Anti-islanding algorithms have been improving during last two decades and were born from photovoltaic inverters. It is possible to find in the literature three categories for anti-islanding detection methods [81–84]:

- Passive methods. Methods based on observe the main grid to take decisions defining a Non-Detection Zone (NDZ) or non-detection window. If the monitored grid parameters, i.e. voltage and frequency, are within the NDZ the grid supervisor system assumes that there is no problem in the grid. Some examples are NDZ or Phase Jump Detection [85].

- Active methods. Methods based on perturb and observe to take decisions. Even though passive methods are fast and robust, they have an important weakness. If a local load is consuming all the power, i.e. active and reactive power, that the inverter delivers when the utility disconnects, neither the voltage nor the frequency will change. This situation is called resonance. Thus, active methods appeared to solve resonance occurrences. It should be remarked that positive methods disturb the system. Consequently, the current or voltage managed by the inverter get worse. Active methods can be classified into:

  - Positive feedback strategy. Active methods try to make unstable some of the controlled current parameters defined by

    $$i(t) = I \cdot \sin(\omega t + \phi) \tag{2.2}$$

    It is possible to modify periodically or asynchronously the amplitude of the controlled current I, the angular frequency ω or the phase ϕ. Some examples of positive feedback methods are Sandia Voltage Shift (SVS), Sandia Frequency Shift (SFS) [86] or Slip-Mode Shift (SMS) [85]. Some of them can be combined to increase the effectiveness of the detection method.

  - Impedance measurement strategy. The operating principle of impedance measurement active methods resides on the measure

of the impedance at the PCC. In order to achieve this objective, the voltage and current values of the PCC are needed, but they must be obtained in a different frequency from the rated grid frequency. A little perturbation is added to cause a non-characteristic harmonic current to the grid. Then, the same harmonic voltage is measured at the PCC. The main challenge is to choose the frequency which makes able the detection without exceeding the maximum harmonic distortion permitted by regulations. Some authors starts using external switching impedance devices [87, 88]. The increase in the computational capabilities of the micro-controllers that manages an inverter make able to inject harmonics via control strategies: simple/double harmonic injection [83, 89] and, also, using inter-harmonics [90–92]. Finally, as an indirect harmonic injection, it can be found PLL based methods, as described in [83, 93].

- Remote methods. Methods based on communications. The utility can inform the inverter through industrial communications of a grid stop due to maintenance or any other abnormal situation. In other words, when the grid and the inverter belongs to the same owner or there is a contractual agreement between them, this option is feasible. One alternative to the use of communications is the use of a battery of capacitors. The utility manages a line breaker and after a controlled time it connects a battery bank of capacitors. The reactive power changes and the frequency resonance is displaced, being possible the disconnection detection.

There are different anti-islanding standards. In Table 2.3.2, it can be seen a review of the clearing time response, i.e. the detection time for three significant standards (VDE 4105, IEEE 1547 and IEC 61727 [16–18]). All the considered standards proposes a detection time that is function of a voltage threshold percentage over the rated voltage and a deviation on the rated frequency. Depending on the amount of displacement of the voltage or frequency, the clearing time is different. Note that in Table 2.3.2 there are some operation ranges in which the clearing time is infinite. These cases are considered within tolerable limits for the utility. Notice that different standards assumes different rated grid frequencies. VDE 4105 and IEC 61727 are thought for 50 Hz grids and IEEE 1547 for 60 Hz networks.

If a local load, called resonant load, is consuming all the power (active and reactive) that the inverter delivers, when the utility disconnects, neither the

	Voltage threshold [%]	Time [s]	Frequency threshold [Hz]	Time [s]
VDE 4105	$V < 80$	0.20	$f < 47.5$	0.20
	$80 \leq V \leq 115$	∞	$47.5 \leq f \leq 51.5$	∞
	$V > 115$	0.20	$f > 51.5$	0.2
IEEE 1547			$f^1 < 59.3$	0.16
	$V < 50$	0.16	$59.3 \leq f^1 \leq 60.5$	∞
	$50 \leq V < 88$	2.00	$f^1 > 60.5$	0.16
	$88 \leq V \leq 110$	∞	$f^2 < 57.0$	0.16
	$110 < V < 120$	1.00	$57.0 \leq f^2 < 59.8$	0.16 - 300[3]
	$V > 120$	0.16	$59.8 \leq f^2 \leq 60.5$	∞
			$f^2 > 60.5$	0.16
IEC 61727	$V < 50$	0.10		
	$50 \leq V < 85$	2.00	$f < 49.0$	0.20
	$85 \leq V \leq 110$	∞	$49.0 \leq f \leq 51.0$	∞
	$110 < V < 135$	2.00	$f > 51.0$	0.20
	$V > 135$	0.05		

[1]DER size ≤ 30 kW
[2]DER size > 30 kW
[3]Adjustable

Table 2.1: Standards review clearing times when non-resonant loads are considered

voltage nor the frequency will change significantly. Anti-islanding regulations suggest that the concept of resonant load will take place when the local consumption is nearly equal to the active power given by the inverter, considering none reactive power. This part is described by an aggregated resistance. Furthermore, it is required that the frequency of the grid will be maintained just after a grid disconnection. A capacitance is connected in parallel with an inductance tuning the resonance frequency of the LC circuit at the grid frequency. Then, when resonant loads are considered, detection times are lax. Table 2.2 exposes the clearing times under the presence of a resonant load. For example VDE 4105 [16] proposes up to 5 s to detect the mains loss. As has been exposed previously, an active method, if the grid disconnection is non-intentional, has to be used.

2.4 Elements of an AC microgrid

An AC microgrid is not only constituted by one or more inverters. It should be also considered all the external devices that will allow to operate an AC system in an optimal way ensuring safety operation for people, devices and

	Time [s]
VDE 4105	5.00
IEEE 1547	2.00
IEC 61727	2.00

Table 2.2: Standards review clearing times when resonant loads are considered

electric infrastructures. In this sense, the main elements that integrate an AC microgrid are the inverter, the main breaker, the protections elements and algorithms, the neutral scheme (re)configuration switches, the management system controller, the communications and the local loads.

2.4.1 The inverter

The inverter is the heart of the AC microgrid. It is constituted by a power converter, usually, a VSI. It is the element that is responsible of applying the voltage and frequency variations in its output in order to match the needs of active and reactive power in both directions at all time. It is also the link between the AC and DC side and interacts with the utility.

If the inverter is grid-connected operated it must support temporary grid transients without generating disturbances. It must be able to communicate with the MGCC and act properly to face the reception of set-points in case of grid fault, for example, if ride-through is implemented.

If the inverter is grid-disconnected operated it must create a grid with nominal values and keep them within secure thresholds also during load (dis)connection transients.

The control strategies on the operation of the microgrid inverters supposes one of the most important challenges.

2.4.2 The main breaker

The main breaker, also known as central switch, enables the (dis)connection of the AC microgrid from/to the utility, allowing to operate the system in grid-(dis)connected. In non-intentional mains loss, this decision is taken according to the anti-islanding implemented strategy.

A smart main breaker will monitor the network to detect any abnormal situation. In Figure 2.8 is proposed an example of a smart main breaker. The use of this type of device implies:

- To consider a main breaker unit to establish a physical controlled way to segregate the utility side from the microgrid side.

- To consider a grounding switch to reconfigure the neutral scheme of the microgrid according to the protections selected. The grounding impedance, operated by the grounding switch, will be function of the selected earthing system and the used transformer.

- In case of considering resonant loads, the power electronics that disturb the system in order to detect the mains loss can be allocated at:

  - The smart main breaker.
  - Each inverter.

  Integrate power electronics in the smart main breaker is an expensive solution when each VSI is based in power electronics. On the other hand, the disturbed magnitude is modified by only one device, avoiding interactions between possible anti-islanding strategies adopted by each VSI.

- Communications. The smart breaker has to include communication with the MGCC. It should be reminded that the Distributed System Operator (DSO) or the Market Operator (MO) can operate according to the price of energy, maintenance, DER availability or other possible motivations. Also, a communication with the inverters allows to inform each VSI that, maybe, they have to change their control strategy, i.e. start to operate as GSI, GCI or GSCI.

In [94, 95] can be seen two examples of smart main breakers (also called anti-islanding relays). On one hand, [94] includes a microprocessor that computes under/over-voltage, under/over-frequency, vector shift, rate of change of frequency, voltage asymmetry determination and phase sequence supervision. Essentially, is based on passive anti-islanding methods. On the other hand, the smart main breaker proposed in [95] is based on a perturbation signal generator thyristor system located at the substation. It creates a controlled short time short-circuit during the grid voltage zero crossing one of each four grid cycles. Then, downstream, each DER connection node has a signal detector. This is a hybrid proposal between active and remote anti-islanding methods.

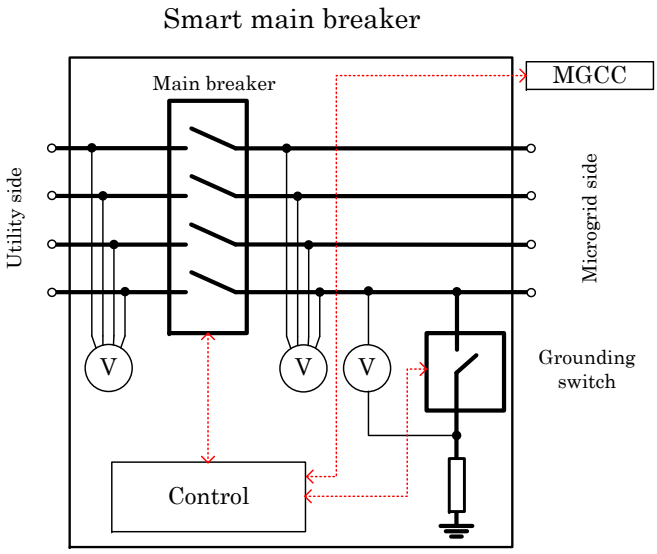

Figure 2.8: Example of a smart main breaker for AC microgrids

2.4.3 Protections

The protections become an essential topic to minimize risks for people and equipment. Although the protections of an AC microgrid are similar, in terms of detection magnitudes, to those of conventional networks, it must be considered some specific challenges. Operating conditions are constantly changing.

Protection in microgrids has to face with two type of faults [96]:

- Utility faults. The protection isolates the main grid from the microgrid as fast as possible to protect the different loads of the microgrid.

- Microgrid faults. The protection isolates the smallest possible section of the feeder where the fault occurs minimizing effects on other microgrid lines.

In the case of a microgrid it has to be taken into account that the energy flow can be bidirectional in some points. All these devices should necessarily communicate with the MGCC or the different LC. As DER are interfaced with the microgrid through power electronics, the possible fault occurrences increase and the required respond times decrease. Power electronics can monitor faults instantaneously and take fast actions, i.e. real-time actions

before high levels of fault current begin to flow. During a fault, a DER has to be controlled in order to limit the fault current. Protection Device units (PD) can be classified into four basic categories [52], see Figure 2.9. All these protections may act differently depending on whether they are operating: grid-(dis)connected. Then, it is exposed how they should act based on active or passive behaviour (considering communications with the MGCC).

- PD1: Point of Common Coupling (PCC) or Microgrid protection. The protection of the PD1 level is conducted by a smart main breaker. It should be reminded that the smart main breaker operation can be according intentional or non-intentional mains loss. This fact implies the combination of anti-islaning mechanisms and communications with the MGCC or LC for the disconnection, synchronization and reconnection of the microgrid.

- PD2: Distribution line protection. A directional over-current relay must act only in case of failures in the correspondent distribution line if the operation is based on local measurements and the microgrid is grid-connected operated. Selectivity at PD1 and PD3 levels should be considered. The hardware selectivity can be complemented with software selectivity implemented by time delays under communications.

  If the microgrid is grid-disconnected operated a voltage relay concept is used. As the AC microgrid disposes of less short-circuit power the over-current detection is complemented with voltage monitoring.

  The PD2 unit can receive the order of (dis)connection via a signal sent by the MGCC. Adaptive algorithms based on multi-voltage and current values monitored during the failure are applied. The objective is to locate and isolate the fault.

- PD3: End-user protection
  - PD3a: Connection service with the end-user. This level feeds various end-users by a same service cable. At this level over-currents protection with no directional breaker or fuse can be considered. Selectivity with PD3b and PD2 based on time delays is required. Reconfiguration of the current thresholds based on the operation mode allows to configure the operation limits according to the microgrid operation mode.
  - PD3b: Load point. This level considers end-users that only consumes from the service line. Over-current protection with smart-

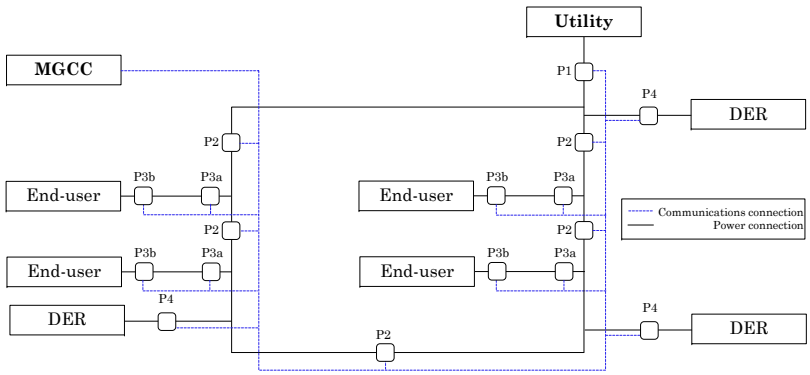

Figure 2.9: Schematic of protection distribution in a microgrid

fuses, requiring communications, is proposed at this level. Selectivity with PD3a and PD2 based on time delays should be considered. Communication are only required in order to inform the MGCC about abnormal occurrences.

- PD4: DER protection. This level assumes active connected systems, being the most significant case of DER. Monitoring system that controls the voltage and frequency through a NDZ should be considered. Selectivity with PD1 and PD2 to avoid unnecessary disconnection of a DER is required. Operation disconnect signals from MGCC have to be included.

In case of medium-voltage microgrids, protections have to be selected with enough cut-off capability and sufficient dynamics, as cited in [97, 98].

2.4.4 The neutral scheme

It is necessary to consider how to face with the neutral and earthing (or grounding) scheme when the system is grid-(dis)connected. The installation must be protected against direct and indirect contacts as any conventional grid. Depending on how the neutral and protective-wire are wired it is crucial to ensure people and device security when a PD is opened.

In [99] is defined the different neutral schemes for conventional low voltage installations. Summing up, the designation of ground systems is performed by two characters, but can be complemented with other characters:

- The first character refers to the situation of the facility with respect to ground. Using a T is called to those networks that have a direct con-

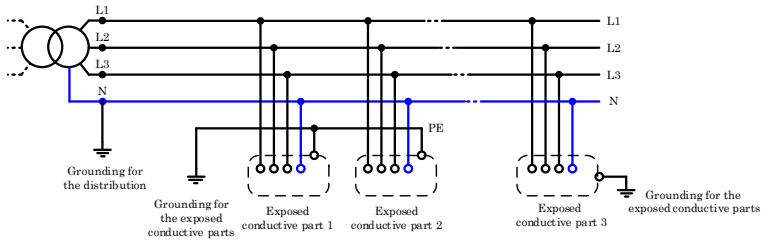

Figure 2.10: TT neutral scheme

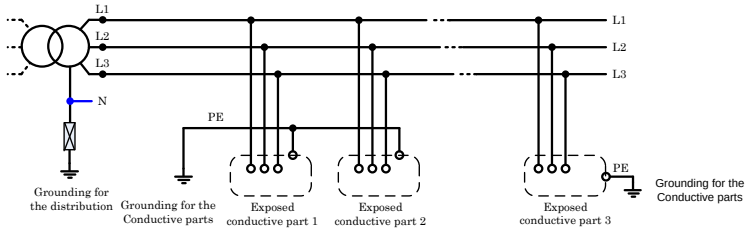

Figure 2.11: IT neutral scheme

nection point on the ground, while the character I is used for isolated networks with respect to ground or connected by high impedances.

- The second character refers to the situation of the electrical installation's exposed conductive parts with respect to ground. The character T indicates that the exposed conductive parts have a separate ground connection of the installation's grounding. The character N is used to refer to those networks that use the neutral point grounded for the distribution to connect the exposed conductive parts.

- The other character, if any, indicates the relation between the neutral wire, designed by the character N and Protection Earth wire (PE). By S it is called to those networks that use two different wires for the neutral and protective earth. By C it is indicated that the neutral cable acts as the protective wire.

Figures 2.10 to 2.12 depicts TT, TI, TN-S/C/C-S neutral schemes.

It is important to remark that when the neutral disconnection is needed, its disconnection will never take place before the open action of the active

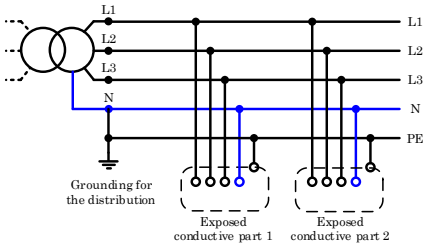

(a) TN-S neutral scheme

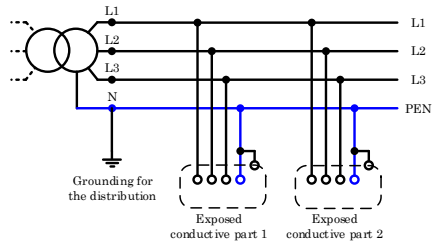

(b) TN-C neutral scheme

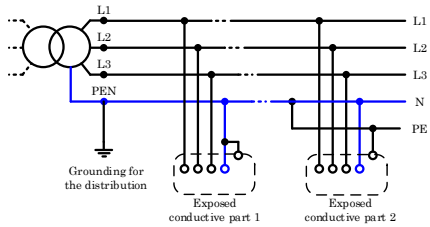

(c) TN-C-S neutral scheme

Figure 2.12: TN neutral schemes

wires L1, L2 or L3. Additionally, during the connection of the neutral, it is necessary to ensure an anticipated or simultaneous connection in respect with the active wires. The different neutral schemes imply different considerations under a fault:

- TT. The disconnection has to be done at the first default. A correct protection is achieved by the interconnection and grounding of all metallic conductive parts. Disconnection is done by differential breakers. The neutral wire disconnection is mandatory.
- TN. The disconnection has to be done at the first default. A correct protection is achieved by interconnection and grounding of all metallic conductive parts. The disconnection is due to over-current detection. In TN-C, the neutral wire is never protected and its disconnection is prohibited. In TN-S, the disconnection is mandatory. The TN-C is not suitable for systems with an important component of the third harmonic because it produce lack of equipotential in the metallic conductive parts and in the PE wire.
- IT. Advice at first default. Disconnection has to be done at the second default. A correct protection is achieved by interconnection and

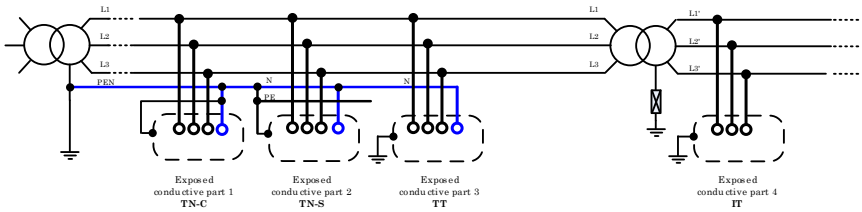

Figure 2.13: Neutral schemes compatibility

	TT	TN-C	TN-S	IT
Flammable storage systems or sensitive power electronics components	✓	✗	✓	✓✓
Robustness of service	✓	✓	✓	✓✓
Components integrity (current acceptance)	✓	✗	✗	✓
People security	✓	✓	✓	✓
Homopolar loads[1] and common-mode filters use	✓	✗	✓✓	✗✗

[1] Multiple single phase-to-neutral loads

Table 2.3: Neutral schemes criteria for microgrids

grounding of all metallic conductive parts. The disconnection is due to over-current detection and over-voltage protection is also imperative. In IT systems with a distributed neutral, a permanent isolation controller is mandatory. This isolation controller has to be connected as close as possible to the origin of the distribution. Thus, in IT configuration a distributed neutral, i.e. L1-L2-L3-N-PE instead of L1-L2-L3-PEN, is not recommended. In case of a distributed neutral scheme, the N-wire has to be protected using a omnipolar breaker.

The various type of distributions are compatible if some consideration are taken, see Figure 2.13. The used neutral configurations has to be TT and TN. The IT has to be interconnected through galvanic isolation. Each installation has to dispose of its own protection wire. All TN scheme used needs its PEN wire connected to ground and to the neutral point of the transformer after its general protection device.

In this sense, depending on the use or not of a transformer the proper neutral scheme can be different. Table 2.3 shows some of the different possible appliances of a neutral schemes in function of different criteria [100, 101].

Whether the microgrid requires galvanic isolation or not, TT or TN-C-S are the most suitable neutral schemes [102]. Note that short-circuit currents have to be controlled properly in the TN-C-S case. However, a microgrid VSI can control these currents, unlike happens when passive components,

as transformers, are considered. IT is not considered as a candidate in [102] because it is indicated that this option is rarely used in practice.

The galvanic isolation and the PCC location

There exists different European regulations for grid-connected low power generators, for example [18, 103]. As a microgrid plays the role of a power generator it can be governed by the same rules that other generators like photovoltaic inverters or wind turbines, directly or indirectly connected to the utility. The most extended and relevant points are:

- The grounding schemes of the interconnected installations will be done in such way that will not modify the grounding scheme of the DSO, ensuring that will not appear default transferences to the distribution grid.
- The installation will dispose of galvanic isolation between the distribution grid and the generation installations using an isolation transformer or another system with the same capabilities.
- The conductive parts of the generation installation will be connected to an independent grounding point of the DSO's neutral. In the same way as the conductive parts of the rest of the supplies.

As has been detailed, a microgrid inverter can operate in grid-(dis)connected modes. Due to different argumentations, as can be regulatory or technical, the inverter can be isolated galvanically from the grid. For this reason, different challenges should be contemplated (detailed in Section 2.7):

- Reactive power injection in grid-(dis)connected operation.
- Frequency variation in grid-(dis)connected operation.
- Inrush currents to provide a black-start for grid-connected to grid-disconnected operation.
- Various parallel inverters with galvanic isolation.
- Unbalanced three-phase loads in grid-disconnected operation or single and three-phase simultaneous consumptions.
- Unbalanced three-phase injection in grid-connected operation. This implies a behaviour as a four-quadrant P/Q inverter.

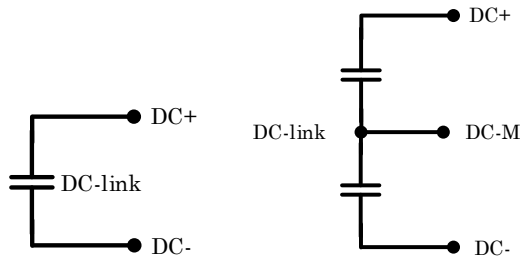

(a) Unipolar DC-side scheme (b) Bipolar DC-side scheme

Figure 2.14: Active wires in DC microgrids

- Three-phase voltage supply with direct, inverse and zero sequence in grid-connected operation.

- Non-linear loads in grid-disconnected operation. In this case currents with direct, inverse and zero sequence components are considered.

On the other hand, the PCC can be located previously or after the isolation stage. This decision implies that the neutral scheme of the distribution could be maintained or not. Also, according to unipolar or bipolar DC microgrids, see Figure 2.14, the AC neutral scheme could be compromised. Unipolar DC microgrids are used for its simplicity but protections requires higher rated voltage. Bipolar DC microgrids are more complex due to the required active balancing of the two semi-buses but are cheaper to protect and more secure for people and devices.

As the substation or Transformer Center (TC) where the microgrid can be interconnected disposes of a transformer and the microgrid, as an active generator, has to include one more, depending on this last, different configurations can be considered.

It is possible to consider that the PCC can be located after or before the microgrid's transformer:

- If the PCC is located after it, all local loads should be removed from conventional location at the TC's secondary side to be connected at this new point. This is a rare situation and will not be considered.

- If the PCC is located previously to the microgrids transformer it is possible to study four scenarios considering star, delta or zig-zag transfomer winding configuration. It is assumed that all DC-side converters

are floating, the utility side is TT (TN follows similar conclusions) and bipolar DC-side scheme is considered. This first analysis only takes into account basic electrical consideration. A more complete analysis is conducted in Section 2.7:

- Delta - star (or zig-zag) microgrid's transformer (Figure 2.15(a)). The secondary-side of the microgrid's transformer distributes the neutral-wire N. The mid-point (M) of the DC side is referenced to N. The PCC is supplied by only three-wires. This situation does not allow single-phase loads due to, commonly, the phase-to-phase voltage is not equal to 230 V.
- Star (or Zig-zag) - delta microgrid's transformer (Figure 2.15(b)). In this case the M wire is directly grounded through a low or high impedance. The secondary side of the microgrid transformer is three-wire implying that it is not possible to control zero-sequence voltage components. Zero sequence currents can be delivered from the inverter but they will not be transmitted to the utility side.
- Star (or Zig-zag) - star (or zig-zag) microgrid's transformer (Figure 2.15(c)). As the inverter side is four-wire, zero voltage and current components can be managed.
- Delta - delta microgrid transformer (Figure 2.15(d)). Same situation than Y(Z)-d scenario presented in Figure 2.15(b).

2.4.5 The management system

The management system is the responsible for monitoring the entire generation and consumption system. It also manages, as well as organizes, the interaction with the public network, constituting the called MGCC. Therefore, forms the brain of the microgrid. Based on communications, using standards when they exists, the MGCC integrates complex algorithms for managing the generation and local demand. Thus, it should communicate with all the elements of generation and consumption, as well as the monitoring systems and protections. It also acts as the information hub and gateway of the entire system to the outside.

The management system incorporates several services that may be local or global. The key issue in the design of this system is the identification of services and their classification, clustering them in optimization algorithms which objective functions can vary according to the time and can be as diverse as maximize profits, minimize losses or maximize resources.

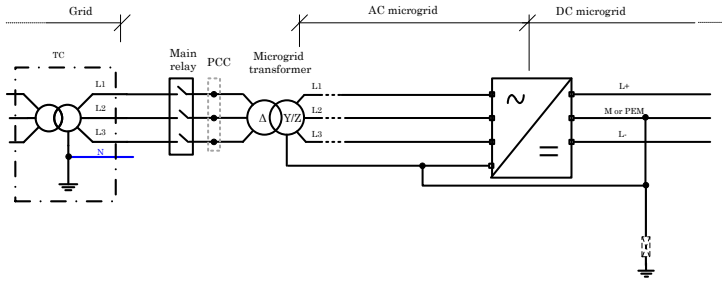

(a) Delta - star (or zig-zag) scenario

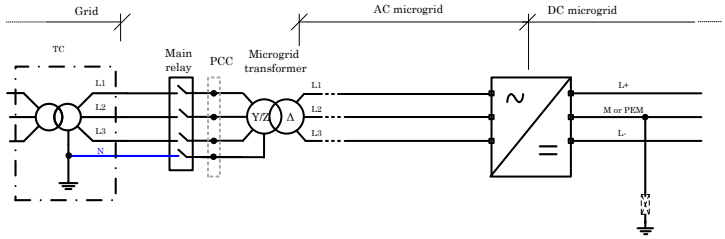

(b) Star (or Zig-zag) - delta scenario

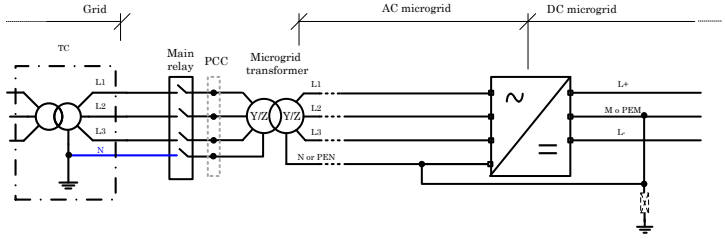

(c) Star (or Zig-zag) - star (or zig-zag) scenario

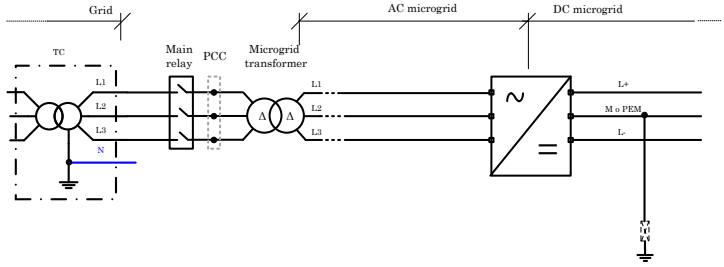

(d) Delta - delta scenario

Figure 2.15: Neutral scheme connections when PCC is located before all microgrid's transformer stages and a bipolar DC microgrid is considered

2.4.6 The communication bus

A microgrid is integrated by a MGCC but also by the LC and the Low Level Devices (LLD) as DER, protections or monitoring systems. As in the Computer Integrated Manufacturing (CIM) model, the integration of the aforementioned different equipment and devices is done by dividing tasks among layers or groups of processes with a hierarchical organization. There exists three regulation mechanisms in conventional public networks:

- The primary regulation procedure operates at short-time (1-20 s) in each local synchronous generator directly acting over the speed of a synchronous machine. This is done to compensate the effect of the unbalances between consumption and generation. A new operation frequency, different from the rated one, is achieved.

- The secondary regulation operates in a medium-time interval (20-120 s). Allows that the synchronous generators can correct its operating frequency following a centralized set-point.

- Tertiary regulation acts at long-time (over 10 min) and manages the power that several generators should supply to optimize the most appropriate resource at any time, taking profit of historical consumption and generation data.

In this sense, it is possible to define different communication requirements according to the considered level:

- I/O level. Integrated by LLD as smart-protections or control sensors for power electronics. This level is related with primary regulation but faster due to the presence of power electronics:
    - Control and manage of the electric basic magnitude: voltage and current.
    - Little information to share.
    - Critical information that requires real-time management.
- Field level. Integrated by LC. This level is related with primary regulation.
    - Control and monitoring of secondary electric magnitude: power or energy.
    - Little information to share.
    - Critical information that requires real-time management

- Process control level. Integrated by LC. This level is related with secondary regulation.
    - System controllers with certain autonomy to take decisions.
    - Gateway for data to higher and lower levels.
    - Pseudo-critical information in real-time but with longer operation times than lower levels.

- Production control level. Integrated by the MGCC unit and its upstream and downstream related layers. This level is related with tertiary regulation.
    - MGCC collects information of all connected LLD and exchange data with the system operator.
    - Not critical information which does not require real-time management but more critical than management level.

- Management level. Integrated by DSO, MO or the MicroGrid Operator (MGO).
    - The system operator analyses the information obtained from the production control level.
    - Includes statistical analysis, forecasting, quality, service and economic boundaries.
    - Not critical information which does not require real-time management.

In this sense, according to the considered communication level there can be found different communication protocols. Some of them matches better with the quantity of data to share, the refreshing time desired, allowed latencies and with the hierarchy (master/slave, client/server, producer/consumer) or structure (star, radial, bus) chosen. In Figure 2.16 can be seen an example of multiple field communication protocols showing the most suitable levels where they can be used. Some examples of used protocols and standards for grid and energy systems are IEC 608070-5-101 or 104, IEC 61850 or IEC 62056 [104–107] where Transmission Control Protocol/Internet Protocol-User Datagram Protocol (TCP/IP-UDP) or Power Line Carrier (PLC) are common applied communication profiles. In this case, they are more related with the production or management levels.

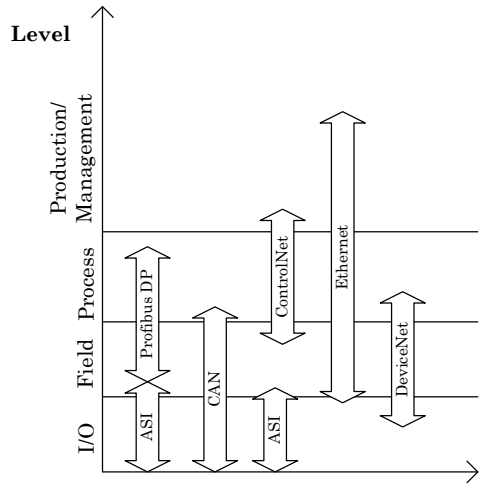

Figure 2.16: Communication protocol versus communication levels for which they are designed

2.4.7 The loads

The loads are connected to the PCC and are commonly called local loads. One important consideration that derives from the local load-microgrid interaction is the control priorities. From this point of view, the loads can be classified as:

- Common load: can be disconnected during long-time periods if necessary.
- Demand Side Management (DSM) loads: can be controlled depending on the needs of the system.
- Critical loads: they should not be left to feed.

An example of DSM loads presents a particular interest in cool climate regions where the electrical heating is achieved by means of static storage. These elements are characterized by the ability to store heat and deliver it to the end-users when it is necessary. This gap between the energy consumption of the network and its use by the end-user provides economic savings rates with time discrimination.

2.5 Operation particularities

This sections presents the different implications on the equivalent models for different three-phase distribution microgrid's VSI options. Also presents some relevant considerations on the transference between the operation modes of these inverters.

2.5.1 Three-wire and four-wire inverter output current state-space models

The main advantage of four-wire topologies lies in the capability to tolerate zero sequence currents. However, the management of zero sequence voltages depends on the controllability of the fourth wire. In this sense, there are two extended inverter choices. The first case is the four-wire three-leg with split capacitor topology, as has been shown in Figure 2.3(b). This option does not allow to manage directly the reference voltage component because the neutral wire is not controlled and it is determined by the neutral scheme of the utility when grid-connected. The other case is a four-wire four-leg topology, see Figure 2.3(c). In this last case, the inverter uses the fourth leg as an extra degree of freedom to manage zero sequence voltages controlling the reference location. The addition of this extra leg supposes to increase the control complexity and the switching losses but permits to synthesize voltages referred to a controlled point.

In case of four-wire systems, the effect of the fourth wire is crucial when the different positive, negative or zero sequences are controlled. Figure 2.17 shows an ideal voltage source model for the mentioned three-phase inverter topologies. In this figure, $\{u', v', w', n'\}$ refers to the grid side, $\{u, v, w, n\}$ to the inverter side output voltages and o to the mid-point of the DC-link.

For the four-wire three-leg with split capacitor case, see Figure 2.17(b), the system can be described in the Laplace domain as

$$\begin{pmatrix} u_{uo} \\ u_{vo} \\ u_{wo} \end{pmatrix} = \begin{pmatrix} R+Ls & 0 & 0 \\ 0 & R+Ls & 0 \\ 0 & 0 & R+Ls \end{pmatrix} \begin{pmatrix} i_u \\ i_v \\ i_w \end{pmatrix} + \begin{pmatrix} u_{u'n'} + u_{n'o} \\ u_{v'n'} + u_{n'o} \\ u_{w'n'} + u_{n'o} \end{pmatrix} \tag{2.3}$$

Notice that o and n' are the same reference point, then $u_{n'o} = 0$. Rewriting Equation 2.3 in a state-space form

$$\frac{d}{dt} \begin{pmatrix} i_u \\ i_v \\ i_w \end{pmatrix} = \frac{-1}{L} \left[\begin{pmatrix} R & 0 & 0 \\ 0 & R & 0 \\ 0 & 0 & R \end{pmatrix} \begin{pmatrix} i_u \\ i_v \\ i_w \end{pmatrix} + \begin{pmatrix} 1 & 0 & 0 \\ 0 & 1 & 0 \\ 0 & 0 & 1 \end{pmatrix} \begin{pmatrix} u_{u'n'} - u_{uo} \\ u_{v'n'} - u_{vo} \\ u_{w'n'} - u_{vo} \end{pmatrix} \right] \tag{2.4}$$

In case of considering a three-wire system, see Figure 2.17(a), it can be also described by Equation 2.3 but $u_{n'o} \neq 0$. In fact,

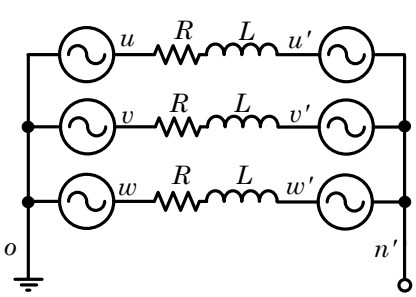

(a) Three-wire three-leg

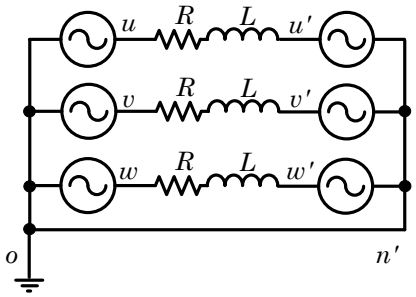

(b) Four-wire three-leg with split capacitor

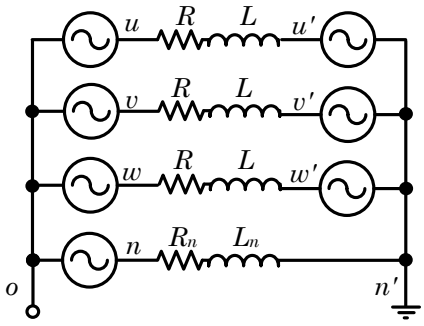

(c) Four-wire three-leg

Figure 2.17: Ideal voltage source schemes for three-phase inverters

$$u_{n'o} = \frac{1}{3}\left(u_{uo} + u_{vo} + u_{wo}\right) \tag{2.5}$$

Applying Equation 2.5 to 2.3 the resulting state-space form is as follows

$$\frac{d}{dt}\begin{pmatrix} i_u \\ i_v \\ i_w \end{pmatrix} = \frac{-1}{L}\left[\begin{pmatrix} R & 0 & 0 \\ 0 & R & 0 \\ 0 & 0 & R \end{pmatrix}\begin{pmatrix} i_u \\ i_v \\ i_w \end{pmatrix} + \begin{pmatrix} 1 & 0 & 0 \\ 0 & 1 & 0 \\ 0 & 0 & 1 \end{pmatrix}\begin{pmatrix} u_{u'n'} \\ u_{v'n'} \\ u_{w'n'} \end{pmatrix} - \frac{1}{3}\begin{pmatrix} 2 & -1 & -1 \\ -1 & 2 & -1 \\ -1 & -1 & 2 \end{pmatrix}\begin{pmatrix} u_{uo} \\ u_{vo} \\ u_{vo} \end{pmatrix}\right] \tag{2.6}$$

If the same analysis is conducted in the four-wire four-leg three-phase case, as depicted in Figure 2.17(c), the use of a neutral inductance to add ripple reduction and current limitation on the controlled fourth leg has to be considered

$$\begin{pmatrix} u_{uo} \\ u_{vo} \\ u_{wo} \end{pmatrix} = \begin{pmatrix} R+Ls & 0 & 0 \\ 0 & R+Ls & 0 \\ 0 & 0 & R+Ls \end{pmatrix}\begin{pmatrix} i_u \\ i_v \\ i_w \end{pmatrix} + \begin{pmatrix} u_{u'n'} + u_{n'n} + u_{no} \\ u_{v'n'} + u_{n'n} + u_{no} \\ u_{w'n'} + u_{n'n} + u_{no} \end{pmatrix} \tag{2.7}$$

Now, assuming

$$i_u + i_v + i_w + i_n = 0 \tag{2.8}$$

it is possible to deduce that

$$u_{n'n} = (R_n + L_n s) i_n \tag{2.9}$$

Applying Equation 2.9 to 2.7 the system can be described in the Laplace domain by

$$\begin{pmatrix} u_{uo} \\ u_{vo} \\ u_{wo} \end{pmatrix} = \begin{pmatrix} R_{eq} + L_{eq}s & R_n + L_n s & R_n + L_n s \\ R_n + L_n s & R_{eq} + L_{eq}s & R_n + L_n s \\ R_n + L_n s & R_n + L_n s & R_{eq} + L_{eq}s \end{pmatrix}\begin{pmatrix} i_u \\ i_v \\ i_w \end{pmatrix} + \begin{pmatrix} u_{u'n'} + u_{no} \\ u_{v'n'} + u_{no} \\ u_{w'n'} + u_{no} \end{pmatrix} \tag{2.10}$$

being $L_{eq} = L + L_n$ and $R_{eq} = R + R_n$. Rewriting Equation 2.10 in a state-space form

$$\begin{aligned} \frac{d}{dt}\begin{pmatrix} i_u \\ i_v \\ i_w \end{pmatrix} = C\Bigg[\begin{pmatrix} LR + LR_n + 2L_n R & LR_n - L_n R & LR_n - L_n R \\ LR_n - L_n R & LR + LR_n + 2L_n R & LR_n - L_n R \\ LR_n - L_n R & LR_n - L_n R & LR + LR_n + 2L_n R \end{pmatrix}\begin{pmatrix} i_u \\ i_v \\ i_w \end{pmatrix} + \\ + \begin{pmatrix} L + 2L_n & L_n & L_n \\ L_n & L + 2L_n & L_n \\ L_n & L_n & L + 2L_n \end{pmatrix}\begin{pmatrix} u_{u'n'} + u_{no} - u_{uo} \\ u_{v'n'} + u_{no} - u_{vo} \\ u_{w'n'} + u_{no} - u_{wo} \end{pmatrix}\Bigg] \end{aligned} \tag{2.11}$$

being $C = \frac{-1}{L(L+3L_n)}$. When $L_n = L$ and $R_n = R$ is assumed, Equation 2.11 is simplified into

$$\frac{d}{dt}\begin{pmatrix} i_u \\ i_v \\ i_w \end{pmatrix} = \frac{-1}{L}\left[\begin{pmatrix} R & 0 & 0 \\ 0 & R & 0 \\ 0 & 0 & R \end{pmatrix}\begin{pmatrix} i_u \\ i_v \\ i_w \end{pmatrix} + \frac{1}{4}\begin{pmatrix} 3 & 1 & 1 \\ 1 & 3 & 1 \\ 1 & 1 & 3 \end{pmatrix}\begin{pmatrix} u_{u'n'} + u_{no} - u_{uo} \\ u_{v'n'} + u_{no} - u_{vo} \\ u_{w'n'} + u_{no} - u_{wo} \end{pmatrix}\right] \tag{2.12}$$

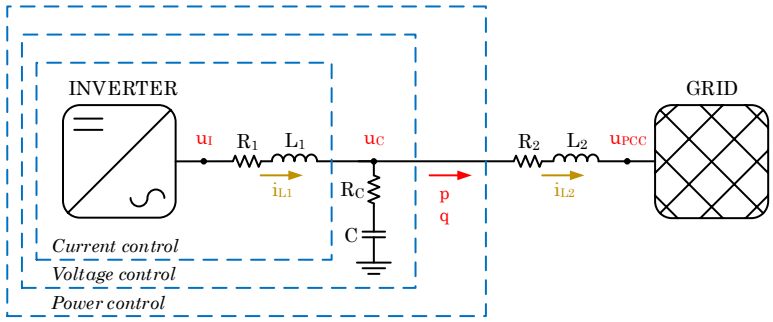

Figure 2.18: General conceptual control scheme

Some authors proposes that the inductance of the fourth wire can be eliminated without affecting substantially the results from when it is considered [77]. It could be deduced that the current through the neutral wire will change according to a slope equal to $L + 3L_n$. Then, if $L_n = 0$, the neutral wire disposes of the same inductive impedance as the active $\{u, v, w\}$ phases.

2.5.2 Control loops

As has been introduced in Section 2.2, an AC microgrid inverter can be integrated by up to three control levels considering LC manage capabilities; power, voltage and current. Figure 2.18 shows a VSI connected with the utility by means of a LCL-type coupling filter. The AC capacitor is sized for filtering in GSI, whereas it is sized for control in GCI or GSCI. This means that the capacitor can be excluded, if required, in GSI.

On the other hand, inner voltage and current control loops offer an important challenge. One of the most relevant considerations is to identify which kind of control problem wants to be solved. In the control theory it is possible to face with tracking of constant or time-varying references. Then, the use of different reference frames can be applied to follow constant or sinusoidal set-points:

- Synchronous Rotating Reference Frame (SRRF). In this reference frame, the electrical magnitudes are seen from a reference in which the considered angular frequency is constant and not null. Then, the electrical magnitudes are constant. To use a SRRF, the use of Clarke's and Park's transforms are widely extended. Appendix A details in which they consist.

- Stationary Reference Frame (SRF). In this reference frame, the electric

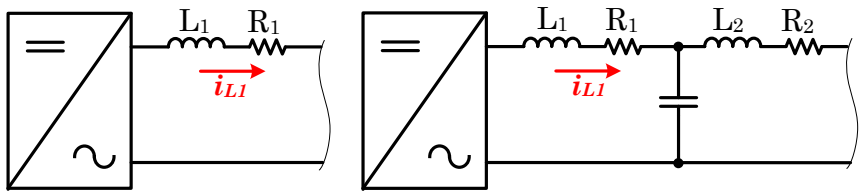

(a) First order coupling filter. L-type

(b) Third order coupling filter. LCL-type

Figure 2.19: CC-VSI with different inductive coupling filters

magnitudes are seen from a reference in which the considered angular frequency is null. Then, the electrical magnitudes are time-varying, i.e. sinusoidal waves. Chapter 3 details the inner loop control when the SRF is used.

The current control loop

The inner current control loop represents the most elemental way to operate a microgrid VSI. An inductance connected at its output is the minimum coupling element to relate the VSI with another voltage source as the grid, see Figure 2.19(a).

As the behaviour of the current through an inductance with its equivalent series resistance is described by

$$v_L = L\frac{di}{dt} + Ri \tag{2.13}$$

it can be deduced that high inductance values ensure low current ripples but also can cause non allowable voltage drops and constitutes considerable space requirements and cost. To prevent high injected or consumed current ripples it is quite common to connect the converter with the grid using high order filters [108, 109], as can be an LCL-type coupling filter constituted by three stages: the converter side inductance, the AC capacitor and the grid side inductance, see Figure 2.19(b). Some of the most relevant transfer functions of a first and third order coupling filter are described in Figure 2.20 and detailed in Table 2.4 [110].

When high order filters are taken into account the location of the current probes, the stability of the control, the power factor or the synchronism with the grid depend on how the system is considered from the control perspective In case of using a LCL-type coupling filters:

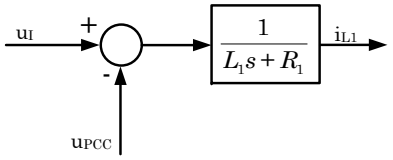

(a) First order coupling filter. L-type

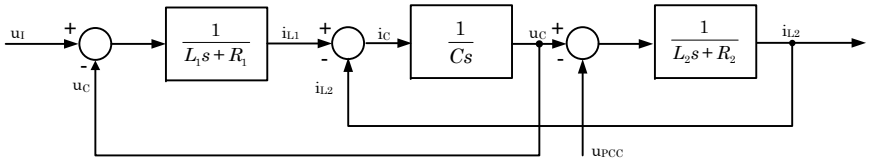

(b) Third order coupling filter. LCL-type

Figure 2.20: Transfer function of different coupling filters for VSI

Transfer functions without considering R_1 and R_2	
$G_{LCL}\vert_{\frac{i_{L1}}{u_I}}(s)$	$\frac{1}{L_1 s}\frac{s^2+\omega_{LC}^2}{s^2+\omega_0^2}$
$G_{LCL}\vert_{\frac{i_{L2}}{u_I}}(s)$	$\frac{1}{L_1 L_2 C s}\frac{1}{s^2+\omega_0^2}$
$G_{LCL}\vert_{\frac{u_C}{i_{L1}}}(s)$	$\frac{L_2 s}{L_2 C s^2+1}$
Transfer functions considering R_1 and R_2	
$G_{LCL'}\vert_{\frac{i_{L1}}{u_I}}(s)$	$\frac{L_2 C s^2+R_2 C s+1}{L_1 L_2 C s^3+C_f(L_2 R_1+L_1 R_2)s^2+(L_1+L_2+R_1 R_2 C)s+(R_1 R_2)}$
$G_{LCL'}\vert_{\frac{i_{L2}}{u_I}}(s)$	$\frac{1}{L_1 L_2 C s^3+C(L_2 R_1+L_1 R_2)s^2+(L_1+L_2+R_1 R_2 C)s+(R_1 R_2)}$
$G_{LCL'}\vert_{\frac{u_C}{i_{L1}}}(s)$	$\frac{L_2 s+R_2}{(L_2 R_2)C s^2+1}$
	$\omega_0^2 = \frac{(L_1+L_2)}{L_1 L_2 C}$
	$\omega_{LC}^2 = \frac{1}{C L_2}$

Table 2.4: Continuous time transfer functions for an LCL-type coupling filter

- **Location of the current probes**. It should be decided where to locate the current probes. This choice will determine the control strategy and other important factors in an electric system, for instance, the power factor.

  The best location of the current probes, from the point of view of observability in terms of control is at both inductances. However, the amount of probes can be considered excessive according to the final application and to cost sensitivity criteria. For this reason, the literature presents different ways to face this topic:

  - Multiple loops in cascade. The current control of a high order system can be reduced to several Single-Input Single-Output (SISO) control loops nested fulfilling some frequency restriction between them [110, 111].
  - Control of the grid side inductance considering one high order transfer function. This strategy implies that easy criteria to tune the system could not be applied due to high order characteristic equations. This case can be solved using a SISO or Multiple-Input Multiple-Output (MIMO) [69, 112] strategies depending on the location of the close loop poles and their dominances. It should be remarked that a direct control of the grid current supposes that the inverter current is not limited.
  - Control of the converter output inductance. Usually, the inductance of the grid is mainly constituted by the leakage inductance of a transformer. Although the capacitor and the grid side inductance shift the phase of the inverter side inductance, usually this angle is considered negligible.

  The presence of high order coupling filters implies resonances that have to be avoided or controlled properly (transfer function numerator or denominator cancellations). One solution is to add damping elements to reduce those resonance peaks. The damping effect can be achieved using passive or active mechanisms [113]:

  - Passive damping. It is based on adding RLC circuits in series or parallel to the coupling components [114, 115]. They have the inherent drawback of reducing the efficiency of the converter.
  - Active damping. It is introduced implementing virtual RLC equations that will compensate the behaviour of some electric magnitudes into the control loop via software, as proposed in [116–118].

- **Stability of the control**. A criterion for choosing the position of the probes is the stability of the current control loop. If the system is not stable with a sufficient margin, any slight variation in the system parameters either due to different operating conditions, deterioration or uncertainty of the values of the plant can carry the system to an unstable situation.

  In general, the size of the LCL-type coupling filter is calculated exhaustively to accomplish low ripples that regulations or loads admit and, then, the parameters of control are tuned according with the obtained plant. There is disparity of opinions according to the different criteria on LCL circuit sizing and tuning procedures. In fact, there is few literature to examine the location of the current probes with a single loop. In [108] an analysis is proposed concluding that using the grid side inductance for current control is more stable. However, in [119] another deep study is conducted and it concludes that it is more stable to locate the probes at the inverter side inductance. In [120] is detailed that for the common values of inductances and capacitors that can be used there is no significant difference between using the measure on the inverter or grid inductance due to conventional PI controllers only affect to low frequencies. This inconsistency may be due to different criteria when sizing the LCL circuit or control aspects as can be the use of feedforward or the chosen settling time.

- **Power Factor**. GSI are widely used for renewable integration purposes. Their objective is to inject active power to the grid. Depending on where the probes are located it can be achieved or not a minimum delay between the controlled current and the grid voltage.

  In [121] four alternatives are presented based on where the current is monitored, see Figure 2.21. The study is based on a current that is imposed to be in phase with the sensed voltage through a Phase Locked Loop (PLL) algorithm:

  - If i_{L1} is controlled in phase with u_c, according with Figure 2.21(a), the grid sees an equivalent circuit constituted by L_2 in series with the parallel R_{eq} and C, where R_{eq} represents the power supplied by the converter. Considering certain assumptions, it is possible to choose appropriately C and L_2 to compensate their reactive power. The current is in phase with the voltage. With this configuration, the converter needs more voltage to provide the same current because it has to be considered L_1 in series

with R_{eq}.

- In Figure 2.21(b) the grid current i_{L2} is not in phase with the grid voltage. In order that the grid can see a unity power factor, L_2 has to be as smallest as possible. Furthermore, to not oversize the converter, the reactive power of L_1 has to be compensated with the C capacitor.
- In the configuration shown in Figure 2.21(c) the grid always sees in phase the current with the voltage, being this the most appropriate way to control the reactive power. Seen from the side of the converter, it is possible to select L_1, C and L_2 to minimize the reactive power supplied by the inverter.
- The configuration shown in Figure 2.21(d) is used to minimize the reactive power that sees the grid. It should be chosen the smallest possible C capacitor to minimize the reactive power provided by the converter L_1 must be reduced.

When the configuration shown in figure 2.21(c) is not used, alternative methods could be considered to provide an I_{L2} current in phase with u_{PCC} and reduce the reactive power that provides or consumes the grid. A possible method is to modify the reference of the current control to take into account the delay that the LCL provides. The problem with this last proposal is that there will be always some uncertainty about the precise value of L_2. It should be added the fact that the values of C and L_1 already present certain tolerances.

- **Synchronization**. As has been mentioned, the PLL algorithm allows to syncronize an inverter with an external voltage reference. In [122] the common approach based on a Clarke transform linearisation is presented. Then, other authors are focused on how decouple the information of the direct and inverse sequences using Park transform as in [123]. PLL based on Clarke or Park transform approach can also be applied for single-phase systems but in this case some consideration should be taken into account. The most important is to look for a proper way to obtain a u'_β virtual voltage delayed $\pi/2$ rad from the current grid voltage to use an $\alpha\beta$ approach. It is also possible to use other concepts as the virtual power or Second Order Generalized Integrator (SOGI) PLLs as in [124, 125]. In [126] a comparison between different possibilities for the single-phase case is carried out.

  It is usual that the grid inductance is not entirely constituted by a imposed design value. For example, if a transformer is used, the grid

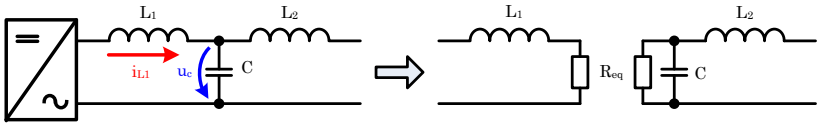

(a) Current control considering L_1 and u_c

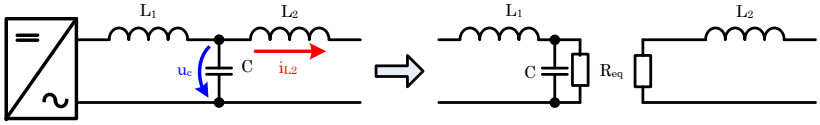

(b) Current control considering L_2 and u_c

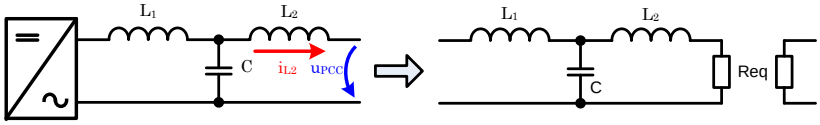

(c) Current control considering L_2 and u_{PCC}

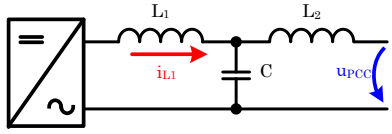

(d) Current control considering L_1 and u_{PCC}

Figure 2.21: Equivalent circuits from the point of view of the grid or the converter

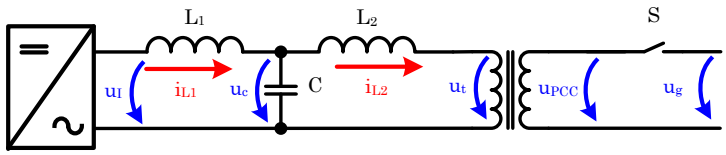

(a) L_2 is added

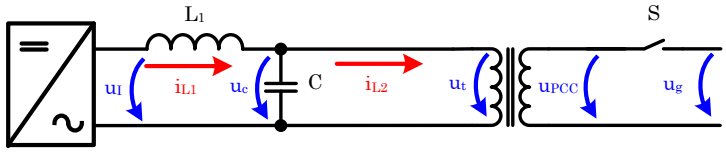

(b) L_2 is not added

Figure 2.22: Equivalent circuits when a transformer is considered

side inductance is split in the leakage inductance of the transformer and the parasitic inductance of the transportation or distribution cables. Depending on the voltage used for synchronization issues, the calculated angle by a PLL algorithm may be shifted or not.

The correct voltage to use is u_{PCC} or u_g corresponding to the point of connection with the grid, see Figure 2.22. However, it is also possible to synchronize the converter with the grid through u_t or u_c, as is shown in Figure 2.22(a). When the grid where the inverter is connected is a medium voltage grid, the voltage measure of u_g or u_{PCC} requires more expensive probes. In these cases the medium voltage transformers usually have lower impedance than in low voltage systems. Then, there is not high phase shifts between u_g and u_t. In these situations it is usual to use u_t for the synchronism.

In some cases, there is no need to use an external inductance L_2, as can be seen in Figure 2.22(b). Then, the leakage inductance of the transformer is considered as negligible. In this case, u_t and u_c are the same. Thus, it is possible to use u_c to synchronize the system with the grid. However, it is not the most suitable point due to the large voltage distortions that can appear.

The voltage control loop

In the case of a microgrid VSI, one of the possible operation modes is when the inverter is grid-disconnected operated. This situation forces the system

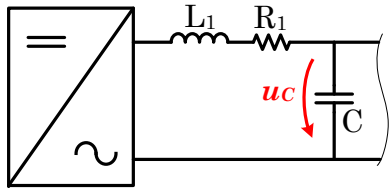

Figure 2.23: VC-VSI scheme

to operate self-generating its own voltage reference to continue supplying energy to any possible local load. The inverter has to operate as a VC-VSI controlling the output AC capacitor voltage u_C, as depicted in Figure 2.23.

To achieve this behaviour the literature contemplates two possibilities:

- V/f control. This strategy is focused on the control of the AC capacitors of a possible LCL-type coupling filter. These capacitors have to be sized for control purposes. The inverter handles the voltage and frequency of the capacitors implying that any other inverter can operate based on the same mechanism. This has to be taken into account when communication are not used to avoid non controlled circulating current between them. The worst case imply short-circuit operation. These inverters under V/f control have to be bidirectional if there are other inverters connected to the microgrid injecting current, as can be photovoltaic inverters. If the inverter has enough power, this technique is more practical due to its simple implementation compared with AC droop alternative. In [127–129] some examples are detailed.

- AC droop with secondary control. This control strategy is based on the concept of a non-ideal voltage reference emulating the behaviour of the synchronous generators. In [55, 130] can be seen some examples of this control methodology. However, a secondary control with low bandwidth communications is needed in order to operate various inverters in parallel under this control algorithm. This methodology has gained momentum during the last years [131–133].

As has been detailed in Chapter 2, the concept of Constant Voltage and Constant Frequency (CVCF) control based in a multi-inverter microgrid synchronization by using high precision GPS has been shown as an alternative to AC droop control.

Any of the aforementioned case implies a cascaded control where the inner current loop is managed by means of the voltage control loop. In this sense,

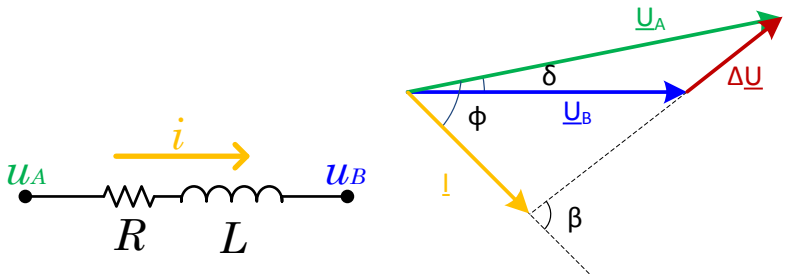

(a) Scheme of a RL impedance (b) Phasorial analysis

Figure 2.24: AC droop analysis

it should be ensured that the inner loop is faster than the output loop. This means that the inner frequency band is higher than the outer one, at least by a factor of two.

The power control loop

The power control loop has the aim of controlling the power exchanged between the VSI and the utility during the grid-connected mode. The referenced power can be translated into a current or into a voltage. GSI appliy a current according to the power set-point and the utility voltage. On the other hand, GSCI applies a voltage modifying the amplitude and the phase to follow the desired power set-point. Then, AC droop control is defined as:

- **Conventional AC droop control**. Its operation principles are obtained from the equations that describe, in steady-state, the power flow between two AC voltage sources or nodes (u_A and u_B) connected by a resistive-inductive line, as is shown in Figure 2.24. R and L represents the equivalent series resistance and inductance of the considered line, respectively.

  The droop control pretends to regulate VSI units with the same mechanisms that can be found in conventional utilities, introduced in Section 2.4. In this sense, there can be found three elemental control levels:

  - The primary AC droop control level. This control level is based on the primary regulation and concerns power reliability. Assuming a static-phasor analysis, if the inductive impedance is predominant (AC droop equations are fully developed in Appendix B,

where it has been considered the general resistive-inductive case and also the simplifications obtained for mainly inductive or resistive lines). When $X_L >> R$ and a small δ angle between u_A and u_B is considered, the active power can be obtained as

$$\delta \approx \frac{X_L}{U_A U_B} P \tag{2.14}$$

where U_A and U_B are the rms voltages at nodes A and B, respectively, X_L is the inductive line impedance and P is the active power transferred from A to B.

Reactive power can be computed as

$$U_A - U_B \approx \frac{X_L}{U_A} Q \tag{2.15}$$

where Q is the reactive power transferred from A to B. In AC droop control U_A is intended to be the AC capacitor voltage U_C and U_B the PCC voltage U_{PCC}, see Figure 2.18. Then, the active and reactive power transmission from the converter to the grid can be managed by controlling the magnitude and phase of the converter voltage by using the droop control law

$$\omega - \omega_0 = -m\,(P - P_0) \tag{2.16a}$$
$$U - U_0 = -n\,(Q - Q_0) \tag{2.16b}$$

where U_0 and ω_0 are the rated voltage and angular frequency of the grid, U and ω are the current values. P_0 and Q_0 are the active and reactive power set-points and P and Q are the current values. The parameters m and n are the slopes used in the AC droop control law. From Equation 2.16 it is possible to deduce a direct linear relationship between the voltages angle and active power, whereas the voltage difference depends on reactive power. Figure 2.25 shows this behaviour.

Note that Equation 2.16 can be applied with two objectives:

- If it is desired that a VSI behaves as a synchronous generator, the vertical axis (ω and U) of Figure 2.25 represents the input and the horizontal axis (P and Q) the output of

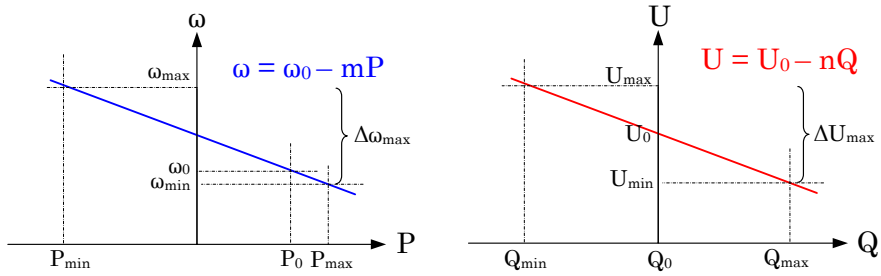

(a) Droop P-ω relationship

(b) Droop Q-U relationship

Figure 2.25: AC droop relationships under predominantly inductive lines

the controlled VSI units. In this sense, the VSI exchanges different apparent power according to the current frequency or voltage amplitude at the PCC. This output is the base for the inner current loop set-point.

- If it is desired that a VSI controls the exchanged power, the horizontal axis (P and Q) of Figure 2.25 represents the input and the vertical axis the output (ω and U) of the controlled VSI units. This output is the set-point for the inner voltage loop.

In [134, 135] can be found the development of the small-signal or quasistatic close-loop model for a connected and stand-alone microgrid VSI under the conventional AC droop control presented in Equation 2.16.

On the other hand, in a general case, the impedance of a microgrid will not be purely inductive. In fact, it is usual to consider a predominant resistive line for a microgrid case. A new relation, proposed in [66], can be obtained using a rotation matrix that takes into account the grid impedance as

$$\begin{pmatrix} P' \\ Q' \end{pmatrix} = \begin{pmatrix} \cos\varphi & -\sin\varphi \\ \sin\varphi & \cos\varphi \end{pmatrix} \begin{pmatrix} P \\ Q \end{pmatrix} = \begin{pmatrix} X_L/Z_L & -R/Z_L \\ R/Z_L & X_L/Z_L \end{pmatrix} \begin{pmatrix} P \\ Q \end{pmatrix} \tag{2.17}$$

where $\varphi = \pi/2 - \phi = \arctan(R/X_L)$ and $Z_L = |R + jX_L|$ is the line impedance value. Using this rotation matrix it is possible

to operate taking into account the same dependences of P' with ω and Q' with U. However, it should be remarked that for the general case, the relationship is obtained through the impedance described by

$$\delta \approx \frac{Z_L}{U_A U_B} P' \tag{2.18a}$$

$$U_A - U_B \approx \frac{Z_L}{U_A} Q' \tag{2.18b}$$

- The secondary AC droop control level. This control level is based on the secondary regulation and concerns power quality. One of the relevant objectives of primary control was to allow operating in parallel several inverters without the use of high bandwidth communications. According to the configured m and n proportional gains of Equation 2.16 it is possible to manage multiple inverters without communications. If all installed inverters have the same droop characteristics, they will operate, theoretically, sharing the same amount of power. However, according to the voltage and current probes error of each inverter and each individual output line impedance it is possible that the system is not being operated at the expected rated values. Then, it is possible that new P_0-Q_0 set-points differ sufficient from current P-Q values to provoke a non acceptable constant operation displacement.

  A secondary control is used for restoration purposes. The voltage and frequency set-points are generated according to a centralized reference, as depicted in Figure 2.26. The restoration is achieved by the use of low bandwidth communications. In a pessimistic case where communications are lost, when the primary control is based on a VC-VSI, the inverter will operate according to maximum/minimum implemented saturation values of the angular frequency and voltage amplitude.

  As it is necessary to contemplate two operation modes:

  - In grid-connected operation, the ${u_{PCC}}^*$ and ${\omega_{PCC}}^*$ references are obtained from a tertiary hierarchical control.
  - In grid-disconnected operation, the value is a pre-configured rated ${u_{PCC}}^*$ and ${\omega_{PCC}}^*$ of the grid.

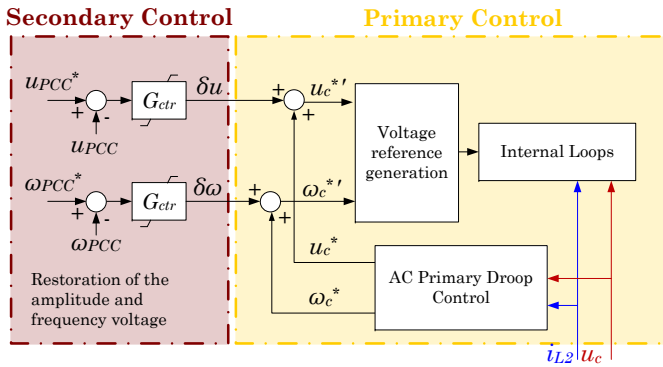

Figure 2.26: Secondary AC droop control

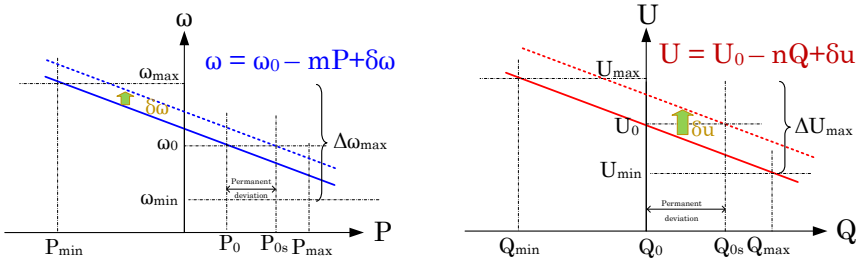

(a) Droop P-ω relationship

(b) Droop Q-U relationship

Figure 2.27: Secondary AC droop relationships under predominantly inductive lines

In both cases, what is obtained is a variation δ_u and δ_ω that implies the vertical displacement of the primary drops selected, as is depicted in Figure 2.27.

- The Tertiary AC droop control level. This control level is based on the tertiary regulation and concerns economics. The tertiary control only operates in grid-connected mode and aggregates the apparent power exchanged at a certain grid point. With this aggregated value, the DSO computes which are the optimal centralized P_g^* and Q_g^* values for the microgrid. Figure 2.28 represents the tertiary control level.

- **AC droop control based on dynamic phasors**. It should be

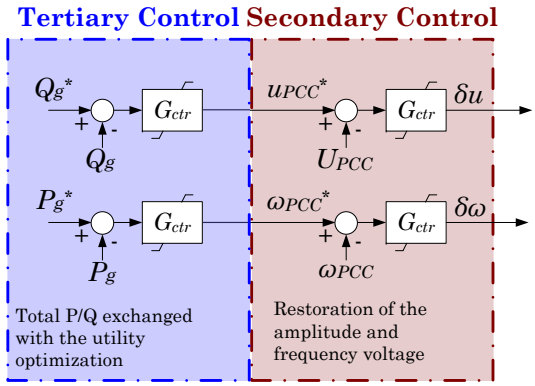

Figure 2.28: Tertiary AC droop control

highlighted that the previously exposed conventional AC droop control law is valid for the steady state and quasistationay state, i.e. for small changes over an equilibrium point varying slowly (no high dynamic behaviours). In fact, Equations 2.14 to 2.18 are based on a small-signal quasistatic model. In [66] it is indicated that for high droop constants, related with high dynamics in VSI operation, the quasistatic model is no longer useful. The use of dynamic phasors or time-varying phasors [136, 137] can be adopted.

A dynamic phasor can be considered as a phasor in which all the parameters are time-varying. For example, when a sinusoidal wave $f(t)$ with a predominant fundamental angular frequency ω is described by

$$f(t) = F(t)\cos(\omega t + \varphi(t)) \tag{2.19}$$

where $F(t)$ is a time-varying amplitude and $\varphi(t)$ is a time-varying phase. Then, the general definition of dynamic or time-varying phasor over a quasi-periodic signal $x(\tau)$ is based on the averaging theory when time-varying Fourier coefficients are considered [138–140]. The time-domain waveform $x(\tau)$ can be represented in the time-moving interval $\tau \in (t - T, t]$ by

$$x(\tau) = \sum_{k=-\infty}^{\infty} X_k(t) e^{jk\omega\tau} \tag{2.20}$$

where $\omega = 2\pi/T$ and $X_k(t)$ are the complex time-varying Fourier coefficients also referred as dynamic phasor. It should be highlighted that the waveform of $x(\tau)$ is seen as periodic for the considered current interval under study. The kth coefficient of a dynamic phasor at time t is determined by the average operation

$$X_k(t) = \langle x \rangle_k = \frac{1}{T} \int_{t-T}^{t} x(\tau) e^{jk\omega\tau} d\tau \tag{2.21}$$

Note that k is the dynamic phasor harmonic component, i.e. when k is zero represents constant signals or when is one the fundamental component and $\langle x \rangle_k = \langle x \rangle_k(t)$. Three key properties should be introduced for dynamic phasors:

- Phasor properties of the derivative of kth coefficient

$$\frac{d\langle x \rangle_k}{dt} = \langle \frac{dx}{dt} \rangle_k - jk\omega \langle x \rangle_k \tag{2.22}$$

- Phasor properties of a product in the time-domain (convolution of the corresponding dynamic phasors)

$$\langle x(t)y(t) \rangle_k = \sum_{m=-\infty}^{\infty} \langle x \rangle_{k-m} \langle y \rangle_m = (X_k(t) * Y_k(t))[k] \tag{2.23}$$

- Phasor properties of the complex-conjugate term

$$\langle x \rangle_{-k} = \langle x \rangle_k^* \tag{2.24}$$

Then, Equation 2.22 can be used to analyse a resistive-inductive line differential equation

$$u_A(t) - u_B(t) = Ri(t) + L\frac{di(t)}{dt} \tag{2.25}$$

from a dynamic phasor perspective. Applying Equation 2.22 to Equation 2.25

$$\langle u_{AB}(t) \rangle_k = R\langle i(t) \rangle_k + L\langle \frac{di(t)}{dt} \rangle_k = R\langle i(t) \rangle_k + L\frac{d\langle i(t) \rangle_k}{dt} + j\omega L\langle i(t) \rangle_k \tag{2.26}$$

is obtained. Hereinafter, if not subscript is explicitly written it is only considered fundamental component for simplicity. In this sense, Equation 2.26 becomes

$$U_{AB}(t) = RI(t) + L\frac{d}{dt}I(t) + j\omega I(t) \tag{2.27}$$

The instantaneous active power of a system is described by

$$p(t) = u(t)i(t) \tag{2.28}$$

but also can be described in terms of dynamic phasors [141]. The average power corresponds to the power 0-phasor

$$\langle p(t)\rangle_0 = \langle u(t)i(t)\rangle_0 = \sum_{m=-\infty}^{\infty} \langle u\rangle_m \langle i\rangle_{-m} \tag{2.29}$$

Applying the conjugate property shown in Equation 2.24

$$\langle p(t)\rangle_0 = \sum_{m=-\infty}^{\infty} \langle u\rangle_m \langle i\rangle_m^* \tag{2.30}$$

and with some rearrangement

$$\langle p(t)\rangle_0 = \left(\langle u\rangle_0\langle i\rangle_0 + \sum_{m=1}^{\infty}\langle u\rangle_m\langle i\rangle_m^*\right) + \left(\langle u\rangle_0\langle i\rangle_0 + \sum_{m=1}^{\infty}\langle u\rangle_m^*\langle i\rangle_m\right) \tag{2.31}$$

Then, $\langle p(t)\rangle_0$ can be expressed in terms of the apparent or average complex power

$$\langle p(t)\rangle_0 = \frac{1}{2}\left(S + S^*\right) \tag{2.32}$$

As indicated by Equation 2.23, the dynamic phasor of two time functions equals the discrete convolution. Then, if the dynamic analysis is conducted in the Laplace's s-domain, the convolution becomes the product. Then, when the apparent power is computed using the conjugate property shown in Equation 2.24

$$S(s) = U(s)I^*(s) \tag{2.33}$$

it can be deduced from Equation 2.33 that

$$I^*(s) = \frac{U_{AB}(s)}{R - j\omega L + sL} \tag{2.34}$$

The average active and reactive power should be calculated to control them individually. However, if the amplitude and phase of each magnitude are time-varying, the analysis becomes complex. As an approach, it is assumed that the dynamics is represented by the term

$$R - j\omega L + sL \tag{2.35}$$

In this sense, the current and voltage phasors are considered, hereinafter, static average rms phasors. Considering $\theta_{U_B} = 0$ and $\theta_{U_A} = \delta$, the apparent power can be computed in the s-domain as

$$S(s) = \frac{\left(U_A U_B \cos\delta - {U_B}^2 - jU_A U_B \sin\delta\right)(R + sL + j\omega L)}{(R + sL - j\omega L)(R + sL + j\omega L)} \tag{2.36}$$

If the real and imaginary part of Equation 2.36 are collected separately, considering a small δ angle,

$$P(s) = \overbrace{\frac{(U_A U_B)\,\omega L}{(R + sL)^2 + (\omega L)^2}}^{G_1}\delta + \overbrace{\frac{U_B\,(R + sL)}{(R + sL)^2 + (\omega L)^2}}^{G_2}(U_A - U_B) \tag{2.37a}$$

$$Q(s) = \overbrace{\frac{-\,(U_A U_B)\,(R + sL)}{(R + sL)^2 + (\omega L)^2}}^{G_3}\delta + \overbrace{\frac{U_B \omega L}{(R + sL)^2 + (\omega L)^2}}^{G_4}(U_A - U_B) \tag{2.37b}$$

Now, the real and imaginary part of Equation 2.37 are linearised by the first Taylor's term as has been done for the quasi-static case in [134,

135]. Some authors applies this same idea on dynamic phasors [66,142, 143]. Then, assuming an inductive line, small δ angle and $U_A \approx U_B$,

$$\Delta P \approx \frac{{U_A}^2 \omega L}{(R+sL)^2 + (\omega L)^2} \Delta\delta \tag{2.38a}$$

$$\Delta Q \approx \frac{U_A \omega L}{(R+sL)^2 + (\omega L)^2} \Delta U_A \tag{2.38b}$$

or for a resistive line

$$\Delta P \approx \frac{U_A (R+sL)}{(R+sL)^2 + (\omega L)^2} \Delta U_A \tag{2.39a}$$

$$\Delta Q \approx \frac{-U_A^2 (R+sL)}{(R+sL)^2 + (\omega L)^2} \Delta\delta \tag{2.39b}$$

where ΔX represents the difference between the operating point of a certain X magnitude and the considered equilibrium point X_e. A more detailed development is done in Appendix B.

The dynamic model for a predominant inductive case when $P_e = 0$, $Q_e = 0$, $\delta_e = 0$ and $U_{A_e} = U_B$ is defined by

$$P \approx \frac{{U_A}^2 \omega L}{(R+sL)^2 + (\omega L)^2} (\theta_{U_1} - \theta_{U_2}) \tag{2.40a}$$

$$Q \approx \frac{U_A \omega L}{(R+sL)^2 + (\omega L)^2} (U_A - U_B) \tag{2.40b}$$

and for the predominant resistive line model it can be deduced

$$P \approx \frac{U_A (R+sL)}{(R+sL)^2 + (\omega L)^2} (U_A - U_B) \tag{2.41a}$$

$$Q \approx -\frac{U_A^2 (R+sL)}{(R+sL)^2 + (\omega L)^2} (\theta_{U_1} - \theta_{U_2}) \tag{2.41b}$$

Figure 2.29 and Figure 2.30 shows the block diagram that describe the small-signal close-loop for the inductive and resistive cases, respectively. The transfer function G_{ctrl} represents the controller that

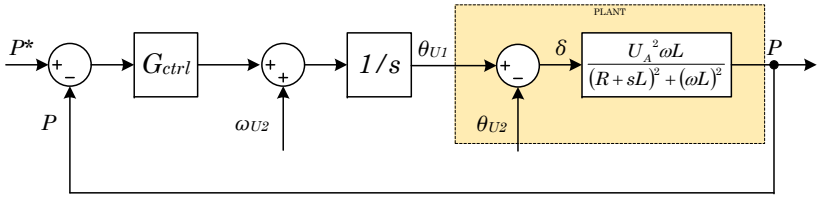

(a) Active power close loop system

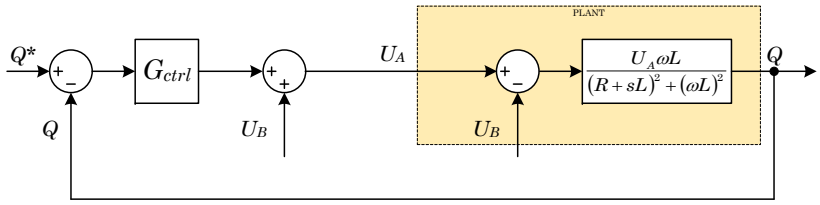

(b) Reactive power close loop system

Figure 2.29: Power small-signal close loop systems under a dynamic phasor model for the inductive line case

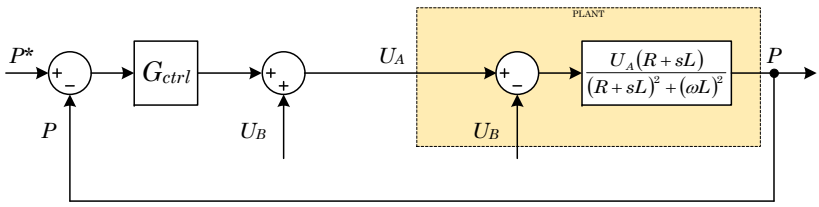

(a) Active power close loop system

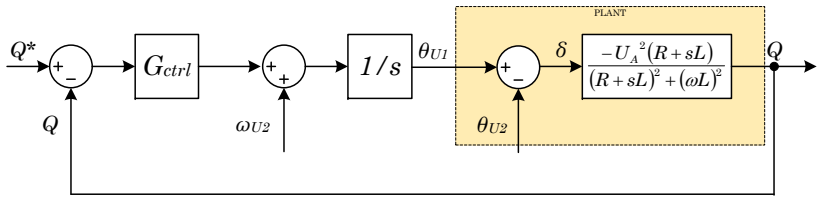

(b) Reactive power close loop system

Figure 2.30: Power small-signal close loop systems under a dynamic phasor model for the resistive line case

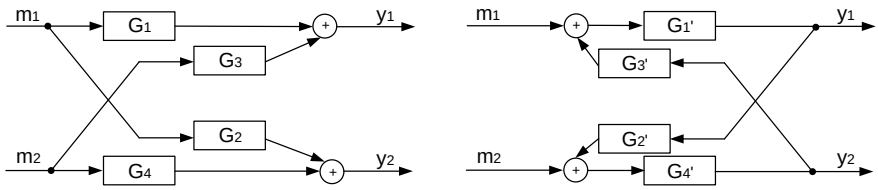

(a) Input-output coupling present in the dynamic phasor PQ transference model

(b) Output-input coupling equivalent model

Figure 2.31: PQ coupling models

can be composed by only proportional gains or more sophisticated controllers.

In a general case where there is not a predominance of a resistive or inductive behaviour $P = P(\delta, U_A)$ and $Q = Q(\delta, U_A)$. The same is applicable to the difference or derivative terms of P and Q if the equilibrium point is different from the proposed one. Then, the system is input-output coupled, as depicted in Figure 2.31(a). Transfer functions G_1 to G_4 have been previously defined in Equation 2.37, $m_1 - m_2$ represent the control actions and $y_1 - y_2$ the outputs, i.e. P and Q.

This coupling will imply a physical and complex decoupling if the plant wants to be analysed as a Single-Input Single-Output (SISO) system for simplicity. From Figure 2.31(a) can be deduced that

$$m_1 G_1 + m_2 G_3 = y_1 \tag{2.42a}$$
$$m_2 G_4 + m_1 G_2 = y_2 \tag{2.42b}$$

To be able to decouple the system it is necessary to transform the input-output coupled system shown in Figure 2.31(a) into an output-input equivalent coupled system shown in Figure 2.31(b). In this last case,

$$(m_1 + y_2 G_3')G_1' = y_1 \tag{2.43a}$$
$$(m_2 + y_1 G_2')G_4' = y_2 \tag{2.43b}$$

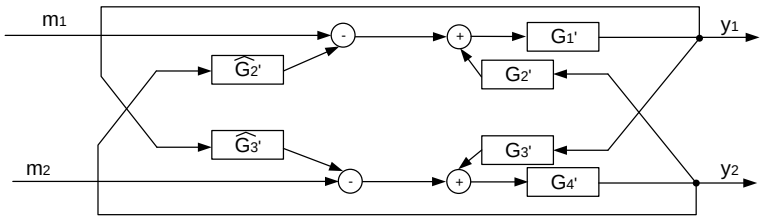

Figure 2.32: Decoupling equivalent PQ proposal

Then, using the rotation matrix defined by Equation 2.17 and considering Equations 2.42 to 2.43 it is possible to find a relationship between them defined by

$$G_1' = \frac{G_1G_4 - G_2G_3}{G_4} = \frac{U_A^2}{L\cos(\phi)s + L\sin(\phi)\omega + R\cos(\phi)} \tag{2.44a}$$

$$G_2' = \frac{G_2}{G_1G_4 - G_2G_3} = \frac{L\sin(\phi)s - L\cos(\phi)\omega + R\sin(\phi)}{U_A^2} \tag{2.44b}$$

$$G_3' = \frac{G_3}{G_1G_4 - G_2G_3} = -\frac{L\sin(\phi)s - L\cos(\phi)\omega + R\sin(\phi)}{U_A} \tag{2.44c}$$

$$G_4' = \frac{G_1G_4 - G_2G_3}{G_1} = \frac{U_A}{L\cos(\phi)s + L\sin(\phi)\omega + R\cos(\phi)} \tag{2.44d}$$

being able to decouple the system by using $\hat{G_2}'$ and $\hat{G_3}'$ estimations of G_2' and G_3' , respectively, as is shown in Figure 2.32.

It should be noticed that to decouple the system, derivative terms would be computed because G_2' and G_3' consists in transfer functions with zeros. This option results in noise excitation when it is implemented in discrete-time due to those derivative terms. Consequently, this alternative is rejected. The rotation matrix of Equation 2.17 results appropiate if the system is clearly resistive or inductive.

2.6 The transference between operation modes

A microgrid VSI has to operate in grid-connected and in grid-disconnected modes, as has been mentioned previously. Independently of the type of inverter, i.e. GSI, GCI or GSCI, the angle of the external reference should be computed. Without this angle is not possible to manage the power factor

of the exchanged power. Also, the operation from one mode to the other one should be performed as smooth as possible ensuring the integrity of any load connected at the PCC.

2.6.1 The synchronism algorithm

In case of VSI that interact with the grid, the used reference is the grid angle that is obtained using PLL algorithms. This angle is employed to manage the power factor of the current that the inverter is delivering to the utility. Thus, the distortion level of the utility, in terms of unbalances, voltage transients or harmonic components, affects the accuracy of the obtained grid angle used for control purposes [144]. However, many authors focus the PLL system to operate the inverter only in grid-connected or in grid-disconnected. In case of a microgrid, the operation of the converter can require a PLL that includes more functional modes than the conventional one. Figure 2.33 illustrates a microgrid PLL algorithm proposal for a three-phase three-wire VSI using a SRRF. It is based on Park transform to obtain the operation angle θ:

- Mode 0: PLL is synchronized with the grid. Phase-to-phase voltages ($u_{PCC_{uv}}$ and $u_{PCC_{vw}}$) are monitored. The outputs of the PLL are the grid frequency f_{PCC}, the grid angle θ_{PCC} and the direct and quadrature voltages $u_{PCC_{dq}}$, respectively.

- Mode 1: output angle is self-generated. The desired frequency is the input of an inner integrator that is used to obtain the angle θ_C to be used on inner control loops, i.e. voltage or current loops. In Figure 2.33, a frequency value of 50 Hz is used.

- Mode 2: for reconnection purposes, the output voltage angle is self-generated, but synchronized with the grid. A PI controller compares θ_{PCC} with the current locally used angle (θ_R) obtaining a differential frequency Δf. This Δf is added to f_{PCC} to speed-up or down this frequency and synchronize the θ_R with θ_{PCC}.

The same scheme can be extrapolated to other single-phase or three-phase PLL strategies and reference frames.

2.6.2 Pattern for transient thresholds

The interconnection between the microgrid and the grid is carried out downstream of the PCC. Thus, the microgrid and, consequently, the inverter(s)

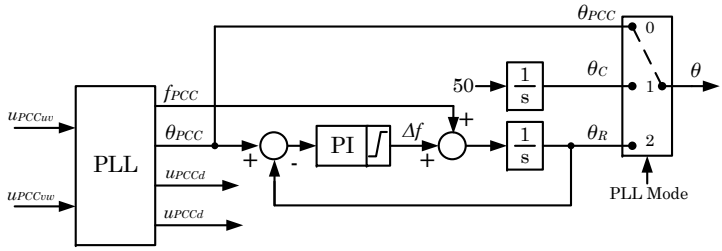

Figure 2.33: PLL proposal for microgrids

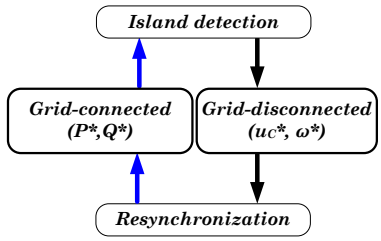

Figure 2.34: Microgrid modes and transitions states simplified scheme

that operate the microgrid can be considered as a single entity by the grid. In this sense, there exists the two operation configurations presented in Section 2.1; grid-tied and grid-isolated. When the microgrid is grid-tied it is possible to define two operation modes: grid-connected and grid-disconnected. The proper comprehension of the transients between operation modes comes from the consideration of the different control strategies defined in Section 2.2: GSI, GCI and GSCI.

When the inverter or the smart main breaker detects the mains loss, the microgrid can be disconnected from the grid and it starts to operate in grid-disconnected mode. One of the transfer key points from grid-connected to grid-disconnected is the detection strategy and the clearing time. Essentially, when an inverter operates in grid-connected it manages power and in grid-disconnected voltage and frequency, as can be seen in Figure 2.34.

In order to provide a pattern to analyse how abrupt is the transference between both configurations, the ITI curve is presented. The ITI curve [145] is a modified version of the CBEMA power acceptability curve with an expanded acceptable power area. It maintains the same idea developed by the working group of the CBEMA, which later changed its name to the Information Technology Industry Council (ITI) in 1994. The ITI curve limits are described in Figure 2.35.

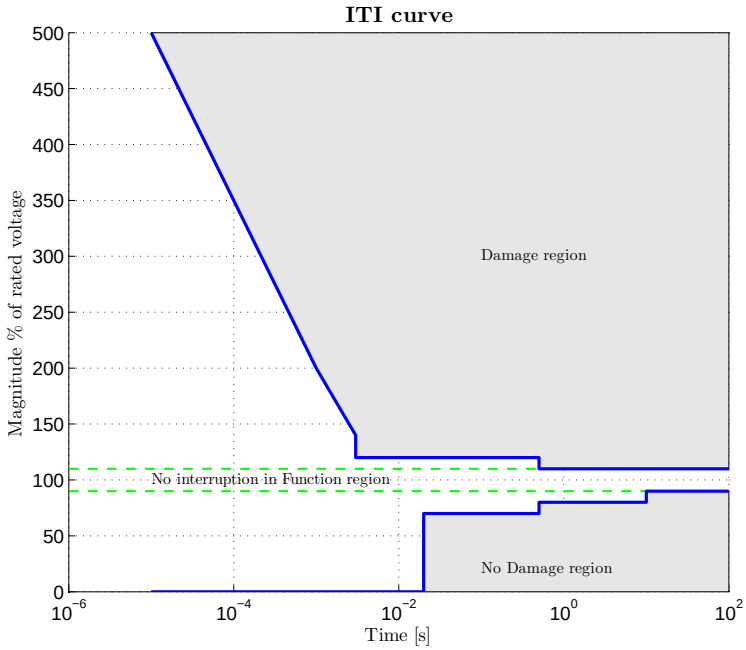

Figure 2.35: The ITI curve limits

The ITI curve was created in collaboration with EPRI's Power Electronics Application Center (PEAC). This curve allows to reflect the performance of typical single-phase, 120 V, 60 Hz computers and their peripherals and other information technologies. Thus, ITI curve is easier to design and implement than CBEMA because of the simplified way that the different regions are represented. It is widely used as a reference to define the withstand capability of various loads and devices for protection taking into account the power quality. However, it is important to consider that the ITI curve is not intended to reflect the performance of all electronic-based devices.

Although this curve was defined for informatics uses supplied by 120 V-60 Hz it has been also applied to 230 V-50 Hz and any kind of devices according to [146, 147]. But, in the preliminary study presented in [146] the results show that equipment connected to Australian 230 V grids has sag immunity considerably greater than that defined by the ITI curve. It concludes that it is highly questionable its application on 230 V devices. Despite of what is detailed in [146], this thesis will consider the 230 V-50 Hz extension of the ITI curve as a pattern to verify the correct operation when a microgrid transient occurs.

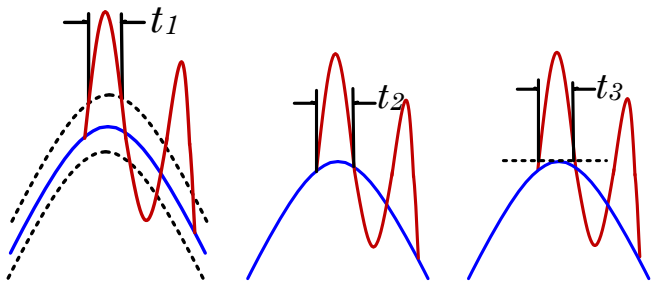

(a) By threshold (b) Difference with the rated wave (c) Difference with the peak value

Figure 2.36: Criteria to define the transient duration. Non abnormal waveform (blue), abnormal value (red), thresholds (dashed)

In [148] is mentioned that one of the important points to be defined when ITI curve is used is the criteria to define the duration of a transient. Figure 2.36 shows different ways to compute the time duration when a transient is detected. In fact, the ITI curve presented in Figure 2.35 only defines transients when they occur close to the peak value. In this sense, is it possible to separate the ITI curve into three regions: instantaneous region ($f > 5$ kHz), transients ($200 < f < 5000$ Hz) and steady state ($f < 200$ Hz). In case of steady state region the rms value needs to be computed.

2.6.3 The anti-islanding challenge over GCI or GSCI

Many anti-islanding regulations, for example, the ones cited in Section 2.1, require that when the grid is lost (grid-disconnected mode), the inverter has to be disconnected in a stipulated time, avoiding the creation of electrical islands. For this reason results essential to analyse the effect of the different anti-islanding mechanisms under GSI and GSCI or GCI behaviours.

The inherent behaviour as CC-VSI or VC-VSI can affect to the effectiveness of the chosen anti-islanding method. An analysis of algorithms is conducted ins this section, resulting into the publication of [49] and summarised in the next lines.

The GSCI and GSI

Anti-islanding methods were developed to operate when GSI are employed. To understand the interactions between the control loops and the anti-

islanding methods it is necessary to remind the key differences between VC-VSI and CC-VSI.

The CC-VSI operates as a current source, as is described in Figure 2.37(a), where it is shown that the apparent power set-point is translated into the controlled current i_L. Then, in this case the power is controlled by means of i_L.

On the other hand, a VC-VSI behaves as a voltage source. In this case the power is controlled by means of the voltage u_C.

The characterisation of the called resonant load is crucial. Both Figures 2.37(a) and 2.37(b) show an inverter connected to the grid with a resonant load connected at the PCC. As has been introduced in Section 2.3.2, this resonant load is used to emulate an aggregation of possible connected local loads with particular features that constituted by a resistance in parallel with an inductance and a capacitance. It should be noticed that when the load is under resonance there is not reactive consumption and the active power consumed suits with the delivered one. However, it results useful to redefine the concept of resonant local load to generalize the anti-islanding detection for all cases; GSI, GCI and GSCI. The resonant load aim is to be the worse scenario for the anti-islanding methods based on voltage and frequency displacements. It takes place when the power flow through the PCC, both active and reactive, is close to zero. Therefore, hereinafter, the concept of zero or non-zero power flow used refers to the resonant condition.

Considering this resonant load definition passive methods and positive feedback, introduced in Section 2.3, methods are discussed when the inverter acts as GSCI, i.e. as VC-VSI:

- Passive methods. If using VC-VSI, the voltage loop makes more difficult the islanding detection, also when the PCC power flow is non zero. When the utility is off, the voltage u_{PCC} is not released, see Figure 2.18. This voltage leaves from being determined by the grid to be conditioned. This is because when grid-disconnected, the grid inertia is released and u_{PCC} becomes indirectly managed by the inverter. The AC capacitor voltage u_C and u_{PCC} are connected only through the output coupling impedance constituted by the inductance L_2 and its equivalent series resistance R_2, that usually are small.

  Although the power flow is suddenly interrupted during a transition from grid-connected to grid-disconnected and this affects on the droop control actions, these effects result slow due to its implicit dynamic behaviour. It should be reminded that the droop control strategy is based on the emulation of the behaviour of synchronous generators

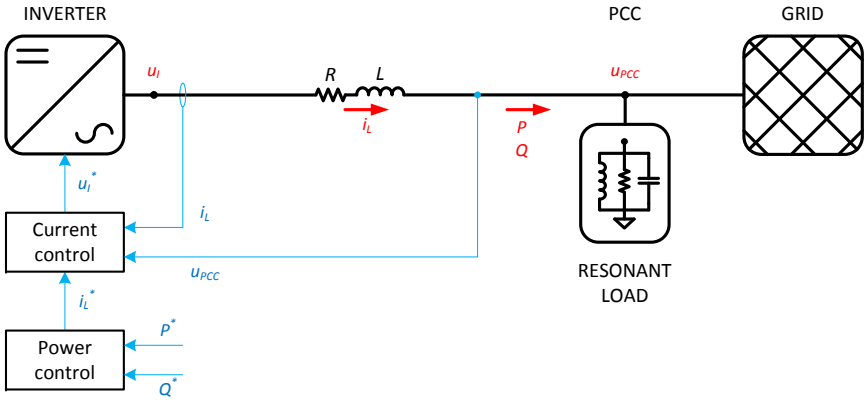

(a) GSI

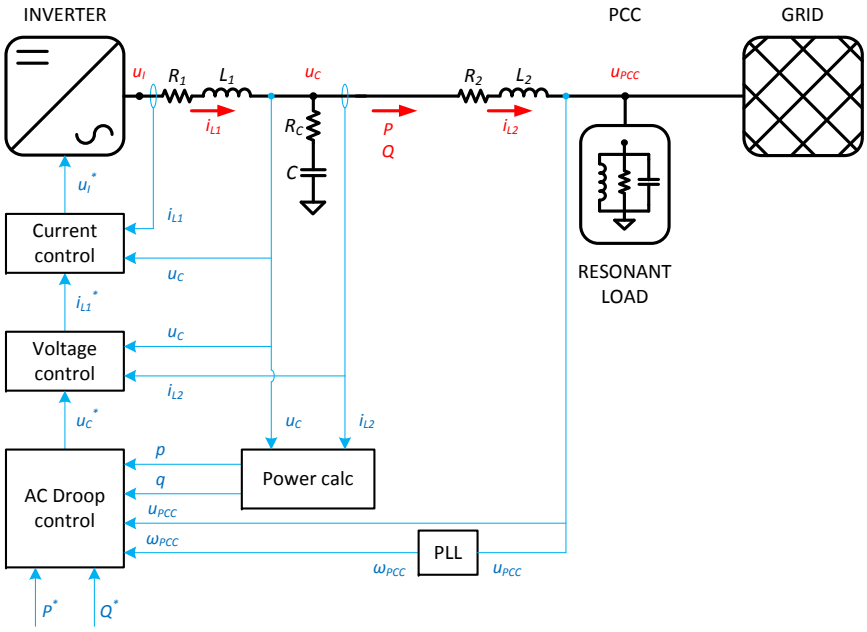

(b) GSCI

Figure 2.37: GSI and GSCI schemes in grid-connected mode when a resonant local load is connected at the PCC

that have big mechanical inertias. In this sense, droop control laws usually includes first order filters for the error calculation whose time constants depends on the power of the inverter. Thus, the not enough dynamic time response in conjunction with the saturation of the droop control actions (voltage amplitude and phase), due to integrity reasons, makes passive methods a non suitable strategy.

- Positive Feedback Active Methods. All active methods base their different detection mechanisms in the perturbation of some of the controlled magnitude parameters. There exists a concrete strategy when active anti-islanding methods are used named positive feedback. Basically, this methods try to make unstable a controlled variable.

  It is usual to define the resonant loads in terms of the quality factor q and the resonant angular frequency ω_r

$$\begin{aligned} q_f &= R_{RL}\sqrt{\frac{C_{RL}}{L_{RL}}} = \frac{\sqrt{|Q_{L_{RL}}||Q_{C_{RL}}|}}{P_{RL}} \\ \omega_r &= \frac{1}{\sqrt{L_{RL}C_{RL}}} \end{aligned} \tag{2.45}$$

  where R_{RL}, L_{RL} and C_{RL} are the resistance, the inductance and the capacitor that constitute the resonant load itself. Besides, $Q_{L_{RL}}$ is the reactive power of the inductive aggregated component, $Q_{C_{RL}}$ the reactive power of the capacitive one and P_{RL} the active power of the resistive one. Then, the resonant load impedance and phase can be expressed as

$$\vec{Z}_{RL} = R_{RL}\frac{1}{1 + j\left(\frac{\omega}{\omega_r} - \frac{\omega_r}{\omega}\right)} \tag{2.46a}$$

$$|\vec{Z}_{RL}| = \frac{R_{RL}}{\sqrt{1 + q_f^2\left(\frac{\omega}{\omega_r} - \frac{\omega_r}{\omega}\right)^2}} \tag{2.46b}$$

$$\theta_{RL} = \arctan\left(-q\left(\frac{\omega}{\omega_r} - \frac{\omega_r}{\omega}\right)\right) \tag{2.46c}$$

  being ω the angular frequency at the PCC. When the inverter goes from grid-connected to grid-disconnected, the power consumption of the resonant load is directly related with the behaviour of the PCC

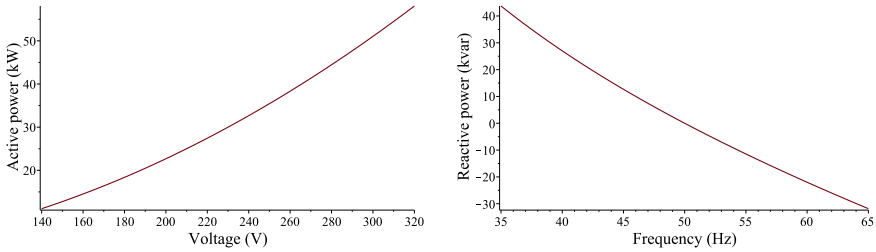

(a) Active power versus voltage. (b) Reactive power versus frequency.

Figure 2.38: Relationship between the power and the voltage of a 30 kW resonant load, 230 V and quality factor $q = 2$.

voltage and frequency. Figure 2.38 shows an example of the dependency of the active power with the voltage and the reactive power with frequency, based on

$$P_{RL} = U_{PCC}^2 \frac{1}{R_{RL}} \tag{2.47a}$$

$$Q_{RL} = U_{PCC}^2 \left(\frac{1}{\omega L_{RL}} - \omega C_{RL} \right) \tag{2.47b}$$

where Q_{RL} is the reactive power at PCC of the resonant load inductive or capacitive component. Also, from the quality factor definition in Equation 2.45 and the module $|\vec{Z}_{RL}|$ in Equation 2.46 it can be deduced that the higher the quality factor is, the narrower the closest region to the resonant frequency. This fact implies that it can be easier to detect the island situation because a little displacement in frequency supposes a high variation in terms of $|\vec{Z}_{RL}|$. However, the considered regulations recommends a quality factor between 1 and 2 [16–18].

The three active methods based on the positive feedback strategy are called Sandia Voltage Shift (SVS), Sandia Frequency Shift (SFS), and Slip Mode frequency Shift (SMS):

- SVS. The difference between the voltage at the PCC and the nominal voltage is added to the active power reference amplified by a k_u gain, as described in Figure 2.39(a). Therefore, while the utility is connected, the voltage error is small and will have a null average value. Thus, it does not affect significantly to the

power reference. But when grid-disconnected, positive/negative little voltage mismatches increase/decrease the active power reference. For the next iterations, the voltage error at the PCC will increase/decrease more, see Figure 2.38(a), producing a positive feedback non stable situation.

- SFS. The difference between the frequency at the PCC and nominal frequencies is added to the reactive power reference amplified by a $-k_\omega$ gain, as described in Figure 2.39(b). In this case, while grid-connected, the frequency error is small and will have a null average value, too. Again, it does not affect significantly to the reactive power reference. But, when grid-disconnected, positive/negative frequency increments decrease/increase the reactive power reference that, in the next iteration, will increase/decrease more the PCC frequency, see Figure 2.38(b). As a result, a positive feedback non stable situation for the frequency occurs.
- SMS tries to destabilise the inverter by changing the frequency. It is based on the phase characteristic of the resonant load. A perturbation on the current injected phase is added according to

$$\theta_{SMS} = \theta_m \sin\left(\frac{\pi}{2}\frac{f - f_r}{f_m - f_r}\right) \tag{2.48}$$

where θ_{SMS} is the phase of the referenced current and θ_m and f_m are the SMS parameters that represent the maximum phase displacement and the particular frequency. Representing Equations 2.46c and 2.48, under grid-connected mode, the utility holds the frequency closed to its fundamental value. Per contra, when the inverter is grid-disconnected, it results an unstable equilibrium point and the frequency is forced to move out from the NDZ (vertical dashed line), detecting the islanding status, as described in Figure 2.40.

The values of the k_ω and k_u gains used by SFS and SVS are significantly different when these methods are applied to GSI (CC-VSI) or GCI-GSCI (VC-VSI). However, the higher the value of the k_ω and k_u gains the higher the perturbation when grid-connected. This will impact on quality indices and may conflict with grid regulations producing that the method could not be applied in a certified installation. Nonetheless, a compatibility problem with the aforementioned positive feedback methods is presented when they

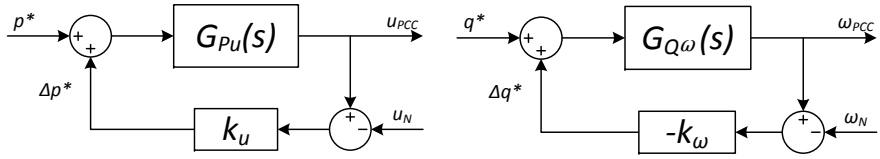

(a) Positive feedback based on voltage error (SVS).

(b) Positive feedback based on angular frequency error (SFS).

Figure 2.39: Positive feedback diagrams.

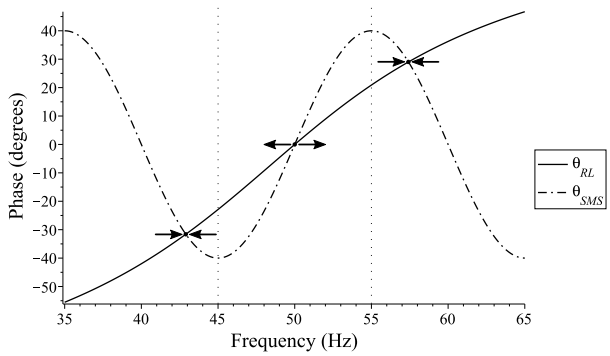

Figure 2.40: SMS perturbation phase with $f_m = 55$ Hz and $\theta_m = 40°$.

Paramater	Value	Units
Current loop settling time	2	ms
Voltage loop settling time	10	ms
Power loop (droop) settling time	8	s
$L1$	250	μH
R_1	50	mΩ
C	350	μF
R_C	0.2	Ω
$L2$	70	μH
R_2	0.25	Ω

Table 2.5: Control and hardware considered parameters for anti-islanding comparison under different control strategies (GSI or GSCI)

are implemented on inverters that operate under droop control. It should be reminded that the droop control strategy is based on a nested loop that controls the active and reactive power through handling the module and phase of the voltage at the AC capacitor u_C. Nevertheless, for its proper operation, the droop control based on grid-connected operation needs the grid to hold the voltage of the PCC (module and phase). In grid-connected mode, the AC droop manages the power flow thanks to the differences of module and phase between the voltages of both nodes where it is applied.

When the inverter operates in grid-disconnected mode, the droop control presents difficulties to modify the power that it injects. When the control loop tries to alter the capacitor voltage (module and phase) in order to modify the power flow, the PCC voltage follows its displacement. This is because the grid it is not fixing the electrical magnitudes any more. This fact is translated to extremely high positive feedback gains to observe the mains loss within tolerable clearance times.

In this sense, Figures 2.41 and 2.42 represent the islanding detection time versus the utility frequency for different k_ω gains for a GSI and a GSCI. For the comparison it is considered a three-phase VSI. The inverter delivers 30 kW per phase to a 230 V-50 Hz grid with a 30 kW resonant local load assuming a quality factor $q_f = 2$. The inner dynamics are set equally. In this sense, Table 2.5 summarises the considered parameters for the comparison.

It can be observed in Figure 2.41 that when the frequency of the grid is close to 50 Hz, the detection becomes slower because of the small error of the positive feedback loop. However, the islanding detection is faster enough to ensure the accomplishment of standards thresholds detailed in Table 2.3.2

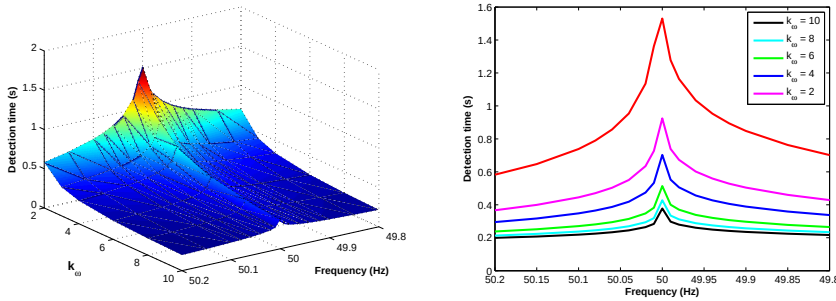

(a) (b)

Figure 2.41: Detection time of the SFS applied to a GSI.

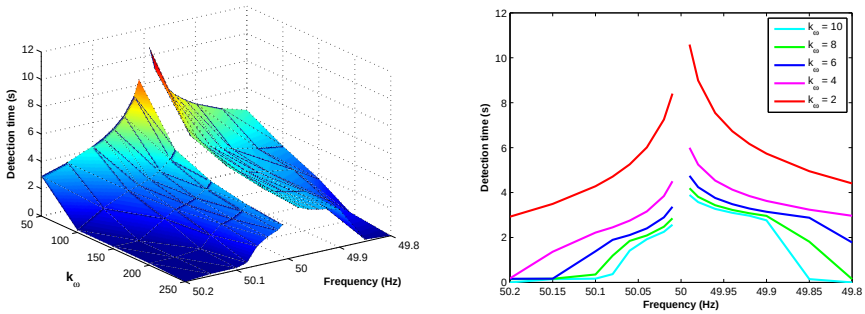

(a) (b)

Figure 2.42: Detection time of the SFS applied to a GSCI.

and 2.2. In contrast, in Figure 2.42 can be noted that the response for a GSCI implies higher amplifying gains to achieve acceptable detection times. Sometimes are not enough to guarantee the aforementioned threshold times. These high amplifier factors will produce non-suitable disturbances.

On the other hand, SMS is not useful for VC-VSI. It is highly sensible with the resonant load quality factor, due to the dependence with its phase.

Taking into account the ineffectiveness of the anti-islanding methods based on the voltage and frequency displacements operating with GSCI, it is necessary to consider other possible active methods. In [49] can be seen that impedance measurement methods are a good alternative to the detection methods based on voltage and frequency displacements.

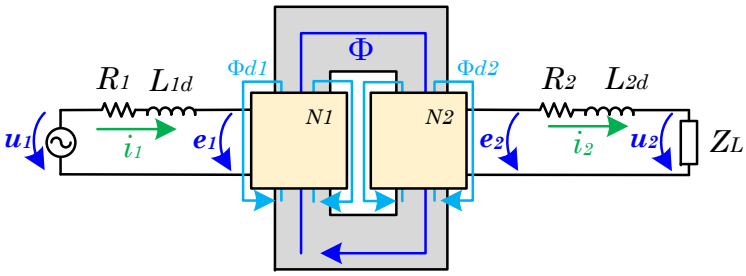

Figure 2.43: Scheme of a single-phase transformer with load scheme connected at the secondary winding

2.7 Galvanic isolation in AC microgrids

2.7.1 Introduction

As has been detailed in Section 2.4, different challenges as reactive power injection, frequency variation, inrush current under black-start, zero-sequence managing or parallel operation have to be considered in microgrid VSI. General concepts of transformer operation and modelling can be found in the literature [149–152]. This section aims to present how the previously mentioned topics affect to a possible required galvanic isolation stage.

Figure 2.43 presents a typical single-phase transformer with a load connected at its secondary side. This load is defined by its impedance Z_L. The total flux that appears when the transformer is powered by the voltage u_1 is divided into the common flux Φ and the leakage flux Φ_d as

$$\Phi_T = \Phi + \Phi_d \tag{2.49}$$

The parasitic winding resistance and leakage inductance are depicted as R_x and L_{xd}, being the subscript x an indication of the primary or secondary side.

2.7.2 Reactive power

When the inverter is gried-tied and it operates in the grid-connected mode, it can receive capacitive or inductive reactive power set-points. Also, in grid-disconnected, the load can be capacitive or inductive. The total flux presented in Equation 2.49 is in quadrature with the primary voltage e_1. The decoupled behaviour between Ψ and e_1 can be deduced from the Faraday's law

$$e = -\frac{d\Psi}{dt} = -N\frac{d\Phi_T}{dt} \tag{2.50}$$

being Ψ the total concatenated flux.

On the other hand, the leakage flux Φ_d is in phase with primary current i_1. Ampere's law is described by

$$\oint \vec{B}d\vec{l} = \mu_0 I_T \tag{2.51}$$

being B the magnetic field, μ_0 the free space magnetic permeability, dl a tangent vector to the chosen trajectory in any point, I_T the current that crosses the surface limited by the trajectory and S the considered surface. Then, applying Equation 2.51 to a leakage line when a load is connected it can be obtained the leakage flux at the primary side as

$$\Phi_{1d} = \frac{N_1 i_1}{\mathcal{R}_d} \tag{2.52}$$

where $\mathcal{R}_d$ is the leakage reluctance and N_1 is the turns of the primary winding. Considering the ordinary differential equation of an inductance, it is possible to define the leakage inductance of the primary side as

$$L_{1d} = \frac{N_1^2}{\mathcal{R}_d} = \frac{N_1 \Phi_{1d}}{i_1} \tag{2.53}$$

deducing the aforementioned in phase behaviour between i_1 and Φ_{1d}.

Thus, according to the direction of Φ_{1d} the common concatenated flux increases or decreases. Under capacitive loads it is higher than in the resistive or inductive cases, refer to Figure 2.44. This situation could saturate the core under and excessive capacitive requirement at the AC grid or microgrid side. Consequently, the transformer should be selected according to the maximum capacitive load that will be required. Usually, the capacitive requirements are low. However, a microgrid VSI can use any phase to compensate reactive power, if necessary. Then capacitive requirements become high.

2.7.3 Frequency and voltage variations

In the framework of the microgrid operation, the frequency at the AC side can be different according to the control strategy used, for instance, when AC droop strategy is applied. This factor can produce undesired results in a transformer. Considering the Faraday's law and a sinusoidal voltage

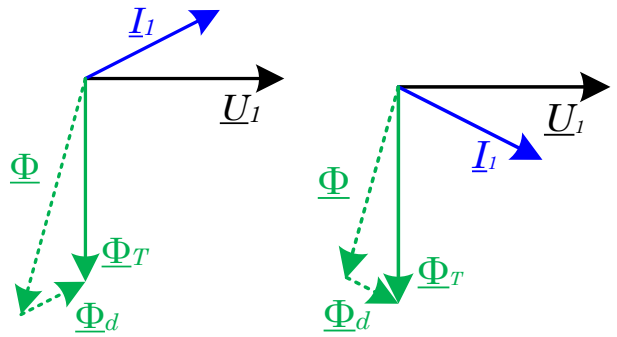

(a) Capacitive load (b) Inductive load

Figure 2.44: Flux behaviour under different types of loads

$$e_1(t) = \sqrt{2}E_1 \sin(\omega t) \tag{2.54}$$

the common flux can be described by

$$\Phi(t) = \Phi_m \cos(\omega t) \tag{2.55}$$

Then, it is possible to deduce that

$$E_1 = 4.44 f N \Phi_m \tag{2.56}$$

Assuming low leakage inductance and low primary resistance,

$$U_1 \approx 4.44 f N \Phi_m \tag{2.57}$$

It is usual to define the concatenation constant as $K = N\Phi_m$. If the transformer is designed for 230 V-50 Hz primary input, the obtained K is 1.03. If the microgrid operates at 40 Hz, U_1 should be 182.93 V. This result implies that when the transformer is supplied with 230 V-40 Hz, as N is fixed, the flux has to increase. The transformer can be saturated depending on the amount of increase.

For higher frequencies there is no problem if the rms value in respect with the rated one is maintained.

In this sense, when the galvanic isolation is required in AC microgrids it has to be considered to size the core of the transformer according to the full-range of frequencies and voltages.

2.7.4 Inrush current for grid-connected to grid-disconnected transition considerations

When the inverter is operating in grid-connected and for any reason it has to start a grid-disconnected operation it will have to energize the system. In this situation, it should be considered the inrush currents of the transformers, power converters and Electro-Magnetic Interference (EMI) filters when zero voltage crossing is accepted between both operation modes. Just when a transformer is connected to a voltage energy source (the converter through the coupling filter or the grid), the Faraday's law is verified. In this sense, the derivative term depends on the current voltage value obtaining a transient that can be more or less abrupt according to

$$\Phi = \int_0^t \frac{e_x}{N_x}\,\mathrm{d}t = \frac{\int_0^t \sqrt{2}E_x \cos(\omega t+\varphi)\,\mathrm{d}t}{N_x} = \frac{\sqrt{2}E_x\,(\sin(\omega t+\varphi)-sin(\varphi))}{\omega N_x} \tag{2.58}$$

where the subscript x indicates the side from which the transformer is powered. In this sense, if the applied voltage is just at its peak ($\varphi = 0$ or $\varphi = \pi$) when the connection is done, the flux increase in absolute value from zero to its maximum value Φ_m.

On the other hand, if the voltage is at a zero-cross point ($\varphi = \pi/2$ or $\varphi = 3\pi/2$), the flux starts at zero and increases in absolute value up to $2\Phi_{max}$. This can imply high inrush currents depending on the magnetic field-magnetic strength ($B - H$) characteristic curve of the transformer.

For these reasons, in a microgrid, the transformer has to be energized progressively from zero voltage up to the rated values when it is in the grid-disconnected mode start-up process after a zero voltage transition. Although the voltage is totally controlled by the inverter, the variability in the open-close times of the controlled circuit breakers rejects other alternatives unless static switches are used. In this last case, the close order of the static switch must be synchronized with one of the generated voltage peaks. If the system is re-started following a programmed voltage ramp, the integrity of the semiconductors of the VSI can be ensured.

2.7.5 Parallel inverters with transformers

An AC microgrid can be constituted by more than one inverter, a common situation when more power is required and it is not desired to replace the existing installed transformer. If different inverters have galvanic isolation it is necessary to apply all conventional rules for operating transformers in parallel. The main requirements are:

- Similar primary voltages, assuming that the primary side is connected to the PCC.

- Same clock hour number.

- It is recommended a maximum power relation of two between them. In this sense, the delivered power will not be excessively unbalanced due to more closer short-circuit impedances.

2.7.6 Unbalanced three-phase loads in grid-disconnected operation

The current exchanged by a transformer of a microgrid can be unbalanced depending on the connected load. The behaviour of the transformer depends on how the windings are connected, the type of core, the type of supplying wires (three or four wires), the type of load and their connection.

When the inverter operates as the master voltage reference, for instance in the grid-disconnected mode, it should be able to provide or compensate direct, inverse and zero voltage and current sequences. In this sense, it is possible to classify the different type of transformer cores, see Figure 2.45 and 2.46, according to their magnetic cores into [153, 154]:

- Free flux cores.

  Single-phase transformers.

  - Two legged wound-core transformers.
  - Shell transformers.
    - Non-distributed (one core).
    - Distributed (dual decoupled core assembled at $\pi/2$ rad).

  Five legged wound-core transformers.

  Triplex core (transformer bank) transformers.

- Linked flux cores.
  - Three legged stack-core transformers.
  - Four legged stack-core transformers.
  - Five legged stack-core transformers.
  - Multiple-phase shell transformers.

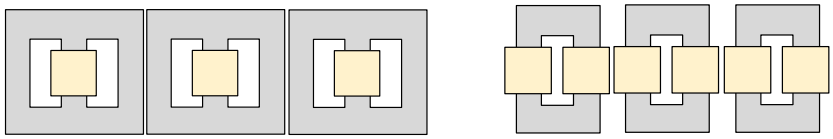

(a) Shell Triplex core transformer diagram (b) Triplex core transformer diagram

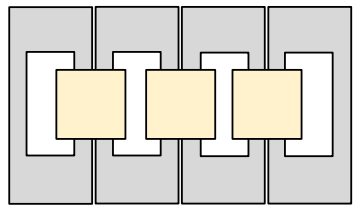

(c) Five legged wound-core transformer diagram

Figure 2.45: Free flux transformer's cores

In free flux transformers there is not a magnetic coupling between phases. There is a preferential magnetic path such that the fluxes of the legs have a trajectory with lower reluctance. Thus, it is possible to close the magnetic circuit through the core and not through the air when zero sequence fluxes are present. Essentially, they can be treated as independent single-phase transformers per phase.

In the case of linked flux cores exists a magnetic coupling between phases. This implies that when a voltage is applied between any phase, a voltage on the other ones will appear. However, the saturation level and the reluctance of the different branches and legs that integrate the core are seen different depending on the winding. That implies that currents can be different even under balanced operation conditions. Thus, concatenated fluxes should be considered to obtain more accurate results.

The following lines detail some important considerations of the aforementioned different type of transformers:

- Shell transformers are static devices where the windings are surrounded by more magnetic material with the aim of minimizing the magnetic air path. This type of transformers are more expensive than the wound-

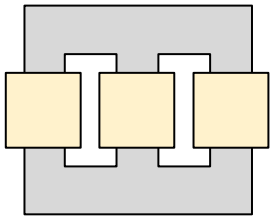

(a) Three legged stack-core transformer diagram

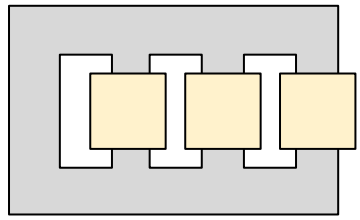

(b) Four legged stack-core transformer diagram

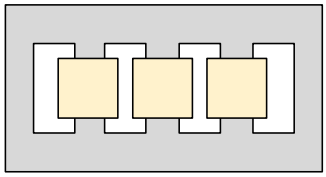

(c) Five legged stack-core transformer diagram

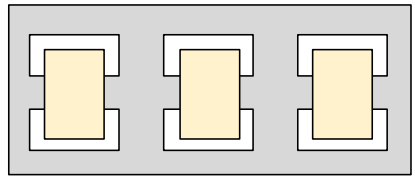

(d) Three-phase shell transformer diagram

Figure 2.46: Linked flux transformer's cores

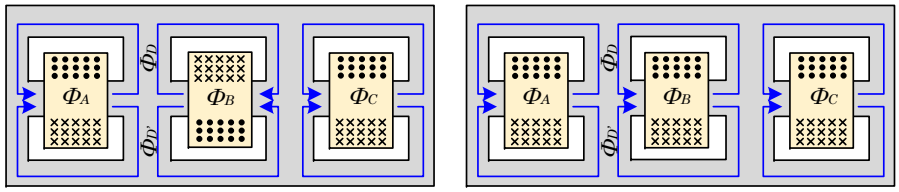

(a) Asymmetric connection for a three-phase shell transformer

(b) Symmetric connection for a three-phase shell transformer

Figure 2.47: Linked flux cores transformer examples

core ones but offer better efficiencies. In the case of the three-phase shell transformers it is possible to optimize the magnetic quantity of material for the core assuming three balanced sinusoidal voltages [153]. If the three windings are connected asymmetrically, according to Figure 2.47(a),

$$|\underline{\Phi}_D| = |\underline{\Phi}_A/2 + \underline{\Phi}_B/2| = 1/2|\underline{\Phi}_x| \tag{2.59}$$

being $\underline{\Phi}_x$ the magnetic flux of any winding. This result shows that the union yokes can be reduced to a half. However, in case of homopolar components $|\underline{\Phi}_D| = |\underline{\Phi}_x|$. In case of a symmetrical winding connection, see Figure 2.47(b),

$$|\underline{\Phi}_D| = \sqrt{3}/2|\underline{\Phi}_x| \tag{2.60}$$

being able to reduce the core in a lower proportion but zero sequence fluxes are avoided.

- Five legged stacked-core transformers are transformers where there are three central legs where the windings are located and two more legs at both sides without windings. These last two legs allow that $\sum \Phi_{\text{winding legs}} \neq 0$. Usually these legs have to be sized 1.5 times the central legs to make as uniform as possible all reluctances. However, all legs are usually sized identically. This means that it is possible to have up to 66% of zero sequence flux component in comparison with the nominal direct or inverse components. In [155] is concluded that five-legged cores produce higher inrush currents than three-legged cores. This supposes an improper condition for a black-start requirement in AC microgrids.

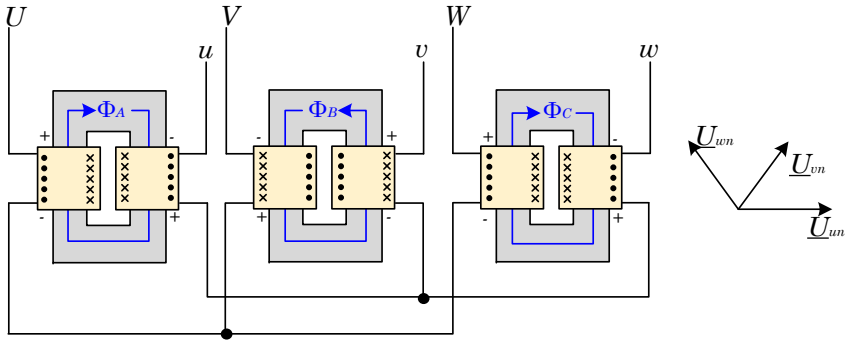

Figure 2.48: Wrong star winding secondary connection of a triplex transformer

- Triplex transformers, also known as transformer banks, are constituted by three single-phase transformers linked by the windings. They constitute a single three-phase unit. When the primary and the secondary windings are connected, it should be taken into account some considerations:

  - Star connection at the primary side. Figure 2.48 shows the primary windings (U, V, W) connected constituting a star. There is no need to take into account any consideration for the primary side. This is because as it has been considered a free-flux core the magnetic flux of each core has an independent path without the need of inferring into the other ones (not true in three legged stack-core transformers). However, for the secondary windings (u, v, w) it is important to consider the relative polarity of the windings in order to avoid unbalanced secondary voltages, as depicted in Figure 2.48.
  - Delta connection at the primary side. For the case of delta connections, the relative polarity has to be taken into account in both windings to avoid unbalanced situations. Figure 2.49(a) and 2.49(b) shows how to consider properly polarities for delta connection at the primary side.

  A triplex transformer results a more expensive option than a three-legged stacked transformer because the use of material is higher. Furthermore, depending on the rated power, a triplex transformer would need three tanks for the oil cooling system. In addition, if the core

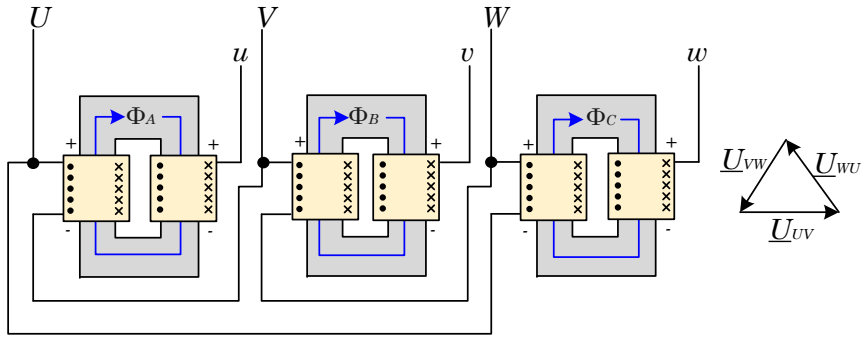

(a) Correct delta connection

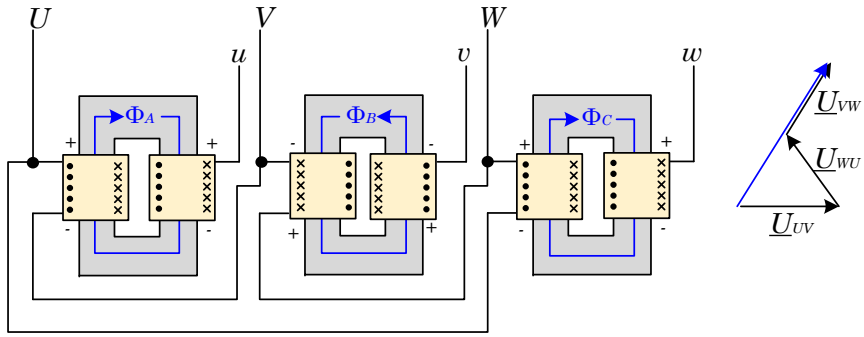

(b) Wrong delta connection

Figure 2.49: Delta winding primary connections of a triplex transformer

losses l are considered as a function of the frequency f, the magnetic field B and the volume V as $l = f(f, B, V)$, the lower the iron quantity the lower the losses.

On the other hand triplex transformer present some advantages:

- Totally independent fluxes between phases.
- In case of failure, it is easier to replace the damaged unit.
- Although the power density of a three-legged transformer is higher than in a triplex transformer each single-phase unit is easy to transport, manipulate and maintain.

Hence, after reviewing the different types of transformers, three legged stack-core transformers are analysed for a microgrid framework operation under single-phase and dual-phase load for delta and star connections. These alternatives are considered to be more standard than other options. Other type of connections will be referred but not developed. To do it analytically, the proposed approaches detailed in [149] are considered:

- Inner drops in the winding resistance and the leakage inductance are neglected, i.e. $R_x \approx 0$ and $Lx_d \approx 0$.
- No losses in the core are considered:
  - No Eddy's currents are present,i.e. $I_{Fe.} \approx 0$
  - The magnetic reluctances of the different legs are infinitely small, i.e. $\mathcal{R}_m \approx 0$.
  - The magnetic reluctance of the air is infinitely big, i.e. $\mathcal{R}_d \approx \infty$.
- The transformation relation ratio r_t will be equal to 1. N_2 is considered equal to 1 and N_1 the needed turns to fix $r_t = 1$. For instance, in case of a primary star connection, the number of turns N_1 is equal to 1 in case of star secondary connection, equal to $1/\sqrt{3}$ in case of delta secondary connection or equal to $\sqrt{3}/2$ in the zig-zag secondary connection.

According with previously exposed considerations, to solve the different cases will be considered:

- At any electric node $\sum i = 0$.
- At any magnetic node $\sum \Phi = 0$.

- At any magnetic closed ring the sum of all magnetomotrive forces follows $\sum fmm = N_1 i_{1m} + N_2 i_{2m} + N_1 i_{1n} + N_2 i_{2n} = \sum \Phi \mathcal{R}_m \approx 0$, being i_{1x} or i_{2x} the primary or secondary winding currents of the m and n core legs, respectively.
- At any electric closed ring the sum of all electromotive forces follows $\sum emm = \sum iZ \approx 0$.

For all the following analysis the load will be considered as a current consumption of 1 A in the single-phase load case or 1 A and 2 A for the dual-phase load case. The connections under study are: Yy, Yyn, YNy, YNyn, Dy, Dyn, Yd, YNd and Dd. As example, the Yy connection is developed. Then, only the interesting situations will be detailed.

- Case 1 Yy, shown in Figure 2.50(a). Applying electrical restrictions

$$i_U + i_V + i_W = 0 \tag{2.61a}$$
$$i_u = 0 \tag{2.61b}$$
$$i_v = -i_w = 1 \tag{2.61c}$$

and applying magnetic restrictions

$$i_U + i_u - 1 - i_V = 0 \tag{2.62a}$$
$$i_U + i_u - 1 - i_W = 0 \tag{2.62b}$$

Then, solving the above equations, can be deduced that the primary and secondary currents are

$$\begin{pmatrix} i_U \\ i_V \\ i_W \end{pmatrix} = \begin{pmatrix} 0 \\ -1 \\ 1 \end{pmatrix}, \begin{pmatrix} i_u \\ i_v \\ i_w \end{pmatrix} = \begin{pmatrix} 0 \\ 1 \\ -1 \end{pmatrix} \tag{2.63a}$$

In this sense, if the primary and secondary currents are added, the sum per core leg is null. This result implies that no problem is present even if a single-load is connected to the secondary side.

Figure 2.50(b) shows the case of a dual-phase load. The same previous analysis can be applied obtaining

$$\begin{pmatrix} i_U \\ i_V \\ i_W \end{pmatrix} = \begin{pmatrix} -1 \\ 3 \\ -2 \end{pmatrix}, \begin{pmatrix} i_u \\ i_v \\ i_w \end{pmatrix} = \begin{pmatrix} 1 \\ -3 \\ 2 \end{pmatrix} \tag{2.64a}$$

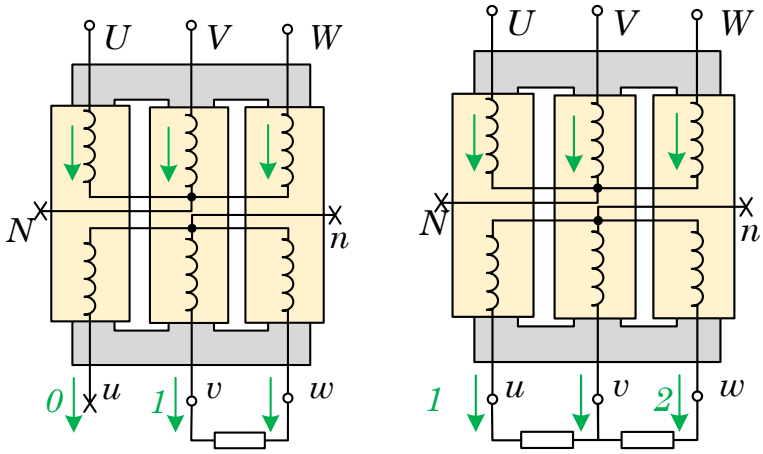

(a) Single-phase load (b) Dual-phase load

Figure 2.50: Yy connection current analysis under different loads

Again, the sum per core leg is null.

- Case 2 Yyn, shown in Figure 2.51. Applying electrical restrictions

$$i_U + i_V + i_W = 0 \tag{2.65a}$$
$$i_w = -i_n = 1 \tag{2.65b}$$
$$i_u = i_v = 0 \tag{2.65c}$$

and, applying magnetic restrictions

$$i_U + i_u - 1 - i_V = 0 \tag{2.66a}$$
$$i_U + i_u - 1 - i_W = 0 \tag{2.66b}$$

Then, solving the above equations, can be deduced that the primary and secondary currents are

$$\begin{pmatrix} i_U \\ i_V \\ i_W \end{pmatrix} = \begin{pmatrix} 0.33 \\ 0.33 \\ -0.66 \end{pmatrix}, \begin{pmatrix} i_u \\ i_v \\ i_w \end{pmatrix} = \begin{pmatrix} 0 \\ 0 \\ 1 \end{pmatrix} \tag{2.67a}$$

In this sense, if the primary and secondary currents are added, the sum per core leg is not null although the sum per ring is null. This

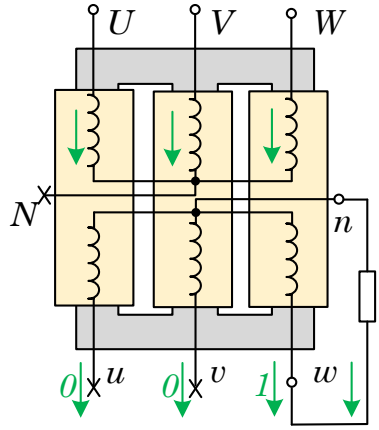

Figure 2.51: Yyn connection current analysis under single load

result implies that there are present zero sequence fluxes. These fluxes will produce efficiency drops and a displacement of the neutral point of the primary side. In other words, the transformer becomes a generator of homopolar voltages that are translated to the secondary side. Dual-phase load produces similar results in terms of zero sequence components.

Any other combination of single-phase or dual-phase load provides wrong operation results.

Voltage supply with positive, negative and zero sequence

In a microgrid each phase of a three-phase system could be managed individually. Then, the amplitude and phase of each one could be totally independent. This supposes that the transformer can be powered by an unbalanced voltage triplet. In this case, considering the upper-case nomenclature as the converter side, the same cases proposed in the previous section are analysed.

- Case with Yx or Dx. As the imposed voltages to the transformer are phase-to-phase, non zero sequence voltages are applied according to Fortescue's decomposition, see Equation A.7 in Apendix A. Then, non zero sequence fluxes are present. This implies currents with only positive and negative sequences.

- Case with YNx. As the imposed voltages are phase-to-neutral and the fluxes are described by Faraday's law, detailed by Equation 2.50, the zero sequence is present in the fluxes and the currents. This effect is translated to the secondary side if YNy or YNyn is used. This situation could be made worse under YNd connection. In this last case as the secondary side ring voltage must sum zero, assuming that the leakage resistance is almost null,

$$e_{uv} + e_{wv} + e_{wu} = 0 \longrightarrow 3N\frac{d\Phi_0}{dt} \simeq 3L_d\frac{di_0}{dt} \tag{2.68}$$

  being e_{xy} the secondary phase-to-phase voltages, N the turns of the secondary side, L_d the leakage inductance and i_0 the current inside the delta. So, the zero sequence currents that are closed in the delta of the secondary side are inversely proportional to the leakage inductance following

$$i_0 \approx \frac{\Phi_0}{L_d} \tag{2.69}$$

  As L_d value is usually small, the zero sequence currents are huge.

2.7.7 Non-linear loads

Non-linear loads are present in most of the devices that are used daily. This type of consumptions implies that the source that supply energy to them should provide these components to propitiate their correct behaviour.

When harmonic currents of the type $n = 3 + 3k \mid k \in \mathbb{Z}$ are consumed by the local loads, they represent homopolar or zero sequence components. These currents have to be generated by homopolar fluxes. This implies that the transformer needs to be able to handle homopolar components.

Considering, as in the previous cases, star or delta connections, the upper-case nomenclature as the converter side, the same cases proposed in the previous section are analysed.

- Case with Yx. To be consistent with Kirchoff's laws, it is non possible to transmit homopolar currents.

- Case YNx.
  - YNy. At the secondary side Kirchoff's laws have to be accomplished. Thus, non zero sequence currents will be transmitted.

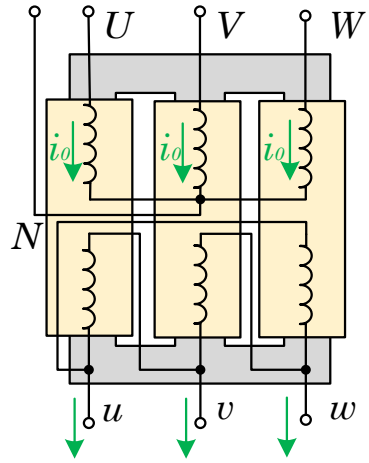

Figure 2.52: YNd connection current analysis for zero sequence primary currents

- YNd. Applying the same analysis done for the example of Figure 2.50(a) to the scheme presented in Figure 2.52 it is possible to obtain

$$\begin{pmatrix} i_{uv} \\ i_{vw} \\ i_{wu} \end{pmatrix} = \begin{pmatrix} i_0 \\ i_0 \\ i_0 \end{pmatrix}, \begin{pmatrix} i_u \\ i_v \\ i_w \end{pmatrix} = \begin{pmatrix} 0 \\ 0 \\ 0 \end{pmatrix} \tag{2.70a}$$

  Zero sequence currents cannot be transmitted because it remains circulating at the delta side.

- Case Ynyn. No restriction in terms of capability to transmit zero sequence currents.

- Case with Dx.
  - Case Dy or Dd. To be consistent with Kirchoff's laws, it is not possible to transmit homopolar currents.
  - Case Dyn. Figure 2.53 is now considered. In this case, the line currents are equal to zero. Although there is a neutral available, no homopolar current can be transmitted to the star side.

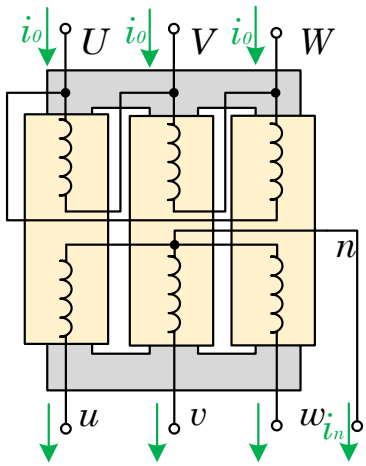

Figure 2.53: Dyn connection current analysis for zero sequence primary currents

2.7.8 Other winding connections and configurations

There are more options than the different combinations of star and delta with or without neutral applied to three legged stack-core transformers. It is possible to use three winding transformers or zig-zag connections.

In case of using three windings, see Figure 2.54, and considering the previous problematic cases for unbalanced loads, some configuration as Yyd, YNyd or Ynyd can be proposed. If it is supposed that the delta winding is opened, taking into account a homopolar component and a leakage impedance, when Kirchoff's laws are applied

$$u_t = u_{uv} + u_{vw} + u_{wu} = -3N_3 \frac{d\Phi_0}{dt} + 3R_d i_0 + 3L_d \frac{di_0}{dt} \tag{2.71}$$

being N_3 the tertiary turns. If, now, the terminals of the tertiary winding in the delta are closed

$$u_t = 0 \longrightarrow 3N_3 \frac{d\Phi_0}{dt} = 3R_d i_0 + 3L_d \frac{di_0}{dt} \tag{2.72}$$

In this sense, according to Lenz's or Faraday's law, the no-load currents i_0 will try to go against their source, in this case the homopolar flux. This type of transformers are more expensive than standard dual winding transformers. Also, the volume is higher due to it is necessary to widen the window to allocate the third winding. Another drawback is their weakness to support

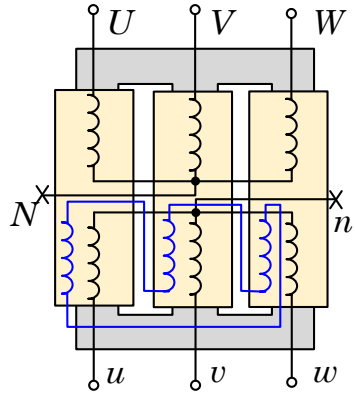

Figure 2.54: Yyd connection

short-circuits due to their inherent circulating current inside the tertiary when homopolar components are present.

On the other hand, a zig-zag connection, as the one depicted in Figure 2.55, can be taken into account. It is based in a secondary winding splitted into two parts with half turns each one. It should be considered the polarities of these two half inductances. One of the terminals sides (same polarity) are connected to generate a neutral point. Each one of the free terminal is connected with the same polarity terminal of other phase of the output side. In this sense, the output line current of any phase also goes through the winding of another phase. If it is supposed that the flux

$$\Phi_{xy} = \Phi_{xd} + \Phi_{xi} + \Phi_{x0} \tag{2.73}$$

where the subscript x concerns a leg and the subscript y to the $dq0$ the direct, inverse and homopolar components of the flux, respectively. If, for example, u_{un} is computed

$$\begin{aligned} u_{un} = u_{ua} + u_{b'n} = -\frac{N_2}{2}\frac{d\Phi_a}{dt} + \frac{N_2}{2}\frac{d\Phi_v}{dt} = \\ = -\frac{N_2}{2}\frac{d(\Phi_{ad} + \Phi_{ai} + \Phi_{a0})}{dt} + \frac{N_2}{2}\frac{d(\Phi_{vd} + \Phi_{vi} + \Phi_{v0})}{dt} \end{aligned} \tag{2.74}$$

Thus, as can be observed in Equation 2.74, the effect of the homopolar fluxes will be cancelled.

On the other hand, if delta or star connection is maintained but now on a triplex configuration, some of the aforementioned problems can be made

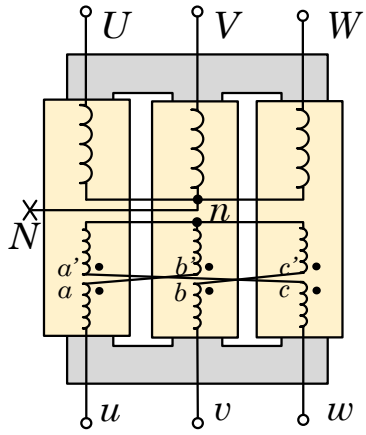

Figure 2.55: YNz connection

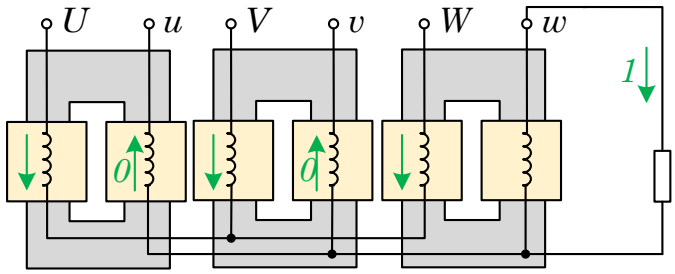

Figure 2.56: Triplex Yyn connection

worse. For example, in the Yyn configuration, as depicted in Figure 2.56, the line input and output currents are

$$\begin{pmatrix} i_U \\ i_V \\ i_W \end{pmatrix} = \begin{pmatrix} 0.33 \\ 0.33 \\ -0.66 \end{pmatrix}, \begin{pmatrix} i_u \\ i_v \\ i_w \end{pmatrix} = \begin{pmatrix} 0 \\ 0 \\ 1 \end{pmatrix} \tag{2.75a}$$

At that point, the transformer bank has two units with no load but with current circulating through its primary side. This current plays the role of no load current but with higher values implying that the two no load units can saturate. This behaviour is known as choke effect [149]. This effect has similar implications in four or five legged with stack or wounded cores.

Type	Single/dual-phase unbalance load	Any type of load (1ϕ & 3ϕ)	Supply considering seq $\{+,-,0\}$
Yy	✓	✗	✓
Yyn	✗✗	✗✗	✓
YNy	✓	✗	✗✗
YNyn	✓	✓	✗✗
Dy	✓	✗	✓
Dyn	✓	✓	✓
Yd	✓	✗	✓
YNd	✓	✗	✗✗
Dd	✓	✗	✓

Table 2.6: Operation of three-legged stack-core transformers under different conditions for grid-disconnected operation

Type	Supply considering seq $\{+,-,0\}$	Capability to inject seq $\{+,-,0\}$
Yy	✓	✗
Yyn	✗✗	✗
YNy	✗✗	✗
YNyn	✗✗	✓
Dy	✓	✗
Dyn	✗✗	✗
Yd	✓	✗
YNd	✗✗	✗
Dd	✓	✗

Table 2.7: Operation of three-legged stack-core transformers under different conditions for grid-connected operation

Conclusions

After analysing various effects that can be present in a microgrid, Table 2.6 and 2.7 provides the proper uses in case of D/Y connections for three-legged stack-core transformers. In the grid-disconnected operation case, upper case type refers to the converter side, while in grid connected mode to the grid side. One ✗ indicates the option is not possible or compatible with the proposed type of connection. When ✗✗ is used, this indicates that the option is possible but it implies improper behaviours of the transformer (mainly due to homopolar fluxes). When ✓ is used implies that there is not inconvenience to use that alternative.

Observing the different scenarios that can be present in any AC microgrid, if a total controlled 4-Quadrant P/Q VSI wants to be operated considering, also, harmonic injection, the last column (Capability to inject $\{+,-,0\}$ sequences) determines that a YNyn transformer is required, but not using a three-leg stack-core transformer.

Depending on the rated power of the final device the best option has to be selected. In this sense, the following is proposed:

- For low power with low zero-sequence currents a four-legged results a

good alternative. It is the most compact option.

- For medium power with significant zero-sequence currents a five-legged core results a better option because the magnetic paths are more uniform than in the previous case and the device is more efficiency sensitive.

- For the high power case, the construction, transport and maintenance of a four or five legged core could result extremely difficult and expensive. For this reason, the use of the standard single-phase transformer constituting a triplex unit could result more attractive. The use of shell triplex core is not necessary if really high performance is not searched.

The three winding YNynd option does not allow to transmit the same zero sequence voltages from the primary to the secondary due to its own behaviour of cancelling the zero sequence fluxes. This alternative is rejected.

If it is desired to use a zig-zag connection, as has been aforementioned, both sides will require four wires. In this sense, the only two possibilities are ZNzn or YNzn. The first option is really rare. Furthermore, both sides will need four wires implying that the zig-zag neutral point should be accessible. This casuistry is even more unusual than the previous one. As the phase to neutral voltage of a zig-zag connection will not be affected by the zero sequence flux, it is not possible to translate zero sequence voltages from one side to the other. In the YNzn case, again, the zero sequence voltages from the primary cannot be generated at the secondary side.

2.8 Summary

Nowadays, most of typical loads are supplied in AC. When microgrids are considered as a solution for the future energy management, it is important to understand the different operation modes and parts of AC microgrids.

AC microgrids are not only constituted by its elemental device, i.e. the Voltage Source Inverter (VSI). The AC microgrid operates under the coexistence of other elements. The main breaker is the gateway between the main grid and the microgrid. Protective devices and smart switches allows to reconfigure the grid topology according to different criteria and modify the neutral scheme according to the operation mode. The management unit(s) will handle these decisions. A first level of protection have to be provided by the own protections or the VSI. The local loads are connected to a common

connection point and can be classified according to their criticism level. The use of industrial communications to exchange data is a remarkable challenge.

The control strategy determines the role of the VSI within the microgrid, being able to behave as a current source (Grid Supply Inverter), an ideal voltage source (Grid Constitution Inverter) or a non-ideal voltage source (Grid Support and Constitution Inverter). As AC microgrids are close to the end-users they have to behave as distribution lines feeding the consumption in a four-wire configuration in grid-disconnected mode. Furthermore, in grid-connected mode, a four-wire system represents a more flexible option for the DSO-MO to request any positive or negative, active or reactive power to be exchanged with the utility. Two conventional VSI topologies can be used; four-wire three-leg with DC-link split-capacitor and four-wire four leg VSI. Per contra, in the conventional vertical distribution scheme, the end-users are more shared defining more regular consumption profiles that do not require a four-wire distribution.

Although a power external control loop controls the operation, the inner control loops, i.e. voltage and current loops, have to be considered. The VSI is connected to the utility through coupling filters. Two options are widely used: L-type or LCL-type coupling filters. The use of LCL-type is followed by a choice of where allocate the control sensors according to reactive power exchanged, stability or synchronization criteria. Also, the operation according to different control strategies influences over the main loss detection capability.

As the AC microgrid VSI can be considered as a generator, galvanic isolation could be required according to some regulations as is the case of Spain. Some challenges can be considered independently of the type of connection chosen for the windings of the transformers, as can be frequency range or reactive supply capability. Others, like unbalance loads, unbalance voltages applied at the primary side and the capability to transmit zero sequence currents are dependent. It has been observed that three-legged stacked-core does not results into a good solution. Thus, it is possible to use a four-legged core, a five-legged core or a triplex transformer depending on cost, maintenance, space required and rated power criteria.

Chapter 3

Inner control loops analysis for AC systems

3.1 Introduction

In the control theory it is possible to consider two control challenges; tracking of constant or time-varying references, as has been exposed in Chapter 2. Depending on the final choice, the use of one or another type of controller can result into a better option.

A huge variety of methods to control a system exists in the literature. Some example are conventional Proportional-Integral-Derivative controllers (PID), conventional PID variations such as PI-D o I-PD, two degree of freedom controllers PI-PD or PID-PD, lead, lag or lead-lag controllers, state space controllers, robust controllers, adaptive controllers, resonant controllers, non-linear controllers, fractal controllers as $PI^{\alpha}D^{\lambda}$, among others [156–159].

The regulation of AC currents and voltages has become an important challenge for VSI from its beginnings. The use of a stationary, a rotating or a synchronous reference frames can be applied not only to voltages and currents values but also to the controller. For example, stationary frame PI regulators are conventionally related with insufficient magnitude and phase tracking capability [160].

This chapter introduces these concepts, analysed them in detail and proposes new alternatives. Thus, it is structured as follows:

- Section 3.2. *Reference frame challenges.* This section introduces some of the most common topics to consider according to different reference frame situations.

- Section 3.3. *Conventional resonant controller analysis.* An exhaustive analysis of the stability based on the Nyquist trajectory for the control of resonant controllers is contributed in this part. This analysis

is conducted for the current and voltage control loops. Also, it is proposed to extend a simple tuning strategy from the current loop to the voltage loop. The results of this section have been published in [161] at EPE'15.

- Section 3.4. *Novel fractional resonant controller proposal.* A new controller based on the $PI^{\alpha}D^{\lambda}$ concept is extended to resonant controllers. This novel controller is presented with the aim of enhance the behaviour at the high frequency region. The outcomes of this section have been published in [162] at EPE'16.

3.2 Reference frame challenges

It is common to observe in the literature different possible reference frames when a VSI wants to be controlled:

- The *abc* stationary reference frame. It refers directly to the natural reference frame where the electric magnitudes are treated without any mathematical transformation. This means that control has to face with a time-varying tracking challenge.

- The $\alpha\beta\gamma$ stationary reference frame. It refers to the natural reference frame base change when Clarke transform is used, see Appendix A. This means that the control has to face with a time-varying tracking challenge. The advantage of this reference is the result obtained under balanced systems. Under this hypothesis, the system order is reduced from $\mathbb{R}^3$ to $\mathbb{R}^2$.

- The *dqh* synchronous reference frame. The *abc* reference frame is translated into a synchronous reference frame when Park transform is used. This last option is widely extended with the aim of apply PI controllers. The *abc* reference is base changed and rotated at the rated angular frequency of the main grid, see Appendidx A. This means that the control has to deal with a constant tracking challenge.

- The rotating reference frame. As for single-phase systems is not possible to take profit directly of Clarke and Park transforms, the rotating frame is also considered. The natural reference frame is directly rotated.

For the following analysis, it is assumed that the minimum control system concerns to the inner current loop. It should be reminded that the inductance behaviour is described in the Laplace's s-domain as

$$\Delta U(s) = LI(s)s + RI(s) \tag{3.1}$$

being ΔU the voltage difference between the inductance terminals, L the self-induction coefficient, R the equivalent series resistance and I the flowing current.

3.2.1 Synchronous reference frame considerations

The unbalance and harmonic effect

When a general three-phase system is considered it is common to find that the phases are not exactly shifted $2\pi/3$ rad. Also, these magnitudes can present different modules or harmonics contents overlapped on the fundamental component. Fortescue's theorem indicates that any system can be decomposed into three balanced systems; one of positive sequence that rotates with the same sequence of the main grid $(+)$, one of negative sequence that rotates with the opposite sequence of the main grid $(-)$ and one of zero sequence that pulses but does not rotate [163]. Then, if X_x represents one electric magnitude in the *abc* reference frame, it is possible to obtain

$$\begin{cases} \underline{X}_a = \underline{X}_a^0 + \underline{X}_a^+ + \underline{X}_a^- \\ \underline{X}_b = \underline{X}_b^0 + \underline{X}_b^+ + \underline{X}_b^- \\ \underline{X}_c = \underline{X}_c^0 + \underline{X}_c^+ + \underline{X}_c^- \end{cases} \tag{3.2}$$

On the other hand, the concatenated Clarke and Park transform, detailed in Apendix A, is described by

$$\begin{pmatrix} x_h(t) \\ x_d(t) \\ x_q(t) \end{pmatrix} = k \begin{pmatrix} 1 & 1 & 1 \\ \cos(\theta) & \cos\left(\theta - \frac{2\pi}{3}\right) & \cos\left(\theta + \frac{2\pi}{3}\right) \\ -\sin(\theta) & -\sin\left(\theta - \frac{2\pi}{3}\right) & -\sin\left(\theta + \frac{2\pi}{3}\right) \end{pmatrix} \begin{pmatrix} x_a(t) \\ x_b(t) \\ x_c(t) \end{pmatrix} \tag{3.3}$$

where θ is equal to ωt and k is a normalization gain to preserve module or power in electric applications. If the *abc* magnitudes are described by

$$x_x(t) = X_x \cos(n(\omega t + \varphi_x)) \tag{3.4}$$

where n is n_{th} harmonic component and the subscript x the referenced abc phase, it can be deduced that

$$x_h(t) = k\left[X_a\cos(n\omega t + n\varphi_a) + X_b\cos(n\omega t + n\varphi_b) + X_c\cos(n\omega t + n\varphi_c)\right] \tag{3.5a}$$

$$\begin{aligned} x_d(t) = \frac{k}{2}\Big[&X_a(\cos((1+n)\omega t + n\varphi_a) + \cos((1-n)\omega t - n\varphi_a)) + \\ &+X_b(\cos((1+n)\omega t + n\varphi_b - \frac{2\pi}{3}) + cos((1-n)\omega t - n\varphi_b - \frac{2\pi}{3})) + \\ &+X_c(\cos((1+n)\omega t + n\varphi_c + \frac{2\pi}{3}) + \cos((1-n)\omega t - n\varphi_c + \frac{2\pi}{3}))\Big] \end{aligned} \tag{3.5b}$$

$$\begin{aligned} x_q(t) = \frac{k}{2}\Big[&X_a(\sin((1+n)\omega t + n\varphi_a) - \sin((1-n)\omega t - n\varphi_a) + \\ &X_b(\sin((1+n)\omega t + n\varphi_b - \frac{2\pi}{3}) - \sin((1-n)\omega t - n\varphi_b - \frac{2\pi}{3})) + \\ &X_c(\sin((1+n)\omega t + n\varphi_c + \frac{2\pi}{3}) - \sin((1-n)\omega t - n\varphi_c + \frac{2\pi}{3}))\Big] \end{aligned} \tag{3.5c}$$

This result allows to deduce that for a synchronous reference frame:

- In an unbalanced system without harmonics, i.e., $n = 1$, a second order harmonic component can appear in the dq transformed magnitudes (this contribution comes from the negative sequence). The homopolar component can present a component that pulses at the rated angular frequency ωt with null average value (this contribution comes from the zero sequence).
- Harmonic components, as the one described in Equation 3.4, contributes with:
  - $(n+1)f$ and $(1-n)f$ hertzs at the direct and quadrature dq components.

- nf hertzs at the homopolar h component.

It should be noticed that the harmonic components can be also decomposed into Fortescue's components presenting positive (n^+), negative (n^-) and zero sequence components (n^0), too. This fact permits to obtain an interesting conclusion when the synchronous reference frame is used. Different information on a same frequency component $n\omega$ is obtained from:

- Zero sequence of the $n\omega$ component.
- Positive sequence of the $(n+1)\omega$ component.
- Negative sequence of $(n-1)\omega$ component.

As an example, if u_n designs the n_{th} harmonic component of a fundamental angular frequency equal to 100π rad/s, u_1^-, u_2^0 and u_3^+ are seen as a 100 Hz component in the synchronous reference frame.

A PI controller can handle, assuming steady state errors, non null frequencies depending on its cut-off bandwidth (ω_{co}). In open-loop, the bode diagram maintains a static gain

$$|G_s| = 20\log(k_p) \tag{3.6}$$

from the cut-off angular frequency

$$\omega_{co} = k_i/k_p \tag{3.7}$$

being k_p and k_i the proportional and integral gains of the controller.

The previous lines pose that to compensate harmonic content or unbalances, ensuring null error in steady state, multiple PI controllers have to be used. A multi-Park reference frame strategy as cited in [164, 165] follows this idea.

If the three-phase system only have three wires the homopolar current is always zero. For the case of voltages, as the only observable voltages are phase-to-phase values, using the Fortescue's decomposition presented in Equation 3.2, if a is defined as $a = e^{\frac{2\pi}{3}j}$, all voltages can be referenced to the u_a voltage. Then, it is possible to deduce

$$\begin{cases} \underline{X}_a = \underline{X}_a^0 + \underline{X}_a^+ + \underline{X}_a^- \\ \underline{X}_b = \underline{X}_a^0 + a^2\underline{X}_a^+ + a\underline{X}_a^- \\ \underline{X}_c = \underline{X}_a^0 + a\underline{X}_a^+ + a^2\underline{X}_a^- \end{cases} \tag{3.8}$$

Computing phase to phase voltages,

$$\begin{cases} \underline{U}_{ab} = (1-a^2)\underline{U}_a^+ + (1-a)\underline{U}_a^- \\ \underline{U}_{bc} = (a^2-a)\underline{U}_a^+ + (a-a^2)\underline{U}_a^- \\ \underline{U}_{ca} = (a-1)\underline{U}_a^+ + (a^2-1)\underline{U}_a^- \end{cases} \tag{3.9}$$

From the last Equation 3.9 can be observed that the zero sequence voltage does not appear. Therefore, the system can only be decomposed into a positive and an negative sequence, reducing the system size. However, the main drawback of the multi-Park control methodology is that several Park transforms are required implying the use of several trigonometric functions. This fact derives in an increase of computational burdens.

The current loop coupling effect

In the case of three-wire three-phase systems, the use of Clarke and Park transforms, detailed in Apendix A, are widely used with the aim of move from a three-phase *abc* sinusoidal reference to a dual-phase *dq* synchronous reference [133, 166–168]. The current open-loop in the *abc* reference frame is described by the introduced Equation 2.6 in Section 2.5. Observing the voltage difference applied to the inductance terminals

$$\frac{d}{dt}\begin{pmatrix} i_u \\ i_v \\ i_w \end{pmatrix} = \frac{-1}{L}\left[\begin{pmatrix} R & 0 & 0 \\ 0 & R & 0 \\ 0 & 0 & R \end{pmatrix}\begin{pmatrix} i_u \\ i_v \\ i_w \end{pmatrix} + \begin{pmatrix} 1 & 0 & 0 \\ 0 & 1 & 0 \\ 0 & 0 & 1 \end{pmatrix}\begin{pmatrix} u_{u'o} - u_{uo} \\ u_{v'o} - u_{vo} \\ u_{w'o} - u_{wo} \end{pmatrix}\right] \tag{3.10}$$

It is possible to express Equation 3.10 as

$$\frac{dI}{dt} = AI + Bv + Ee \tag{3.11}$$

being I the current state space vector, A the state space matrix and B, E the identity matrix that affects the input voltage vector $v = u_{xo}$ and the disturbance vector $e = u_{x'o}$, respectively. The subscript x indicates the considered phase. According to the exposed in the previous chapters, when v is considered it refers to the inverter side voltage and e to the grid or PCC voltage, see Figure 2.18.

Applying the Park transform to Equation 3.11

$$P\frac{d(P^{-1}PI)}{dt} = PAP^{-1}PI + PBP^{-1}Pv + PEP^{-1}Pe \tag{3.12}$$

is deduced that in the Laplace's s-domain

$$\begin{pmatrix} \Delta U_d \\ \Delta U_q \end{pmatrix} = \begin{pmatrix} Ls+R & -\omega \\ \omega & Ls+R \end{pmatrix}\begin{pmatrix} I_d \\ I_q \end{pmatrix} \tag{3.13}$$

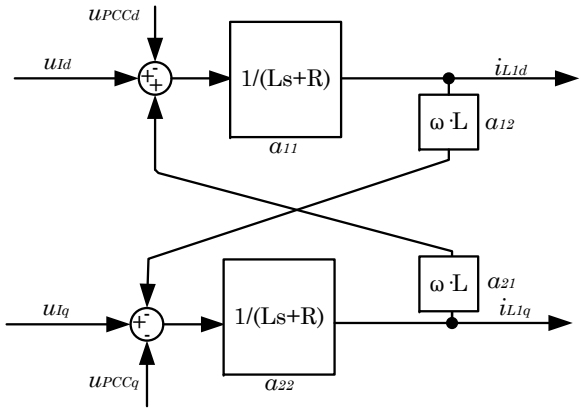

Figure 3.1: Output-input coupling of a three-wire current loop system in the synchronous reference frame

where ΔU_{dq} is the difference between v_{dq} and e_{dq}. Note that Equation 3.13 shows the conventional coupled dq current open-loop matrix. In this sense, the advantage of translate sinusoidal signals to constant values in steady state is that the control problem can be faced using conventional PI controllers. These controllers are tuned for a constant reference tracking. However, the use of Park transforms sets two challenges:

- The electric variables have only to be defined by positive sequence without harmonic components to obtain pure constant dq components.
- The system in dq variables is coupled. Figure 3.1 shows the equivalent scheme of the current open-loop system presented in Equation 3.13.

Three alternatives can be used in the case of the coupling topic:

- Decouple the system via software. Figure 3.2 shows the typical decoupling strategy, as is proposed in [169], where the estimation of the grid angular frequency ($\hat{\omega}$) and the inductance value ($\hat{L}$) are used. In [170] another decoupling strategy using integral decoupling factors is presented.
- Use a multi-variable control law, for example, by means of the state space formulation

$$\begin{cases} \dot{\vec{x}} = A\vec{x} + B\vec{u} & \longrightarrow Dynamic\,equation \\ \vec{y} = C\vec{x} + D\vec{u} & \longrightarrow Static\,equation \end{cases} \tag{3.14}$$

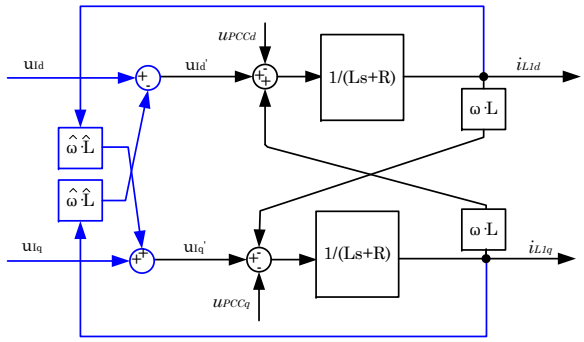

Figure 3.2: Conventional decoupling strategy (in blue) of a current loop system in the synchronous reference frame

where A is the plant matrix, B is the input matrix, C the output matrix and D the perturbation matrix. The drawback of this alternative is the amount of needed operations. Also, the basic state space feedback matrix is only a linear combination of the state variables

$$\begin{cases} \dot{\vec{x}} = (A - K)\vec{x} + B\vec{u} & \longrightarrow \textit{Dynamic equation} \\ \vec{y} = C\vec{x} + D\vec{u} & \longrightarrow \textit{Static equation} \end{cases} \tag{3.15}$$

being K the feedback state matrix. Furthermore, if the plant matrix has not pure integrators, to obtain null errors in steady state it is also necessary to add new states that corresponds to the integral of the output variables that wants to be controlled. The new state-space formulation is

$$\begin{cases} \begin{bmatrix} \dot{\vec{x}}_i \\ \dot{\vec{x}} \end{bmatrix} = \begin{bmatrix} 0 & C \\ 0 & A \end{bmatrix} \begin{bmatrix} \vec{x}_i \\ \vec{x} \end{bmatrix} + \begin{bmatrix} D \\ B \end{bmatrix} \vec{u} \\ \vec{y} = \begin{bmatrix} 0 & C \end{bmatrix} \begin{bmatrix} \vec{x}_i \\ \vec{x} \end{bmatrix} + D\vec{u} \end{cases} \tag{3.16}$$

where

$$\vec{x}_i = \int_0^t \vec{y}_i \, \mathrm{d}t. \tag{3.17}$$

A new feedback state matrix has also to be expanded adding K_i. In this sense, the derived control law results into:

$$\vec{u} = -\begin{bmatrix} K_i & K_r \end{bmatrix} \begin{bmatrix} \vec{x_i} \\ \vec{x} \end{bmatrix} \tag{3.18}$$

- Analyse the strength of the coupling using, for example, the Relative Gain Array (RGA) [156, 171] method. It is also known as Bristol method. When the coupling is weak it can be controlled each component independently, as is proposed in [172].

  The inputs of the system u_{PCCd} and u_{PCCq} are considered null. This assumption is possible because a feedforward in the inner controller is considered and the synchronization of the VSI with the grid is assumed. For the calculations of the RGA matrix, it is interesting that the system presents the structure of interaction that is shown in Figure 3.3, where G_{xx} and G_{xy} are the direct and coupling transfer functions, respectively. The system to control has an output-input coupling instead of the desired input-output coupling. Thus, considering the relations from Figure 3.1, y_1 and y_2 can be obtained as

$$y_1 = (m_1 + y_2\ a_{21})\ a_{11} = (m_1 + ((m_2 - y_1 a_{12})a_{22})a_{21})a_{11} \tag{3.19a}$$
$$y_2 = (m_2 - y_1\ a_{12})\ a_{22} = (m_2 - ((m_1 + y_2 a_{21})a_{11})a_{12})a_{22} \tag{3.19b}$$

  and, rearranging terms,

$$y_1(1 + \prod^{\forall i,j}[a_{ij}]) = m_1\ a_{11} + m_2\ a_{21}\ a_{11}\ a_{22} \tag{3.20a}$$
$$y_2(1 + \prod^{\forall i,j}[a_{ij}]) = m_2\ a_{22} - m_1\ a_{12}\ a_{11}\ a_{22} \tag{3.20b}$$

  So, according to Figure 3.3, the G_{xx} and G_{xy} transfer functions are

$$G_{11} = G_{22} = \frac{a_{11}}{(1 + \prod^{\forall i,j}[a_{ij}])} \tag{3.21a}$$
$$G_{12} = -G_{21} = \frac{a_{11}a_{22}a_{12}}{(1 + \prod^{\forall i,j}[a_{ij}])} \tag{3.21b}$$

  For the RGA method it is necessary to follow four steps:

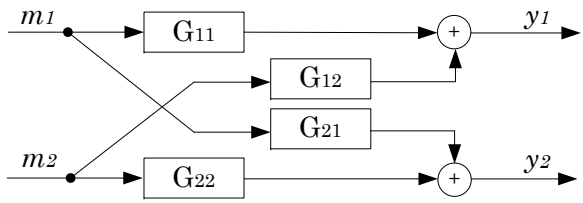

Figure 3.3: Desired input/output coupling scheme for RGA application

- Determination of the relative gain matrix of Bristol. Once the four required transfer functions are obtained (G_{11}-G_{12}-G_{21}-G_{22}), it is necessary to proceed making the calculations of static gains using the final value theorem. It has to be computed considering the input as a unit step.

$$K_{11} = K_{22} = \lim_{s\to 0} sG_{11}\frac{1}{s} = \lim_{s\to 0} s\frac{Ls+R}{(Ls+R)^2+\omega L)^2}\frac{1}{s} \tag{3.22a}$$

$$K_{12} = -K_{21} = \lim_{s\to 0} sG_{12}\frac{1}{s} = \lim_{s\to 0} s\frac{\omega L}{(Ls+R)^2+\omega L)^2}\frac{1}{s} \tag{3.22b}$$

The static gain matrix and its transpose inverse are defined as

$$K = \begin{pmatrix} K_{11} & K_{12} \\ K_{21} & K_{22} \end{pmatrix} \tag{3.23a}$$

$$K^{-t} = \frac{1}{K_{11}K_{22} - K_{12}K_{21}} \begin{pmatrix} K_{22} & -K_{12} \\ -K_{21} & K_{11} \end{pmatrix} \tag{3.23b}$$

Therefore, the Λ RGA is defined as the Hadammard product of KxK^{-t}.

- Choose the best coupling between inputs and outputs. Summarising all the possibilities, if the component λ_{ij} of Λ is close to one, input-i controls independently output-j. If the value is close to zero practically there is no interaction between input-i and output-j.
- Check if the pairing is quite significant. Proceed with independent tuning of the controller if all previous steps are valid. If not, a

classical decoupling strategy or multi-variable control has to be applied.

As an example, if a coupling inductance of 1 mH and an equivalent series resistance of 1 Ω is considered, the RGA matrix obtained is

$$\Lambda = \begin{pmatrix} \lambda_{11} & \lambda_{12} \\ \lambda_{21} & \lambda_{22} \end{pmatrix} = \begin{pmatrix} \frac{K_{11}K_{22}}{K_{11}K_{22}-K_{12}K_{21}} & 1-\lambda_{11} \\ 1-\lambda_{11} & \lambda_{11} \end{pmatrix} = \tag{3.24a}$$

$$= \begin{pmatrix} 0.9102 & 0.0898 \\ 0.0898 & 0.9102 \end{pmatrix} \tag{3.24b}$$

implying that direct components ($u_d - i_d$ and $u_q - i_q$) are strongly correlated while coupling terms shows weakly interactions ($u_q - i_d$ and $u_d - i_q$).

Single-phase systems

The control of single phase inverters using a synchronous reference frame results more complex than in the three-phase case. Clarke and Park transforms cannot be applied directly to single-phase systems. By using the Clarke transform can be deduced that the α component is totally decoupled of the β component.

As in a single-phase system there is only one voltage and one current, there is a common idea behind all synchronous reference frame strategies. It consists on the generation of a second virtual reference lagged $\pi/2$ rad in respect of the real magnitude. In [173] a brief review on conventional methods based on the delay of a quarter of the period using a fixed buffer applied on the current is done. The use of mathematical expressions that generates a signal delayed $\pi/2$ rad is also common in Phase Locked Loop (PLL) algorithms for single-phase systems. They offer faster convergence results than when a buffer alternative is chosen, as can be observed in [124, 174].

The rotating reference frame

A rotating frame can be achieved multiplying the differential order equation of an inductance, see Equation 2.13, by the term $e^{-j\omega t}$. Then, if the Laplace transform is applied

$$\Delta U(s) = (L(s + j\omega) + R)I(s) \tag{3.25}$$

Note that this results is equivalent to the one obtained when dynamic phasors are considered. In [175] a comparative study of three controller types is conducted. In [175] is considered as:

- Mutiple Rotating Integrators (MRI). The controller transfer function with respect to harmonic k is

$$H_{k_{\mathrm{MRI}}} = \frac{k_{p_k} s + k_{i_k}}{s} \tag{3.26}$$

- Stationary frame Second Order Generalized Integrators (SGI or SOGI). The controller transfer function with respect to harmonic k is obtained applying a rotation of $e^{\pm jk\omega t}$ on Equation 3.26, deriving into

$$H_{PIk_{\mathrm{SGI}}} = H_{PIk_{\mathrm{SGI+}}} + H_{PIk_{\mathrm{SGI-}}} = 2k_{p_k} + \frac{2k_{i_k} s}{s^2 + (k\omega)^2} \tag{3.27}$$

  where $H_{PIk_{\mathrm{SGI+}}}$ or $H_{PIk_{\mathrm{SGI-}}}$ indicates the sense of the applied rotation.

- Vector Proportional Integral controller (VPI). The controller is designed using the pole-zero cancellation technique. As Equation 3.25 presents a complex pole it can be considered a controller with a complex transfer function. The VPI controller is achieved applying $e^{\pm jk\omega t}$ to the integrator term

$$H_{PIk_{\mathrm{VPI}}} = H_{PIk_{\mathrm{VPI+}}} + H_{PIk_{\mathrm{VPI-}}} = 2\frac{k_{p_k} s^2 + k_{i_k} s}{s^2 + (k\omega)^2} \tag{3.28}$$

The aforementioned controllers can be also applied to three-phase systems.

3.2.2 The reference frame of the controller

An interesting perspective results from the analysis of different reference frame controllers over different reference frames [160, 176].

Synchronous frame PI to stationary $\alpha\beta$ reference frame

Considering a PI controller and a synchronous reference frame, the close-loop transfer function of a three-wire three-phase system, see Figure 3.4, system can be expressed as

$$\begin{pmatrix} x_\alpha(t) \\ x_\beta(t) \end{pmatrix}^* = \begin{pmatrix} \cos(\omega t) & -\sin(\omega t) \\ \sin(\omega t) & \cos(\omega t) \end{pmatrix} \left\{ [G_{ctrl}(t)] * \begin{pmatrix} \cos(\omega t) & \sin(\omega t) \\ -\sin(\omega t) & \cos(\omega t) \end{pmatrix} \begin{pmatrix} e_\alpha(t) \\ e_\beta(t) \end{pmatrix} \right\} \tag{3.29}$$

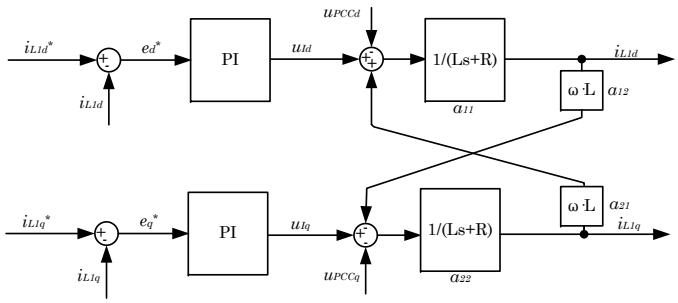

Figure 3.4: Current close-loop scheme under synchronous frame PI controller in the synchronous dq reference frame

Note that the real and complex convolution relationship between the time-domain and the s-domain have been applied. It should be reminded that a product in the s-domain becomes a convolution in the time-domain and viceversa. In this case, x^* is the error set-point, e_x is the error and $[G_{ctrl}(t)]$ represents the controller matrix that follows

$$[G_{ctrl}(s)] = \begin{pmatrix} \frac{k_p s + k_i}{s} & 0 \\ 0 & \frac{k_p s + k_i}{s} \end{pmatrix} \tag{3.30}$$

If the x_α component of Equation 3.29 is developed

$$\begin{aligned} x_\alpha^*(t) = &\{G_{ctrl}(t) * (e_\alpha \cos(\omega t) + e_\beta \sin(\omega t))\} \cos(\omega t) + \\ &+ \{G_{ctrl}(t) * (e_\alpha \cos(\omega t) - e_\beta \sin(\omega t))\} \sin(\omega t) \end{aligned} \tag{3.31}$$

and the x_β component is calculated

$$\begin{aligned} x_\beta^*(t) = &\{G_{ctrl}(t) * (e_\alpha \cos(\omega t) + e_\beta \sin(\omega t))\} \sin(\omega t) + \\ &+ \{G_{ctrl}(t) * (-e_\alpha \cos(\omega t) + e_\beta \sin(\omega t))\} \cos(\omega t) \end{aligned} \tag{3.32}$$

Now, the Laplace's transform is applied to the term multiplied by $cos(\omega t)$ in Equation 3.31 obtaining

$$X_\alpha^*(s) = G_{ctrl}(s) \mathcal{L}\{e_\alpha \cos(\omega t) + e_\beta \sin(\omega t)\} * \frac{s}{s^2 + \omega^2} \tag{3.33}$$

Using the Euler's formula

$$\cos(\omega t) = \frac{e^{j\omega t} + e^{-j\omega t}}{2} \tag{3.34a}$$

$$\sin(\omega t) = \frac{e^{j\omega t} + e^{-j\omega t}}{2j} \tag{3.34b}$$

into Equation 3.33 follows

$$\begin{aligned} X^*_\alpha(s) =& \frac{1}{4}\left[G_{ctrl}(s+j\omega)\left(E_\alpha(s+2j\omega) + E_\alpha(s) + jE_\beta(s+2j\omega) - jE_\beta(s)\right) + \right. \\ &\left. + G_{ctrl}(s-j\omega)\left(E_\alpha(s-2j\omega) + E_\alpha(s) - jE_\beta(s-2j\omega) + jE_\beta(s)\right)\right] \end{aligned} \tag{3.35}$$

When the other three terms of Equation 3.31 to 3.32 are computed and rearranging terms

$$\begin{pmatrix} x_\alpha(t) \\ x_\beta(t) \end{pmatrix}^* = \begin{pmatrix} k_p + \frac{k_i s}{s^2+\omega^2} & -\frac{k_i \omega}{s^2+\omega^2} \\ \frac{k_i \omega}{s^2+\omega^2} & k_p + \frac{k_i s}{s^2+\omega^2} \end{pmatrix} \begin{pmatrix} e_\alpha(t) \\ e_\beta(t) \end{pmatrix} \tag{3.36}$$

It can be seen that a synchronous frame PI controller presents cross-coupled elements in the stationary reference frame.

Synchronous frame PI to stationary *abc* reference frame

Defining a non normalized Clarke transform restricted to the $\alpha\beta$ components by

$$T = k \begin{pmatrix} 1 & -1/2 \\ 0 & \sqrt{3}/2 \end{pmatrix} \tag{3.37}$$

if T^{-1} is applied to Equation 3.36

$$T^{-1} \begin{pmatrix} x_\alpha(t) \\ x_\beta(t) \end{pmatrix}^* = T^{-1} \begin{pmatrix} k_p + \frac{k_i s}{s^2+\omega^2} & -\frac{k_i \omega}{s^2+\omega^2} \\ \frac{k_i \omega}{s^2+\omega^2} & k_p + \frac{k_i s}{s^2+\omega^2} \end{pmatrix} T T^{-1} \begin{pmatrix} e_\alpha(t) \\ e_\beta(t) \end{pmatrix} \tag{3.38}$$

then

$$\begin{pmatrix} x_a(t) \\ x_b(t) \end{pmatrix}^* = \begin{pmatrix} \frac{\sqrt{3}k_i\omega + 3k_p\omega^2 + 3k_p s^2 + 3k_i s}{3(\omega^2+s^2)} & \frac{2\sqrt{3}k_i\omega}{3(\omega^2+s^2)} \\ \frac{2\sqrt{3}k_i\omega}{3(\omega^2+s^2)} & \frac{-\sqrt{3}k_i\omega + 3k_p\omega^2 + 3k_p s^2 + 3k_i s}{3(\omega^2+s^2)} \end{pmatrix} \tag{3.39}$$

Stationary frame PI in the synchronous reference frame

In case that Equation 3.30 refers to the stationary abc or $\alpha\beta$ frame, the controller matrix is called stationary frame PI matrix. As it is diagonal, the application of a linear base change, as the one presented in Equation 3.37, does not affect to its expression. On the other hand, when the stationary matrix controller is translated to the synchronous reference frame, a similar analysis as the one conducted in Equation 3.29 to 3.33 can be applied, concluding that

$$\begin{pmatrix} x_d(t) \\ x_q(t) \end{pmatrix}^* = \begin{pmatrix} k_p + \frac{k_i s}{s^2+\omega^2} & \frac{k_i \omega}{s^2+\omega^2} \\ -\frac{k_i \omega}{s^2+\omega^2} & k_p + \frac{k_i s}{s^2+\omega^2} \end{pmatrix} \begin{pmatrix} e_d(t) \\ e_q(t) \end{pmatrix} \tag{3.40}$$

Rotation frame controller in the synchronous reference frame

Now, the controller matrix is based on a resonant or rotation frame. If the conventional PI expression in Equation 3.30 is substituted by the SOGI controller expression, see Equation 3.27, then

$$[G_{ctrl}(s)] = \begin{pmatrix} k_p + \frac{2k_i s}{s^2+\omega^2} & 0 \\ 0 & k_p + \frac{2k_i s}{s^2+\omega^2} \end{pmatrix} \tag{3.41}$$

Again, a similar analysis as the one conducted in Equation 3.29 to 3.33 can be applied, concluding that

$$\begin{pmatrix} x_d(t) \\ x_q(t) \end{pmatrix}^* = \begin{pmatrix} k_p + \frac{k_i}{s} + \frac{k_i s}{s^2+4\omega^2} & -\frac{2k_i \omega}{s^2+4\omega^2} \\ \frac{2k_i \omega}{s^2+4\omega^2} & k_p + \frac{k_i}{s} + \frac{k_i s}{s^2+4\omega^2} \end{pmatrix} \begin{pmatrix} e_d(t) \\ e_q(t) \end{pmatrix} \tag{3.42}$$

Controller frame comparison in the synchronous reference frame

In [160] a comparison by means of the final value theorem is done applied to the close-loop matrix transfer function [CL(s)], too. The [CL(s)] has to be computed by the negative feedback expression obtained according to the corresponding term of the matrix controller and Equation 3.1.

The comparison is calculated for the three aforementioned controller frames under the synchronous reference frame. If the $\lim_{s\to 0} s\,[\mathrm{CL}(s)]$ is computed for the stationary frame PI in the synchronous reference frame, considering an unitary step input set-point, then

$$\lim_{s\to 0}[\mathrm{CL}(s)] = \begin{pmatrix} \frac{(Rk_p+k_p^2-k_i)\omega^2+k_i^2}{\omega^4+(R^2+2Rk_p+k_p^2-2k_i)\omega^2+k_i^2} & \frac{\omega(k_p\omega^2+Rk_i)}{\omega^4+(R^2+2Rk_p+k_p^2+2k_i)\omega^2+k_i^2} \\ \frac{-\omega(k_p\omega^2+Rk_i)}{\omega^4+(R^2+2Rk_p+k_p^2+2k_i)\omega^2+k_i^2} & \frac{(Rk_p+k_p^2-k_i)\omega^2+k_i^2}{\omega^4+(R^2+2Rk_p+k_p^2-2k_i)\omega^2+k_i^2} \end{pmatrix} \tag{3.43}$$

For the synchronous frame PI and the resonant frame controller, the steady state error is

$$\lim_{s\to 0}[\mathrm{CL}(s)] = \begin{pmatrix} 1 & 0 \\ 0 & 1 \end{pmatrix} \tag{3.44}$$

This results shows that the synchronous frame PI obtains proper results, being able to track the set-point with null gain steady state error. However, a coupled gain error matrix is achieved when a stationary frame PI is translated to the synchronous reference frame. To solve this issue, the rotation frame controller achieves same results of null gain error in steady state.

3.3 Conventional resonant controller analysis

3.3.1 Introduction

As has been mentioned, tracking a sinusoidal reference signal with zero steady state error is a crucial aspect in single-phase or three-phase VSI. Current regulation in Voltage-Source Converters (VSC) is present in many applications such as AC motor drives, parallel active filters, wind turbines, static synchronous compensator and photovoltaic systems [177]. On the other hand, some of the most remarkable applications that require voltage regulation are uninterruptible power supplies, series active filters and microgrid inverters [178].

In the case of AC microgrid VSI, as has been cited in Chapter 2, the electrical distribution is usually done in a four-wire configuration. This fact implies that the system can be treated as three independent single phase subsystems. As has been presented in Equation 3.27, a rotation frame controller can be used. Then, the controller matrix becomes

$$[G_{ctrl}(s)] = \begin{pmatrix} k_p + \frac{2k_i s}{s^2+\omega^2} & 0 & 0 \\ 0 & k_p + \frac{2k_i s}{s^2+\omega^2} & 0 \\ 0 & 0 & k_p + \frac{2k_i s}{s^2+\omega^2} \end{pmatrix} \tag{3.45}$$

This type of controller is also called Proportional-Resonant controller (PR) [179–181]. Taking into account the feature of compensating for both

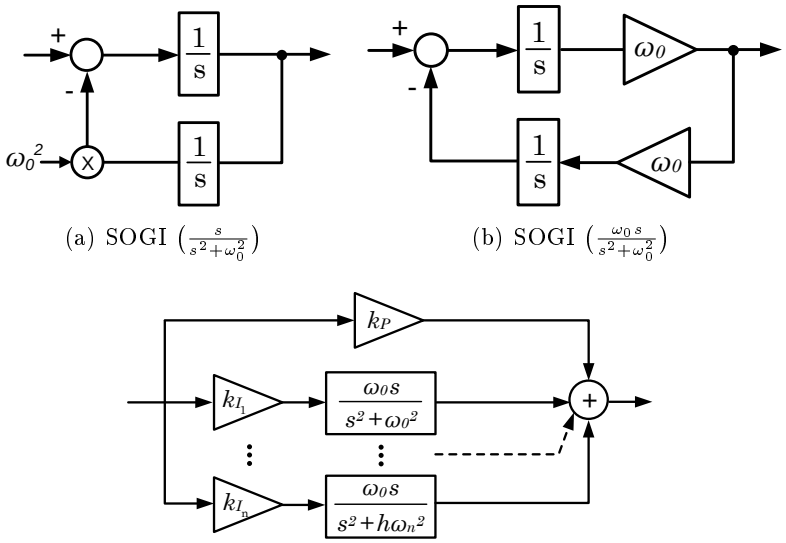

(a) SOGI $\left(\frac{s}{s^2+\omega_0^2}\right)$

(b) SOGI $\left(\frac{\omega_0 s}{s^2+\omega_0^2}\right)$

(c) PR-HC

Figure 3.5: Block diagrams of resonant controllers

positive and negative sequence components simultaneously, PR technique is perfectly able to deal with unbalanced three-phase systems [180, 182].

3.3.2 Fundamentals of the PR controller in continuous time

The transfer function of a PR controller, Figure 3.5(a), contains two poles located at $\pm j\omega_0$, see Figure 3.6, where ω_0 is the desired frequency to control.

On Figures 3.7 and 3.8 can be observed the behaviour of the frequency for a PR controller varying the k_p and k_i factors. The parameter k_p gives gain at all frequencies providing a "tail-up" behaviour altering the phase. The parameter k_i gives gain, shifting up the gain diagram without any effect on the phase when k_p is null.

A little modification consist of including a gain of ω_0 at the numerator [43], and it is useful for quadrature signal generation [183], see Figure 3.5(b). Hereinafter, the PR transfer function will be in accordance with this last concept.

Considering more than one frequency to control, i.e. Harmonic Compen-

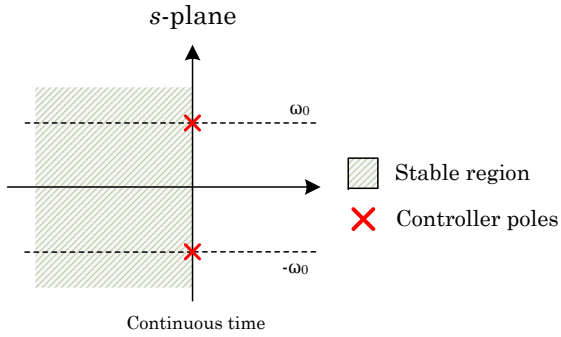

Figure 3.6: Continuous time SOGI pole location in the s-domain

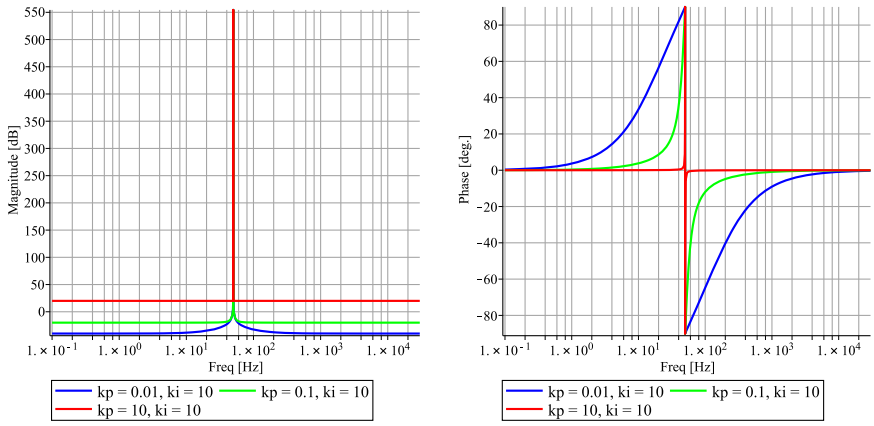

(a) Gain diagram (b) Phase diagram

Figure 3.7: Open-loop PR controller bode diagram under different k_p maintaining $k_i = 10$

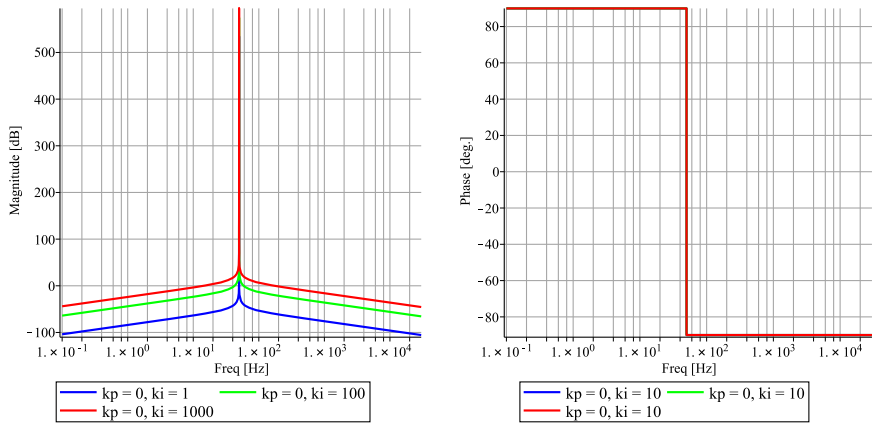

(a) Gain diagram (b) Phase diagram

Figure 3.8: Open-loop PR controller bode diagram under different k_i maintaining $k_p = 0$

sation, the transfer function of a PR-HC controller derives into

$$G_{\text{PR}-\text{HC}}(s) = k_P + k_I \frac{s\omega_0}{s^2 + \omega_0^2} + \sum_{k=2}^{n} \frac{k_{I_k}}{h} \frac{s\omega_k}{s^2 + \omega_k^2} \tag{3.46}$$

with k_P, k_I and k_{I_k} being the proportional and the integral gains of each resonant term, respectively, and h the harmonic component of the fundamental frequency ω_0. Figure 3.5(c) shows an scheme in a block diagram of a PR-HC. The k_{I_k} factor is divided by k in order to compensate the additional gain provided by ω_k and, thus, all integral gains are homogeneously scaled.

A sequence-decoupled resonant controllers was proposed in [184], in which the gains for positive and negative sequences are adjusted individually. To do so, a multi-state variable structure is constructed.

An alternative to the standard PR controller becomes the previously mentioned vector proportional integral (VPI) controllers [185], see Equation 3.28.

Another alternative is to apply a delay compensation to the PR controller. For large values of ω_0, the delay caused by the sampling time and the modulation can affect the system performance and the stability, too. For this reason, using a rotational transformation in the standard PR transfer function of a phase lead ϕ_k allows to compensate possible delays [186] using

$$H_{PI^d k_{VPI\pm}} = k_{p_k} + \frac{k_{i_k}}{s \mp jk\omega} e^{\pm\phi_k} \tag{3.47}$$

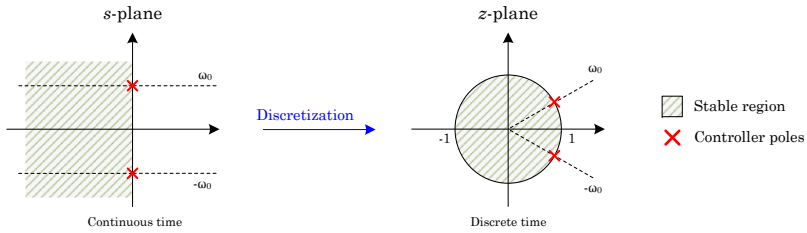

Figure 3.9: Ideal mapping of resonant poles from s to z domain

then,

$$G_{PR}^{d}(s) = H_{PI^{d}k_{VPI+}} + H_{PI^{d}k_{VPI-}} = k_P + k_I \frac{s\cos(\phi_k) - \omega_0 \sin(\phi_k)}{s^2 + k^2\omega_0^2} \quad (3.48)$$

The discrete implementation

Several options are available to discretize the PR transfer function, which is specially sensitive to this process because of the obtained infinite gain and the narrow band [187]. Continuous time poles are expected to be mapped in the unity circle of the z-plane, as is shown in Figure 3.9. Thus, the infinity gain will be preserved. Moreover, as it is deeply detailed in [177], some discrete techniques map the poles either inside or outside the unity circle, whereas others lead to a deviation of the resonant peak that worsens as $h\omega_0$ increases. In general, it can be stated that for low frequencies (50/60 Hz) and even for low order harmonics, any continuous to discrete technique offers satisfactory results. However, they should not be used for applications in which higher frequencies have to be tracked [187].

The different digital implementations of resonant controllers are obtained either discretizing the continuous transfer function directly or discretizing each integrator separately, which lead to several combinations. Best alternatives regarding performance and, in essence, fidelity to continuous time, are tustin with prewarping and triangle-equivalent hold methods [177]. Then, the implementation of such controllers can be carried out in two ways:

- Considering the double-integrator scheme. In this manner, each integrator is discretized separately and intermediate saturations or anti-windup methods can be applied.
- Considering the filter form, i.e. difference equations. In this case, several implementations are available: direct form I, direct form II

and the transposed forms of previous both. In general, quantification errors affect significantly all these methods, and filters of a higher order than two should be implemented in cascaded forms to avoid this effect [188]. The main difference between them is the number of necessary memory positions and mathematical operations. The direct form II takes advantage in regard to this. However, it is not suitable for resonant filters because internal calculations are more susceptible to produce overflows. An alternative for low cost fixed-point digital signal processor is called delta (δ) operator. It has proven to outperform the standard z-based filter due to its less sensibility to the coefficients rounding errors, even at very low representation precision [189, 190].

3.3.3 Stability analysis in continuous time

As a microgrid VSI has to operate in grid-connected mode and, also, in grid-disconnected mode, the system under study is a VSI with an LCL-type coupling filter. In this section, the system is described in the continuous time domain and the stability areas using PR controllers for each of the inner control loops of a VSI are identified, i.e. for the voltage and current loops. Nyquist diagrams supports the analysis. From now on, subscripts i and u mean current or voltage loop, respectively.

The double closed-loop control block diagram is depicted in Figure 3.10. An inner current loop allows to control the current through the the output inductance L_1. A feedforward structure is assumed to compensate the u_C voltage disturbance. Regarding the voltage loop, the magnitude to be controlled is the voltage of the capacitor u_C. In this case, the disturbance is the output current i_{L2}, and a feedforward structure is used as well. The Pulse-Width Modulator (PWM) block used for modulation can be considered as a gain K. A computational delay could also be considered and it can be modelled as one sampling period delay in the direct control chain. For simplicity the delay is considered null and the gain K is set to one. The delay will be considered in the discrete time analysis.

Next sections analyses the stability in the continuous time domain for the inner control loops under resonant controllers. The study is conducted by means of Nyquist characteristic frequencies analysis; when ω is null, when ω equals to ω_0 and when ω tends to infinite.

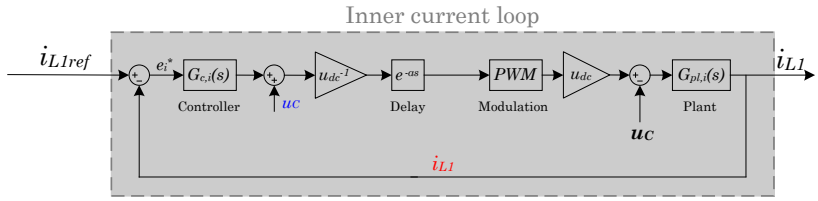

(a) Inner current control loop

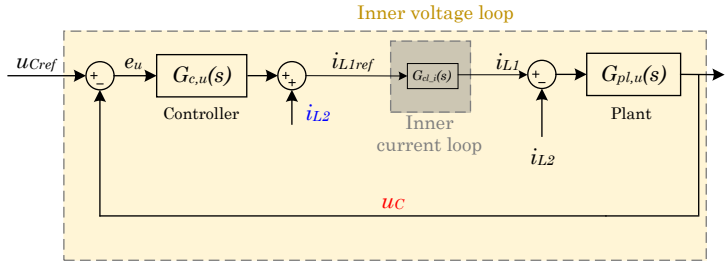

(b) Inner voltage control loop cascaded with the inner current control loop

Figure 3.10: Continuous time double close-loop block diagram control system, with feedback (red) and feedforward (blue) signals

Current loop analysis

For the current loop case, the plant transfer function for an inductance is defined by

$$G_{pl,i}(s) = \frac{I(s)}{\Delta U(s)} = \frac{1}{Ls + R} \tag{3.49}$$

and the open loop transfer function, considering only a fundamental ω_0 component, for the PR controller presented in Equation 3.46, is

$$OL_i(s) = \frac{k_{P_i}(s^2 + \omega_0^2) + k_{I_i}\omega_0 s}{(s^2 + \omega_0^2)(Ls + R)} \tag{3.50}$$

The significant frequency values of the Nyquist plot are:

- $\omega = 0$ (Start point). $\Re(OL_i(j\omega)) = \frac{k_{P_i}}{R}$ and $\Im(OL_i(j\omega)) = 0$.
- $\omega = \omega_0$ (Resonance). When the limits to ω_0 are computed
  - $\lim_{\omega \to \omega_0^{\mp}} \{\Re(OL_i(j\omega))\} = \pm\infty$
  - $\lim_{\omega \to \omega_0^{\mp}} \{\Im(OL_i(j\omega))\} = \pm\infty$

  An asymptote with $\frac{R}{L\omega_0}$ slope is followed. An infinite clockwise encirclement takes place at this frequency because of the π phase lag inherent to the resonant term.
- $\omega \longrightarrow +\infty$ (End point). When the limits to $+\infty$ are computed
  - $\lim_{\omega \to +\infty} \{\Re(OL_i(j\omega))\} = 0$
  - $\lim_{\omega \to +\infty} \{\Im(OL_i(j\omega))\} = 0$

  describing a slope that tends to $\frac{k_{P_i} L}{k_{I_i} L\omega_0 - k_{P_i} R}\omega$ (the sign of this slope will depend on the denominator). If an asymptotic analysis of the phase is done, the numerator contributes with $+\pi$ rad, the resonant pole with -π rad and the plant with -$\pi/2$ rad. Therefore, the final phase tends to $-\pi/2$ rad.

Taking into account these frequencies and that the possible values of ω that make $\Im(OL_i(\omega)) = 0$ are $\{0, \pm\frac{\sqrt{Lk_{P_i}\omega_0(Lk_{P_i}\omega_0 - Rk_{I_i})}}{Lk_{P_i}}\}$, if the positive root is substituted in $\Re(OL_i(\omega))$ it can be pointed out that the solution is $\frac{k_{P_i}}{R}$, which is always a positive value. It can be deduced that in continuous time, if $k_{P_i} > 0$ and $k_{I_i} > 0$, the system is always stable because $Z = N + P =$

0 (Nyquist criterion), being P the number of poles with positive real part and N the number of counter-clockwise encirclements around $(-1+j0)$ (in this case, $P=0$ and $N=0$).

If a PR-HC controller is considered, the results can be extended: the asymptote for a harmonic component k has a slope of $\frac{R}{L\omega_h}$ and will take place at $\varphi_h = \tan^{-1}(\frac{R}{L\omega_h}) - \frac{\pi}{2}$.

Figure 3.11 shows Nyquist diagrams considering $L = 250\,\mu$H, $R = 0.05\ \Omega$, $\omega_0 = 100\pi$ rad/s, $k_{P_i} = 1.5$, $k_{I_i} = 0.01$ and $k_{I_3} = \frac{k_{I_i}}{3}$. Figure 3.11(a) shows that the slope is inversely proportional to ω_0. Figure 3.11(b) presents how the starting point is displaced to the right side of the real axis, being proportional to the new k_{P_i} gain and making the Nyquist trajectory wider maintaining the slope values. Finally, Figure 3.11(c) shows how k_{I_i} widens the trajectory at each $h\omega_0$ but maintains the slope values, too. In conclusion, the stability of the current loop in continuous time is not compromised by ω_0, k_{P_i} or k_{I_i}.

If the plant parameters are modified, it can be seen in Figure 3.11(d) that L affects the angle and the slope of the resonance but it does not affect the main trajectory. Finally, Figure 3.11(e) shows that R has a bigger effect on the diagram, changing both the asymptotes and the start point.

Voltage loop analysis

For simplicity, the inner current loop (Figure 3.10) is substituted by a unity gain block. This allows to simplify the tuning procedure of the outer voltage loop. This assumption is consistent if the rules of nested loops are respected (the most external loop has to be slower presenting a narrow bandwidth). In this case, the passive element considered for control purposes is an AC capacitor C and its equivalent series resistance R_C:

$$G_{pl,u}(s) = \frac{1}{Cs} + R_C \tag{3.51}$$

The open loop transfer function using Equation 3.46, Equation 3.51 and considering only the fundamental ω_0 component is

$$OL_u(s) = \frac{(k_{P_u}(s^2+\omega_0^2) + k_{I_u}\omega_0 s)(R_C C s + 1)}{(s^2+\omega_0^2)Cs} \tag{3.52}$$

The frequency values of interest in the Nyquist plot are:

- $\omega = 0$ (Start point). In this case, the capacitor acts as a pure integrator. Analysing the limits to 0, $\lim_{\omega\to 0}\{\Re(OL_u(j\omega))\} = \frac{(CR_C k_{P_u}\omega_0^2 + k_{I_u})}{C\omega_0^2}$

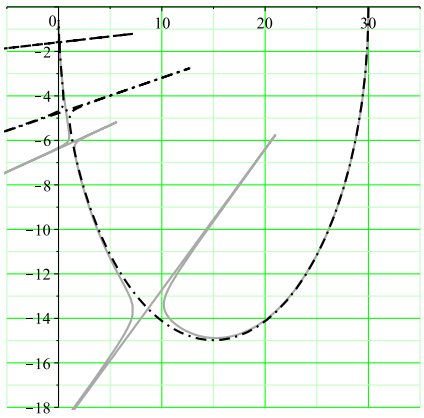

(a) ω_0 and $4\omega_0$

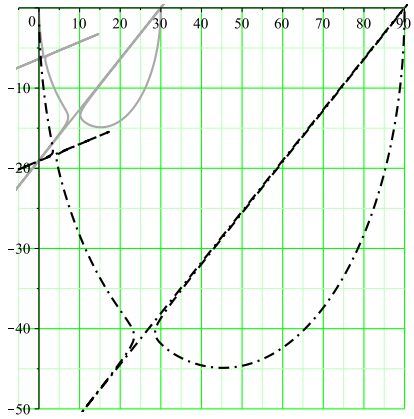

(b) k_P and $3k_P$

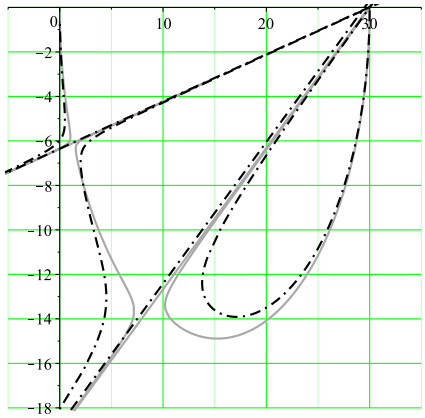

(c) k_I and $10k_I$

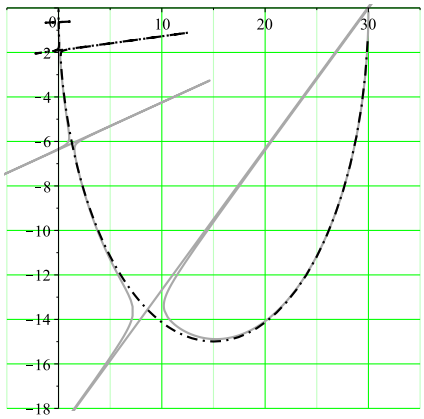

(d) L and $10L$

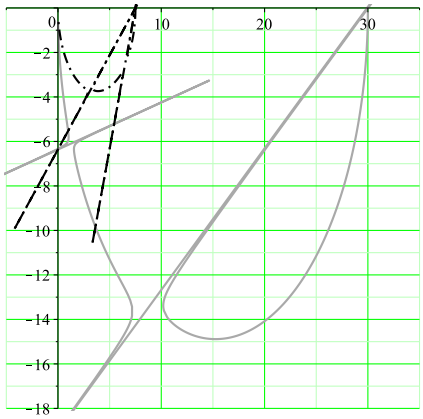

(e) R and $4R$

Figure 3.11: Nyquist plots of $OL_i(s)$ with the base parameter (solid gray) and the modified parameter (dashed black).

and $\lim_{\omega\to 0}\{\Im(OL_u(j\omega))\} = -\infty$.

- $\omega = \omega_0$ (Resonance). When the limits to ω_0 are computed
  - $\lim_{\omega\to\omega_0^{\mp}}\{\Re(OL_u(j\omega))\} = \pm\infty$
  - $\lim_{\omega\to\omega_0^{\mp}}\{\Im(OL_u(j\omega))\} = \pm\infty$

  describing an asymptote with a slope of $CR_C\omega_0$. The asymptote is horizontal for an ideal capacitor.

- $\omega \longrightarrow +\infty$ (End point). When the limits to $+\infty$ are computed
  - $\lim_{\omega\to+\infty}\{\Re(OL_u(j\omega))\} = R_C k_{P_u}$
  - $\lim_{\omega\to+\infty}\{\Im(OL_u(j\omega))\} = 0$

  If $k_{P_u} > 0$ and $R_C \geq 0$, the end point of the Nyquist diagram is always located at the right side of the s-plane. Doing an asymptotic analysis of Equation 3.52, it can be seen that the final phase tends to 0 rad.

As in the current loop case, taking into account these frequencies and considering that the possible ω values that satisfy $\Im(OL_u(\omega)) = 0$ are $\{\pm\frac{\omega_0\sqrt{(CR_C k_{I_u}\omega_0 + k_{P_u})k_{P_u}}}{CR_C k_{I_u}\omega_0 + k_{P_u}}\}$, if the positive root is substituted in $\Re(OL_u(\omega))$ it can be seen that the solution is $\frac{C^2R_C^2 k_{P_u}\omega_0^2 + CR_C k_{I_u}\omega_0 + k_{P_u}}{C^2R_C\omega_0^2}$, being always a positive value. Thus, for $k_{P_u} > 0$ and $k_{I_u} > 0$, the system is stable for any ω_0. These results can be extended to the PR-HC system, where each harmonic component k has a slope of $R_C\omega_h$ and will take place at $\varphi_k = \tan^{-1}(R_C\omega_k) - \frac{\pi}{2}$.

In the same way than in the current loop case, Figure 3.12 shows Nyquist diagrams considering $C = 350\,\mu$F, $R_C = 0.1\ \Omega$, $\omega_0 = 100\pi$ rad/s, $k_{P_u} = 1.5$, $k_{I_u} = 0.01$ and $k_{I_{u3}} = \frac{k_{I_u}}{3}$. Figures 3.12(a)-3.12(c) show the relation between the Nyquist plot and ω_0, k_{P_u} and k_{I_u}, respectively. The stability of the system in continuous time is not compromised by these values. Changing the plant parameters, it can be seen in Figure 3.12(d) that the bigger C value, the bigger the slope and the smaller the asymptotic angle over the real axis. Finally, Figure 3.12(e) shows that the bigger R_C, the higher the slope and the displacement of the trajectory to the right.

If the direct chain is computed without neglecting the inner loop

$$OL'_u(s) = \frac{(k_{P_u}(s^2+\omega_0^2) + k_{I_u}\omega_0 s)(k_{P_i}s^2 + k_{P_i}\omega_0^2 + k_{I_i}\omega_0 s)(CR_C s + 1)}{(s^2+\omega_0^2)(Ls^3 + (R+k_{P_i})s^2 + (L\omega_0^2 + k_{I_i}\omega_0)s + R\omega_0^2 + k_{P_i}\omega_0^2)Cs} \tag{3.53}$$

Superscript ($'$) indicates that the transfer function considers both loops. The three relevant frequencies are analysed as in the previous cases:

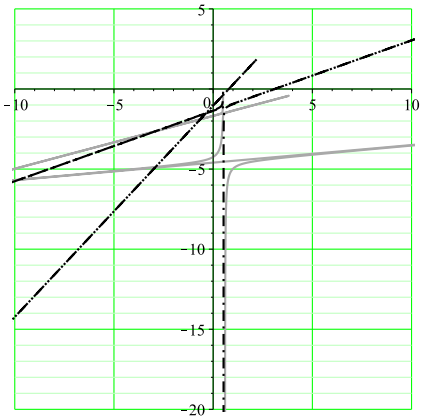

(a) ω_0 and $4\omega_0$

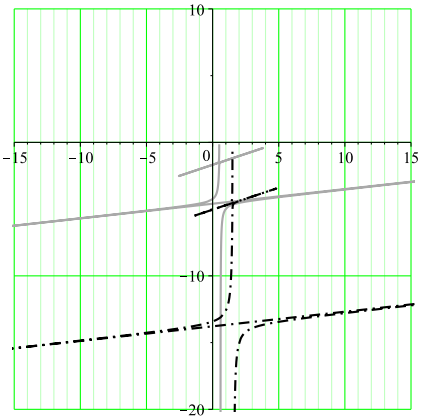

(b) k_{P_v} and $3k_{P_u}$

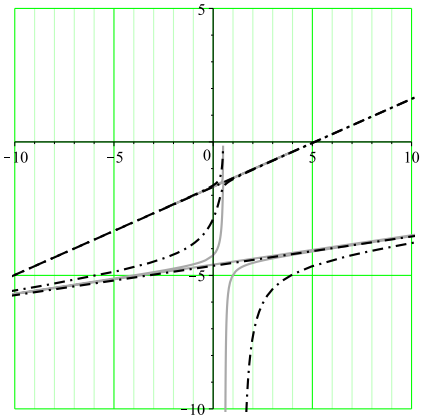

(c) k_I and $10k_I$

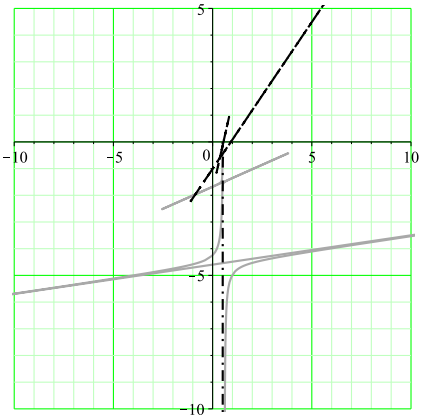

(d) C and $10C$

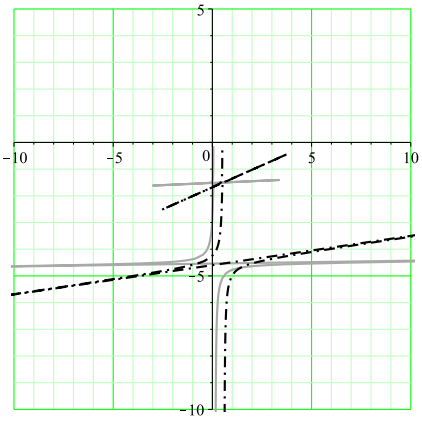

(e) R_C and $10R_C$

Figure 3.12: Nyquist plots of $OL_u(s)$ with the base parameter (solid grey) and the modified parameter (dashed black).

- $\omega = 0$ (Start point). Analysing the limit to 0
  - $\lim_{\omega\to 0}\{\Re(OL'_u(j\omega))\} =$
    $= \frac{R_C C R k_{P_i} k_{P_u} \omega_0 + C R_C k_{P_i}^2 k_{P_u} \omega_0 - L k_{P_i} k_{P_u} \omega_0 + R k_{I_i} k_{P_v} + R k_{I_u} k_{P_i} + k_{I_u} k_{P_i}^2}{\omega_0 C (R^2 + 2R k_{P_i} + k_{P_i}^2)}$
  - $\lim_{\omega\to 0}\{\Im(OL'_u(j\omega))\} = -\infty$
- $\omega = \omega_0$ (Resonance). When the limits to ω_0 are computed
  - $\lim_{\omega\to \omega_0^{\mp}}\{\Re(OL'_u(j\omega))\} = \pm\infty$
  - $\lim_{\omega\to \omega_0^{\mp}}\{\Im(OL'_u(j\omega))\} = \pm\infty$

  An asymptote that is described by $CR_C\omega_0$ is followed. It is important to remark that if an ideal capacitor is considered, the asymptote is horizontal.
- $\omega \longrightarrow +\infty$ (End point). When the limits to ω_0 are computed
  - $\lim_{\omega\to +\infty}\{\Re(OL'_u(j\omega))\} = 0$
  - $\lim_{\omega\to +\infty}\{\Im(OL'_u(j\omega))\} = 0$

  If an asymptotic analysis is done as in the previous cases, see Equation 3.53, the final phase tends to $-\pi/2$ rad.

In this case, the stability cannot be guaranteed analytically as in the previous two cases. It will depend on the inner loop. Thus, the maximum resonant frequency $h\omega_0$ is limited. Because of the complexity of the resultant equations and the large amount of parameters, a possible method to prove this fact is with a practical case. In Figure 3.13, a comparison between $OL_u(s)$ and $OL'_u(s)$ is presented. The bandwidth of the inner loop must be higher than the outer loop, so that a faster inner dynamic will be ensured. As k_P determines the bandwidth of the system, a reduction of the inner loop bandwidth (for a fixed outer loop bandwidth) may lead to an unstable system. In this example, for $k_{P_i} = 1.0$, see Figure 3.13(a), the system is unstable, whereas for $k_{P_i} = 2.5$ and $k_{P_i} = 5.0$, observe Figures 3.13(b)-3.13(c), the system becomes stable. In these examples, $k = 13$, $k_{P_u} = 0.5$ and $k_{I_u} = 1.0$. The plant parameters are set equal as the base values previously used. Moreover, k_I values are also important. In Figures 3.13(c)-3.13(d), the difference between $k_{I_i} = 1$ and $k_{I_i} = 5$ is shown. It can be seen that the effect of the inner loop is lower if k_{I_i} increases in relation with k_{I_u}. When k_{P_i} and k_{I_i} tend to high values, $OL'_u(s)$ is close to $OL_u(s)$. A higher resonant frequency without compromising the stability could be achieved in this last case.

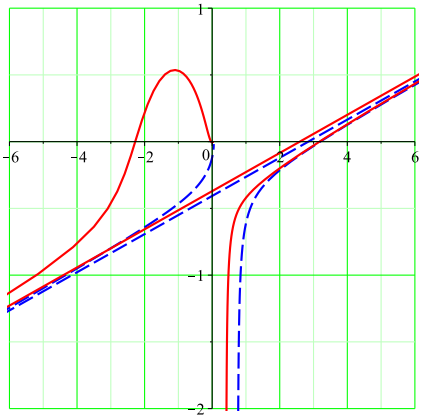

(a) $k_{P_i} = 1.0$, $k_{I_i} = 1.0$

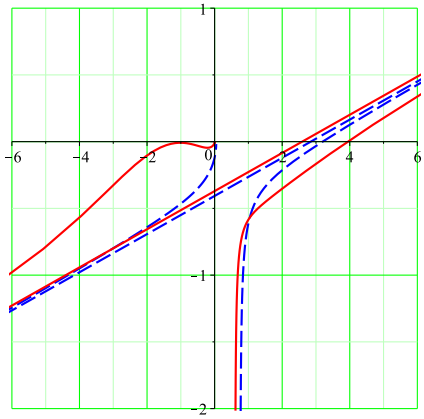

(b) $k_{P_i} = 2.5$, $k_{I_i} = 1.0$

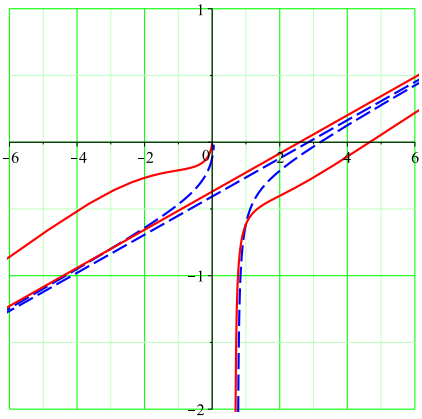

(c) $k_{P_i} = 5.0$, $k_{I_i} = 1.0$

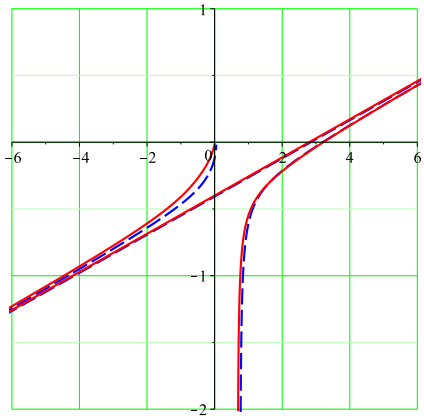

(d) $k_{P_i} = 5.0$, $k_{I_i} = 5.0$

Figure 3.13: Nyquist plots of $OL_u(s)$ and $OL'_u(s)$ to demonstrate the effect of the inner loop.

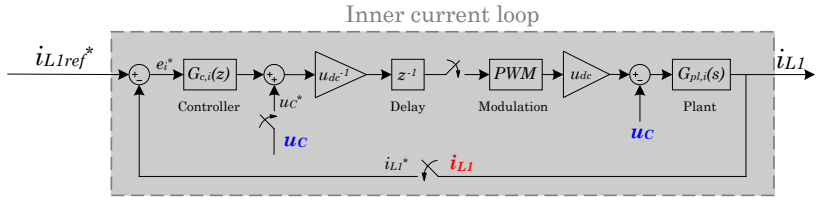

(a) Inner current control loop

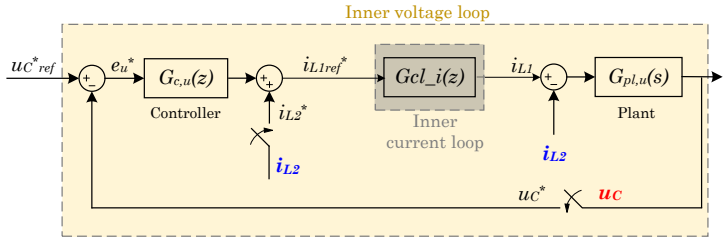

(b) Inner voltage control loop cascaded with the inner current control loop

Figure 3.14: Discrete time double close-loop block diagram control system, with feedback (red) and feedforward (blue) signals

3.3.4 Stability analysis of the discrete time system

Results obtained in Section 3.3.3 cannot be directly extended to discrete time. In this case, Figure 3.14 represents the considered system for the discrete time analysis.

In discrete time domain, equation $z = e^{sT_s}$ is satisfied. However, if this relation is used to analyse the system in the frequency domain, obtained expressions become complex. To avoid the use of exponential terms, the bilinear transformation $z = \frac{2+T_s w}{2-T_s w}$ is applied. To discuss in the frequency domain, relation $w = j\omega_w$ must be used. The relation between ω_w and ω is described by $\omega_w = \frac{2}{T_s}\tan\left(\frac{\omega T_s}{2}\right)$. Thus, the interval $[0, \frac{\omega_s}{2}]$ in the z-domain becomes $[0, \infty]$ in the w-domain. When low frequencies are considered (in relation with the sampling frequency), $\omega_w \simeq \omega$ is satisfied [157].

As in the continuous time analysis of Section 3.3.3, three relevant frequencies are used to study the stability of the system by means of the Nyquist diagram for the discrete time case.

Current loop analysis

Discretizing the current controller of Equation 3.46 with the Triangular Equivalent Hold (TEH) method, applying Zero-Order-Hold (ZOH) to Equation 3.49 and neglecting the delay of one sampling period (otherwise, an extra z multiplies the denominator), the open loop transfer function becomes

$$OL_i(z) = \frac{(K_1 z^2 - k_{P_i} f z + k_{P_i} z^2 - K1 + k_{P_i}) K_2}{(z^2 - f z + 1)(z - b)} \tag{3.54}$$

The parameters are grouped as $K_1 = k_{I_i} d$, $f = 2\cos(a)$, $K_2 = kc$, $c = 1-b$, $b = e^{-RT_s/L}$, $d = \frac{1-\cos(a)}{a}$, $k = \frac{1}{R}$ and $a = h\omega_0$.

- $\omega_w = 0$ (Start point). $\Re(OL_i(j\omega_w)) = \frac{k_{P_i}}{R}$ and $\Im(OL_i(j\omega_w)) = 0$. The starting point will be located always at the right half-plane of the polar diagram.

- $\omega_w = \omega_0$ (Resonance). When the limits to ω_0 are computed
  - $\lim_{\omega_w \to \omega_0^{\mp}} \{\Re(OL_i(j\omega_w))\} = \infty$
  - $\lim_{\omega_w \to \omega_0^{\mp}} \{\Im(OL_i(j\omega_w))\} = \infty$

  The sign will depend on the slope, which in turn depends on all parameters. Qualitatively, for low $k\omega_0$ values the slope will be positive, whereas for high values will be negative.

- $\omega_w \longrightarrow +\infty$ (End point). When the limits to $+\infty$ are computed
  - $\lim_{\omega_w \to +\infty} \{\Re(OL_i(j\omega_w))\} = \frac{k_{P_i}(e^{\frac{RT_s}{L}} - 1)}{R(e^{\frac{RT_s}{L}} + 1)}$
  - $\lim_{\omega_w \to +\infty} \{\Im(OL_i(j\omega_w))\} = 0$

The first limit for the stability depends on the end point of the Nyquist trajectory. For a given plant and a given T_s, this limit is determined by

$$k_{P_{max}} = R(1 + e^{\frac{RT_s}{L}})(e^{\frac{RT_s}{L}} - 1)^{-1} \tag{3.55}$$

A higher value of k_{P_i} will make the system unstable, whereas for lower values the stability will depend on the resonant frequency and, also, on k_{I_i}. Figure 3.15 shows the conceptual possible trajectories of the Nyquist diagram for the current loop. It can be deduced that stability and stability margins depend on the sign of the slope and on the existence and position of points with null imaginary part, too. If the slope is positive, it is necessary

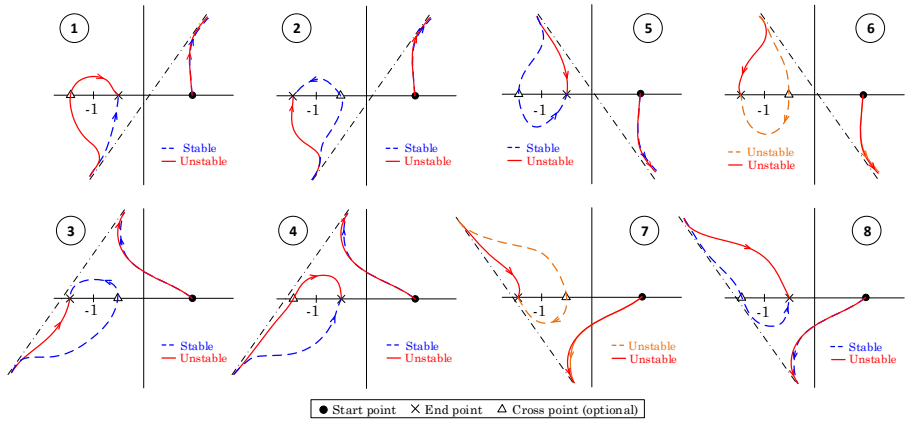

Figure 3.15: Conceptual possible trajectories of the Nyquist diagram for the current loop.

to guarantee the non-existence of a point with null imaginary part. On the other hand, if it exists, it has to be located on the right side of $(-1+0j)$. For a negative slope, the situation is the opposite: it is always necessary the existence of a point with null imaginary part and it has to be located on the left side of $(-1+0j)$.

The effect of z^{-1} is depicted in Figure 3.16. The considered parameters are $L = 250\ \mu$H, $R = 0.05\ \Omega$, $\omega_0 = 100\pi$ rad/s, $k_{P_i} = 1.0$ and different k_{I_i}: 0.1 and 1.0. It can be seen that the stability margins are reduced if the delay is included into the model. If the asymptote is far enough from the end point of the Nyquist trajectory, i.e. it does not distort too much this part of the diagram, the new $k'_{P_{max}}$ gain is limited to half. This is the limit that determines the stability of the system, see Figure 3.16(a). However, if the asymptote is close to the ending part of the diagram, observe Figure 3.16(b), this maximum value is not a sufficient condition to ensure the stability and the critical point can be encircled due to the position of the asymptote. Finally, Figure 3.16(c) shows that high k_{I_i} gain values can also lead to instability.

Considering the parameters L, R and T_s, the maximum $h\omega_0$ that maintains the system within stable conditions for different k_{P_i}-k_{I_i} values can be computed numerically. Three-dimensional representations are shown in Figure 3.17 representing different stability threshold surfaces. It can be seen that the highest values of k_{max} are obtained with high k_{P_i} and low k_{I_i}. Nevertheless, using a k_{P_i} value very close to $k_{P_{max}}$ should be avoided because

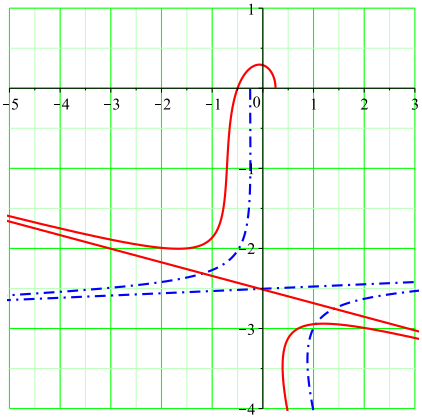

(a) $h = 5$, $k_{I_i} = 0.1$

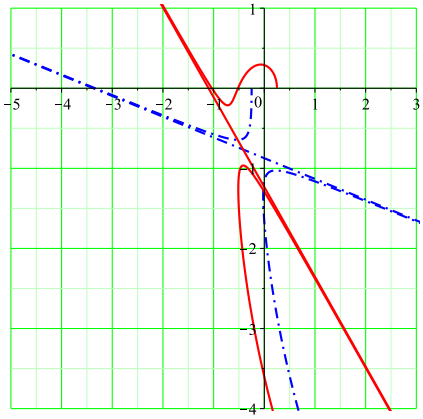

(b) $h = 15$, $k_{I_i} = 0.1$

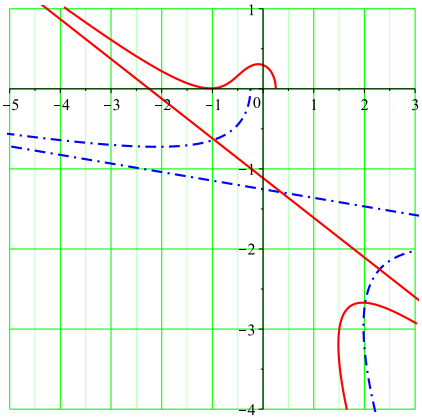

(c) $h = 9$, $k_{I_i} = 1.0$

Figure 3.16: Nyquist diagrams of $OL_i(z)$ with (red) or without (blue) one sampling period delay.

the stability margins would be low and this could lead to an unstable situation [177]. The k_{P_i} interval and k_{max} are proportional to the sampling frequency. Figures 3.17(a)-3.17(b) depict this behaviour. When computational delay is considered, see Figure 3.17(c), the shape of the surface changes slightly but $k_{P_{max}}$ remains equal, as can be compared with Figure 3.17(b).

Voltage loop analysis

Now, the voltage loop for the discrete case study is considered. As a first approach, the current loop is simplified as an unity gain. The controller is discretized using TEH. The plant is discretized applying ZOH method because it is more restrictive in terms of stability than First-Order-Hold (FOH). The open loop transfer functions results in

$$OL_u(z) = \frac{(K_{1_u} z^2 - k_{P_u} f z + k_{P_u} z^2 - K_{1_u} + k_{P_u})(T_s + CR_C z - CR_C)}{(z^2 - fz + 1)(z-1)C} \tag{3.56}$$

In this case, the parameters are grouped as $K_{1_u} = k_{I_u} d$, $f = 2\cos(a)$, $d = \frac{1-\cos(a)}{a}$ and $a = k\omega_0$. As in all aforementioned cases, the three relevant frequencies are analysed.

- $\omega_w = 0$ (Start point). $\Re(OL_u(j\omega_w)) = \frac{k_{P_u}(CR_C f - 2CR_C - 0.5T_s f + T_s) - 2K1_v T_s}{C(f-2)}$ and $\Im(OL_u(j\omega_w)) = -\infty$. The starting point location will be determined by the sign of $\Re(OL_u(j\omega_w))$.

- $\omega_w = \omega_0$ (Resonance).When the limits to ω_0 are computed
  - $\lim_{\omega_w \to \omega_0^{\mp}} \{\Re(OL_u(j\omega_w))\} = \mp\infty$
  - $\lim_{\omega_w \to \omega_0^{\mp}} \{\Im(OL_u(j\omega_w)\} = \mp\infty$

- $\omega_w \to +\infty$ (End point). When the limits to $+\infty$ are computed
  - $\lim_{\omega_w \to +\infty} \{\Re(OL_u(j\omega_w))\} = \frac{1}{2}\frac{k_{P_u}(2CR_C - T_s)}{C}$
  - $\lim_{\omega_w \to +\infty} \{\Im(OL_u(j\omega_w)\} = 0.$

When the inner loop with delay is considered, $OL'_u(z)$ has an 8^{th} order characteristic equation. For this reason, a qualitative analysis has been conducted. The proposed parameters are $C = 350\ \mu$F, $R_C = 0.1\ \Omega$, $\omega_0 = 100\pi$ rad/s, $k_{P_i} = 1.2$, $k_{I_i} = 0.5$, $k_{P_u} = 0.5$ and $k_{I_u} = 0.1$ ($k_{I_{j_h}} = k_{I_j}/h$, $j = i, u$). Considering a PR-HC controller ($h = 3, 5, 7, 9$), the effect of the

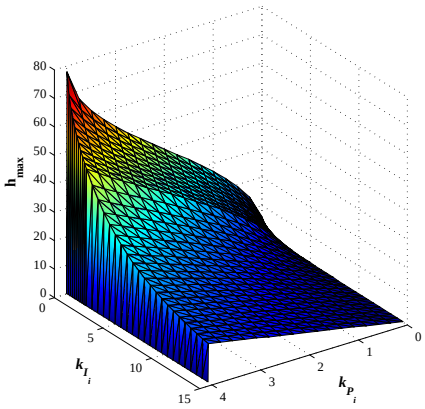

(a) $f_s = 8000$ Hz ($k_{P_{max}} = 4.00$)

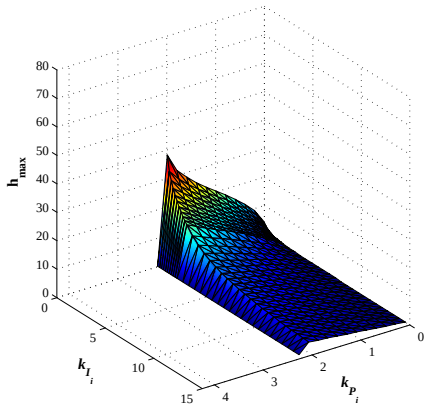

(b) $f_s = 4000$ Hz ($k_{P_{max}} = 2.00$)

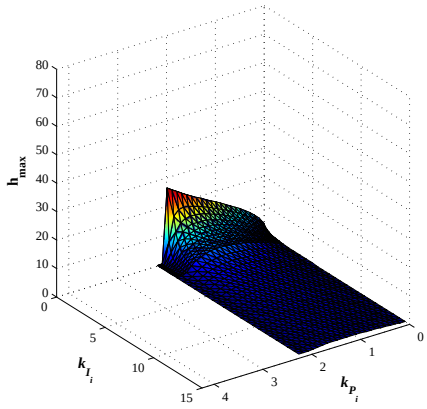

(c) $f_s = 8000$ Hz with delay

Figure 3.17: Effect of the delay and the sampling frequency in the highest stable harmonic for the current loop.

inner loop is shown in Figure 3.18(a). It should be noted that for low k_{I_u} values, the stability of the system is only constrained by the highest frequency controller. Therefore, Figure 3.18(b) supports that there is an interval of stable values for k_{I_i}, which is approximately $[0.10, 0.60]$. In Figure 3.18(c), the same behaviour is observed for k_{P_i} ($[1.05, 1.65]$ approximately). These intervals are relatively small because the example is near the stability limit.

The effect of the sampling frequency and the inner loop delay is shown in Figure 3.19. Thus, the maximum feasible frequency preserving the stability of the system, for a given k_{I_u} and k_{P_u}, is depicted.

In Figure 3.20, the effect of different R_C, k_{P_i} and k_{I_i} values is shown. When R_C is increased, the maximum value of k_{P_u} is reduced. Consequently, the 3D chart is compressed (Figure 3.20(a)-3.20(b)). If k_{I_i} is reduced, the stability of the system improves, see Figures 3.20(c)-3.20(d). An analogous behaviour is observed in Figure 3.18(b). Finally, it can be noticed that higher frequencies can be achieved with a higher k_{P_i} but, in such cases, the maximum k_{P_u} value is more constrained, observe Figures 3.20(e)-3.20(f). Consequently, a compromise solution must be taken for each particular situation.

3.3.5 Tuning of conventional PR controllers

Tuning methods for a PR controller can be performed by means of either time response [43] or frequency specifications [175, 191, 192]. In the last case, k_P defines the bandwidth of the closed loop system and each k_{I_k} defines the bandwidth at the vicinity of each resonant frequency, allowing more or less frequency sensitivity.

In this thesis, the controller is tuned according to time response criterion following the proposal of [43] for the current loop and extended to the voltage loop.

The current loop tuning

The current control loop under study is shown in Figure 3.14 as the gray shadowed region. In this case, the discrete time current plant, obtained by applying ZOH, is described by

$$G_{pl,i}(z) = (1 - z^{-1})\mathcal{Z}\left\{\mathcal{L}^{-1}\left[\frac{G_{pl,i}(s)}{s}\right]\Bigg|_{t=kT_s}\right\} = \frac{1}{R}\frac{1 - e^{\frac{-RT_s}{L}}}{z - e^{\frac{-RT_s}{L}}} \tag{3.57}$$

In [43] is proposed to use the discrete form based on the conversion from

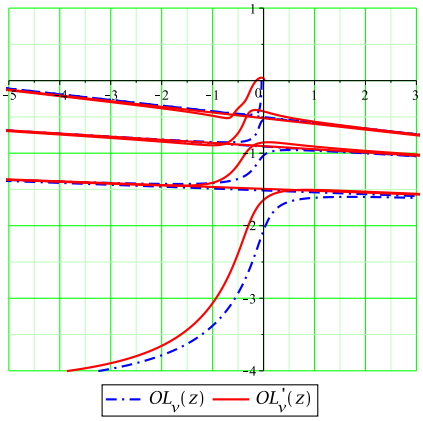

(a) Comparison of both systems

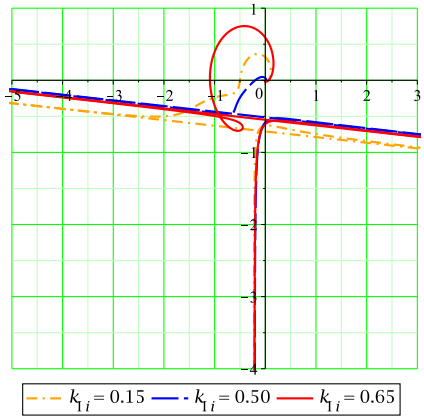

(b) k_{I_i} effect in $OL_v'(z)$

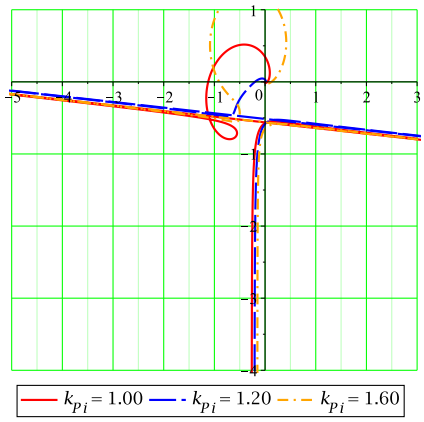

(c) k_{P_i} effect in $OL_v'(z)$

Figure 3.18: Inner current loop effect on the Nyquist diagram of the voltage loop.

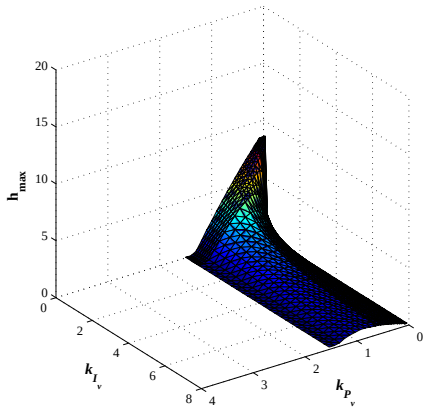

(a) $f_s = 8000$ Hz with delay

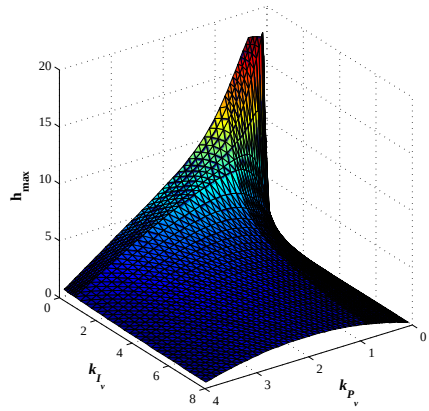

(b) $f_s = 8000$ Hz without delay

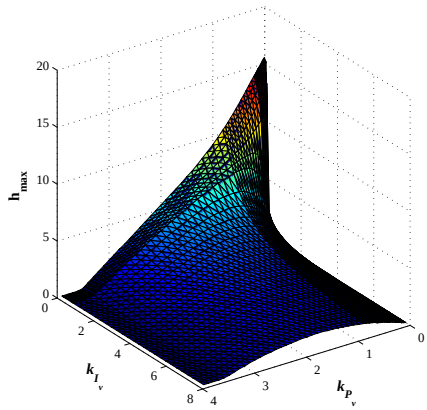

(c) $f_s = 16000$ Hz with delay

Figure 3.19: Effect of the delay and the sampling frequency in the highest stable harmonic for the voltage loop.

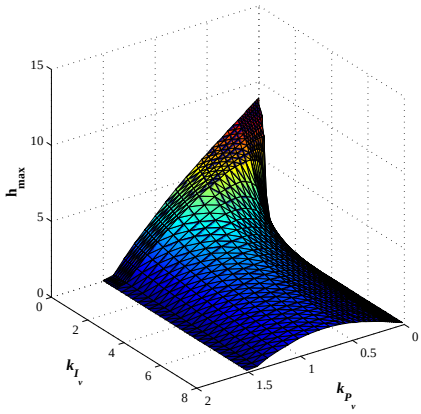

(a) $R_C = 0.5\ \Omega$

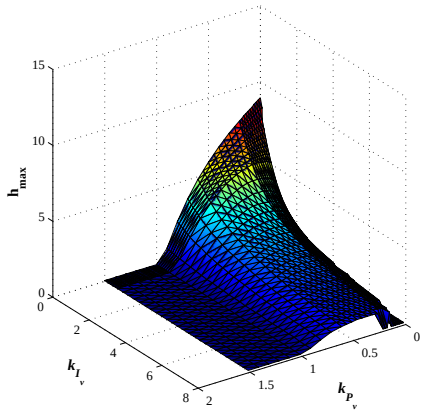

(b) $R_C = 1.0\ \Omega$

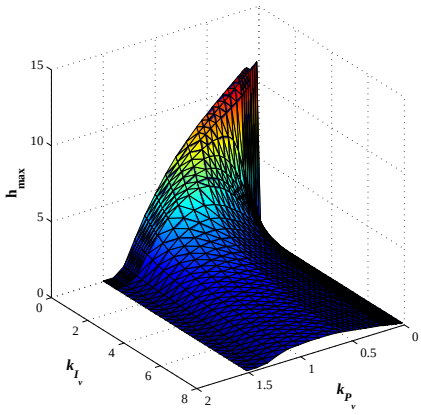

(c) $k_{I_i} = 0.5$

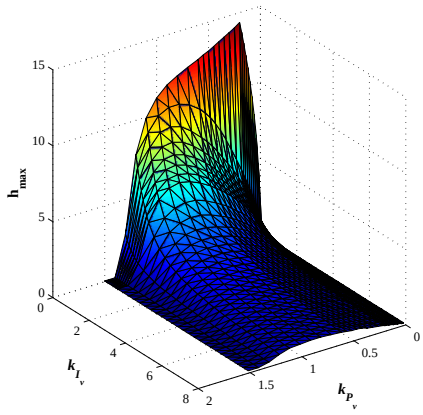

(d) $k_{I_i} = 0.1$

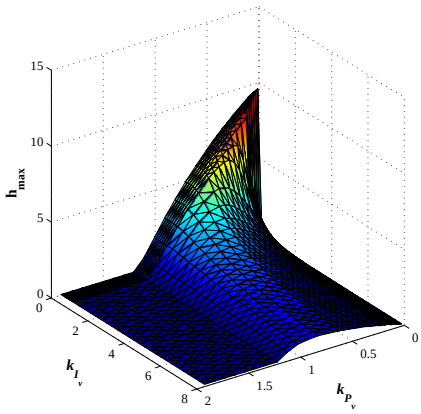

(e) $k_{P_i} = 1.25$

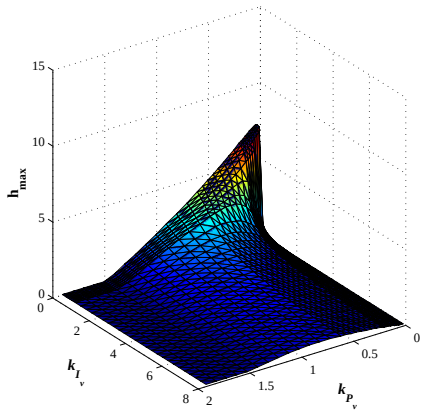

(f) $k_{P_i} = 0.75$

Figure 3.20: Effect of the delay and the sampling frequency in the highest stable harmonic for the voltage loop.

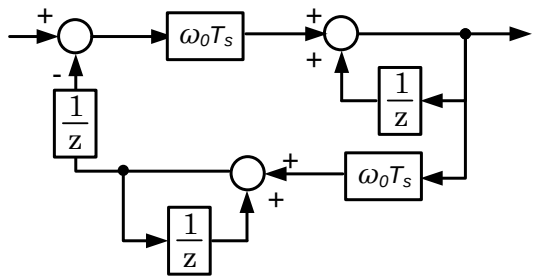

Figure 3.21: Discrete time proposal of a PR controller based on using backward Euler's integrators and introducing a delay in the positive feedback chain

continuous to discrete time of each integrator using backward Euler's introducing a delay in the positive feedback chain, as depicted in Figure 3.21.

If the desired waveform does not have harmonic components higher than the 5th or 7th, this discretization is adequate, especially if the sampling frequency f_s is high. One important point is that this option does not involve trigonometric components. So, the computational load is low. Its transfer function in z is described as

$$G'_{c,i}(z) = k_{p_i} + k_{i_i} \frac{\omega_0 T_s z(z-1)}{z^2 + (\omega_0^2 T_s^2 - 2)z + 1} \tag{3.58}$$

Another option, if the accuracy of the controlled frequencies must be ensured, is the discretization using the TEH alternative, because is one of the alternatives that offers best results [177]. Per contra, it introduces trigonometric components. This point can be an inconvenient in terms of computational time if the controlled ω_0 wants to be dynamically changed. In this last case, the transfer function is

$$G''_{c,i}(z) = k_{p_i} + k_{i_i} \frac{1 - \cos(\omega_0 T_s)}{\omega_0 T_s} \frac{z^2 - 1}{z^2 - 2z\cos(\omega_0 T_s) + 1} \tag{3.59}$$

Both methodologies derives into similar controller constants. Then, hereinafter, $G'_{c,i}(z)$ is considered. In [43] is exposed that the denominator term $\omega_0 T_s$ is considered really small in order to simplify the controller, assuming

$\omega_0^2 T_s^2 - 2 \backsimeq -2$. In this sense, the close loop is represented by

$$\begin{aligned} G'_{cl,i}(z) &= \frac{G'_{c,i}(z)G_{pl,i}(z)}{1 + G'_{c,i}(z)G_{pl,i}(z)} = \\ &= \frac{((T_s k_{i_i}\omega_0 + k_{p_i})z - k_{p_i})\alpha}{z^2 + (T_s k_{i_i}\omega_0\alpha + k_{p_i}\alpha - \beta - 1)z - k_{p_i}\alpha + \beta} \end{aligned} \tag{3.60}$$

with $\alpha = \frac{1-\beta}{R}$, $\beta = e^{-RT_s/L}$, $a = \omega_0 T_s$ and $b = 1 - \beta$. Imposing a second order system in discrete time

$$D(z) = (z - \rho e^{-j\theta})(z - \rho e^{+j\theta}) = z^2 - 2\rho\cos(\theta)z + \rho^2 \tag{3.61}$$

The module and angle of the poles are determined by

$$\rho = e^{-\xi\omega_n T_s} \tag{3.62}$$

$$\theta = \omega_n T_s \sqrt{1 - \xi^2} \tag{3.63}$$

If Equation 3.61 is compared coefficient by coefficient with the denominators of Equation 3.60 and, also, the damping factor ξ and natural frequency ω_n are set to the desired values, the controller can be tuned. The parameters ξ and ω_n are related by the establishment time to arrive into $\pm 2\%$ of the final value as

$$t_{set} \simeq \frac{4}{\xi\omega_n} \tag{3.64}$$

Thus, for the system $G'_{cl,i}(z)$, comparing and rearranging terms

$$(T_s k_{i_i}\omega_0\alpha + k_{p_i}\alpha - \beta - 1) = -2\rho\cos(\theta) \tag{3.65}$$

$$-k_{p_i}\alpha + \beta = \rho^2 \tag{3.66}$$

Finally, if the constants of the controller are isolated

$$k_{p_i} = \frac{\beta - \rho^2}{\alpha} \tag{3.67}$$

$$k_{i_i} = \frac{-2\rho cos(\theta) - k_{p_i}\alpha + \beta + 1}{\omega_0 T_s \alpha} \tag{3.68}$$

It has to be remarked that k_{p_i} is no dependent of ω_0 while k_{i_i} is inversely dependent of it. This indicates that to adapt the fundamental resonant frequency to a different value only one parameter needs to be recomputed.

It is relevant to consider two possible effects that can distort the tuned time response. To analyse the effect of this two situations it is proposed to consider $T_s = 125$ μs, $L = 250$ μH and $R = 50$ mΩ. The parameter ξ is set to 0.8 and the settling time is swept in the interval $[0.001, 0.02]$ s.

The first effect is the consideration of a sample delay in the direct chain if the computed constants are used directly. In this case, the characteristic equation without the delay changes from

$$z^2 + (K_1 K_2 k_i + K_2 k_{p_i} - b - 1)z - K_2 k_{p_i} + b \tag{3.69}$$

when no delay is assumed to

$$z^3 + (-b - 1)z^2 + (K_1 K_2 k_i + K_2 k_{p_i} + b)z - K_2 k_{p_i} \tag{3.70}$$

when the delay is considered. The parameters has been aggregated as $K_1 = \omega T_s$, $K_2 = kc$, $k = 1/R$, $c = 1 - b$ and $b = e^{-\frac{RT_s}{L}}$. The zeros remains equal in both cases.

Figure 3.22(a) details a comparison of an ideal case without delay and the use of the obtained constants on a system considering the delay effects. It can be observed that the response with the delay differs in respect to the ideal case but the obtained settling time delay is almost constant from a determinate target settling time.

On the other hand, for sinusoidal tracking the references are sine waves. Thus, depending on the settling time it can occur that the error sign changes while the feedback is following the reference producing a non expected higher settling time. This behaviour is shown in Figure 3.22(b). In this case, the system tends to not be able to accomplish with the targeted settling time.

The voltage loop tune

The voltage control loop under study is shown in Figure 3.14 as the yellow shadowed region. It can be observed that the new control diagram is constituted by the voltage controller, the current controller, the inductance and the new plant that is an AC capacitor. This loop is the responsible to control the voltage of the capacitor for AC applications.

In this case, for two nested loops correct operation it is necessary to guarantee that the outer loop responds slower than the inner one and the bandwidth of the external close loop has to be, at least, more than two times

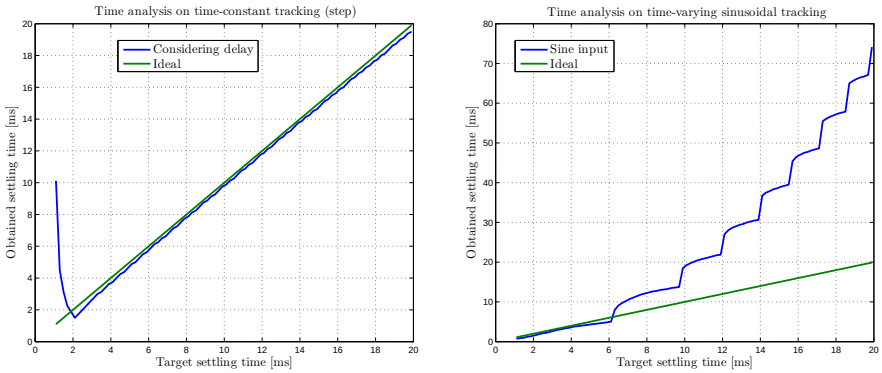

(a) Settling time effect on delay consideration

(b) Settling time effect on sine input

Figure 3.22: Effects on the settling time

the inner one. The action of the inverter to the plant is through the PWM module, so it is quite common to discretize the system using a ZOH, as has been done in the current loop development. If the ZOH is considered, the plant discretized is defined by

$$G_{pl,u}^{zoh}(z) = (1-z^{-1})\mathcal{Z}\left\{\mathcal{L}^{-1}\left[\frac{G_{pl,u}(s)}{s}\right]\Bigg|_{t=kT_s}\right\} = \\ = \frac{T_s z + C_{AC}R_{C_AC}(z-1)^2}{C_{AC}z(z-1)} \tag{3.71}$$

For the analytic tune, $R_{C_{AC}}$ is considered negligible because usually represents a low value ($\sim 10^{-3} - 10^{-2}\ \Omega$). Therefore, $R_{C_{AC}}C_{AC} << T_s$ is taken into account. The voltage controller $G'_{c,u}(z)$ is described also by the same transfer function as in Equation 3.58.

For simplicity, it should be remarked that next equations are developed considering that the inner loop acts as an unit gain and the ZOH is used to discretize the system. If the ideal inner current loop simplifications is not assumed, the obtained system has an order superior to two, and the same tuning as the current loop cannot be applied directly. Other techniques would be necessary, as pole dominance, making more difficult the automation of the tuning procedure. The close-loop transfer function of the system for the voltage control, considering again that the denominator term $\omega_0 T_s$ is considered really small, is

$$G'_{cl,u}(z) = \frac{G'_{c,u}(z)G_{pl,u}(z)}{1 + G'_{c,u}(z)G_{pl,u}(z)} = \\ = \frac{(z(T_s k_{i_u}\omega_0 + k_{p_u}) - k_{p_u})D}{z^2 + (DT_s k_{i_u}\omega_0 + Dk_{p_u} - 2)z - k_{p_u}D + 1} \tag{3.72}$$

being $D = T_s/C_{AC}$ and $a = \omega_0 T_s$. Rearranging and comparing the denominators of Equation 3.72 with a desired second order system like in Equation 3.61

$$DT_s k_{i_u}\omega_0 + Dk_{p_u} - 2 = -2\rho\cos(\theta) \tag{3.73}$$

$$-k_{p_u}D + 1 = \rho^2 \tag{3.74}$$

Solving the system and isolating the controller constants

$$k_{p_u} = \frac{1 - \rho^2}{D} \tag{3.75}$$

$$k_{i_u} = \frac{1 + \rho^2 - 2\rho cos(\theta)}{DT_s\omega_0} \tag{3.76}$$

An example is proposed considering a fundamental ω_0 of 100π rad/s, a $C_{AC} = 350$ μF, $t_{set} = 10$ ms, $\xi = 0.8$ and $Ts = 125$ μs to validate if the controller tuning operates properly. The obtained controller constants are $k_{p_u} = 0.2665$ and $k_{i_u} = 0.2650$. Thus, Figure 3.23 shows a simulation of the close loop where a sinusoidal reference is changed at time $t = 0.1$ s from 1 to 2 of peak amplitude. Figure 3.23 shows that for $f_0 = 50$ Hz the time specifications to arrive at 98% of the final value takes place after 18 ms. This is almost the double of the specified settling time. This is a clear evidence of the inversion sign issue of the error during the transient, as has been indicated in Figure 3.22(b).

3.4 Novel fractional resonant controller proposal

3.4.1 Fractional Calculus Fundamentals

The Factional Order Calculus (FOC) is a generalization of integration and differentiation considering non integer orders. Thus, the considered order can be rational, irrational or even complex. The possibility to use this

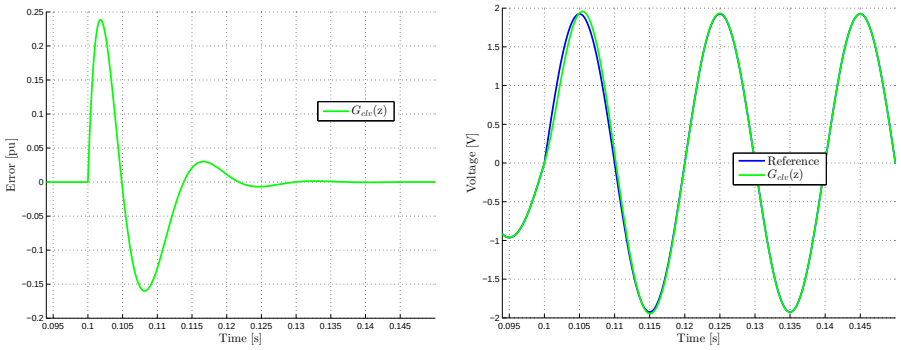

(a) Error evolution when the step response is targeted

(b) Time simulation

Figure 3.23: Simulation for the tune of the voltage controller at $f_0 = 50$ Hz

generalization allows to describe more accurately real systems. This fact permits to expand the possibilities of using different combination between the representation of the system and the controllers in the control field. For close-loop systems four options can be combined; integer-order plant and integer-order controller, integer-order plant and fractional-order controller, fractional-order plant and integer-order controller and, finally, both transfer functions using a fractional-order representation.

The fractional calculus has been proposed in 1695 by Leibniz and Hôpital when a half-order derivative was mentioned. The integro-differential operator ${}_aD_t^\alpha$ is defined as [193–195]

$$ {}_aD_t^\alpha = \begin{cases} \frac{d^\alpha}{dt^\alpha} & if \quad \Re(\alpha) > 0 \\ 1 & if \quad \Re(\alpha) = 0 \\ \int_a^t d(\tau)^{-\alpha} & if \quad \Re(\alpha) < 0 \end{cases} \tag{3.77} $$

where a and t are the limits of the operation (a is related with initial conditions) and α the order of the differ-integration (usually $\alpha \in \mathbb{R}$).

There exists multiple definitions for the description of a fractal derivative. The three most usual ones are [196]:

- Grunlawald-Letnikov's definition

$$ {}_aD_t^{\alpha} f(t) = lim_{h \to 0} h^{-\alpha} \sum_{j=0}^{[\frac{t-a}{h}]} (-1)^j \binom{\alpha}{j} f(t - jh) \tag{3.78} $$

  The binomial $\binom{\alpha}{j}$ is

$$ \binom{\alpha}{j} = \frac{\Gamma(\alpha + 1)}{\Gamma(j + 1)\Gamma(\alpha - j + 1)} \tag{3.79} $$

  h the time increment and $\Gamma(.)$ represents de Gamma function.

- Riemann-Liouville's definition

$$ {}_aD_t^{\alpha} f(t) = \frac{1}{\Gamma(n - \alpha)} \frac{d^n}{dt^n} \int_a^t \frac{f(\tau)}{(t - \tau)^{\alpha - n + 1}} d\tau \tag{3.80} $$

  where the term $\Gamma(.)$ represents, again, the Gamma function valid for $n - 1 < \alpha < n$.

- Caputo's definition

$$ {}_aD_t^{\alpha} f(t) = \frac{1}{\Gamma(n - \alpha)} \int_a^t \frac{f^n(\tau)}{(t - \tau)^{\alpha + n - 1}} d\tau \tag{3.81} $$

  also for $n - 1 < \alpha < n$.

Some of the most relevant properties of fracto-differ-integrals are summarised in the following lines:

- If $f(t)$ is analytical of t, ${}_0D_t^{\alpha} f(t)$ is analytical of α.
- For $\alpha = n$, where $n \in \mathbb{Z}$, gives the same result as classical operation with integer order n.
- For $\alpha = 0$, ${}_0D_t^0 f(t) = f(t)$.
- Fractional differentiation and integration are linear operations:
  ${}_0D_t^{\alpha}(\lambda f(t) + \mu g(t)) = \lambda\, {}_0D_t^{\alpha} f(t) + \mu\, {}_0D_t^{\alpha} g(t))$.
- Additive law:
  ${}_0D_t^{\alpha}\, {}_0D_t^{\beta} f(t) = {}_0D_t^{\beta}\, {}_0D_t^{\alpha} f(t) = {}_0D_t^{\alpha+\beta} f(t)$
  and
  $\frac{d^n}{dt^n}\left({}_aD_t^{\alpha} f(t)\right) = {}_aD_t^{\alpha}\left(\frac{d^n f(t)}{dt^n}\right)$

Each of the three aforementioned definitions has its advantages and drawbacks. Focusing on control challenges it is well known that the Laplace transform is widely used because of its easy use in the s-space. Applying the definition of Laplace's transform over the fractal differ-integration, it can be obtained

$$\begin{aligned}\mathcal{L}\left\{{}_aD_t^{\alpha}f(t)\right\} &= \int_0^{\infty} e_0^{-st}D_t^{\alpha}f(t)dt = \\ &= s^{\alpha}F(s) - \sum_{m=0}^{n-1} s^m(-1)^j\,{}_0D_t^{\alpha-m-1}f(t)|_{t=0}\end{aligned} \tag{3.82}$$

where α lies within $(n-1) < \alpha < n$. If initial conditions are equal to zero, then the Laplace transform can be expressed as

$$\mathcal{L}\left\{{}_aD_t^{\alpha}f(t)\right\} = s^{\alpha}F(s) \tag{3.83}$$

Fractional derivatives and integrators have been used in the control field since 1999 [197]. In that year, I. Poflubony proposed the fractional order $\mathrm{PI}^{\lambda}\mathrm{D}^{\mu}$ controller, where λ and μ are non integer order coefficients for the integrator and the derivative terms with respect to conventional PID controllers. In this thesis, a new hybrid controller based on fractional coefficients and PR controllers is developed and tested.

3.4.2 Proposal of the Fractional Proportional-Resonant controller in continuous time

The interest on analysing new resonant controllers using integro-differential operators resides in the idea behind its form in the Laplace domain. In this sense, $1/s^{\alpha}$ involves a Fractal Integrator (FI) with the same infinite gain at continuous frequencies but with less delay in the high frequency range than a convention pure integrator $1/s$. Analytically, if $\alpha \in (0,1)$ the delay provided by $1/s^{\alpha}$ is $\frac{\alpha\pi}{2}$ [198]. Although the gain at higher frequency decreases with the same relationship as the phase does (-20α [dB/dec]), the key issue for a following problem usually is focused in delay terms. Figure 3.24 illustrates this behaviour for various ideal fractal integrators in the frequency domain. The key frequency in the gain diagram is $f = 1$ Hz: if α increases, the gain is higher for frequencies below 1 Hz, and lower for frequencies above 1 Hz.

Then, a new resonant controller transfer function is proposed being described by

$$G_{\mathrm{FPR}} = \frac{s^{\alpha}}{s^2 + \omega_k^2} \tag{3.84}$$

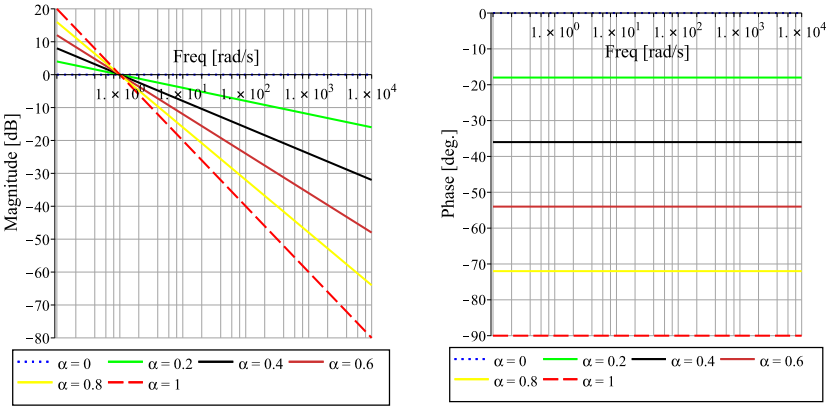

Figure 3.24: Bode diagram of a Fractal Integrator (FI)

where $\alpha \in \mathbb{R} \subset [0, 2]$ is the fractional exponent. Complex exponents will not be considered in this work. Hereinafter, this controller will be named as Fractional Proportional Resonant (FPR) controller. Other possibilities, as

$$G_{\text{FPR}} = \frac{s}{s^{\alpha} + \omega_k^2} \tag{3.85}$$

have been evaluated but without obtaining better results than conventional PR controllers.

The proposed FPR controller is analysed in terms of the close-loop bode behaviour for a first order system. As a VSI needs to control the output current, the plant is described by Equation 3.49. Then, to describe the frequency response of a current loop control of a converter, it is proposed to consider the following transfer function

$$G_{\text{CL FPR}}(s) = \frac{\frac{1}{Ls+R}\left(k_p + k_i \frac{s^{\alpha}\omega_0}{s^2+\omega_0^2}\right)}{1 + \frac{1}{Ls+R}\left(k_p + k_i \frac{s^{\alpha}\omega_0}{s^2+\omega_0^2}\right)} \tag{3.86}$$

where L and R are the inductance and its parasitic impedance, k_p and k_i the FPR constants tuned as if a standard PR is considered and α the fractal real exponent. The considered values for the system are detailed in Table 3.1.

Figure 3.25 shows the behaviour of the proposed controller for a set of different α exponents that goes from zero to two. When $\alpha = 1$, a pure standard PR behaviour is obtained. It should be noticed that two different trends appears, depending if $\alpha \in [0, 1]$ -dotted line- or if $\alpha \in [1, 2]$ -dashed

Parameter	Value	Units
L	350	μH
R	100	mΩ
k_p	0.99	–
k_i	3.08	–

Table 3.1: Proposed parameters for the close loop analysis of the FPR controller

line-. It can be seen, that in terms of gain or delay, the first subset where $\alpha \subset [0, 1]$ offers frequency specification close to an standard PR. However, the second subset where $\alpha \subset [1, 2]$ expands the operation bandwidth. This means that it is possible to control a wider range of frequencies in terms of gain or phase without using a PR-HC controller structure, as is proposed in Equation 3.46.

However, the use of higher exponents on the numerator of Equation 3.84 implies that the overshoot that appears on the gain is shifted to the left and amplified. When $\alpha = 2$ a resonance appears, as can be observed clearly in Figure 3.26. Although this peak on the gain or the phase, the use of this new controller allows to obtain a new degree of freedom that permits to tune, for instance, the maximum desired delay at a different frequency of the fundamental frequency.

3.4.3 Implementable forms of the FPR controller analysed in continuous time

The implementation in a DSP or a μcontroller it is not feasible using fractional exponents. Regarding these challenges the use of Continued fraction expansion (CFE) can be a good alternative as an approximation, but there are other options. The following lines shows the most relevant possibilities.

Continued fraction expansions of s^α

CFE is a method to evaluate functions that offers better results in terms of convergence-time that using power expansions. Considering $G(s)^{-\alpha}$, with $0 < \alpha < 1$, two transfer functions can be defined [199]:

- For high frequency

$$G_h(s) = \frac{1}{(1 + sT)^\alpha} \tag{3.87}$$

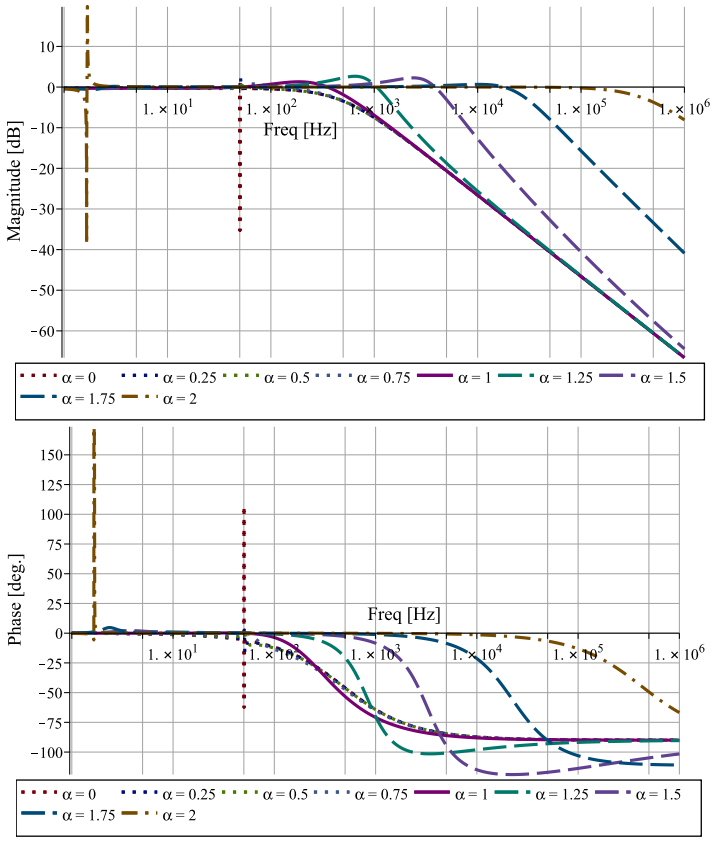

Figure 3.25: Close loop when α is swept from 0 to 2.0

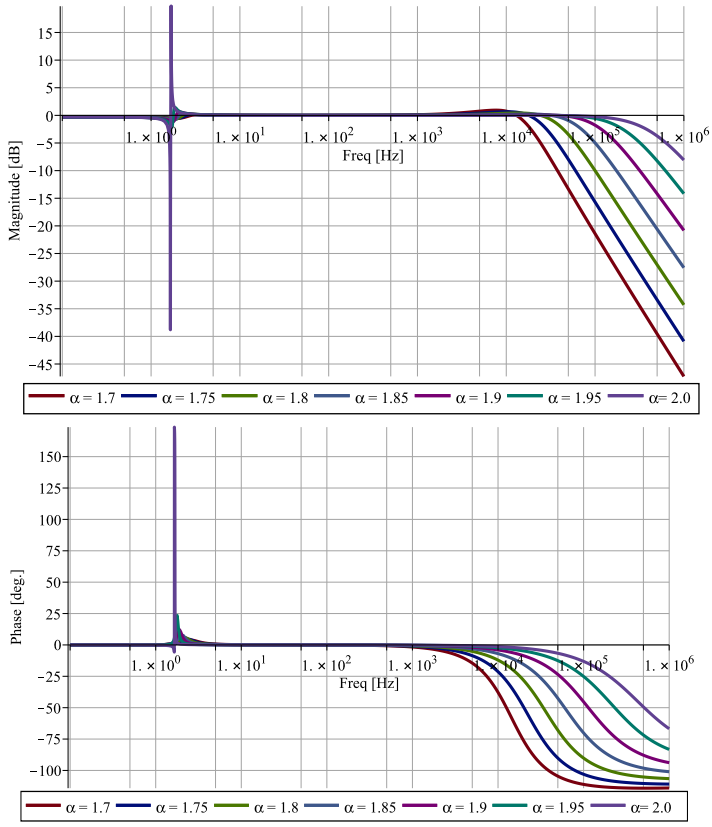

Figure 3.26: Zoom of the close loop when α is swept from 1.7 to 2.0

- For low frequency

$$G_h(s) = \left(1 + \frac{1}{s}\right)^{\alpha} \tag{3.88}$$

Considering that $G_h(s)$ is valid if $\omega T >> 1$ and $G_l(s)$ for $\omega << 1$. In this sense, T is a parameter that helps to accomplish that $\omega T >> 1$.

The CFE is an expansion that takes the form of [200]

$$f(x) = a_0 + \cfrac{h}{a_1 + \cfrac{h}{a_2 + \cfrac{h}{a_3 + \cfrac{h}{\cdots}}}} \tag{3.89}$$

where a_i are the CFE coefficients, h is a variable whose power may match with an equivalent power series expansion of $f(x)$. Thus,

$$f_0(x) = a_0 + \frac{h}{f_1(x)} \tag{3.90}$$

Assuming $x = 0$, h will be x, x^2,... depending on the case. Considering that $f_1(x)$ is different off zero, a_0 can be calculated as

$$a_0 = f_0(x)|_{x \to 0} \tag{3.91}$$

Applying the last step it is possible to find a recursive relationship where the next formula for the coefficients a's is obtained

$$a_i = \frac{h}{f_{i-1}(x) - a_{i-1}}|_{x \to 0} \tag{3.92}$$

The above recursive Equation 3.92 always has an indetermination of the type 0/0. This form is not really useful for digital computation but allows analytic developments.

Considering that for a microgrid VSI it is necessary to control frequencies higher than 50 Hz, $G_h(s)$ can be used when $T >> 0.0032$. Expanding $G_h^{-1}(s)$ using Equation 3.92,

$$\text{CFE}\left\{G_h(s)\right\} = \text{CFE}\left\{(1+x)^r\right\} = 1 + \cfrac{x}{\frac{1}{r} + \cfrac{x}{-\frac{2r}{r-1} + \cfrac{x}{\frac{-3(r-1)}{r(r+1)} + \cfrac{x}{\frac{2(r+1)r}{r^2-3r+2} + \cfrac{x}{\frac{5(r^2-3r+2)}{r^2+3r+2} + \cdots}}}}} \tag{3.93}$$

So, taking into account different order approximations (order numerator plus order denominator). For

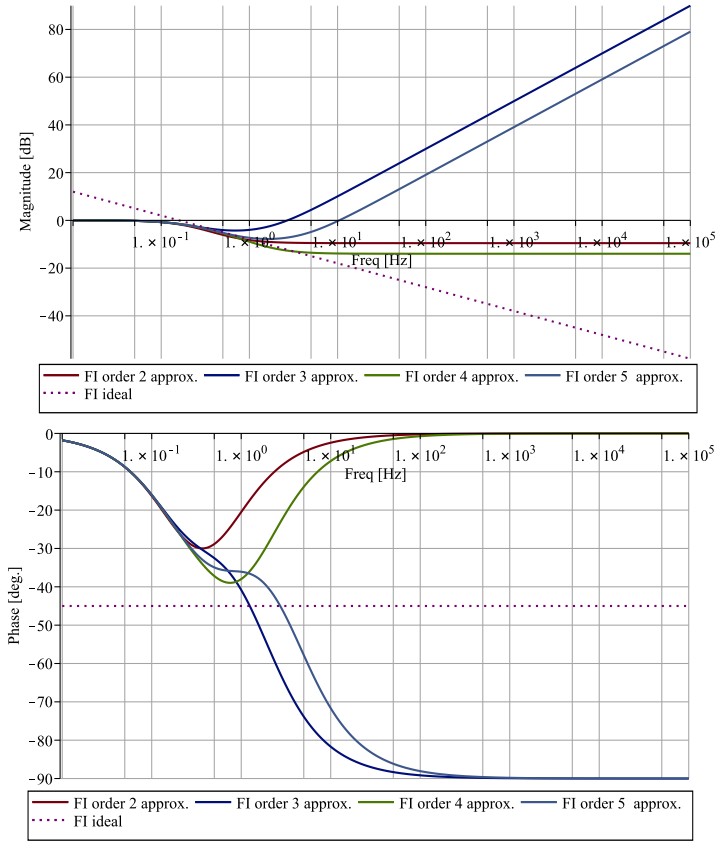

Figure 3.27: Bode diagram of $s^{-0.5}$ approximated using CFE option for high frequencies

- Order 3: $-\frac{1}{2}\frac{r^2x^2+rx^2+4rx+4x+6}{rx-2x-3}$
- Order 4: $\frac{r^2x^2+3rx^2+6rx+2x^2+12x+12}{r^2x^2-3rx^2-6rx+2x^2+12x+12}$
- Order 5: $\frac{1}{3}\frac{r^3x^3+3r^2x^3+9r^2x^2+2rx^3+27rx^2+36rx+18x^2+72x+60}{r^2x^2-5rx^2-8rx+6x^2+24x+20}$
- Order 6: $-\frac{r^3x^3+6r^2x^3+12r^2x^2+11rx^3+60rx^2+6x^3+60rx+72x^2+180x+120}{r^3x^3-6r^2x^3-12r^2x^2+11rx^3+60rx^2-6x^3+60rx-72x^2-180x-120}$

  where r represents the fractional exponent and x has to be substituted by $x = sT$. Considering $r = 0.5$ and $x = s$, the results of using this approximation are detailed in Figure 3.27.

It can be seen that all options only approximates to the ideal fractal 0.5

integrator in the neighbourhood of 1 Hz even in case of high order approximations. This option does not seem a good alternative to obtain adequate approximations in a wide operation frequency range.

Carlson's rational approximations of s^α

Carlson proposed a method that derives from the Newton's approximation to obtain an iterative formula for the α-root. The first step of the method implies the relationship [201]

$$(H(s)^{1/\alpha} - (G(s)) = 0 \tag{3.94}$$

If α is defined as $\alpha = 1/q$ and $m = q/2$, in each iteration, considering $H_0(s) = 1$, the approximation for the i-th iteration is defined by

$$H_i(s) = H_{i-1}(s)\frac{(q-m)(H_{i-1}(s))^2 + (q+m)G(s)}{(q+m)(H_{i-1}(s))^2 + (q-m)G(s)} \tag{3.95}$$

Considering $\alpha = 0.5$ the results of using this approximation for different iteration levels are detailed in Figure 3.28. It can be observed in Figure 3.28 that as the higher the order expressed by i, the better the approximation results. However, to obtain acceptable approximations for a range up to 1 kHz, the transfer function obtained is really extensive, implying terms of order 40 in the case of H_4.

Matsuda's rational approximations of s^α

The Matsuda's approach [201,202], also known as Thiele's continued fraction approximation, suggests a CFE where the values of the function under study is known at some frequencies w_k, with $k = 0, 1, 2, ..., n$. The frequencies are obtained by means of a logarithmic spaced set. The number of frequencies is equal to $n + 1$. The approximations takes the form of

$$f(x) = a_0 + \frac{x - x_0}{x_1 +} \frac{x - x_1}{x_2 +} \frac{x - x_2}{x_3 +} ... \frac{x - x_n}{x_{n+1} +} \tag{3.96}$$

If it is applied considering Laplace's s-domain [203]

$$a_0(w) = |H(w_0 j)| \tag{3.97}$$

$$a_{k+1}(w) = \frac{w - w_k}{d_k(s) - d_k(s_k)} \tag{3.98}$$

So, the approximation looks as

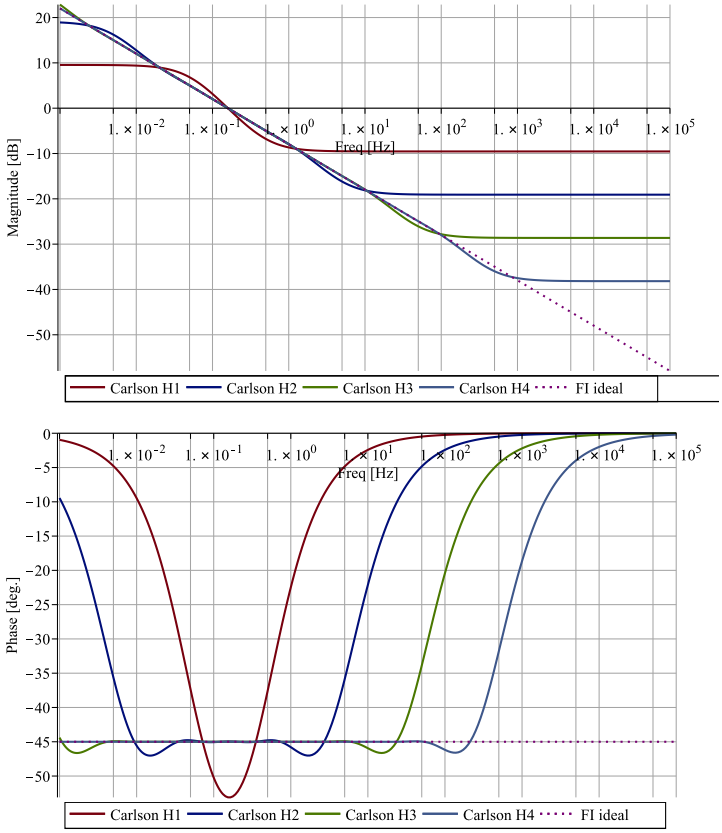

Figure 3.28: Bode diagram of $s^{-0.5}$ approximated using Carlson's option

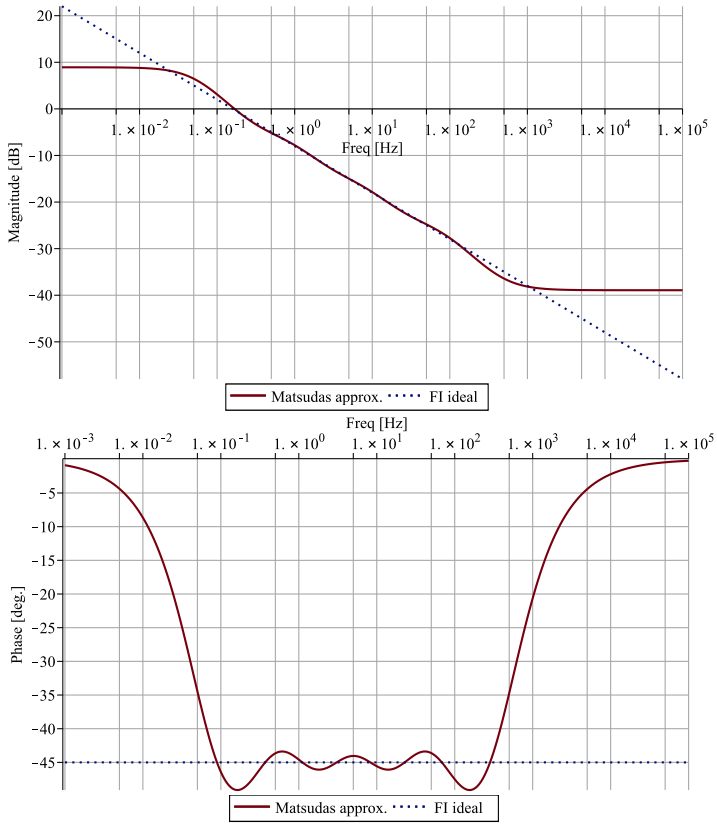

Figure 3.29: Bode diagram of $s^{-0.5}$ approximated using Matsuda's option

$$H(s) \simeq a_0(w_0) + \cfrac{s - w_0}{a_1(w_1) + \cfrac{s-w_1}{a_2(w_2) + \cfrac{s-w_2}{a_3(w_3) + \cfrac{s-w_3}{\ldots}}}} \tag{3.99}$$

The result of using this approximation considering $H(s) = 1/s^{0.5}$ and $w_k = \{1, 2.3713, 5.6234, 13.3352, 31.6227, 74.9894, 177.8279, 421.6965, 1000\}$ are detailed in Figure 3.29. This approximation offers low errors for a wide range of frequencies with an approach of relative low order. In the example used, as the last k is the $8th$, the order of the numerator and the denominator of the obtained transfer function is four.

Oustaloup's rational approximations of s^α

This case, together with Chareff's approximation, are two options whose fundamentals are based on the minimization of a cost function focused on the frequency domain [201, 204, 205]. An example of the cost function can be described by

$$J = \int W(\omega)|G(\omega) - G'(\omega)|^2 d\omega \tag{3.100}$$

being $W(\omega)$ the weighting function, $G(\omega)$ the original frequency response and $G'(\omega)$ the approximation of the rational function.

This approach considers that $H(s) = s^\delta$ where $\delta \in \mathbb{R}^+$. The approximation proposed is calculated as a rational function of the form

$$H(s) \simeq C^\delta \prod_{k=-N}^{N} \frac{1 + s/\omega'_k}{1 + s/\omega_k} \tag{3.101}$$

being $2N+1$ the number of total poles or zeros. It is possible to compute the recursive formulation using the following set of intermediate relationships

$$C = \frac{\omega_u}{\omega_h} = \frac{\omega_l}{\omega_u} \tag{3.102}$$

$$\omega_k = \omega_l \left(\frac{\omega_h}{\omega_l}\right)^{\frac{k+N+1/2+\delta/2}{2N+1}} \tag{3.103}$$

$$\omega'_k = \omega_l \left(\frac{\omega_h}{\omega_l}\right)^{\frac{k+N+1/2-\delta/2}{2N+1}} \tag{3.104}$$

with $\omega_u = \sqrt{\omega_h \omega_l}$ being the unit gain frequency and the frequency midpoint band of a band of frequencies geometrically distributed around it, ω_h and ω_l. If $N = 2$ the order of the obtained Oustaloup's approximation is five. Considering $w_l = 10^{-3}$ and $w_h = 10^3$ the results of the approximation can be observed in Figure 3.30.

This choice supports a good frequency range approach but it is important to notice that the w_u must be 1 to match properly to the ideal bode curves of the fractal integrator. If w_u is different from 1, the obtained approximation is shifted in the positive frequency axis sense.

Chareff's rational approximations of s^α

This proposal [206] is close to Oustaloup's method but the approximation's coefficients are computed to set a maximum deviation in magnitude of y dB

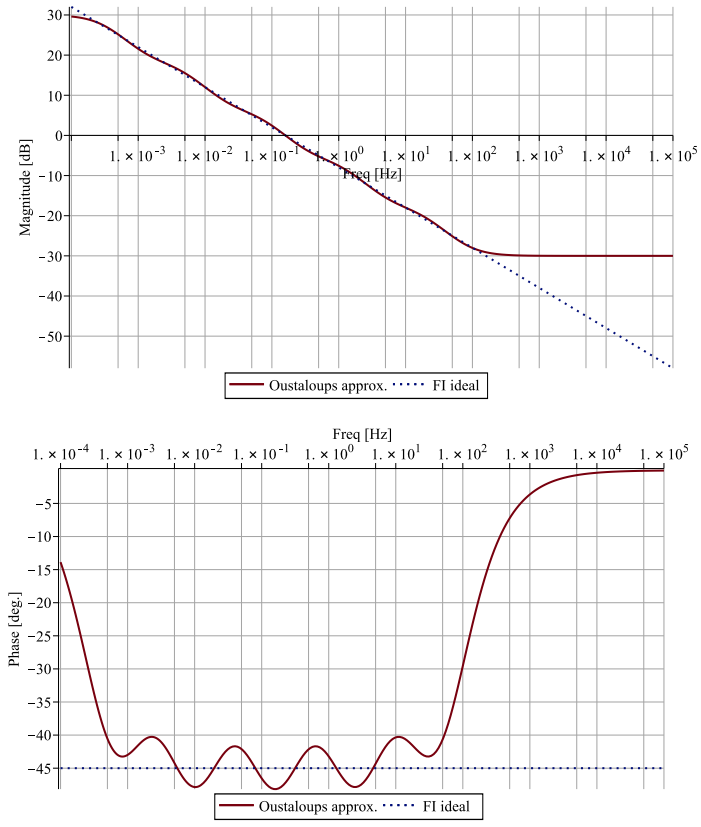

Figure 3.30: Bode diagram of $s^{-0.5}$ approximated using Oustaloup's option with $w_u = 1$

in respect with the original response. If the desired transfer function has the form of

$$H(s) = \frac{1}{\left(1 + \frac{s}{p_T}\right)^{\alpha}} \tag{3.105}$$

the proposed approach is based on a factorization

$$H(s) \simeq \frac{\prod_{i=0}^{n-1}\left(1 + \frac{s}{z_i}\right)}{\prod_{i=0}^{n}\left(1 + \frac{s}{p_i}\right)} \tag{3.106}$$

As has been indicated, the coefficients are chosen to set a maximum difference in magnitude of y dB respect the original response. In this sense, the intermediate required values are

$$a = 10^{\frac{y}{10(1-\alpha)}} \tag{3.107a}$$

$$b = 10^{\frac{y}{10\alpha}} \tag{3.107b}$$

$$ab = 10^{\frac{y}{10\alpha(1-\alpha)}} \tag{3.107c}$$

being the poles and zeros of the approximation

$$p_0 = p_T\sqrt{b} \tag{3.108a}$$

$$p_i = p_0(ab)^i \tag{3.108b}$$

$$z_i = ap_0(ab)^i \tag{3.108c}$$

The number of zeros and poles are chosen as a function related with the bandwidth by the formula

$$N = \frac{\log\left(\frac{\omega_{max}}{p_0}\right)}{\log(ab)} + 1 \tag{3.109}$$

where ω_{max} determines the frequency bandwidth fixed according to

$$p_{N-1} < \omega_{max} < p_N \tag{3.110}$$

Setting a maximum deviation y of 2 dB, $p_T = 1$ and $n = 4$, the obtained approximation can be observed in Figure 3.31.

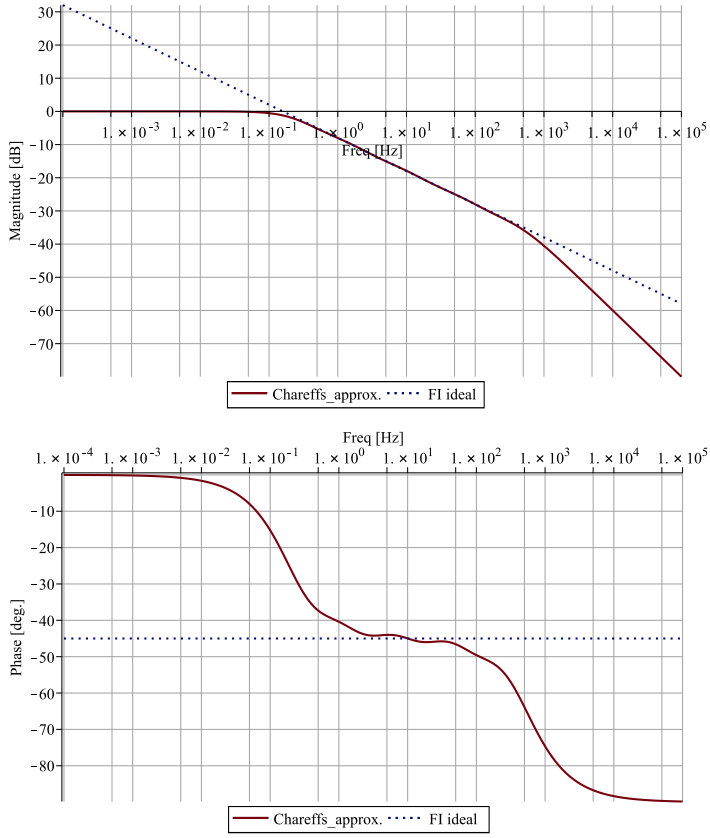

Figure 3.31: Bode diagram of $s^{-0.5}$ approximated using Chareff's option

CFE	
α	0.5
Order	5
T	0.05
Carslon	
α	0.5
$_i$	2
Matsuda	
α	0.5
$_k$	8
ω_k	1-1000 rad/s

Oustaloup	
α	0.5
ω_b	0.001 rad/s
ω_h	1000 rad/s
N	2
Chareff	
α	0.5
p_T	1
y	2 dB
n	4

Table 3.2: Summary of $s^{-0.5}$ continuous time fractal approximation controller parameters

Fractional Proportional Integral controller under different continuous time approximations

As has been proposed previously, all the continuous approximation detailed in the above sections are compared to select the ones with more potential to control a wide range of frequencies with only one controller. The comparison is based on the current control close-loop with the parameters detailed in Table 3.1. The different parameters of the FPR proposed for the comparison are summarised in Table 3.2.

Figure 3.32 shows the result of applying a FPR controller on a current loop compared simultaneously with an ideal FPR -continuous line- and the standard PR controller - separated dotted line-.

It can be seen that in terms of overshoot the best approximations are CFE and Chareff's approximation. In terms of gain bandwidth are CFE, Chareff's and Matsuda's approximations. Finally, in terms of phase all options offers good response up to 500 Hz, but it is possible to assume that Carlson's approach is the worst one.

3.4.4 Proposal of the Fractional Proportional-Resonant controller in discrete time

For discrete time applications a finite difference equation is required to be implemented in a DSP or μcontroller. There are different options to obtain the discrete form of an FPR. Numerical integration, invariant simulation,

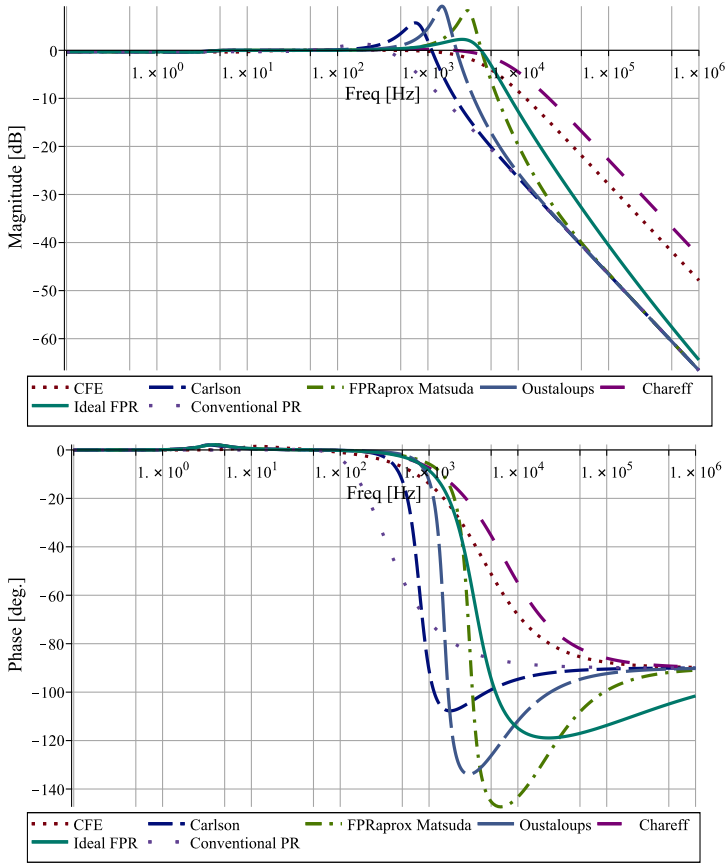

Figure 3.32: Bode diagram comparison when different continous time aproximations are applied

pole-zero transformation can be used but also the discrete time form can be performed by using the power series expansion (PSE) [196, 201, 207]. The PSE and a combination of numerical integration are presented in the following lines.

- PSE. $D^{\pm\alpha}(z) = T^{\mp\alpha}\text{PSE}\{f(z)\}$. $D^{\pm\alpha}$ denotes the discrete equivalent of the fractal operator, T the sampling period and α the fractional exponent. Assuming that in discrete time there are three options for applying PSE: backward Euler, forward Euler and trapezoidal. Forward Euler is not developed because as is detailed in [208] it is not suitable due to causal problems.

- Combination of numerical integration. It is possible to combine different numerical integration alternatives as can be backward Euler with Tustin integration or Simpson's and Tustin to obtain better behaviours on different frequencies bands.

Firstly, for the PSE option, if the backward choice is assumed, the Grünwald-Letnikov formula with the short-memory approach is obtained

$$D_b^{\pm\alpha}(z) = T^{\mp\alpha}\text{PSE}\{(1-z^{-1})^{\pm\alpha}\} = T^{\mp\alpha}z^{-[L/T]}\sum_{j=0}^{[L/T]}(-1)^j\binom{\pm\alpha}{j}z^{[L/T]-j} \tag{3.111}$$

and if the trapezoidal option is assumed, $\text{PSE}\{\left(\frac{2(1-z^{-1})}{T(1+z^{-1})}\right)^{\pm\alpha}\}$ has to be computed. Then applying substitution replacing z by $-z$ on the denominator and using Equation 3.111

$$D_t^{\pm\alpha}(z) = \left(\frac{T}{2}\right)^{\mp\alpha}\frac{z^{-[L/T]}\sum_{j=0}^{[L/T]}(-1)^j\binom{\pm\alpha}{j}z^{[L/T]-j}}{(-z)^{-[L/T]}\sum_{j=0}^{[L/T]}(-1)^j\binom{\pm\alpha}{j}(-z)^{[L/T]-j}} \tag{3.112}$$

being L the length memory, the subscript b or t indicates backward or tustin alternative, respectively, and $(-1)^j\binom{\pm\alpha}{j}$ are the binomial coefficients.

Thus, considering $T = 0.1$ s and $L = 10$ (implying 101 coefficients), both approximations -backward and Tustin- can be observed in Figure 3.33.

What can be deduced from Figure 3.33 is that Tustin's approximation is better in terms of phase. It should be remarked that to obtain this approximation the number of coefficients is 101, implying non acceptable time computation and memory reservation on a μcontroller. Furthermore, it has been noticed that the approximation is acceptable one decade before

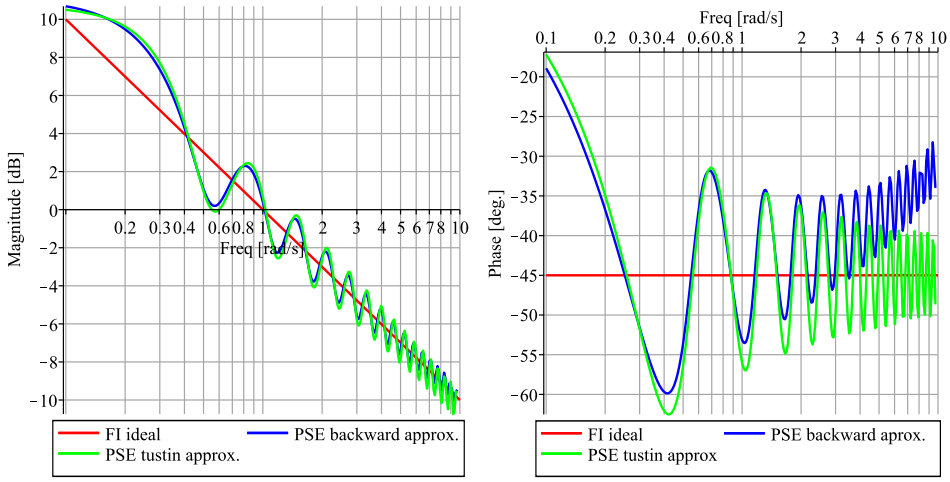

Figure 3.33: Bode diagram for backward and tustin PSE approximations of $s^{-0.5}$ with $T = 0.1$ s

the selected sampling time. Figure 3.34 helps to illustrate this issue when $T = 0.00005$ s, $L = 0.005$ and 101 coefficients are used. In this sense, the PSE alternative is rejected. Also, in the literature it is possible to find that CFE is a method that have, in general, faster convergence and large domain of convergence than PSE [196].

Secondly, for the numerical integration combination it should be detailed that the discretization of the fractional differentiator or integrator, s^{α} or $\frac{1}{s^{\alpha}}$, respectively, being $|\alpha| < 1$, can be expressed by the called generating function $s = \omega(z^{-1})$ [207]. The function $\omega(z^{-1})$ can be expanded using different options. For example, as proposed in [209], considering

$$z = e^{sT} = e^{((1-\alpha)+\alpha)Ts} = \frac{e^{(1-\alpha)Ts}}{e^{-\alpha Ts}} \tag{3.113}$$

and computing separately the PSE of the obtained numerator and denominator

$$z = \frac{\frac{\sum_{n=0}^{\infty}((1-\alpha)Ts)^n}{n!}}{\frac{\sum_{k=0}^{\infty}\left((-1)^k\alpha Ts\right)^k}{k!}} \tag{3.114}$$

that if only the terms up to the first order are used it is possible to obtain

$$z \simeq \frac{1+(1-\alpha)Ts}{1-\alpha Ts} \tag{3.115}$$

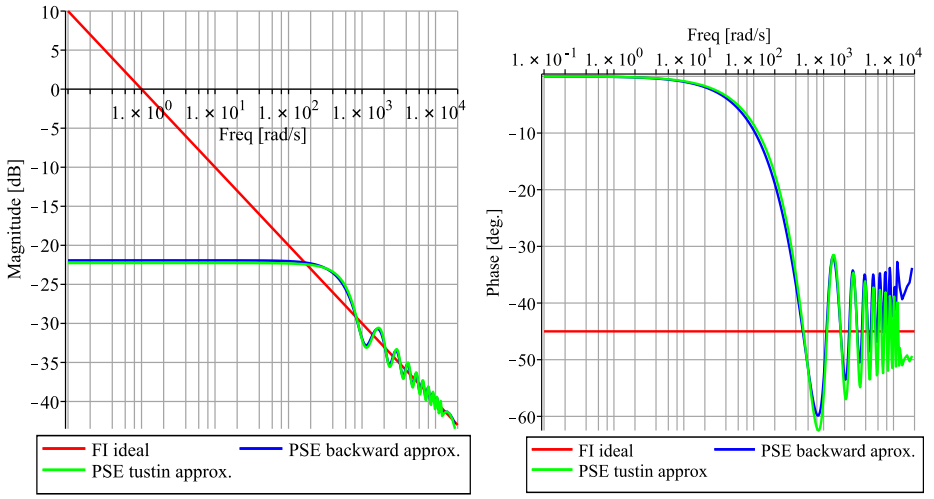

Figure 3.34: Bode diagram for backward and tustin PSE approximations of $s^{-0.5}$ with $T = 0.00005$ s

implying that the inverse relationship is described by

$$s \simeq \frac{1}{T}\frac{z-1}{1+\alpha(z-1)} \tag{3.116}$$

Equation 3.116 is equivalent to the Al-Alaoui's [209] operator where a hybrid digital integrator is proposed using a combination of the backward Euler integrator and Tustin integrator form

$$H(z) = aH_{\text{backward}}(z) + (1-a)H_{\text{tustin}}(z) \tag{3.117}$$

being a the weighting factor. The most known Al-Alaoui's relationship is described using $a = 3/4$ [210]. Thus,

$$s = \omega(z^{-1})^{\pm\alpha} = \left(\frac{8}{7T}\frac{1-z^{-1}}{1+z^{-1}/7}\right)^{\pm\alpha} \tag{3.118}$$

is obtained. Now, the PSE or CFE of Equation 3.117 can be calculated. In this case, only the CFE is developed. The approximation is analysed in function of a in Figure 3.35 and in function of the CFE's order of the parameter n in Figure 3.36.

When $a = 0$ the trapezoidal approach is obtained, while if $a = 1$ backward Euler rule is followed. In Figure 3.35 can be deduced that if the trapezoidal strategy is assumed, the magnitude gain and the phase are closer to the ideal

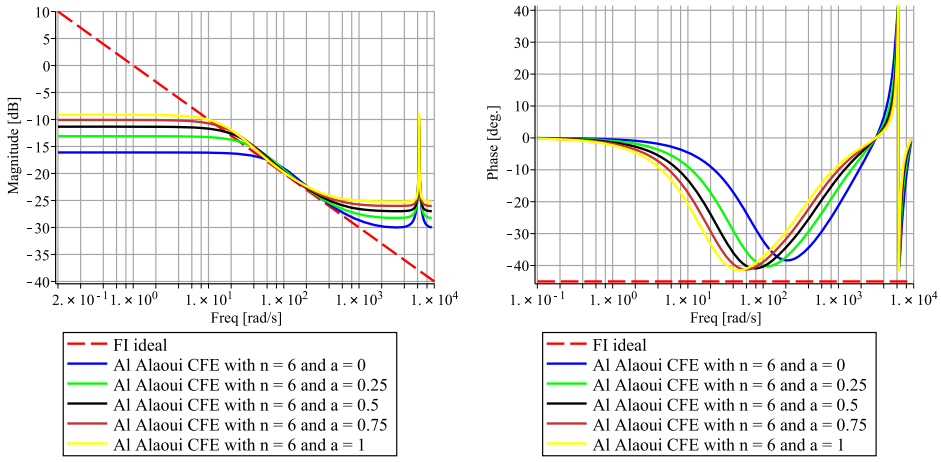

Figure 3.35: Bode diagram for the Al Aloui's hybrid digital integrator with T = 0.001 s, CFE $n = 6$ and different knob factors

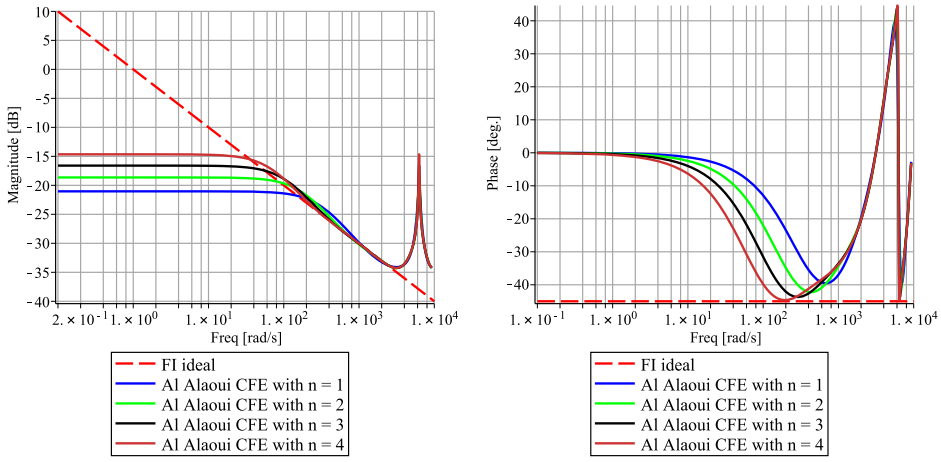

Figure 3.36: Bode diagram for the Al Alaoui's hybrid digital integrator with T = 0.001 s for different CFE n orders when $a = 0.75$

one for high frequencies. For this reason, the use of a knob factor a could result interesting to obtain better dynamics results. Figure 3.36 shows how the higher the CFE order used, the better the approximation results.

It is mentioned in [207] that Al-Alaoui stated in 1997 that the magnitude of the frequency response of the integrator $1/s$ is a trade-off in the discrete time domain represented by an average weighted relationship between the Simpson ($G_s(z)$) and trapezoidal ($G_t(z)$) digital integrators, as

$$G(z) = aG_s(z) + (1-a)G_t(z), \quad a \in [0,1] \tag{3.119}$$

being a the weighting factor, $G_s(z) = \frac{T(z^2+4z+1)}{3(z^2-1)}$, $G_t(z) = \frac{T(z+1)}{(2(z-1)}$. Rearranging terms,

$$G(z) = \frac{T(3-a)(z+r_1)(z+r_2)}{6(z^2-1)} \tag{3.120}$$

where $r_1 = \frac{3+a+2\sqrt{3a}}{3-a}$ and $r_2 = \frac{3+a-2\sqrt{3a}}{3-a}$. It should be pointed that $r_1 = 1/r_2$ and that $|r_1| >= 1$, $\forall a \subset [0,1]$. Thus, a non-minimum phase pole or zero appears due to r_1 depending on if $G(z)$ represents and hybrid differentiator or integrator, respectively. Then, [207] proposes to use

$$\widehat{G}(z) = K\frac{T(3-a)(z+r_2)^2}{6(z^2-1)} \tag{3.121}$$

as an approximation with no non-minimum phases elements. K is determined using the final value of the impulse response on $G(z)$ obtaining $K = r_1$. Rearranging terms, the generating function derives into

$$G(z^{-1}) = (w(z^{-1}))^{\pm\alpha} = k_0\left(\frac{1-z^{-2}}{(1+bz^{-1})2}\right)^{\pm\alpha} \tag{3.122}$$

with $k_0 = \left(\frac{6r_2}{T(3-a)}\right)^{\pm\alpha}$ and $b = r_2$. As in the case of Equation 3.118, only the CFE is developed. The approximation is analysed as a function of parameter a and depicted in Figure 3.37. The order of the parameter n is analysed in Figure 3.38.

The trapezoidal approach is obtained when $a = 0$, while if $a = 1$ the Simpson's rule is followed. In Figure 3.37 can be deduced that if the trapezoidal strategy is assumed, the magnitude gain does follows adequately the ideal magnitude gain at high frequencies. However, it is the option with better phase behaviour at high frequency. For this reason, the use of a knob factor a could result interesting to obtain better results. Figure 3.38 shows how the higher the CFE order used, the better the approximation is.

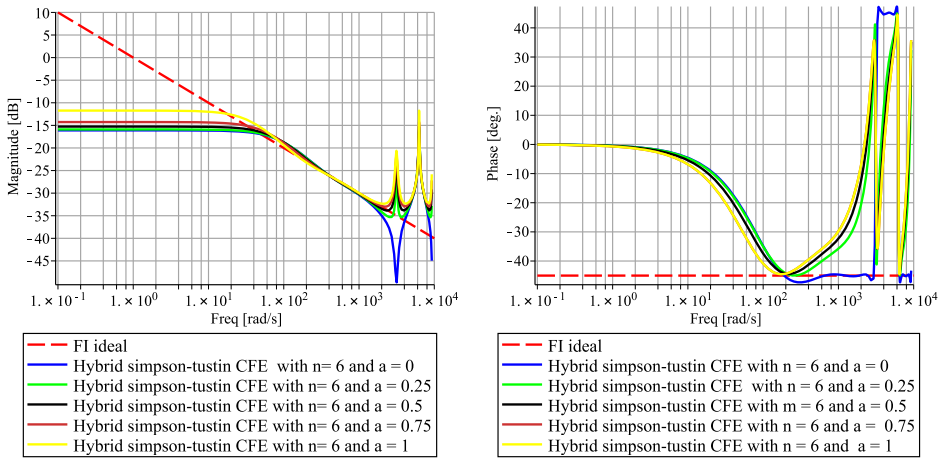

Figure 3.37: Bode diagram for the hybrid digital integrator mixing Simpson and Tustin with T = 0.001 s, CFE $n = 6$ and different knob factors

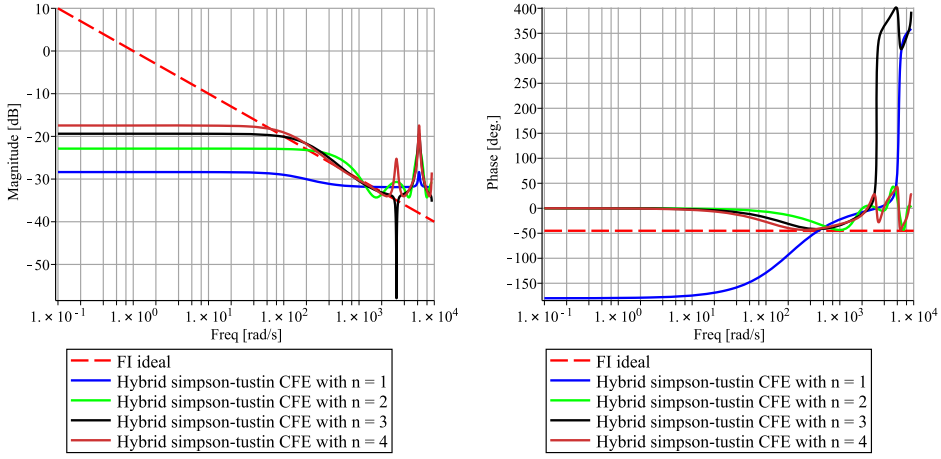

Figure 3.38: Bode diagram for the hybrid digital integrator mixing Simpson and Tustin with T = 0.001 s for different CFE n orders when $a = 0.5$

Discrete time implementation

In [201] is detailed that good continuous approximations, considering the ones exposed in this work, are: Carlson, Oustaloup, Matsuda and Chareff. In this sense, [201] also details that there are two suitable strategies to obtain a good discrete form of s^{α} and, consequently, of the new proposed FPR controller: the discretization of an adequate continuous time approximation or the CFE of a generating function. In this case, as has been analysed in section 3.4.3, the selection that seems better in continuous time for the FPR controller in terms of gain magnitude and phase is Chareff's approximation. The Chareff's approximation will be studied in discrete time discretizing the controller via Al-Alaoui's operator and the hybrid Simpson-Tustin's options. These options allow, implicitly, to analyse backward Euler's, Tustin's and Simpson's alternatives alone, too. To do that, the general formulation of Al-Alaoui's operator is described as [209]

$$s = \frac{2(z-1)}{T\left((1-a)+(1+a)z\right)} \tag{3.123}$$

where it is possible to demonstrate that when $\alpha = (1+a)/2$, Equation 3.116 and 3.123 are equivalent. For the hybrid Simpson-Tustin case the obtained relationship is

$$s = \frac{6(z^2-1)}{T\left((a-3)z^2+(-2a-6)z+(a-3)\right)} \tag{3.124}$$

that will be used on Chareff's approximation. To allow the possibility to illustrate some results for both options, Chareff's alternative proposed in Table 3.2 is used and the sampling period is $T = 50 \cdot 10^{-6}$. Figure 3.39 depicts how the use of Al-Alaoui's discrete relationship affects on the Chareff's continuous time transfer function

$$s^{0.5} \simeq \frac{63.09575s^4 + 74931.8162s^3 + 1.213339077 \cdot 10^7 s^2 + 2.98308 \cdot 10^8 s + 1.0 \cdot 10^9}{1.0s^5 + 2984.6743s^4 + 1.2181 \cdot 10^6 s^3 + 7.6855 \cdot 10^7 s^2 + 7.4972 \cdot 10^8 s + 1.0 \cdot 10^9} \tag{3.125}$$

obtained applying the cited parameters of Table 3.2 for Chareff's rational approximation.

It can be seen that when the trapezoidal relationship is applied (a =0 in Equation 3.123) the discrete transfer function obtained is closer to the continuous time approximation. However, when the backward Euler is directly computed ($a = 1$), the magnitude is a more suitable approximation to the continuous time Chareff's approximation and the phase is more close to the ideal case. That implies that backward Euler or Tustin are good options.

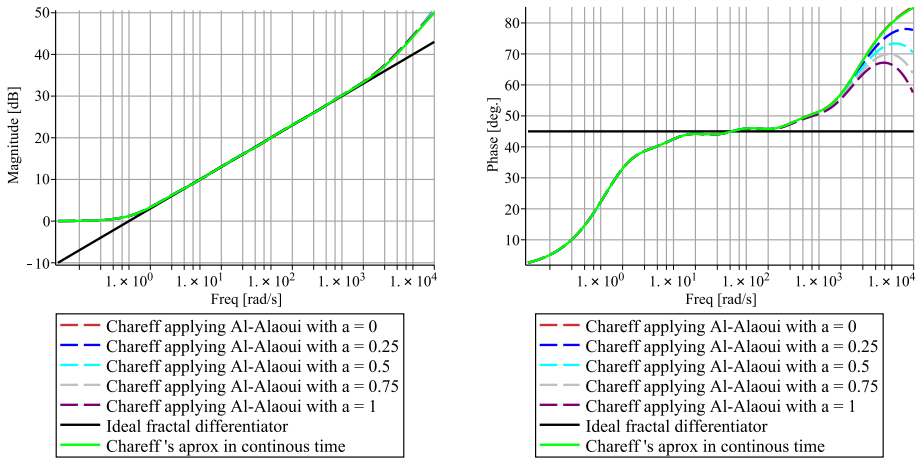

Figure 3.39: Bode diagram for the Al Aloui's continous to discrete time relationships for different knob a factors

On the other hand, Figure 3.40 shows the effect of the hybrid Simpson-Tustin's discrete relationship on Equation 3.125. In that case, there are no significant differences between the use of a trapezoidal approach or a Simpson's second order approach applied on the continuous time Chareff's approximation. This means that there is no need to increase the order of the discrete transfer function using a hybrid Simpson-Tustin's choice.

Finally, the option of using the CFE of the generating functions will not be considered. This is due to high CFE's orders are needed to obtain appropriate approximations.

Once the approximation for the implementation of the FPR controller has been achieved it is necessary to apply it to the topic under study that is the control of sinusoidal electrical variables. As this thesis is focused on the AC control of microgrids, the controller will be applied to the inner current control loop cited along this chapter.

Current loop stability and sensitivity analysis

The use of Chareff's approximation in discrete time will be applied to the inner current control loop. The tuning will be focused on a controller that will enhance the current response up to 1 kHz finding a lower order implementation than conventional proportional-resonant controllers. In this sense, computation time burdens can be improved. As this new proposed

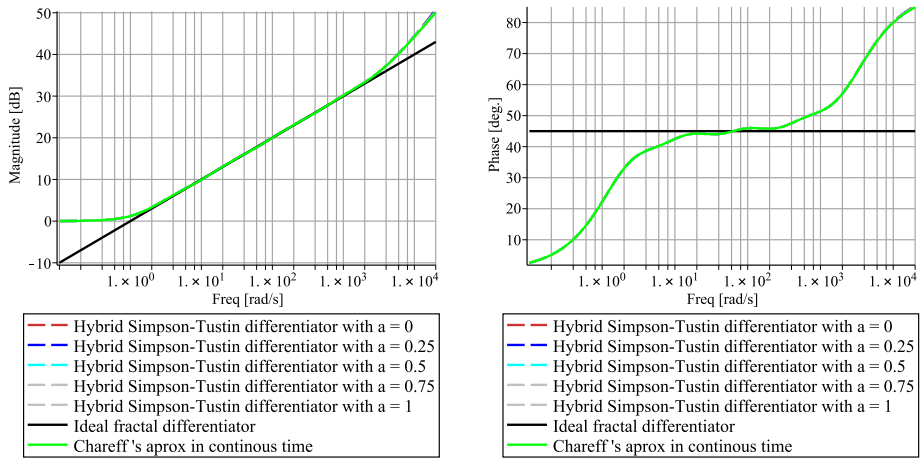

Figure 3.40: Bode diagram for the hybrid Simpson-Tustin continous to discrete relationship for different knob factors

controller gives one extra degree of freedom, the controller is going to be tuned in three main steps:

- Step 1. Tune of k_{p_i} and k_{i_i} based on section 3.3.5.
- Step 2. Selection of α based on a maximum desired delay at high frequencies
  - Stability analysis. If the system is unstable, it will be used the first stable α with the delay as close as possible to the previously specified one.
- Step 3. Analysis of the obtained controller
  - Zero-Pole map analysis.
  - Partial fraction decomposition.
  - Correction of the poles and zeros of the controller due to quantification error challenges. Normalization application if necessary.
    - Analysis of the goodness of the normalization.

The previous steps are applied to the system with the parameters summarised in Table 3.3.

If Step 1 is applied using Equation 3.67 and Equation 3.68, k_{p_i} is equal to 1.44 and k_{i_i} to 4.2.

Chareff approximation	
Integration approximation	Tustin
α	Depends on step 2
p_T	1
y	3 dB
n	3

Control parameters	Value	Units
Inductance	0.49	mH
Parasitic resistance	0.045	Ω
ω_0	100π	rad/s
Controller settling time	2.5	ms
ξ	0.95	–
Sampling time	33.33	μs
Delay at 650 Hz	0.175	rad

Table 3.3: Summary of FPR tuning example parameters

Step 2 consists in computing the close loop bode diagrams for a swept of α coefficients obtaining, in the present case, the results shown in Figure 3.41.

As can be observed, as α increases, the close loop response increases controllable capability at the high frequency range. However, it is necessary to analyse the stability and sensitivity of the controller. At first, it is necessary to set the extra degree of freedom α based on the obtained bode diagrams to select a specific α value according to a desired delay at design frequency. In this case, the minimum delay available at 650 Hz is 1.8° corresponding to $\alpha = 1.995$ and the maximum is 69° concerning to $\alpha = 1.085$. In this sense, it is proposed to fix a 10° delay at 650 Hz, obtaining an approximate α of 1.39 derived from the linear interpolation between the bode diagrams obtained in Figure 3.41. Figure 3.42 shows the obtained close loop response with and without one sample delay introduced in the direct control chain once $\alpha = 1.39$. It should be considered that the effect of the delay increases the amplification region in terms of bandwidth and gain.

Then, the FPR transfer function is described by

$$\mathrm{FPR}(z) = \frac{5.047810z^5 - 23.690598z^4 + 44.3206122z^3 - 41.296290z^2 + 19.154083z - 3.535618}{z^5 - 4.9182478z^4 + 9.6734735z^3 - 9.5109255z^2 + 4.674420z - 0.918721} \tag{3.126}$$

If a zero-pole gain analysis is computed, the following values are obtained

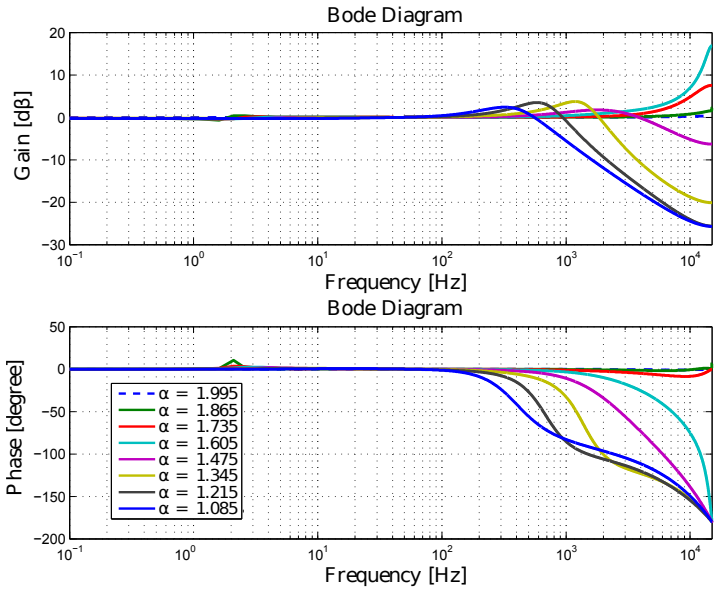

Figure 3.41: Bode diagram for the inner current loop controlled by a FPR for different α coefficients

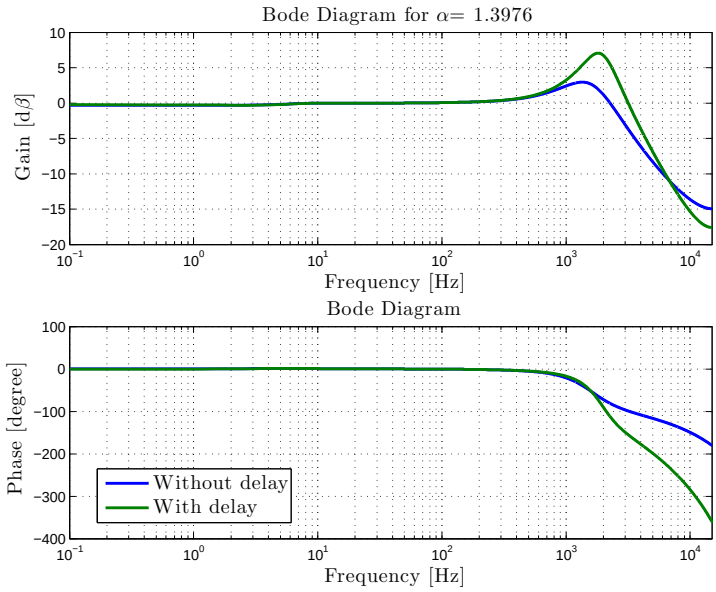

Figure 3.42: Bode diagram for inner current close loop controlled by a FPR with $\alpha = 1.3947$

- Gain: 5.0478
- Zeros:

  0.999701623027697

  0.976390495224586

  0.718662311808648

  0.999243995285733 + 0.0008889074577886 45i

  0.999243995285733 - 0.0008889074577886 45i
- Poles:

  0.999945169942248 + 0.0104716893527957i

  0.999945169942248 - 0.0104716893527957i

  0.999749919603353

  0.995536603631299

  0.923070916709077

It should be pointed out two important points. The first one is the proximity of the real part of the different poles to one. The second one resides in that some poles could have a module higher than one.

The first point could present significant problems to be implemented in a single transfer function due to quantification limitations. The second one is not an issue if the close loop is stable but it will be discussed later on. In case of non-stable systems, the norm of the poles will be normalized to close to one as possible.

To decrease the quantification problem due to the zeros and poles proximity to one and to some operations as multiplications it is proposed to use a partial fraction decomposition of the controller that has to be computed with the maximum possible precision. Doing that, all the transfer function of the controller will be split in sub-transfer functions of order 1 and 2. In this sense, each sub-transfer functions can be implemented with higher precision. It is necessary to define the arithmetic number representation that will be used. As fixed-point is better in terms of precision, if no extremely big or small values have to be represented, it is considered fixed-point instead of floating point. Considering a nowadays common DSP or μcontroller with 32 bits, the data type range and resolution for 32 bits can be seen in Table 3.4. It can be observed that up to a maximum of 8 digits can be accurately represented if all the coefficient of the controller have a value lower than 4.

Data type	Range		Resolution
	min	max	
Q30	-2	1.999999999	0.000000001
Q29	-4	3.999999998	0.000000002
...	...	...	...
Q21	-1024	1023.999999523	0.000000477
...	...	...	...
Q1	-1073741824	1073741823.5	0.5

Table 3.4: 32 bits resolution using fixed-point arithmetic

If some term of Equation 3.126 has a module higher than one, it can be normalized maintaining the angle of the zeros and poles. Thus, if $|z_i| > 1$ or $|p_i| > 1$ with the maximum available precision used, then

$$z_i' = \frac{z_i}{|z_i|} \tag{3.127a}$$

$$p_i' = \frac{p_i}{|p_i|}. \tag{3.127b}$$

Figure 3.43 shows a comparison in the frequency domain between the close loop response of a FPR and a PR-HC with all the odd harmonics up the the 9th paralleled (order 10). For the PR-HC has been considered the same fundamental constants aforementioned in step 1 and for the harmonics regulators, the different $k_{i_{i_k}} = k_{i_{i_0}}/k$. It can be observed that the PR-HC controller allows to have null steady state errors at the desired harmonic components. On the other hand, the FPR shows an error in gain and phase at all the bandwidth except at 50 Hz. However, the error is acceptable and it should be remarked that the inter-harmonic excitation is minimized with a lower order controller (order 5). This fact can help to avoid real implementation issues when the hardware resonant or parasitic frequencies are excited. Figure 3.44 shows a comparison in the time domain between the same two controllers considering a reference that contains 40 A on the 150 Hz component, 10 A on the 450 Hz, 10 A on the 550 Hz and 2 A on the 750 Hz.

To ensure the robustness off the controller, the plant parameters are changed and the zero-pole map is depicted. The parameter L is changed between the range $[0.1L_r, 2L_r]$, being L_r the rated value of 490 μH used. The results are shown in Figure 3.45. The modification of the parasitic re-

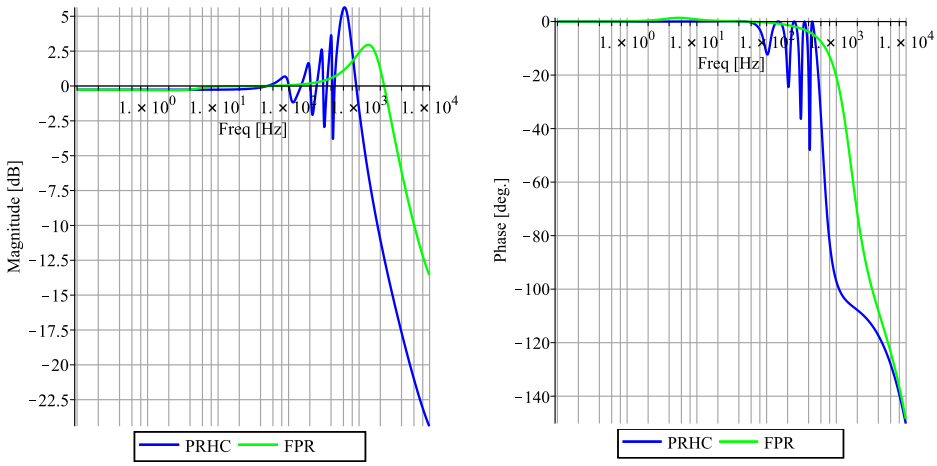

Figure 3.43: Bode diagram comparison between the use of a PRHC or the new proposed FPR controller

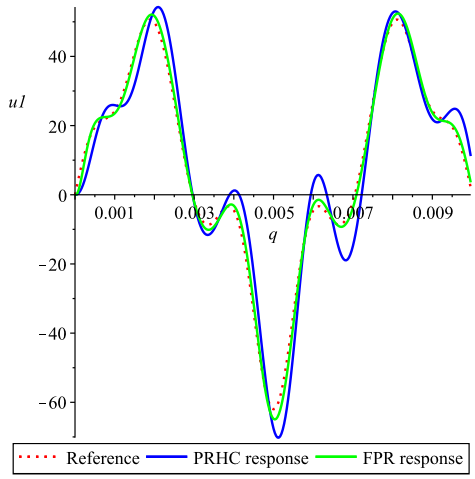

Figure 3.44: Sinusoidal tracking response comparison between PR-HC and FPR

sistance does no affect substantially the position of the poles considering the range $[0R_r, 10R_r]$, being R_r the rated value of 45 mΩ used.

All the sensitivity bode diagrams gains are plotted in Figure 3.46. In this figure the conventional sensitivity $S(s)$, the complementary sensitivity $T(s)$, the input sensitivity $S_i(s)$ and the control sensitivity $S_u(s)$ are considered. These transfer functions are described as

$$S(s) = \frac{1}{1 + C(s)G(s)} \tag{3.128}$$

$$T(s) = \frac{C(s)G(s)}{1 + C(s)G(s)} \tag{3.129}$$

$$S_i(s) = \frac{G(s)}{1 + C(s)G(s)} \tag{3.130}$$

$$S_u(s) = \frac{C(s)}{1 + C(s)G(s)} \tag{3.131}$$

obtained from a system like the one depicted in Figure 3.47:

$$Y(s) = \frac{C(s)G(s)}{G_{ce}(s)}(R(s) - N(s)) + \frac{G(s)}{G_{ce}(s)}D_i(s) + \frac{1}{G_{ce}(s)}D_o(s) \tag{3.132}$$

$$U(s) = \frac{C(s)}{G_{ce}(s)}(R(s) - N(s) - D_o(s)) - \frac{C(s)G(s)}{G_{ce}(s)}D_i(s) \tag{3.133}$$

being $G_{ce}(s) = 1 + C(s)G(s)$ the characteristic equation of the system.

All obtained points in the bode diagrams above a gain of zero decibels supposes an amplification of the correspondent frequency component. As can be deduced from Figure 3.47 the most suitable amplification becomes from $S_u(s)$ that is produced by $R(s)$, $D_o(s)$ and $N(s)$. In a VSI, $D_o(s)$ and $N(s)$ can be considered really small if the measures are sufficient accurate and filtered.

3.4.5 Experimental results

Firstly, a test platform constituted by an active filter integrated by a two-level three-phase four-wire with split DC-link inverter and a two-level three-leg interleaved DC/DC stage, as shown in Figure 3.49(a) is proposed to validate the goodness of the novel controller proposed. This active filter is connected to a reference non-linear load (according to the IEC 62040-3/Annex E [211]), as the one depicted in Figure 3.49(b) ($R_1 = 1\ \Omega$, $R_2 = 22\ \Omega$ and $C = 2.2$ mF). A Sinusoidal Pulse Width Modulation (SPWM) for the four-wire three-leg inverter has been selected. The converter is based

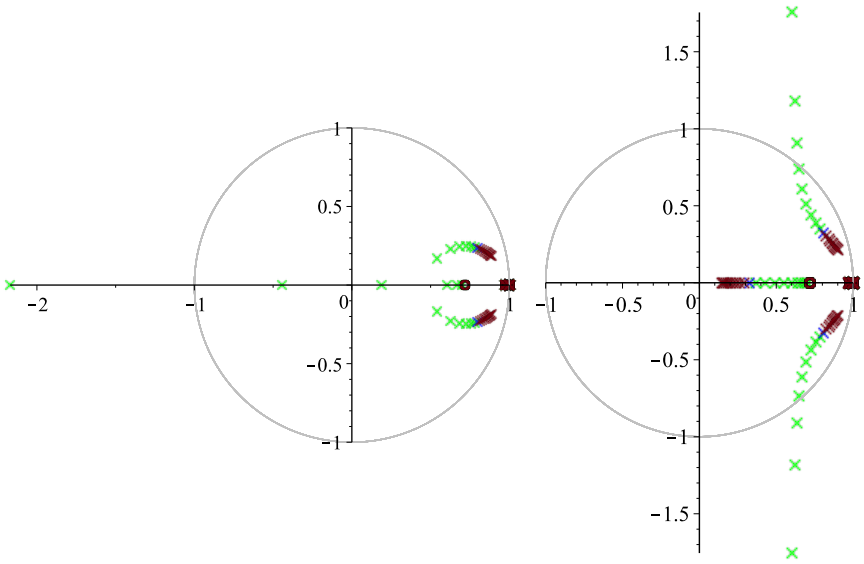

(a) No delay considered (b) Delay considered

Figure 3.45: Robustness analysis varying the tolerance of the parameter L from 0.1 to 2.0

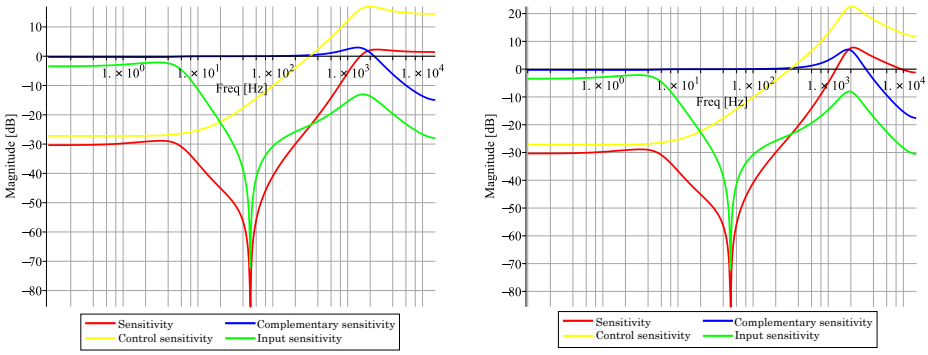

(a) No delay considered (b) Delay considered

Figure 3.46: Sensitivity gain bode diagram analysis

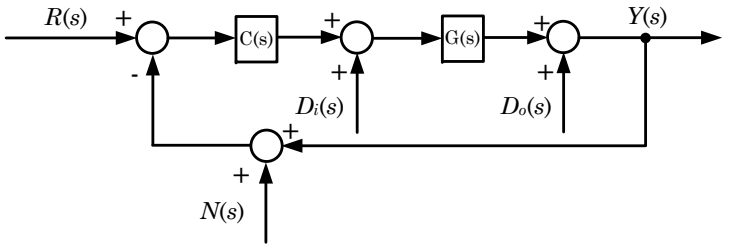

Figure 3.47: Complete control scheme when all disturbance inputs are considered

Figure 3.48: Setup picture

on a 20 kVA SiC module (CCS050M12CM2), the sampling and switching frequency is set at 30 kHz and the current references are computed at 10 kHz. It should be clarified that although a switching frequency of 30 kHz may seem a low value for SiC it is a good trade-off between high efficiency and time for all the required computational burdens (remind that the sampling and switching frequencies are the same). The parameters of the plant and the controller are shown in Table 3.3. The FPR controller used is described by Equation 3.126.

It can be observed in Figure 3.50 that the controller is able to compensate a high number of harmonic components. The non-linear load presents a THD of 62.8%. The controller is able to inject most of the harmonic components reducing up to a 3.2% the THD delivered by the main grid.

Secondly, the same inverter stage is used and all the hardware and soft-

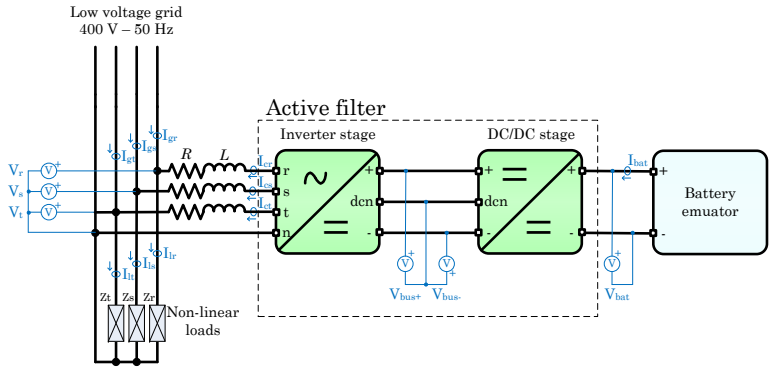

(a) Active filter setup framework

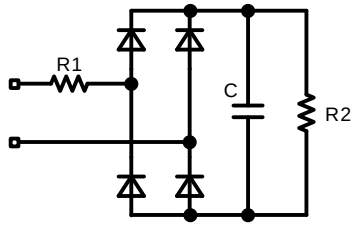

(b) Proposed non-linear load for the active filter setup framework according to IEC62040-3 [211]

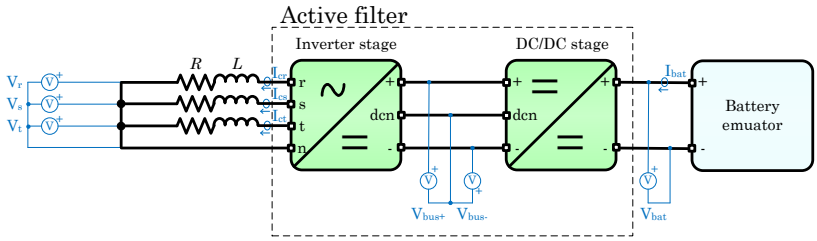

(c) Short-circuited setup framework

Figure 3.49: Setup schemes.

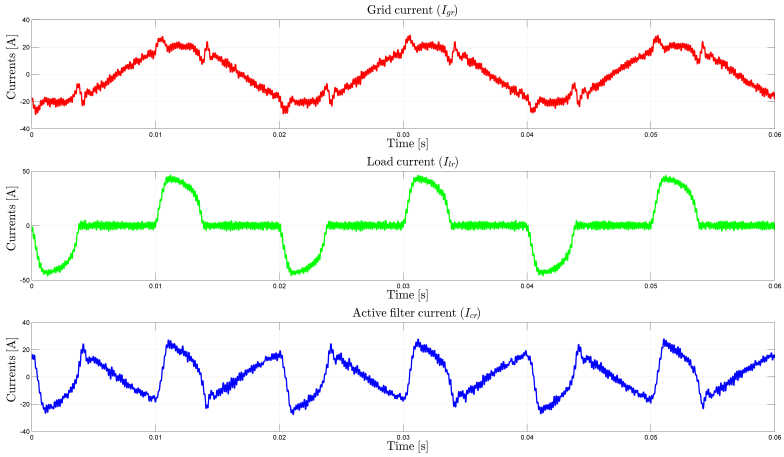

(a) Current waveforms when operated as an active filter

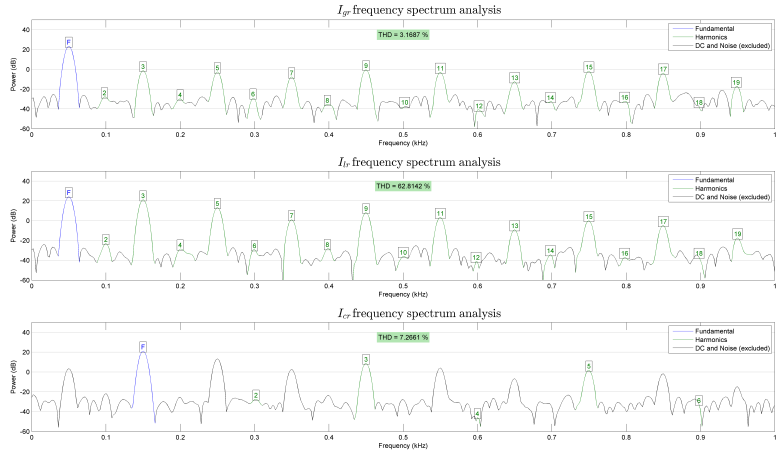

(b) Harmonic content distribution and THD

Figure 3.50: Experimental results obtained operating as an active filter for the delivered grid current, the consumed load current and the injected inverter current

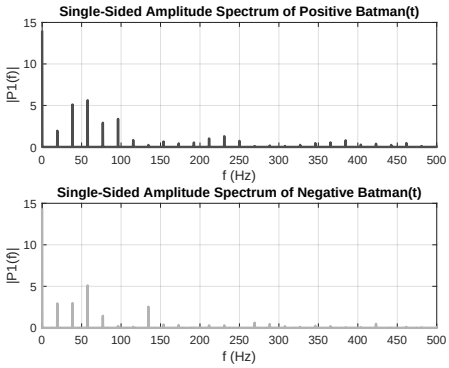

(a) FFT of the reference

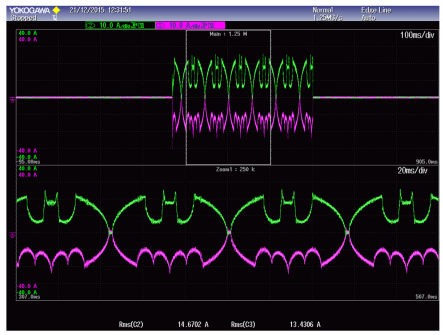

(b) Tracking response

Figure 3.51: Multi-harmonic ("Batman") tracking signal.

ware is maintained. Now, the inverter's output is short-circuited, see Figure 3.49(c). A complex multi-harmonic reference is generated. Phase r is used to generate the positive part of about 55 ms period "Batman" signal, whereas phase s is used for the negative part. In Fig. 3.51(a), the Fast Fourier Transform (FFT) of both parts is represented, thus detailing the multi-harmonic content. Fig. 3.51 shows an oscilloscope capture in which it is demonstrated that the controller is able to track complex multi-harmonic set-points.

3.5 Summary

One of the challenges on AC systems, as AC microgrids, is the control without steady state error of AC setpoints. For this situation is not only important to control correctly the fundamental component but also a widespread range of frequencies concerning harmonic component control.

This chapter has exposed the possibility to use different reference frames from the electrical magnitude or the controller perspective. In this case, the resonant controller and the stationary reference frame has been studied in more detail.

This chapter demonstrates that in continuous time there is no limitation in the frequencies to be controlled, in terms of stability, for the single current loop when resonant controllers are used. When a double nested loop structure is considered, the maximum frequency limit depends on the obtained controller gains of both loops. A high performance can still be obtained

with an appropriate tuning. Continuous time analysis has been extended to discrete time domain concluding that, in this last case, the system is significantly constrained. Ideal high frequency current control (no delay consideration) can be achieved. However, the stability worsens considerably when computational delay is taken into account. On the other hand, the maximum controllable frequency for the voltage loop, when no simplifications are done on the inner loop, is hardly constrained. It is highly dependent on both controllers constants. The results obtained in this study are an approach to the theoretical system stability and they help to understand the global behaviour of a voltage-current cascaded control. In addition, for a particular converter, the electrical limits have to be taken into account to ensure feasible transient responses.

Also, a method to tune the voltage control loop for conventional PR controllers is extended considering a desired time response and damping factor. The effect of a time-varying set-point is also analysed for the current loop.

A novel controller based on the application of fractional order calculus into resonant controllers has been presented. The existence of a fractional proportional-resonant controller formulation that enhances the frequency behaviour considering a non-integer order coefficient is demonstrated. Moreover, this single controller reduces the inter-harmonic excitation inherent to a resonant multi-harmonic controller. Several approximation alternatives have been considered and compared with regard to the implementation. The proposed controller has been implemented in a real test platform and its harmonic compensating capability has been validated operating the system as an active filter against a highly non-linear load and following complex trajectories when it is short-circuited.

Chapter 4

Grid Supply Inverters operation proposals for AC microgrids

4.1 Introduction

An AC microgrid is mainly integrated by two type of Voltage Source Inverters (VSI), as has been introduced in Chapter 2; the Current Controlled-VSI (CC-VSI) named Grid Supply Inverters (GSI), and the Voltage Controlled-VSI (VC-VSI) named Grid Constitution Inverter (GCI) or Grid Support and Constitution Inverter (GSCI). The GCI or GCSI designation concerns to an ideal or non-ideal voltage source behaviour, respectively

In this chapter, two proposals to operate conventional GSI when they are in the grid-connected mode, i.e. acting as CC-VSI, are proposed. The aim is to enhance the GSI operation when they are operated in an AC microgrid operation framework because GDSI is the most common photovoltaic and wind-turbine grid-connected inverters. A Grid Constitution Inverter (GCI) operation is adopted for the grid-disconnected mode in both proposals to supply the end-used acting as the voltage refernce for other systems. In this sense, the chapter is divided as follows:

- Section 4.2. *Grid-connected to/from grid-disconnected PV GSI operation.* This section presents a methodology to move from a grid-connected GSI to a grid-disconnected GCI operation. This transition is done without stopping the operation of the GSI. This proposal has been presented in [212, 213] published at PCIM2013 and IECON2013, respectively. Also, the control algorithm has been patented at European level [2].

- Section 4.3. *Extended execution of the MPPT algorithm for a Photovoltaic (PV) inverter with back-up.* This section proposes a control strategy to extend the operation capabilities of a PV GSI when there

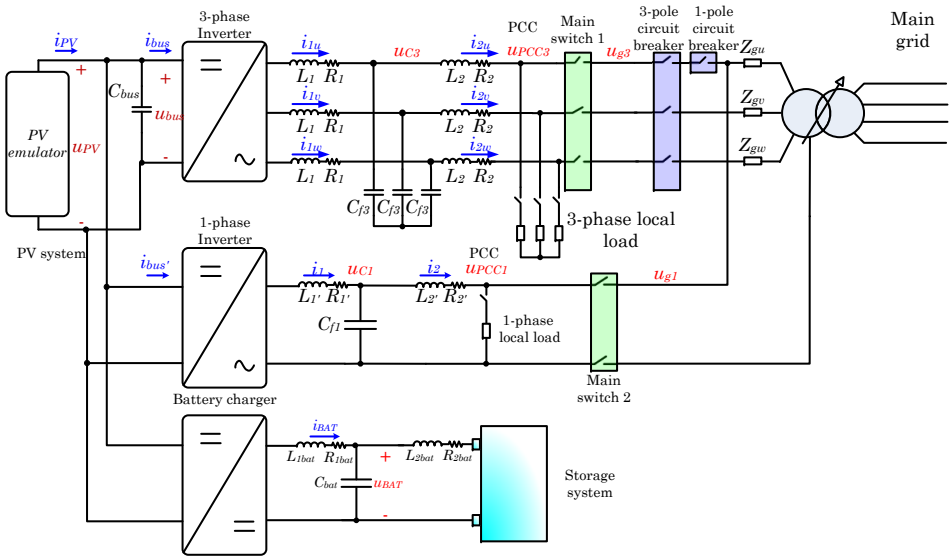

Figure 4.1: General conceptual scheme of the considered PV system

is a storage back-up system. This proposal has resulted in the publication of an article on PEDG2015 [214] and a Spanish patent [215].

The conceptual scheme shown in Figure 4.1 is considered as the PV grid feeding-forming system along this chapter. In this case, a PhotoVoltaic (PV) inverter is assumed. It is constituted by a three-phase inverter, a single-phase inverter and a battery charger converter. An experimental set-up will support the proposed control strategies according to the scheme of Figure 4.1.

4.2 Grid-connected to/from grid-disconnected PV GSI operation

This sections presents a flying transference proposal between grid-connected and grid-disconnected operation modes of a PV-GSI. In this direction, the objective is to provide a non-zero voltage crossing transference between both operation modes. The cited transference between modes implies two possibilities:

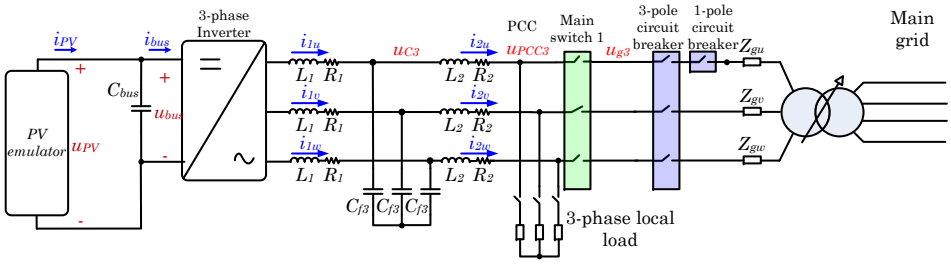

Figure 4.2: Conceptual scheme of the proposed three-phase PV-GSI for the grid-connected to/from grid-disconnected transfer operation

- The grid-connected to grid-disconnected transference. This situation is, commonly, non-intentional.

- The grid-disconnected to grid-connected transference. This situation is, as a rule, intentional.

The proposed procedure presents a strategy to move from GSI to GCI operation minimizing the effect of the transference at the Point of Common Coupling (PCC) voltage. It also details a methodology for reconnection purposes. In the published author's cites [212, 213], a comparison operating the inverter always as a Grid Supply and Constitution Inverter (GSCIs) extends the present proposal.

The case study is focused on the three-phase inverter of Figure 4.1, depicted in Figure 4.2, but it is also applicable to single-phase systems.

The inverter is operated as GSI under a Maximum Power Point Tracker (MPPT) algorithm in the grid-connected mode. Then, the PV inverter operates as a GCI in the grid-disconnected mode. For the present section, a synchronous reference frame control is adopted. Thus, all control loops are managed by Proportional-Integral (PI) controllers. Figure 4.3 shows the control scheme implemented for both operation modes. The subscripts dq refer to the direct/quadrature sequences, the subscript C to the AC capacitor, the subscript bus designates the PV DC-link, the subscript g adduces the grid-side and the superscript x^* alludes control references. The variables u and i indicates the AC capacitor voltage and the current through the inductance L_1, respectively. The AI block is the anti-islanding algorithm, explained next.

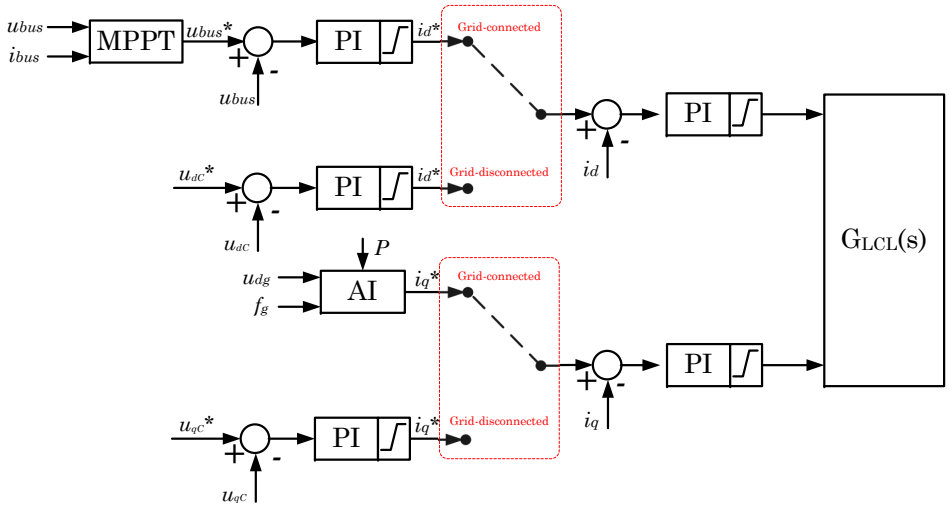

Figure 4.3: Considered control scheme for a three-phase PV inverter with an LCL-type coupling filter

4.2.1 The grid-connected to grid-disconnected transference

The key point of the transference from GSI to GCI is the detection of the mains loss. Once the island situation occurs, the change of operating mode from current source to voltage source involves extra control algorithms to ensure the integrity of the local loads. The transference strategy is divided into:

- The island detection algorithm.
- The transference decision.

The island detection algorithm

The island detection must be as fast as possible in order to not incur in extremely high voltage transients that will be, at the end, applied to the local loads. In other words, the clearance time results relevant. As in this case the inverter operates as a GSI when it is grid-connected, an active anti-islanding method based on the Sandia Frequency Shift (SFS) [86] strategy has been selected. In this sense, resonant loads and non-resonant loads will be taken into account. However, as the

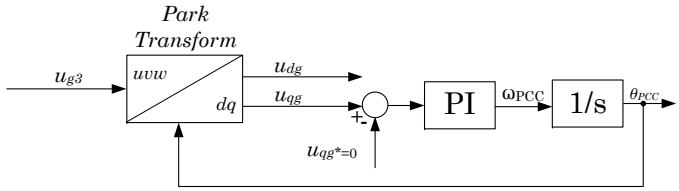

Figure 4.4: Conventional dq-based PLL

detection time is crucial, the active anti-islanding method is combined with real time voltage envelopes that are used to monitor the voltage at the PCC. The detection algorithm is described in the following lines.

The angle at the PCC voltage is obtained from a conventional Phase Locked Loop (PLL) mechanism, as the one depicted in Figure 4.4. Note that when the inverter is grid-connected $u_{PCC3} \simeq u_{g3}$, being u_{PCC3} the voltage at the PCC and u_{g3} the grid voltage.

The quadrature current of the L_1 inductance, i_q^*, is targeted by the anti-islanding calculation action as

$$i_q^* = k_1 k_2 (f - f_r) \tag{4.1}$$

The parameter f is the PCC frequency. This frequency is obtained from the angular frequency of the PCC, ω_{PCC}, and it matches f_g under grid-connected operation. The parameter f_r is the considered resonance or rated grid frequency, k_1 is a proportionality gain whose objective is changing the time spent to move out of an implemented Non Detection Zone (NDZ) and k_2 is described by

$$k_2 = \frac{2Pq_f}{u_{dg} f_r} \tag{4.2}$$

where P represents the average active power delivered by the inverter, $u_{d_{PCC}}$ the direct sequence voltage at the PCC and q_f the quality factor, see Equation 2.45.

While the GSI is grid-connected, the term $(f - f_r)$ is, in average, a null value if the PLL algorithm is properly tuned. In the grid-disconnected mode, the computed subtraction produces a constant effort to increase the difference term $(f - f_r)$, positive or negative, each control cycle.

During normal operation mode, i.e. operating as GSI in grid-connected mode, the LCL capacitor voltages u_C are continuously monitored and

compared with two envelope curves. If any u_C voltage is out of the envelope thresholds, a detection situation is presumed. These thresholds are self-generated sine-waves obtained from the computed PLL angle, $\omega_{PCC}t$. The envelopes are calculated as

$$u'_{env}(t) = Usin(\omega_{PCC}t) \pm A \tag{4.3}$$

being U the rated peak voltage value and A a selected offset. Each one of these curves and the AC capacitor voltage needs to be filtered to avoid that the process noises will affect the procedure. Another option is to consider an envelope as

$$u''_{env}(t) = kUsin(\omega_{PCC}t) \tag{4.4}$$

where k is a design gain. It should be noticed that $u''_{env}(t)$ can cause false detecting situations when a zero crossing takes place. For this reason, the option proposed in Equation 4.4 is desisted.

The transference decision

Once the system has detected a possible island situation, due to the implemented anti-islanding procedure or because the AC capacitor voltage is out of the aforementioned envelopes indicated in Equation 4.3, the transference occurs. Then, the inverter starts to operate as a GCI. However, two challenges appear:

- How to initialize the AC controller?
- Which is the most suitable initial AC voltage reference according to different grid fault types?

From the transference event, the references to the inner loop are provided by a non initialized AC voltage controller. For this reason, it can appear not desirable voltage transients at the PCC. In this case, it is proposed to analyse the effect of two possible solutions to initialize the voltage controller properly:

- Reset. All previous errors and the controller output are set to zero.
- Bumpless. All previous errors are set to zero and the controller output is set to the previous current reference.

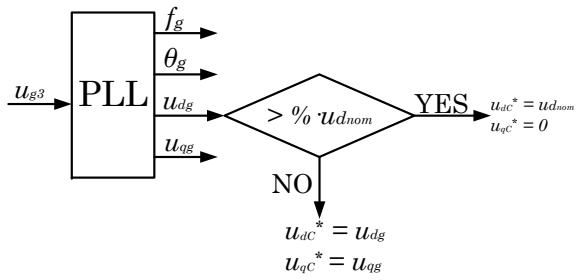

Figure 4.5: Criterion for grid fault consideration

It is also convenient to consider different kinds of grid faults; short-circuits and non-stipulated grid disconnections. A strategy to identify the type of fault is proposed based on the LCL filter capacitor voltage reference. This strategy is focused on forcing a specific voltage level, setting the reference to the rated grid values, during a short time interval just after the transference takes place and observe how the system reacts. The operation of the converter requires a PLL with the three functional modes detailed in Chapter 2-Figure 2.33. Then, the PCC voltage is observed to make a decision:

- If the u_{dg} value is below a certain limit, the fault will be considered as a depth dip or a short-circuit and the new reference is the present voltage value.
- If the u_{dg} value is above the chosen threshold, it is considered that grid is really disconnected and the new reference is the nominal voltage value ($u_{d_{nom}}$).

The decision criterion has been established as a percentage of the direct voltage $u_{d_{nom}}$, as can be seen in Figure 4.5.

On the other hand, it has to be considered that the opening process of the main switch, see Figure 4.2, usually an electro-mechanical switch, is not instantaneous. It is necessary to implement a wait stage which objective is to continue with the same decision made in the previous step. Finally, the disconnection procedure ends with a final part in which the AC voltage reference is set to rated grid values operating, from that instant, as a GCI.

Figure 4.6 summarises the exposed procedure for the GSI to GCI trans-

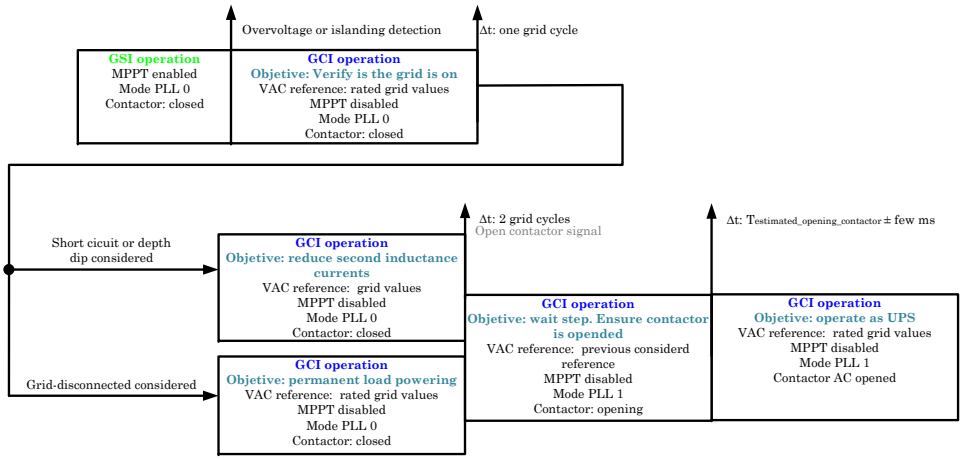

Figure 4.6: Grid-connected to grid-disconnected proposal operation scheme

ference. Note than when the overvoltage or island detection occurs, the MPPT is disabled to match the DER with the requirements of the AC load. This is a consequence of thee absence of back-up systems. This idea is developed in Section 4.3.

4.2.2 The grid-disconnected to grid-connected transference

During the grid-disconnected operation, the voltage u_{g3} at the grid side is constantly monitored. Once the frequency and the grid voltage, obtained from a PLL algorithm, are inside a predefined NDZ window, a counter measuring a prefixed time (determined according to the considered regulation) is initialized. During this time it could happen that any instant can be out of the NDZ. If this event occurs, the inverter continues operating as a GCI but the synchronization process is disabled until new grid values are again inside the NDZ. Then, the PLL algorithm is forced to mode 2, detailed in Chapter 2-Figure 2.33. This PLL mode manages the microgrid voltage u_{PCC3}. The PLL imposes progressively u_{PCC3} to have the same amplitude, frequency and phase than the u_{g3} voltage. The synchronization is achieved when the difference between the grid angle and the microgrid angle is almost zero. When the synchronization procedure is finished, the main switch, see Figure 4.2, is closed and the converter begins the operation in the GSI

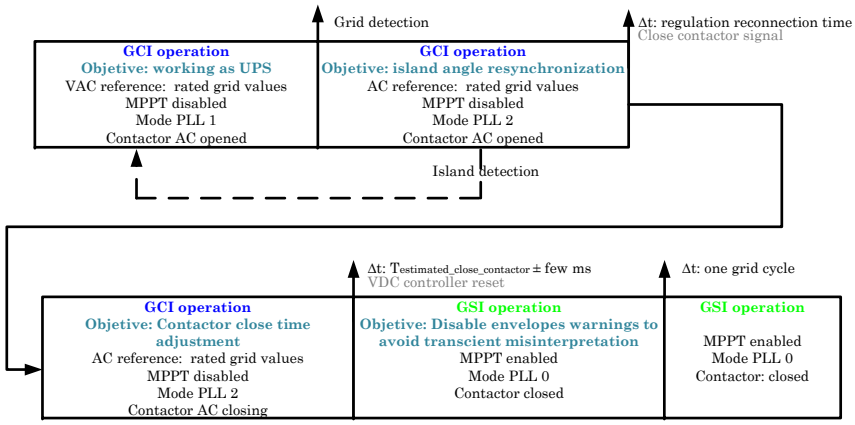

Figure 4.7: Grid-disconnected to grid-connected proposal operation scheme

mode. In this case, it is also necessary to consider the close time of the main switch.

Figure 4.7 summarises the exposed procedure for GCI to GSI transference.

4.2.3 Full transference proposal strategy

To show a clear picture of the full proposed process, Figure 4.8 depicts the patented scheme in [2].

4.2.4 Simulation and experimental results

The methodology proposed in this section is simulated using Matlab/Simulink and validated in an experimental set-up to contrast both obtained outcomes.

The PV string characteristic curve is depicted in Figure 4.9 in which the open-circuit voltage is set to 350 VDC. The considered AC grid side is 230 V phase-to-phase and 50 Hz to match with the mentioned PV string open-circuit voltage. The three-phase inverter is operated at 2.5 kW under a P&O MPPT algorithm for the simulated and experimental case studies. The control algorithm and switching frequency is 19 kHz. The parameters values of the inverter LCL-type coupling filter

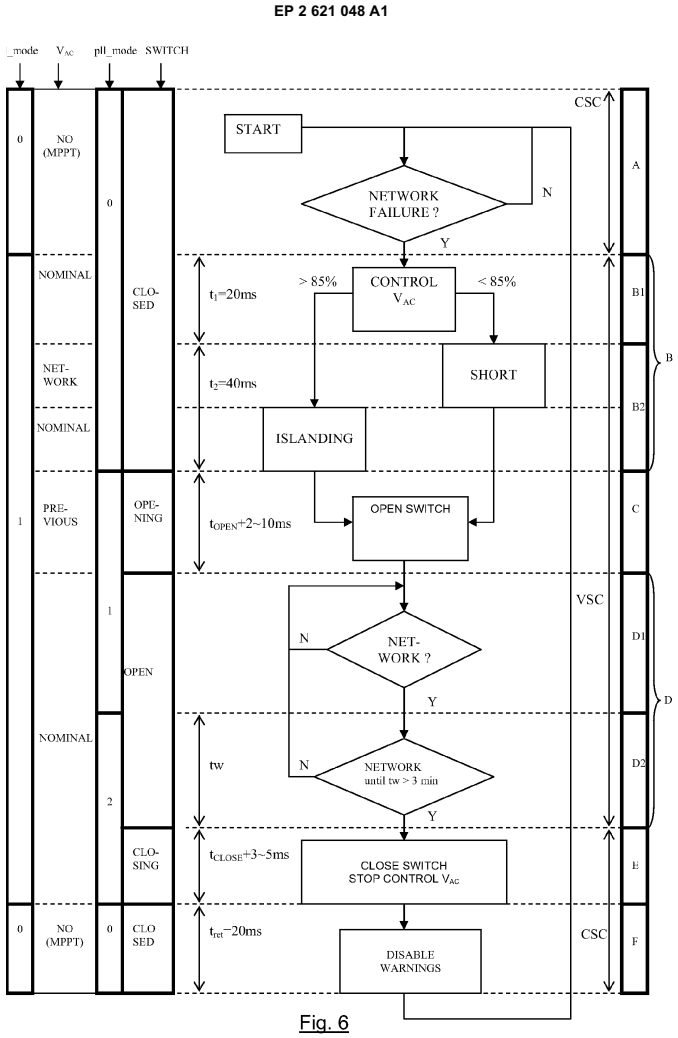

Figure 4.8: Patented scheme of the method for disconnecting and reconnecting a GSI system to/from the electrical network [2]

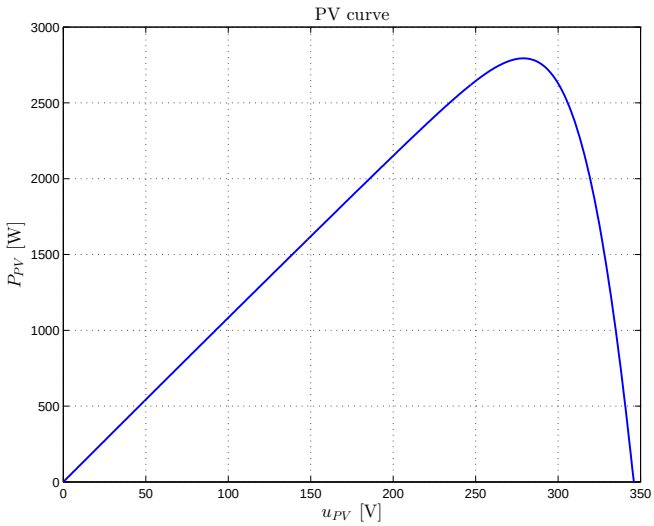

Figure 4.9: PV curve used for the flying transference algorithm validation

used are shown in Table 4.1. In Table 4.2 can be observed the controllers parameters of the inverter. As has been mentioned, all control strategies are developed using a *dq* reference frame.

For the experimental set-up it should be considered that all control algorithms have been implemented in the Texas Instrument TMS320-F2808. Figure 4.10 shows a picture of the full PV system proposed in Figure 4.1. Block (1) is a battery charger, block (2) a single-phase inverter, block (3) a resistive load bank, block (4) a three-phase inverter and block (5) a PV emulator. For this section, it only has

Symbol	**Parameter**	**Value**	**Units**
L_1	Output inverter inductance	2	mH
R_1	Equivalent series resistance of L_1	1	Ω
C_{f3}	Capacitor of the LCL filter (Δ)	2	μF
L_2	Leakage inductance of the transformer	2	mH
R_2	Equivalent series resistance of L_2	0.3	Ω

Table 4.1: Simulation LCL used parameters

Symbol	Parameter	Value
k_{p_i}	AC current loop proportional gain	20
k_{i_i}	AC current loop integral gain AC current loop	20000
k_{p_u}	AC voltage loop proportional gain	0.040
k_{i_u}	AC voltage loop integral gain	120.0
$k_{p_{udc}}$	DC voltage loop proportional gain	0.10
$k_{i_{udc}}$	DC voltage loop integral gain	5.0

Table 4.2: *dq* AC current and voltage controller parameters

to be considered blocks (3) to (5). The PV string is emulated. It has been programmed according to the control technique assumption cited in [172]. This emulator is pre-configured to match the PV curve shown in Figure 4.9. Different local resistive loads will be used for the validation; 10 kΩ (close to no-load situation: ≈5 W), 70 Ω (≈725 W) and 35 Ω (≈1450 W).

Four scenarios will constitute the test framework to validate the three-phase inverter flying transference from GSI to GCI. Each case contemplates four sub-cases monitoring the voltages at the PCC; one related with bumpless initialization and a three-pole disconnection, one concerning bumpless initialization and one-pole disconnection, one involving reset initialization and three-pole disconnection and, finally, one joining reset initialization and one-pole disconnection. The three and one pole disconnection are intentionally produced by the 3-pole and 1-pole circuit breakers shown in Figure 4.2.

On the other hand, one more scenario for the reconnection sequence has been considered also plotting the voltages at the PC. The case in which the outer voltage loop transference is done before and after the real closure of the main switch is analysed. It has been assumed a response time of the electro-mechanical switch around 55 ms and has been simulated the transference 50 and 60 ms after sending the order of closing that switch.

Simulations

Figure 4.11 to 4.13 shows the obtained simulated results according to the previous four planned scenarios for the GSI to GCI transference. Each figure

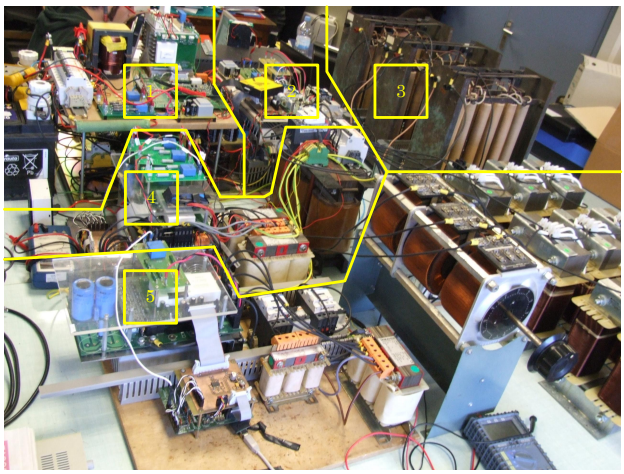

Figure 4.10: Proposed set-up

considers a different local load connected to illustrate the effect of the ratio between the PV-inverter delivered power and the consumed power when the transference from GSI to GCI takes place. From these figures it can be deduced that, in general, reset alternative produces better results considering the maximum voltage value obtained at the local load terminals. However, this option produces a short oscillating transient due to a more abrupt control action. This fact permits that the rms value can be lower than in the bumpless case. Thus, the bumpless option does not oscillate but the maximum rms voltages obtained are higher than in the reset case. This last result should be avoided to ensure local load integrity.

Figure 4.14 shows the results after simulating the reconnection situation under a 725 W local load. It can be observed that, as indicated in the transference proposal strategy, the fact of operating the inverter as a GCI during a small time interval (few milliseconds) after the main switch is really closed offers better reconnection results.

Experimental results

The experimental results presented in Figure 4.15 to 4.17 shows the same set of scenarios depicted in the simulation section but obtained with the set-up of Figure 4.10. The obtained results are quite similar to those presented at the simulation section. The differences between the simulations and the real cases can be attributed to the different instant when the grid has been

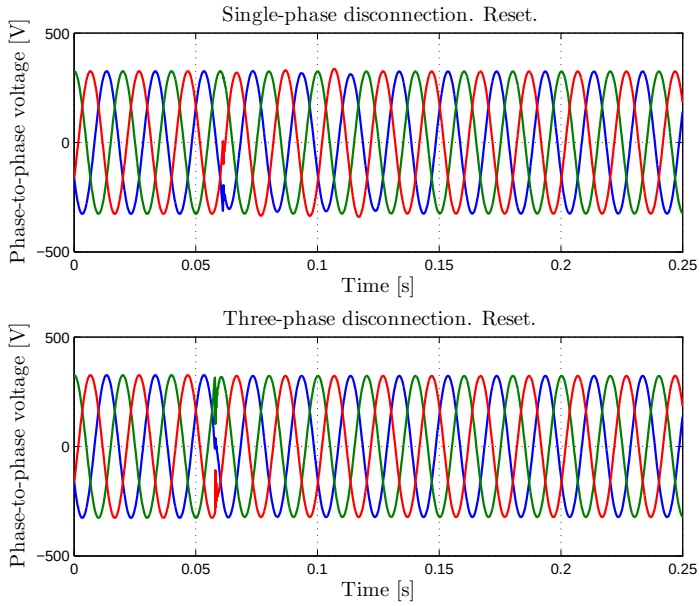

(a) Reset AC voltage controller initialization

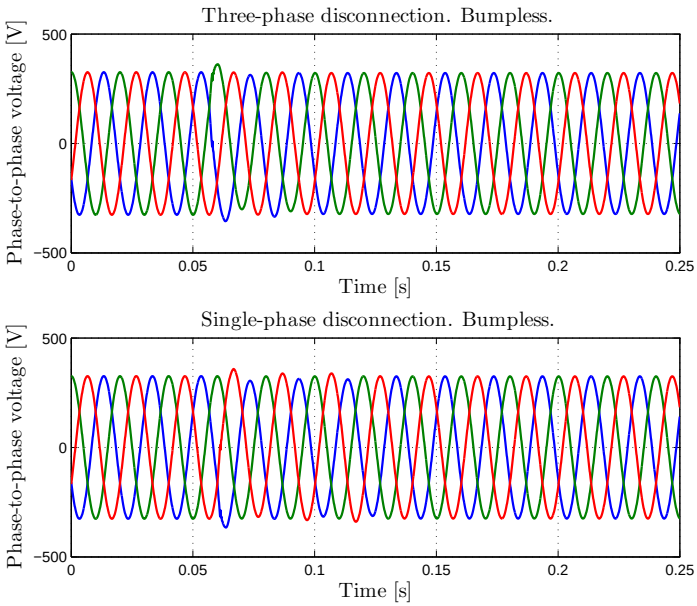

(b) Bumpless AC voltage controller initialization

Figure 4.11: Simulation PCC phase-to-phase voltages for the disconnection with a 70 Ω local load

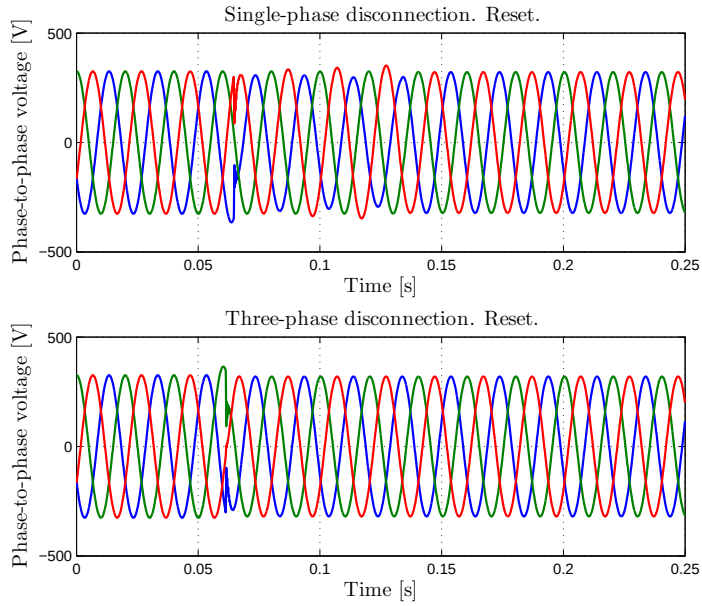

(a) Reset AC voltage controller initialization

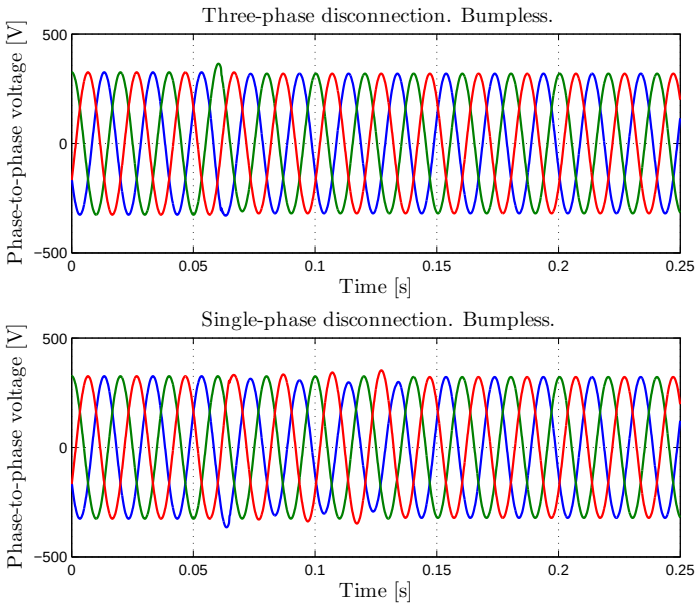

(b) Bumpless AC voltage controller initialization

Figure 4.12: Simulation PCC phase-to-phase voltages for the disconnection with 35 Ω local load

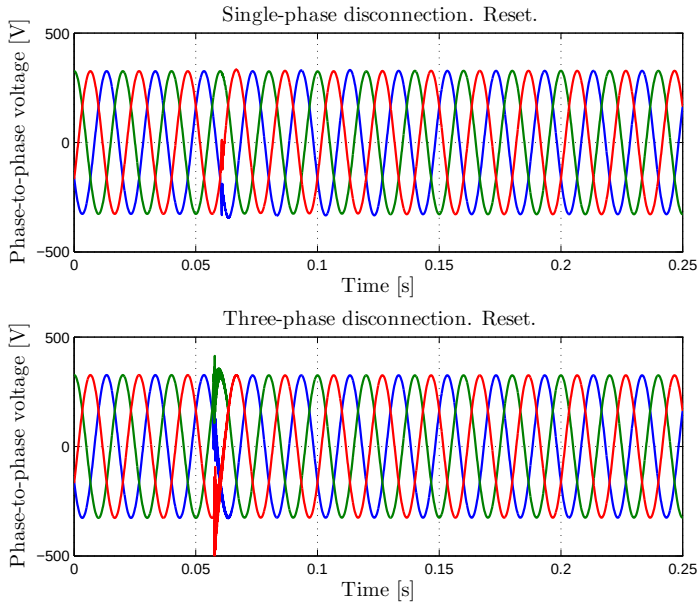

(a) Reset AC voltage controller initialization

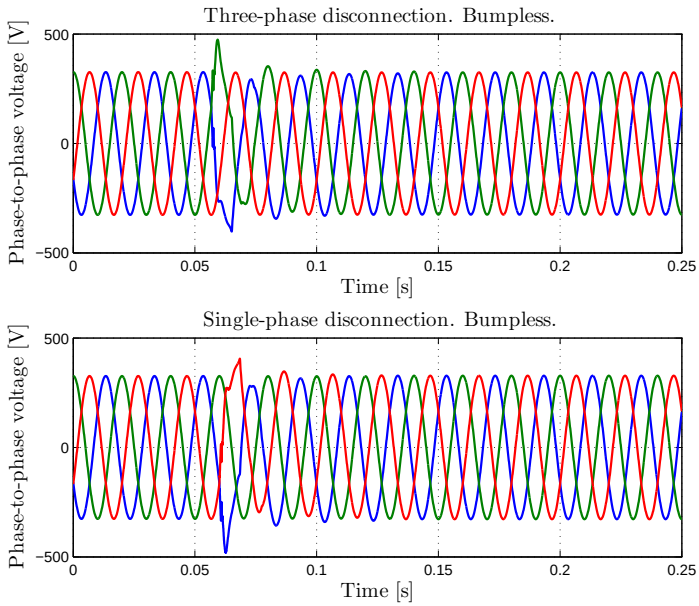

(b) Bumpless AC voltage controller initialization

Figure 4.13: Simulation PCC phase-to-phase voltages for the disconnection with a 10 kΩ local load

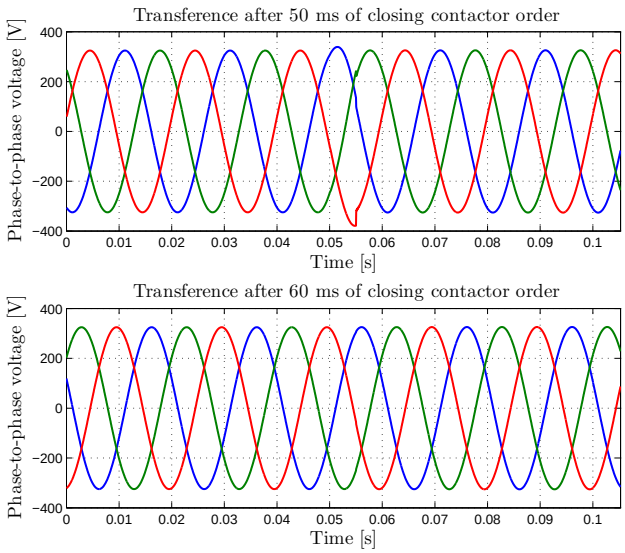

Figure 4.14: Simulation PCC phase-to-phase voltages for the reconnection with a 725 Ω local load

forced to be disconnected and due to the model of the circuit breaker used.

Figure 4.18 depicts the real obtained PCC voltages after the reconnection situation under a 725 W local load. In the real case it has been observed an average close-time response of the main switch closer to 58 ms. It can be seen that it is crucial to force the transference from GCI to GSI after few milliseconds after the main switch is really closed. This action produces a smooth transference.

All the results in the experimental section have been contrasted with the grid analyser Dranetz Power Explorer PX-5. This device allows to generate reports according to the ITI curve presented in Section 2.6. Although some of the exposed results show points out of the ±10% steady state thresholds, any one is out of the limitations according to the ITI pattern. Figure 4.19 shows an example for the worst case, 10 kΩ load under reset and bumpless initialization.

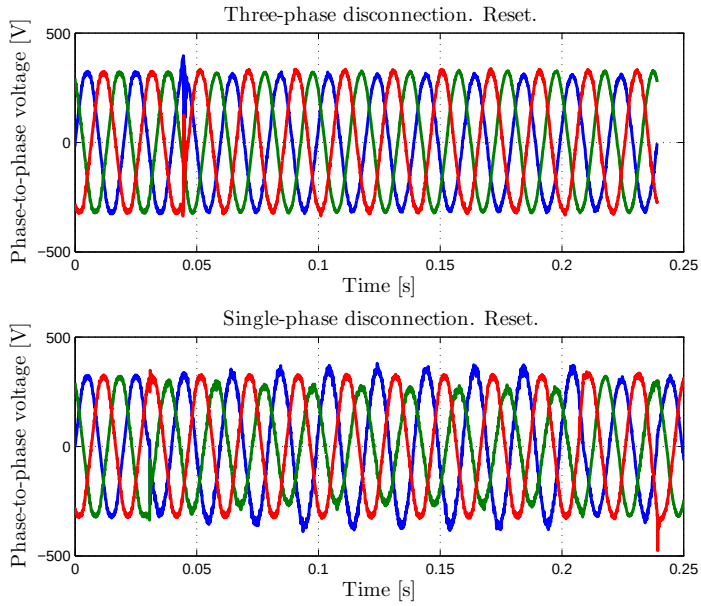

(a) Reset AC voltage controller initialization

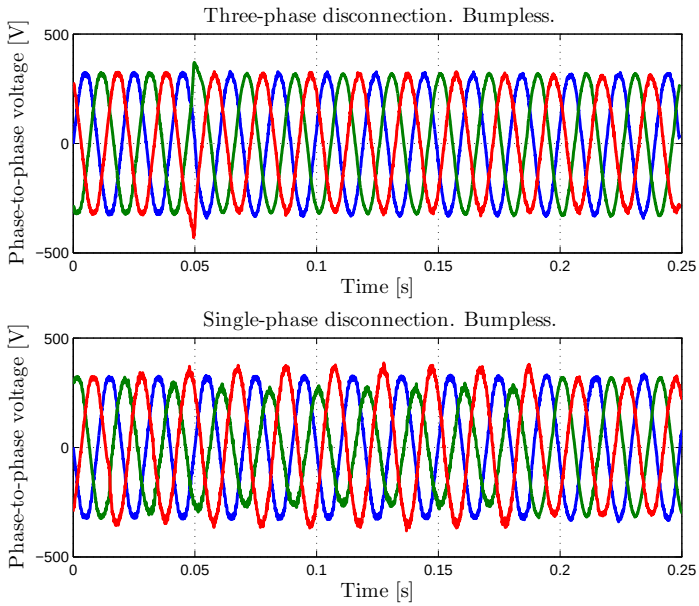

(b) Bumpless AC voltage controller initialization

Figure 4.15: Experimental PCC phase-to-phase voltages for the disconnection with 70 Ω

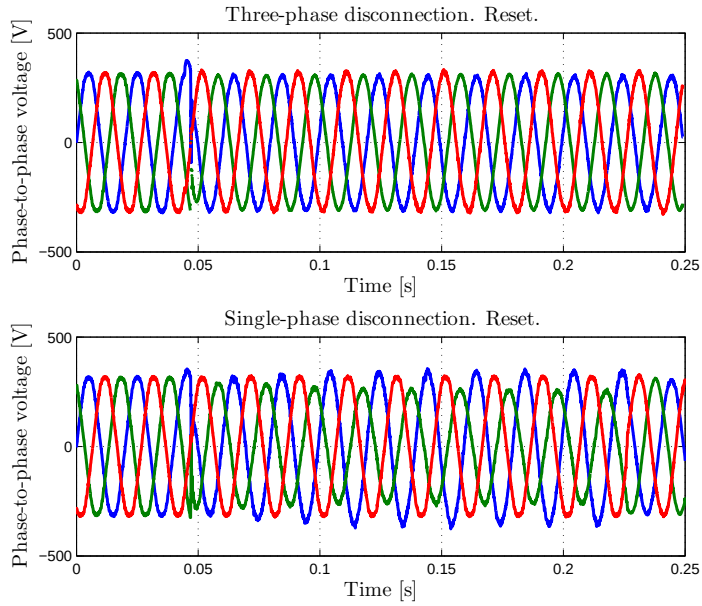

(a) Reset AC voltage controller initialization

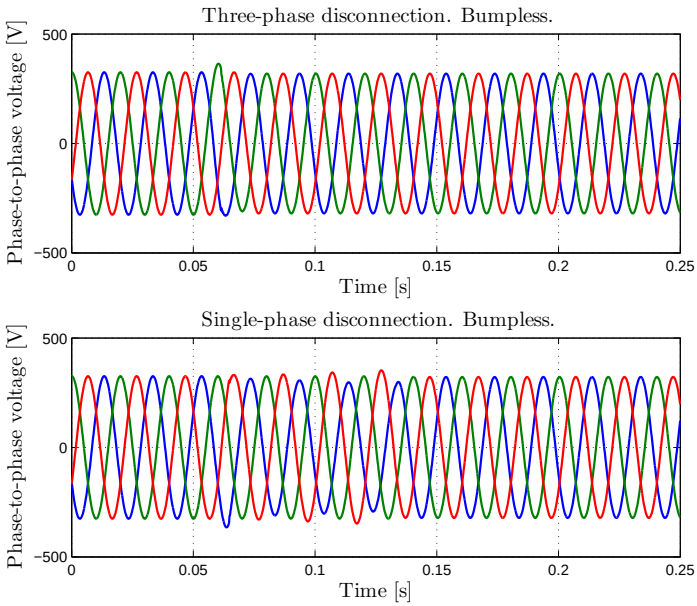

(b) Bumpless AC voltage controller initialization

Figure 4.16: Experimental PCC phase-to-phase voltages for the disconnection with 35 Ω

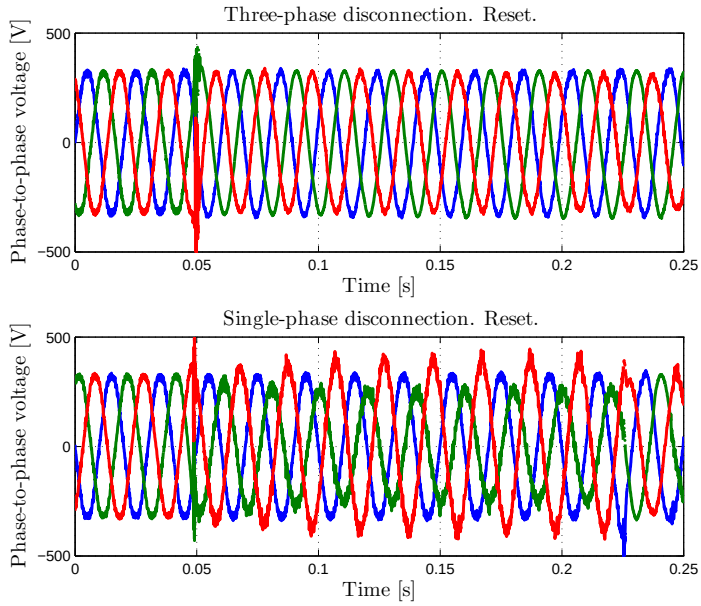

(a) Reset AC voltage controller initialization

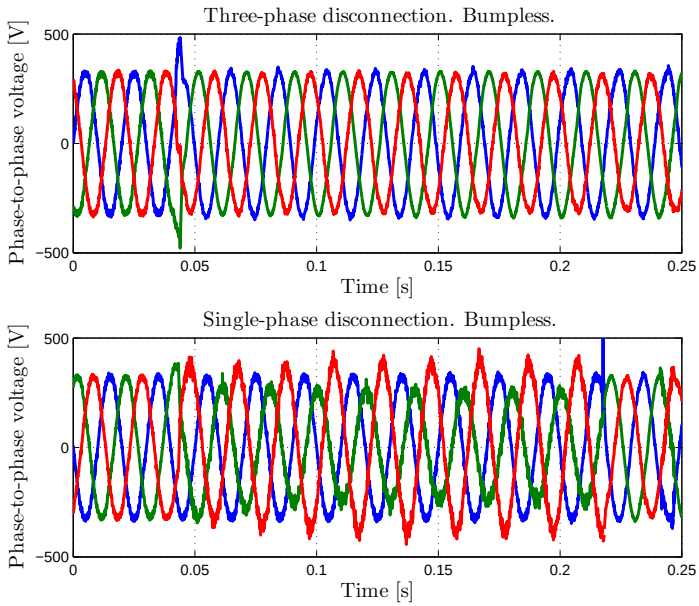

(b) Bumpless AC voltage controller initialization

Figure 4.17: Experimental PCC phase-to-phase voltages for the disconnection with 10 kΩ

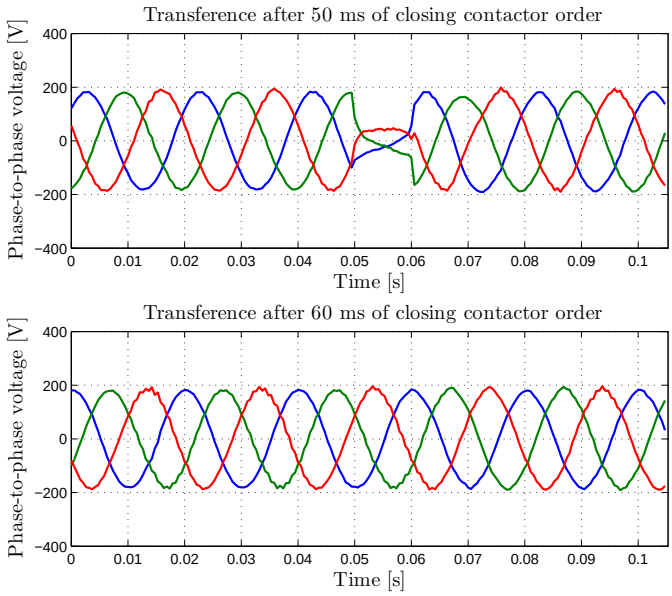

Figure 4.18: Experimental results for the reconnection with 70 Ω

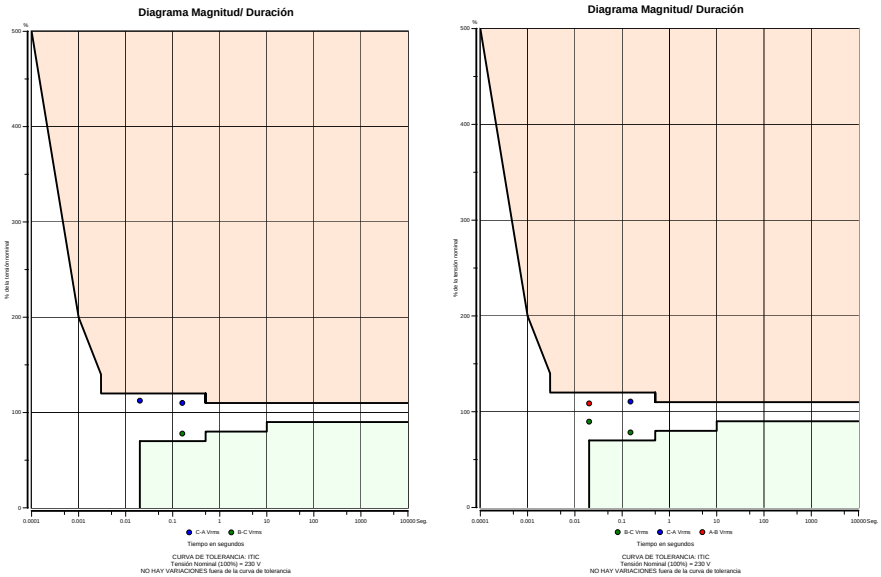

(a) Bumpless initialization (b) Reset initialization

Figure 4.19: ITI Dranetz's report for the disconnection with 10 kΩ

4.3 Extended execution of the MPPT algorithm for a PV inverter with back-up

PV inverters, as one of the most relevant Distributed Energy Resources (DER) nowadays, will play an important role in the years ahead. For this reason it is not possible to conceive PV inverters as a mere grid feeding DER from now on. Their participation as grid-forming DER in grid-disconnected mode combined with conventional grid feeding behaviour constitutes hybrid solutions as grid feeding-forming DER, as has been introduced in Chapter 1. Then when a PV inverter is thought to be operated in an AC microgrid, it should be considered:

- If the PV inverter is operated as a PV-GCI in the grid-disconnected mode the power at the AC side could be less than the maximum power of the PV modules. Thus, the MPP (Maximum Power Point) is not attained at any time whereas in the grid-connected mode the power delivered to the grid is controlled by the AC current loop of the inverter. Then, in the last case, the MPP is steadily reached due to the grid can be considered as an infinite energy buffer.

- As exposed in the previous point, during the grid-disconnected operation the power flow at the AC side of the inverter is imposed by the AC local loads. One way to change the power requested to the PV modules is by using an energy back-up storage system. This situation provides a new degree of freedom that can be used for energy management purposes.

In order to optimize the use of the available energy of a conventional grid feeding photovoltaic system, a grid-connected PV-GSI supported with a backup storage system is considered in this section. A novel strategy to extend the execution of the MPPT algorithm on photovoltaic inverters is proposed. The control strategy takes into account local loads and the battery limitations. The main objective of this technique are:

- Supply power to the local loads while extracting the maximum power during the battery charge and discharge processes.

- Contribute to the restoration of the grid operation in case of overcharge in the electric network.

- Provide extra power to the local loads during peak-demand hours or store the surplus of energy during less-demand hours using the storage system.

- Maintain the MPPT active whenever possible using the new degree of freedom that offers the energy storage.

- Manage the amount of energy that the PV system will deliver to the storage system.

The case study is focused on the single-phase inverter and the battery charger of Figure 4.1, depicted in more detail in Figure 4.20, but it is also applicable to three-phase systems. The single-phase inverter and the battery charger are considered individual devices. As the power electronics which need to be controlled has been separated into two different parts managed by independent control boards they are linked using industrial communications. The CAN (Communication Area Network) bus has been selected for this commitment. With the aim of simplifying the power balance in the whole system, the control of the inverter and the battery charger is treated assuming a master-slave hierarchy. The inverter (master) is responsible for giving a power reference to the battery charger (slave) to store or to deliver.

The main device is constituted by a H-bridge one-stage single-phase PV inverter. It has been considered a PV string at the DC-side and an LCL-type coupling filter for control and ripple filtering purposes. The main switch disconnects all the elements from the utility to start operation in the grid-disconnected mode. The other relevant converter's stage is the battery charger. It is implemented as a bidirectional current half bridge DC-DC converter with an LCL-type filter. The LCL-type output filter is used to decrease the current switching ripple at the input of the battery and to ensure more cyclability. Some local loads completes the set-up.

The explanation of the different control strategies is divided into three different sections:

- The battery charger control.

- The inverter control.

- The MPTT algorithm.

The bases for the control strategies are substantiated by the grid-connected and grid-disconnected operation modes. It will be assumed that while the system is operating in the grid-connected mode, a fraction of the amount of power produced is used for charging the batteries and the remaining is delivered to the grid. Essentially, the grid will not be used for charging purposes. Per contra, it should be reminded that when the system is grid-disconnected,

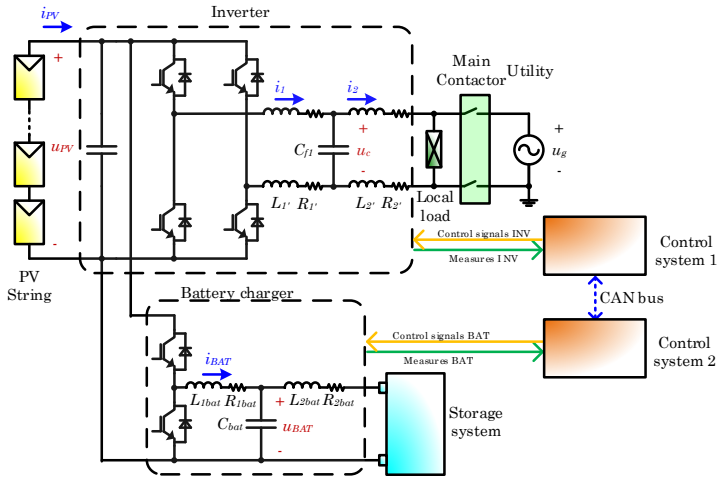

Figure 4.20: Power stage of the considered PV-System

the MPP could not be reached, mainly, because the storage system does not allow to be more charged with the available power of the PV system and the AC load consumption is too low or due to the AC power consumption is too high and the storage system is close to be fully discharged.

4.3.1 The battery charger control

Firstly, as has been aforementioned, the battery limitations are relevant to ensure the battery integrity. For this reason, the battery charger algorithm has to take into account some thresholds for the power flow in the input or output direction according to the battery State of Charge (SoC). Usually, there is a different maximum value for the battery current in consonance with the charging direction. Hereinafter, $i_{BAT_{MAXCHR}}$ refers to the maximum charging current and $i_{BAT_{MAXDCHR}}$ to the maximum discharging current. These saturations may be modified by the charging and discharging processes and must be controlled at any time in order to avoid any damage on the accumulator.

The control scheme of the battery charger is shown in Figure 4.21. As has been cited in the previous section, the inverter computes the power reference P_{BAT}* for the battery charger. The power reference P_{BAT}* is translated to a current magnitude by dividing it by the battery voltage u_{BAT}. This value is saturated by the upper and lower limits of the accumulator, $i_{BAT_{MAXCHR}}$ and $i_{BAT_{MAXDCHR}}$. The result is used as the upper saturation of the voltage

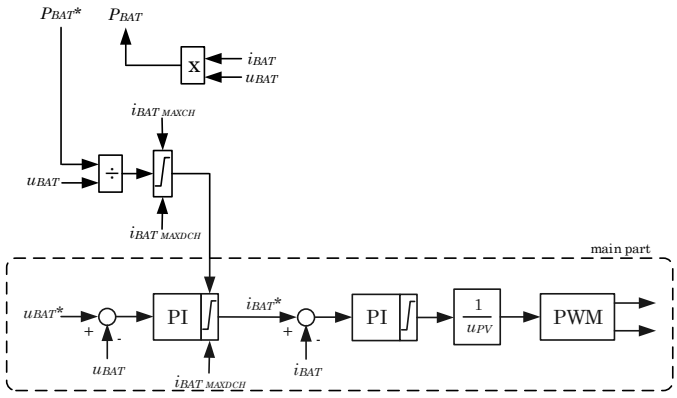

Figure 4.21: Control scheme of the battery charger

controller which is, in fact, the upper limit for the final current reference. The lower saturation is fixed at $i_{BAT\ MAX\ DCH}$. At each voltage close-loop execution cycle, the power flow data P_{BAT} in the accumulator is returned to the inverter through the communication channel.

The main part of the control scheme of Figure 4.21 is based on two cascaded loops. The outer one refers to the u_{BAT} voltage and the inner one to i_{BAT} current. This two nested loops permits to charge the battery, firstly, at a constant current rate and, finally, at a constant voltage rate. To achieve this behaviour autonomously the voltage reference $u_{BAT}{}^*$ is set to be the maintenance voltage. Note that the current reference is forced to the upper saturation of the voltage controller until the voltage level of the battery reaches a value close to the charge maintenance one.

4.3.2 The inverter control

Because the inverter has to operate as a GSI in the grid-connected and as a GCI in the grid-disconnected mode, it is usual to assume two nested control loops. The inner one refers to the first inductance $L_1{}'$ current i_1 and it is a common loop for all the following proposals. In Figure 4.22, a control scheme diagram of the current loop is shown. The main goal of this inner current loop is to regulate the power delivered to the AC side of the converter. The main structure is a PI controller complemented by a feed-forward of the u_c voltage to reject, as maximum as possible, the second inductance $L_2{}'$ current disturbances i_2 and to reduce the control action required effort. By using the DC voltage u_{PV} and a Sinusoidal Pulse Width Modulation (SPWM),

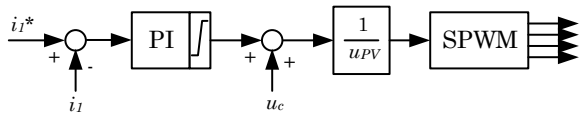

Figure 4.22: Control scheme of the inverter current loop

the switching signals of the IGBTs can be generated.

The origin of the current reference for the inner loop depends on the operation mode of the system; grid-connected or grid-disconnected operation mode. In Figure 4.23, a block diagram of the outer control control loop is presented according to these operation modes:

- In the grid-connected operation, the MPPT algorithm determines the u_{PV}* reference for the PV-string voltage, which matches with the DC side of the inverter. In steady state, this reference is the MPP voltage of the PV string. However, as the MPPT algorithm used is based on a P&O (Perturbation and Observation) method [216], if there is no certain control of the PV consumption, the maximum power cannot be ensured. Due to the fact that the system is connected to the grid, the only limit is that the addition of the nominal power of the inverter and the battery charger has to be higher than the maximum power of the PV string for the optimal conditions. Thus, the MPP is attainable in any condition.

  Once u_{PV}* has been obtained, it is controlled by the DC voltage controller which control action will be the power reference, P_{PV}*, for the PV modules. A portion of this power, defined by the $K_{BAT} \subset [0, 1]$ gain, is referenced to the storage system. Note that this K_{BAT} gain should be controlled by a MGCC and will depen on several factors as demand profiles, state of health of the back-up system, among others. The term (P_{PV}*-P_{BAT}) is the power reference, P_{INV}*, for the inverter. The block (1) expresses the power in terms of current which is, in fact, the current reference i_1* for the inner loop presented in Figure 4.22. The K gain is obtained as $(1 - K_{BAT})$ and θ_g refers to the grid angle.

- In grid-disconnected operation, the voltage at the AC side must be controlled in order to keep powering the local loads. This is achieved thanks to an outer loop that control the u_c voltage at the capacitor of the LCL-type coupling filter. The output of the controller is directly the current reference i_1* for the inner loop presented in Figure 4.22.

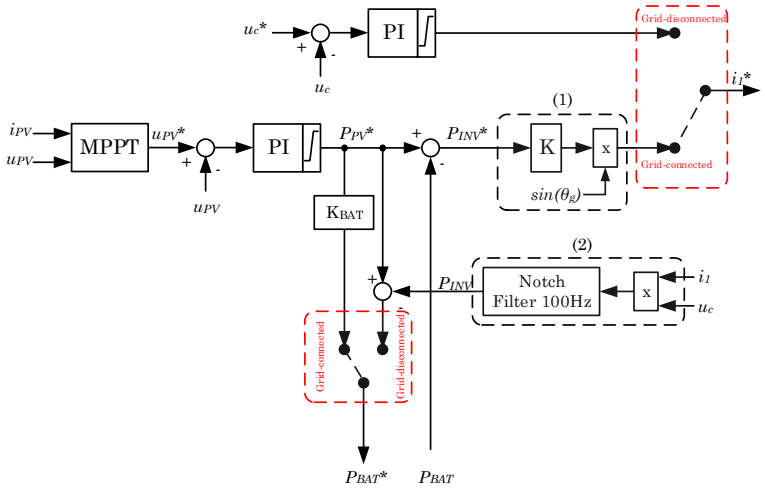

Figure 4.23: Full control scheme of the inverter

The power at the AC side of the inverter is not controlled and it is imposed by the local load. The block (2) calculates the power at the AC side of the inverter, P_{INV}, as the product of the i_1 current and the u_c voltage. Note that this is a single-phase system and the instantaneous power is affected by a 100 Hz oscillating component that should be suppressed using, for instance, a notch filter. Now, the subtraction (P_{PV}*-P_{INV}) is referenced to the battery charger as P_{BAT}*. This value can be negative in the case that there is no enough power available in the PV string to supply the local loads.

Some extreme cases can be considered:

- If the limits of the battery charger are exceeded, the PV voltage regulator is not be able to operate. As a result, the MPPT system can fail into some errors and its output achieves the saturation in the steady state.
- In case of a lack of power in the isolated system, the DC voltage falls until the under-voltage alarm of the inverter and the local load will be permanently non supplied. P_{INV} falls down to zero and all the PV power is injected to the battery. Otherwise, if there is a surplus of non storable energy, the DC voltage increases, while the PV power decreases, due to the PV string voltage-current characteristics. The voltage that equals the PV power with the storable power and the local load power is now the operating

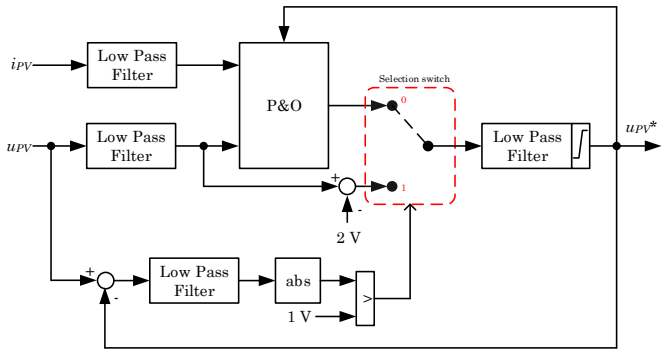

Figure 4.24: Control scheme of the MPPT system

point for the DC voltage.

4.3.3 MPPT algorithm

In the Sections 4.3.1 and 4.3.2 there is no explanation on how the MPPT system operates to enhance the use of the PV available resources. It is assumed a base operation principle substantiated on the widely used P&O method. The P&O MPPT algorithm introduces a step in the PV voltage u_{PV} producing a variation in the PV power (perturbation) that is seen after the PV voltage transient (observation). According to this information it can be decided how to proceed with the next step in the PV voltage, i.e. keep the same step sign or change it.

In the grid-connected operation mode there are no remarks to do about the conventional operation of the MPPT algorithm. Otherwise, during the grid-disconnected operation, in some situations, the control of the DC voltage can be lost if a mismatch between the available PV power and the consumed power occurs (battery plus AC loads). In that circumstance, the targeted u_{PV}* voltage and the u_{PV} will not match, even after a certain time (action of the low-pass filter). This situation should be detected by the MPPT system. Figure 4.24 shows a control scheme of the proposed MPPT system adding extra elements to a conventional P&O MPPT algorithm.

If there is a lack of power in the system, the PV voltage is going to fall under the disconnection alarm level, so there is nothing to do more than disconnecting the loads and switching off the inverter.

In an extra-powered PV system, the DC voltage increases and a non controllable error between the reference u_{PV}* and the measure u_{PV} appears. The extracted power from the PV panels cannot be delivered to any load,

even considering the battery. Thus, as soon as this error exceeds a certain threshold value (in this case 1 V), the P&O algorithm is disabled (the input port of the selection switch changes from 0 to 1). Obviously, this error should not contemplate the transients in the DC voltage loop, so a filter is added. In this situation, the voltage reference u_{PV}* is set close to the measured voltage in order to avoid hard transients under a step in the local load. This value is established below the measured one (in Figure 4.24 a value of 2 V is proposed), forcing the voltage to decrease and, consequently, trying to increase the power that the PV system can deliver. Note that the proposed value for this commitment is different form the threshold used to detect. This is done to create such kind of hysteresis avoiding switching excessively between MPPT enabling and disabling occurrences. As soon as the local load increases, P_{BAT}* falls inside the battery operating range, the control of the PV voltage is restored and the P&O algorithm is enabled again (the input port of the selection switch changes from 1 to 0).

4.3.4 Simulation and experimental results

The methodology proposed is simulated using Matlab/Simulink and validated in the same experimental set-up shown in Figure 4.9 to contrast both obtained outcomes. In this case, block (1) that is the battery charger, block (2) that refers to the single-phase inverter, block (3) constituted by a resistive load bank and block (5) that concerns to the PV emulator are used.

The PV string is emulated as in Section 4.2. The emulator is pre-configured to operate under the PV curve shown in Figure 4.25 with a maximum power of 1.5 kW (at G = 1 kW/m^2), an open-circuit voltage about 610 VDC and a MPP around 500 VDC. The storage system is constituted by four series 12 VDC lead-acid batteries. The allowed loads are 0 W, 587 W and 1174 W. The considered single-phase AC grid side is set at 230 V and 50 Hz.

Table 4.3 to 4.5 presents the battery charger, the inverter and the MPPT hardware and control parameters.

The following lines describe a selected set of six scenarios used illustrate how can be used the extended MPPT strategy in island mode, even under suddenly irradiation changes, but also in transference situations. These case studies permits to validate the extended execution MPPT control strategy proposed previously under complex situation when a grid-tied inverter with back-up is assumed:

- For the three first scenarios the single-phase inverter is permanently in the grid-disconnected mode. The system is evaluated under different

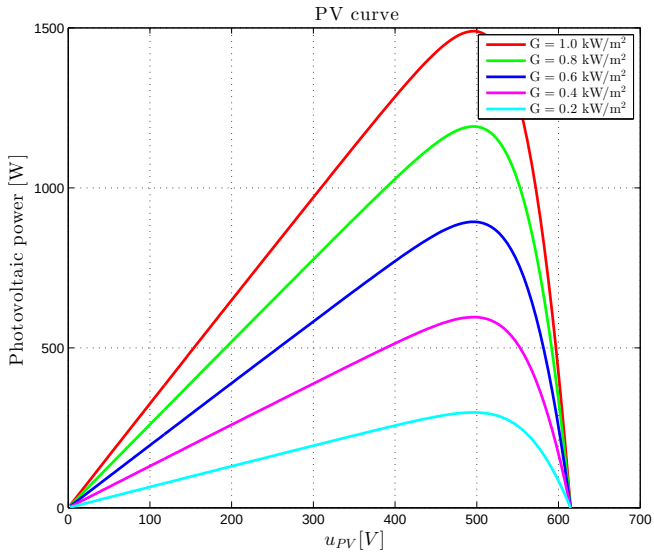

Figure 4.25: PV curve used for testing the extended execution of the MPPT algorithm

Block	Parameter	Value	Units
Battery charger	Execution frequency of the current loop	16	kHz
	Execution frequency of the voltage loop	1	kHz
	$i_{BAT_{MAXCHR}}$	9.0	A
	$i_{BAT_{MAXDCHR}}$	-32.0	A
	$L_{1_{bat}}$	1.62	mH
	C_{bat}	47.0	μF
	$L_{2_{bat}}$	21.4	μH
	k_p voltage loop	1	
	k_i voltage loop	720	
	k_p current loop	3.4	
	k_i current loop	3280	

Table 4.3: Battery charger parameters

Block	Parameter	Value	Units
Inverter	Execution frequency of the current /AC voltage loop	16	kHz
	Execution frequency of the DC voltage loop	1	kHz
	DC under voltage alarm threshold	400	V
	DC voltage controller saturation	2.2	kW
	AC voltage controller saturation	10	A
	Current controller saturation	400	V
	AC grid voltage	230	V
	AC grid frequency	50	Hz
	DC-link	2.35	mF
	$L_1{}'$	6	mH
	C_f	26	μF
	$L_2{}'$	33	μH
	k_p DC voltage loop	0.03	
	k_i DC voltage loop	0.5	
	k_p AC voltage loop	0.02	
	k_i AC voltage loop	20	
	k_p AC current loop	71	
	k_i AC current loop	40000	

Table 4.4: Single-phase inverter parameters

Block	Parameter	Value	Units
MPPT algorithm	u_{PV}/ i_{PV}/ u_{PV}* voltage low pass filter	0.4	Hz
	$u_{PV} - u_{PV}$* error voltage low pass filter	10.0	Hz
	P&O execution time	20	ms
	Voltage step of the P&O	4	V
	u_{PV}* lower/upper saturation	450/650	V

Table 4.5: MPPT parameters

load transients at a constant irradiation G = 0.6 kW/m^2 (MPP $\approx$ 900 W, refer to Figure 4.25). When t<40 s no load is connected, then when 40 s<t<80 s a first 587 W load is added and for 80 s<t<100 s the full load is connected. The loads are disconnected following a symmetric disconnection pattern over the time instant t = 100 s.

  - Scenario 1. Study of the system behaviour considering that the batteries are practically full charged.
  - Scenario 2. Identical scenario in respect with scenario 1 but the SoC of the storage system is now at 80%.
  - Scenario 3. Identical scenario in respect with 1 and 2 but the SoC of the storage system is practically at 0%.

- Other two scenarios are used to analyse the effect of a transference from grid-connected to grid-disconnected and viceversa, at a constant irradiation G = 0.4 kW/m^2 (MPP $\approx$ 600 W). Two sub-cases are considered per scenario: full-load (1174 W) or with no-load (0 W). Each sub-case takes into account three different levels of SoC for the storage system: 100%, 80% and 0%. Both scenarios contemplates a zero crossing transference step between operation modes. During this zero crossing step, the inverter does not switch and the power reference for the batteries is zero.

  - Scenario 4. The grid-connected to grid-disconnected transition is evaluated. In this case, the zero crossing step time is set at 0.14 s.
  - Scenario 5. The grid-disconnected to grid-connected transition is evaluated. In this case, the zero crossing step time is set at 1 s.

- Finally, a sixth scenario shows how suddenly irradiation changes affects the MPPT tracking in island mode. The considered SoC is set at 80% for three different load demands; full-load (1174 W), half-load (587 W) or with no-load (0 W). The energy balance between the available irradiation and AC load consumptions will establish a continuously operation enabling and disabling the MPPT operation.

For the validation results it is presented how the power flow of the three main devices (PV emulator, inverter and battery charger) is shared and how evolves the u_{PV}. For the experimental case, the power flow values between the three devices are obtained monitoring the power values exchanged using the CAN field bus. The evolution of the PV voltage u_{PV} is presented as an oscilloscope capture. The measure has been obtained via a differential

voltage probe in which it should be considered a 2-scale factor due to the selected voltage probe range.

- Scenario 1. The evolution of P_{PV}, P_{INV} and P_{BAT} is shown in Figure 4.26(a) and 4.26(b). The bus voltage behaviour is depicted in Figure 4.26(c) and 4.26(d). During the time that no-load is present (t<40 and t>160 s), the P_{PV} can be only used to compensate the battery charger and the inverter losses in the experimental case. It should be remarked that the inverter is operating generating the voltage at the AC side and the battery charger is controlling the maintenance voltage. When the first load is connected (40 s<t<80 s and 120 s<t<160 s), the inverter starts to deliver energy but cannot fulfil the MPP. When the load consumes enough power (80 s<t<120 s), the inverter automatically operates at the MPP and the battery supplies the remaining power. It is possible to validate the on-state of the MPPT algorithm observing the behaviour of the bus voltage in Figure 4.26(c) and 4.26(d) that oscillates around 500 V.

- Scenario 2. The evolution of P_{PV}, P_{INV} and P_{BAT} is shown in Figure 4.27(a) and 4.27(b). The bus voltage is depicted in Figure 4.27(c) and 4.27(d). As now the battery can absorb some power, during no-load operation (t<40 and t>160 s) the inverter can supply some power to charge the storage system. The MPP is not reached due to the battery limits. Now, when the first load is connected (40 s<t<80 s and 120 s<t<160 s), as there is enough P_{PV} available, the battery is charged and it is possible to supply the local loads. When the full load is connected, some energy is supplied by the back-up system and all the available P_{PV} is delivered to the load allowing to operate at the MPP. In this scenario, from t = 40 s to t = 160 s the MPPT is active.

- Scenario 3. The evolution of P_{PV}, P_{INV} and P_{BAT} is shown in Figure 4.28(a) and 4.28(b). The bus voltage is depicted in Figure 4.28(c) and 4.28(d). In this case, when the full-load is connected (t = 80 s), as the battery level is too low, there is no way to supply the loads. Although the systems is not able to supply the loads, the inverter is switched-off but the PV systems delivers all power that admits the storage system to charge it. In this sense, the system is focused on the minimization of this situation because it always try to charge the storage system. It should be remembered that the system has been designed with the aim of avoid to charge the storage system from the grid.

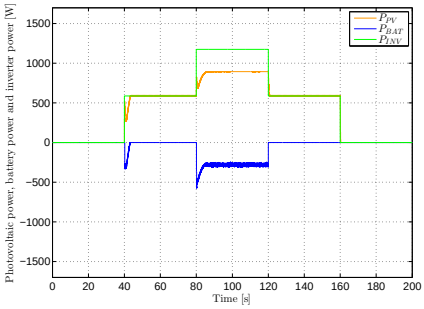

(a) Simulated results. P_{PV}, P_{INV} and P_{BAT}

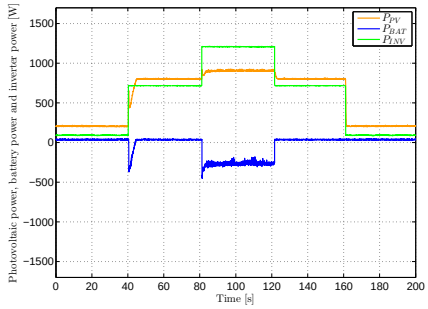

(b) Experimental results. P_{PV}, P_{INV} and P_{BAT}

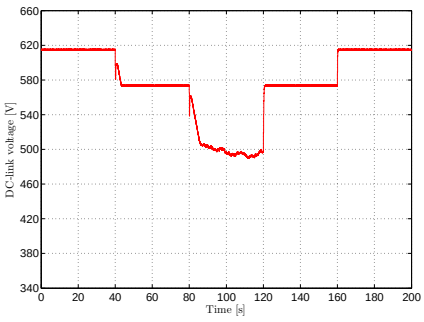

(c) Simulated results. u_{PV} voltage

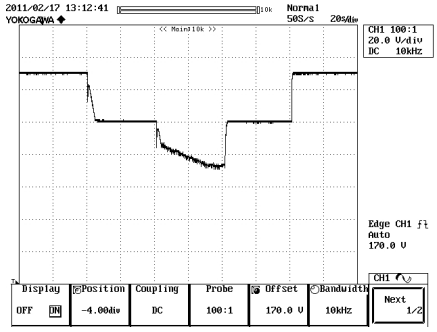

(d) Experimental results. u_{PV} voltage

Figure 4.26: Scenario 1. Grid-disconnected operation at G = 0.6 kW/m^2, different loads and SoC at $\simeq$ 100%

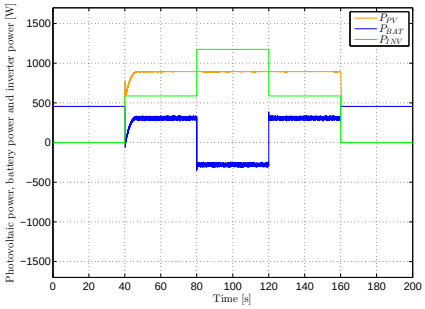

(a) Simulated results. P_{PV}, P_{INV} and P_{BAT}

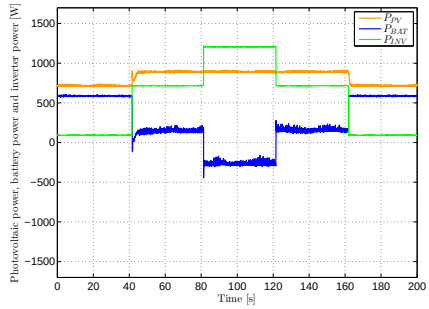

(b) Experimental results. P_{PV}, P_{INV} and P_{BAT}

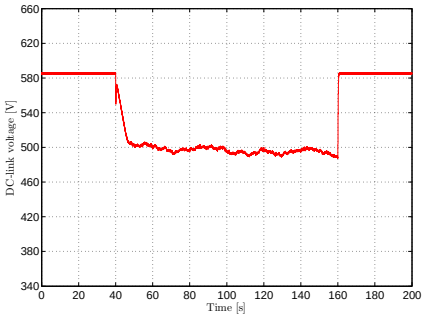

(c) Simulated results. u_{PV} voltage

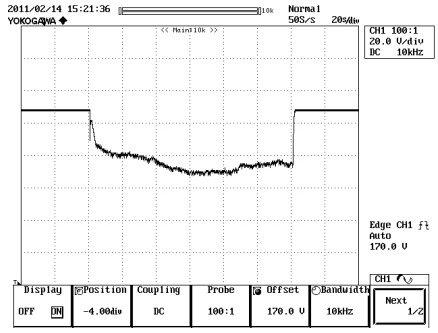

(d) Experimental results. u_{PV} voltage

Figure 4.27: Scenario 2. Grid-disconnected operation at G = 0.6 kW/m^2, different loads and SoC at 80%

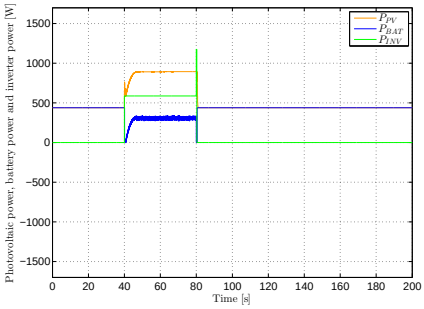

(a) Simulated results. P_{PV}, P_{INV} and P_{BAT}

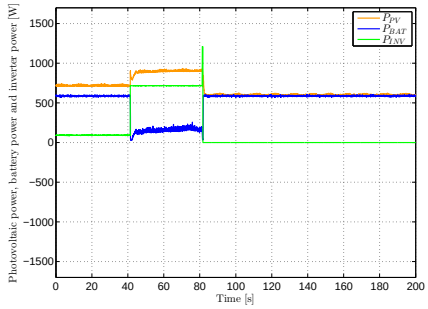

(b) Experimental results. P_{PV}, P_{INV} and P_{BAT}

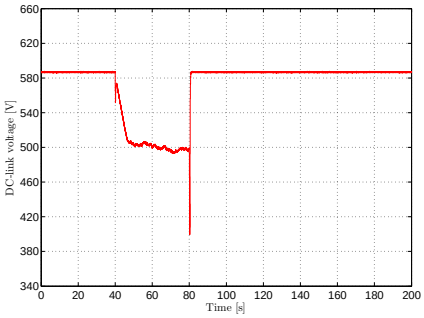

(c) Simulated results. u_{PV} voltage

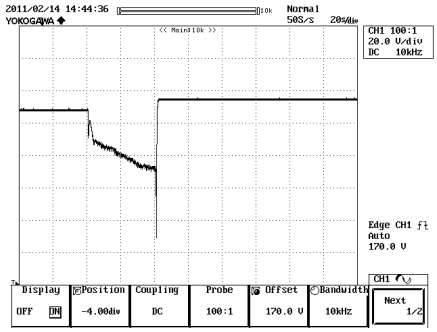

(d) Experimental results. u_{PV} voltage

Figure 4.28: Scenario 3. Grid-disconnected operation at G = 0.6 kW/m^2, different loads and SoC at $\simeq$ 0%

- Scenario 4. Grid-connected to grid-disconnected transition considering G = 0.4 kW/m^2. In this case, at time t = 2 s the grid is off.

  - Scenario 4.a. Full-load connected. It should be highlighted that when a grid-connection to grid-disconnected transition occurs, the behaviour of the inverter in grid-connected mode is as a GSI and in grid-disconnected mode is as a GCI. The evolution of P_{PV}, P_{INV} and P_{BAT} is shown in Figure 4.29. Then, the voltage u_{PV} is depicted in Figure 4.30.

    When the inverter is in the grid-connected mode (t < 2 s), the load is supplied by the grid and all the available P_{INV} is delivered to the grid. Thus, the system is operating at the MPP. When it is grid-disconnected, as the available PV power is not close to the demand side, the capability to supply the AC loads is dependent on the SoC. If there is enough energy available at the battery the inverter does not stop to deliver energy and, consequently, it operates at the MPP with the support of the storage system. In case of 0% of SoC, the inverter is not able to supply sufficient power. Although the AC side is disconnected, all the available P_{PV} is used for charge the storage system. Then, the MPP is attained after the inverter switch-off process. It should clarified that in the case of the results shown when SoC is at 0% some differences can be appreciated. This is due to the internal losses in the experimental test platform produces an extra consumption that enables to operate at the MPP, i.e. $\approx$ 9 ADC to charge the storage system plus the charger losses.

  - Scenario 4.b. No-load connected. This is a complementary situation of the previous one. The evolution of P_{PV}, P_{INV} and P_{BAT} is now shown in Figure 4.31. Then, the voltage u_{PV} is depicted in Figure 4.32.

    In this scenario, the worst case occurs when the battery is at 100% of SoC. The energy storage system cannot absorb the available P_{PV} and, in this situation, it is wasted because there is any device, neither the batteries nor the inverter, that can take profit of the PV energy. Only the internal losses can be consumed in the real case. In the case of SoC at 80% or 0%, the available P_{PV} is used to generate the AC voltage by the inverter implying some inner losses ($\approx$ 80 W). Also, the remaining available P_{PV} is used to charge the batteries close to the maximum allowable current

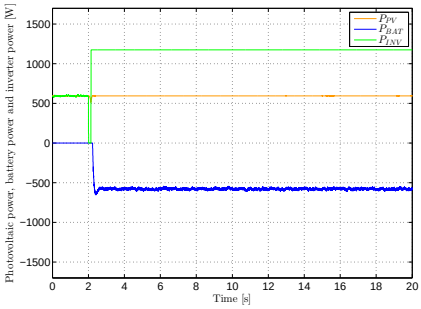

(a) Simulated results. SoC at 100%

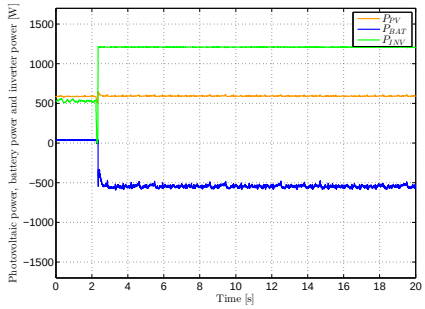

(b) Experimental results. SoC at 100%

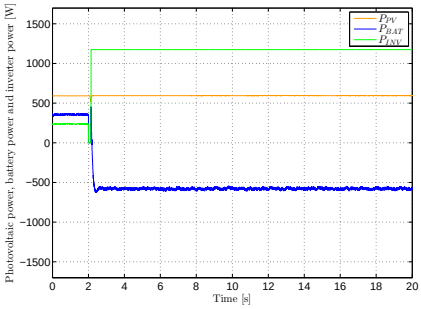

(c) Simulated results. SoC at 80%

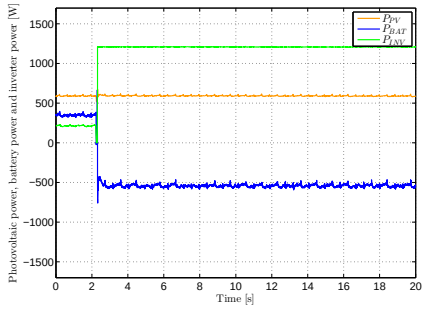

(d) Experimental results. SoC at 80%

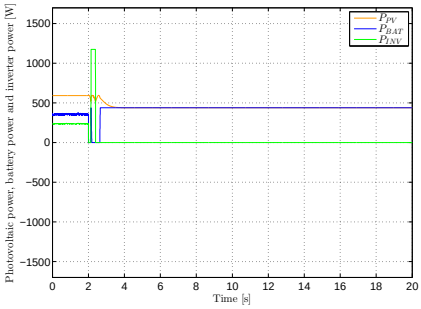

(e) Simulated results. SoC at 0%

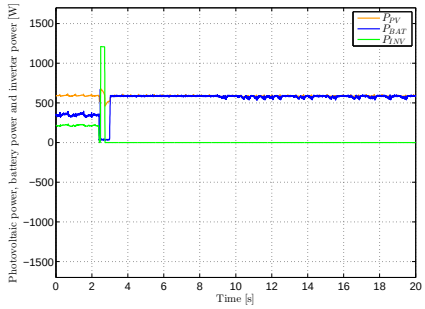

(f) Experimental results. SoC at 0%

Figure 4.29: Scenario 4.a. Grid-connected to grid-disconnected transition at G = 0.4 kW/m^2, full-load and different SoC. P_{PV}, P_{INV} and P_{BAT}

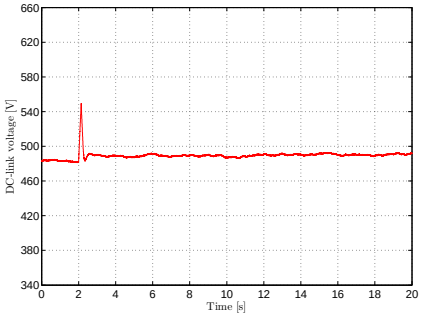

(a) Simulated results. SoC at 100%

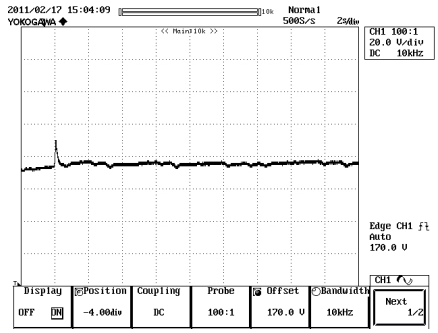

(b) Experimental results. SoC at 100%

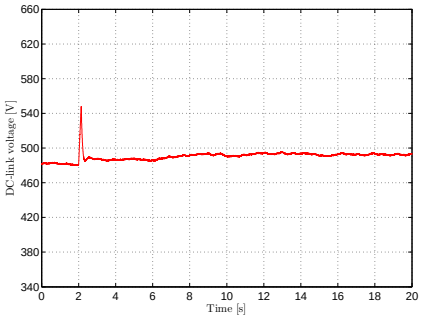

(c) Simulated results. SoC at 80%

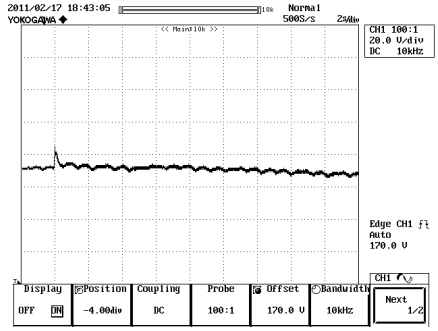

(d) Experimental results. SoC at 80%

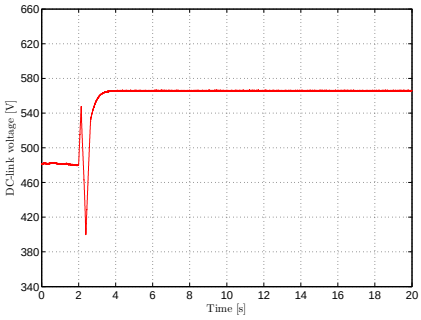

(e) Simulated results. SoC at 0%

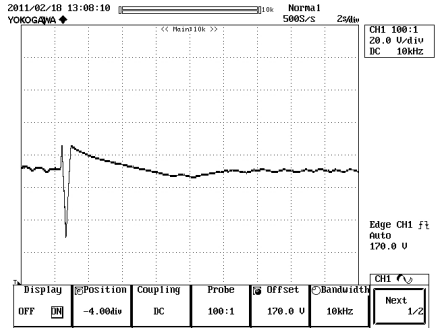

(f) Experimental results. SoC at 0%

Figure 4.30: Scenario 4.a. Grid-connected to grid-disconnected transition at G = 0.4 kW/m^2, full-load and different SoC. u_{PV} voltage

($\approx$ 7.5 ADC - 480 W). Once more, these inner losses justifies the difference between the simulation and experimental results for these last cases.

- Scenario 5. Grid-disconnected to grid-connected transition considering G = 0.4 kW/m^2. In this case, at time t = 2 s the inverter starts the reconnection procedure and the MPPT is disabled during 1 s (zero crossing transference step).
  - Scenario 5.a Full-load connected. During the time before 2 s, the MPPT is operating properly and the extra needed power for the loads is delivered by the batteries except in case of SoC at 100%. In this situation, the inverter is switched-off and the P_{PV} is used to charge the back-up system. Then, as has been mentioned, between t = 2 s and 3 s all systems are disconnected transiently to change the operation mode. After the first three seconds, the system evolves to a new state where the 60% of the available P_{PV} is used to charge the battery ($K_{BAT} = 0.6$), except when the storage system is at 100% of its SoC. The remaining power is injected to the grid, as can be seen in Figure 4.33 and 4.34.
  - Scenario 5.b. No-load connected. In this case, the only difference in respect with Scenario 5.a is before t = 2 s. The transference begins from a different start point when it has to face the transference from GCI to GSI. In case of SoC at 100%, the P_{PV} is wasted. In the other cases, if the back.up system does not limit in terms of current the available power, the MPPT can be attained. The evolution of P_{PV}, P_{INV} and P_{BAT} is shown in Figure 4.35 and the voltage u_{PV} is depicted in Figure 4.36.
- Scenario 6. Response to an irradiation, G, change from 0.2 kW/m^2 to 1.0 kW/m^2 in steps of 0.4 kW/m^2 and 40 s (increasing and decreasing) under different AC loads consumptions when the SoC is set at 80%. It should be taken into account that the considered irradiations suppose a maximum available PV power of approximately 298 W, 894 W and 1490 W. As the considered consumptions are 0 W, 587 W and 1174 W, and the exchangeable power with the back-up system is around 432 W for charging or 1536 W for discharging, this scenario presents how the extended execution of the MPPT algorithm is able to operate. In fact, this scenario permits to emulate a sudden shadowing of the PV panels. Partial shadowing is beyond the scope of this case study. The evolution of P_{PV}, P_{INV} and P_{BAT} is shown in Figure 4.37 and the voltage u_{PV} is

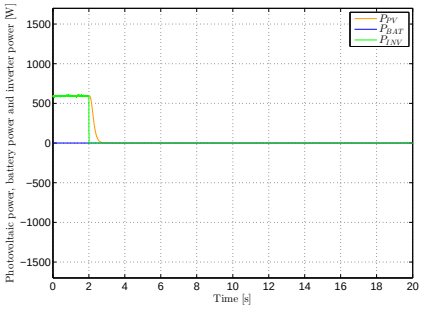

(a) Simulated results. SoC at 100%

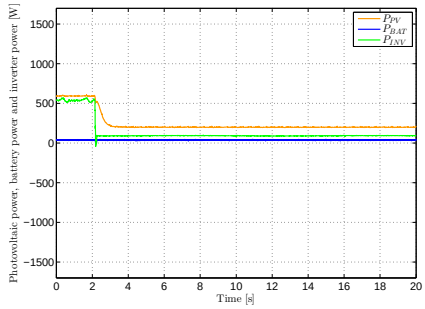

(b) Experimental results. SoC at 100%

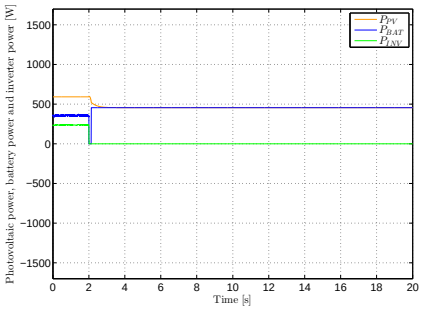

(c) Simulated results. SoC at 80%

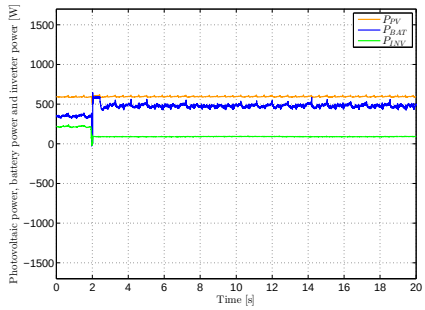

(d) Experimental results. SoC at 80%

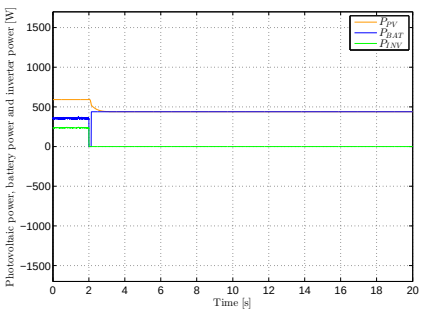

(e) Simulated results. SoC at 0%

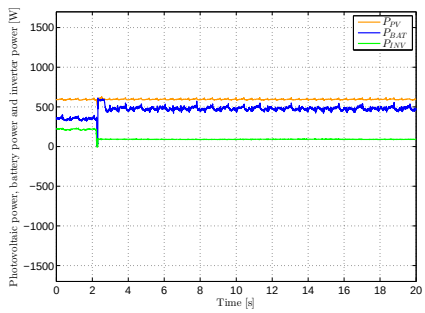

(f) Experimental results. SoC at 0%

Figure 4.31: Scenario 4.b. Grid-connected to grid-disconnected transition at G = 0.4 kW/m^2, no-load and different SoC. P_{PV}, P_{INV} and P_{BAT}

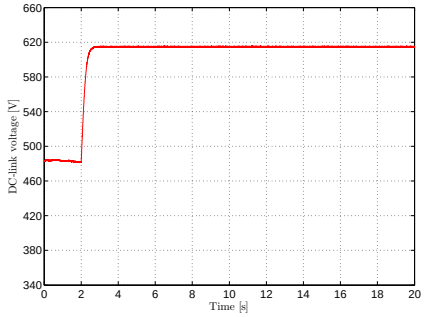

(a) Simulated results. SoC at 100%

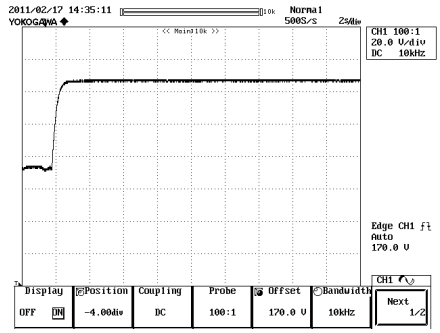

(b) Experimental results. SoC at 100%

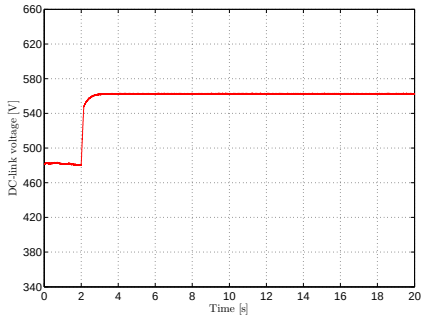

(c) Simulated results. SoC at 80%

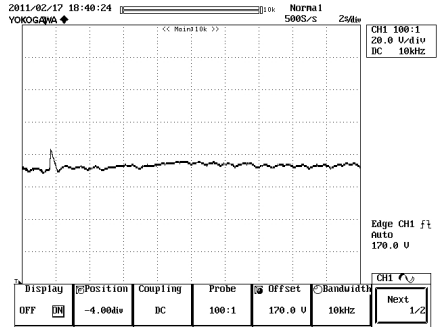

(d) Experimental results. SoC at 80%

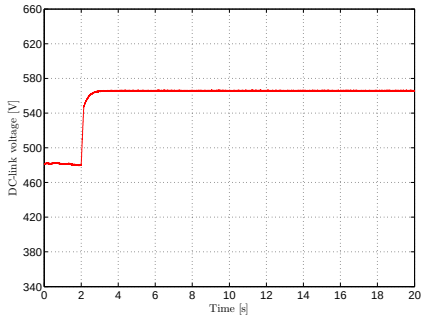

(e) Simulated results. SoC at 0%

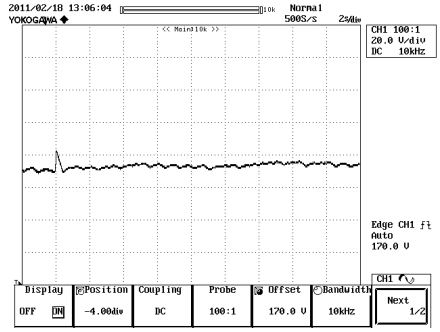

(f) Experimental results. SoC at 0%

Figure 4.32: Scenario 4.b. Grid-connected to grid-disconnected transition at G = 0.4 kW/m^2, no-load and different SoC. u_{PV} voltage

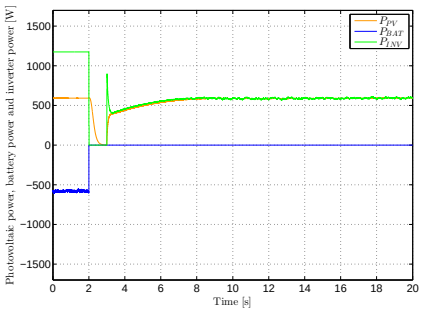

(a) Simulated results. SoC at 100%

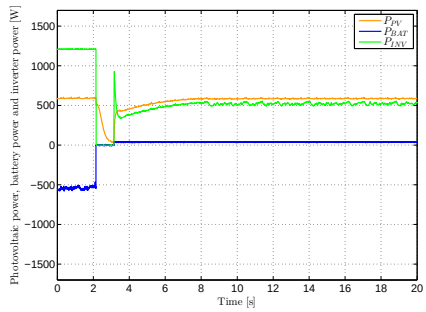

(b) Experimental results. SoC at 100%

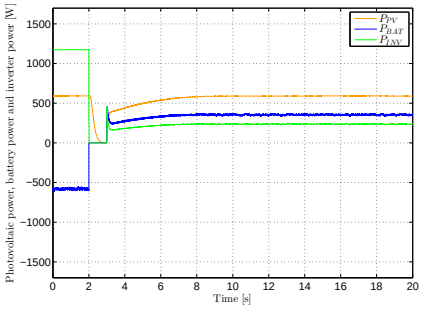

(c) Simulated results. SoC at 80%

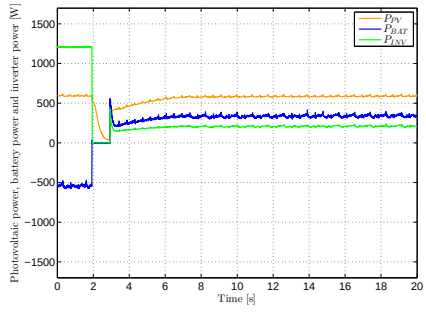

(d) Experimental results. SoC at 80%

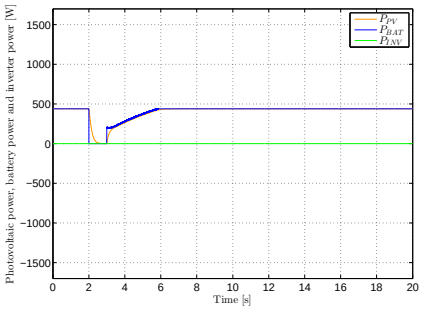

(e) Simulated results. SoC at 0%

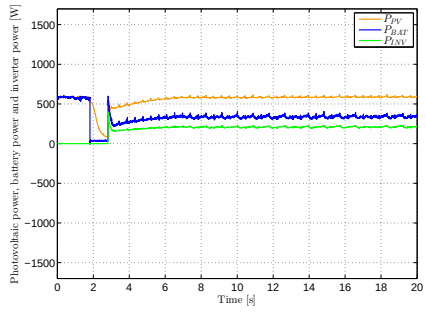

(f) Experimental results. SoC at 0%

Figure 4.33: Scenario 5.a. Grid-disconnected to grid-connected at G = 0.4 kW/m^2, full-load and different SoC. P_{PV}, P_{INV} and P_{BAT}

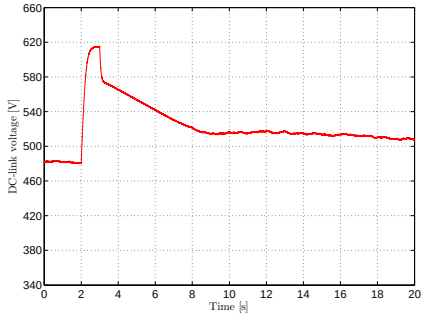

(a) Simulated results. SoC at 100%

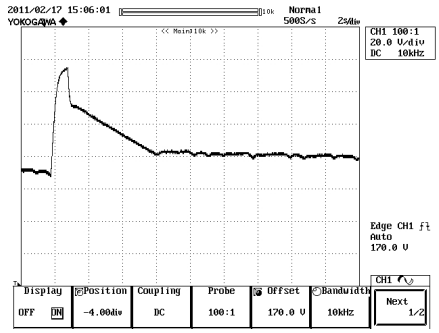

(b) Experimental results. SoC at 100%

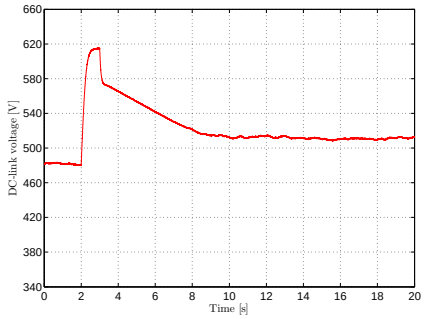

(c) Simulated results. SoC at 80%

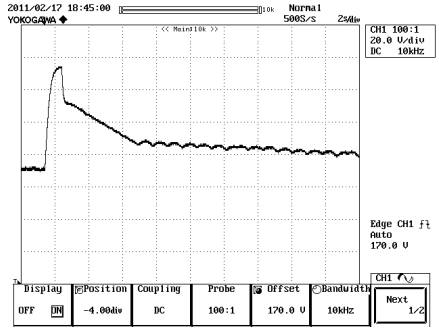

(d) Experimental results. SoC at 80%

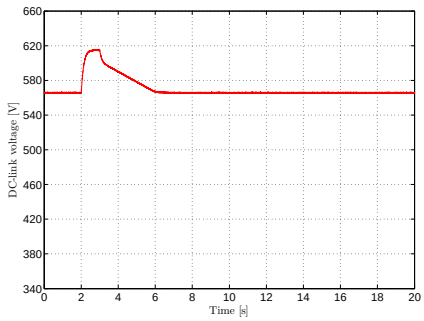

(e) Simulated results. SoC at 0%

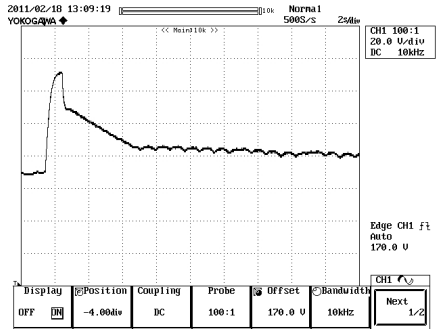

(f) Experimental results. SoC at 0%

Figure 4.34: Scenario 5.a. Grid-disconnected to grid-connected transition at G = 0.4 kW/m^2, full-load and different SoC. u_{PV} voltage

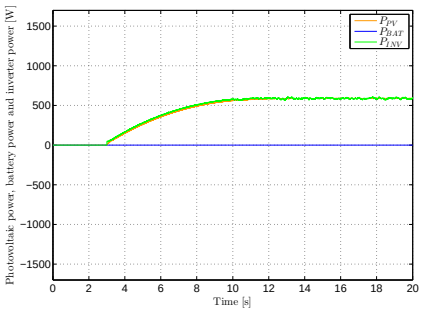

(a) Simulated results. SoC at 100%

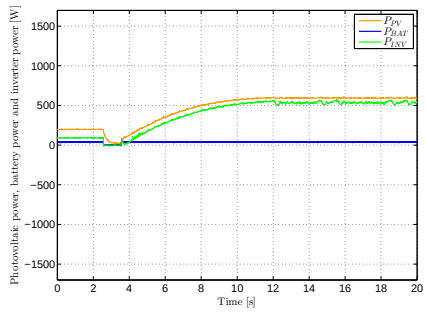

(b) Experimental results. SoC at 100%

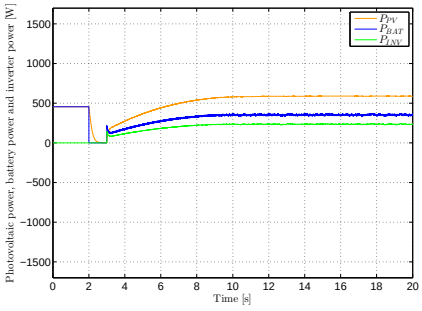

(c) Simulated results. SoC at 80%

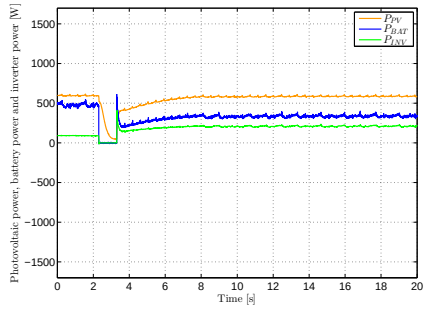

(d) Experimental results. SoC at 80%

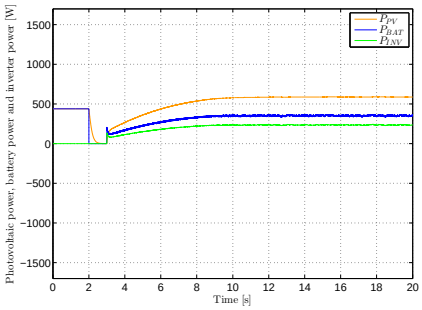

(e) Simulated results. SoC at 0%

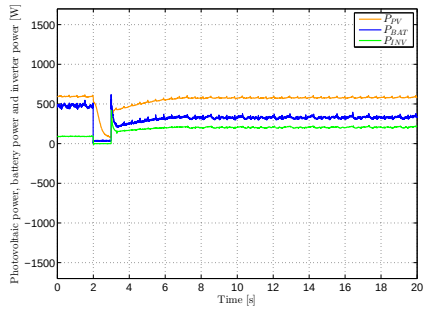

(f) Experimental results. SoC at 0%

Figure 4.35: Scenario 5.b. Grid-disconnected to grid-connected at G = 0.4 kW/m^2, no-load and different SoC. P_{PV}, P_{INV} and P_{BAT}

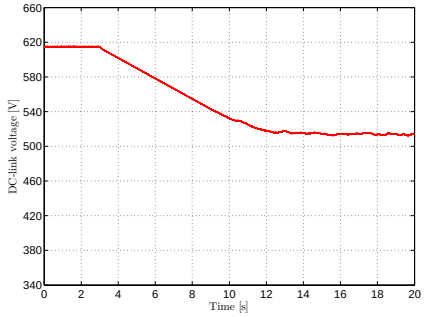

(a) Simulated results. SoC at 100%

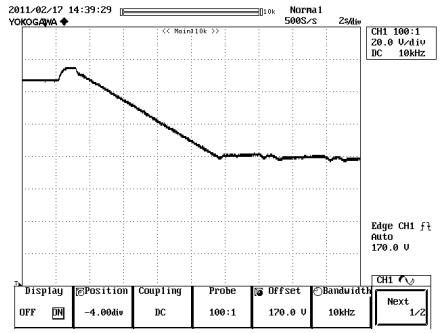

(b) Experimental results. SoC at 100%

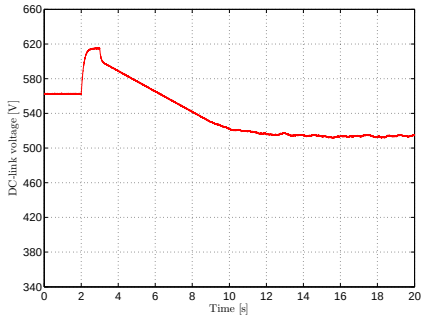

(c) Simulated results. SoC at 80%

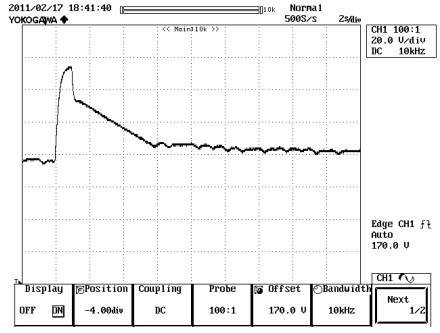

(d) Experimental results. SoC at 80%

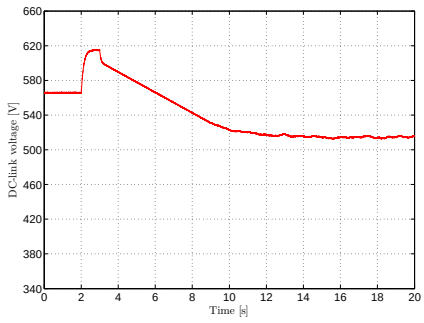

(e) Simulated results. SoC at 0%

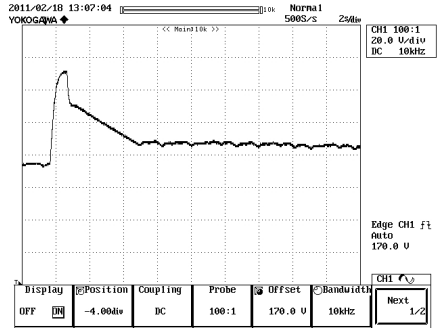

(f) Experimental results. SoC at 0%

Figure 4.36: Scenario 5.b. Grid-disconnected to grid-connected transition at G = 0.4 kW/m^2, no-load and different SoC. u_{PV} voltage

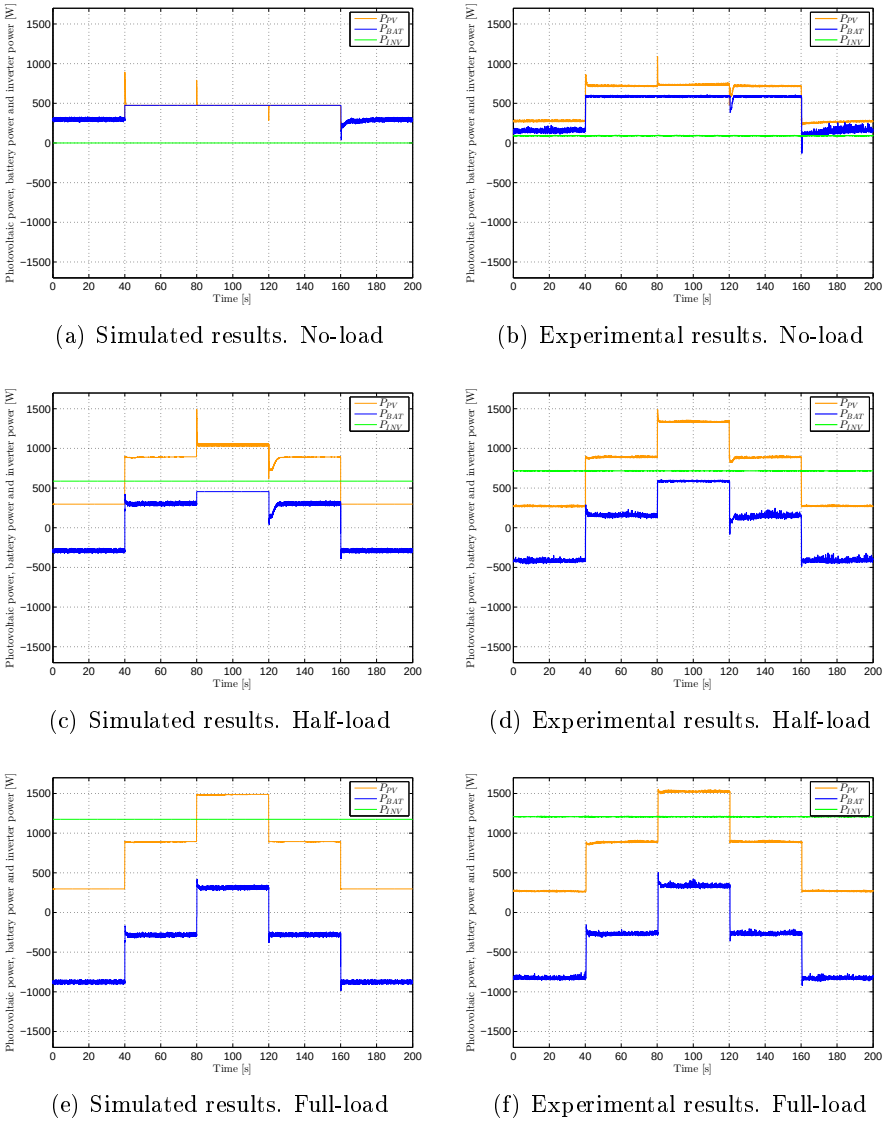

(a) Simulated results. No-load

(b) Experimental results. No-load

(c) Simulated results. Half-load

(d) Experimental results. Half-load

(e) Simulated results. Full-load

(f) Experimental results. Full-load

Figure 4.37: Scenario 6. Response to an irradiation change from 0.2 kW/m^2 to 1.0 kW/m^2 in steps of 0.4 kW/m^2 and 40 s (increasing and decreasing) under different AC loads consumptions when the SoC is set at 80%. P_{PV}, P_{INV} and P_{BAT}

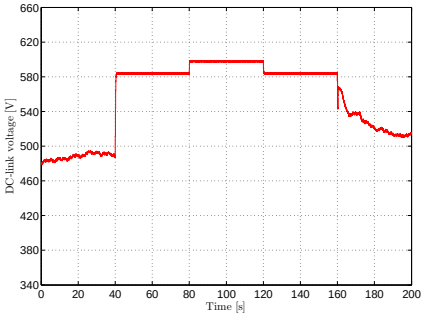

(a) Simulated results. No-load

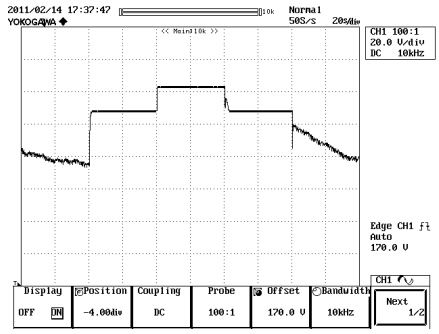

(b) Experimental results. No-load

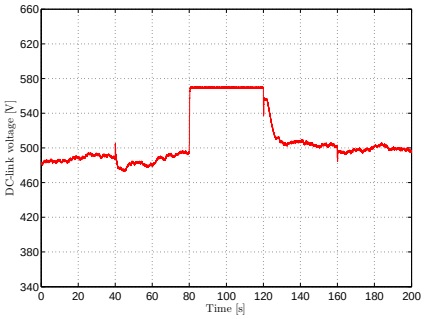

(c) Simulated results. Half-load

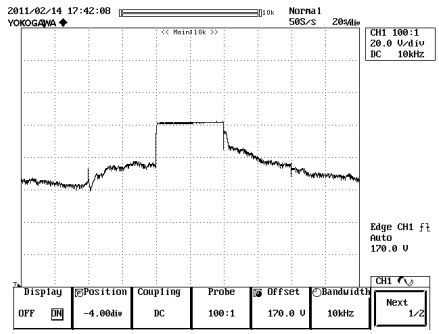

(d) Experimental results. Half-load

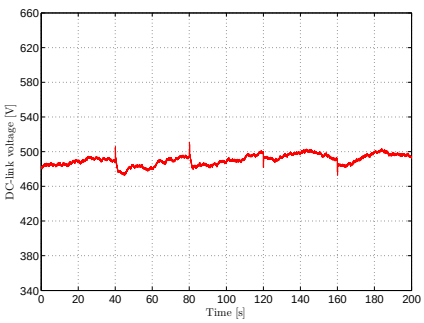

(e) Simulated results. Full-load

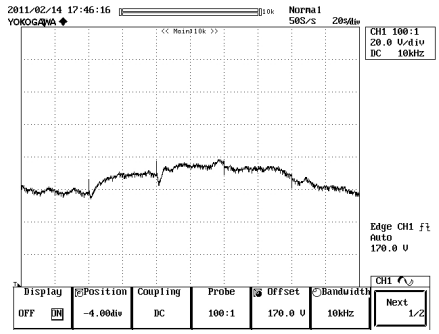

(f) Experimental results. Full-load

Figure 4.38: Scenario 6. Response to an irradiation change from 0.2 kW/m^2 to 1.0 kW/m^2 in steps of 0.4 kW/m^2 and 40 s (increasing and decreasing) under different AC loads consumptions when the SoC is set at 80%. u_{PV} voltage

depicted in Figure 4.38. In all cases, a difference between simulations and experimental results appears due to the operative consumption of the inverter.

For the no-load case, Figures 4.37(a)-4.37(b) and 4.38(a)-4.38(b), the only time interval where the MPP can be tracked is before the time is 40 s and after 160 s. During those time intervals all the available PV power is used for charging the back-up system. In all the other cases, the system is over-powered, implying that the MPPT should be disabled during long time intervals. However, as can be seen after time is 160 s, the MPPT is again operative.

In case of half-load a more favoured situation is analysed. Now, an AC consumption permits to extend the MPPT operation before time is 80 s and after time is 120 s. In those time intervals, the P_{PV} is about 300 W or 900 W, and the maximum aggregated consumption amounts to 1019 W. Thus, the loads are supplied and the back-up system is discharged when G is 0.2 kW/m^2. However, under G equal to 0.6 kW/m^2 there is enough P_{PV} to supply the AC loads and the surplus is used to charge the batteries under MPP operation. As in G equal to 1.0 kW/m^2 the P_{PV} surplus exceeds the maximum aggregated consumption, the MPPT is disabled transiently.

Finally, for the full load-case, the maximum aggregated consumption amounts to 1609 W. As the back-up system assumed considers a SoC at 80%, the system can operate always with the MPP. When G is not enough to supply the AC loads, the back-up system is used for this commitment (cases before time is 80 s and after time is 120 s).

4.4 Summary

Due to the high penetration of renewable in the energy mix during last decades, especially concerning photovoltaic and wind-turbines systems, the implantation of Grid Supply Inverters (GSI) is a common used alternative. GSI suppose important challenges when they have to be operated within an AC microgrid, acting as voltage sources in the grid disconnected mode. This chapter has presented two different strategies to enhance the behaviour of conventional PV-GSI under grid-connected operation when it is considered that it can be also operated as PV-GCI under the grid-disconnected mode.

In the first case, the converter is operated as GSI when grid-connected and a non zero voltage crossing transfer is provided when the inverter is

grid-disconnected operated. The difference in the control strategy between the operation modes adds complexity to the control algorithm and to the detection of the mains loss. A fast fault grid detection method is presented to overcome the transients based on combination of an active anti-islanding method and a monitoring voltage system consisting of voltage envelopes. Another challenge of this method is the proper initialization of the AC voltage controller, concluding that is better to reset the controller than use a bumpless strategy. The reset option produces an oscillation in the voltage during the transient between operation modes but is better than bumpless alternative in terms of transient rms values. A knowledge of the opening and closing times of the main switch helps to obtain seamless and smooth transferences in both senses.

In the second case, a control strategy to extend the use of the MPPT algorithm for PV inverters has been proposed. This PV inverter can be operated in grid-connected mode as GSI and in grid-disconnected mode as GCI. The proposed algorithm prioritizes the charging of the batteries from the PV system. It allows to operate the PV inverter at the MPP during the maximum time possible when it is supported by a back-up system based on batteries. Six different scenarios with sub-cases have been selected to illustrate the proper operation of the autonomous enable/disable of the MPPT operation in grid-disconnected mode. These case studies consider suddenly changes in the AC consumptions or in the received irradiation (emulating sudden shadowing). Also, the effect of the transference between grid-connected and grid-disconnected has been studied.

Both algorithms have been validated on an experimental set-up contrasting that the expected simulated behaviours matches properly with the real obtained data.

Chapter 5

Four-wire three-phase AC inverter proposal for AC microgrids

5.1 Introduction

Nowadays, most inverters operate as Current Controlled-Voltage Source Inverters (CC-VSI) behaving as Grid Support Inverters (GSI) when are grid connected, as has been presented in Chapter 2 and 4. During the first years of Distributed Energy Resource (DER) integration, most countries avoid the creation of unintentional electrical islands by the use of different regulations, as the VDE 4105, IEEE 1547 or IEC 61727 [16–18] to prevent risk situations. However, electrical grids are expected to be smarter in the next times when the grid is lost. In this sense, microgrids play an important role to overcome a forced stop when the grid must be disconnected because of maintenance or malfunction. Microgrids are a consequence of the DER. In this sense, the electrical energy distribution scenario has to change and big generators, utilities and regulators must change to a new and smart energy scenario. This new scenario is full of interconnected small microgrids (no more than hundreds of kW) to create the Smart Grid. In this new paradigm, power electronics and communications are playing a major role and are the key technologies to make this change possible. Furthermore, conventional GSI used by different DER, as in the photovoltaic case, needs to evolve.

This chapter details the design, simulation and implementation of a three-phase four-wire AC inverter for microgrids which can be interfaced with a DC microgrid, battery or supercapacitor bank with a wide voltage swing. The converter proposed in this chapter has been designed and installed on the experimental microgrid ATENEA at CENER, Sangüesa, Spain (introduced in Chapter 1).

This chapter is divided into:

- Section 5.2. *General system specifications.* This section defines the operation modes and electrical considerations for the proposed microgrid

inverter.

- Section 5.3. *Microgrid VSI proposal.* This section defines the main components of the two power stages considered; a DC/DC converter and a DC/AC inverter. The motivation of the structures selected are also introduced.

- Section 5.4. *The three-phase four-wire inverter coupling filter design.* In this section, the size of a coupling LCL-type filter is developed based on a new Space Vector Pulse Width Modulation (SVPWM) technique for three-phase four-wire inverters to optimize the required program memory digital implementation. Firstly, a brief review on the SVPWM techniques is conducted. Then, the new SVPWM proposal is proposed and used to define a methodoloy to size the cited coupling filter.

- Section 5.5. *Three-phase four-wire DC/AC inverter control.* The proposed VSI is based on a hybrid combination of dynamic droop control when it is grid-connected and a voltage-frequency control when it is grid-disconnected operated. In this sense, the operation of the inverter is maintained as a VC-VSI (Voltage Controlled Voltage Source Inverter) in both operation modes. Some special control requirements are considered as over-load capability when grid-connected or sinusoidal short-circuit proof when grid-disconnected.

- Section 5.6. *The three-leg interleaved DC/DC converter coupling filter design.* A LC-type filter is designed according to the modulation technique for DC/DC converter detailed in Section 5.3.

- Section 5.7. *The three-leg interleaved DC/DC converter control.* This section presents the tuning procedure of the DC current and the DC-link voltage control. An analysis on the the DC-link is conducted to validate that the voltage ripples are acceptable for a four-wire inverter operation. A control scheme to avoid over-modulation at the DC/AC inverter is proposed.

- Section 5.8. *Simulation and experimental results.* This section presents several scenarios considered for the operation validation. These scenarios consider power control, disturbance response, energy quality, DC-link behaviour, transients between grid-(dis)connected and short-circuit capability.

5.2 General system specifications

5.2.1 The AC side

The converter must act as a bidirectional interface between a DC side, where a energy storage device will be connected and the AC side constituted by a three-phase four-wire microgrid. The energy storage device could be a battery, a supercapacitor bank or a DC microgrid.

Different operation modes, configurations and control challenges need to be considered to make compatible a real microgrid, in this particular case ATENEA's microgrid.

Configurations and operation modes

The AC microgrid scope is as follows:

- Grid-tied (Configuration 1)
    - o Grid-connected (Operation mode 1)
    - o Grid-disconnected (Operation mode 2)
- Grid-isolated (Configuration 2)

The converter must be able to operate focused on two different strategies:

- P/Q control (Grid-tied $\rightarrow$ Grid-connected). The power is referenced independently per phase, active and reactive, positive or negative. This means a four-quadrant P/Q operation of the three-phase system.
- V/f control (Grid-tied $\rightarrow$ Grid-disconnected or Grid-isolated). The converter is the responsible device to manage the microgrid's voltage and frequency, providing this voltage to other converters or any kind of load (non-linear or unbalanced).

One of the most important challenges to overcome is the consideration that the converter has to manage proper transitions between the operating modes when grid-tied configured. In the case study, in grid-disconnected operation there is only one voltage and frequency master in the whole AC microgrid. To accomplish with this restriction AC droop control is used for grid-connected operation mode and V/f control is used for grid-disconnected operation behaviour. As droop and V/f control treats the converter as a voltage source there is not a control change on the operation mode. In this sense, a different approach from the one presented in Chapter 4-Section 4.2

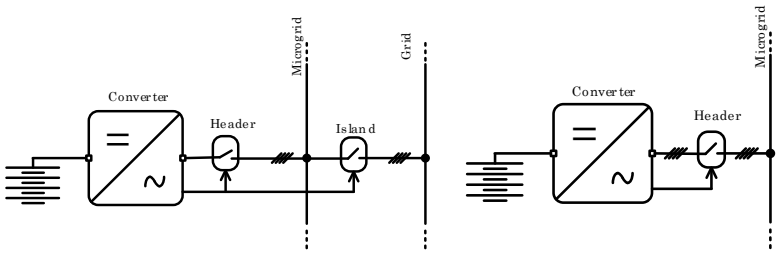

(a) Dual configuration switches (b) Only-connected switch

Figure 5.1: Main AC handling switches

is now considered. A combination of GCI (when grid-disconnected) and GCSI (when grid-connected) is proposed. In this way, in grid-disconnected operation the dynamics is not compromised by droop constrains.

On the other hand, to interoperate properly with other converters of the microgrid and set all the possibilities, the converter is composed by two possible operation options:

- Only-connected. In this operation option, the converter only obeys active/reactive power references. The utility or another microgrid's converter is the responsible for fixing the voltage and the frequency.

- Dual. The dual operation option is more complex than only-connected. The converter must manage connection-disconnection procedures. Thus, the converter obeys active/reactive power references when grid-connected but fixes the voltage and the frequency when it is in the isolated configuration or operation in grid-disconnected mode.

In the dual converter operation option, the converter is able to control a microgrid main switch, called island switch, and also its own header switch, see Figure 5.1(a), while in the only-connected mode, the converter only controls the header switch, see Figure 5.1(b).

Electrical considerations

The converter is sized for 135 kVA but the rated considered power is 90 kVA. The electrical specifications for the AC side are 400 VAC phase-to-phase ($\pm$ 10%) and 50 Hz ($\pm$ 10 Hz) considering a four-wire distribution. This four-wire feature concerns to face unbalances and asymmetries. Each phase

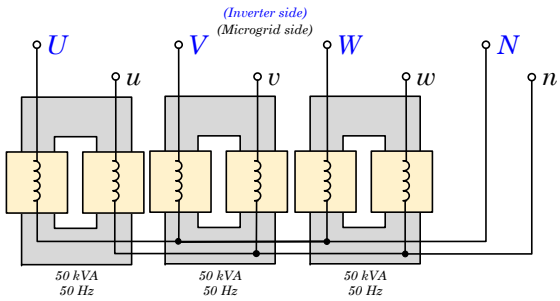

Figure 5.2: Galvanic isolation proposed

can be controlled individually, in terms of power when grid-connected and in terms of voltage in grid-disconnected operation.

The wide range in voltage and frequency allows to implement different control strategies that have to be adaptive around an operation point, as can be AC droop control.

As explained in Chapter 2, there are different regulations that detail some mandatory consideration for grid-tied energy producers. In this sense, it has been considered that the converter should include galvanic isolation between the AC microgrid and the converter. According to Chapter 2, and for the power involved in this proposal, the use of the standard single-phase transformer constituting a triplex unit results a good option to operate a microgrid inverter. In Figure 5.2 can be seen the proposed YNyn triplex connection.

The converter must be short-circuit proof. This means that it has to be able to maintain at its output a sinusoidal maximum predetermined current during a configurable time in short-circuit. This feature applies only to grid-disconnected mode. The sinusoidal waveform behaviour permits that the protections reacts as in conventional grids.

As a final requisite, the converter has to handle severe overloads of 20% to 50% during some tenths of seconds. This overload capability has been considered with the aim of emulating the behaviour of a rotatory machine, in terms of power, during big load (dis)connection transients. This fact implies that if a power converter needs to support certain over-currents during tenths of seconds requires to size the semiconductors to support the maximum current during the over-load operation but also all the heat-dissipation system (as heat-sinks, fans or filters). This makes bigger the power modules but represents a first approach between conventional distribution generators and future smart-grids. The heat-dissipation system design is not included

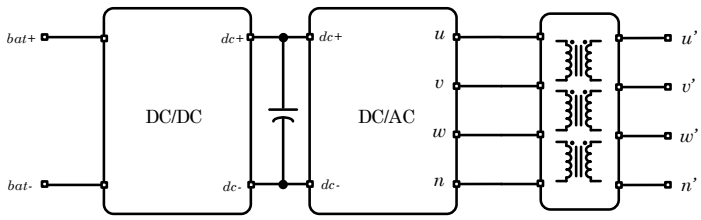

Figure 5.3: Simplified scheme of the microgrid inverter proposal

in the present thesis.

5.2.2 The DC side

Electrical considerations

For the DC side, the input voltage range is 150 VDC to 500 VDC. The maximum rated DC current is fixed to be 250 A, but with an overload capability to increase up to 360 A during tenths of seconds.

5.3 Microgrid VSI proposal

5.3.1 General scheme proposal

As the microgrid VSI has to face with wide DC voltage ranges and needs to manage AC different voltage and frequency values, a structure constituted by two stages with low frequency galvanic isolation is proposed, as can be observed in Figure 5.3. It should be remarked that with the aim of obtaining an useful and flexible microgrid VSI, all the power stacks used will be identical. In this sense, the minimal considered unit is a three-phase full-bridge IGBT stack.

Firstly, a four-wire three-phase DC/AC bidirectional VSI is dedicated to the AC interface using two three-phase full-bridge IGBT stacks, one stack is used for the active phases u, v and w. Another one is operated in parallel and responds to the neutral wire commitment. Secondly, an interleaved DC/DC converter is considered for the DC side interface using one more three-phase full-bridge IGBT stack.

The complete proposed scheme of the microgrid inverter is shown in Figure 5.4.

The converter is based on a four-phase VSI plus an LCL-type output filter with a DC side interface implemented thanks to a three-leg interleaved

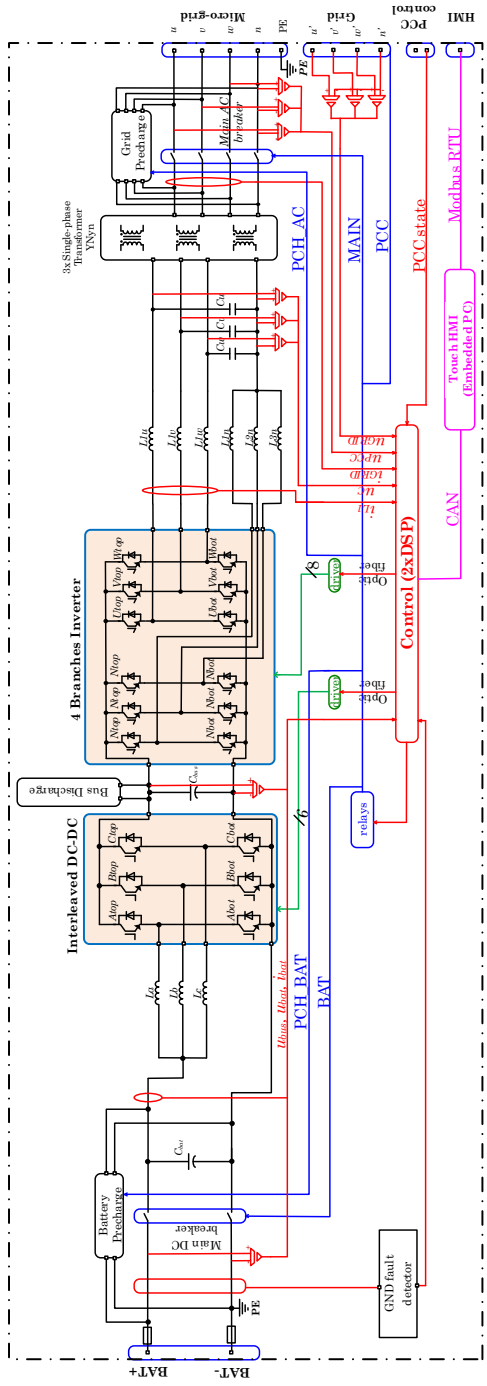

Figure 5.4: Scheme of the full DC/DC and DC/AC proposed converter

converter. The inverter is controlled by means of an internal current controller. To operate as a VC-VSI, the voltage at the LCL filter capacitor is controlled in cascade with a more external loop based on AC droop with a dynamic virtual resistor strategy to provide hot-swapping capability in the grid-connected mode. An active damping algorithm to reduce inherent resonance excitations of the LCL-type filter is also considered.

Due to the inherent slow behaviour of the AC droop control it has been decided to change the control strategy to a voltage-frequency (V/f) control in the grid-disconnected mode. Obviously, this strategy is conditioned by ensuring that there is only one GCI in the microgrid islanded system or a Constant Voltage Constant Frequency (CVCF) synchronized mechanism. The following sub-sections details the design of the different components integrated in the proposed microgrid VSI.

Note that, as has been detailed in Section 2.5, the neutral inductances can be neglected. However, it has been considered useful to include them to avoid excessive current ripples under predominant homopolar current components. Also, it should be clarified that a GND fault detector has been included to detect leakage currents in case of a fault between the DC terminals (BAT+ and BAT-) and the transformer secondary terminals (microgrid side). A header differential switch will allow to detect any leakage current between the transformer primary terminals and the location of such protective device.

5.3.2 The four-wire three-phase DC/AC motivation

The transportation lines provide their services in a three-wire topology. The distribution lines provide their services in a four-wire topology to supply electricity to three-phase and single-phase consumptions. As a microgrid is close to the end-users, it can be treated as a distribution line. For this reason, the inverter of the microgrid has to distribute a three-phase four-wire system. As detailed in Chapter 2, this option can be achieved by power converters with three controlled legs using the mid-point of the DC-link as the neutral wire or controlling also the neutral wire adding a fourth controlled leg.

Four-wire three-leg split capacitor topologies imply:

- Less switching elements for the main converter and less extra circuitry.
- DC-link active balancing. Depending on the operation of the inverter it is possible to consume or deliver more power from one of the two semi-buses that constitutes the DC-link. Although the total DC-link is controlled, if no action is applied to set the voltage difference of the semi-buses to zero it is possible to collapse one semi-bus or produce

an over-voltage situation on the other one. When grid-connected, this effect is solved injecting some DC current to the AC side. This is not possible when the VSI is grid-disconnected operated.

- It is possible to modulate any voltage and control any current sequence but the neutral point is determined according to where it is externally referenced.
- No SVPWM can be applied taking more profit of the DC-link voltage to synthesize higher AC voltages.
- High frequency voltages produced by the switching behaviour of the inverter affects to the mid-point of the DC-link but not to the DC wires because the two semi DC-link act as a considerable low-pass filter. This means that a storage system can be connected directly to the DC-link without considering premature ageing due to high frequency components. In this direction, the DC wires will present a low-frequency oscillation that mainly is consequence of the active balancing of the DC-link, the control of the total DC-link and the AC connected load type.

The required hardware of the two four-wire alternatives results similar because the three-leg split capacitor topology could require a fourth leg for balancing purposes. Furthermore, the four-leg topology permits the application of SVPWM techniques improving the use of the DC-link voltage. In this thesis, the chosen option is the four-leg inverter. Figure 5.4 shows the DC/AC three-phase four-wire scheme proposed with an output LC coupling filter.

When using a four-leg inverter it should be considered that, in grid-connected operation, the isolation has to be included by the inverter to make compatible a possible distribution transformer. If not, the neutral high frequency oscillation is connected to the ground wire of the transformer producing undesired effects. Both situations are depicted in Figure 5.5.

5.3.3 The three-leg interleaved DC/DC motivation

A microgrid is constituted, usually, for a DC side where different DER are integrated. It is necessary to consider that it can operate with large voltage swings that usually do not match with the adequate inverter operation voltage level. Due to this voltage swing, a DC/DC converter to step-up the voltage of the DC microgrid side is considered. The proposed converter is formed by a three-phase full-bridge stage operating as the interface between

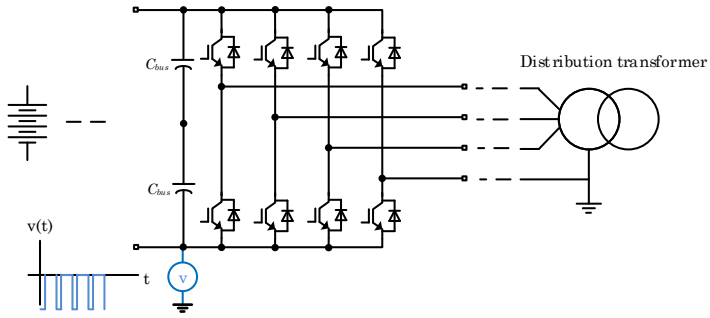

(a) Directly connected

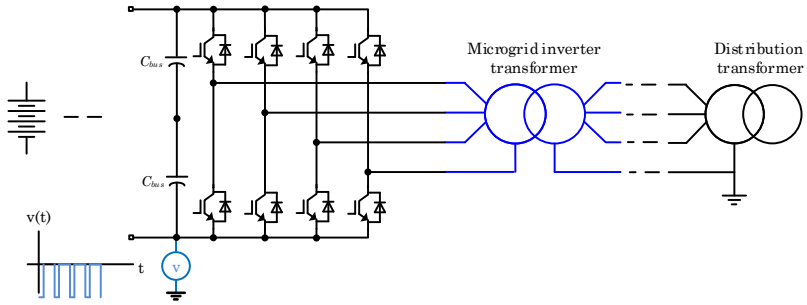

(b) Connected by an ancillary transformer

Figure 5.5: Neutral interconnection of a four-wire inverter with the utility transformer when a SVPWM technique is used

the DC bus of the microgrid and the DC-link of the inverter stage. The three output inductances are connected each other at the input side of the converter, as depicted in Figure 5.4. It is also common the use of a DC capacitor at the DC microgrid to obtain high filter attenuation ratios. In this case, the voltage control capability of this capacitor is beyond the scope of this work. However, for storage systems where a constant voltage charge is required it has to be considered, as indicated in [217, 218].

By the use of an interleaved topology, the output inductive filter volume is split, making easier the maintenance tasks and wiring. At the same time, high power converters can be designed with lower current modules. The utilization of a commonly used power electronics structure could permit to achieve a lower production cost. As three legs are available according with the selected stack structure a three-phase interleaving or a parallel commutation can be applied. The parallel operation implies the reduction of the controlled current per leg. However, no benefits on the current ripple are achieved. On the other hand, an interleaved commutation, where the switching signals are 2π/N rad phase shifted (being N the number of interleaved legs), can be applied in order to obtain lower ripples in the DC microgrid, reduce the voltage and current ripples in the DC link and decrease the power capacity of the inductors [219]. Furthermore, as explained in [220, 221], the ripple is a non-linear function of the duty cycle. The maximum ripple depends on the number of interleaved legs used. In [222] is deduced that the absolute peak-to-peak ripple can be expressed by

$$\Delta i(\alpha) = \frac{u_{bus}}{L f_s}\left[1 - \frac{m}{N\alpha}\right][1 + m - N\alpha] \tag{5.1}$$

being $m = floor(N\alpha)$. In Figure 5.6 is shown the normalized ripple

$$\kappa = \Delta i \frac{L f_s}{u_{bus}} \tag{5.2}$$

evolution as a function of the duty cycle for the one, two and three-leg interleaved case.

It can be observed that from one to two interleaved legs the ripple is divided by a factor 2, implying 50% of enhancement. Adding a third leg, the improvement over two interleaved legs is 16%. In case of a fourth leg less than 10% is achieved in respect with the three-leg alternative. As can be deduced, the improvement of Δi when N is considered over the case when N-1 is used follows the hyperbolic normalized behaviour as

$$\frac{\Delta i(N)}{\Delta i(N-1)} = \frac{1}{N(N-1)} \tag{5.3}$$

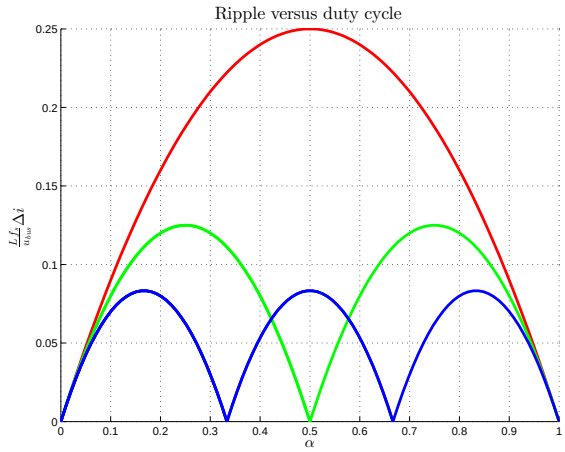

Figure 5.6: DC/DC interleaved normalized ripple as a function of the duty cycle α. One-leg (red), two-legs (green) and three-legs (blue).

being N≥1. For this reason, three interleaved legs results a good trade-off between number of switching elements and maximum ripple. It should be noticed that each leg presents its maximum ripple when the duty cycle α is equal to 0.5. In the three-leg case the duty cycle equal to 0.5 represents the worst case. In this situation the ripple per leg is maximum and the total current ripple is maximum, too. However, in any case, the DC microgrid is affected by a 1/N part of one leg ripple and by a N factor of the switching frequency if all inductances are exactly equal. The asymmetric case is considered for the design of the interleaving stage developed in Section 5.6. Also, as can be seen in [223], the reliability of an interleaving DC/DC converter increases in comparison with a conventional DC/DC converter (one-leg). Mainly, due to the decrease on the thermal stress as consequence of sharing of the current magnitude and ripple. Also, in terms of cost, a three-leg results a good candidate if the used power stack is identical to the other ones used for the AC/DC converter.

5.4 The three-phase four-wire inverter coupling filter design

The modulation technique results into a factor that conditions the hardware design. In this section, firstly, a review on classical space vector modulation techniques is done for three and four-wire inverters. Then, a novel simplified

3D-SVPWM modulation is presented as an extension of the 2D-SVPWM but applied to four-leg three-phase VSI. Once this new modulation strategy is presented, the hardware design of the LCL-type filter at the AC side is developed. The methodology for the LCL coupling filter design proposed is as follows:

1. The output inductance L_{1_x} is sized according to a desired maximum ripple at the output of the inverter and depending on the applied modulation technique. The subscript x refers to one of the four legs u, v, w or n.

2. The grid side inductance L_{2_x} and the capacitor C is sized to produce a high attenuation at high frequency. Also, the AC capacitor should have to accomplish with a maximum reactive power consumption. This last situation can be compensated by the injection of some amount of reactive power by the inverter implying an efficiency drop.

   It is also common to assume that the grid side inductance is constituted by the leakage inductance of the transformer when galvanic isolation is considered.

5.4.1 SVPWM for three-phase VSI review

The most extended modulation technique for power converters is the Pulse Width Modulation (PWM) strategy. The control of three-phase inverter switches under Space Vector-PWM (SVPWM) has been proved to be more optimal than other modulation possibilities [224–226]. Among its main advantages can be included some as low output voltage harmonic distortion, more available output AC voltage, good utilization of the available DC-link, low switching losses or simple digital implementation in three-wire inverters.

The SVPWM technique is based, mainly, on the abstraction of considering the converter as a state machine. Each state is defined according to the conduction or blockage situation of each inverter's switch.

The space vector **s** concept can be described as an instantaneous vector that represents each voltage in the canonic orthonormal *abc* reference $C = \{[1\,0\,0],[0\,1\,0],[0\,0\,1]\}$ at any instant. In this sense $u_a(t)$ is linked with $\vec{u}_1 = [1\,0\,0]$, $u_b(t)$ with $\vec{u}_2 = [0\,1\,0]$ and $u_c(t)$ with $\vec{u}_3 = [0\,0\,1]$. However, other references as Clarke's or Park's basis can be applied.

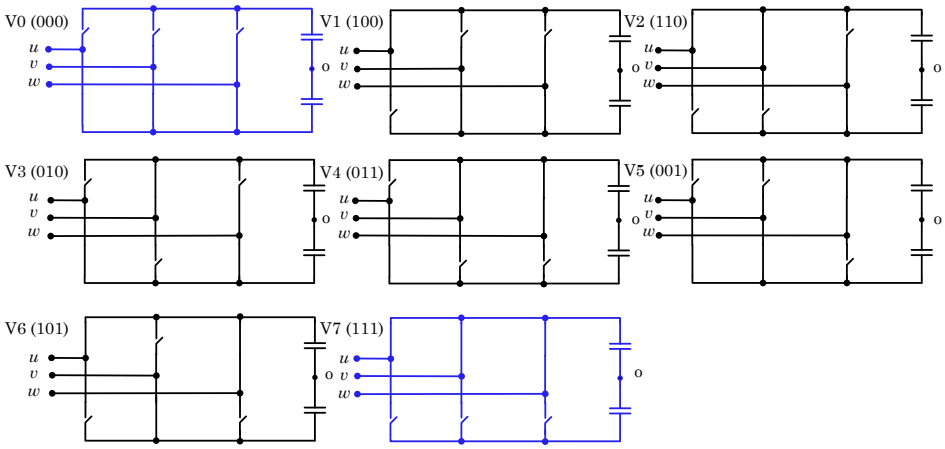

Figure 5.7: Symbolic representation of the possible states of the converter when SVPWM is applied (three-leg topology)

Three-wire three-leg inverters

In case of three-wire three-phase converters, the SVPWM technique is widely used due to its higher efficiency in terms of profit of the DC-link.

As has been mentioned, the SVPWM technique is based, mainly, on the abstraction of considering the converter as a state machine where the desired output voltage is obtained from the superposition of the different switching vectors [227]. One prohibited state results from both switches of the same leg closed simultaneously. In this sense, up to eight switching states are possible. Figure 5.7 shows the eight possible switching states that constitutes the three-wire VSI. It should be remarked that V0 (000) and V1 (111) provide null voltage at the output of the inverter and are usually called null vectors or Zero Switching Vectors (ZSVs). The other six are active vectors or Non-ZSV (NZSVs) [3].

Figure 5.8 shows the eight possible states of the converter in the space and Table 5.1 presents the output voltages imposed by the inverter from the natural abc reference and $\alpha\beta\gamma$ reference. These states conform a cube which edge is equal to the voltage applied at the DC-link side, u_{bus}, hereinafter. The origin of coordinates is at the center of the cub (red star) if a splitted DC link is considered (o is the voltage reference). If the negative wire of the DC-link is used as the voltage reference, the origin of coordinates is displaced to V0.

If these switching vectors are projected over the plane π, which normal

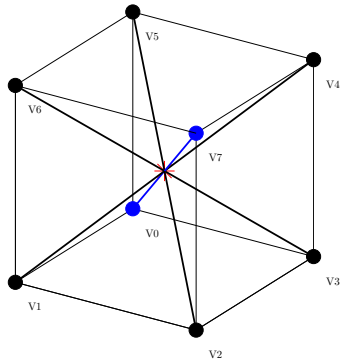

Figure 5.8: Possible states of the converter under SVPWM respect o. ZSVs in blue and NZSVs in black

Output voltages when SVPWM										
Vector	State	u_{ao}	u_{bo}	u_{co}	$u_{\alpha o}$ (module invariant)	$u_{\beta o}$	$u_{\gamma o}$	$u_{\alpha o}$ (power invariant)	$u_{\beta o}$	$u_{\gamma o}$
V0	000	-1	-1	-1	0	0	$-\sqrt{2}$	0	0	$-\sqrt{3}$
V1	100	1	-1	-1	$\frac{4}{3}$	0	$-\frac{\sqrt{2}}{3}$	$\frac{2\sqrt{6}}{3}$	0	$-\frac{\sqrt{3}}{3}$
V2	110	1	1	-1	$\frac{2}{3}$	$\frac{2}{\sqrt{3}}$	$\frac{\sqrt{2}}{3}$	$\frac{\sqrt{6}}{3}$	$\sqrt{2}$	$\frac{\sqrt{3}}{3}$
V3	010	-1	1	-1	$-\frac{2}{3}$	$\frac{2}{\sqrt{3}}$	$-\frac{\sqrt{2}}{3}$	$-\frac{\sqrt{6}}{3}$	$\sqrt{2}$	$-\frac{\sqrt{3}}{3}$
V4	011	-1	1	1	$-\frac{4}{3}$	0	$\frac{\sqrt{2}}{3}$	$-\frac{2\sqrt{6}}{3}$	0	$\frac{\sqrt{3}}{3}$
V5	001	-1	-1	1	$-\frac{2}{3}$	$-\frac{2}{\sqrt{3}}$	$-\frac{\sqrt{2}}{3}$	$-\frac{\sqrt{6}}{3}$	$-\sqrt{2}$	$-\frac{\sqrt{3}}{3}$
V6	101	1	-1	1	$\frac{2}{3}$	$-\frac{2}{\sqrt{3}}$	$\frac{\sqrt{2}}{3}$	$\frac{\sqrt{6}}{3}$	$-\sqrt{2}$	$\frac{\sqrt{3}}{3}$
V7	111	1	1	1	0	0	$\sqrt{2}$	0	0	$\sqrt{3}$

Table 5.1: Possible normalized voltages of a three-wire tree-phase converter under SVPWM from different references (base value $u_{bus}/2$)

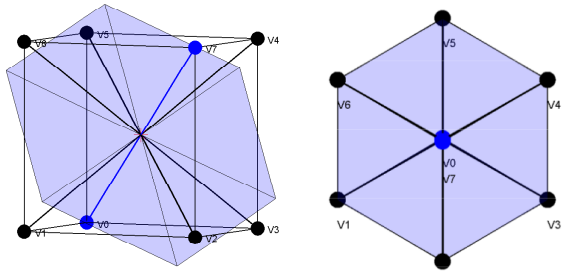

(a) Perspective 1 (b) Perspective 2

Figure 5.9: Projected hexagon over the plane π

vector is $\vec{n} = (111)$, an hexagon is obtained, as is shown in Figure 5.9. It should be noticed that ZSVs have a null projection over π. The plane π represents the space where positive and negative sequences are located.

Also, it can be seen in Figure 5.9 that all possibles states are out of the plane π. This means that when a switching vector is applied, in the *abc* coordinates, a homopolar component respect with o is generated. Assuming that o is the reference and n is another floating reference (obtained from an external triangle or star connection without neutral), u_{kn} does not dispose of homopolar components while u_{ko} presents them, being the subscript k the corresponding phase u, v or w. The fact of not be able to observe homopolar component in respect with n can also be computed analytically as a displacement of the state vectors. In this sense, one degree of freedom is lost when the voltage space is seen from n. The cube constituted by the eight states collapses to the vertices of the aforementioned hexagon applying a displacement equal to the average value of u_{ko} voltages. A component with a period three times the fundamental one can be seen in the u_{ko} voltages. In this fact resides the benefit of this modulation technique.

Figure 5.10(a) shows how the average space vector trajectory of the synthesized voltage moves. It can be observed that this trajectory takes more profit of the possible voltages that can be synthesized in respect with other modulation techniques, for example, Sinusoidal-PWM (SPWM). This is due to the value of the space vector trajectory of the synthesized voltage is more close to the vertices of the cube.

In the SPWM strategy each phase is obtained by comparing a low frequency sinewave reference (modulation signal) with a high-frequency signal (carrier signal). If over-modulation is avoided, the maximum voltage that can be synthesized is limited by the DC link to $u_{bus}/2$ (ideal peak value

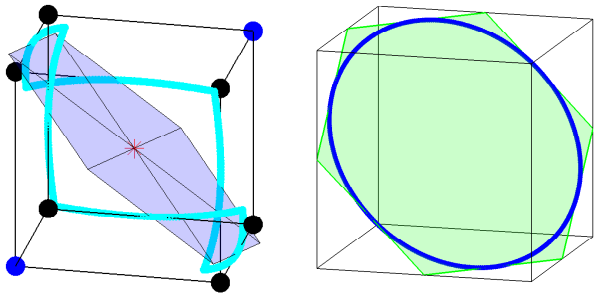

(a) SVPWM (b) SPWM

Figure 5.10: Trajectory of $\mathbf{s}$ in the *abc* reference frame for different modulation techniques

of the synthesized voltages). This limit is a new hexagon obtained by the intersection of the plane π with the cube constituted by the possible states of the inverter. If the space vector trajectory of the synthesized voltage is represented in the space it generates a circle over π. This circle is circumscribed in the green hexagon presented in Figure 5.10(b). The maximum available radius is $u_{bus}/2$. The available output voltage that SVPWM can synthesize is up to 15.47% more than when SPWM is used considering the same DC-link. SPWM can be on a par with SVPWM when a third harmonic component is added, obtaining the same modulation index [225, 228].

The conventional 2-D SVPWM technique assumes that the desired vector in $\alpha\beta\gamma$ is contained in π and it is also common to consider balance set-points (non negative or zero sequence). Thus, the reference space vector $\bar{s}^*_{abc}$, hereinafter $\mathbf{s}_{abc}$, is computed in the $\alpha\beta\gamma$ reference frame, obtaining the vector $\mathbf{s}_{\alpha\beta}$. Figure 5.11 illustrates the procedure considering as inputs $\mathbf{s}_{\alpha\beta}$ for a predetermined sequencing and class criterion.

Then, it is necessary to follow next three steps:

1. Sextant determination. Selection of the adjacent vectors $\mathbf{V}_{adj_{xy}}$ according with the location of $\mathbf{s}_{\alpha\beta}$ in one of the sextants S_i of the projected hexagon, being $i = 1 : 6$. Subscripts x and y represents the corresponding adjacent vectors of the hexagon at any time.

2. Projection. Projection of $\mathbf{s}_{\alpha\beta}$ onto the selected $\mathbf{V}_{adj_{xy}}$ in order to obtain $\text{Proj}(_{V_{adjx}}\mathbf{s}_{\alpha\beta})$ and $\text{Proj}(_{V_{adjy}}\mathbf{s}_{\alpha\beta})$. Figure 5.12 shows an example when the position of $\mathbf{s}_{\alpha\beta}$ is located at the first sextant S_1 (limited by V1 and V2). The amount of time in which the switching vectors

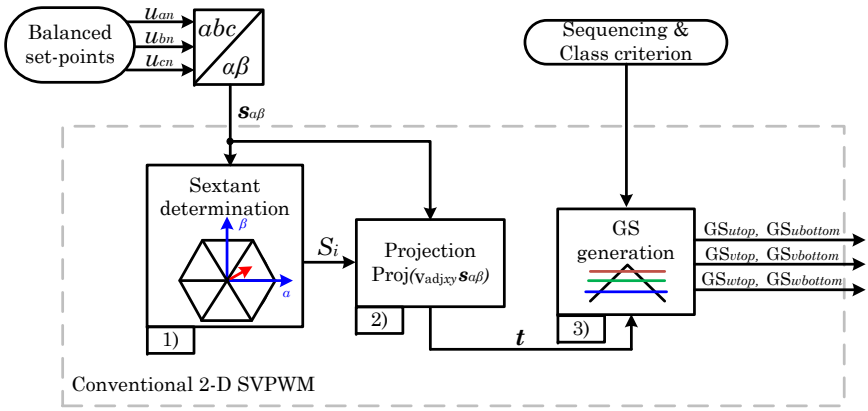

Figure 5.11: Conventional 2-D SVPWM algorithm

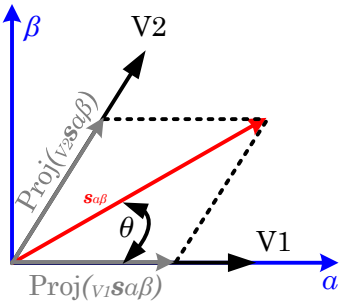

Figure 5.12: Projection example when $\mathbf{s}_{\alpha\beta}$ is located at S_1

are applied during a switching period T_s is defined by the time vector $\mathbf{t} = T_s(t_i, t_j, t_k)$, in which

$$(t_i, t_j, t_k) = \left(\frac{|\text{Proj}(V_{adj_x}\, \mathbf{s}\alpha\beta)|}{|V_{adj_x}|}, \frac{|\text{Proj}(V_{adj_y}\, \mathbf{s}\alpha\beta)|}{|V_{adj_y}|}, |1 - t_i - t_j| \right) \quad (5.4)$$

3. Gate Signal (GS) generation. One sequencing and class has to be selected for the switching vectors to obtain the gate signals. It has to be chosen how will be sequenced the switches of the transistors in order to optimize the process, mainly, according to high order harmonic reduction, minimization of switching losses or minimization of conducting losses. Depending on how the ZSVs are used the sequencing

can be classified into two categories: Class I and Class II. Class I sequencing schemes uses both ZSVs while Class II only uses one of them. Each class has four possible sequencing schemes suitable for different purposes [3, 6]:

- Rising-edge aligned. Suitable for soft switching converters.
- Falling-edge aligned. Suitable for soft switching converters.
- Symmetrically aligned. Convenient for low output current ripples.
- Alternative sequence. Adequate for optimal switching losses.

Then, the different GS to operate the converter can be obtained comparing the desired application duty ratios with a carrier signal. The selection of the type of carrier signal will determine the four possible sequences; up sawtooth (rising-edge), down sawtooth (falling-edge), triangle waveform up-down (symmetrical) or triangle waveform up-down (alternative).

Different authors have proposed optimal algorithms to determine the location of the space vector **s** and compute the switching vectors duty ratios for conventional 2-D SVPWM, as in [164, 227].

Four-wire four-leg inverters

The first possible case to consider is a four-wire three-leg with DC-link split capacitor topology. This option allows to manage zero sequence voltages but restricted to the neutral scheme where the neutral wire is connected. Also, as the mid-point of the DC-link is tied with the neutral wire it is not possible to use optimally the DC-link. The states are exactly the same than in a three-wire inverter but now it is lost the benefit of use a SVPWM from the AC side perspective, as is indicated in [229]. In [230] the SVPWM is applied to this topology to provide a controllability criteria of the converter. This analysis is conducted as a direct extension presented in [231] for three-wire active filters under SVPWM operation. Thus, due to all above cited issues, SPWM is commonly preferred for the operation of four-wire three-leg inverters.

The other case is a four-wire four-leg topology. In this last case, the inverter uses the fourth leg as an extra degree of freedom to manage zero sequence voltages. In the four-leg case, the possible output voltages of the VSI in respect with the mid-point of the DC-link constitutes a 4-D hypercube. The 4-D analysis is not practical to operate with it. To overcome this challenge it is common to use the fourth leg as the reference. In this

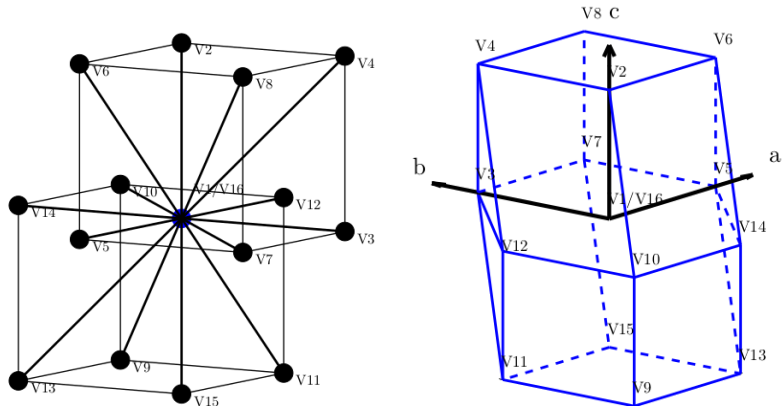

(a) Possible states under SVPWM respect n'. (b) Available space where $\mathbf{s}_{abc}$ can be ZSVs (blue) and NZSVs synthesized in a four-leg converter (black)

Figure 5.13: Four-leg SVPWM space representations

sense, the fourth leg can be understood as a short-circuit (limited by the neutral coupling filter inductance, if any) between the fourth-phase and the AC side neutral point. Then, the 4-D hypercube is projected over the normal vector $\vec{n} = (1, 1, 1, 1)$ obtaining a dodecahedron, where the sixteen possible switching vector combinations are shown in Figure 5.14. If overmodulation is avoided, the limit of the space where $\mathbf{s}$ is able to be synthesized is limited by that dodecahedron obtained when the vertices of the two partial cubes, presented in Figure 5.13(a), are joined. Each partial cube presents an edge length of u_{bus} where V1 to V8 are all on the positive space region while V9 to V16 are all in the negative octant. The common vertex of both cubes is defined by two ZSV (V1 and V16). Figure 5.13(b) illustrates this available space in the *abc* reference frame. This 3-D projection contains 24 tetrahedrons which are divided into 6 per each partial cube and 12 more defined by the available space between these partial cubes. Table 5.2 resumes the output voltages referenced to the fourth leg versus all possible switching states in the *abc* and $\alpha\beta\gamma$ reference frame. Table 5.3 shows the available tetrahedrons according to the possible NZSV [232].

As in the previous Section 5.4.1, the SVPWM technique is analysed but now extending the state machine to a four-wire converter. In the literature, the SVPWM is widely analysed from a 3-D perspective. In [233] is presented the first 3-D SVPWM proposal for four-leg inverters. Then, in [4, 234] an analysis and comparison of space vector modulation schemes for a four-

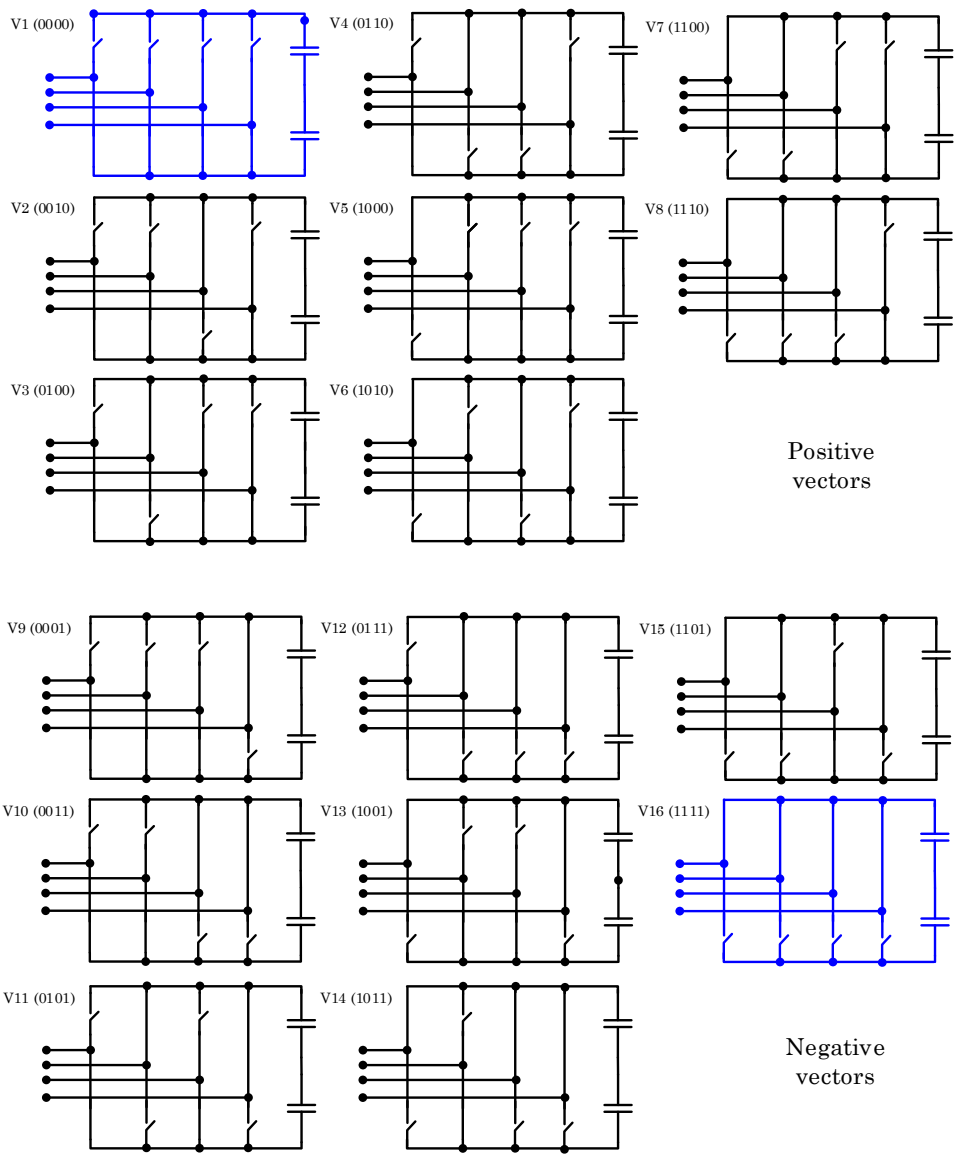

Figure 5.14: Symbolic representation of the possible states of the converter when SVPWM is applied (four-leg topology)

Output voltages when SVPWM										
Vector	State (s_u, s_v, s_w, s_n)	u_{an}	u_{bn}	u_{cn}	$u_{\alpha n}$ (module invariant)	$u_{\beta n}$ (module invariant)	$u_{\gamma n}$ (module invariant)	$u_{\alpha n}$ (power invariant)	$u_{\beta n}$ (power invariant)	$u_{\gamma n}$ (power invariant)
V01	0000	0	0	0	0	0	0	0	0	0
V02	0010	0	0	1	$-\frac{1}{3}$	$-\frac{1}{\sqrt{3}}$	$\frac{\sqrt{2}}{3}$	$-\frac{\sqrt{6}}{6}$	$-\frac{1}{\sqrt{2}}$	$\frac{1}{\sqrt{3}}$
V03	0100	0	1	0	$-\frac{1}{3}$	$\frac{1}{\sqrt{3}}$	$\frac{\sqrt{2}}{3}$	$-\frac{\sqrt{6}}{6}$	$\frac{1}{\sqrt{2}}$	$\frac{1}{\sqrt{3}}$
V04	0110	0	1	1	$-\frac{2}{3}$	0	$\frac{2\sqrt{2}}{3}$	$-\frac{\sqrt{6}}{3}$	0	$\frac{2}{\sqrt{3}}$
V05	1000	1	0	0	$\frac{2}{3}$	0	$\frac{\sqrt{2}}{3}$	$\frac{\sqrt{6}}{3}$	0	$\frac{1}{\sqrt{3}}$
V06	1010	1	0	1	$\frac{1}{3}$	$-\frac{1}{\sqrt{3}}$	$\frac{2\sqrt{2}}{3}$	$\frac{\sqrt{6}}{6}$	$-\frac{1}{\sqrt{2}}$	$\frac{2}{\sqrt{3}}$
V07	1100	1	1	0	$\frac{1}{3}$	$\frac{1}{\sqrt{3}}$	$\frac{2\sqrt{2}}{3}$	$\frac{\sqrt{6}}{6}$	$\frac{1}{\sqrt{2}}$	$\frac{2}{\sqrt{3}}$
V08	1110	1	1	1	0	0	$\sqrt{2}$	0	0	$\sqrt{3}$
V09	0001	-1	-1	-1	0	0	$-\sqrt{2}$	0	0	$-\sqrt{3}$
V10	0011	-1	-1	0	$-\frac{1}{3}$	$-\frac{1}{\sqrt{3}}$	$-\frac{2\sqrt{2}}{3}$	$-\frac{\sqrt{6}}{6}$	$-\frac{1}{\sqrt{2}}$	$-\frac{2}{\sqrt{3}}$
V11	0101	-1	0	-1	$-\frac{1}{3}$	$\frac{1}{\sqrt{3}}$	$-\frac{2\sqrt{2}}{3}$	$-\frac{\sqrt{6}}{6}$	$\frac{1}{\sqrt{2}}$	$-\frac{2}{\sqrt{3}}$
V12	0111	-1	0	0	$-\frac{2}{3}$	0	$-\frac{\sqrt{2}}{3}$	$-\frac{\sqrt{6}}{3}$	0	$-\frac{1}{\sqrt{3}}$
V13	1001	0	-1	-1	$\frac{2}{3}$	0	$-\frac{2\sqrt{2}}{3}$	$\frac{\sqrt{6}}{3}$	0	$-\frac{2}{\sqrt{3}}$
V14	1011	0	-1	0	$\frac{1}{3}$	$-\frac{1}{\sqrt{3}}$	$-\frac{\sqrt{2}}{3}$	$\frac{\sqrt{6}}{6}$	$-\frac{1}{\sqrt{2}}$	$-\frac{1}{\sqrt{3}}$
V15	1101	0	0	-1	$\frac{1}{3}$	$\frac{1}{\sqrt{3}}$	$-\frac{\sqrt{2}}{3}$	$\frac{\sqrt{6}}{6}$	$\frac{1}{\sqrt{2}}$	$-\frac{1}{\sqrt{3}}$
V16	1111	0	0	0	0	0	0	0	0	0

Table 5.2: Possible normalized voltages of a four-wire three-phase converter under SVPWM from different references perspectives (base value u_{bus})

Tetrahedron	Active vectors			Tetrahedron	Active vectors		
T_{01}	V05	V13	V15	T_{13}	V09	V13	V15
T_{02}	V05	V07	V15	T_{14}	V05	V07	V08
T_{03}	V03	V07	V15	T_{15}	V09	V11	V15
T_{04}	V03	V11	V15	T_{16}	V03	V07	V08
T_{05}	V03	V11	V12	T_{17}	V09	V11	V12
T_{06}	V03	V04	V12	T_{18}	V03	V04	V08
T_{07}	V02	V04	V12	T_{19}	V09	V10	V12
T_{08}	V02	V10	V12	T_{20}	V02	V04	V08
T_{09}	V02	V10	V14	T_{21}	V09	V10	V14
T_{10}	V02	V06	V14	T_{22}	V02	V06	V08
T_{11}	V05	V13	V14	T_{23}	V09	V13	V14
T_{12}	V05	V06	V14	T_{24}	V05	V06	V08

Table 5.3: Tetrahedron mapping according to the defined switching vector in four-leg inverters

leg voltage source inverter is developed. In [235, 236] hysteresis modulation techniques in a 3-D space are proposed. This last option is beyond the scope of this thesis and will not be considered. The most relevant details about how SVPWM operates in four-leg inverters will be explained in the following lines.

Once the allowable space is splitted into 24 tetrahedrons, different procedures are presented in order to know which switching vectors have to be applied. It should be noticed that in the 3-D SVPWM technique there are three adjacent NZSVs unlike in the 2-D SVPWM case where there are only two.

Although there are more adjacent vectors, the procedure of SVPWM is analogue to 2-D SVPWM:

- Tetrahedron determination. Selection of the adjacent vectors $\mathbf{V}_{adj_{xyz}}$ according with the location of $\mathbf{s}_{\alpha\beta\gamma}$ in one of the 24 tetrahedrons T_i, being $i = 1 : 24$. Subscripts x, y and z represents the corresponding adjacent vectors of the selected tetrahedron at any time.

- Projection. Projection of $\mathbf{s}_{\alpha\beta\gamma}$ onto the selected $\mathbf{V}_{adj_{xyz}}$, in order to obtain $\text{Proj}(_{V_{adj_x}}\mathbf{s}_{\alpha\beta\gamma})$, $\text{Proj}(_{V_{adj_y}}\mathbf{s}_{\alpha\beta\gamma})$, $\text{Proj}(_{V_{adj_z}}\mathbf{s}_{\alpha\beta\gamma})$ and the time vector $\mathbf{t} = T_s(t_i, t_j, t_k, t_l)$, in which

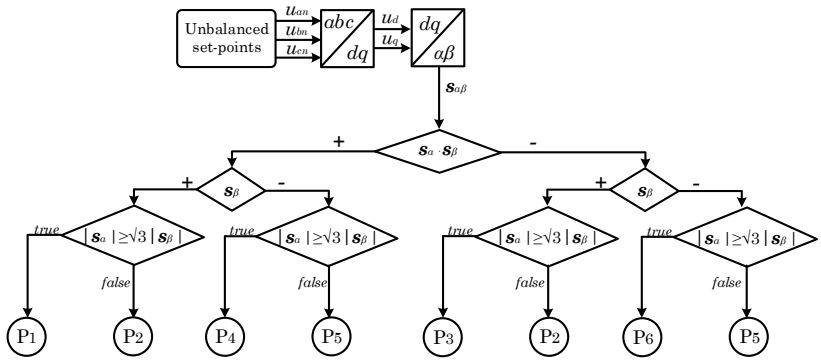

Figure 5.15: Determination of prisms

$$(t_i, t_j, t_k, t_l) = \left(\frac{|\text{Proj}(_{V_{adj_x}} \mathbf{s}_{\alpha\beta\gamma})|}{|V_{adj_x}|}, \frac{|\text{Proj}(_{V_{adj_y}} \mathbf{s}_{\alpha\beta\gamma})|}{|V_{adj_y}|}, \frac{|\text{Proj}(_{V_{adj_z}} \mathbf{s}_{\alpha\beta\gamma})|}{|V_{adj_z}|}, |1 - t_i - t_j - t_k| \right) \quad (5.5)$$

- Gate Signal (GS) generation. Select one sequencing and class type in order to achieve one or other benefit in terms of number of stitchings, current ripple or losses and obtein the GS for the four legs.

One of the key points of 3-D SVPWM is to find in an easy or optimal way to implement the tetrahedron location of $\mathbf{s}$. Unlike in 2-D SVPWM there is not a clear preference for the use of the *abc* or the $\alpha\beta\gamma$ reference frames in 3-D SVPWM. Different authors prefer one or the other in function of their criterion on which is the best option to analyse the space. Thus, next list summarises different proposed algorithms according to the used reference frame:

- Based in $\alpha\beta\gamma$ - *abc* coordinates. In [3, 4] is presented a 3-D SVPWM focused on the selection of the adjacent vectors based in two steps; determination of a prism P_i and determination of the tetrahedron. The dodecahedron is divided into six prisms, $i = 1 : 6$. Each prism is constituted by one sextant of the hexagon in $\alpha\beta$ and extruded up to V8 for positive vectors and to V9 for negative vectors. The selection of the prism is indicated in Figure 5.15.

  Then, each prism contains four tetrahedrons T_k, being $k = 1 : 4$. It should be noticed that the P_i determination is only a function of $\alpha\beta$. The second step is the determination of the tetrahedron in which

Prism	Tetrahedron	Active vectors			$\mathbf{s}_{abc}$		
					$u_{an'}$	$u_{bn'}$	$u_{cn'}$
P_1	T_{01}	V15	V13	V5	$\geq$	$<$	$<$
	T_{02}	V05	V07	V15	$\geq$	$\geq$	$<$
	T_{13}	V09	V13	V15	$<$	$<$	$<$
	T_{14}	V08	V07	V05	$\geq$	$\geq$	$\geq$

Table 5.4: Tetrahedron determination example [3, 4]

the reference vector is located. This location is computed according to the polarity of $\mathbf{s}$ in the *abc* reference frame due to the tetrahedron identification is more complex in $\alpha\beta\gamma$ coordinates. For example, for P_1 Table 5.4 shows how to determine the position of the reference vector $\mathbf{s}_{abc}$ in terms of a tetrahedron.

- Based in *abc* coordinates. In [5] is indicated that the dodecahedron in Figure 5.13(b) is defined by twelve planes that can be represented using simple expressions. Six of them are parallel to the coordinates planes, expressed by equations $v_a = \pm 1$, $v_b = \pm 1$ and $v_c = \pm 1$. The last six have $\pi/4$ rad over the coordinate planes and are described by $v_a - v_b = \pm 1$, $v_b - v_c = \pm 1$ and $v_c - v_a = \pm 1$. In this case, instead of determining a prism in $\alpha\beta\gamma$ coordinates, as in the previous case, it will be determined directly the tetrahedron that includes $\mathbf{s}$. As has been mentioned, the dodecahedron can be splitted into 24 tetrahedrons that contains three NZSVs and the two ZSVs. It should be remarked that all tetrahedrons are equal in size. This facts propitiates a symmetrical division of the control region. In this sense, a region pointer RP, optimized for computing, is defined as [4, 5]

$$RP = 1 + \sum_{i=1}^{6} C_i 2^{(i-1)} \tag{5.6}$$

where C_i

$$C_i = \mathtt{sign}(INT(\mathbf{x}(i) + 1)) \quad i = 1:6 \tag{5.7}$$

and $\mathbf{x}(i)$ is a normalized vector constituted by [$\mathbf{s}_a$,$\mathbf{s}_b$,$\mathbf{s}_c$,$\mathbf{s}_{ab}$,$\mathbf{s}_{bc}$,$\mathbf{s}_{ca}$]. This pointer RP can only take 24 different values from 1 to 64. Considering as an example the same tetrahedrons shown in Table 5.4, the different RP pointer values are represented in Table 5.5.

- Based in $\alpha\beta\gamma$ coordinates. In [226] it is presented a 3-D SVPWM algorithm based on the determination of a truncated triangular prism

Tetrahedron	Active vectors			RP
T_{01}	V05	V13	V15	58
T_{02}	V05	V07	V15	60
T_{13}	V09	V13	V15	57
T_{14}	V05	V07	V08	64

Table 5.5: Tetrahedron determination example [5]

called TTP. Assuming n as the voltage reference it can be verified that when $\mathbf{s}$ is computed using $\alpha\beta\gamma$ coordinates there is no effect of the fourth leg on the $\mathbf{s}_{\alpha\beta}$

$$\mathbf{s}_\alpha = k\left(\mathbf{s}_a - \frac{1}{2}\mathbf{s}_{bc}\right) \tag{5.8}$$

$$\mathbf{s}_\beta = k\left(\frac{\sqrt{3}}{2}\mathbf{s}_{bc}\right) \tag{5.9}$$

$$\tag{5.10}$$

Taking again the TTP concept, it can be defined by four coefficients. These four coefficients, noted as C_0, C_1, C_2 and C_3, can be determined as

$$C_0 = 1 \tag{5.11}$$

$$C_1 = INT\left(\frac{5}{2} - x - \epsilon\right) \tag{5.12}$$

$$C_2 = INT\left(1 - y - \epsilon\right) \tag{5.13}$$

$$C_3 = INT\left(\frac{5}{2} + x + \epsilon\right) \tag{5.14}$$

where

$$x = \frac{\mathbf{s}_\alpha}{\|\mathbf{s}\|} \tag{5.15}$$

$$y = \frac{\mathbf{s}_\beta}{\|\mathbf{s}\|} \tag{5.16}$$

being

$$\|\mathbf{s}\| = \sqrt{\mathbf{s}_\alpha^2 + \mathbf{s}_\beta^2} \tag{5.17}$$

and ϵ is used to face with boundary conditions between two adjacent triangles in the $\alpha\beta$ frame. It is not true that the reference space vector

Tetrahedron	$u_1 \geq u_2 \geq u_3 \geq u_4$
T_{01}	$u_{an'} \geq 0 \geq u_{bn'} \geq u_{cn'}$
T_{02}	$u_{an'} \geq u_{bn'} \geq 0 \geq u_{cn'}$
T_{13}	$0 \geq u_{an'} \geq u_{bn'} \geq u_{cn'}$
T_{14}	$u_{an'} \geq u_{bn'} \geq u_{cn'} \geq 0$

Table 5.6: Tetrahedron determination [6]

moves along the full prism as indicated in [3]. In fact, the reference space vector **s** passes only in six pentahedron or six TTPs [226]. Then, the TTP can be determined according to

$$TTP = 3C_2 + \sum_{i=0}^{2}(-1)^i C_i C_{i+1} \tag{5.18}$$

Each TTP contains six switching vectors that defines four tetrahedrons that at the same time contains three active NZSVs. For the tetrahedron identifications the following formula is proposed

$$T = 4(TTP - 1) + 1 + \sum_{i}^{3} a_i \tag{5.19}$$

where $a_i = 1$ if $u_i \geqslant 0$. In the opposite case, $a_i = 0$. The subscript i refers to u, v and w.

In [6] a new algorithm for tetrahedron determination is proposed. In this case, it exposes the relation between the adjacent vectors and the corresponding tetrahedron. The concept behind this proposal is to assume that the adjacent vectors are in a tetrahedron but the identification of this last is dispensable. The authors expose that as the relation between abc and $\alpha\beta\gamma$ coordinates are based on rotations, as detailed in Apendix A, any vector in abc or $\alpha\beta\gamma$ have different spatial position and can have different scales but the time in which one is applied is independent of the coordinates. Thus, if $\mathbf{s}_{abc}$ and zero value (used for polarity determination) are ordered in descending order it is possible to obtain 24 combinations that appoints one tetrahedron and, consequently, defines the adjacent vectors to apply. Special care has to be considered for boundary conditions when more that one equality occurs. Considering again as an example the same tetrahedrons shown in Table 5.4, the location of these tetrahedra is illustrated in Table 5.6.

5.4.2 Novel space vector modulation for three-phase four-wire inverters

A new fast computing modulation technique for four-wire four-leg three-phase inverters is developed. The goal is to simplify computation burdens compared with other techniques. In this case, the main idea is to take profit of the conventional 2-D SVPWM algorithm in terms of computation times and the existing optimized implementation alternatives without considering 3-D SVPWM techniques. In other words, in case of unbalanced set-points, they will be decoupled into non-homopolar and homopolar components. The non-hompolar components will follow classical 2-D SVPWM techniques. A simple treatment to the homopolar term permits to recover the original set-point at the output of a four-leg inverter.

Algorithm proposal

As has been mentioned, when $\mathbf{s}$ is computed using $\alpha\beta$ coordinates there is no effect of the fourth leg on the $\mathbf{s}_{\alpha\beta}$. Thus, according to Figure 2.17(c), the u_{xo} voltages can be computed as

$$u_{xo} = u_{xn'} + u_{n'n} + u_{no} \tag{5.20}$$

being $x = u, v, w$. Then,

$$u_{xn'} = u_{xo} - u_{no} - u_{n'n} \tag{5.21}$$

In this sense, considering the average voltage values of the midpoint of each leg in respect with n' during one switching cycle

$$\hat{u}_{xn'} = (d_x - d_n)u_{bus} - \hat{u}_{n'n} \tag{5.22}$$

where d_u, d_v and d_w are the duty cycles of the corresponding active phase x leg and d_n the one of the neutral fourth leg. In case of considering n as the voltage reference

$$\hat{u}_{xn} = (d_x - d_n)u_{bus} \tag{5.23}$$

Applying the module invariant Clarke transform, see Equation A.18 in Ap-

pendix A, to Equation 5.23,

$$\hat{u}_\alpha = \frac{2}{3} u_{bus} \left(d_u - \frac{1}{2}(d_v + d_w) \right) \tag{5.24a}$$

$$\hat{u}_\beta = \frac{\sqrt{3}}{3} u_{bus} \left(d_v - d_w \right) \tag{5.24b}$$

$$\hat{u}_h = \frac{\sqrt{2}}{3} \left((d_u + d_v + d_w) u_{bus} - 3 d_n u_{bus} \right) \tag{5.24c}$$

It is remarkable that $\hat{u}_{\alpha\beta}$ is not dependent on the voltage generated at neutral leg, being this point the key of the extended SVPWM for four-branch inverters presented in Figure 5.16.

As it is possible that the desired voltages to synthesize are not constituted by a balanced system and, therefore, it can contain homopolar components, the following steps are proposed for a predetermined unbalanced set-points, class and sequencing input set (note that at this point $\mathbf{s} \in \Re^3$ considering n as the voltage reference):

1. Free-homopolar system calculation. From any unbalanced desired voltages of $\mathbf{s}$ a new virtual three-phase system without homopolar component is obtained:
   a) Compute from any unbalanced phase-to-neutral a phase-to-phase voltage vector. The phase-to-phase reference spacial vector voltage $\mathbf{s}'$ is computed obtaining a new vector without homopolar components.
   b) Compute from phase-to-phase voltages a virtual phase-to-neutral (n'') voltage vector without homopolar component. A new spacial vector $\mathbf{s}''$ reference is obtained.

   Note after applying step 1 the obtained space vector $\mathbf{s}'' \in \Re^2$ (reference to n'').

2. 2-D space vector determination in the stationary $\alpha\beta$ reference frame. Thus, applying the Clarke transform, see Appendix A, $\mathbf{s}''_{\alpha\beta}$ is obtained.

3. Sextant determination. Same procedure than in the conventional 2-D SVPWM approach but considering $\mathbf{s}''_{\alpha\beta}$ as the input reference spacial vector instead of $\mathbf{s}_{\alpha\beta}$.

4. Projection. Projection of $\mathbf{s}''_{\alpha\beta}$ onto the selected $\mathbf{V}_{adj_{xy}}$, in order to obtain $\text{Proj}(_{V_{adj_x}}\mathbf{s}''_{\alpha\beta})$, $\text{Proj}(_{V_{adj_y}}\mathbf{s}''_{\alpha\beta})$ and the time vector $\mathbf{t} = T_s(t_i, t_j, t_k)$,

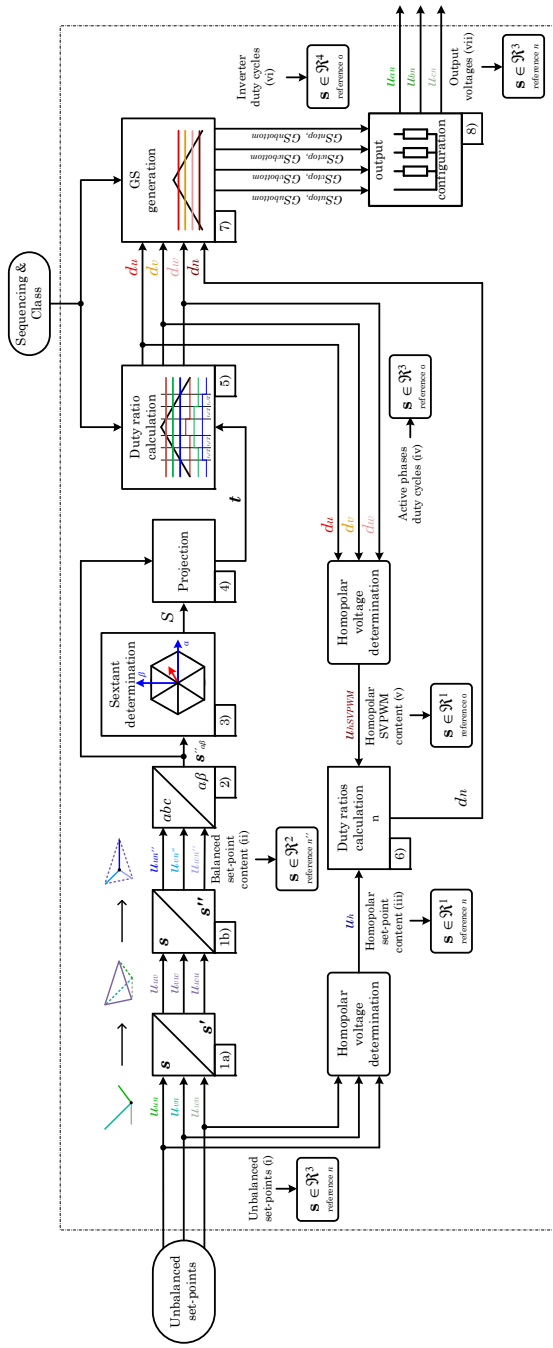

Figure 5.16: Proposed SVPWM algorithm for four-wire four-leg inverters

in which

$$(t_i, t_j, t_k) = \left(\frac{|\text{Proj}(_{V_{adj_x}} \mathbf{s}_{\alpha\beta})|}{|V_{adj_x}|}, \frac{|\text{Proj}(_{V_{adj_y}} \mathbf{s}_{\alpha\beta})|}{|V_{adj_y}|}, |1 - t_i - t_j| \right) \quad (5.25)$$

as in the conventional 2-D SVPWM case.

5. Duty ratios calculation of active phases. Analogous procedure than in the conventional 2-D SVPWM according to the sequencing and class criterion previously selected. The computation of these duty ratios are commonly referenced to the mid-point of the DC-link. In consequence, the obtained duty cycles d_u, d_v and d_w accomplishes that

$$d_u + d_v + d_w \neq 0 \quad (5.26)$$

implying that the equivalent space vector $\mathbf{s} \in \Re^3$ (reference to o, see Figure 5.7 and 5.8).

6. Duty ratio calculation of the neutral leg n. According to the module invariant Clarke transform, see Equation A.18 in Appendix A, the instantaneous homopolar voltage component of the initial unbalanced set-point can be computed as

$$u_h = \frac{\sqrt{2}}{3}(u_{un} + u_{vn} + u_{wn}) \quad (5.27)$$

that has been previously described by its average equivalent formulation in Equation 5.24.

The duty cycle for the fourth leg can be calculated independently and it is a function of the duty cycle obtained previously for the active three legs (u, v and w). For a switching period it is assumed that $\hat{u}_h = u_h$, then, the duty ratio of the neutral leg n can be obtained by

$$d_n = \frac{1}{3}(d_u + d_v + d_w) - \frac{1}{\sqrt{2}u_{bus}} u_h \quad (5.28)$$

It should be highlighted that Equation 5.28 introduces two relevant components. The term $(d_u + d_v + d_w)/3$ compensates the homopolar component introduced by the 2-D SVPWM, u_{hSVPWM}, and the term $u_h/(\sqrt{2}u_{bus})$ is related with the duty cycle of the desired homopolar term in the initial voltage set-points. Both terms, u_{hSVPWM} and u_h implies an equivalent $\mathbf{s} \in \Re^1$.

7. Generate gate signals. According to the same sequencing and class of step 5, the duty cycle of the fourth leg is added and the gate signals for each switch of the four-leg inverter is obtained. In this step there are involved the four-legs. Thus, du, dv, dv and d_n are considered and four degrees of freedom have to be taken into account, therefore, $\mathbf{s} \in \Re^4$.

8. Output voltage attainment. Considering the neutral point n as the reference, one degree of freedom is lost in respect with step 7, implicating that the fourth dimension is cancelled and the space vector dominion is located $\mathbf{s} \in \Re^3$. In fact, the converter states suffer a displacement through the four-dimension homopolar vector $\vec{m} = (1,1,1,1)$ to a volume $\Omega|\{n' = 0\}$, see Figure 2.17(c). In other words, a three-dimensional space appears as a conjunction of two three-phase dominions (cubes) as was depicted in Figure 5.13.

Limitation analysis of the extended 2-D SVPWM from a over-modulation perspective

The proposed method can take profit of any optimized 2-D SVPWM only requiring simple operations to overcome step 1 and step 5, see Fig. 5.16. However, some limitations are offered by this modulation strategy compared with conventional 3-D SVPWM.

The methodology is based on, first, compute the associated d_u, d_v and d_w as in a three-wire case. This point implies that the possible vectors to apply are conditioned, as indicated in Table 5.4.2. In this sense, the fourth-wire is the only responsible not only to cancel the homopolar component inherent to the 2-D SVPWM but also to generate the desired homopolar component present in case (i) -unbalanced set-point-. In other words, step 6 does not propitiate to take advantage of the homopolar component achieved in the conventional 2-D SVPWM technique. According to this fact, the maximum u_h that is possible to synthesize is limited unlike in conventional 3-D SVPWM alternatives.

The possible switching vectors to use are predetermined by the previous computation of d_u, d_v and d_w. Consequently, the maximum u_h (u_γ) that is possible to synthesize is limited. This homopolar or γ voltage component can not be simplified easily. However, it can be treated as the addition of three sinusoidal voltages with different amplitudes and different initial angles. The result is another sinusoidal signal. With this assumption, it is possible to deduce that u_h can be expressed as

$$u_h = u_\gamma = \sqrt{2} U_h \sin(\omega t + \phi_h) \tag{5.29}$$

being ϕ_h the angle shift between the positive and the homopolar voltages. The duty cycle of the active phases u, v and w can be expressed for the first sextant as [227]

$$d_u = \frac{1}{2}(1 + t_i + t_j) \tag{5.30a}$$

$$d_v = d_u - t_i \tag{5.30b}$$

$$d_w = d_v - t_j \tag{5.30c}$$

when an up-down sequencing and class I is selected. the addition of them divided by a factor of three can be expressed as

$$\frac{d_u + d_v + d_w}{3} = \frac{1}{2} - \frac{1}{6}\sqrt{3} M \cos(\omega t + \frac{\pi}{3}) \tag{5.31}$$

where M is defined as the positive sequence modulation index described by

$$M = \frac{U}{u_{bus}} \tag{5.32}$$

being U the phase-to-phase peak voltage value.

Another modulation is defined. In this sense, m_h is the time-based homopolar modulation index described by

$$m_h = \frac{u_h}{u_{bus}} \tag{5.33}$$

Thus, as $d_n \in [0, 1]$ when no over-modulation is desired, if d_n is expressed as

$$d_n = \frac{1}{2} - \frac{1}{6}\sqrt{3} M \cos(\omega t + \frac{\pi}{3}) - \frac{m_h}{\sqrt{2}} \tag{5.34}$$

it is possible to impose that $d_n = 0$ or $d_n = 1$. Then, isolating m_h

$$m_h|_{d_n=0} = -\frac{\sqrt{2}}{6}\left(-3 + \sqrt{3} M \cos(\omega t + \frac{\pi}{3})\right) \tag{5.35a}$$

$$m_h|_{d_n=1} = -\frac{\sqrt{2}}{6}\left(3 + \sqrt{3} M \cos(\omega t + \frac{\pi}{3})\right) \tag{5.35b}$$

In this sense, Equation 5.35a and 5.35b provides the lower and upper limit 3-D surfaces for the maximum module of m_h and are a function of the modulation index M of the active phases and the angle (time instant). Figure 5.17

3-leg VSI SV	4-leg VSI SV	3-leg VSI SV	4-leg VSI SV
000 (V0)	0000 (V00)	011 (V4)	0110 (V04)
	0001 (V08)		0111 (V12)
100 (V1)	1000 (V05)	001 (V5)	0010 (V02)
	1001 (V13)		0011 (V10)
110 (V2)	1100 (V02)	101 (V6)	1010 (V06)
	1101 (V15)		1011 (V14)
010 (V3)	0100 (V03)	111 (V7)	1110 (V08)
	0101 (V11)		1111 (V16)

Table 5.7: Possible vector application when the simplified 3-D is applied for an up-down sequencing and class I SV modulation strategy

shows these limit surfaces. As can be deduced, this modulation technique does not allow to synthesize $m_h = 1$. However, although in a microgrid each phase can operate individually, the consideration of providing only homopolar voltage at the maximum available voltage is a rare situation. It should be reminded that this surfaces are valid for an up-down sequencing and class I modulation. For other alternatives, different surfaces are obtained.

Implemantion comparison

The implementation for the conventional 2-D SVPWM is based on the DMC MATH v13.1 library for digital motor control of Texas Instruments [237]. The proposed SVPWM for four-leg inverters add the calculations required to compute Equation (5.28) and the extra gate signal generation for the fourth leg. Besides, the 3-D SVPWM based on the region pointer (RP) concept and proposed in [5] is also implemented to have a wider comparison view.

The three considered modulation strategies run on a Texas instruments TMS320F28335 DSP and have been implemented within a synchronous interruption at 12.5 kHz, and a clock speed of 150 MHz. The results of the computational burdens and the required program memory for the exposed three cases are summarised in Table 5.8. It can be noted that the computation burdens added represent 45% of extra time over the conventional 2-D SVPWM required time, and 12.4% of the considered 3-D SVPWM technique. However, according to our estimations it is possible to save about 50% respect with a conventional 3-D SVPWM strategy in terms of program memory. In this sense, the proposed SVM procedure for four-leg inverters can be considered as a good trade-off between required memory and com-

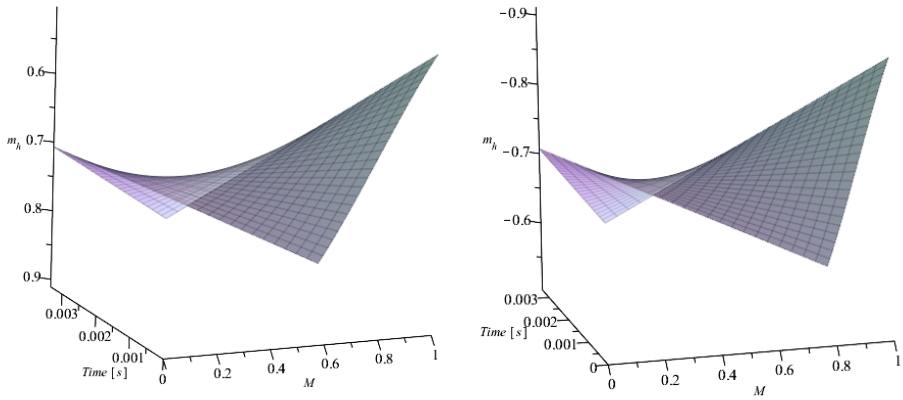

(a) Solution surface for Eq. (5.35a) (b) Solution surface for Eq. (5.35b)

Figure 5.17: Limit surfaces of m_h as a function of the modulation index M used and the time instant for the first sextant

SVM Strategy	Time	Units	Program memory	Units
Conventional 2-D SVPWM (under DMC MATH v13.1)	1.78	μs	600	Bytes
Proposed SVPWM (considering the conventional 2-D SVPWM common part)	2.53	μs	706	Bytes
3-D SVPWM in *abc* coordinates by RP determination (proposed in [5])	2.25	μs	1751	Bytes

Table 5.8: Implementation comparison

putational burdens when digitally implemented.

Validation results

To validate the extended 2-D SVPWM, a set of three arbitrary voltages in respect with n is proposed. In this sense,

$$\begin{aligned} u_{un} &= -1\sin(100\pi t) \\ u_{vn} &= 1.2\sin(100\pi t - \pi/2) \\ u_{wn} &= -0.3\sin(100\pi t + \pi/4) \end{aligned}$$

Figure 5.18 shows the desired input voltages. It also splits this desired voltages into the homopolar and the positive/negative components considering as a reference the virtual neutral n'', see Figure 5.16.

Then, the obtained duty cycles for the active phase u, v, w and the neutral leg n are presented in Figure 5.19. The different homopolar components that

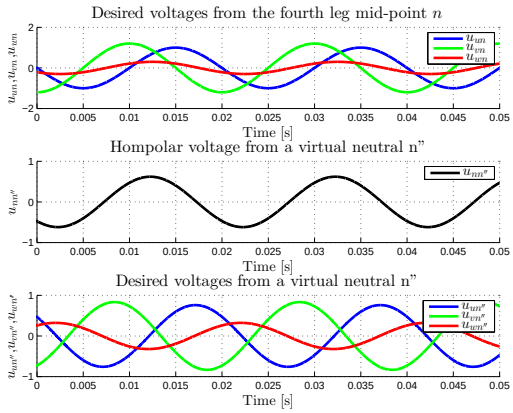

Figure 5.18: Input voltages to the extended 2-D SVPWM

are involved are depicted. Note that this strategy basically determines what homopolar component u_{no} must be synthesized in order to obtain the desired $u_{nn''}$ but considering that the conventional 2-D SVPWM participates with $u_{on''}$.

On the other hand, as the harmonics can be seen also as components of direct, inverse and homopolar sequence, Figure 5.20 shows the duty ratios and average output voltages obtained when a direct, inverse or homopolar individual components are desired under the proposed extended 2-D SVPWM. For these three cases, the AC base value is 230 V considering a DC-link voltage u_{bus} of 700 VDC.

Also, to validate that the duty ratios of the active phases u, v or w are not affected by the homopolar voltage a desired voltage combination of fundamental (230 V) and third harmonic component (35.5 V) is considered. Figure 5.21 depicts a comparison between only fundamental and the new combined voltage (indicated with the subscript 2). It can be observed that only the neutral leg has to be modified while the duty ratios of the active phases are maintained invariant.

5.4.3 Design of the LCL-type coupling filter for the AC side

The effect of the used modulation technique on a three-wire three-leg inverter determines how to size the output coupling inductance.

In this section, in order to introduce the ripple calculation procedure for the extended 2-D SVPWM it is first presented the conventional 2-D SVPWM applied methodology.

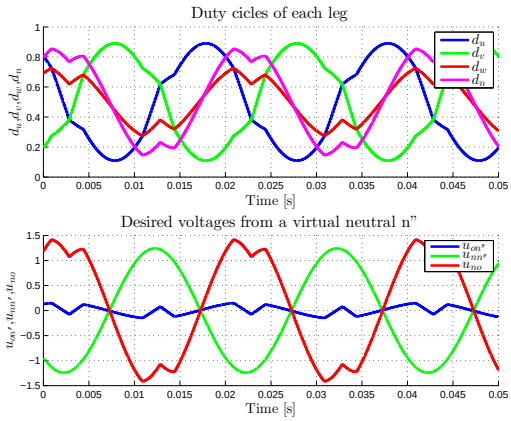

Figure 5.19: Output duty cycles and voltages when the extended 2-D SVPWM is applied

Effect of the conventional SVPWM on the size of the output VSI inductance for an up-down sequencing and class I modulation strategy

From one side, the 2-D conventional SVPWM is constituted by eight possible states or vectors that determines the state machine of the inverter, see Figure 5.7. Table 5.1 summarizes the different possible voltages in different reference frames. Hereinafter, the power invariant Clarke transform

$$T = \sqrt{\frac{2}{3}} \begin{pmatrix} 1 & -\frac{1}{2} & -\frac{1}{2} \\ 0 & \frac{\sqrt{3}}{2} & -\frac{\sqrt{3}}{2} \\ \frac{1}{\sqrt{2}} & \frac{1}{\sqrt{2}} & \frac{1}{\sqrt{2}} \end{pmatrix} \quad T^{-1} = T^t = \sqrt{\frac{2}{3}} \begin{pmatrix} 1 & 0 & \frac{1}{\sqrt{2}} \\ -\frac{1}{2} & \frac{\sqrt{3}}{2} & \frac{1}{\sqrt{2}} \\ -\frac{1}{2} & -\frac{\sqrt{3}}{2} & \frac{1}{\sqrt{2}} \end{pmatrix} \tag{5.36}$$

is used, being $X_{\alpha\beta\gamma} = TX_{abc}$ and $X_{abc} = T^{-1}X_{\alpha\beta\gamma}$.

On the other hand, if the three-wire three-leg system is described by equivalent average voltage sources, as shown in Figure 2.17(a) in Chapter 2, it is possible to determine that when the active phase currents (i_u, i_v and i_w) are considered as the state variables, the system described by Equation 2.6 can be expressed in the $\alpha\beta\gamma$ reference frame after applying T as

$$\frac{d}{dt}\begin{pmatrix} i_\alpha \\ i_\beta \end{pmatrix} = -\begin{pmatrix} \frac{R}{L} & 0 \\ 0 & \frac{R}{L} \end{pmatrix}\begin{pmatrix} i_\alpha \\ i_\beta \end{pmatrix} + \frac{1}{L}\begin{pmatrix} u_\alpha - u'_\alpha \\ u_\beta - u'_\beta \end{pmatrix} \tag{5.37}$$

Note that the γ component is not considered. This is due to three-wire inverters under SVPWM techniques considers an isolated neutral at the AC

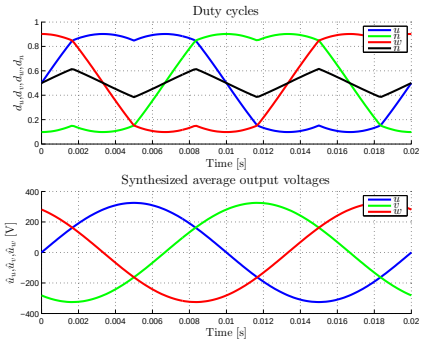

(a) Fundamental component setpoint

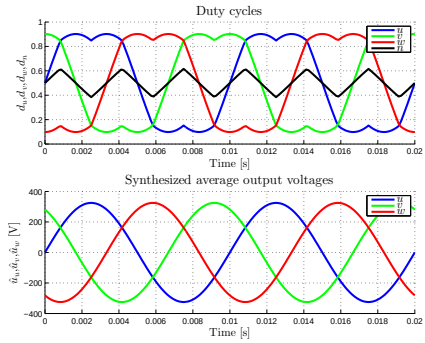

(b) Second harmonic component setpoint

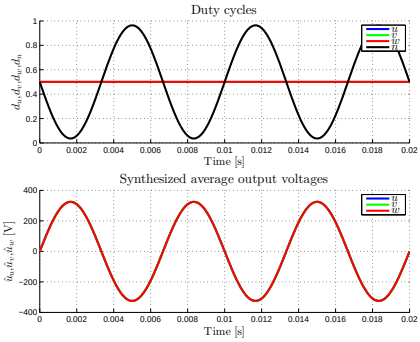

(c) Third harmonic component setpoint

Figure 5.20: Duty ratios and synthesized voltages under direct, inverse or homopolar setpoints

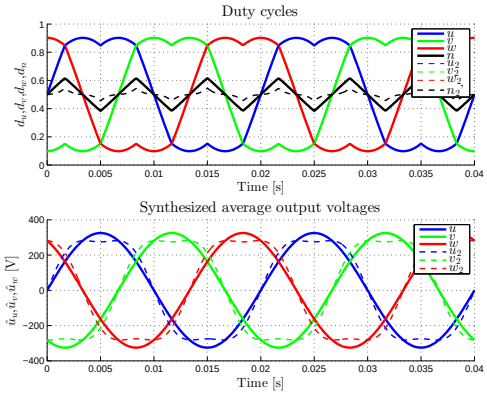

Figure 5.21: Comparison of duty ratios and synthesized voltages under direct and homopolar setpoints

side, then, is not possible to inject homopolar components. Assuming that the grid only presents positive sequence voltage, the phase-to-neutral grid side voltages are defined as

$$u_{u'n'} = \sqrt{2}\frac{U'}{\sqrt{3}}\cos(\omega t) \tag{5.38a}$$

$$u_{v'n'} = \sqrt{2}\frac{U'}{\sqrt{3}}\cos(\omega t - 2\pi/3) \tag{5.38b}$$

$$u_{w'n'} = \sqrt{2}\frac{U'}{\sqrt{3}}\cos(\omega t + 2\pi/3) \tag{5.38c}$$

being U' the phase-to-phase grid voltage amplitude. Using Equation 5.36 into 5.38,

$$u'_\alpha = \sqrt{\frac{2}{3}}\left(u_{u'n'} - \frac{1}{2}u_{v'n'} - \frac{1}{2}u_{w'n'}\right) = U'\cos(\omega t) \tag{5.39a}$$

$$u'_\beta = \sqrt{\frac{2}{3}}\left(\frac{\sqrt{3}}{2}u_{v'n'} - \frac{\sqrt{3}}{2}u_{w'n'}\right) = U'\sin(\omega t) \tag{5.39b}$$

Considering that the reference space vector $\mathbf{s}$ is located at the first sector, a switching period of t_{sw}, a switching sequencing up-down and class I, the $\mathbf{s}_{\alpha\beta}$ can be expressed as

$$\mathbf{s}_{\alpha\beta} = \alpha_1\underline{U}_1 + \alpha_2\underline{U}_2 + \frac{\alpha_0}{2}\underline{U}_0 + \frac{\alpha_0}{2}\underline{U}_7 \tag{5.40}$$

being α_x the application time (in the previous Section 5.4.1 and 5.4.2 referred as a component of $\mathbf{t}$) and $\underline{U}_x$ the voltage of the corresponding state or SVPWM vector x, such that $x = 0:7$. It should be noticed that the application during a same time interval of V0 and V7 produces a self-cancellation in a switching interval of the γ component. Thus, when the first sextant is considered, the duty cycles are ordered as $d_u > d_v > d_w$ producing that, if the carrier signal is symmetrical up-down, the SVPWM vectors follows a stipulated order ($\cdots$-V0-V1-V2-V7-V2-V1-V0-$\cdots$), as can be seen in Figure 5.22.

It is considered that the LCL-type coupling filter will not introduce excessive delay or voltage drop between the converter side and the grid side. Then, it is assumed that the grid side voltage is equal to the converter output voltage and the output current is in phase with the utility voltage. If not, an equivalent delay can be introduced in Equation 5.38 or 5.39.

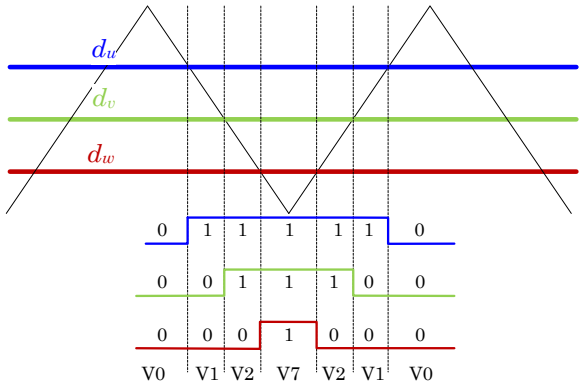

Figure 5.22: Vector application when SVPWM is applied using a symmetrical carrier signal in a three-phase three-wire inverter

Then, splitting $\mathbf{s}_{\alpha\beta}$ in the corresponding $\alpha\beta$ components it is possible to generalize the time application α_x for the first sextant using Equation 5.39 as

$$u'_\alpha = U' \cos(\omega t) = \sqrt{\frac{2}{3}} u_{bus} (\alpha_1 + \frac{1}{2}\alpha_2) \tag{5.41}$$

$$u'_\beta = U' \sin(\omega t) = \sqrt{\frac{2}{3}} u_{bus} (\frac{\sqrt{3}}{2}\alpha_2) \tag{5.42}$$

where, operating,

$$\alpha_1 = M \cos(\omega t + \pi/6) \tag{5.43a}$$

$$\alpha_2 = M \sin(\omega t) \tag{5.43b}$$

$$\alpha_0 = \alpha_7 = \frac{1 - \alpha_1 - \alpha_2}{2} \tag{5.43c}$$

and M the modulation index described in Equation 5.32 but now referred to the grid side voltage U'. To simplify the calculations, the parasitic resistance of Equation 5.37 is neglected. As the converter is a variable time system, Equation 5.37 is translated to the discrete time domain as

$$\Delta i_{\alpha_x} = \frac{u_\alpha - u'_\alpha}{L f_{sw}} \alpha_x \tag{5.44a}$$

$$\Delta i_{\beta_x} = \frac{u_\beta - u'_\beta}{L f_{sw}} \alpha_x \tag{5.44b}$$

obtaining the ripple at any instant in the $\alpha\beta$ reference frame. L is the considered ideal inductance value and f_{sw} is the switching frequency ($1/T_{sw}$). If Equation 5.44 is applied to any of the four possible states linked with the first sextant, i.e. V0, V1, V2 and V7, it is possible to obtain the ripple when they are used. Thus, for instance, the associate ripple for the state 000 (V0) is

$$\Delta i_{\alpha_0} = \frac{-u_{\alpha'}}{L f_{sw}} \alpha_0 = -\frac{u_{bus} M \cos(\omega t)}{\sqrt{2} L f_{sw}} \alpha_0 \tag{5.45a}$$

$$\Delta i_{\beta_0} = \frac{-u_{\beta'}}{L f_{sw}} \alpha_0 = -\frac{u_{bus} M \sin(\omega t)}{\sqrt{2} L f_{sw}} \alpha_0 \tag{5.45b}$$

Now, the obtained ripple for each state is computed in the natural uvw reference frame using the inverse matrix T^{-1} of Equation A.16. The different active phase ripples for the state 000 (V0) are

$$\Delta i_{u_0} = \sqrt{\frac{2}{3}} \Delta i_{\alpha_{V0}} = -\frac{u_{bus} M}{\sqrt{3} L f_{sw}} \cos(\omega t) \alpha_0 \tag{5.46a}$$

$$\Delta i_{v_0} = \sqrt{\frac{2}{3}} \left(-\frac{\Delta i_{\alpha_0}}{2} + \frac{\sqrt{3} \Delta i_{\beta_{V0}}}{2} \right) = -\frac{u_{bus} M}{\sqrt{3} L f_{sw}} \cos(\omega t + \pi/3) \alpha_0 \tag{5.46b}$$

$$\Delta i_{w_0} = \sqrt{\frac{2}{3}} \left(-\frac{\Delta i_{\alpha_0}}{2} - \frac{\sqrt{3} \Delta i_{\beta_{V0}}}{2} \right) = -\frac{u_{bus} M}{\sqrt{3} L f_{sw}} \cos(\omega t - \pi/3) \alpha_0 \tag{5.46c}$$

If the ripple base value is defined as

$$\Delta I_b = \frac{u_{bus}}{\sqrt{3} L f_{sw}} \tag{5.47}$$

Equation 5.46 results into

$$\Delta i_{u_0} = -M \Delta I_b \cos(\omega t) \alpha_0 \tag{5.48a}$$

$$\Delta i_{v_0} = -M \Delta I_b \cos(\omega t + \pi/3) \alpha_0 \tag{5.48b}$$

$$\Delta i_{w_0} = -M \Delta I_b \cos(\omega t - \pi/3) \alpha_0 \tag{5.48c}$$

This same procedure can be applied to V1, V2 and V7 for the analysis on the first sextant. Although the ripples are located at different time instants when the other sextants are considered, the maximum ripple can be extracted from the information of the first one.

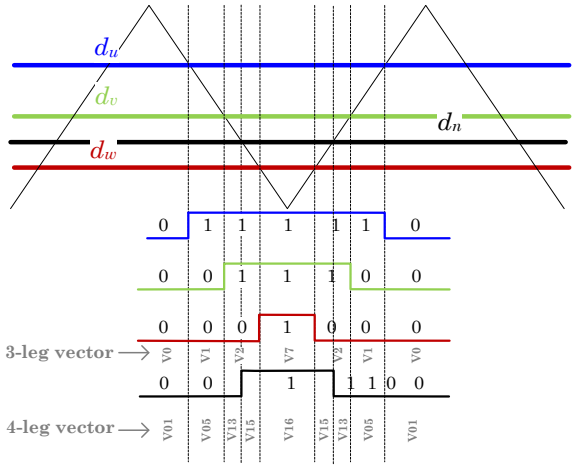

Figure 5.23: Vector application when SVPWM is applied using a symmetrical carrier signal in a three-phase four-wire inverter using the proposed extended 2-D SVPWM

Effect of the extended 2D-SVPWM on the size of the output VSI inductance for the up-down sequencing and class I modulation strategy

The extension of the previous sizing ripple procedure derives from the understood of the behaviour of the applied possible vectors in the 2-D case. This means that unlike conventional methodologies of 3-D SVPWM, in which there exists different proposals to find the three closest adjacent vectors that surrounds the current space vector location, in the extended 2-D SVPWM the possible vectors are predetermined, as shown in Table 5.4.2 for an up-down sequencing and class I modulation strategy. In this sense, the analysis deduced from Figure 5.22 can be broaden considering the effect of the switching state of the fourth leg. In Figure 5.23 can be seen an example. However, the possible states to be applied depends directly on d_n. Note that the switching state 1 is always at the middle for each leg. Table 5.4.2 relates all possible state vectors when the extended 2-D SVPWM is used.

If the four-wire three-leg system is described by equivalent voltage sources, as shown in Figure 2.17(c) in Chapter 2 and the active phases u, v and w dispose of the same inductance and equivalent series resistance than the neutral phase

$$\begin{pmatrix} u_{un} \\ u_{vn} \\ u_{wn} \end{pmatrix} = \begin{pmatrix} 2(Ls+R) & Ls+R & Ls+R \\ Ls+R & 2(Ls+R) & Ls+R \\ Ls+R & Ls+R & 2(Ls+R) \end{pmatrix} \begin{pmatrix} i_u \\ i_v \\ i_w \end{pmatrix} + \begin{pmatrix} u_{u'n'} \\ u_{v'n'} \\ u_{w'n'} \end{pmatrix} \quad (5.49)$$

If the transformation matrix T, presented in Equation A.16, is applied to Equation 5.49 and is rewritten in its state-space form

$$\frac{d}{dt} \begin{pmatrix} i_\alpha \\ i_\beta \\ i_\gamma \end{pmatrix} = - \begin{pmatrix} \frac{R}{L} & 0 & 0 \\ 0 & \frac{R}{L} & 0 \\ 0 & 0 & \frac{R}{L} \end{pmatrix} \begin{pmatrix} i_\alpha \\ i_\beta \\ i_\gamma \end{pmatrix} + \begin{pmatrix} \frac{1}{L} & 0 & 0 \\ 0 & \frac{1}{L} & 0 \\ 0 & 0 & \frac{1}{4L} \end{pmatrix} \begin{pmatrix} u_\alpha - u'_\alpha \\ u_\alpha - u'_\alpha \\ u_\gamma - u'_\gamma \end{pmatrix} \quad (5.50)$$

As in the 2-D conventional SVPWM, when the parasitic resistance is neglected, Equation 5.50 is translated to the discrete time domain as

$$\Delta i_{\alpha_x} = \frac{u_\alpha - u'_\alpha}{L f_{sw}} \alpha'_x \quad (5.51a)$$

$$\Delta i_{\beta_x} = \frac{u_\beta - u'_\beta}{L f_{sw}} \alpha'_x \quad (5.51b)$$

$$\Delta i_{\gamma_x} = \frac{u_\gamma - u'_\gamma}{4L f_{sw}} \alpha'_x \quad (5.51c)$$

In this case α'_x is used to differentiate the fourth-leg application times from the three-leg ones. Then, using Equations 5.29 to 5.34, and considering Table 5.4.2 it is possible to find the application times for the corresponding vectors according to the procedure shown in Figure 5.24. In this figure $t(\mathrm{Vx})$ indicates the time that a vector of a three-phase four-wire inverter is applied, $t(1-d_n)$ is the application time of the state xxx0 (bottom switch closed) of the fourth-leg, RV is a remaining value in terms of time and α'_x represents the application time of the corresponding vector of a three-phase three-wire inverter.

Once the application times $t(\mathrm{Vx})$ for the eight possible states in the three-phase four-wire case are obtained, derived from V0, V1, V2 and V7 in the three-phase three-wire case, Equation 5.51 can be applied substituting α'_x by $t(\mathrm{Vx})$. Then, the procedure is analogue to the three-phase three-wire analysis for the first sextant. Thus, the different steps for the ripple computation are as follows:

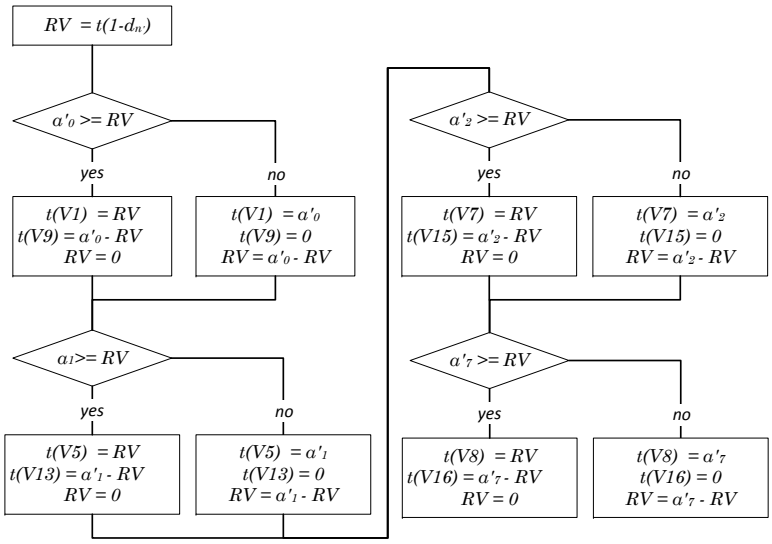

Figure 5.24: Time application algorithm for the application of the extended 2-D SVPWM obtained from α'_0, α'_1, α'_2, α'_7 and the complementary time of the duty cycle d_n

1. Step 1. Obtain application times of the vectors shown in Table 5.4.2 by setting one modulation index M using the algorithm presented in Figure 5.24. Then, apply the complementary to Equation 5.34.
   - It is recommended to use a predefined M using a positive sequence voltage about 0.8. This will represent the major cases if the output inductance is sized with a good trade-off between filtering and efficiency.
   - Select a voltage swing for M_h according to the maximum available homopolar current.
2. Step 2. Use the ripple expressions presented in Equation 5.51 in the $\alpha\beta\gamma$ reference frame.
3. Step 3. Translate the ripples obtained in step 2 to the natural reference frame. This has to be computed by using an inverse Clarke transform matrix according to the normalization chosen in step 2. Note that the proposed algorithm aggregate the partial application times, so it should be remarked that the obtained ripples if a up-down or up-down strategy is used should be divided by a factor 2.

4. Step 4. Decide the maximum desired ripple according to a maximum homopolar voltage.

An example is developed in order to clarify the aforementioned steps. For this example:

- Solid line. The homopolar phase shift in respect with the positive sequence is $\phi_h = 0$ rad.

- Dot line. The homopolar phase shift in respect with the positive sequence is $\phi_h = \pi/2$ rad.

- Dash line. The homopolar phase shift in respect with the positive sequence is $\phi_h = \pi$ rad.

- Dashdot line. The homopolar phase shift in respect with the positive sequence is $\phi_h = 3\pi/2$ rad.

and the green to blue colour degradation indicates that the u_h peak value is swept from 0 to 108 V, respectively. The example is as follows:

1. Step 1. Obtain application times of the vectors in four-legs. Equation 5.34 is applied considering:
   - u_{bus} is equal to 700 VDC
   - M is set to 0.8.
   - m_h is swept from 0 to 0.25 in ten steps.
   - ϕ_h is swept from 0 to 360 in eight steps.

   Figure 5.25 shows the application time of $t(1 - d_n)$ for different ϕ_γ angles in the example of the case study.

   Then, using the obtained application times of $t(1 - d_n)$ and the algorithm proposed in Figure 5.24 it is possible to determine the application times of each vector or state of the three-phase four-leg inverter α'_x . Figure 5.26 to 5.29 show the application times for vectors V1, V5, V7, V8, V9, V13, V15 and V16 under the proposed different m_h and ϕ_h values.

2. Step 2. To use the ripple expressions presented in Equation 5.51 considering α'_x as the applications times found in step 1. In this case, it

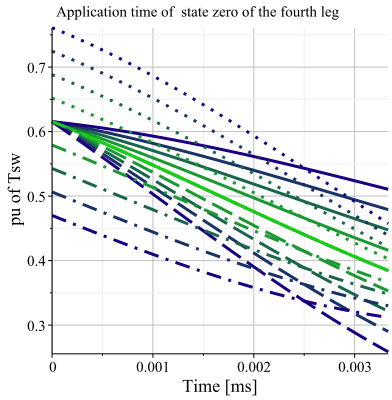

Figure 5.25: Application time of $t(1-d_n)$ in base of the switching period T_{sw} for different ϕ_h and m_h indexes

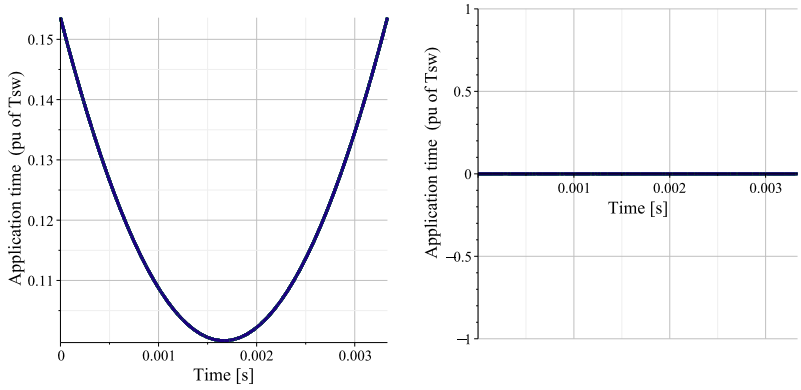

(a) V1 (b) V9

Figure 5.26: Application time of V1 and V9 in base of the switching period T_{sw} for different $\phi_h$and m_h indexes

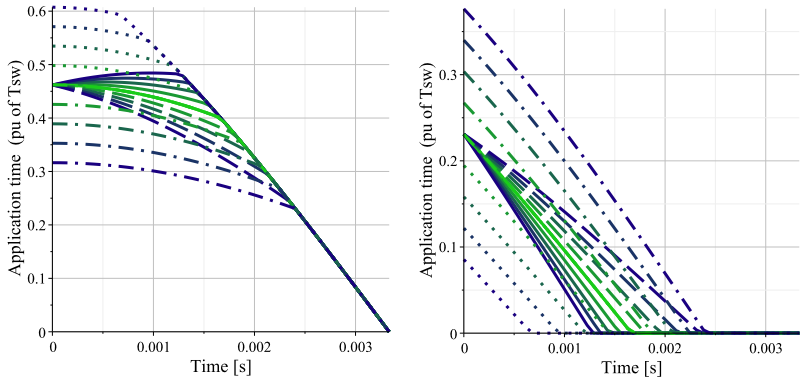

(a) V5 (b) V9

Figure 5.27: Application time of V5 and V13 in base of the switching period T_{sw} for different $\phi_h$and m_h indexes

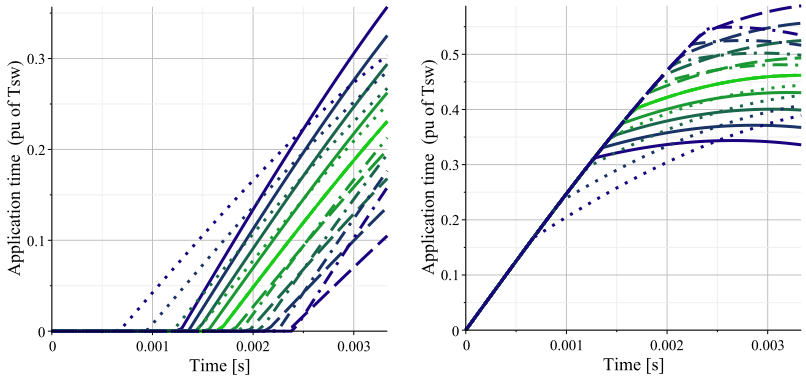

(a) V7 (b) V15

Figure 5.28: Application time of V7 and V15 in base of the switching period T_{sw} for different $\phi_h$and m_h indexes

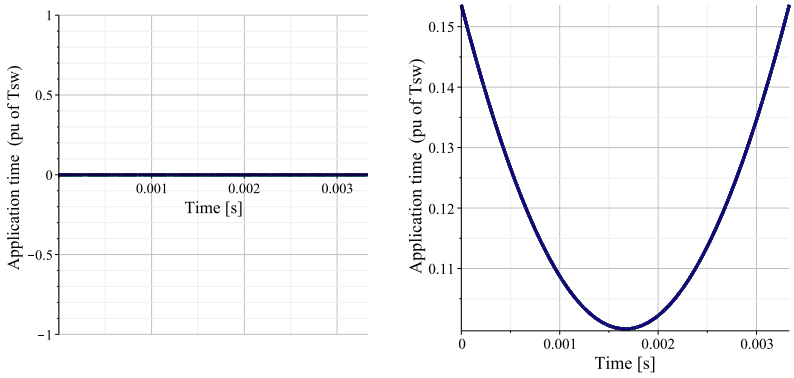

(a) V8 (b) V16

Figure 5.29: Application time of V8 and V16 in base of the switching period T_{sw} for different $\phi_h$and m_h indexes

has been selected the power invariant Clarke transform. For example, in case of V1, the ripples are

$$\Delta i_{\alpha_1} = \frac{u_{\alpha_1} - u'_{\alpha_1}}{Lf_{sw}}\alpha'_1 = -\frac{u_{bus}M\cos(\omega t)}{\sqrt{2}Lf_{sw}}\alpha'_1 \tag{5.52a}$$

$$\Delta i_{\beta_1} = \frac{u_{\beta_1} - u'_{\beta_1}}{Lf_{sw}}\alpha'_1 = -\frac{u_{bus}M\sin(\omega t)}{\sqrt{2}Lf_{sw}}\alpha'_1 \tag{5.52b}$$

$$\Delta i_{\gamma 1} = \frac{u_{\gamma 1} - u'_{\gamma 1}}{Lf_{sw}}\alpha'_1 = 0 \tag{5.52c}$$

or in case of V5

$$\Delta i_{\alpha_5} = \frac{u_{\alpha_5} - u'_{\alpha_5}}{Lf_{sw}}\alpha'_5 = \frac{\left(\frac{\sqrt{6}}{3} - \frac{M\cos(\omega t)}{\sqrt{2}}\right)u_{bus}}{Lf_{sw}}\alpha'_5 \tag{5.53a}$$

$$\Delta i_{\beta_5} = \frac{u_{\beta_5} - u'_{\beta_5}}{Lf_{sw}}\alpha'_5 = \frac{\left(0 - \frac{M\sin(\omega t)}{\sqrt{2}}\right)u_{bus}}{Lf_{sw}}\alpha'_5 \tag{5.53b}$$

$$\Delta i_{\gamma_5} = \frac{u_{\gamma_5} - u'_{\gamma_5}}{4Lf_{sw}}\alpha'_5 = \frac{\left(\frac{\sqrt{3}}{3} - 0\right)u_{bus}}{4Lf_{sw}}\alpha'_5 \tag{5.53c}$$

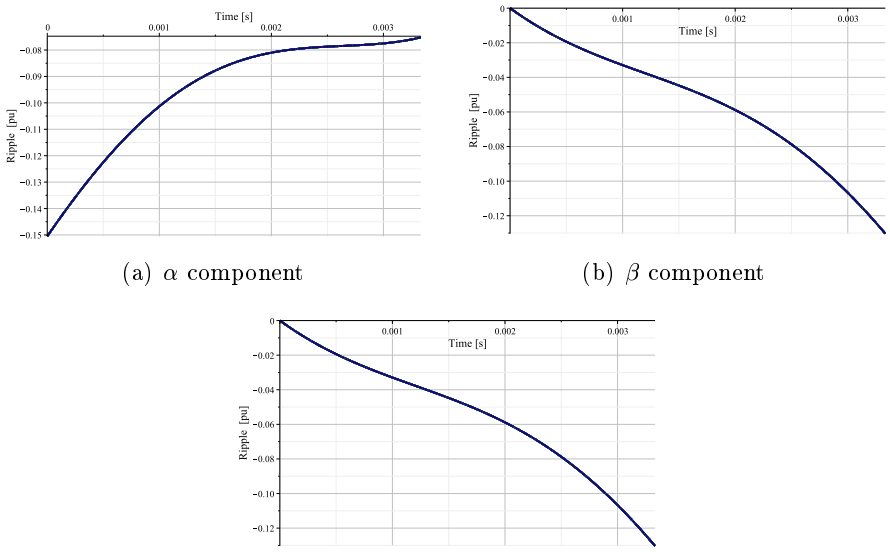

(a) α component

(b) β component

(c) γ component

Figure 5.30: Ripple in pu (base value ΔI_b) when V1 is applied ($\alpha\beta\gamma$ frame)

The same strategy can be applied to the rest of the vectors. Figure 5.30 to 5.34 shows the ripple in pu (using as base value Equation 5.47) when V1, V5, V7, V13, v15 are applied on the example (V8-V9 are not applied switching vectors in the case study and V16 output is null).

3. Step 3. To translate the ripples obtained in step 2 to the natural reference frame using the inverse Clarke transform T^{-1}. Unlike in Equation 5.46, now the γ component should be considered. Thus, the ripple in the natural uvw reference frame for any vector is

$$\Delta i_{u_{\mathrm{x}}} = \sqrt{\frac{2}{3}}\left(\Delta i_{\alpha_{\mathrm{x}}} + \frac{\Delta i_{\gamma_{\mathrm{x}}}}{\sqrt{2}}\right) \tag{5.54a}$$

$$\Delta i_{v_{\mathrm{x}}} = \sqrt{\frac{2}{3}}\left(-\frac{\Delta i_{\alpha_{\mathrm{x}}}}{2} + \frac{\sqrt{3}\Delta i_{\beta_{\mathrm{x}}}}{2} + \frac{\Delta i_{\gamma_{\mathrm{x}}}}{\sqrt{2}}\right) \tag{5.54b}$$

$$\Delta i_{w_{\mathrm{x}}} = \sqrt{\frac{2}{3}}\left(-\frac{\Delta i_{\alpha_{\mathrm{x}}}}{2} - \frac{\sqrt{3}\Delta i_{\beta_{V0}}}{2} + \frac{\Delta i_{\gamma_{\mathrm{x}}}}{\sqrt{2}}\right) \tag{5.54c}$$

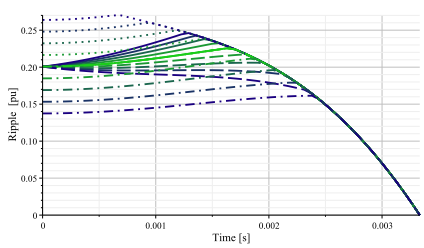

(a) α component

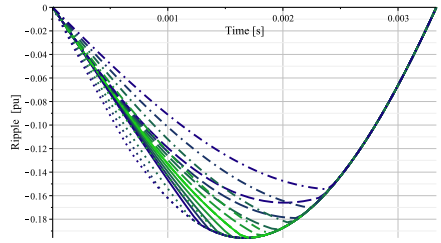

(b) β component

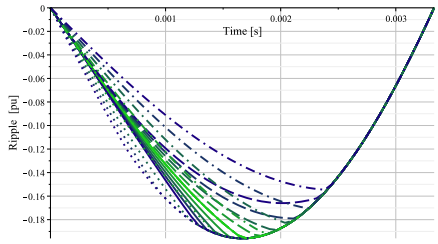

(c) γ component

Figure 5.31: Ripple in pu (base value ΔI_b) when V5 is applied ($\alpha\beta\gamma$ frame)

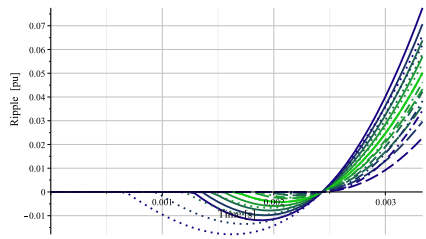

(a) α component

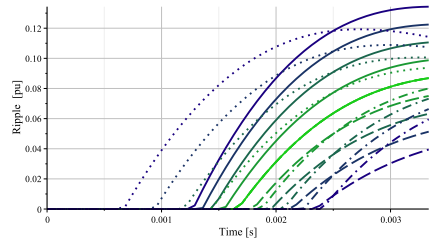

(b) β component

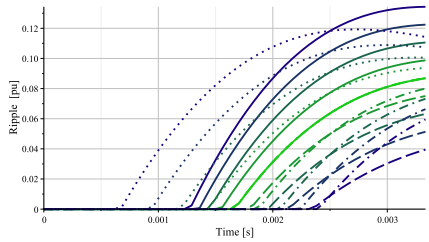

(c) γ component

Figure 5.32: Ripple in pu (base value ΔI_b) when V7 is applied ($\alpha\beta\gamma$ frame)

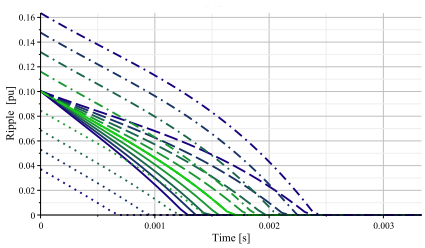

(a) α component

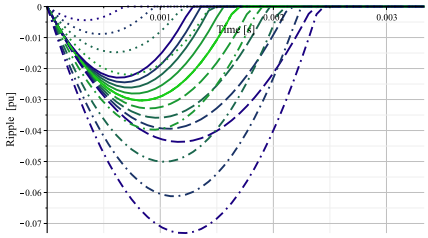

(b) β component

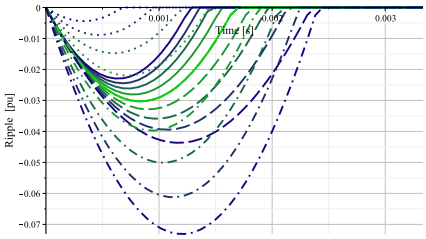

(c) γ component

Figure 5.33: Ripple in pu (base value ΔI_b) when V13 is applied ($\alpha\beta\gamma$ frame)

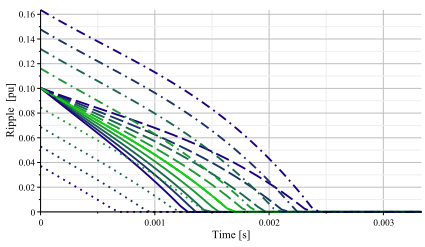

(a) α component

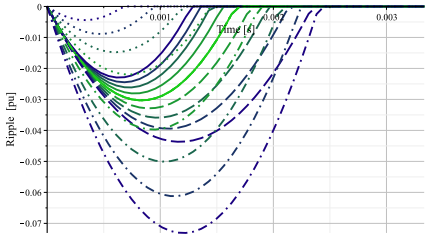

(b) β component

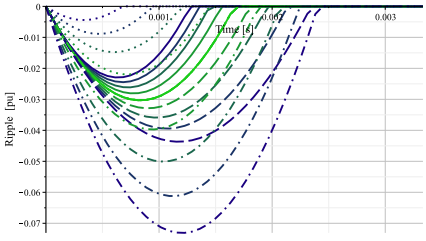

(c) γ component

Figure 5.34: Ripple in pu (base value ΔI_b) when V15 is applied ($\alpha\beta\gamma$ frame)

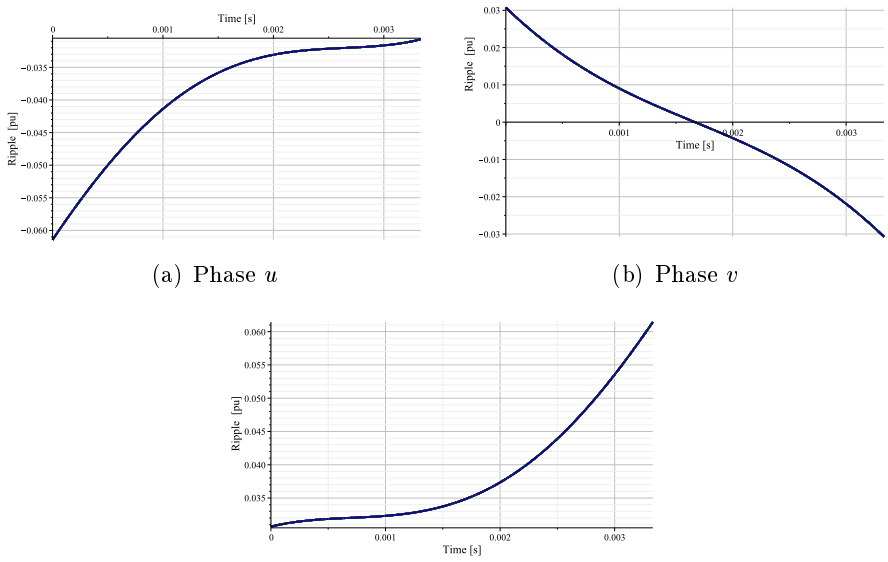

(a) Phase u

(b) Phase v

(c) Phase w

Figure 5.35: Ripple in pu (base value ΔI_b) when V1 is applied (uvw frame)

From the results obtained in steps 1 and 2 and applying Equation 5.54, Figure 5.35 and 5.39 shows the obtained ripples on the example. It should be remarked that the correction of the factor 2 is already applied on the showed plots.

4. Step 4. To decide the maximum desired ripple according to a maximum homopolar voltage. If step 3 is applied for all ϕ_h and to all corresponding first sextant vectors in the four-wire situation, the worst case occurs for Figure 5.36(a) supposing a ripple of 0.16 in pu, approximately. This means that, in real magnitude, the ripple is

$$\Delta I = \Delta i \Delta I_b = \Delta i \frac{u_{bus}}{\sqrt{3} L f_{sw}} \tag{5.55}$$

Thus, considering an average u_{bus} voltage equal to 700 VDC, a switching frequency of 8 kHz and a maximum desired ripple of 32 A, the obtained inductance is

$$L = \frac{0.16 \cdot 700}{\sqrt{3} \cdot 32 \cdot 8000} \approx 250\ \mu\text{H}$$

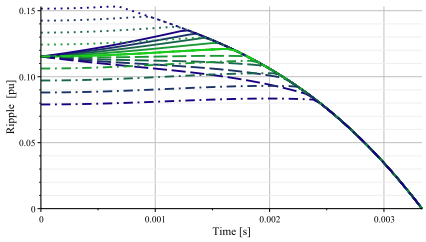

(a) Phase u

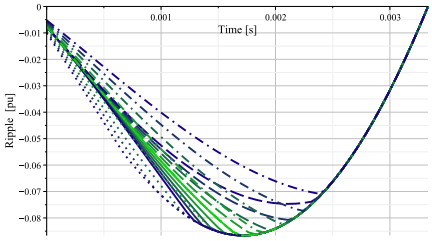

(b) Phase v

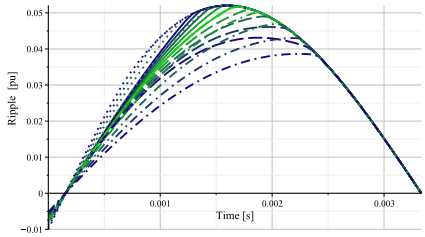

(c) Phase w

Figure 5.36: Ripple in pu (base value ΔI_b) when V5 is applied (uvw frame)

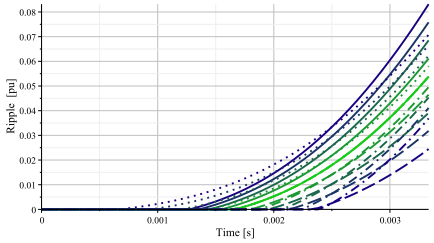

(a) Phase u

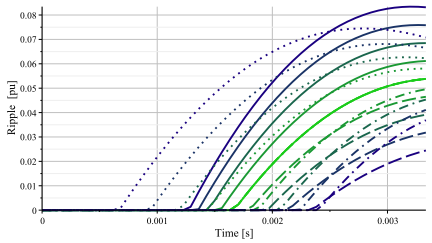

(b) Phase v

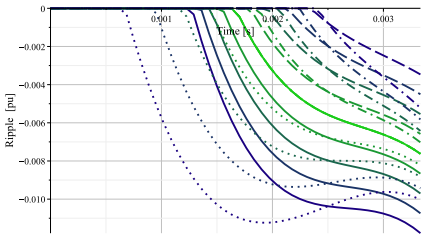

(c) Phase w

Figure 5.37: Ripple in pu (base value ΔI_b) when V7 is applied (uvw frame)

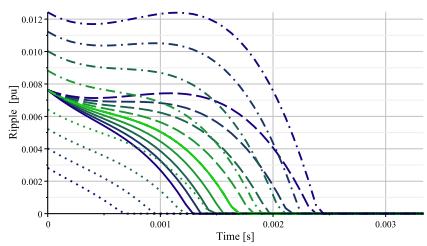

(a) Phase u

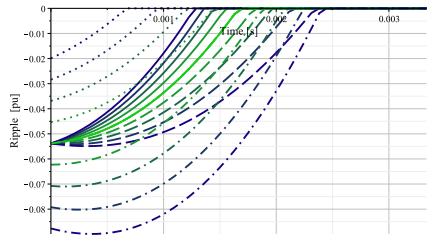

(b) Phase v

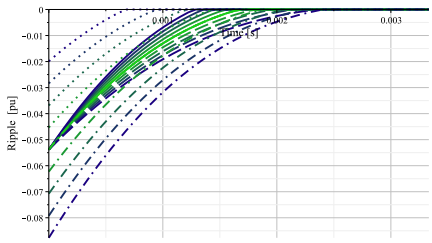

(c) Phase w

Figure 5.38: Ripple in pu (base value ΔI_b) when V13 is applied (uvw frame)

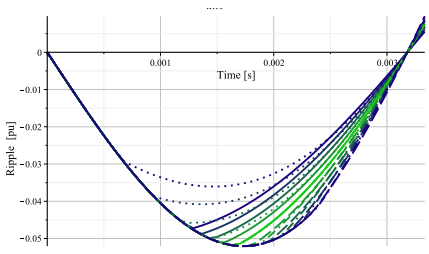

(a) Phase u

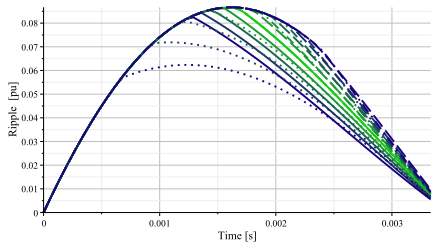

(b) Phase v

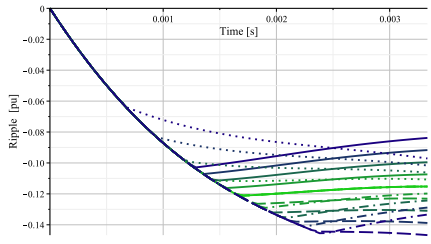

(c) Phase w

Figure 5.39: Ripple in pu (base value ΔI_b) when V15 is applied (uvw frame)

This inductance will be the one chosen for the active phases and the neutral wire of the converter.

The grid inductance design

The grid side inductance is predetermined by the leakage inductance of the transformer.

According to Figure 5.2, three independent 50 kVA transformers in a triplex configuration are proposed. In this case, after the short-circuit test, the obtained value is L_2 equal to 70 μH.

The AC capacitor design

If the transfer function between the delivered current and the output current is computed

$$G(s) = \frac{I_{L2}(s)}{I_{L1}(s)} = \frac{1}{CL_2s^2 + 1} \tag{5.56}$$

Computing the isochronous transfer function substituting s by $j\omega$, the gain can be computed as

$$\frac{I_{L2}(\omega)}{I_{L2}(\omega)} = \frac{1}{-CL_2\omega^2 + 1} \tag{5.57}$$

If an attenuation of 99.5% wants to be achieved at the switching frequency of 8 kHz,

$$\frac{I_{L2}(\omega)}{I_{L2}(\omega)} = \left| \frac{1}{-CL_2\omega^2 + 1} \right| = 0.015 = G \tag{5.58}$$

Considering $L_2 = 70$ μH and that the switching frequency is at the right of the resonance where $\omega^2 = L_2C$, the capacitor is

$$C = \frac{\frac{1}{G} + 1}{\omega^2 L_2} \approx 382\,\mu\text{F} \tag{5.59}$$

On the other hand, assuming that the rated voltage at the AC side is 230 VAC and a maximum reactive consumption by the capacitor bank of 10% of the maximum power of the inverter, i.e 135 kVA divided by 3, the X_c impedance should be about 11.7 Ω. This implies about 270 μF.

Although, the reactive consumption is a little bit high, the chosen size of the AC capacitor is 350 μF. This results a trade-off between the previous obtained values. It also results crucial for short-circuit proof algorithms

Element	Value	Units
L_1	250	μH
C	350	μF
L_2	70	μH

Table 5.9: Final LCL-type coupling filter parameters

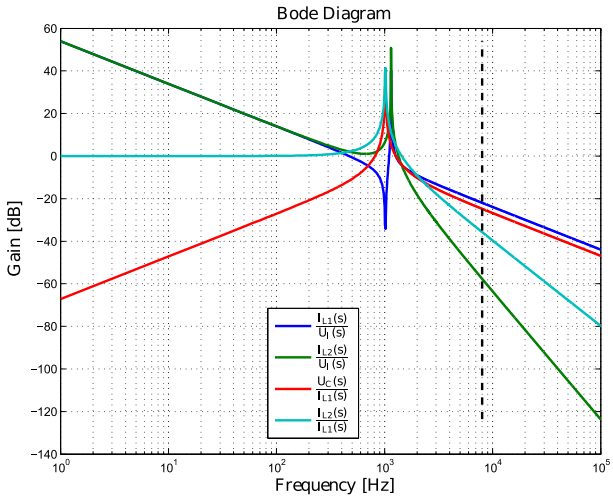

Figure 5.40: Relevant trasnfer functions of the final LCL-type coupling filter

to provide, in terms of hardware, enough electrical inertia when a fault is produced in grid-disconnected mode. On the other hand, the reactive consumption can be compensated when grid-connected at expenses of drop the efficiency.

The LCL-type coupling filter final design

After all the previous analysis, the final proposed LCL-type coupling filter according to the selected modulation are summarised in Table 5.9. Figure 5.40 shows different interesting transfer functions for the selected parameters. The vertical black dashed line marks the switching frequency chosen of 8 kHz.

As indicated in [120], it is recommended that

$$10f_{\text{base}} \leqslant f_0 \leqslant f_{sw}/2 \tag{5.60}$$

where f_{base} represents the maximum frequency that wants to be controlled,

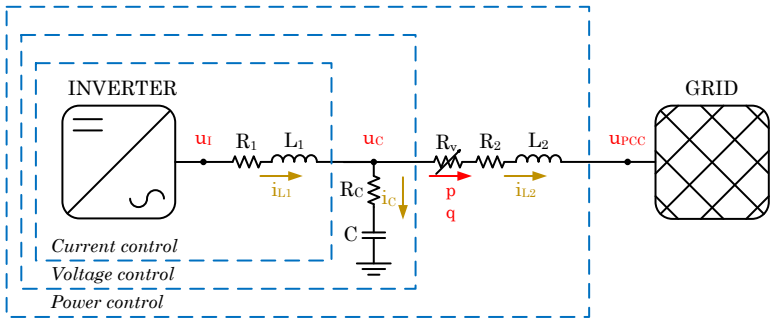

Figure 5.41: Proposed general conceptual control scheme

f_0 the resonance frequency and f_{sw} the switching frequency. As will be detailed in the next chapters, only the third and fifth harmonics would be controlled. Considering a nominal frequency of 50 Hz, all the inequalities proposed in Equation 5.60 are accomplished.

5.5 Three-phase four-wire DC/AC inverter control

The proposed three-phase four-leg hardware topology will be controlled by means of three independent single phase systems in order to provide direct, inverse and homopolar voltage sequence control capability. Each phase has its own adaptive AC droop controller [66, 238] in grid-connected operation. Also, two inner cascaded proportional-resonant controllers, for voltage and current control, in grid-connected and grid-disconnected operation are considered, respectively. Thus, the inverter will operate as three non-ideal voltage sources in grid-connected mode and as an ideal source in grid-disconnected mode.

For this section, the general scheme of Figure 5.41 will be assumed. Note that it is, basically, the one shown in Figure 2.18 but with a little modifications including a new virtual resistance R_v that is detailed in the following lines.

5.5.1 The power control loop for grid-connected operation

Proposal

The non-adaptive AC droop control operation presents some inconveniences. As has been detailed in Chapter 2, it only considers steady-state. For this reason, a dynamic droop with a dynamic phasor model is adopted. The

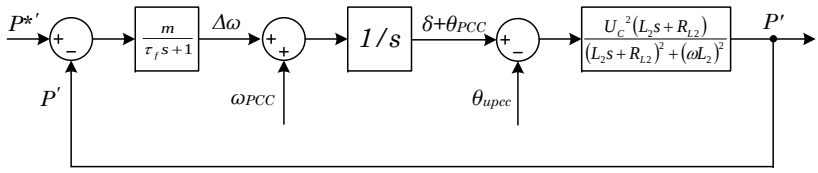

(a) Active power close loop system

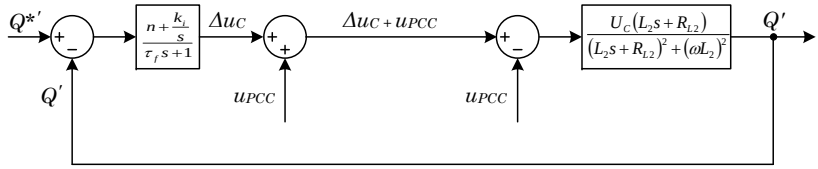

(b) Reactive power close loop system

Figure 5.42: Power close loop systems under a dynamic phasor model for the resistive line case after the rotation matrix is applied

proposed control scheme for the power loop considers a predominant resistive line according to Figure 5.42, where m and n represents the proportional droop constants for the active and reactive loops, respectively. The k_i is an integral gain justified in the following lines. Notice that a low-pass filter has been added in order to emulate the inertia when big synchronous generators are used in conventional lines. This low-pass filter follows

$$G_{\mathrm{LPF}}(s) = \frac{1}{\tau_f s + 1} \tag{5.61}$$

being τ_f the time constant.

However, considering that the grid-side inductance L_2 is constituted, essentially, by the leakage inductance of the transformer and its equivalent series resistance, the obtained PQ model is coupled, as depicted in Figure 2.31(a), and Figure 5.42 conducts to errors. In order to avoid this situation, a virtual resistance R_v is added to ensure the resistive behaviour of the system. Although a decoupled scheme is obtained, practically without rotation because $\varphi \approx 0$ when a predominant resistive model, see Equation 2.17, the rotated variables $P'Q'$ are used to maintain positive plants and positive controller constants. In this sense, Figure 5.43 shows the voltage generation reference for the AC capacitor and in Figure 5.44 is depicted the open loop virtual resistance concept. In this sense, $u_c{}^*$ is equal to u_{droop} of Figure 5.43 and u_C represents the voltage Set-Point (SP) for the inner voltage loop yielding to

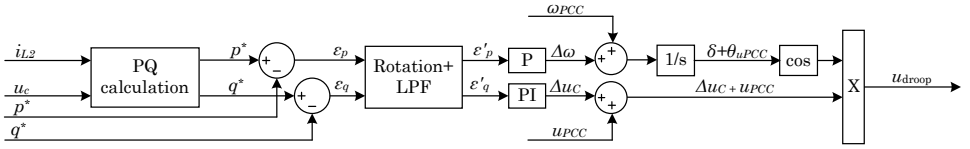

Figure 5.43: Scheme of the P/Q droop control with hot-swap for booting-up AC voltage capacitor reference generation

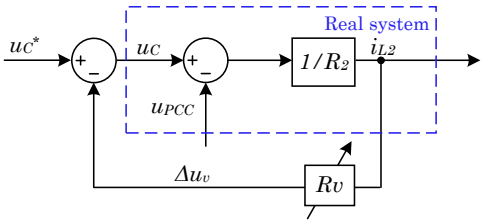

Figure 5.44: Virtual resistance added at the generataed reference from the dynamic droop loop

$$u_{\text{droop}} = u_C^{SP} - i_{L2} R_v \tag{5.62}$$

Other options as as virtual impedances, for instance, inductive impedances, are not considered by practical implementation problems as noise amplification when derivative terms are applied.

The objective of the virtual output impedance is not only change the output line behaviour but also to limit the dynamics of the hot-swap, to smooth the transference between operation modes without producing real losses and to reduce possible resonance downstream the capacitor connection. The proposed algorithm consists in a high initial virtual series resistance that is used to start-up the system from a black-out or from grid-disconnected operation when the system starts to operate in the grid-connected mode. The effect of a high virtual resistance implies low inrush currents and slow dynamics compared with the desired one when the system is operated in steady-state and a new set-point is required. In this sense, when a VSI with this control strategy is connected to a microgrid where there are other inverters already operating it will start to operate in a progressive way. Figure 5.45 shows a comparison for the active power close loop of Figure 5.42. Then, this virtual resistance is decreased until a minimum level is reached. This minimum threshold represents a trade-off between damping, dynamics and the line

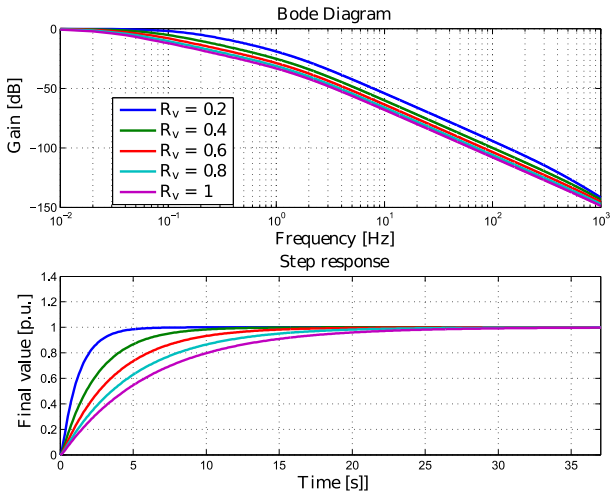

Figure 5.45: Analysis of the effect of modify R_v from the start-up value to the steady state-value for a rotated and decoupled active power close loop resistive model. R_v is swept from 0.2 to 1 Ω, m is set to 0.000003, U_C is set to 230 V and $\omega = 100\pi$ rad/s

characterization. When the system operates in the grid-disconnected mode, during some time the virtual series resistance will be decreased continuously until a null value is obtained.

Design and simulations

It is proposed that the equivalent series resistance and the virtual resistance added sums about one magnitude order higher than the inductive impedance. Then, considering a 50 Hz line, the corresponding inductive impedance is

$$X_{L2} = 2\pi f L_2 = 0.022\ \Omega \tag{5.63}$$

the steady-state virtual resistance considered is 0.2 Ω.

The time constant τ_f for the filter has been set to 100 ms limiting any fast dynamics when a new set-point is required. Thus, from the models presented in Figures 5.42 it is possible to deduce the characteristic equation for the active power

$$s(\tau_f s + 1)((sL_2 + R_2')^2 + (\omega L_2)^2) + m\omega L_2 U_C^2 = 0 \tag{5.64}$$

and for the reactive power when k_i is null

$$(\tau_f s + 1)((sL_2 + R_2')^2 + (\omega L_2)^2) + n\omega L_2 U_C^2 = 0 \tag{5.65}$$

where R_2' represents the equivalent series resistance obtaiend by the addition of the real resistance R_2 and the virtual resistance R_v. In the active power case, see Figure 5.42(a), it can be observed that the frequency control chain includes a pure integrator in the direct control chain to obtain the angle of the voltage to be synthesized. Moreover, in the case of reactive power this does not occur, see Figure 5.42(b). For this reason, an integrator is usually added in order to obtain a zero steady state error although the system is not operating at the design point, obtaining the adaptive AC droop control approach. Then, a proportional-integral controller for the reactive case is used. This integrator has to be properly managed in grid-disconnected mode when the droop strategy is used in both modes (grid-connected and disconnected). This is because the local load will not match with the reference. Then, the characteristic equation for the reactive power becomes

$$s(\tau_f s + 1)((sL_2 + R_2')^2 + (\omega L_2)^2) + ns\omega L_2 U_A^2 + k_i \omega L_2 U_C^2 = 0 \tag{5.66}$$

being k_i the integral constant of the proposed PI controller for the reactive loop.

Considering the parameters summarised in Table 5.5.1, the simulated dynamics shown in Figure 5.46 for the active and reactive loops are obtained. In this case, a dynamics with a time constant of around 1 s is achieved for both power control loops.

As has been aforementioned, the inner control loop is composed of two nested control loops. The voltage control loop, or outer, fixes the output voltage from the reference voltage provided by the droop controller, remind Figure 5.43 and 5.44. As can be seen in Figure 5.41, this voltage is set at the capacitor of the output LCL filter. The inner control loop concerns the current loop through L_1.

The voltage and the current control loops are implemented in then natural *uvw* stationary reference frame. To obtain the required dynamics, Proportional-Resonant (PR) controllers with Harmonic Compensation (HC) have been used to follow the sinusoidal voltage references and possible distorted currents. Other control strategies can be applied. However, PR controllers are widely used in time-varying reference tracking, as is discussed in Chapter 4. From Chapter 2 it can be deduced that the plant model changes when positive/negative or zero sequence wants to be controlled. It has been

	Parameter	Value	Units
Droop controller	m for active power loop	0.000003	
	n for reactive power loop	0.000004	
	k_i for reactive power loop	0.0009	
PRHC Voltage controller	k_p	0.27	
	k_{i_0}	0.26	
	k_{i_3}	0.001	
	k_{i_5}	0.001	
PRHC Current controller	k_p	0.7468	
	k_{i_0}	3.93	
	k_{i_3}	0.1	
	k_{i_5}	0.04	
Short-circuit algorithm	K	0.9	
	I	130	A
Virtual impedances	R_v (initial-state grid-connected)	1.0	Ω
	R_v (steady-state grid-connected)	0.2	Ω
	R_v (grid-disconnected)	0	Ω
	R_v change ratio	±0.16	Ω/s
	R_{Cv}	0.1	Ω
DC/AC converter	Switching & control frequency	8	kHz
	L_1 (active phases & neutral wire)	250	μH
	ESR_{L_1}	50	mΩ
	C (star connected)	350	μF
	L_2 (leakage transformer inductance)	70	μH
	ESR_{L_2}	50	mΩ

Table 5.10: Four-wire DC/AC converter parameters

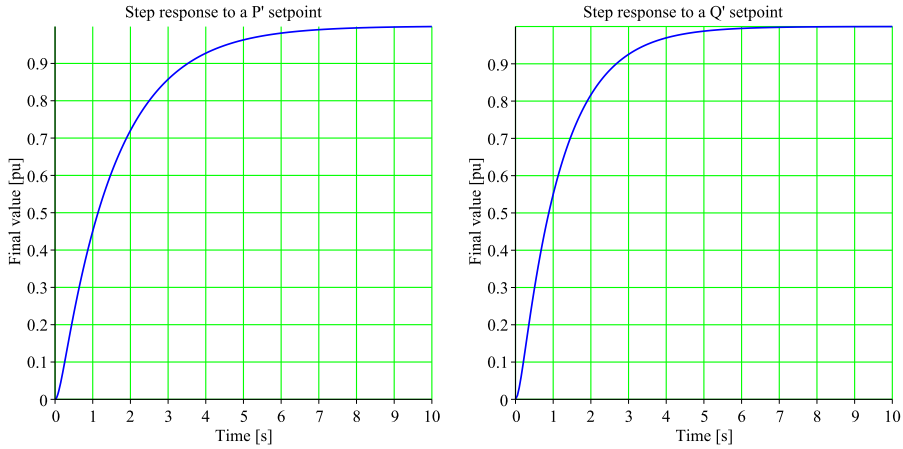

(a) Active power loop P' (b) Reactive power loop Q'

Figure 5.46: Step responses for the power loops in the rotated frame

Parameter	Value	Units
Damping factor ξ	0.80	
Settling time t_{set} ($\pm 2.00\%$ of the final value)	2	ms
Switching frequency f_s	8.00	kHz

Table 5.11: Parameters for the current loop tune (L_1)

considered to tune the voltage and current loops according to positive (or direct) sequence and maintain the gains for the zero sequence cases.

The current loop

Considering the discrete time control scheme presented in Figure 3.14, the tuning procedure proposed in [43] (see Equations 3.58 to 3.68) and the parameters summarised in Table 5.11, the resulting controller gains are $k_{p_i} = 0.7468$ and $k_{i_i} = 3.9310$. Figure 5.47 shows a simulation with a step produced when the time is 10 ms and 25 ms considering that the system disposes of an ideal feed-forward and the output inductance can be treated as short-circuited. The first step matches with a zero-crossing of the reference and the second one with a peak. In both cases can be verified that in the expected 2 ms the response is inside a $\pm 2\%$ of the final value, see red dashed line on the error analysis.

The voltage loop

Considering the discrete time control scheme presented in Figure 3.14, assuming the inner current loop as a unity gain and taking into account the extended tuning procedure proposed in this thesis for the voltage loop, detailed in Section 3.3.5 (see Equations 3.71 to 3.76), and setting the parameters summarised in Table 5.12 the resulting controller constants are $k_{p_v} = 0.2665$ and $k_{i_v} = 0.2650$. Figure 5.48 shows a simulation with a step produced when the time is 10 ms and 45 ms considering that the system disposes of an ideal feed-forward and, consequently, the AC capacitor can be treated as it operates in open loop. Also, the inner loop is considered as an unit gain. The first step matches with a zero-crossing of the reference and the second one with a peak. In both cases can be verified that in the expected 10 ms the response is not inside a $\pm 2\%$ of the final value, see red dashed line on the error analysis. This is due to the change of sign of the error during the tracking, as has been detailed in Chapter 3. However, in

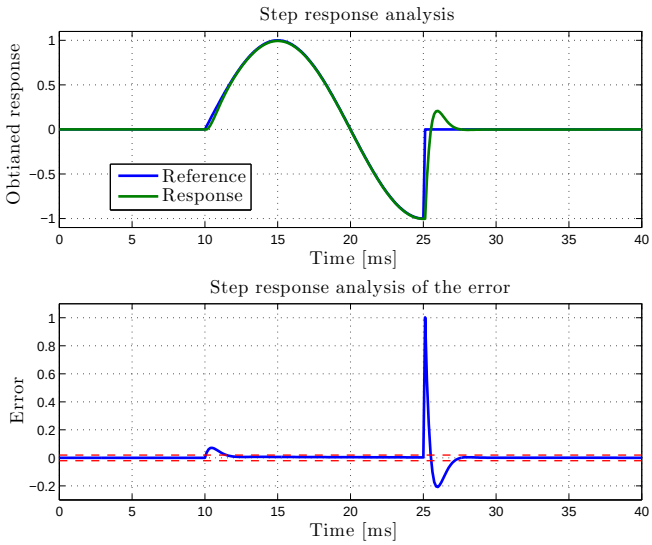

Figure 5.47: Step response analysis for the current loop according the parameters exposed in Table 5.11 assuming that the output inductance L_1 is short-circuited

Parameter	**Value**	**Units**
Damping factor ξ	0.80	
Settling time t_{set} ($\pm 2.00\%$ of the final value)	10.0	ms
Switching frequency f_s	8.00	kHz

Table 5.12: Parameters for the voltage loop tuning

about 20 ms the system is inside an acceptable threshold of $\pm 2\%$ of the final value, being the voltage loop tune accepted.

The inter-harmonic excitation challenge under PR operation

When multiple harmonic compensators are used in the stationary reference frame an inter-harmonic excitation appears [239]. Figure 5.49 shows the aspect of the inter-harmonic excitation when the third and the fifth HC are added to the fundamental PR controller, also developed in Chapter 3. The image considers that the integral gain constant of the k harmonics is $k_{i_k} = k_{i_0}/k$ either for the current or the voltage control loop.

One option is to decrease the HC integral gains heuristically to attenuate

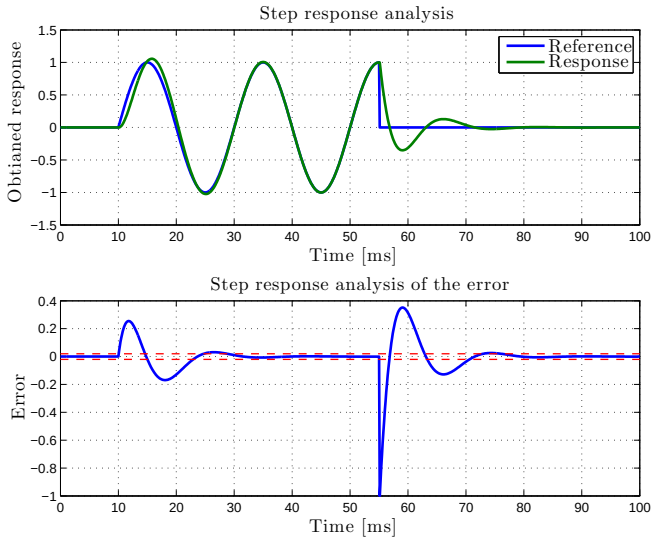

Figure 5.48: Step response analysis for the voltage loop according the parameters exposed in Table 5.12 assuming that the AC is without load and ideal inner loop

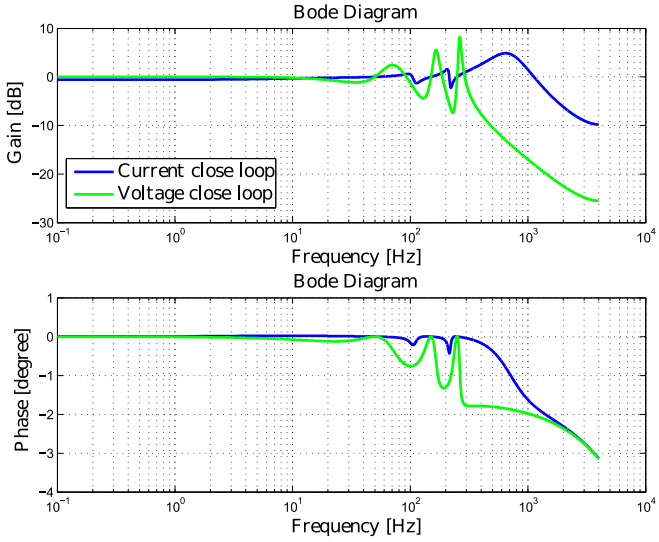

Figure 5.49: Inter-harmonic excitation when a PR-HC controller is used. Included fundamental component plus the third and the fifth HC

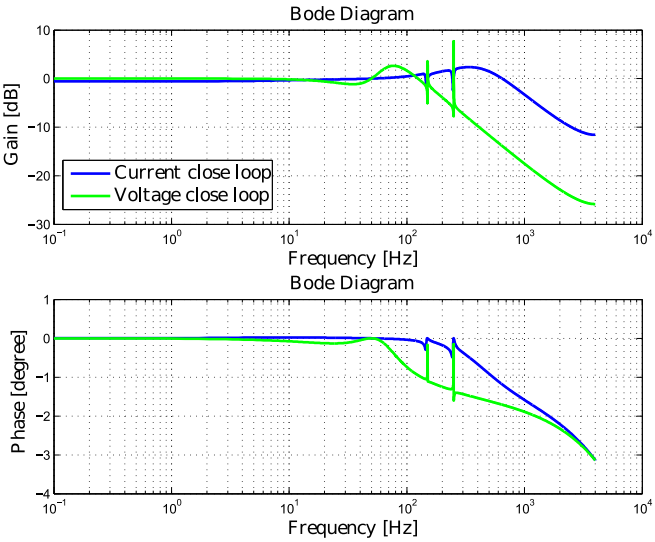

Figure 5.50: Inter-harmonic excitation when a PR-HC controller is used when ki_{i_k} are reduced in respect with the theoretical values. Included fundamental component plus the third and the fifth HC

a little bit the inter-harmonic effect. Figure5.50 shows the results when ki_{i_3} is set to 0.1, ki_{i_5} to 0.04 and ki_{v_3} or ki_{v_5} to 0.001. This solution affects to the dynamics of the harmonic compensation.

Other options is to attenuate possible resonances. To damp frequencies exists different alternatives when an LCL-type filter is used; apply passive or active damping elements or use a control structure that minimizes the inter-harmonic excitation. In this case, a virtual active series resistor using the current of the AC capacitors, i_C, is added at the current loop according to [240]. The objective is to avoid translating as much as possible any current excitation from the system to the utility. Figure 5.51(a) shows the proposed active damping model. The converter current reference $i^*_C(k)$ is

$$i^*_{L1}(k) = i_{L1}(k) - \frac{CR_{C_v}}{T_{sw}}\left(i_C(k) - i_C(k-1)\right) \tag{5.67}$$

k indicates the sampling instant and R_{C_v} the virtual equivalent series resistance of the capacitor. Note that Equation 5.67 represents an open loop control law. In this sense, $i^*_{L1}(k)$ is the final reference for the current loop while $i_{L1}(k)$ has to be substituted by the current reference obtained form the

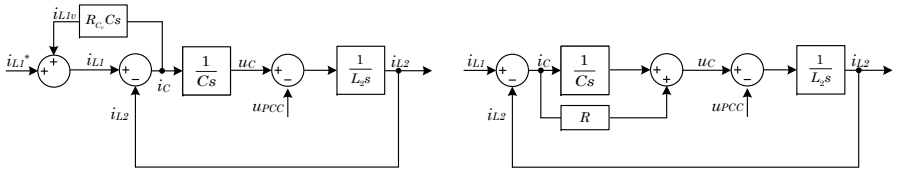

(a) Proposed active resistive damping in series with the capacitor model in [240]

(b) Passive resistive damping in series with the capacitor model

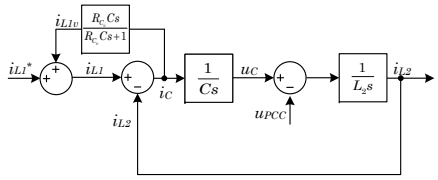

(c) Complete active resistive damping in series with the capacitor model

Figure 5.51: Series resistive damping models for the AC side capacitor when a LCL-type coupling filter is used

control action of the voltage loop. It should be clarified that Equation 5.67 is obtained by using a backward-Euler derivative term

$$s = \frac{z-1}{zT_{sw}} \tag{5.68}$$

It should be noted that the I_C value is computed because the system does not provide a measure of these currents, see Figure 5.4. Although [240] proposes Equation 5.67, it should be clarified that is not valid fow all operation parameters. In fact, the correct equivalent model to a passive damping, as the one shown in Figure 5.51(b), is the one depicted in Figure 5.51(c). If the virtual current i_{L1v} is computed for Figure 5.51(c)

$$\frac{I_{L1v}(s)}{I_C(s)} = \frac{R_{C_v}C(1-z^{-1})}{(R_{C_v}C+T_{sw})-R_{C_v}Cz^{-1}} \tag{5.69}$$

and for Figure 5.51(a) yields to

$$\frac{I_{L1v}(s)}{I_C(s)} = \frac{R_{C_v}C(1-z^{-1})}{T_{sw}} \tag{5.70}$$

When $T_{sw} >> R_{C_v}C$ Equation 5.69 behaves like Equation 5.70.

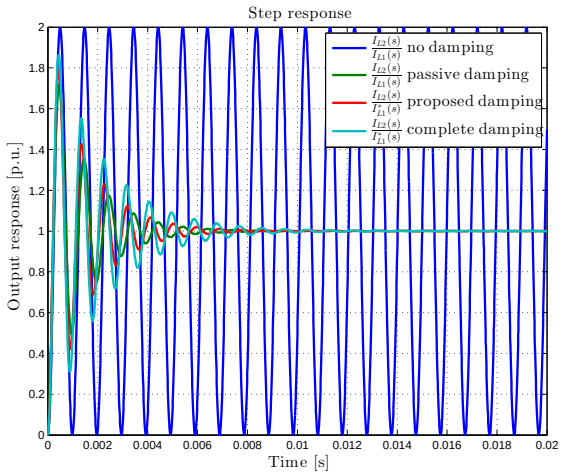

Figure 5.52: Step response comparison when resistive damping in series with the capacitor

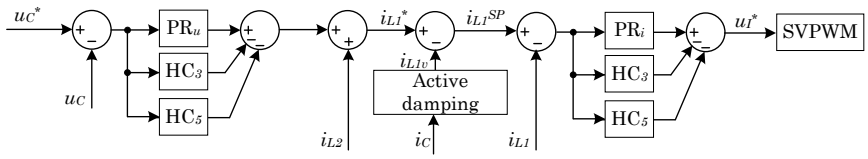

Figure 5.53: Scheme of inner control loops for normal operation in grid-connected mode

In this case, if the the R_{C_v} is set to 0.1 Ω, the capacitor is about 350 μF and the T_{sw} is determined by 8 kHz^{-1}, the proposed model of Figure 5.51(a) results sufficient accurate, as can be seen in Figure 5.52.

It is proposed to use both alternatives; reduce HC gains and introduce active damping. According with all previous sections, the final set-point generator scheme for the inner loops is depicted in Figure 5.53. It should be reminded that the virtual resistance change the output model behaviour for the outer droop control when grid-connected and that the active damping enhances the output current attenuation that can be excited by the inherent operation of the PR controllers in grid-(dis)connected operation.

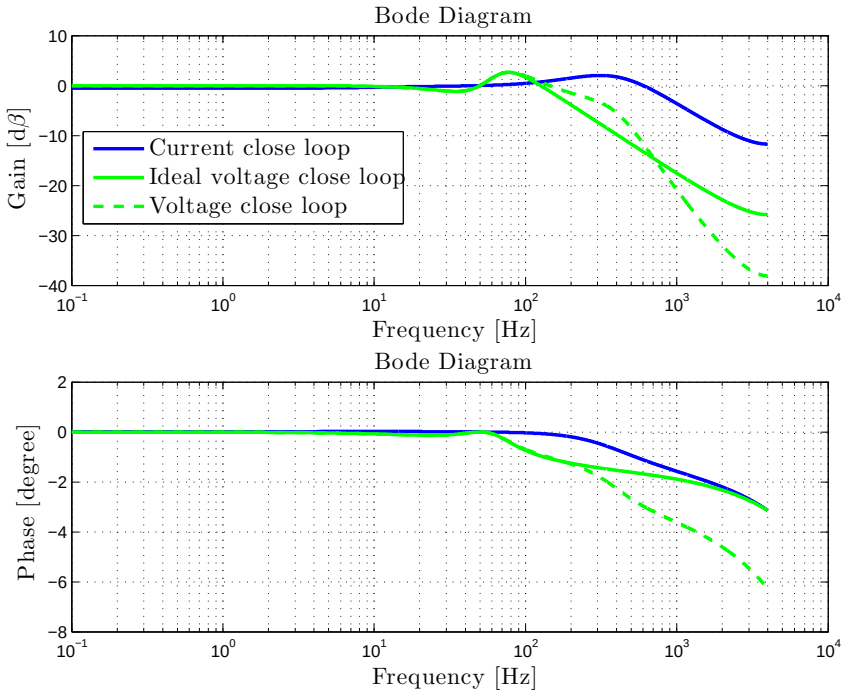

Figure 5.54: Discrete time close loop bode diagrams for the current and voltage close loop (only fundamental component)

Validation of decoupled double loop

In order to ensure that there is a minimum interference between the two nested loops it is recommended not only that the settling time of the outer loop has to be slower than the inner one but also to decouple close-loop bandwidths. In this sense, the inner loop bandwidth (-3 dB) should be at least two times the outer one (recommended 10 times). Figure 5.54 represents the current and voltage close loop bode diagrams. In this figure it is represented the voltage loop when the inner one is considered as a unity gain and when the full current close loop is taken into account. It can be seen that, in the worst case, there are around 500 Hz between the voltage close loop (290 Hz) and the current close loop (951 Hz) bandwidth. Then, the inner loops are considered properly tuned.

5.5.2 Special control features

This section will detail the proposed algorithms to provide a microgrid VSI with controlled over-load and short-circuit proof capabilities.

Over-load capability

In the grid-connected mode, one important challenge is the management of the active/reactive power target values. External per phase active/reactive power references are provided to the converter. The consistency of these references is first checked, mainly, by two possible reasons. First the active power is limited but this action is not enough. Also the current must be limited in order to not destroy the converter. The current limitation is done by means of apparent power s (in per unit).

- Active power limitation. The active power must not exceed the maximum power available from the storage system as

$$-u_{bat} i_{max\,dch\,bat} < (p_u + p_v + p_w) < u_{bat} i_{max\,ch\,bat} \tag{5.71}$$

  where u_{bat} is the battery voltage, $i_{max\,dch\,bat}$ is the maximum battery discharge current provided by the Energy Management System (EMS) of the storage system, $i_{max\,ch\,bat}$ is the maximum battery charge current provided by the EMS and p_u, p_v and p_w are phase u, v and w active power references, respectively. When Equation 5.71 is not fulfilled, the three power references are equally saturated and a warning signal is generated and sent to the MGCC.

- Current limitation. An overload observer, ol_o, will limit the power per phase. It will fulfil this task by means of a calculation based on the i^2t computation as

$$ol_o = \int_0^t \left(i^{*2} - 1\right) dt \tag{5.72}$$

  where ol_o is an indicator of the overload energy exchanged, i^* is the desired current and t is the interval time of the over-current. Time t begins when $|s^*| > 1$, being s^* the maximum apparent power per phase reference. The algorithm that handles the overload mechanism is managed according to the state diagram depicted in Figure 5.55. When $|s^*| > 1$, the observer wakes-up and starts to compute ol_o according to Equation 5.72 and ol_t that is the accumulative time under the over-load situation. If the ol_o value reaches zero, the observer returns to a sleep stage, where ol_o and ol_t are reset. If the ol_o is bigger

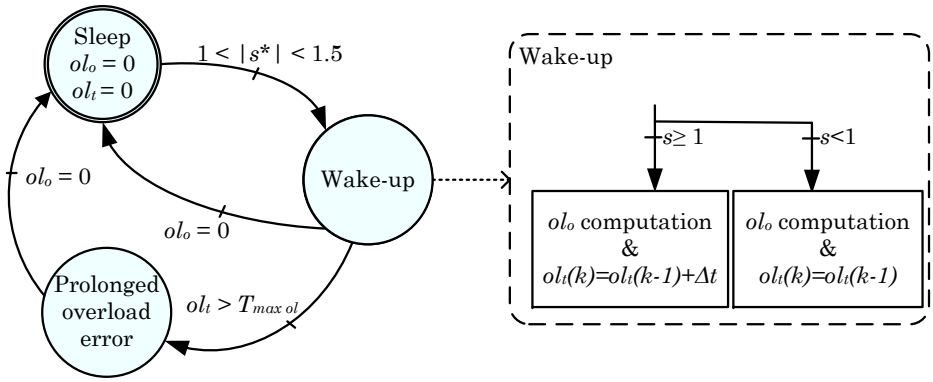

Figure 5.55: Scheme of the overload algorithm

than zero, depending on the present s value, the accumulated time ol_t is incremented or maintained. Keeping constant the ol_t time, it is ensured that the VSI is not over-loaded intermittently producing a possible degradation by thermal reasons. In case that the ol_t becomes higher than a pre-set threshold $T_{max\,ol}$, the system evolves to the Prolonged overload error state and it is internally limited. This limitation is in terms of maximum apparent power. This situation is transmitted to the MGCC. Figure 5.56 shows the behaviour of the algorithm presented in Figure 5.55.

Short-circuit proof capability

When the VSI is grid-disconnected operated, it must set the microgrid voltage and frequency. In this operating mode, the converter must not only provide sinusoidal currents when overload but also when short-circuited. In this sense, Figure 5.57 shows the proposed block diagram of the algorithm that implements the short-circuit proof algorithm considering, also, sinusoidal current control (in blue the new parts added to the scheme presented in Figure 5.53). The algorithm is based on the per phase rms value of the reference current, i^*, and two gains k_1 and k_2. The first gain k_1 allows to regulate the voltage target in order to attenuate it under short-circuit or high over-load, as follows

$$k_1 = \begin{cases} 1 & \text{if} \quad i_{\text{rms}} \leq I \\ (K+1) - \frac{K}{I} i_{\text{rms}} & \text{if} \quad I < i_{\text{rms}} < (K+1)\, I \\ 0 & \text{if} \quad i_{\text{rms}} \geq (K+1)\, I \end{cases} \tag{5.73}$$

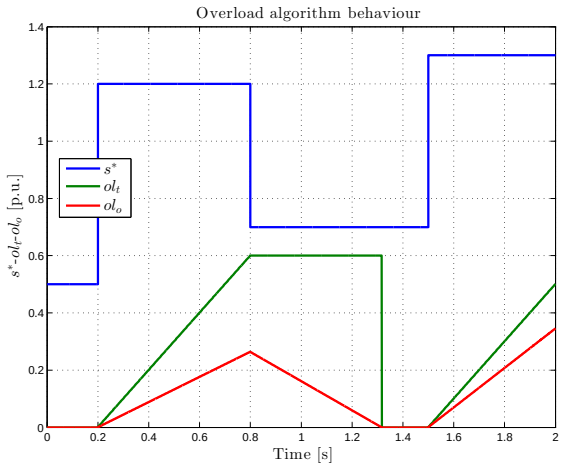

Figure 5.56: Example of the behaviour of the overload algorithm

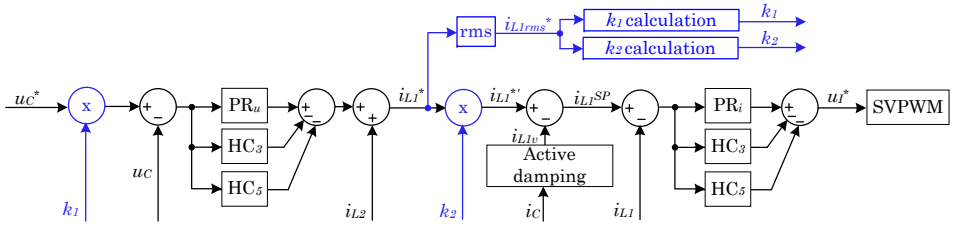

Figure 5.57: Short-circuit proof implementated algorithm

where I is the maximum desired rated output current (at the L_1 inductance). In this sense, it is possible to obtain a dynamic adaptation to the load connected voltage at the controlled voltage node u_C and, consequently, at the PCC. The parameter K in k_1 calculation allows to adapt the speed of response of the system to face short-circuits. However, the higher the K value, the higher an undesired oscillation in k_1 appears.

The second gain $k2$ limits the current to the rated valued when short-circuit as

$$k_2 = \begin{cases} 1 & \text{if} \quad i_{rms} < I \\ \frac{I}{i^*_{L1rms}} & \text{if} \quad i_{\text{rms}} \geq I \end{cases} \tag{5.74}$$

However, if only this action is taken into account, the behaviour when a fault recovery appears is undesired. This is due the fast response of the k_1 gain. To avoid this dynamic, when the current $k_{1in}(k)$ value is higher than

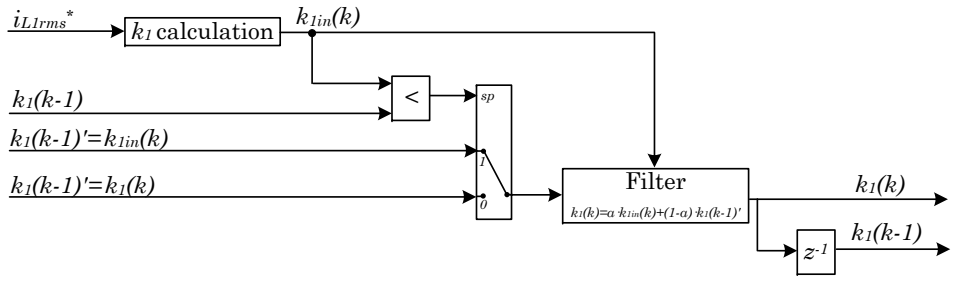

Figure 5.58: k_1 calculation proposed for fault recovery behaviour enhancement

the previous computed one $k_1(k-1)$, i.e., this criterion is used as a fault recovery indicator, the $k_1(k)$ used for the inner current control reference is filtered according to the scheme described in Figure 5.58.

Simulated validation of short-circuit proof algorithm

Considering the parameters summarised in Table 5.5.1, the proposed four-leg VSI is modelled and four type of short-circuit situations are considered, see Figure 5.59. All the different scenarios will detail the behaviour of the VSI when the fault is produced and recovered in terms of I_{L1u}, I_{L1v}, u_{PCCu} and u_{PCCv}. The short-circuit fault is produced at time t equal to 20 ms and there is a fault clearance at 30 ms.

- Scenario 1. Phase u to neutral n short-circuit, see Figure 5.59(a). Figure 5.60 shows the behaviour of the voltage and current of phases u and v when a phase u to the neutral wire n short-circuit is generated and when it is recovered. It can be seen that the voltage goes to zero when the fault appears maintaining the current limited with a sinusoidal waveform during all time the short-circuit is hold. Note that just when the short-circuit takes place, the current increases to 600 A. This will be a common situation for all the scenarios. Assuming that the control loop is closed every 125 μs, the capacitor is discharged without control during this time. The discharge time constant is dependent on the capacitance C. This is the reason why in the AC capacitor size section it has been decided to use a 350 μF capacitor instead o a lower value. On the other hand, the settling time of the current loop is about 2 ms and for the voltage loop about 20 ms. Then, a possible solution is to increase the switching and control frequency to improve

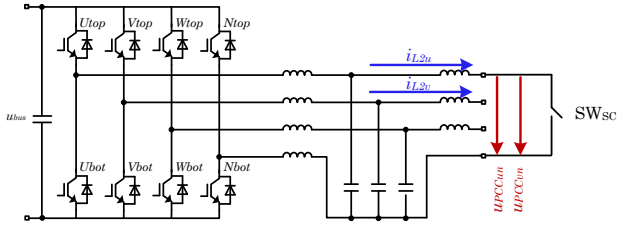

(a) Phase u to neutral n short-circuit

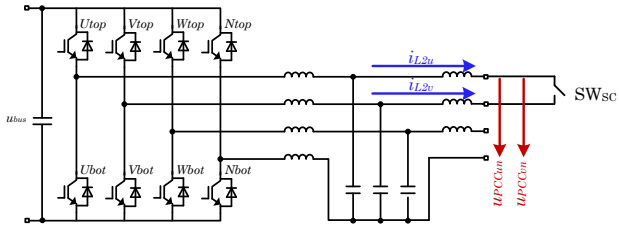

(b) Phase u to phase v short-circuit

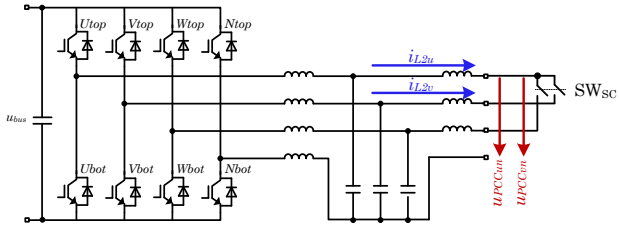

(c) Three-phase uvw short-circuit

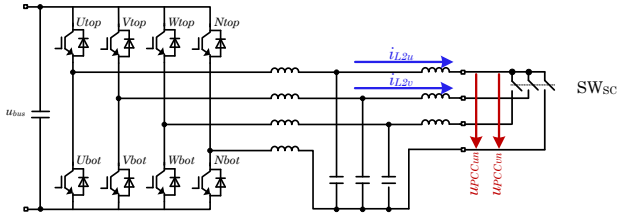

(d) Three-phase uvw to neutral $n$short-circuit

Figure 5.59: Proposed short-circuited scenarios

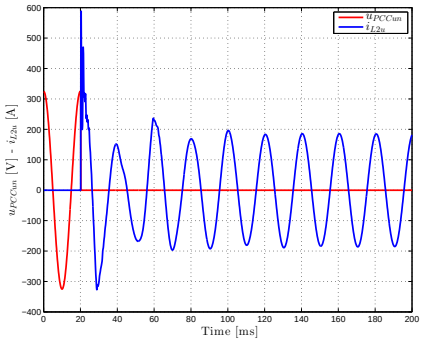

(a) u_{PCCu} and i_{L2u} when the short-circuit fault occurs

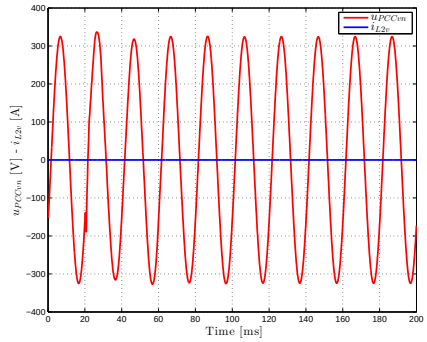

(b) u_{PCCv} and i_{L2v} when the short-circuit fault occurs

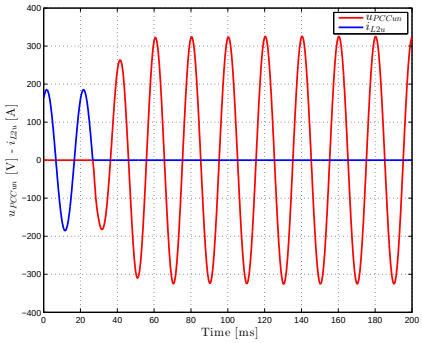

(c) u_{PCCu} and i_{L2u} when the short-circuit fault is recovered

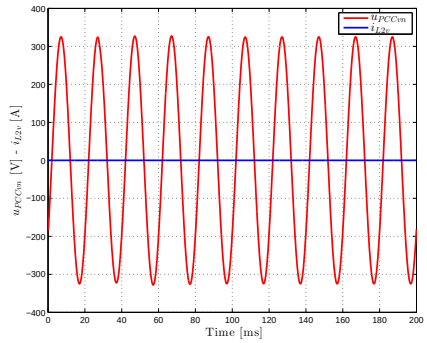

(d) u_{PCCv} and i_{L2v} pwhen the short-circuit fault is recovered

Figure 5.60: Phase u to n short-circuit time response simulated results

the close loop specifications. However, this option will compromise the efficiency of the real platform. As the time duration is really short, it is assumed to be valid.

When the fault is recovered, the voltage increases progressively without producing any dangerous over-voltage thanks to the algorithm proposed in Figure 5.58.

- Scenario 2. Phase u to v short-circuit, see Figure 5.59(b). Figure 5.61 shows the behaviour of the voltage and current of phases u and v when a phase u to phase v short-circuit is generated and when it is recovered. It can be deduced that $i_{L2u} = -i_{L2v}$ and $u_{PCCun} = u_{PCCvn}$, as can be also observed in Figure 5.61. This case is particularly interesting

because although the current is perfectly managed in steady-state, it can be seen that the voltage does not go to zero when the fault appears. When the fault occurs the present current per phase will produce that in one of the two involved phases its voltage control action plus the short-circuit current sums more than in the other case. That phase with more error rapidly produces a k_1 gain that moves from one to zero. As the other phase operates with higher k_1 values, it starts to control the current without necessarily a k_1 gain equal to zero, i.e. without the correspondent phase-to-neutral equal to zero. Then, the other phase-to-neutral voltage of the PCC is determined by hardware boundaries. Lets assume that phase v can manage u_{Cv} because k_{1v} is not null. Then, in steady-state, depending on k_{1v}, the $u_{Cu}{}^*$ and $u_{Cv}{}^*$ take different values. In the simulated case, it can be observed that when the fault is recovered, u_{PCCu} is close to 319 V. This means that $k_{1v} = 1$ and $k_{1u} = 0$ for this scenario.

Again, when the fault is recovered, the voltage increases progressively without producing any dangerous over-voltage thanks to the algorithm proposed in Figure 5.58.

- Scenario 3. Three phase uvw short-circuit, see Figure 5.59(c). Figure 5.62 shows the behaviour of the voltage and current of phases u and v when a three-phase uvw short-circuit is generated and when it is recovered. In this case, $u_{PCCuv} = u_{PCCvw} = u_{PCCwu}$. This implies that, as a difference from the scenario 2, when the short-circuit occurs the voltages at the PCC keeps constituting a balanced system. As, the amplitude in steady state is equal to

$$|u_C| = \sqrt{2} I \|X_{sc}\| \tag{5.75}$$

being the $\|X_{sc}\|$ the short-circuit impedance norm, those voltages will be close to zero. This result can be seen in this simulated scenario where it can be observed that i_{L2v} is $2\pi/3$ rad lagged from i_{L2u}.

Once more, when the fault is recovered, the voltage increases progressively without producing any dangerous over-voltage thanks to the algorithm proposed in Figure 5.58.

- Scenario 4. Three phase uvw to n short-circuit, see Figure 5.59(d). Figure 5.63 shows the behaviour of the voltage and current of phases u and v when a three-phase to neutral short-circuit is enforced and when it is recovered. Again, as in the single-phase to neutral case

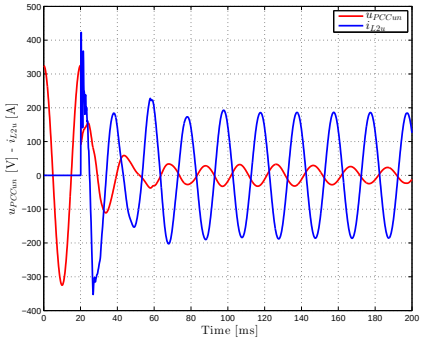

(a) u_{PCCu} and i_{L2u} when the short-circuit fault occurs

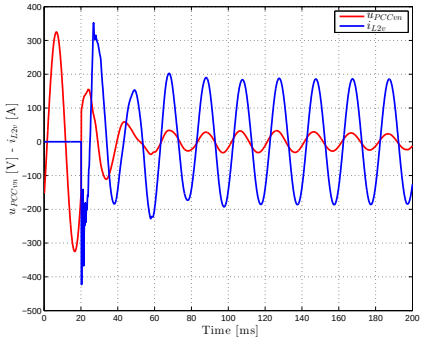

(b) u_{PCCv} and i_{L2v} when the short-circuit fault occurs

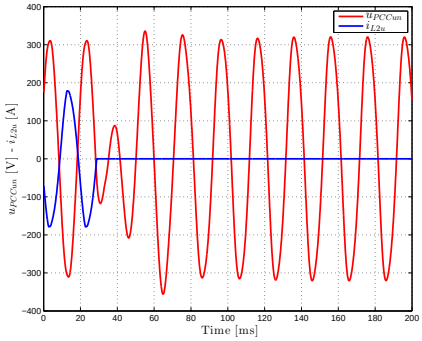

(c) u_{PCCu} and i_{L2u} when the short-circuit fault is recovered

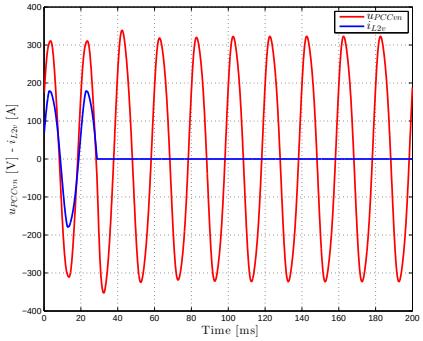

(d) u_{PCCv} and i_{L2v} pwhen the short-circuit fault is recovered

Figure 5.61: Phase u to v short-circuit time response simulated results

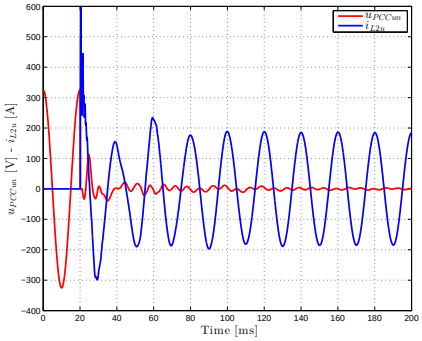

(a) u_{PCCu} and i_{L2u} when the short-circuit fault occurs

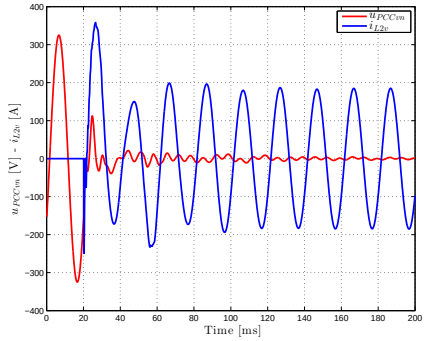

(b) u_{PCCv} and i_{L2v} when the short-circuit fault occurs

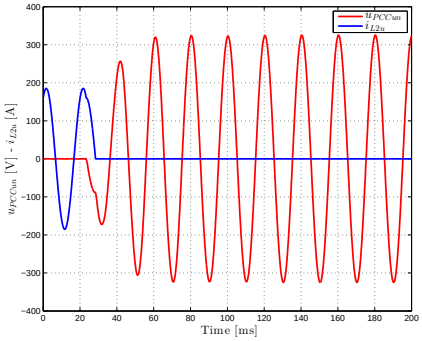

(c) u_{PCCu} and i_{L2u} when the short-circuit fault is recovered

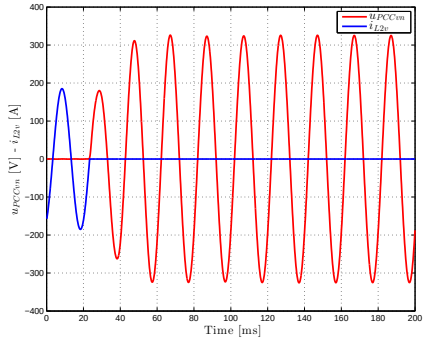

(d) u_{PCCv} and i_{L2v} pwhen the short-circuit fault is recovered

Figure 5.62: Three phase *uvw* short-circuit time response simulated results

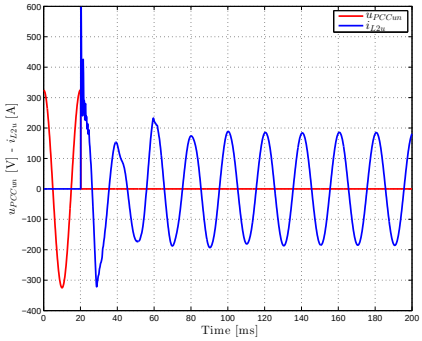

(a) u_{PCCu} and i_{L2u} when the short-circuit fault occurs

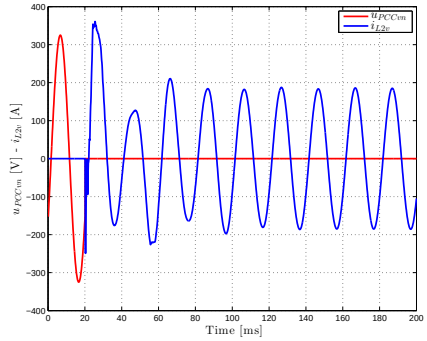

(b) u_{PCCv} and i_{L2v} when the short-circuit fault occurs

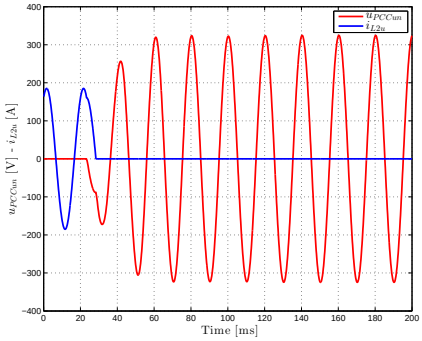

(c) u_{PCCu} and i_{L2u} when the short-circuit fault is recovered

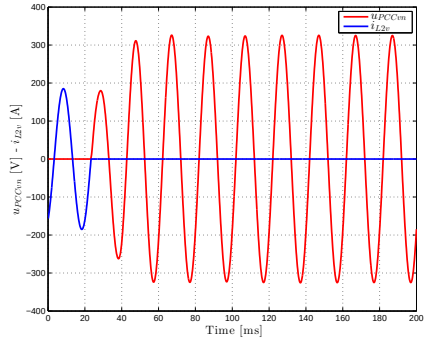

(d) u_{PCCv} and i_{L2v} pwhen the short-circuit fault is recovered

Figure 5.63: Three phase uvw to n short-circuit

(scenario 1), the behaviour of the current and the voltage follows the expected transients without producing severe peaks. As in scenarios 1 to 3, when the fault is recovered, the voltage increases progressively without producing any dangerous over-voltage

5.6 The three-leg interleaved DC/DC converter coupling filter design

5.6.1 Hardware design

Design of the output inductance

In Section 5.2 it has been indicated that the input DC voltage swing is 150-500 VDC. Due to the wide voltage operation range of the DC microgrid it is not possible to design the interleaved inductances for optimal operation, i.e. according to a specific duty cycle, see Figure 5.6. Then, if the required DC-link is about 700 VDC, the duty cycle required moves from 0.21 to 0.71, approximately.

Observing Figure 5.6 it should be assumed a maximum normalized ripple, κ, of 0.083 when three-legs are used for the interleaving operation. Thus, if it is desired that Δi would be equal to 20 A when u_{bus} is set to 700 VDC and a switching frequency f_s to 8 kHz, the inductance value is

$$L = \frac{u_{bus}\kappa}{f_s \Delta i} = \frac{700 \cdot 0.083}{8000 \cdot 20} = 363.3\ \mu\text{H} \tag{5.76}$$

However, in an interleaved configuration, when each leg output inductance is not exactly like the other ones the obtained total current presents unbalances. As an example, Figure 5.64 shows the expected leg currents and the total current considering L_a, L_b and L_c equal to 250 μH, a parasitic resistance of 60 mΩ, a switching frequency of 8 kHz, u_{bus} equal to 600 VDC and a duty cycle α equal to 0.237.

The effect of a different inductance affects to the obtained ripple and to the interleaved current frequency components, as can be seen in Figure 5.65. If the Fast Fourier Transform (FFT) is computed on the interleaved currents of Figure 5.65 it is obtained that there are components of one, two and three times the switching frequency.

When the duty cycle $\alpha \leq 0.33$, the effect on the ripple can be analysed and extrapolated to the the other two parts defined from $0.33 < \alpha \leq 0.66$ and $0.66 < \alpha \leq 1$. Thus, k will define the relation between the different inductance and the other ones.

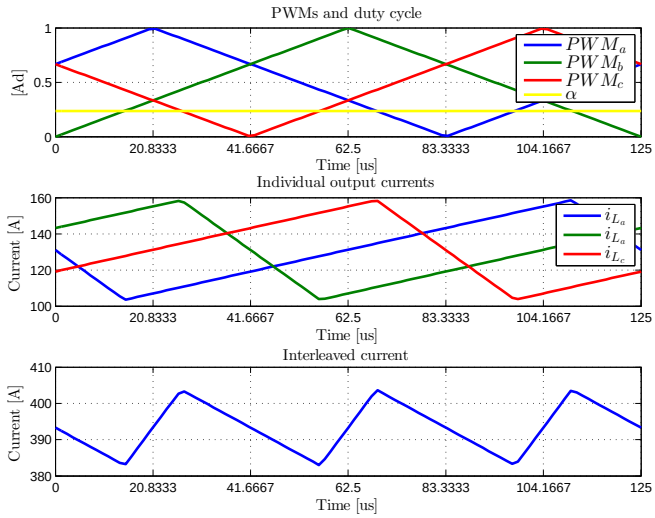

Figure 5.64: Simulation for a totally balanced interleaved control

It can be deduced from Figure 5.65(a) that if $k > 1$, the maximum ripple is obtained adding the ripple of two sections where all currents increase during a time equal to 1/3-α. The result is subtracted by the ripple of one section where the current of the two equal inductances increases and the different one decreases during a time equal to α. In Figure 5.65(b) ($k < 1$), the maximum ripple is obtained adding the ripple effect of one section where the current of the two equal inductances increases and the different one deceases during a time equal to α. Then, Figure 5.66 can be obtained. For a reasonable tolerance of $\pm 10\%$ on the inductance value it can be obtained that the worst case is when $k = 0.9$. In this situation, the maximum κ value is 0.098. Recalculating the inductance required and maintaining Δi equal to 20 A the obtained L is 428 μH. Then, the selected $L_a = L_b = L_c$ is 400 μH.

On the other hand, if there is a difference in the parasitic equivalent series resistance of one interleaved inductance, the ripple of each current is maintained but its average value not. Assuming steady state, the average voltage of a parasitic resistance R is determined by

$$\overline{u}_R = \alpha u_{bus} - u_{bat} \tag{5.77}$$

where u_{bat} represents the voltage of the DC microgrid. Then, applying the Ohm's law it can be deduced that if k_R defines the relation between two

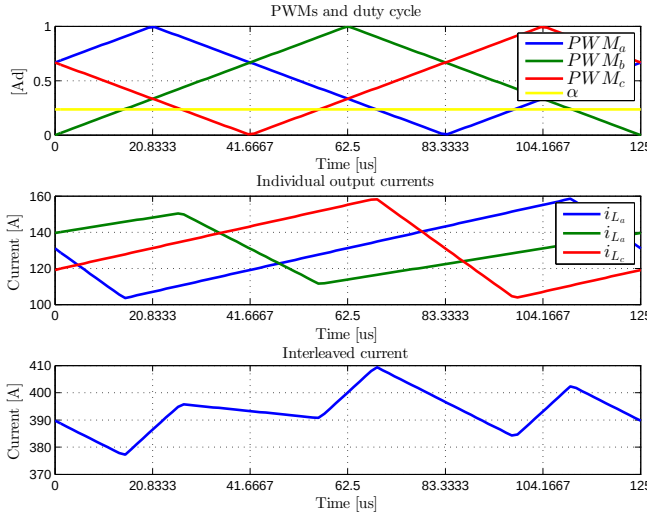

(a) $L_b = 1.4L_a,\ L_a = L_c$

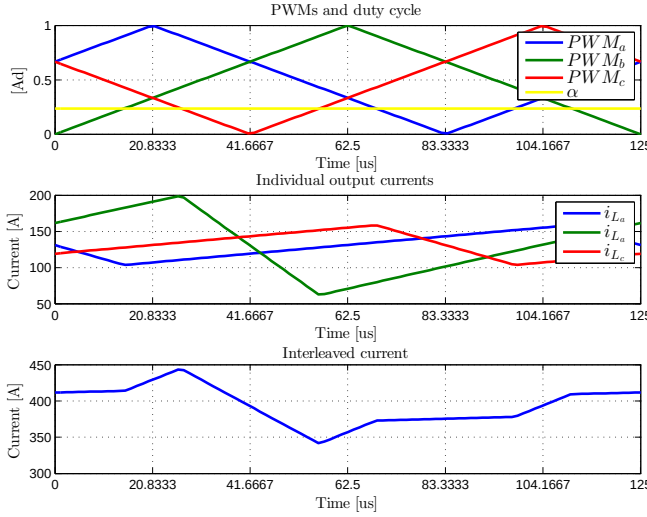

(b) $L_b = 0.4L_a,\ L_a = L_c$

Figure 5.65: Simulation for different inductances for the interleaved control.

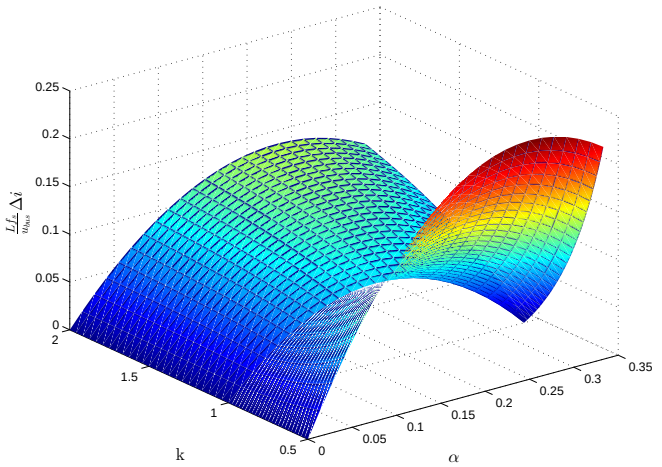

Figure 5.66: Simulation for an unbalanced inductance interleaved system

different equivalent series resistances x and y

$$k_R = \frac{R_x}{R_y} \tag{5.78}$$

the average current of leg y will be k_R times the current of leg x. Thus, the individual leg current ripple is equal than in a total balanced interleaved system but not the average value. In Figure 5.67 can be observed the effect for different k_R gains. This effect is specially relevant if the converter is not oversized.

It is possible to conclude that the tolerance between the interleaved inductactes must be as better as possible to avoid exchanging currents and obtaining non tolerable ripples.

Design of the output capacitor

The capacitor C_{bat} is defined by its differential equation as

$$i_{C_{bat}} = C_{bat} \frac{du_{bat}}{dt} \tag{5.79}$$

Then, assuming that a symmetrical triangular current signal of period T and amplitude A has its first and predominant sinusoidal component at a period T with a value of $8A/\pi^2$, the C_{bat} can be computed from its isochronous transfer function as

$$U_{C_{bat}}(\omega) = I_{C_{bat}}(\omega) \frac{1}{C_{bat}\omega} \tag{5.80}$$

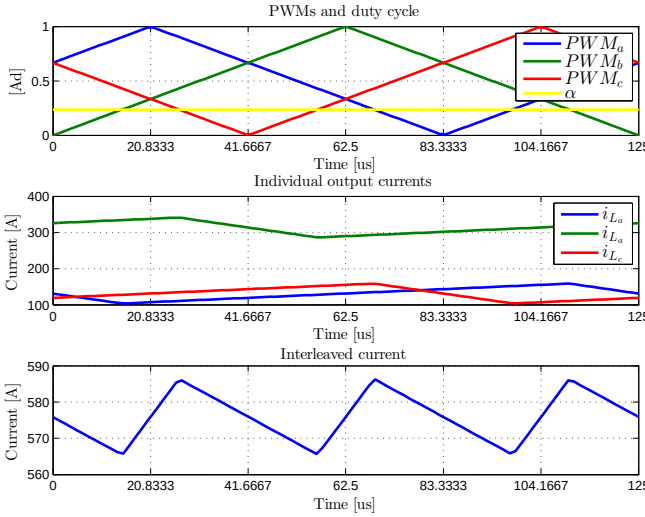

(a) $R_b = 1.4R_a,\ R_a = R_c$

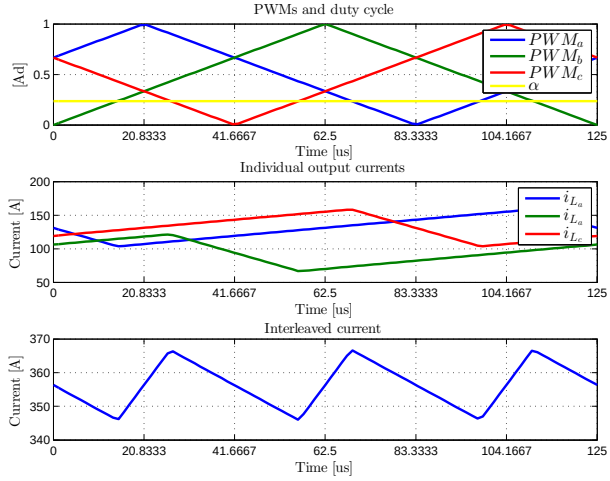

(b) $R_b = 0.4R_a,\ R_a = R_c$

Figure 5.67: Simulation for different parasitic resistances for the interleaved control.

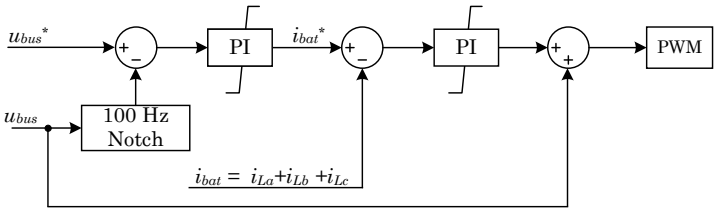

Figure 5.68: Control scheme of the proposed DC/DC interleaved converter

Thus, considering $i_{C_{bat}}$ as a triangular symmetrical current of 35 A peak to peak, f equal to 24 kHz (interleaved obtained switching frequency) and $U_{C_{bat}}$ equal to 0.45 VDC

$$C_{bat} = \frac{I_{C_{bat}}(\omega)}{\omega U_{C_{bat}}(\omega)} = \frac{35\frac{8}{\pi^2}}{(2 \cdot \pi \cdot 24000) \cdot 0.45} = 418\ \mu\text{F} \tag{5.81}$$

5.7 The three-leg interleaved DC/DC converter control

5.7.1 DC current and voltage control

Despite the high complexity in hardware implementation, the converter is controlled as a conventional voltage source DC/DC converter composed by a single leg and a single inductance of a third of each individual value. As a result, the control loop needs to manage a single duty cycle. The DC/DC converter is controlled by means of two nested control loops, as shown in Figure 5.68. The inner control loop is used to control the interleaved current i_{bat}. This control loop is also used to limit the output current of the DC/DC converter.

The Internal Model Control (IMC) [241] is used to set the current controller constants. In the IMC it is indicated that if the control system corresponds to a first order system, only establishing the rise time t_r (time for the response to go from 10% to 90% of the final value) as

$$t_r = \frac{ln(9)}{\nu} \tag{5.82}$$

and knowing the parameters a and b of a first order system

$$G(s) = \frac{1}{\frac{a}{b}s + 1} \tag{5.83}$$

it is possible to compute the controller proportional and integral constants as

$$k_{p_{idc}} = a\nu \tag{5.84}$$
$$k_{i_{idc}} = b\nu \tag{5.85}$$

Thus, considering t_r equal to 1.8 ms, a equal to $L_a/3$ (133.3 μH) and b equal to 82.8 mΩ, the current controller constants are

$$k_{p_{idc}} \approx 0.164$$
$$k_{i_{idc}} \approx 36.75$$

The outer control loop is intended to manage the DC bus voltage. Due to unbalanced AC connected loads, low frequency voltage ripples in the DC bus can be severe. As can be observed in Figure 5.68, a 100 Hz notch filter is applied to the feedback to eliminate this component of the control action. In this sense, Figure 5.69 shows a simulation when a current sweep is applied (any type of current, i.e. positive, negative or zero sequence) and the objective function is focused on the worst case in terms of u_{bus} ripple (Δu_{bus}). Figure 5.69(a) considers an inverter under SVPWM without neutral current and Figure 5.69(b) with neutral current. In both cases u_{bus} is equal to 700 VDC, S is equal to 135 kVA, C_{bus} is equal to 7 mF and the grid is 230 V-50 Hz considering only positive sequence. The AC LCL-type filter is summarised in Table 5.9. It is considered a DC-link of 7 mF.

It should be clarified that Figure 5.69 represents the worst case found according to the meshing applied at the simulation routine, but exists a family of solutions closed to the depicted one. It can be observed that the worst case is derived from a situation with neutral current. In concrete, the maximum Δu_{bus} is close to 96 VDC. If the same type of analysis is conducted for a four-wire three-leg split capacitor topology but considering that u_{bus} is equal to 800 VDC the results can be observed in Figure 5.70. In this case, it can be seen that the u_{bus} low frequency ripple is higher than in the four-leg topology although the use of a higher u_{bus} voltage. Figure 5.70(a) analyses the worst case for the maximum ripple of one of the two DC semi-buses of this topology. Figure 5.70(b) takes into account the most pessimistic situation for the full DC-link.

The situation presented in Figure 5.69 determines that it is possible that over-modulation at the AC side occurs. A dynamic bus value control depending on AC demands, considering non-balanced possibilities, is proposed. In this sense, a preventive DC voltage controller is added at a higher level.

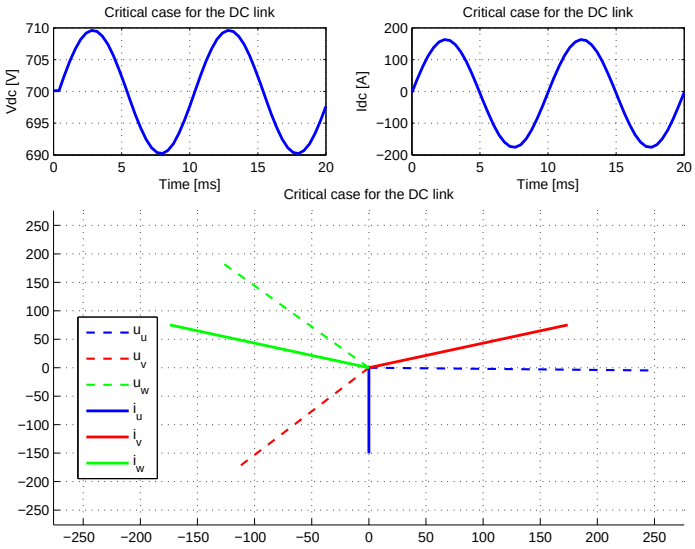

(a) Three-phase inverter under SVPWM when no neutral current is considered

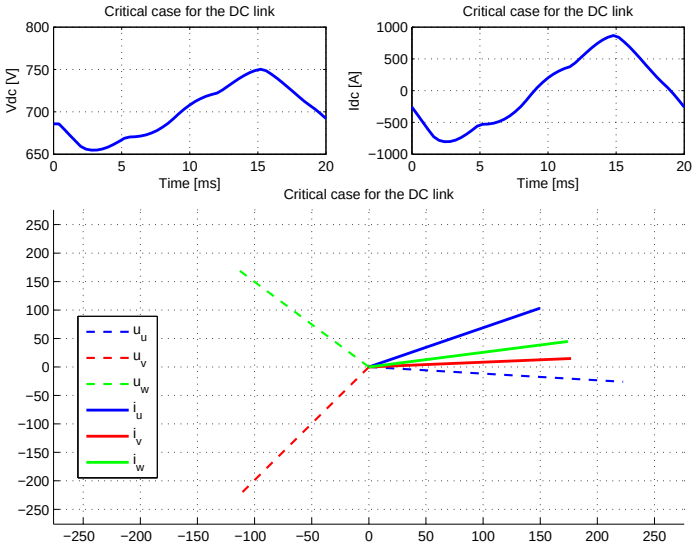

(b) Three-phase inverter under SVPWM when neutral current is considered

Figure 5.69: Current sweep analysis of the worst case for the DC-link ripple in a four-leg topology

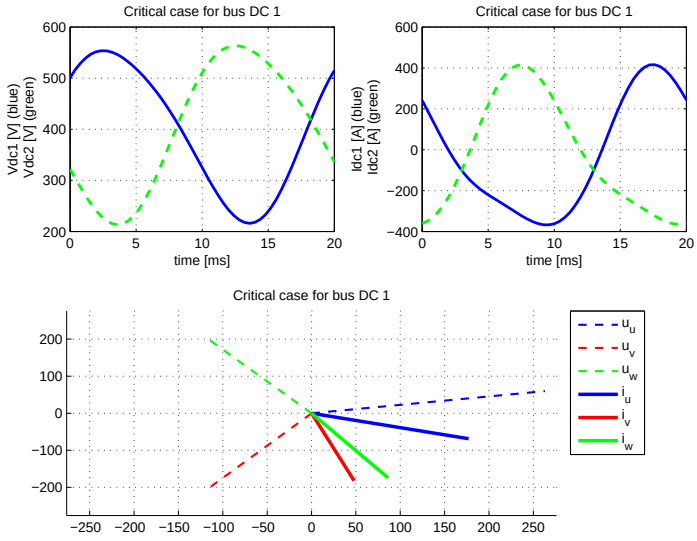

(a) Worst Δu_{bus} situation of the positive semi-bus

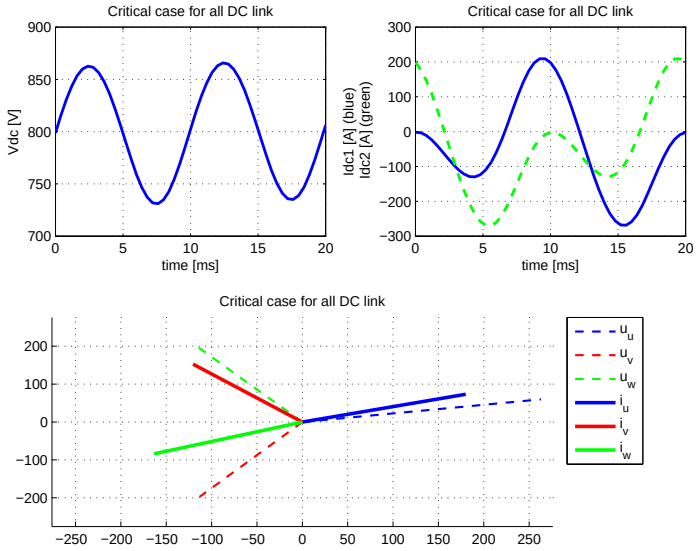

(b) Worst Δu_{bus} situation of the full bus

Figure 5.70: Current sweep analysis of the worst case for the DC-link ripple in a three-leg split capacitor topology

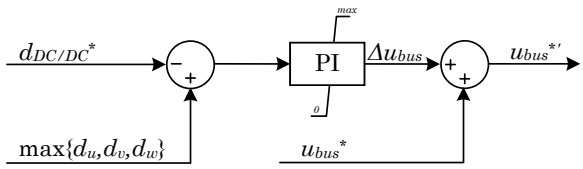

Figure 5.71: Control scheme to avoid over-modulation situation in the DC/DC converter

It will provide a voltage increment Δu_{bus} to the rated D-link voltage, in this case 700 VDC, generating the reference ${u_{bus}}^{*\prime}$. The maximum available duty cycle ${d_{DC/DC}}^*$ is compared with the maximum of the inverter duties (d_u, d_v and d_w). If there is not enough DC bus voltage for the inverter needs, the DC reference is increased up to a maximum threshold thanks to an upper saturation, taking into account the limitations of the DC-link. In other case, Δu_{bus} is equal to zero in steady state thanks to a lower saturation equal to zero. This high level control scheme is depicted in Figure 5.71.

Once has been determined that the selected C_{bus} of 7 mF can be operated properly, the outer DC voltage controller is tuned. In this case, the inner current loop is considered as a unity gain. Then, the close loop transfer function is

$$G_{CL_u}(s) = \frac{G_C(s)G(s)}{1 + G_C(s)G(s)} \tag{5.86}$$

being $G_C(s)$ the transfer function of a PI controller and $G(s)$ the transfer function of a capacitor. It is usual to consider only the poles of the system neglecting the effect of the zeros of the system. In this case, has to be ensured the final over-shoot to guarantee the integrity of the DC-link. Thus, the characteristic equation of $G_{CL_u}(s)$ is

$$1 + G_C(s)G(s) = C_{bus}s^2 + k_{p_u}s + k_{i_u} \tag{5.87}$$

where k_{p_u} and k_{i_u} are the proportional and integral gains of the DC-link voltage controller. If the desired response is under-damped, when the over-shoot is set equal to 2% and the peak-time equal to 60 ms, the controller constant results in

$$k_{p_{u_{dc}}} \approx 0.9 \tag{5.88}$$

$$k_{i_{u_{dc}}} \approx 50.3 \tag{5.89}$$

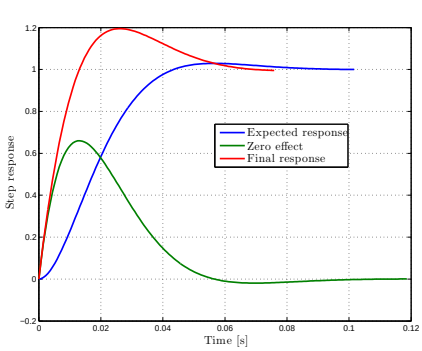

(a) Step response for the u_{bus} control

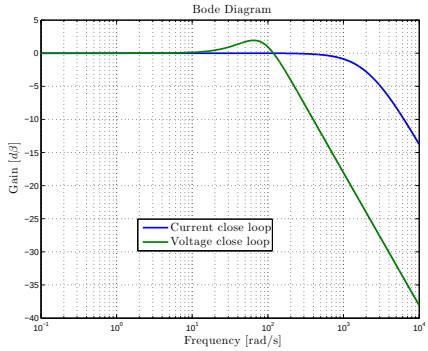

(b) Diagram bode of the current and voltage loop for the DC/DC converter

Figure 5.72: Control time and frequency responses

The zero effect is shown in Figure 5.72(a). It affects distorting the time response increasing the final over-shoot and reducing the peak-time. Furthermore, in a cascaded loop it is important to ensure that the bandwidths (-3 dB) of both loops are sufficient separated being the inner current loop bandwidth higher than the voltage control loop one. Figure 5.72(b) shows that this is obtained for the proposed current and voltage controller constants.

5.8 Simulation and experimental results

5.8.1 Set-up

According to all exposed in this chapter, Figure 5.73 shows a control scheme of the set-up used for the validation of the different proposed algorithms. Figure 5.74 shows the proposed experimental microgrid VSI electrical cabinet. It is sized to manage up to 135 kVA and it is based on three Semikube IGD-2-424-P1N6-DH-FA power stacks from Semikron. The chosen switching and control frequency is 8 kHz.

All control algorithms are implemented in two control boards based on the TMS320F2809 DSP from Texas Instruments. These two DSP are interfaced with an external MGCC through a Human Machine Interface (HMI). The different used communication buses and routines of each device are summarised in Figure 5.75.

The interaction between AC output side of the converter and the micro-

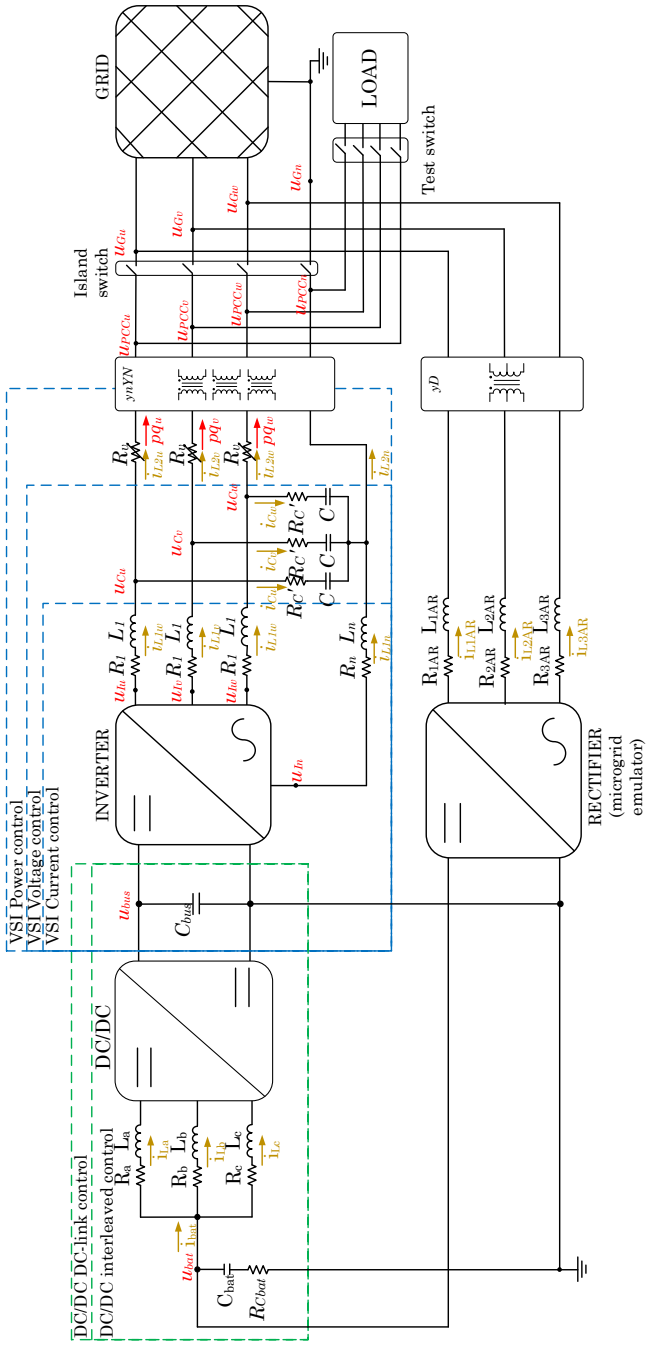

Figure 5.73: Proposed set-up scheme

(a) Outer electrical cabinet view

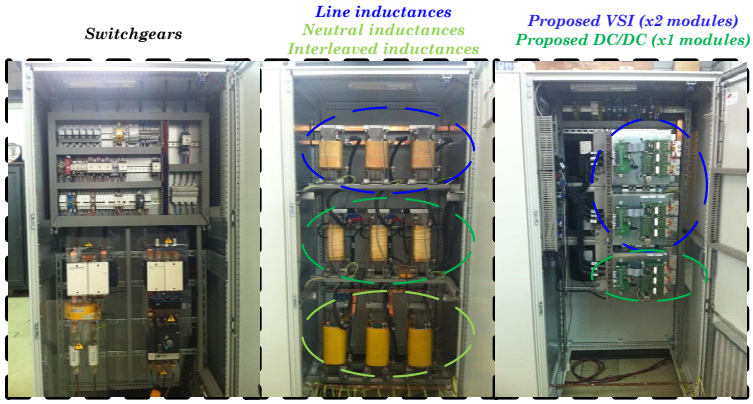

(b) Inner electrical cabinet view

Figure 5.74: Developed VSI

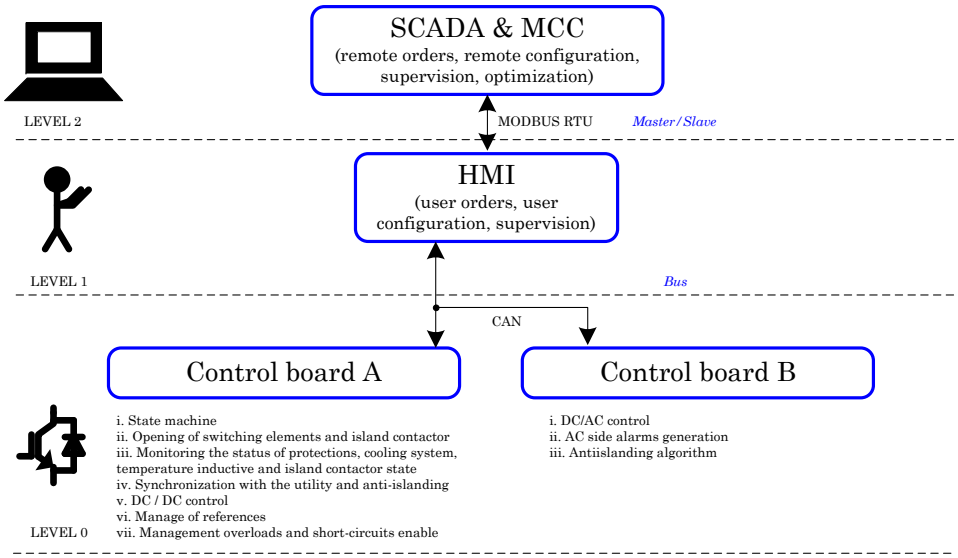

Figure 5.75: Manage and control interfacing

grid is at 400 VAC (±10%) phase to phase and 50 Hz (±10%). TT or TN-S ground schemes have been considered. This is obtained with a galvanic isolation done by a transformer bank of 50 kVA per phase in a YNyn configuration. The DC microgrid is emulated by means of a 50 kVA active rectifier that supplies the DC required input voltage, see Figure 5.76. The selected input voltage range of the converter in the DC microgrid side is 150-500 VDC. Table 5.13 summarises the hardware parameters described in Figure 5.73. The box called Load is variable and depends on the validation scenario.

5.8.2 The four-wire three-phase DC/AC VSI in grid-connected operation

In this section three different type of tests are proposed:

- PQ unbalance tracking
- Dynamic droop analysis
- Energy quality analysis at rated power (non over-loaded)

(a) Outer electrical cabinet view (b) Inner electrical cabinet view

Figure 5.76: Used active rectifier (DC microgrid emulator)

Block	Element	Value	Unit
AC LCL filter	Output phase inductance L_1	248	μH
	Equivalent series resistance R_1	30	mΩ
	Equivalent output neutral inductance L_n	245	μH
	Equivalent series resistance R_n	15	mΩ
	Transformer leakage inductance L_2	69	μH
	Equivalent series resistance R'_2 $(R_{L2} + R_v)$	250	mΩ
	AC Capacitor	350	μF
	Equivalent series resistance R'_C $(R_{Cv} + R_C)$	200	mΩ
DC-link	DC-link Capacitor C_{bus}	6.9	mF
DC LC filter	Output phase inductance $L_a/3$	142	μH
	Equivalent series resistance $R_a/3$	15.2	mΩ
	DC Capacitor	420	μF
	Equivalent series resistance R_{Cbat}	10	mΩ
Island switch	Turn-on delay	40	ms
	Turn-off delay	120	ms

Table 5.13: Experimental hardware parameters

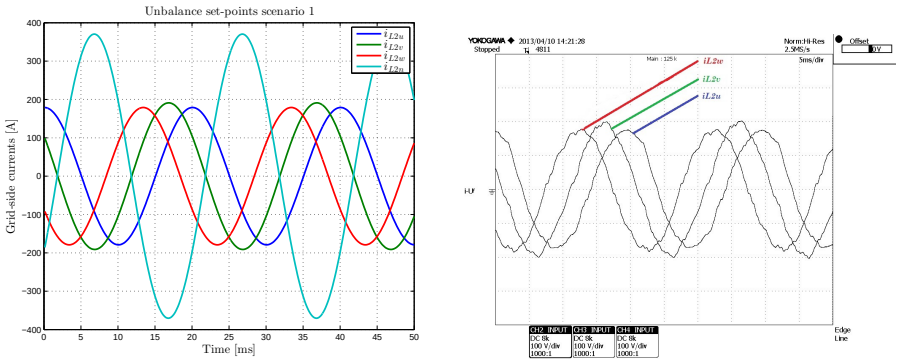

(a) Simulated results (b) Experimental results

Figure 5.77: Scenario 1. Inverter in grid-connected mode. Unbalanced reference: $P_u = 30$ kW, $P_u = -30$ kW and $P_w = 30$ kW. $Q_u = 0$ kvar, $Q_v = 0$ kvar and $Q_w = 0$ kvar

Unbalanced PQ set-points

In this section two different scenarios are proposed:

- Scenario 1. Inverter operating in grid-connected mode with rated (non over-loaded) unbalanced PQ set-points. The targets are: $P_u = 30$ kW, P_v = -30 kW, P_w = 30 kW and Q_u, Q_v, Q_w all nulls. Figure 5.77 shows that the inverter is capable to synthesize non balanced currents from non-balanced PQ references. Figure 5.77(a) shows a simulation of the expected active phase and neutral wire currents, respectively. Figure 5.77(b) presents the captured oscilloscope active currents.

- Scenario 2. Inverter operating in grid-connected with a particular set of references that implies to exchange only homopolar currents. The targets are: $P_u = 15$ kW, P_v = -7.5 kW, P_w = -7.5 kW, $Q_u = 0$ kvar, Q_v = -13 kvar and $Q_w = 13$ kvar. Figure 5.78 shows that the inverter is capable to synthesize homopolar currents currents from non-balanced PQ references. Figure 5.78(a) shows the expected active phase and neutral wire currents, respectively. Figure 5.78(b) presents the captured oscilloscope active currents of the active phases.

Dynamic droop dynamics

This sections proposes four scenarios for the validation of the dynamic droop. Scenario 3 and 4 involves a step response on the active power set-point.

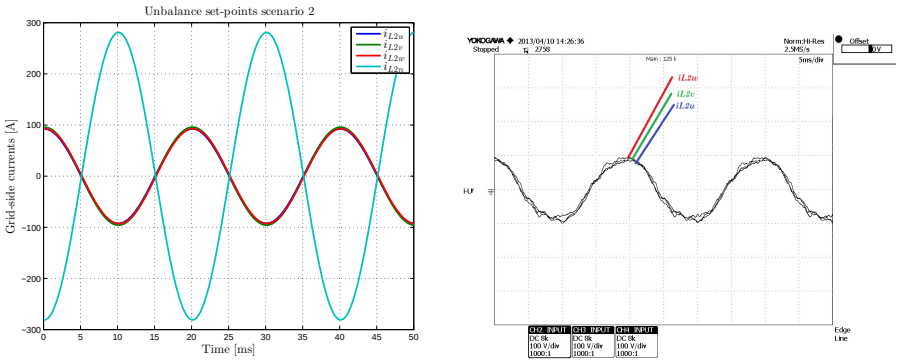

(a) Simulated results (b) Experimental results

Figure 5.78: Scenario 2. Inverter in grid-connected mode when maximum neutral current scaled by a factor 2 is targeted. Unbalanced reference: $P_u = 15$ kW, $P_v = -7.5$ kW and $P_w = -7.5$ kW. $Q_u = 0$ kvar, $Q_v - 13$ kvar and $Q_w = 13$ kvar

Scenario 3 proposes a positive step from P^*= 0 to 30 kW and scenario 4 a negative one from P^*= 30 to 0 kW.

On the other hand, scenario 5 and 6 involves a step response on the reactive power set-point. Scenario 5 proposes a positive step from Q^*= 0 to 30 kvar and scenario 6 a negative one from Q^*= 30 to 0 kvar.

In Section 5.5.1 has been described the tuning procedure for the dynamic droop control implemented when the inverter is grid-connected. Reminding Figure 5.46 it is possible to contrast that the expected time constant (±63% of the final value) is around 1.5 s for the active power and 1.2 s for the reactive power loop. Figure 5.79 shows the results obtained for scenarios 3 and 4 when all the control loop are considered, i.e. dynamic droop plus AC voltage control plus the output current control. In Figure 5.80 can be seen similar results for scenarios 5 and 6.

Energy quality analysis

When the VSI is operated in grid-connected mode at rated power per phase (non over-loaded situation), i.e. 30 kW per phase, it should be verified that the quality of the exchanged current and the voltage controlled at PCC are adequate. The quality analysis has been computed by suing the grid analyser Dranetz PowerExplorer PX-5.

Figure 5.81(a) depicts the grid-side currents and Figure 5.81(b) the rms

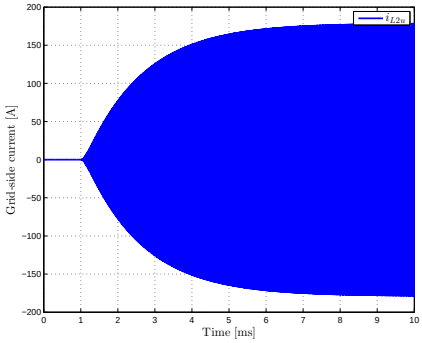

(a) Simulation results 0 to 30 kW

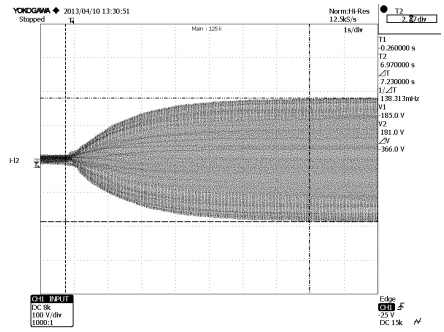

(b) Experimental results 0 to 30 kW

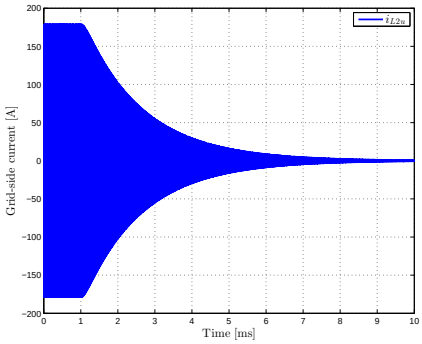

(c) Simulation results 30 to 0 kW

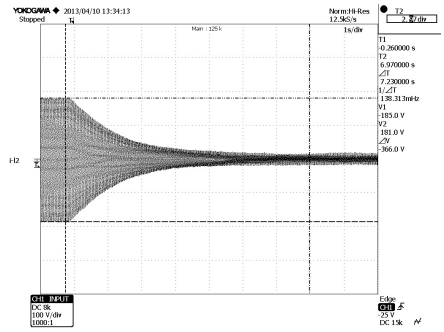

(d) Experimental results 30 to 0 kW

Figure 5.79: Scenarios 3-4. Inverter in grid-connected mode. Active power step response analysed in terms of current through L_1

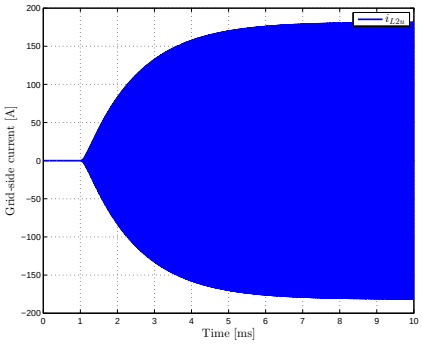

(a) Simulation results 0 to 30 kvar

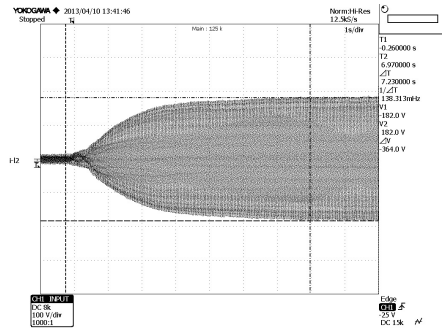

(b) Experimental results 0 to 30 kvar

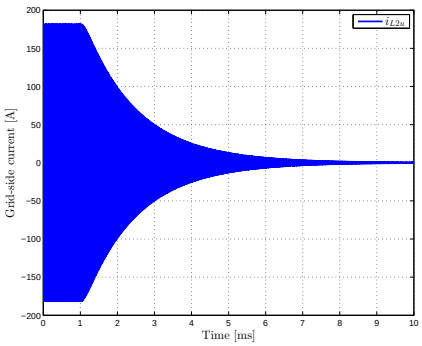

(c) Simulation results 30 to 0 kvar

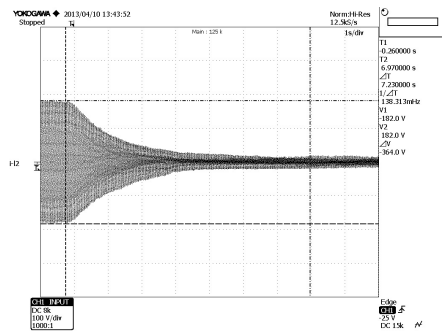

(d) Experimental results 30 to 0 kvar

Figure 5.80: Scenarios 5-6. Inverter in grid-connected mode. Reactive power step response analysed in terms of current through L_1

value, the DC component and the THD of the voltages at the PCC and, also, of the grid-side currents. It can be seen that the worst case in distortion is in terms of current THD and it is below 6%. In this sense, the inner controllers are considered properly tuned and no more HC will be added for the grid-connected mode operation.

5.8.3 The four-wire three-phase DC/AC in grid-disconnected operation

In this section three different type of test are proposed:

- Disturbance response
- Short-circuits proof capability
- Energy quality analysis

Disturbance response

In Section 5.5.1 has been described the tuning procedure for the inner control loops, i.e. the voltage and current loops. However, when the microgrid VSI is operating in grid-disconnected mode it should be validate that under a rated power local load connection or disconnection disturbance the voltage at the AC capacitor or the PCC is kept within adequate thresholds. Scenario 9 is defined to study the local load connection and scenario 10 for the local load disconnection effects. Then, for instance, the ITI curve could be used to analyse these effects (see Chapter 2). Figure 5.82 and Figure 5.83 show the simulated and experimental results when a load of 1.81 Ω resistance between u_{PCCu} and u_{PCCn} is connected and disconnected, respectevely (see Figure 5.73). The Test switch is considered ideal for the simulation results. It can be deduced that although there is a short voltage sag or peak transient at the PCC ,it accomplishes with the ITI curve. Then, it is considered that the voltage and current loops are dynamically well tuned. To increase the integral gain of higher HC than the considered (third and fifth) can improve the disturbance behaviour but can compromise the nested loop decoupled interaction, the system stability or the inter-harmonics excitation.

Short-circuits proof capability

In Section 5.5.2 has been proposed an algorithm that is based in the two gains k_1 and k_2 that allows to regulate the controlled voltage according the grid-side current plus voltage controller control action rms value and scales the

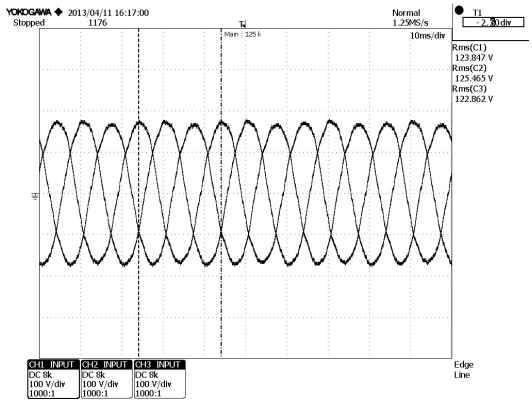

(a) Exchanged grid-side currents oscilloscope capture

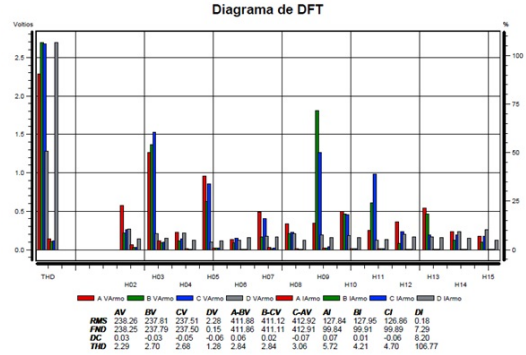

	AV	BV	CV	DV	A-BV	B-CV	C-AV	AI	BI	CI	DI
RMS	238.26	237.81	237.51	2.28	411.88	411.12	412.92	127.84	127.95	126.86	0.18
FND	238.25	237.79	237.50	0.15	411.86	411.11	412.91	99.84	99.91	99.89	7.29
DC	0.03	-0.03	-0.05	-0.06	0.06	0.02	-0.07	0.07	0.01	-0.06	6.20
THD	2.29	2.70	2.68	1.28	2.84	2.84	3.06	5.72	4.21	4.70	106.77

(b) Obtained grid-side quality results. XV indicates phase-to-neutral voltage information. XYV indicates phase-to-phase voltage information. XI indicates currents information

Figure 5.81: Scenario 7. Electrical quality analysis at 90 kW when grid-connected

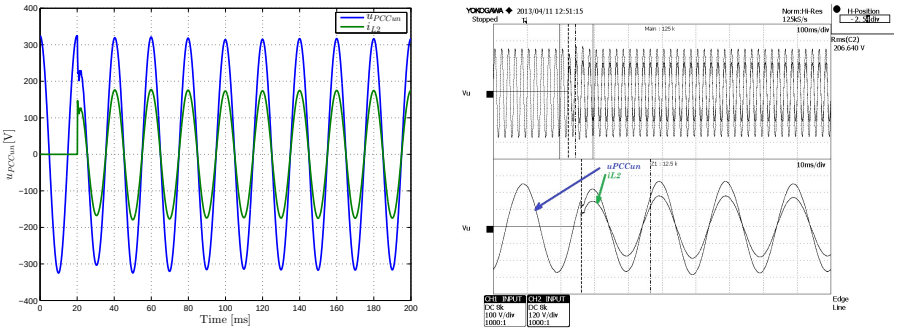

(a) Simulation results (b) Experimental results

Figure 5.82: Scenario 8. Behaviour on load change disturbance: no-load to 1.81 Ω

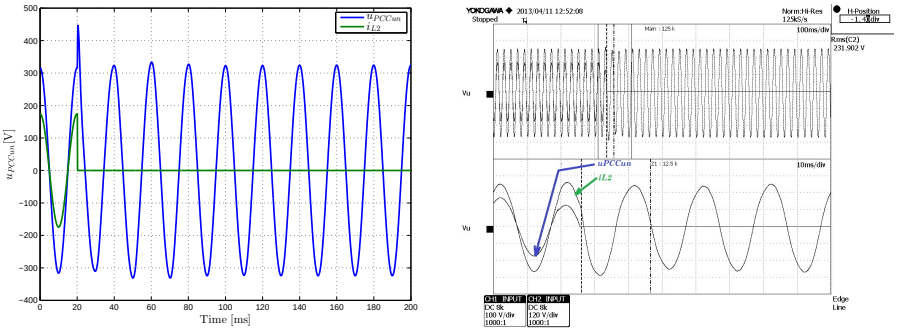

(a) Simulation results (b) Experimental results

Figure 5.83: Scenario 9. Behaviour on load change disturbance: 1.81 Ω to no-load

maximum current reference for the current loop. Simulation results shown in Figure 5.60 to 5.63 have proved a proper expected behaviour. Then, in order to validate them, the same four scenarios are replicated in the experimental set-up, see Figure 5.73. This four scenarios are:

- Scenario 10-11. Scenario 10 defines a phase-to-neutral short-circuit ($u_{PCCun} \approx 0$). Scenario 11 recovers normal operation coming from scenario 10.

- Scenario 12-13. Scenario 12 defines a phase-to-phase short-circuit ($u_{PCCuv} \approx 0$). Scenario 13 recovers normal operation coming from scenario 12.

- Scenario 14-15. Scenario 14 defines a three-phase short-circuit. In this case $u_{PCCuv} = u_{PCCvw} = u_{PCCwu}$, being $u_{PCCuv} \approx 0$. Scenario 15 recovers normal operation coming from scenario 14.

- Scenario 16-17. Scenario 16 defines a three-phase to neutral short-circuit. Now, $u_{PCCun} = u_{PCCvn} = u_{PCCwn}$, being $u_{PCCun} \approx 0$. Scenario 17 recovers normal operation coming from scenario 16.

Figures 5.84 to 5.87 depict experimental results when the considered load is constituted by a 30 cm wire with a section of 35 mm^2 connected between the corresponding terminals according to the case study. The Test switch is operated manually producing the corresponding short-circuit fault and clearance in the same oscilloscope capture. Comparing simulated and experimental results it can be seen that the proposed algorithm produces matching results.

In this sense, under a fault, the VSI can be protected by conventional protection designed to operate under sinusoidal currents but the short-circuit power should be reconfigured when a short-circuit situation is detected by the MGCC.

Energy quality analysis

In the same direction that in scenario 7, it should be verified that the quality of the exchanged current and the voltage controlled at PCC is adequate but, now, in grid-disconnected mode. The quality analysis has been computed by suing the grid analyser Dranetz PowerExplorer PX-5. Scenario 18 is defined by no-load connected at the PCC and scenario 19 by a rated power per phase local load, i.e. 30 kW per phase.

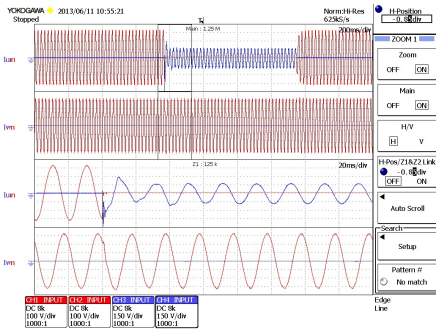

(a) u_{PCCu} and i_{L2u} when the short-circuit fault occurs

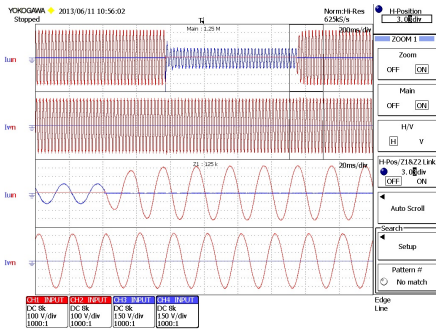

(b) u_{PCCv} and i_{L2v} when the short-circuit fault occurs

Figure 5.84: Scenarios 10-11. Phase u to n short-circuit time response experimental results. Phase to neutral voltages in red and line currents in blue.

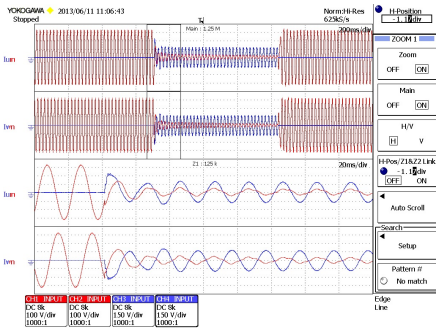

(a) u_{PCCu} and i_{L2u} when the short-circuit fault occurs

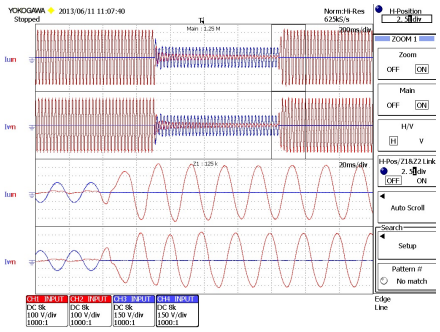

(b) u_{PCCv} and i_{L2v} when the short-circuit fault occurs

Figure 5.85: Scenarios 12-13. Phase u to v short-circuit time response experimental results. Phase to neutral voltages in red and line currents in blue.

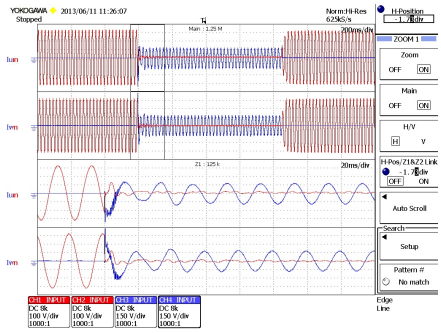

(a) u_{PCCu} and i_{L2u} when the short-circuit fault occurs

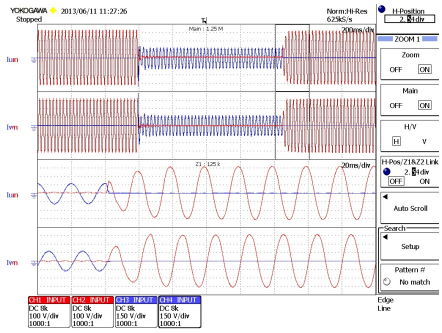

(b) u_{PCCv} and i_{L2v} when the short-circuit fault occurs

Figure 5.86: Scenarios 14-15. Three phase uvw short-circuit time response experimental results. Phase to neutral voltages in red and line currents in blue.

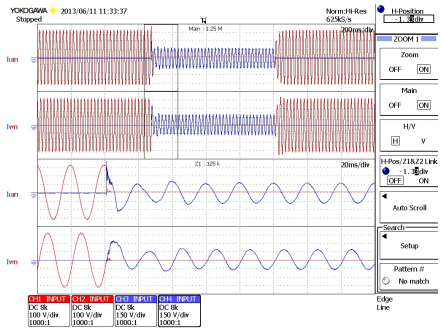

(a) u_{PCCu} and i_{L2u} when the short-circuit fault occurs

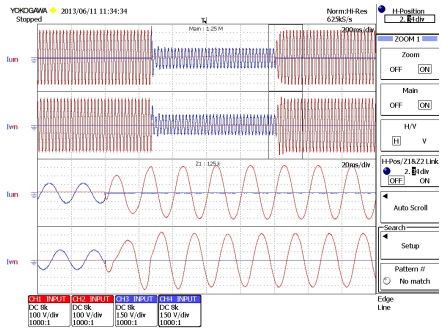

(b) u_{PCCv} and i_{L2v} when the short-circuit fault occurs

Figure 5.87: Scenarios 16-17. Three phase uvw to n short-circuit. Phase to neutral voltages in red and line currents in blue.

Figure 5.88(a) depicts the voltages at the PCC and Figure 5.88(b) the rms value, the DC component and the THD of the voltages at the PCC and, also, of the microgrid side currents when no-load is connected at the PCC. It can be seen that the worst case in distortion is terms of voltage THD at the PCC and it is below 3%. In this sense, the inner controllers are considered properly tuned and no more HC will be added for the grid-disconnected mode operation.

Figure 5.89(a) depicts the voltages at the PCC and Figure 5.89(b) the rms value, the DC component and the THD of the voltages at the PCC and, also, of the microgrid side currents when a 30 kW per phase is connected at the PCC. It can be seen that the worst case in distortion is terms of voltage THD at the PCC and it is below 2.1% and 2.26% in terms of current.

Considering the maximum THD values obtained, the inner controllers are considered properly tuned and no more HC will be added for the grid-disconnected mode operation.

5.8.4 The four-wire three-phase DC/AC transients

One of the most important challenges of a microgrid VSI is to provide smooth transients between operation modes. To validate that the proposed control algorithms operates properly, the VSI is analysed considering ten different scenarios. Four of them involves intentional transient form grid-connected to grid-disconnected operated when there is no load connected at the PCC. Another four involves the same situation when a resistive load of 30 kW is already connected. Finally, the last two presents a reconnection when no-load and the a rated local load is already connected.

In order to be as close as possible to the reality, the Island switch has been simulated with turn-on and turn-off delay, as indicated in Table 5.13. For all the simulated grid-connected to grid-disconnected intentional transition results, next steps are followed:

1. Time 0 to 50 ms. The system is operating in grid-connected steady state ($R_v = 0.2\ \Omega$) with a determined PQ reference per phase under the proposed dynamic droop control strategy.

2. Time 50 ms. A transition to grid-disconnected mode order is received (intentional disconnection). The virtual resistance R_v starts to decrease up to 0 Ω, according to the exposed in Section 5.5.1. It is proposed a decrease ratio of 0.16 Ω/s. The dynamic droop is disabled and the voltage reference is the last one provided by the power loop but, from this instant, it is self-generated per phase (delayed $2\pi/3$ rad

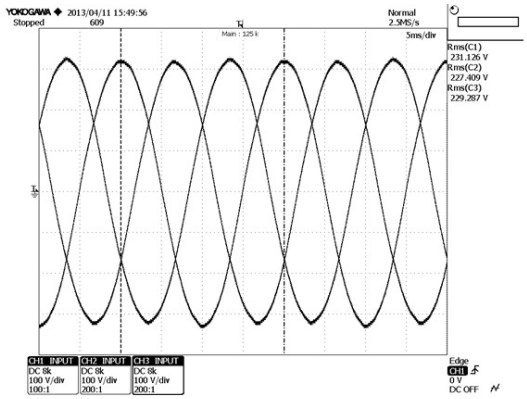

(a) Exchanged grid-side currents oscilloscope capture

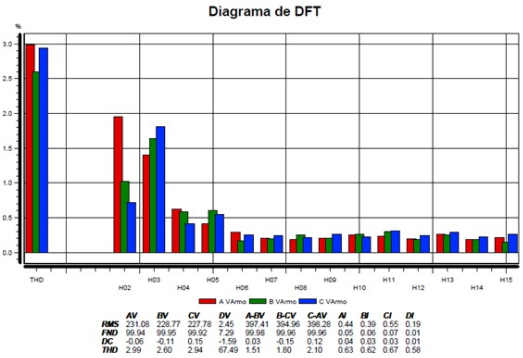

(b) Obtained grid-side quality results. XV indicates phase-to-neutral voltage information. XYV indicates phase-to-phase voltage information. XI indicates currents information

Figure 5.88: Scenario 18. Electrical quality analysis when grid-disconnected and no-load

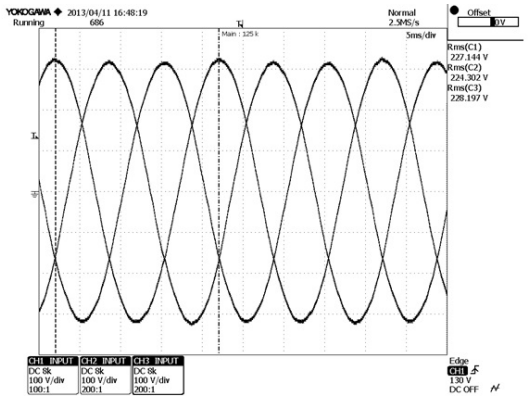

(a) Exchanged grid-side currents oscilloscope capture

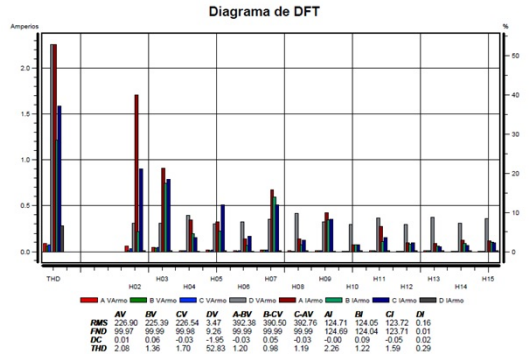

(b) Obtained grid-side quality results. XV indicates phase-to-neutral voltage information. XYV indicates phase-to-phase voltage information. XI indicates currents information

Figure 5.89: Scenario 19. Electrical quality analysis when grid-disconnected and 30 kW per phase load connected at the PCC

to constitute a balance voltage set), i.e. the VSI starts to operate under the V/f control strategy.

3. Time 50 to 170 ms. Turn-off time of the Island switch.

4. Time 170 ms. The Island switch is opened.

5. Time 170 ms to ∞ ms. The system is operated in grid-disconnected mode under the V/f control strategy until a reconnection order is received.

- Scenario 20-23. For all these scenarios it is considered that there is no load connected at the PCC just before, during or just after the transient operation to grid-disconnected operation is conducted. Figure 5.90 to 5.91 illustrates the obtained grid-side currents and PCC voltages when the four extreme set-points are targeted. This means that scenario 20 is conducted when P_u^* =45 kW, scenario 21 when P_u^* =-45 kW, scenario 22 when Q_u^* =45 kvar and, finally, scenario 23 when Q_u^* =-45 kvar.

  It can be seen from the simulation results that when the transition order is received (t = 50 ms) the current is not able to follow the power set-point because the control strategy is changed. When the Island switch is opened a short transient occurs, no more than 100 ms. Observing the ITI curve shown in Figure 2.35, it can be seen that the voltage simulated results are at the limit of the damage region. However, observing the experimental results, the maximum rms value is about 116% and the minimum about 80% for 20 to 30 ms. This is located within the ITI curve no interruption region.

  A possible reason of the difference between the simulated and real results might be due to the real behaviour of the Island switch. The fact of open electrically the inner terminals consumes some energy that helps to maintain more controlled the voltage peaks during the opening process.

- Scenario 24-27. For all this scenarios it is considered that there is connected a load of around 1.81 Ω at the PCC just before, during or just after the transient operation to grid-disconnected operation is conducted. Figure 5.92 to 5.93 illustrated the obtained grid-side currents and PCC voltage when the four extreme set-points are targeted. This means that scenario 24 is conducted when 45 kW is referenced to phase u during the grid-connected operation interval, scenario 25

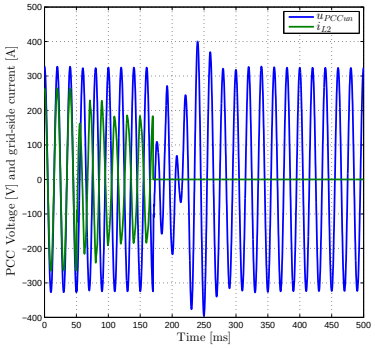

(a) Simulated results. $P_u^* = 45$ kW

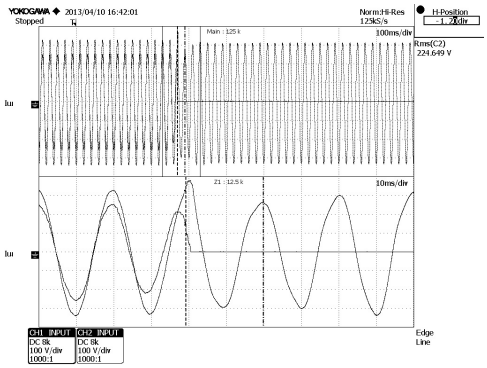

(b) Experimental results. $P_u^* = 45$ kW

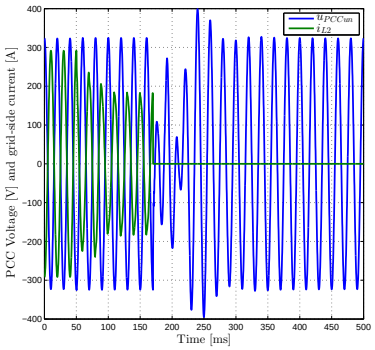

(c) Simulated results. $P_u^* = -45$ kW

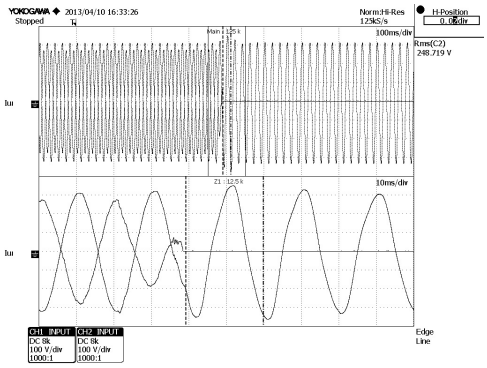

(d) Experimental results. $P_u^* = -45$ kW

Figure 5.90: Scenarios 20-21. Grid disconnection transient response when no-load under maximum active power set-point. Phase u

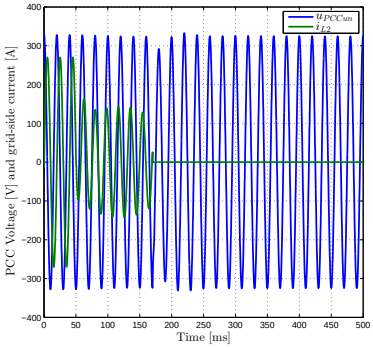

(a) Simulated results. $Q_u^* = 45$ kvar

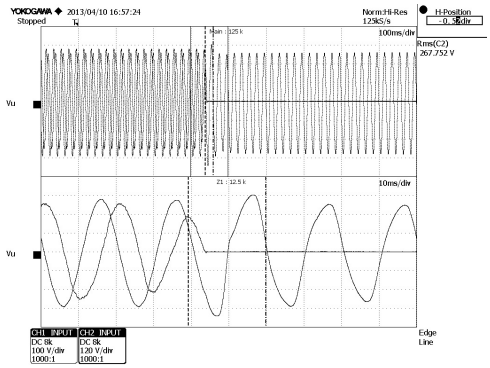

(b) Experimental results. $Q_u^* = 45$ kvar

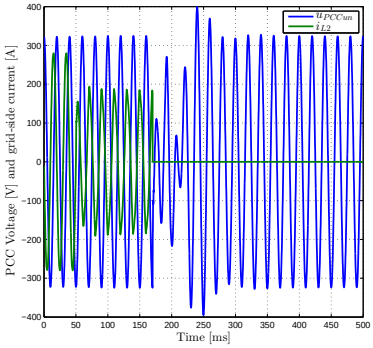

(c) Simulated results. $Q_u^* = -45$ kvar

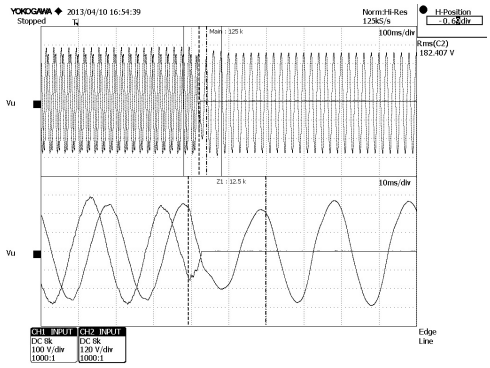

(d) Experimental results. $Q_u^* = -45$ kvar

Figure 5.91: Scenarios 22-23. Grid disconnection transient response when no-load under maximum reactive power set-point. Phase u

when -45 kW, scenario 26 when 45 kvar and, finally, scenario 27 when -45 kvar.

It can also be seen from the simulation results that when the transition order is received (t = 50 ms) the current is not able to follow the power set-point because the control strategy is changed. When the Island switch is opened a short transient occurs, not more than 100 ms. Observing the ITI curve shown in Figure 2.35, it can be seen that the voltage simulated results are at the limit of the damage region. However, observing the experimental results, the maximum RMS value is about 80.5% and the minimum about 78% for 20 to 30 ms. Once more, this is located in the no interruption region of the ITI curve.

- Scenario 28-29. In this case, a reconnection procedure is ordered. It should be noted that the reconnection procedure is intentional and totally controlled when the mains is sufficient stable according to the applied regulation. For all the simulated grid-disconnected to grid-connected intentional transition results analysis, the next steps are followed:

  1. Time 0 to 20 ms. The system is operating in grid-disconnected steady state ($R_v = 0\ \Omega$) under the proposed V/f control strategy. The system is synchronized with the utility by using the modified PLL algorithm presented in Figure 2.33.
  2. Time 20 ms. A reconnection order is received. The virtual resistance R_v is set to 1 Ω and starts to decrease up to the steady-state value of 0.2 Ω, according to the exposed in Section 5.5.1. It is proposed a decrease ratio of 0.16 Ω/s. The dynamic droop is enabled. Thus, the VSI starts to operate under the dynamic droop control strategy with null PQ set-points.
  3. Time 20 to 60 ms. Turn-on time of the Island switch.
  4. Time 60 ms. The Island switch is closed.
  5. Time 60 ms to ∞ ms. The system is operated in grid-connected mode under the dynamic droop control strategy control strategy until a new disconnection order is received. New PQ set-point are accepted after 1 s. This times is the considered to have stable voltages at the AC capacitors after the reconnection process.

  Figure 5.94 shows the transient simulated and experimental results for scenario 28, i.e. with no-load connected at the PCC. As, for this

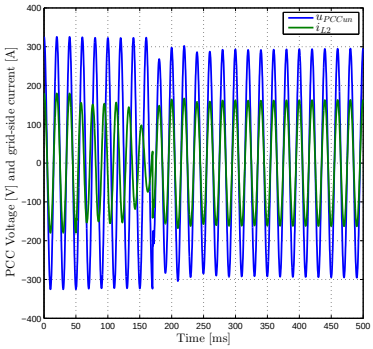

(a) Simulated results. $P_u^* = 45$ kW

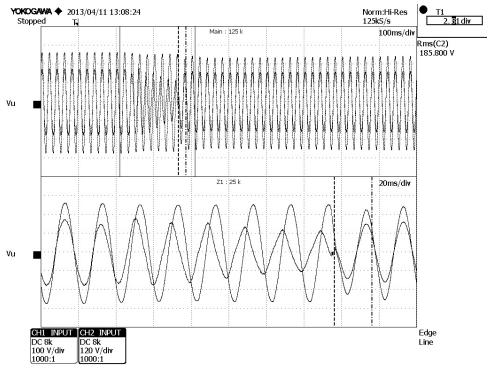

(b) Experimental results. $P_u^* = 45$ kW

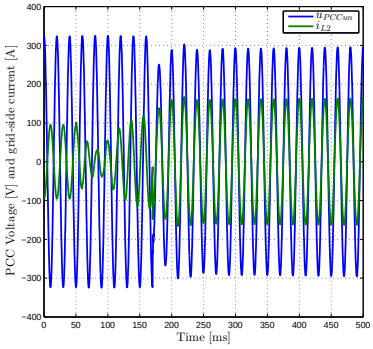

(c) Simulated results. $P_u^* = -45$ kW

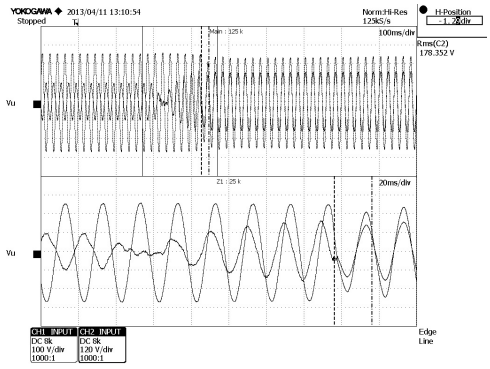

(d) Experimental results. $P_u^* = -45$ kW

Figure 5.92: Scenarios 24-25. Grid disconnection transient response when a resistive 30 kW load is connected under maximum active power set-point. Phase u

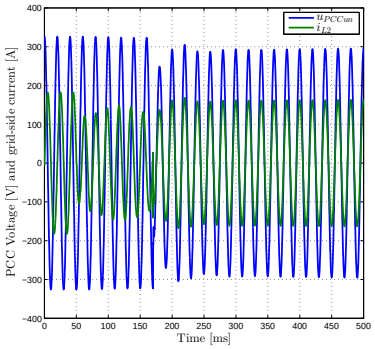

(a) Simulated results. $Q_u^* = 45$ kvar

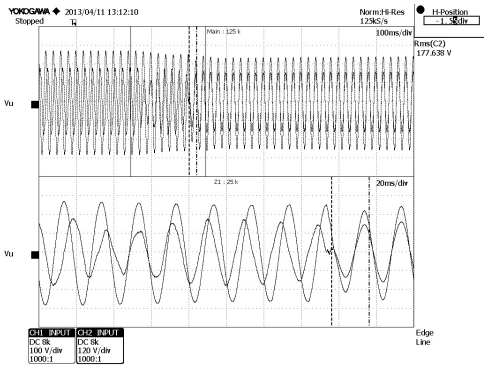

(b) Experimental results. $Q_u^* = 45$ kvar

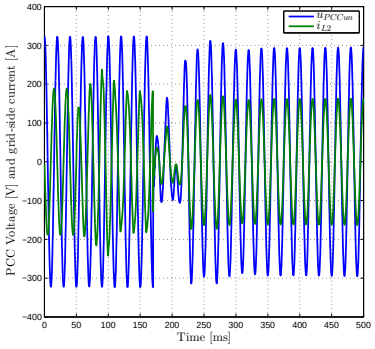

(c) Simulated results. $Q_u^* = -45$ kvar

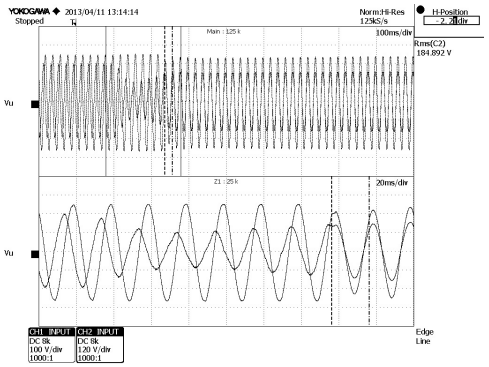

(d) Experimental results. $Q_u^* = -45$ kvar

Figure 5.93: Scenarios 26-27. Grid disconnection transient response when resistive 30 kW load is connected under maximum reactive power set-point is referenced. Phase u

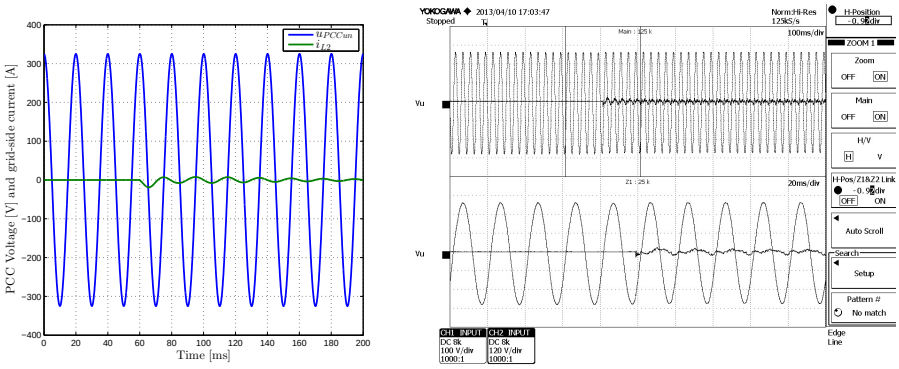

(a) Simulated results. (b) Experimental results

Figure 5.94: Scenarios 28. Reconnection transient response when no-load connected at the PCC

scenario, there is not a grid-side consumption during the close time of the Island switch, there is no effect of R_v. Then, the reconnection transient effect is practically non-existent.

Figure 5.95 shows the transient simulated and experimental results for scenario 29, i.e., with a resistive 30 kW local load. In this case, there is a grid-side consumption during the close time of the Island switch. Consequently, the voltage at the PCC and the grid-side current are related through R_v. This effect can be observed in the voltage sag of Figure 5.95(a). When the Island switch is close, the PCC voltage is determined by the utilty.

5.8.5 The three-leg interleaved DC/DC ripple analysis in grid-connected operation

To analyse the robustness on the stability of the DC-link, scenario 30 is proposed to study the DC-link oscillation under the same case presented in scenario 1. Figure 5.96 shows a maximum ripple on the DC-link of 35 VDC.

5.8.6 The three-leg interleaved DC/DC time response in grid-disconnected operation

Two more scenarios based on analyse the effect of a disturbance at the DC-link while it is controlled by the three-leg interleaved DC/DC controllers, proposed in Section 5.7, are presented.

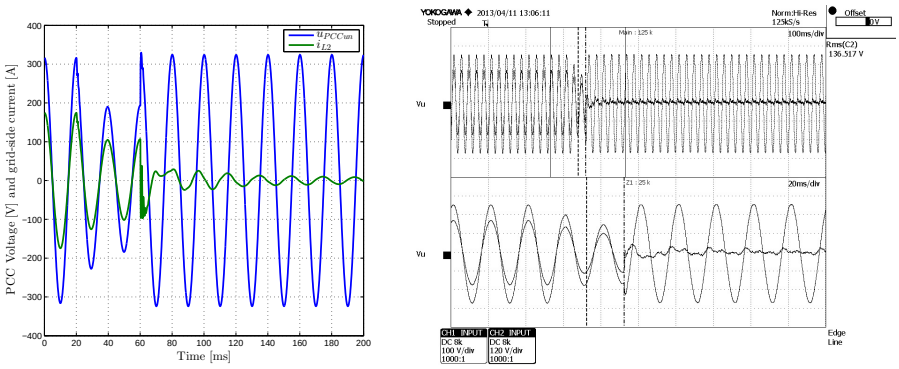

(a) Simulated results (b) Experimental results

Figure 5.95: Scenarios 29. Reconnection transient response when resistive 30 kW load is connected at the PCC

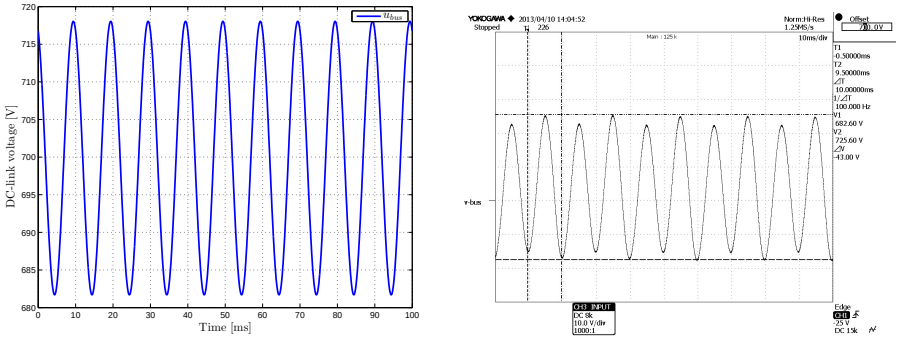

(a) Simulated results. (b) Experimental results.

Figure 5.96: Scenarios 30. Ripple oscillation analysis on the DC-link under unbalance PQ set-point of the VSI side

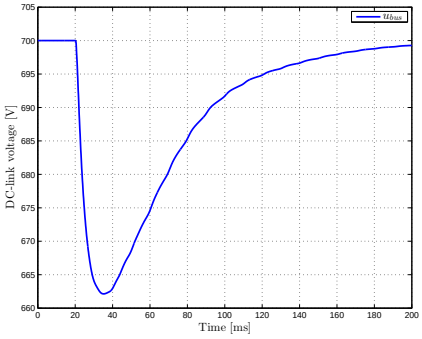

(a) Simulated results. Increasing disturbance from $P^* = -15$ kW to 0 kW

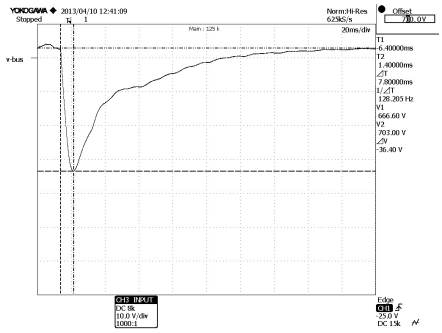

(b) Experimental results. Increasing disturbance from $P^* = -15$ kW to 0 kW

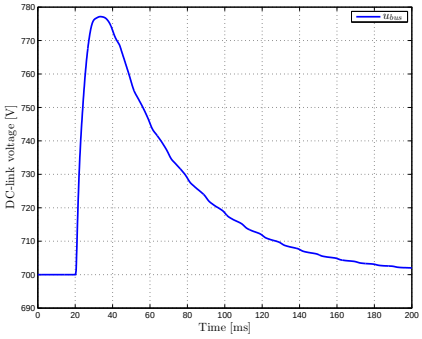

(c) Simulated results. Decreasing disturbance from $P^* = 30$ to 0 kW

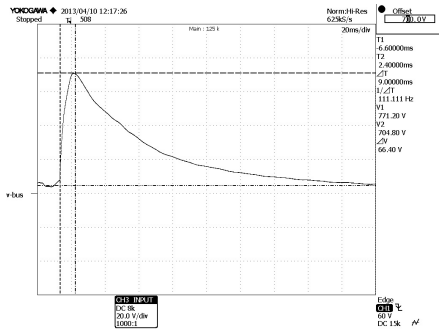

(d) Experimental results. Decreasing disturbance from $P^* = 30$ kW to 0 kW

Figure 5.97: Scenarios 31-32. Disturbance analysis on the DC-link

In scenario 31, a negative active power set-point is targeted to the VSI in grid-connected mode. Then, suddenly, the VSI is disabled. In this way, it is possible to analyse the effect of a disturbance on the DC-link as if the VSI is operating in grid-disconnected mode.

Scenario 32 is analogous to 31 but the difference is that the active power reference is positive. Now, when the VSI side will be disabled, a negative disturbance on the DC-link is applied.

Figure 5.97 shows a maximum simulated and experimental response of about -40 VDC for scenario 31 and 80 VDC for scenario 32. This means that the DC-link should be sized to support, at least, 800 VDC if the overload capability of the microgrid VSI proposed and a security margin range is considered.

5.9 Summary

Although most installed inverters during last years operate as Current Controlled Voltage Source Inverters (CC-VSI) when they are grid-connected, the use of concepts related to microgrids to enhance the electric system is changing this trend. New regulations are pushing renewable inverters to operate not only in grid-connected but also in grid-disconnected. The transference between this operation modes is relevant and use the same voltage source behaviour in both modes is a strong foothold to ensure a seamless transient. However, in grid-connected mode it is no possible to operate as an ideal voltage source if it is desired to exchange power with the utility. In this sense, the AC droop control is used for this purpose. Besides, AC droop control, static or dynamic, implies poor dynamics responses in grid-disconnected mode due to its implementation emulation as rotatory machines.

A hybrid control strategy based on the dynamic AC droop control strategy when the inverter is grid-connected and on a V/f control strategy when it is grid-disconnected supports the whole operation. The master loop in grid-connected mode is based on a predominant resistive line model. To ensure this situation, the use of a dynamic virtual resistance has been considered. With this hybrid control criterion, the most complex situation in terms of control, that is the possible dynamic requirements in grid-disconnected mode (non linear-loads) can be supported but maintaining a voltage source behaviour for both operation modes. The inner loops (voltage and current) are implemented by adaptive proportional-resonant with harmonic compensator controllers. In this sense, the desired AC frequency setpoint can be recomputed according to the AC requirements each switching period. In order to attenuate possible resonances produced by the LCL-type filter at the AC side or excited by the PR controller, an active damping series resistor at the AC capacitor has been implemented.

According to the previous lines, this chapter presents the design and control of a special converter for an experimental microgrid based on a DC/DC interface converter and a three-phase four-leg inverter with a LCL-type coupling filter. The design is done considering the same power stack for all the converters. The set-up is based on a 135 kVA development (rated power 90 kVA). This converter is intended to interface a DC microgrid with a voltage range from 150 to 500 VDC and an AC microgrid of 400 V-50 Hz ($\pm$10%). It also requires a short-circuit proof capability during grid-disconnected operation and up to 50% overload capability during grid-connected operation. The converter is able to operate in grid-connected and grid-disconnected allowing hot-transients between the operation modes (non zero-crossing volt-

age transients).

With reference to the design, the coupling elements (inductances, DC-link and AC capacitors) are sized. Furthermore, a simplified SVPWM strategy for a four-leg based on three-leg inverters SVPWM and Fortescue's decompositions has been proposed and used. The methodology limitations in terms of over-modulation are also studied. The design of the LCL-type coupling filter of the AC side has been done according to the novel modulation proposed. The computation required time and the program memory are compared with conventional SVPWM for three-wire inverters and with a conventional 3-D SVPWM.

About the special algorithms detailed, an over-modulation supervisor is proposed to autonomously adapt the DC-link voltage level between the DC/DC converter and the four-leg inverter according to the AC-side consumption needs. Also, for the inverter, an over-load manager handles the overload requirements based on an overloaded energy exchange criterion, and a short-circuit proof algorithm based on the computation of rms values is introduced.

A wide set of simulated and experimental scenarios supports the different ideas developed along the chapter. These scenarios contemplates:

- For the grid-connected mode: PQ unbalance tracking, dynamic droop analysis, energy quality.

- For the grid-disconnected mode: disturbance response, short-circuit proof capability and energy quality analysis.

- Transferences between operation modes under different situations: intentional transient from grid-connected to grid-disconnected and reconnection under no-load operation and at rated power.

Chapter 6

Conclusions

A microgrid can be defined as a localized small-scale bidirectional energy grid system, AC or DC, supported by the increasing proliferation of distributed energy resources. These microgrids dispose of the control capability to handle delicate processes, as can be the mains disconnection to start an autonomously operation as an electric island. Likewise, these microgrids can be reconnected to the area or local electric power system with minimal disruption to the local loads by using a point of common coupling. Nonetheless, the implication of the different involved layers; physical (switches, protections, power converters, storage systems or renewable resources), informative (information and communications technologies), energetic (service operators, energy managers or electric markets), ownership, control (power, voltage or current), among others, makes a microgrid a really complex, transversal and challenging system to contribute with cutting-edge ideas and technologies.

Nowadays, AC loads compose a relevant part of the different type of loads that constitutes the end-consumptions. The proper operation of AC microgrids ensures the safely operation of the microgrid itself and the public utility permitting to enhance different energy quality indices. After a deep study of the present AC microgrids paradigm, this thesis concludes with different control proposals to enhance and support their operation under different approaches.

6.1 Realized tasks

In this section, a summary of the realized tasks presented is listed:

- From Chapter 1: It has been analysed the definition behind the general concept of microgrid, describing microgrids from different contexts; the operation aspects, roles, standards or types of designation. It has been also presented a set of ongoing operative microgrids around the world.

- From Chapter 2: It has been studied the different operation modes and components for the particular case of AC microgrids. From this search, a clear picture of the operation particularities in terms of control is deduced. Pining AC microgrid control down, it has been faced the mains loss.

  The galvanic isolation challenge for AC microgrids complements the previous topic.

- From Chapter 3: An important effort on the analysis of tracking AC references for the inner loops (voltage and current) has been done. This aspect has conducted to the study of the different reference frames that can be used in electric systems from a control outlook. Conventional synchronous reference frame controllers have been examined and new control possibilities based on fractional calculus have been explored.

- From Chapter 4: The classic operation of grid supply inverters commonly applied extensively in DER, as in the photovoltaic or wind cases, have been expanded to optimize their use in AC microgrids. Two main case studies have been contemplated; the transference between grid-connected and grid-disconnected operation, and the MPPT extended execution when the inverters are supported by back-up systems under three representative situations; the transference, irradiation changes and consumptions variations.

- From Chapter 5: A proposal of a four-wire converter thought for an AC-DC microgrid interconnection has been evaluated. A mixed control strategy based on known concepts as dynamic AC droop or V/f control is developed to improve the dynamics in grid-disconnected mode. The operation of the inverter has been analysed taking into consideration wide DC voltage swings, high order coupling filters (LCL-type), active damping control strategies, hot-swapping skills and special features as over-load (inverter), short-circuit proof capabilities (inverter) or over-modulation supervisor (DC/DC). It has been also developed a new SVPWM methodology for four-leg inverters based on three-leg inverters and Fortescue's decomposition, and compared with other conventional 2-D or 3-D options in terms of computational burdens and program memory.

  Chapters 3 to 5 are supported by simulations and experimental results.

6.2 Conclusions

This section details a synopsis of the most relevant conclusions and results of this thesis.

- From Chapter 2: *AC microgrids control and operation* can conclude that AC microgrids are not only constituted by its elemental device, i.e. the inverter. The AC microgrid operates under the coexistence of other elements as the main breaker, the protection devices or smart switches, the management unit(s), the local loads and all integrated thanks to the use of industrial communications to exchange data. Notwithstanding, it is paramount to analyse in detail the different possible inverters that can coexist side-by-side in a microgrid. A review of different type of inverters, coupling filters and controls has been performed.

  The applied control strategy will define the role of the inverter within the microgrid and will present some challenges that have been coped; the mains loss detection effectiveness according to the applied control strategy and the suitable selection of galvanic isolation.

  Different anti-islanding detection mechanisms have been widely used in conventional distributed energy resources, i.e. grid-feeding distributed energy resources. Although there exists several proved detection algorithms for those cases, it has been verified that most of them are ineffective when the operation framework is an AC microgrid, especially the active ones based on the voltage and frequency displacements of the point of common coupling.

  As the AC microgrid inverter can be considered as a generator, the possible incorporation of galvanic isolation could be a requisite. In conventional grids, transformers feeds power in only one sense. However in AC microgrids this situation is extended to a more complex operation condition. A microgrid can operate at different frequency ranges, can work in a four-quadrant P/Q scenario and can be subjected to any positive, negative or zero sequence current demand or voltage feed. All these circumstances are studied and some recommendations according to the type of core and windings are outlined according to space, cost, maintenance or rated apparent power restrictions.

- From Chapter 3: *Inner control loops analysis* can conclude, from a Nyquist trajectory study, that in case of using resonant controllers in the continuous time domain there is no limitation in the frequencies to be controlled, in terms of stability, for the single current or voltage

control loop. Per contra, when a cascaded control loop is considered, the maximum frequency limit depends on the obtained controller gains of both loops.

Nowadays, the continuous time domain can be considered as a start point but it does not result enough useful for digital implementations. The same analysis done for the continuous time is broaden to the discrete-time domain. Due to the complexity of an analytical stability analysis in this case, numerical three-dimensional plots define a surface that shows the maximum theoretical controllable harmonic component. This surface is according to the controller gains and the switching frequency contemplating, also, a possible pure delay in the control chain.

A method to tune the voltage control loop for conventional resonant controllers is extended from an existing current loop proposal. The methodology is based on the time response design specifications. The effect of a time-varying set-point on the settling time is analysed for the current loop under two assumptions; a pure delay in the control chain and the settling-time over the target time ratio. It has been observed that the major effect in time-varying set-points concerns to the second case resulting in non tolerable errors as the mentioned ratio increases.

On the other hand, a novel controller based on the application of fractional order calculus into resonant controllers is developed. The existence of a fractional proportional-resonant controller formulation that improves the frequency behaviour considering a non-integer order coefficient is demonstrated. This single controller reduces the inter-harmonic excitation inherent to resonant multi-harmonic controllers. Several approximation of the non-integer order coefficient have been considered and compared regarding implementation challenges. The proposed controller has been implemented in a real test platform and its harmonic compensating capability has been validated. The set-up system assumed is an active filter against a highly non-linear load and a short-circuited inverter to illustrate the complex trajectory tracking capabilities.

- From Chapter 4: *Grid supply Inverters operation proposal for AC microgrids* can be concluded that is possible to extend conventional grid-feeding inverters operation to AC microgrids. Instead of only deal with the grid-connected mode, two proposals are studied; how to face

a flying transference between the operation modes (grid-connected and grid-disconnected) and how to extend the maximum power point operation if it is connected to a back-up system.

In the flying transference case, a control strategy based on the hybridation of voltage monitoring envelopes and an active anti-islanding algorithm is proposed to detect rapidly a possible mains loss situation. A criterion concerning the type of grid-side fault occurrence is performed according to the response of certain AC voltage reference. The proper initialization of the AC voltage controller is also considered as a key point; bumpless and reset options are compared. The reset alternative presents a better transient behaviour. On the other hand, the reconnection procedure has been also examined. It has been observed that the opening and closing times of the controlled switch that segregates the grid from the inverter are crucial for a good transference in both senses. The control strategy is supported by a set of simulation and experimental results for a three-phase inverter and different local load consumptions.

In the second case, a control strategy to extend the use of the maximum power point tracking algorithm for photovoltaic inverters that can operate in the grid-connected and grid-disconnected mode has been proposed. The presented algorithm prioritizes the charging of the batteries from the PV system. It allows to operate the photovoltaic inverter at the maximum power point during the maximum time possible when it is supported by a back-up system based on batteries. As in the previous case, the control strategy is supported by a set of simulation and experimental results but now for a single-phase inverter case, different state of charge of the back-up system, and different local load or irradiation sudden variations.

- From Chapter 5: *Proposal of a four-wire three-phase AC inverter for microgrids* can conclude that a special converter to assist an experimental AC microgrid has been developed. It is based on a DC/DC interface converter plus a three-phase four-leg inverter. The set-up is a 135 kVA device (rated power 90 kVA) intended to interface a DC microgrid with a voltage range from 150 to 500 VDC and a four-wire three-phase AC microgrid of 400 V-50 Hz ($\pm$10%).

  The DC/DC converter is focused on step-up the voltage of the storage system. Thus, an autonomously way to regulate the DC-link voltage level is presented according to the AC-side needs.

The proposed control and topology of the AC-side converter allows managing non-balanced injected power with power overload capability when it is grid-connected. It is suggested a control mechanism to manage sinusoidal short-circuit currents when grid-disconnected presenting smooth voltage transients under fault clearance. The inverter is operated by using a hybrid combination between an AC droop control strategy based on dynamic phasors when grid-connected, and a voltage-frequency control strategy when it grid-disconnected operated. An adaptive resistive model applying the virtual resistance concept is considered for this purpose. For both operation modes a LCL-type coupling filter is adopted examining an active damping strategy for the grid-(dis)connected operation.

The size of the coupling filters for both the inverter (based on a space vector modulation) and the DC/DC (based on interleaving modulation) is analysed. For the particular case of the inverter, a new simplified space vector modulation is proposed for two-level four-leg converters taking profit of conventional modulation techniques for three-wire inverters. This strategy is based on conventional 2-D space vector modulation with minor changes. The proposed modulation permits a better implementation than other conventional 3-D alternative in terms of program memory without increasing excessively the computational burdens.

All the proposed control strategies are supported by a set of simulation and experimental results for the grid-(dis)connected modes.

6.3 Future work

The microgrid regulation is often changing and being updated. Then, from Chapter 1 and 2, the most recent regulation and standards about microgrids can be reviewed. The new technical considerations can determine some upgrades into the content of the full thesis.

From Chapter 2, a more depth study of the limitations of conventional anti-islanding methods applied to droop-based inverters can be extended. In this sense, it should be analysed and tested other alternatives rather than active methods based on positive feedback, as can be impedance measurements methods. In this line, the development of an intelligent and autonomous main-switch that will include an anti-islanding method is an interesting topic.

From Chapter 3, the controller tune procedures based on frequency features can be analysed in detail and the present theoretical limitations can be adjusted to these new premises. Also, the new fractional-resonant formulation for current controllers can be extended to the voltage loop, analysing the effect of the controllability region due to the obtained cascaded close-loop wide bandwidth.

Chapters 4 and 5 are focused on the utilisation of only one inverter. Although some of the applied control strategies contemplates the possibility to operate in parallel with other inverters, this alternative has not been studied. A deep analysis of the interactions when more than one inverter is assumed can be done. Also, the controllability limits according to the number of inverters and the ancillary algorithms (maximum power point trackers, anti-islanding, phase locked loops, among others) could require to be redesigned.

In case of chapter 4 the improvement of the detection criterion for grid fault consideration should be improved for unbalanced systems and the consideration of a static-switch instead of a conventional contactor should be studied.

The extended MPPT depends, essentially, on a microgrid manager. In this sense, to develop an intelligent agent that manages, local or globally, the energy fluxes, is determinant. Not only for the MPPT but also for the whole strategies considered along these chapters. In the particular case of the MPPT operation, the effect of partial shadowing will be relevant to ensure robustness. Also, the inclusion of demand side management (DSM) loads will help to increase the effectiveness of the proposal.

The stability of AC microgrids when the different type of inverters, i.e. the grid-supply inverters, grid constitution inverters or grid supply and constitution inverters, cooperate is a challenging topic. Furthermore, the consideration of different type of storage systems can support the microgrid stability according to different inertia criteria. On the same topic, these possible high inertial skills could require new converter topologies.

In case of chapter 5, a redesign of the converter can be considered. For example, the use of the neutral inductances can be omitted. In case of considering multi-level topologies, it will be required a redefinition of the space vector modulation technique developed for two-level four-wire inverters.

6.4 Publications

6.4.1 Directly related with the thesis content

Articles/Proceedings

- Published
  - **Title**: *A novel fractional proportional-resonant current controller for Voltage Source Converters*
    Authors: Daniel Heredero, Enric Sánchez, Cristian Chillón, Daniel Montesinos and Samuel Galceran
    Citation: Proceedings of the EPE. Karlsruhe. 2016
  - **Title**: *Understanding the three and four-leg inverter Space Vector*
    Authors: Marc Llonch, Daniel Heredero, Daniel Montesinos and Joan Rull
    Citation: Proceedings of the EPE. Karlsruhe. 2016
  - **Title**: *Understanding the three and four-leg inverter Space Vector*
    Authors: Francesc Girbau, Andreas Sumper, Daniel Heredero, Cristian Chillón, Marc Pagès, Roberto Villafáfila, and Ramon Gallart
    Citation: Proceedings of the EPE. Karlsruhe. 2016
  - **Title**: *An anti-islanding method for voltage controlled VSI*
    Authors: Marc Llonch, Daniel Heredero and Daniel Montesinos
    Citation: Proceedings of the EPE. Geneve. 2015
  - **Title**: *Inverter design for four-wire microgrids*
    Authors: Daniel Heredero, Marc Pagès and Daniel Montesinos
    Citation: Proceedings of the EPE. Geneve. 2015
  - **Title**: *Stability analysis of current and voltage resonant controllers for Voltage Source Converters*
    Authors: Enric Sánchez, Daniel Heredero and Daniel Montesinos
    Citation: Proceedings of the EPE. Geneve. 2015
  - **Title**: *Permanent execution of MPPT algorithm for PV systems with energy storage*
    Authors: Daniel Heredero, Marc Pagès, Gabriel Gross and Daniel Montesinos
    Citation: Proceedings of the PEDG. Aachen. 2015
  - **Title**: *Convertidores smart para la redes eléctricas del futuro*
    Authors: Daniel Heredero, Marc Pagès and Daniel Montesinos
    Citation: Automática e Instrumentación. Vol. 470. 2015

- **Title**: *Implementation of grid-connected to/from off-grid transference for micro-grid inverters*
  Authors: Daniel Heredero, Cristian Chillón, Marc Pagès, Gabriel Gross and Daniel Montesinos
  Citation: Proceedings of the IECON. Vienna. 2013

- **Title**: *Grid-connected to/from off-grid transference for micro-grid inverters*
  Authors: Daniel Heredero, Cristian Chillón, Marc Pagès, Gabriel Gross and Daniel Montesinos
  Citation: Proceedings of the PCIM. Nürnberg. 2013

- Journal articles under review

  - Title: *AC control contributions to assist the operation of four-wire microgrids*
    Authors: Daniel Heredero, Marc Pagès, Daniel Montesinos, Mónica Aguado, David Rivas and Mikel Santamaría
    Citation: IEEE PES Transactions on Power Delivery 2016. Reviewed and expected major revisions.

  - **Title**: *Tuning procedure proposal for fractional proportional-resonant current controllers*
    Authors: Daniel Heredero, Cristian Chillón, Enric Sánchez and Daniel Montesinos
    Citation: IIEEE PES Transactions on Power Delivery 2016. Regular paper under review.

  - **Title**: *Simplified Space Vector PWM for four-wire three-phase inverters*
    Authors: Daniel Heredero, Marc Llonch, Marc Pagès and Daniel Montesinos
    Citation: IEEE PES Transactions on Power electronics 2016. Reviewed and expected to include experimental results.

Patents

- **Title**: *Equipo fotovoltaico y procedimiento para controlar dicho equipo fotovoltaico*
  Publication number: ES2421857 B1
  Inventors: Eduardo Gálvez, Martí Torné, Ramon Carreras, Marc Pagès, Daniel Heredero, Gabriel Gross, Daniel Montesinos

Applicant: CIRCUTOR, S.A.
Granted: 27/08/2014

- **Title**: *Device and method for the disconnection and subsequent reconnection of an inverter to/from an electrical network*
  Publication number: EP2621048 B1
  Inventors: Eduardo Gálvez, Martí Torné, Ramon Carreras, Marc Pagès, Daniel Heredero, Gabriel Gross, Daniel Montesinos
  Applicant: CIRCUTOR, S.A.
  Granted: 04/11/2015

6.4.2 Indirectly related with the thesis content

Articles/Proceedings

- Published
  - **Title**: *Resonant load emulator for distributed energy resources to test anti-islanding algorithms*
    Authors: Daniel Heredero, Fernando Jorge, Daniel Montesinos and Tomàs Lledó
    Citation: Proceedings of the PCIM. Nürnberg. 2016
  - **Title**: *Development and implementation of a dynamic PV emulator with HMI interface for high power inverters*
    Authors: Daniel Heredero, Macià Capó, Carlos Miguel, Tomàs Lledó and Daniel Montesinos
    Citation: Proceedings of the EPE. Lappeenranta. 2014
  - **Title**: *Charging/discharging process for electric vehicles: proposal and emulation*
    Authors: Miquel Barnola, Daniel Heredero, Roberto Villafáfila, Daniel Montesinos, Joan Bergas, Narcís Vidal
    Citation: Proceedings of the IEVC. Florence. 2014
  - **Title**: *Assessment of the Impact of Electric Vehicles on Iberian Day-ahead Electricity Market*
    Authors: Pol Olivella, Guillem Bosch, Roberto Villafáfila, Daniel Heredero, Mario Kovacevic, Niels Leemput
    Citation: Proceedings of the IEVC. Florence. 2014
  - **Title**: *El ecosistema del vehículo eléctrico*
    Authors: Roberto Villafáfila, Pol Olivella, Daniel Heredero and Antoni Sudrià
    Citation: Automática e Instrumentación. Vol. 452. 2013

- **Title**: *Emulador de paneles fotovoltaicos para el ensayo de onduladores*
  Authors: Carlos Miguel, Daniel Montesinos, Gabriel Gross, Daniel Heredero, Guillermo Martín
  Citation: Automática e Instrumentación. Vol. 440. 2012
- **Title**: *Electric vehicles in power systems with distributed generation: Vehicle to Microgrid (V2M) project*
  Authors: Roberto Villafáfila, Pau Lloret, Daniel Heredero, Andreas Sumper, Ignasi Cairó, Miguel Cruz, Narcís Vidal
  Citation: Proceedings of the EPQU. 2011
- **Title**: *Gestión de baterías en los vehículos eléctricos e híbridos enchufables*
  Authors: Daniel Montesinos and Daniel Heredero
  Citation: Automática e Instrumentación. Vol. 434. 2011

Utility model

- **Title**: *Dispositivo para la carga y descarga de baterías de vehículo eléctrico*
  ID number: ES1077796 Y
  Inventors: Roberto Villafáfila, Daniel Heredero, Narcís Vidal Tejedor y Jorge Sànchez
  Applicant: Endesa
  Granted: 10/01/2013

Appendix A

The space vector and Clarke & Park transforms

A.1 Introduction

It is usual to depict three balanced voltage vectors delayed 120^o between them to represent a three-phase system in a phasor perspective. This option is applied when a steady-state analysis wants to be conducted. However, if it is desired to use these axes as a reference basis for an instantaneous vectorial analysis it can result ambiguous in the plane. The main reason is due to the lineal dependency of the third component. Thus, it is only necessary two of them for vector generation. When a three-wire grid is balanced there are only two degrees of freedom justified by

$$u_{an}(t) + u_{bn}(t) + u_{cn}(t) = 0 \tag{A.1}$$

being $u_{xn}(t)$ the instantaneous voltage between the active phase x and the reference, in this case, n. Equation A.1 is moving in a plane π defined by the normal vector [1 1 1]. On the other hand, in case of unbalanced systems this relation is not true and it is possible to define that

$$u_{an}(t) + u_{bn}(t) + u_{cn}(t) \neq 0 \tag{A.2}$$

It can be deduced that Equation A.2 is moving in the space. Fortescue's theorem [163] supports that any unbalanced system can be decoupled in three balanced systems; one of positive sequence, a second one of negative sequence and a final one of zero sequence. Fortescue's theorem, also known as the theorem of symmetrical components, was developed by D. L. Fortecue in 1918. This theorem states that three unbalanced phasors of a three-phase system can be decomposed into three balanced systems of phasors. This set of three systems is as follows:

- Direct sequence. Same magnitude, 120° between phases and clockwise rotation.

- Inverse sequence. Same magnitude, 120° between phases and counter-clockwise rotation.
- Homopolar sequence. Same magnitude and 0° between phases.

Then, in Figure A.1, it is possible to see an example of an unbalanced currents system and their decomposition in a three phasorial balanced systems:

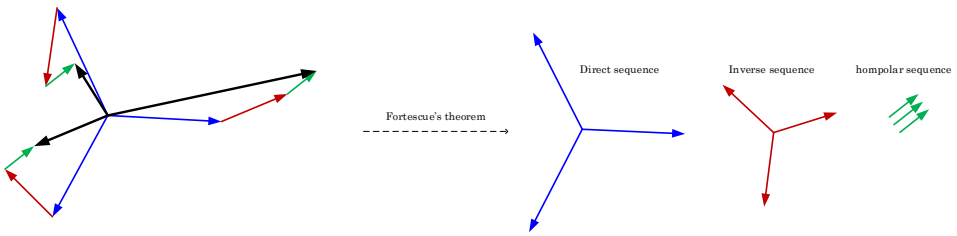

Figure A.1: Example of Fortescue's decomposition of an unbalanced system

Writing Fortescue's theorem in equations

$$\begin{cases} u_a = u_a^d + u_a^i + u_a^h \\ u_b = u_b^d + u_b^i + u_b^h \\ u_c = u_c^d + u_c^i + u_c^h \end{cases} \tag{A.3}$$

If a defined as $a = e^{\frac{2\pi}{3}j}$, all referencing to the voltage V_a, it is possible to deduce:

$$\begin{cases} u_a = u_a^d + u_a^i + u_a^h \\ u_b = a^2\, u_a^d + a\, u_a^i + u_a^h \\ u_c = a\, u_a^d + a^2\, u_a^i + u_a^h \end{cases} \tag{A.4}$$

where can easily be extracted the transformation matrix between the original voltages and direct, inverse and homopolar voltage is

$$\begin{pmatrix} u_a \\ u_b \\ u_c \end{pmatrix} = \begin{pmatrix} 1 & 1 & 1 \\ a^2 & a & 1 \\ a & a^2 & 1 \end{pmatrix} \begin{pmatrix} u_a^d \\ u_a^q \\ u_a^h \end{pmatrix} \tag{A.5}$$

This matrix is invertible. The relation A.4 can be expressed in reverse, leaving to

$$\begin{cases} u_d = 1/3(u_a + a\, u_b + a^2\, u_c) \\ u_i = 1/3(u_a + a^2\, u_b + a\, u_c) \\ u_h = 1/3(u_a + u_b + u_c) \end{cases} \tag{A.6}$$

In Equation A.6, can be drawn that if the system is balanced, it do not have homopolar component. Similarly, if it is considered that the device is a three-phase without neutral, voltages are composed like

$$\begin{cases} u_{ab} = (1-a^2)\, u_a^d + (1-a)\, u_a^i \\ u_{bc} = (a^2-a)\, u_a^d + (a-a^2)\, u_a^i \\ u_{ca} = (a-1)\, u_a^d + (a^2-1)\, u_a^i \end{cases} \tag{A.7}$$

From the last expression A.7 can be observed that the homopolar voltage does not appear, therefore, the system can only be decomposed into direct and inverse sequence. To clarify the use of direct, inverse and homopolar or positive, negative and zero nomenclature it is possible to stablish a relation between them as depicted in FigureA.2 [242].

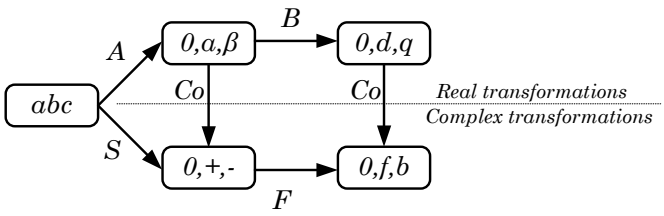

Figure A.2: Overview of different transformations

S is the complex transformation matrix introduced by Fortescue

$$S = \begin{pmatrix} 1 & 1 & 1 \\ a^2 & a & 1 \\ a & a^2 & 1 \end{pmatrix} \tag{A.8}$$

A and B are Clarke and Park transforms detailed in the following subsections A.2 and A.3 as T and P, respectively. F is the forward-backward transformation

$$F = \begin{pmatrix} 1 & 0 & 0 \\ 0 & e^{j\theta} & 0 \\ 0 & 0 & e^{-j\theta} \end{pmatrix} \tag{A.9}$$

and, finally, Co is the complex transformation

$$Co = \frac{1}{\sqrt{2}} \begin{pmatrix} \sqrt{2} & 0 & 0 \\ 0 & 1 & 1 \\ 0 & -j & j \end{pmatrix} \tag{A.10}$$

On the other hand, from Equations A.1 and A.2 can be concluded that the positive and negative components are contained on the plane π and the zero sequence components are perpendicular to that plane. Given any three-phase magnitude, the space vector $\vec{s}(t)$ concept can be described as a vector that represents each voltage in the canonic orthonormal *abc* reference $C = \{[1\,0\,0],[0\,1\,0],[0\,0\,1]\}$ when a spacial analysis is applied. In this sense $u_a(t)$ is linked with $\vec{u}_1 = [1\,0\,0]$, $u_b(t)$ with $\vec{u}_2 = [0\,1\,0]$ and $u_c(t)$ with $\vec{u}_3 = [0\,0\,1]$. Although C reference is perfectly useful it is not practical for electric systems where the habitual case is more related with positive and negative sequences rather than with zero sequence. Figure A.3 allows to see how is described the trajectory of the space vector $\vec{s}(t)$ over time for a considered positive fundamental component. The green hexagon represents the plane π. The trajectory of $\vec{s}(t)$ turns at the ω rad/s.

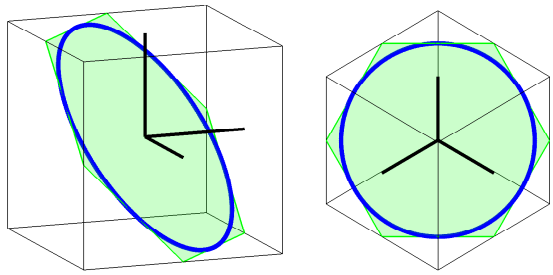

(a) Persepecive 1 (b) Persepecive 2

Figure A.3: 3D representation of basis C (black axes) and the space vector trajectory over time for a positive sequence component (blue trajectory)

To decouple the information of positive/negative sequences from the zero sequence a new axes reference can be considered. The widely used one for the instantaneous case is known as Clarke transformation [242]. Essentially, it consists in the projection of the vector $\vec{v}_1 = [1\,0\,0]$ over the plane π. This mathematical application implies a rotation over $\vec{v}_2$ of $acos(\sqrt{\frac{2}{3}})$ rad, obtaining $\vec{v}_1\,'$, $\vec{v}_3\,'$ with $\vec{v}_2\,' = \vec{v}_2$. To provide a new orthonormal reference with two vectors contained on the plane π, a new rotation over $\vec{v}_1\,'$ of $acos(\frac{\sqrt{2}}{2})$ rad is applied, obtaining $\vec{v}_2\,''$, $\vec{v}_3\,''$ and $\vec{v}_1\,'' = \vec{v}_1\,'$.

Thus, the new basis $C_1 = \{[\sqrt{\frac{2}{3}}\ \frac{-1}{\sqrt{6}}\ \frac{-1}{\sqrt{6}}],[0\ \frac{1}{\sqrt{2}}\ \frac{-1}{\sqrt{2}}],[\frac{1}{\sqrt{3}}\ \frac{1}{\sqrt{3}}\ \frac{1}{\sqrt{3}}]\}$ can be achieved. Figure A.4(a) shows basis C in black and C_1 in fuchsia.

Once this second rotation is applied a decoupled axis over π is achieved,

where the information of the positive and negative sequence is described by $\vec{v}_1{}''$ and $\vec{v}_2{}''$ whereas the zero sequence is completely described by $\vec{v}_3{}''$. Figure A.4(b) shows how the space trajectory of $\vec{s}(t)$ over π is seen in the natural *abc* reference and when the new basis C_1 is considered.

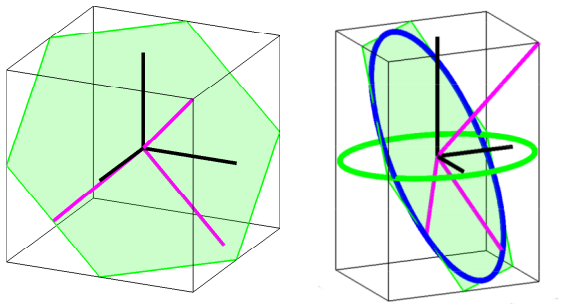

(a) *abc* axes and Clarke axes (b) $\vec{s}(t)$ trajectory over *abc* axes and over Clarke axes

Figure A.4: Orthonormal basis C (black axes) and C_1 (fuchsia axes). Space vector $\vec{s}(t)$ trajectory over time for a positive sequence component (blue line) and when Clarke transformed (green line)

A.1.1 Other space vector trajectories

In case of a system with positive and inverse sequence of the fundamental component the trajectory of $\vec{s}(t)$ follows an elliptical path over the plane π, as is shown in Figure A.5.

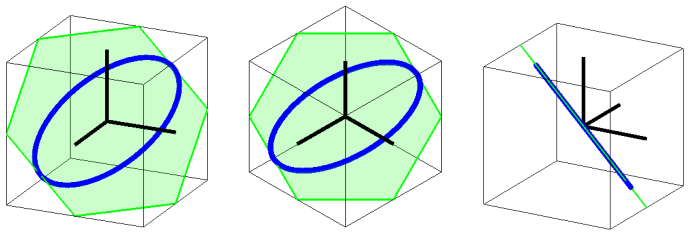

Figure A.5: Space vector $\vec{s}(t)$ trajectory over time for a 50 Hz positive and inverse component

When harmonics components or unbalanced systems are taken into account $\vec{s}(t)$ adopts different trajectories that can be contained in π or not.

Figure A.6 shows different possibilities when different harmonics components are added to the fundamental component. It is possible to confirm that only harmonics that are a multiple of the third harmonic component follow a trajectory out of π.

As a conclusion, can be deduced that positive and negative sequence components are contained in π and moves following an elliptical trajectory while zero sequence components moves only over the homopolar axis following a linear trajectory.

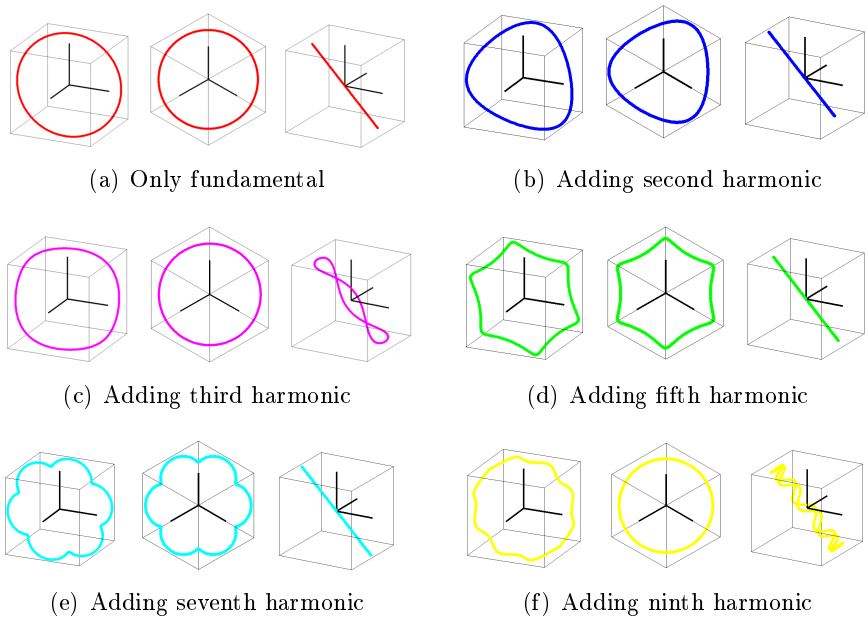

(a) Only fundamental (b) Adding second harmonic

(c) Adding third harmonic (d) Adding fifth harmonic

(e) Adding seventh harmonic (f) Adding ninth harmonic

Figure A.6: Space vector $\vec{s}(t)$ trajectory over time for a 50 Hz direct component plus a 10% of harmonic content

A.2 Clarke transform

Once introduced the behaviour of a three-phase system in space, can be confirmed that Clarke transformation is a useful mathematical tool for three-phase electric magnitudes. However, in the electrical scope different requirements could be required. In this sense, the norm of the Clarke application can be focused on a module invariant or power invariant perspective [110]. Concatenating the rotations cited above, a T matrix and its inverse can be

obtained

$$T = \sqrt{\frac{2}{3}} \begin{pmatrix} 1 & -\frac{1}{2} & -\frac{1}{2} \\ 0 & \frac{\sqrt{3}}{2} & -\frac{\sqrt{3}}{2} \\ \frac{1}{\sqrt{2}} & \frac{1}{\sqrt{2}} & \frac{1}{\sqrt{2}} \end{pmatrix} \quad T^{-1} = T^t = \sqrt{\frac{2}{3}} \begin{pmatrix} 1 & 0 & \frac{1}{\sqrt{2}} \\ -\frac{1}{2} & \frac{\sqrt{3}}{2} & \frac{1}{\sqrt{2}} \\ -\frac{1}{2} & -\frac{\sqrt{3}}{2} & \frac{1}{\sqrt{2}} \end{pmatrix} \tag{A.11}$$

In this sense, $X_{\alpha\beta\gamma} = TX_{abc}$ and $X_{abc} = T^{-1}X_{\alpha\beta\gamma}$. It should be noticed that T is orthonormal.

A.2.1 Power invariant

The instantaneous power of a balanced three-wire three-phase system is defined in the *abc* reference as

$$p_{abc} = u_a i_a + u_b i_b + u_c i_c \tag{A.12}$$

and using T, in the $\alpha\beta\gamma$ reference, as

$$p_{\alpha\beta\gamma} = u_\alpha i_\alpha + u_\beta i_\beta \tag{A.13}$$

Thus,

$$\begin{aligned} u_\alpha &= \sqrt{\frac{2}{3}} \left(u_{an} - 1/2u_{bn} - 1/2u_{cn}\right) \\ i_\alpha &= \sqrt{\frac{2}{3}} \left(i_a - 1/2i_b - 1/2i_c\right) \\ u_\beta &= \sqrt{\frac{2}{3}} \frac{\sqrt{3}}{2} \left(u_{bn} - u_{cn}\right) \\ i_\beta &= \sqrt{\frac{2}{3}} \frac{\sqrt{3}}{2} \left(i_b - i_c\right) \end{aligned}$$

Expanding $p_{\alpha\beta\gamma}(t)$ using previous defined $u_{\alpha\beta}$ and $i_{\alpha\beta}$,

$$p_{\alpha\beta\gamma} = p_{abc} \tag{A.14}$$

In case of an electrical system with homopolar sequence, this can be computed in a decoupled way as

$$p_\gamma = u_\gamma i_\gamma = -i_n(u_{an} + u_{bn} + u_{cn}) \tag{A.15}$$

being i_n the current of the neutral wire. Thus, for the power-invariant case, the Clarke transformation T_1 and its inverse T_1^{-1} are

$$T_1 = \sqrt{\frac{2}{3}} \begin{pmatrix} 1 & -\frac{1}{2} & -\frac{1}{2} \\ 0 & \frac{\sqrt{3}}{2} & -\frac{\sqrt{3}}{2} \\ \frac{1}{\sqrt{2}} & \frac{1}{\sqrt{2}} & \frac{1}{\sqrt{2}} \end{pmatrix} \quad T_1^{-1} = T^t = \sqrt{\frac{2}{3}} \begin{pmatrix} 1 & 0 & \frac{1}{\sqrt{2}} \\ -\frac{1}{2} & \frac{\sqrt{3}}{2} & \frac{1}{\sqrt{2}} \\ -\frac{1}{2} & -\frac{\sqrt{3}}{2} & \frac{1}{\sqrt{2}} \end{pmatrix} \tag{A.16}$$

A.2.2 Module invariant

If the matrix T is normalized with a factor k it is possible to obtain a Clarke transformation that maintains the module of the magnitudes in respect with the *abc* reference. In this sense, a new T_2 transformation is considered

$$T_2 = k \begin{pmatrix} 1 & -\frac{1}{2} & -\frac{1}{2} \\ 0 & \frac{\sqrt{3}}{2} & -\frac{\sqrt{3}}{2} \\ \frac{1}{\sqrt{2}} & \frac{1}{\sqrt{2}} & \frac{1}{\sqrt{2}} \end{pmatrix} \tag{A.17}$$

Considering a balanced three-phase system where

$$\begin{aligned} f_a &= sin(\omega t) \\ f_b &= sin(\omega t - \frac{2\pi}{3}) \\ f_c &= sin(\omega t + \frac{2\pi}{3}) \end{aligned}$$

then

$$f_\alpha = k \left(sin(\omega t) - 0.5 sin(\omega t - \frac{2\pi}{3}) - 0.5 sin(\omega t + \frac{2\pi}{3}) \right) = \cdots = k \frac{3}{2} sin(\omega t)$$

$$f_\beta = k \frac{\sqrt{3}}{2} \left(sin(\omega t - \frac{2\pi}{3}) - sin(\omega t + \frac{2\pi}{3}) \right) = \cdots = k \frac{3}{2} sin(\omega t + \frac{\pi}{2})$$

where it is possible to observe that when $k = \frac{2}{3}$, the norm in both references are equal, implying that $\|X_{\alpha\beta}\| = \|X_{abc}\|$.

In this case, for the homopolar component, if $k = \frac{2}{3}$, f_γ results

$$f_\gamma = \frac{\sqrt{2}}{3} (f_a + f_b + f_c)$$

Thus, for the module invariant case, the Clarke transformation T_2 and its inverse T_2^{-1} are

$$T_2 = \frac{2}{3}\begin{pmatrix} 1 & -\frac{1}{2} & -\frac{1}{2} \\ 0 & \frac{\sqrt{3}}{2} & -\frac{\sqrt{3}}{2} \\ \frac{1}{\sqrt{2}} & \frac{1}{\sqrt{2}} & \frac{1}{\sqrt{2}} \end{pmatrix} \quad T_2^{-1} = \frac{1}{2}\begin{pmatrix} 2 & 0 & \sqrt{2} \\ -1 & \sqrt{3} & \sqrt{2} \\ -1 & -\sqrt{3} & \sqrt{2} \end{pmatrix} \tag{A.18}$$

A.3 Park transform

Park's transformation is widely known in its final form that concatenates Clarke transformation with a new rotation that can be or not time dependent. Thus, when the rotation is in clockwise (same sense that positive sequence in electric systems), Park's transformation is defined by

$$P = \begin{pmatrix} \cos(\theta) & -\sin(\theta) & 0 \\ \sin(\theta) & \cos(\theta) & 0 \\ 0 & 0 & 1 \end{pmatrix} T \tag{A.19}$$

In this sense, $X_{dqh} = PX_{abc}$ and $X_{abc} = P^{-1}X_{dqh}$. The subscripts d, q and h represents the direct, quadrature and homopolar components, respectively. It is possible to observe that the rotation is done over the $\alpha\beta$ components whereas γ is maintained invariant. The idea behind this transformation is move from a static reference to a synchronous reference frame. In this sense, the rotation angle θ used will depend on the final application. For example, in the electric motor literature there are three remarkable cases [243]:

- Synchronous reference. The angle $\theta = \omega_s t$ where ω_s is the synchronism angular frequency.
- Rotor reference. The angle $\theta = 0$.
- Stator reference. The angle $\theta = \omega_m$ where ω_m is the rotor angular frequency. In asynchronous machines

$$s = \frac{\omega_s - \omega_m}{\omega_s} \tag{A.20}$$

being s the slip.

Thus, for the case of grid-connected inverters, $\theta = \omega_g t$ where ω_g is the angular frequency of the grid. Then, when the power invariant Clarke transformation is used,

$$P = \sqrt{\frac{2}{3}}\begin{pmatrix} \cos(\theta) & \cos(\theta - \frac{2\pi}{3}) & \cos(\theta + \frac{2\pi}{3}) \\ -\sin(\theta) & -\sin(\theta - \frac{2\pi}{3}) & -\sin(\theta + \frac{2\pi}{3}) \\ \frac{1}{\sqrt{2}} & \frac{1}{\sqrt{2}} & \frac{1}{\sqrt{2}} \end{pmatrix} \tag{A.21}$$

and its inverse

$$P^{-1} = P^t = \sqrt{\frac{2}{3}} \begin{pmatrix} \cos(\theta) & -\sin(\theta) & \frac{1}{\sqrt{2}} \\ \cos(\theta - \frac{2\pi}{3}) & -\sin(\theta - \frac{2\pi}{3}) & \frac{1}{\sqrt{2}} \\ \cos(\theta + \frac{2\pi}{3}) & -\sin(\theta + \frac{2\pi}{3}) & \frac{1}{\sqrt{2}} \end{pmatrix} \tag{A.22}$$

When the module invariant is used,

$$P' = \frac{2}{3} \begin{pmatrix} \cos(\theta) & \cos(\theta - \frac{2\pi}{3}) & \cos(\theta + \frac{2\pi}{3}) \\ -\sin(\theta) & -\sin(\theta - \frac{2\pi}{3}) & -\sin(\theta + \frac{2\pi}{3}) \\ \frac{1}{\sqrt{2}} & \frac{1}{\sqrt{2}} & \frac{1}{\sqrt{2}} \end{pmatrix} \tag{A.23}$$

and its inverse

$$P'^{-1} = \begin{pmatrix} \cos(\theta) & -\sin(\theta) & \frac{1}{\sqrt{2}} \\ \cos(\theta - \frac{2\pi}{3}) & -\sin(\theta - \frac{2\pi}{3}) & \frac{1}{\sqrt{2}} \\ \cos(\theta + \frac{2\pi}{3}) & -\sin(\theta + \frac{2\pi}{3}) & \frac{1}{\sqrt{2}} \end{pmatrix} \tag{A.24}$$

Appendix B

Droop control

B.1 Introduction

Classical distribution airlines are usually considered predominantly inductive. For this reason the ordinary differential equation that describe an inductance L with a parasitic series resistance R is

$$u_1(t) - u_2(t) = Ri(t) + L\frac{di(t)}{dt} \tag{B.1}$$

where $u_1(t)$ and $u_2(t)$ are the voltages applied at its terminals and i the current flowing through the inductance. Figure B.1 shows an scheme of the system under study. Applying the Laplace transformation to Equation B.1 is deduced

$$U_1(s) - U_2(s) = RI(s) + sLI(s) \tag{B.2}$$

Thus, it is possible to obtain the transmittance

$$\frac{I(s)}{U_1(s) - U_2(s)} = \frac{1}{Ls + R} \tag{B.3}$$

The droop control equations will be presented in the following section from an static and a dynamic perspective.

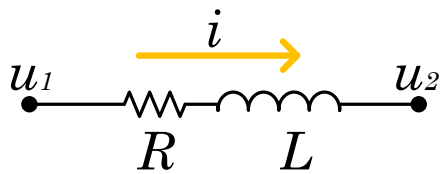

Figure B.1: Scheme of a RL impedance

B.2 Static model

The current I that flows through and impedance accomplishes the Ohm's law

$$\underline{I} = \frac{\underline{U_1} - \underline{U_2}}{\underline{Z}} \tag{B.4}$$

In this sense, the power computed at node 2 is

$$\underline{S} = \underline{U_2}\underline{I}^* = \underline{U_2}\left(\frac{\underline{U_1} - \underline{U_2}}{\underline{Z}}\right)^* \tag{B.5}$$

If $\theta_{U_2} = 0$ and $\theta_{U_1} = \delta$ is considered, then

$$\begin{aligned}\underline{S} &= U_2\left(\frac{U_1\cos\delta + jU_1\sin\delta - U_2}{R + j\omega L}\right)^* \\ &= \frac{U_1U_2\cos\delta - {U_2}^2 - jU_1U_2\sin\delta}{R - j\omega L} \\ &= \frac{\left(U_1U_2\cos\delta - {U_2}^2 - jU_1U_2\sin\delta\right)(R + j\omega L)}{R^2 + \omega^2L^2}\end{aligned} \tag{B.6}$$

Collecting the real part as the active power P and the imaginary part as the reactive power Q

$$P = \frac{\left(U_1U_2\cos\delta - {U_2}^2\right)R}{R^2 + \omega^2L^2} + \frac{(U_1U_2\sin\delta)\,\omega L}{R^2 + \omega^2L^2} \tag{B.7}$$

$$Q = \frac{\left(U_1U_2\cos\delta - {U_2}^2\right)\omega L}{R^2 + \omega^2L^2} - \frac{(U_1U_2\sin\delta)\,R}{R^2 + \omega^2L^2} \tag{B.8}$$

For small δ angles it can be used the approximation of $\sin\delta \approx \delta$ and $\cos\delta \approx 1$. Thus,

$$P = \frac{\left(U_1U_2 - {U_2}^2\right)R}{R^2 + \omega^2L^2} + \frac{(U_1U_2\delta)\,\omega L}{R^2 + \omega^2L^2} \tag{B.9}$$

$$Q = \frac{\left(U_1U_2 - {U_2}^2\right)\omega L}{R^2 + \omega^2L^2} - \frac{(U_1U_2\delta)\,R}{R^2 + \omega^2L^2} \tag{B.10}$$

B.2.1 Inductive lines

In a predominantly inductive line where $\omega L >> R \;\rightarrow\; R \approx 0$ it is possible to simplify Equations B.9 and B.10 as

$$P \approx \frac{U_1U_2}{\omega L}\delta \tag{B.11}$$

$$Q \approx \frac{U_2}{\omega L}(U_1 - U_2) \tag{B.12}$$

B.2.2 Resistive lines

In a predominantly inductive line where $R >> \omega L \ \rightarrow \ L \approx 0$) it is possible to simplify Equations B.9 and B.10 as

$$P \approx \frac{U_2}{R}\left(U_1 - U_2\right) \tag{B.13}$$

$$Q \approx -\frac{U_1 U_2}{R}\delta \tag{B.14}$$

B.3 Dynamic model

It is desired to obtain a dynamic model that decouples the relation between two complex variables; power (active and reactive) and voltage (module and phase). With this purpose the use of dynamic phasors [137–140, 142, 143] is considered. Equation B.1 in phasorial terms is

$$\underline{U}_1(t) - \underline{U}_2(t) = R\underline{I}(t) + L\frac{d}{dt}\underline{I}(t) \tag{B.15}$$

It can be understood that any phasor can be represented by separating the amplitude and the phase. However, identifying the dynamics of the phasor, the phase itself can also be separated in a constant rotation (no dynamics), altered by a $\delta(t)$ time-varying function, that symbolizes the dynamics that affects the rotation variations. Thus, the current can be expressed as

$$\underline{I}(t) = I(t)e^{j(\omega t + \delta(t))} = I(t)e^{j\omega t}e^{j\delta(t)} \tag{B.16}$$

Defining the dynamic current phasor $\underline{I}_D(t) = I(t)e^{j\delta(t)}$ as that one that collects the dynamics of the original phasor

$$\underline{I}(t) = e^{j\omega t}\underline{I}_D(t) \tag{B.17}$$

it is possible to rewrite Equation B.15 as

$$\underline{U}_1(t) - \underline{U}_2(t) = Re^{j\omega t}\underline{I}_D(t) + L\frac{d}{dt}\left[e^{j\omega t}\underline{I}_D(t)\right] \tag{B.18}$$

Expanding the derivative term of Equation B.18

$$\underline{U}_1(t) - \underline{U}_2(t) = Re^{j\omega t}\underline{I}_D(t) + Lj\omega e^{j\omega t}\underline{I}_D(t) + Le^{j\omega t}\frac{d\underline{I}_D(t)}{dt} \tag{B.19}$$

Now, if the Laplace transformation is applied and considering the rotation term $e^{j\omega t}$ as a constant (it rotates at constant speed),

$$\underline{U}_1(s) - \underline{U}_2(s) = Re^{j\omega t}\underline{I}_D(s) + Lj\omega e^{j\omega t}\underline{I}_D(s) + Le^{j\omega t}s\underline{I}_D(s) \tag{B.20}$$

from where recombining it with Equation B.17, but in the Laplace domain

$$\underline{U}_1(s) - \underline{U}_2(s) = R\underline{I}(s) + j\omega L\underline{I}(s) + sL\underline{I}(s) \tag{B.21}$$

$$\underline{I}(s) = \frac{\underline{U}_1(s) - \underline{U}_2(s)}{R + j\omega L + sL} \tag{B.22}$$

Thus, from Equation B.22, the power transmitted is defined by

$$\underline{S} = P + jQ = \underline{U}_2\underline{I}^* = \underline{U}_2\left(\frac{\underline{U}_1 - \underline{U}_2}{R + j\omega L + sL}\right)^* \tag{B.23}$$

Considering $\theta_{U_2} = 0$ and $\theta_{U_1} = \delta$

$$\begin{aligned}\underline{S} &= U_2\left(\frac{U_1\cos\delta + jU_1\sin\delta - U_2}{R + sL + j\omega L}\right)^* \\ &= U_2\left(\frac{U_1\cos\delta - jU_1\sin\delta - U_2}{R + sL - j\omega L}\right) \\ &= \frac{\left(U_1U_2\cos\delta - {U_2}^2 - jU_1U_2\sin\delta\right)(R + sL + j\omega L)}{(R + sL - j\omega L)(R + sL + j\omega L)}\end{aligned} \tag{B.24}$$

Collecting the real part as the active power P and the imaginary part as the reactive power Q

$$P = \frac{\left(U_1U_2\cos\delta - {U_2}^2\right)(R + sL)}{(R + sL)^2 + (\omega L)^2} + \frac{(U_1U_2\sin\delta)\,\omega L}{(R + sL)^2 + (\omega L)^2} \tag{B.25}$$

$$Q = \frac{\left(U_1U_2\cos\delta - {U_2}^2\right)\omega L}{(R + sL)^2 + (\omega L)^2} - \frac{(U_1U_2\sin\delta)(R + sL)}{(R + sL)^2 + (\omega L)^2} \tag{B.26}$$

For small δ angles it can be used the approximation of $\sin\delta \approx \delta$ and $\cos\delta \approx 1$. Thus,

$$P = \frac{\left(U_1U_2 - {U_2}^2\right)(R + sL)}{(R + sL)^2 + (\omega L)^2} + \frac{(U_1U_2\delta)\,\omega L}{(R + sL)^2 + (\omega L)^2} \tag{B.27}$$

$$Q = \frac{\left(U_1U_2 - {U_2}^2\right)\omega L}{(R + sL)^2 + (\omega L)^2} - \frac{(U_1U_2\delta)(R + sL)}{(R + sL)^2 + (\omega L)^2} \tag{B.28}$$

B.3.1 Inductive lines

In a predominantly inductive line where $\omega L >> R \ \rightarrow \ R \approx 0$ it is possible to simplify Equations B.27 and B.28 by

$$P \approx \frac{U_1 U_2 \delta \omega L}{(R + sL)^2 + (\omega L)^2} \tag{B.29}$$

$$Q \approx \frac{\left(U_1 U_2 - {U_2}^2\right) \omega L}{(R + sL)^2 + (\omega L)^2} \tag{B.30}$$

Linearising, using a first order Taylor term around an equilibrium point $P_0 = 0$, $Q_0 = 0$, $\delta_0 = 0$ and $U_{10} = U_2$,

$$\Delta P \approx \frac{\partial P}{\partial U_1} \Delta U_1 + \frac{\partial P}{\partial \delta} \Delta \delta \tag{B.31}$$

$$\Delta Q \approx \frac{\partial Q}{\partial U_1} \Delta U_1 + \frac{\partial Q}{\partial \delta} \Delta \delta \tag{B.32}$$

where Δ represents the variation around the equilibrium point

$$\Delta P \approx \frac{U_2 \delta \omega L}{(R + sL)^2 + (\omega L)^2} \Delta U_1 + \frac{U_1 U_2 \omega L}{(R + sL)^2 + (\omega L)^2} \Delta \delta \tag{B.33}$$

$$\Delta Q \approx \frac{U_2 \omega L}{(R + sL)^2 + (\omega L)^2} \Delta U_1 - \frac{U_1 U_2 \delta \omega L}{(R + sL)^2 + (\omega L)^2} \Delta \delta \tag{B.34}$$

For small δ angles and $U_1 \approx U_2$

$$\Delta P \approx \frac{{U_1}^2 \omega L}{(R + sL)^2 + (\omega L)^2} \Delta \delta \tag{B.35}$$

$$\Delta Q \approx \frac{U_1 \omega L}{(R + sL)^2 + (\omega L)^2} \Delta U_1 \tag{B.36}$$

Evaluating in the equilibrium point and substituting the delay between voltages U_1-U_2 by $\delta = \theta_{U_1} - \theta_{U_2}$,

$$P \approx \frac{{U_1}^2 \omega L}{(R + sL)^2 + (\omega L)^2} \left(\theta_{U_1} - \theta_{U_2}\right) \tag{B.37}$$

$$Q \approx \frac{U_1 \omega L}{(R + sL)^2 + (\omega L)^2} \left(U_1 - U_2\right) \tag{B.38}$$

B.3.2 Resistive lines

In a predominantly inductive line where $R >> \omega L \ \rightarrow \ L \approx 0$) it is possible to simplify Equations B.27 and B.28 by

$$P \approx \frac{\left(U_1 U_2 - {U_2}^2\right)(R + sL)}{(R + sL)^2 + (\omega L)^2} \tag{B.39}$$

$$Q \approx -\frac{U_1 U_2 \delta (R + sL)}{(R + sL)^2 + (\omega L)^2} \tag{B.40}$$

Linearising, using a first order Taylor term around an equilibrium point $P_0 = 0$, $Q_0 = 0$, $\delta_0 = 0$ and $U_{10} = U_2$,

$$\Delta P \approx \frac{\partial P}{\partial U_1}\Delta U_1 + \frac{\partial P}{\partial \delta}\Delta\delta \tag{B.41}$$

$$\Delta Q \approx \frac{\partial Q}{\partial U_1}\Delta U_1 + \frac{\partial Q}{\partial \delta}\Delta\delta \tag{B.42}$$

where Δ represents the variation around the equilibrium point

$$\Delta P \approx \frac{U_2 (R + sL)}{(R + sL)^2 + (\omega L)^2}\Delta U_1 - \frac{U_1 U_2 \delta (R + sL)}{(R + sL)^2 + (\omega L)^2}\Delta\delta \tag{B.43}$$

$$\Delta Q \approx -\frac{U_2 \delta (R + sL)}{(R + sL)^2 + (\omega L)^2}\Delta U_1 - \frac{U_1 U_2 (R + sL)}{(R + sL)^2 + (\omega L)^2}\Delta\delta \tag{B.44}$$

For small δ angles and $U_1 \approx U_2$

$$\Delta P \approx \frac{U_1 (R + sL)}{(R + sL)^2 + (\omega L)^2}\Delta U_1 \tag{B.45}$$

$$\Delta Q \approx -\frac{{U_1}^2 (R + sL)}{(R + sL)^2 + (\omega L)^2}\Delta\delta \tag{B.46}$$

Evaluating in the equilibrium point and substituting the delay between voltages U_1-U_2 by $\delta = \theta_{U_1} - \theta_{U_2}$,

$$P \approx \frac{U_1 (R + sL)}{(R + sL)^2 + (\omega L)^2}(U_1 - U_2) \tag{B.47}$$

$$Q \approx -\frac{{U_1}^2 (R + sL)}{(R + sL)^2 + (\omega L)^2}(\theta_{U_1} - \theta_{U_2}) \tag{B.48}$$

Bibliography

[1] "Plan de energías renovables 2011-2020," Ministerio de Industria, turismo y comercio, Tech. Rep., 2011. xiii, 1, 2

[2] R. Carreras-Margalef, E. Galvez-Moreno, D. Heredero-Peris, G. Gross, D. Montesinos-Miracle, M. Pagès-Giménez, and M. Torne-Pibernat, "Device and method for the disconnection and subsequent reconnection of an inverter to/from an electrical network," European Patent EP 2 621 048 A1, 2012. xviii, 207, 215, 216

[3] R. Zhang, V. H. Prasad, D. Boroyevich, and F. C. Lee, "Three-dimensional space vector modulation for four-leg voltage-source converters," *IEEE Transactions on Power Electronics*, vol. 17, no. 3, pp. 314–326, 2002. xxvi, 42, 270, 275, 280, 281, 283

[4] A. Kouzou, *The Space Vector Modulation PWM Control Methods Applied on Four Leg Inverters*, 2011. [Online]. Available: http://www.intechopen.com/source/pdfs/14094/InTech-The_space_vector_modulation_pwm_control_methods_applied_on_four_leg_inverters.pdf xxvi, 276, 280, 281

[5] M. Perales, M. Prats, R. Portillo, J. Mora, J. Leon, and L. Franquelo, "Three-dimensional space vector modulation in abc coordinates for four-leg voltage source converters," *IEEE Power Electronics Letters*, vol. 99, no. 4, pp. 104–109, 2003. xxvi, 281, 282, 290, 291

[6] X. Li, Z. Deng, Z. Chen, and Q. Fei, "Analysis and Simplification of Three-Dimensional Space Vector PWM for Three-Phase Four-Leg Inverters," *IEEE Transactions on Industrial Electronics*, vol. 58, no. 2, pp. 450–464, Feb 2011. xxvi, 275, 283

[7] R. Lasseter, "MicroGrids," *Power Engineering Society Winter Meeting, IEEE*, vol. 1, pp. 305 – 308, 2002. 1

[8] B. Kroposki, R. Lasseter, T. Ise, S. Morozumi, S. Papatlianassiou, and N. Hatziargyriou, "Making micro-grids work," *Power and Energy Magazine, IEEE*, vol. 6 , Issue: 3, pp. 40 – 53, 2008. 1

[9] N. Hatziargyriou, *Architectures and Control*, Wiley, Ed. John Wiley and Sons Ltd, Chichester, 2014. 1

[10] A. Rathnayaka, V. Potdar, O. Hussain, and T. Dillon, "Identifying prosumer's energy sharing behaviours for forming optimal prosumer-communities," in *International Conference on Cloud and Service Computing (CSC)*, Dec 2011, pp. 199–206. 2

[11] J. Rocabert, A. Luna, F. Blaabjerg, and P. Rodriguez, "Control of Power Converters in AC Microgrids," *IEEE Transactions on Power Electronics*, vol. 27, no. 11, pp. 4734–4749, Nov 2012. 2

[12] D. Hohm and M. Ropp, "Comparative study of maximum power point tracking algorithms using an experimental, programmable, maximum power point tracking test bed," in *Photovoltaic Specialists Conference, IEEE*, 2000, pp. 1699–1702. 2, 39

[13] F. Katiraei, R. Iravani, N. Hatziargyriou, and A. Dimeas, "Microgrids management," *Power and Energy Magazine, IEEE*, vol. 6, no. 3, pp. 54–65, May 2008. 4, 6, 12

[14] "Evaluation of islanding detection methods for photovoltaic utility interactive power systems," IEA PVPS, Tech. Rep., 2002. 7

[15] *VDE 0126-1-1. Automatic disconnection device between a generator and the public low-voltage grid*, VDE Std., 2012. 7

[16] *VDE-AR-N 4105 2011-08 Power generation systems connected to the low-voltage distribution network - Technical minimum requirements for the connection to and parallel operation with low-voltage distribution networks*, VDE Std., 2011. 7, 10, 47, 48, 96, 257

[17] *IEC 61727. Photovoltaic (PV) systems - Characteristics of the utility interface*, IEC Std., 2004. 7, 47, 96, 257

[18] *IEEE Standard 1547 Standard for Interconnecting Distributed Resources with Electric Power Systems*, IEEE Std. July, 2003. 7, 10, 47, 57, 96, 257

[19] C. Marnay, H. Asano, S. Papathanassiou, and G. Strbac, "Policymaking for microgrids," *Power and Energy Magazine, IEEE*, vol. 6, no. 3, pp. 66–77, May 2008. 7

[20] G. Venkataramanan and C. Marnay, "A larger role for microgrids," *Power and Energy Magazine, IEEE*, vol. 6, no. 3, pp. 78–82, May 2008. 7

[21] D. E. Christopher Villarreal and M. Zafar, "Microgrids: A Regulatory Perspective," 2014. 7

[22] F. Girbau-Llistuella, J. Rodriguez-Bernuz, E. Prieto-Araujo, and A. Sumper, "Experimental validation of a single phase intelligent power router," in *Innovative Smart Grid Technologies Conference Europe (ISGT-Europe), 2014 IEEE PES*, Oct 2014, pp. 1–6. 8

[23] Q. Yu, "Applications of flexible AC transmissions system (FACTS) technology in SmartGrid and its EMC impact," in *IEEE International Symposium on Electromagnetic Compatibility (EMC)*, Aug 2014, pp. 392–397. 8

[24] H. Liu, X. Xu, and M. Ding, "The energy management system of the smartgrid characterized by multi-parts interactions," in *China International Conference on Electricity Distribution (CICED)*, Sept 2014, pp. 1056–1063. 8

[25] S. Jang, S. Han, S. H. Han, and K. Sezaki, "Optimal decision on contract size for V2G aggregator regarding frequency regulation," in *12th International Conference on Optimization of Electrical and Electronic Equipment (OPTIM)*, May 2010, pp. 54–62. 9

[26] R. Wang, Y. Li, P. Wang, and D. Niyato, "Design of a V2G aggregator to optimize PHEV charging and frequency regulation control," in *IEEE International Conference on Smart Grid Communications (SmartGridComm)*, Oct 2013, pp. 127–132. 9

[27] M. Wang, M. Ismail, R. Zhang, X. Shen, E. Serpedin, and K. Qaraqe, "A semi-distributed V2V fast charging strategy based on price control," in *Global Communications Conference (GLOBECOM), IEEE*, Dec 2014, pp. 4550–4555. 9

[28] *IEEE 2030. Guide for Smart Grid Interoperability of Energy Technology and Information Technology Operation with the Electric Power System (EPS), and End-Use Applications and Loads*, IEEE Std., 2011. 10

[29] *Generating Plants Connected to the Medium-Voltage Network (Technical Guideline)*, BDEW - Bundesverband der Energie- und Wasserwirtschaft e. V. Std., 2008. 10

[30] J. Driesen and F. Katiraei, "Design for distributed energy resources," *Power and Energy Magazine, IEEE*, vol. 6, no. 3, pp. 30–40, May 2008. 12

[31] M. Salcone and J. Bond, "Selecting film bus link capacitors for high performance inverter applications," in *Electric Machines and Drives Conference, 2009. IEMDC '09. IEEE International*, May 2009, pp. 1692–1699. 18

[32] E. Karfopoulos, P. Papadopoulos, S. Skarvelis-Kazakos, I. Grau, L. Cipcigan, N. Hatziargyriou, and N. Jenkins, "Introducing electric vehicles in the microgrids concept," 2011. 18

[33] G. Christophe and G. George, "Design of a Conceptual Framework for the V2G Implementation," *Energy 2030 Conference, ENERGY, IEEE*, vol. 1, pp. 1–3, 2008. 18

[34] F. Berthold, B. Blunier, D. Bouquain, S. Williamson, and A. M. A., "PHEV Control Strategy Including Vehicle to Home (V2H) and Home to Vehicle (H2V) functionalities," *Vehicle Power and Propulsion Conference (VPPC), IEEE*, vol. 1, pp. 1 – 6, 2011. 18

[35] R. Villafáfila-Robles, P. Lloret-Gallego, D. Heredero-Peris, A. Sumper, I. Cairo, M. Cruz-Zambrano, and N. Vidal, "Electric vehicles in power systems with distributed generation: Vehicle to Microgrid (V2M) project," in *Electrical Power Quality and Utilisation (EPQU), 2011 11th International Conference on*, Oct 2011, pp. 1–6. 18

[36] H. Lotfi and A. Khodaei, "AC Versus DC Microgrid Planning," *IEEE Transactions on Smart Grid*, vol. PP, no. 99, pp. 1–1, 2015. 18

[37] N. Hatziargyriou, H. Asano, R. Iravani, and C. Marnay, "Microgrids," *Power and Energy Magazine, IEEE*, vol. 5, no. 4, pp. 78–94, July 2007. 19

[38] http://smartruralgrid.eu/. 19

[39] http://www.cener.com/es/integracion-red-energias-renovables/121220microrred.asp. 19

[40] http://galvinpower.org/resources/microgrid-hub/smart-microgrids-faq/examples. 19

[41] L. Schmitt, S. Kayal, and J. Kumar, "Microgrids and the future of the European city," in *Smart Grid Conference (SASG), Saudi Arabia*, Dec 2014, pp. 1–3. 19

[42] A. Vojdani, "Smart Integration," *Power and Energy Magazine, IEEE*, vol. 6, no. 6, pp. 71–79, November 2008. 26

[43] F. J. Rodríguez, E. Bueno, M. Aredes, L. G. B. Rolim, F. a. S. Neves, and M. C. Cavalcanti, "Discrete-time implementation of second order generalized integrators for grid converters," *IECON, IEEE*, no. 1, pp. 176–181, 2008. 32, 139, 158, 162, 319

[44] J. J. Justo, F. Mwasilu, J. Lee, and J.-W. Jung, "AC-microgrids versus DC-microgrids with distributed energy resources: A review ," *Renewable and Sustainable Energy Reviews*, vol. 24, pp. 387 – 405, 2013. 35

[45] F. Inthamoussou, J. Pegueroles-Queralt, and F. Bianchi, "Control of a Supercapacitor Energy Storage System for Microgrid Applications," *IEEE Transactions on Energy Conversion*, vol. 28, no. 3, pp. 690–697, Sept 2013. 36

[46] A. Zeng, Q. Xu, M. Ding, K. Yukita, and K. Ichiyanagi, "A classification control strategy for energy storage system in microgrid." *IEEJ Transactions on Electric and Electronic Engineering*, vol. 10, p. 396 403, 2015. 36

[47] J. Rocabert, G. Azevedo, I. Candela, F. Blaabjerg, and P. Rodriguez, "Connection and disconnection transients for micro-grids under unbalance load condition," in *Proceedings of the 2011-14th European Conference on Power Electronics and Applications (EPE)*, Aug 2011, pp. 1–9. 36

[48] H. Minxiao, S. Xiaoling, L. Shaobo, and Z. Zhengkui, "Transient analysis and control for microgrid stability controller," in *PowerTech (POWERTECH), 2013 IEEE Grenoble*, June 2013, pp. 1–6. 36

[49] M. Llonch-Masachs, D. Heredero-Peris, and D. Montesinos-Miracle, "An anti-islanding method for voltage controlled VSI," in *European Conference on Power Electronics and Applications (EPE-ECCE Europe), IEEE.* EPE, 2015. 37, 92, 100

[50] ——, "Anti-islanding challenges analysis for Voltage-Controlled Voltage Source Inverters," *IEEE transactions on smart grids*, 2016. 37

[51] F. Peng, Y. W. Li, and L. Tolbert, "Control and protection of power electronics interfaced distributed generation systems in a customer-driven microgrid," in *Power Energy Society General Meeting, PES, IEEE*, July 2009, pp. 1–8. 37

[52] H. Laaksonen, "Protection Principles for Future Microgrids," *IEEE Transactions on Power Electronics*, vol. 25, no. 12, pp. 2910–2918, Dec 2010. 37, 52

[53] A. Kwasinski, "Advanced power electronics enabled distribution architectures: Design, operation, and control," in *IEEE 8th International Conference on Power Electronics and ECCE Asia (ICPE ECCE)*, May 2011, pp. 1484–1491. 37, 42

[54] J. R. Delgado, "Intelligent Connection Agent for Three-Phase Grid-Connected Microgrids," Ph.D. dissertation, UPC, 2010. 38

[55] J. Guerrero, L. Hang, and J. Uceda, "Control of Distributed Uninterruptible Power Supply Systems," *Industrial Electronics, IEEE Transactions on Power Electronics*, vol. 55, Issue: 8, pp. 2845 – 2859, 2008. 39, 75

[56] F. Liu, Y. Kang, Y. Zhang, and S. Duan, "Comparison of P&O and hill climbing MPPT methods for grid-connected PV converter," in *3rd IEEE Conference on Industrial Electronics and Applications, ICIEA*, June 2008, pp. 804–807. 39

[57] A. M. Babaa, S.E. and V. Pickert, "Overview of Maximum Power Point Tracking Control Methods for PV Systems," *Journal of Power and Energy Engineering*, pp. 59–72, 2014. 39

[58] O. Gomis-Bellmunt, A. Junyent-Ferre, A. Sumper, and J. Bergas-Jan, "Ride-Through Control of a Doubly Fed Induction Generator Under Unbalanced Voltage Sags," *IEEE Transactions on Energy Conversion*, vol. 23, no. 4, pp. 1036–1045, Dec 2008. 39

[59] F. Z. Peng, "Application issues of active power filters," *Industry Applications Magazine, IEEE*, vol. 4, no. 5, pp. 21–30, Sep 1998. 39

[60] Z. Chen, F. Blaabjerg, and J. Pedersen, "A study of parallel operations of active and passive filters," in *Power Electronics Specialists Conference, PESC, IEEE*, vol. 2, 2002, pp. 1021–1026 vol.2. 39

[61] M. Routimo, M. Salo, and H. Tuusa, "Comparison of Voltage-Source and Current-Source Shunt Active Power Filters," *IEEE Transactions on Power Electronics,*, vol. 22, no. 2, pp. 636–643, March 2007. 39

[62] W. Jian, H. Na, and X. Dianguo, "A 10 kV shunt hybrid active filter for a power distribution system," in *Applied Power Electronics Conference and Exposition, APEC, IEEE*, Feb 2008, pp. 927–932. 39

[63] T.-L. Lee, Y.-C. Wang, J.-C. Li, and J. Guerrero, "Hybrid Active Filter With Variable Conductance for Harmonic Resonance Suppression in Industrial Power Systems," *IEEE Transactions on Industrial Electronics*, vol. 62, no. 2, pp. 746–756, Feb 2015. 39

[64] K. Zhou and D. Wang, "Unified robust zero-error tracking control of CVCF PWM converters," *IEEE Transactions on Circuits and Systems I: Fundamental Theory and Applications*, vol. 49, no. 4, pp. 492–501, Apr 2002. 39

[65] E.-C. Chang, L.-P. Yin, R.-C. Wu, and L.-S. Yang, "Terminal Sliding Mode Controlled CVCF inverters," in *IEEE International Conference on Fuzzy Systems (FUZZ)*, June 2011, pp. 236–240. 39

[66] K. D. Brabandere, "Voltage and frequency droop control in low voltage grids by distributed generators with inverter front-end," Ph.D. dissertation, Katholike Universiteit Leuven, 2006. 40, 78, 81, 85, 313

[67] J. M. Guerrero, J. C. Vasquez, J. Matas, L. G. De Vicuña, and M. Castilla, "Hierarchical control of droop-controlled AC and DC microgrids - A general approach toward standardization," *IEEE Transactions on Industrial Electronics*, vol. 58, no. 1, pp. 158–172, 2011. 40

[68] H. Avelar, W. Parreira, J. Vieira, L. de Freitas, and E. Coelho, "A State Equation Model of a Single-Phase Grid-Connected Inverter Using a Droop Control Scheme With Extra Phase Shift Control Action," *Industrial Electronics, IEEE Transactions on Power Electronics*, vol. 59 Issue: 3, pp. 1527–1537, 2012. 40

[69] X. Zhang, J. Liu, and Z. You, "A state space model of paralleled inverters based on droop control in grid-connected microgrid," in *Applied Power Electronics Conference and Exposition (APEC), Twenty-Ninth Annual IEEE*, March 2014, pp. 1815–1820. 40, 70

[70] S. Peng, A. Luo, Z. Lv, J. Wu, and L. Yu, "Power control for single-phase microgrid based on the PQ theory," in *6th IEEE Conference on Industrial Electronics and Applications (ICIEA)*, June 2011, pp. 1274–1277. 40

[71] S. Dasgupta, S. Mohan, S. Sahoo, and S. Panda, "Application of Four-Switch-Based Three-Phase Grid-Connected Inverter to Connect Renewable Energy Source to a Generalized Unbalanced Microgrid System," *IEEE Transactions on Industrial Electronics*, vol. 60, no. 3, pp. 1204–1215, March 2013. 40

[72] G. Kim, C. Hwang, J. Jeon, G. Byeon, J. Ahn, and C. Jo, "Characteristic analysis of three-phase four-leg inverter based load unbalance compensator for stand-alone microgrid," in *9th International Conference on Power Electronics and ECCE Asia (ICPE-ECCE Asia)*, June 2015, pp. 1491–1496. 40

[73] Q. Sun, J. Zhou, J. Guerrero, and H. Zhang, "Hybrid Three-Phase Single-Phase Microgrid Architecture With Power Management Capabilities," *IEEE Transactions on Power Electronics*, vol. 30, no. 10, pp. 5964–5977, Oct 2015. 40

[74] C. Quinn and N. Mohan, "Active filtering of harmonic currents in three-phase, four-wire systems with three-phase and single-phase nonlinear loads," in *Applied Power Electronics Conference and Exposition, APEC, Conference Proceedings*, Feb 1992, pp. 829–836. 41

[75] F. Peng, H. Akagi, and A. Nabae, "A novel harmonic power filter," in *Power Electronics Specialists Conference, PESC, IEEE*, April 1988, pp. 1151–1159 vol.2. 41

[76] H. Akagi, Y. Kanazawa, and A. Nabae, "Instantaneous Reactive Power Compensators Comprising Switching Devices without Energy Storage Components," *IEEE Transactions on Industry Applications*, vol. IA-20, no. 3, pp. 625–630, May 1984. 41

[77] R. Torres-Olguin, G. Escobar, A. Valdez, and M. Martinez-Montejano, "A model-based controller for a three-phase four-leg shunt active

filter with homopolar current compensation," in *Power Electronics Congress, CIEP, IEEE*, Aug 2008, pp. 63–68. 42, 67

[78] J. Chen, J. Wang, Q. Chen, and D. Wu, "Optimal Dispatch of Medium-Voltage Microgrid Using an Adaptive PSO Algorithm," in *7th International Conference on Intelligent Human-Machine Systems and Cybernetics (IHMSC)*, vol. 1, Aug 2015, pp. 324–329. 42

[79] J. Song, M. Bozchalui, A. Kwasinski, and R. Sharma, "Microgrids availability evaluation using a Markov chain energy storage model: a comparison study in system architectures," in *Transmission and Distribution Conference and Exposition, IEEE*, May 2012, pp. 1–6. 42

[80] Y. X. Aleks Dimitrovski and L. T. Tom King, "Microgrid Protection and Control Technologies," DOE Microgrid Workshop, August 2011, san Diego, CA. 45

[81] IEA-PVPS-Report, "Evaluation of islanding detection methods for photovoltaic utility-interactive power systems," *Report IEA PVPS T5-09*, no. March, 2002. [Online]. Available: http://apache.solarch.ch/pdfinter/solar/pdf/PVPSTask509.pdf 46

[82] M. Bower, Ward Ropp, "Evaluation of islanding detection methods for utility-interactive inverters in photovoltaic systems," *Sandia Report*, 2002. 46

[83] P. Rodriguez, R. Teodorescu, and M. Liserre, *Grid Converters for Photovoltaic and wind power systems.* Wiley, 2011. 46, 47

[84] M. El-Moubarak, M. Hassan, and A. Faza, "Performance of three islanding detection methods for grid-tied multi-inverters," in *IEEE 15th International Conference on Environment and Electrical Engineering (EEEIC)*, June 2015, pp. 1999–2004. 46

[85] B. Singam and L. Y. Hui, "Assessing SMS and PJD schemes of anti-islanding with varying quality factor," *First International Power and Energy Conference, PECon Proceedings*, pp. 196–201, 2006. 46

[86] H. Zeineldin, "A Q-f Droop Curve for Facilitating Islanding Detection of Inverter-Based Distributed Generation," *IEEE Transactions on Power Electronics*, vol. 24, Issue: 3, pp. 665 – 673, 2009. 46, 210

[87] P. Hopewell, N. Jenkins, and a.D. Cross, "Loss-of-mains detection for small generators," *IEE Proceedings - Electric Power Applications*, vol. 143, no. 3, p. 225, 1996. 47

[88] P. O. Kane and B. Fox, "Loss of Mains Detection for Embedded Generation By System Impedance Monitoring," in *Developments in Power System Protection*, 1997, pp. 95–98. 47

[89] M. Ciobotaru, R. Teodorescu, and F. Blaabjerg, "On-line grid impedance estimation based on harmonic injection for grid-connected PV inverter," *IEEE International Symposium on Industrial Electronics*, no. i, pp. 2437–2442, 2007. 47

[90] L. Asiminoaei, R. Teodorescu, F. Blaabjerg, and U. Borup, "A new method of on-line grid impedance estimation for PV inverter," *Nineteenth Annual IEEE Applied Power Electronics Conference and Exposition, APEC*, vol. 3, no. C, 2004. 47

[91] ——, "Implementation and test of on-Line embedded grid impedance estimation for PV-inverters," *IEEE Annual Power Electronics Specialists Conference, PESC*, vol. 4, no. 4, pp. 3095–3101, 2004. 47

[92] ——, "A digital controlled PV-inverter with grid impedance estimation for ENS detection," *IEEE Transactions on Power Electronics*, vol. 20, no. 6, pp. 1480–1490, 2005. 47

[93] M. Ciobotaru, V. G. Agelidis, R. Teodorescu, and F. Blaabjerg, "Accurate and less-disturbing active antiislanding method based on PLL for grid-connected converters," *IEEE Transactions on Power Electronics*, vol. 25, pp. 1576–1584, 2010. 47

[94] [Online]. Available: http://www.ipdgroup.com.au/wms/upload/catalogues/Relays/HTML/files/assets/common/downloads/Relays.pdf 50

[95] W. Xu, G. Zhang, C. Li, W. Wang, G. Wang, and J. Kliber, "A Power Line Signaling Based Technique for Anti-islanding Protection of Distributed Generators: Part I: Scheme and Analysis," in *2007 IEEE Power Engineering Society General Meeting*, June 2007, pp. 1–1. 50

[96] A. Oudalov, "Microgrid Protection: Microgrids Evolution and Integration in Modern Power Systems," IEEE PES Swiss Chapter Workshop, April 2014, ABB Switzerland Ltd. 51

[97] M. Madan and B. Chowdhury, "Solid state fault interruption devices in medium voltage microgrid distribution systems with distributed energy resources," in *Power and Energy Society General Meeting, 2012 IEEE*, July 2012, pp. 1–6. 53

[98] C. Yuan, M. Haj-ahmed, and M. Illindala, "Protection Strategies for Medium-Voltage Direct-Current Microgrid at a Remote Area Mine Site," *IEEE Transactions on Industry Applications*, vol. 51, no. 4, pp. 2846–2853, July 2015. 53

[99] *IEC 60364-1. Low-voltage electrical installations - Part 1: Fundamental principles, assessment of general characteristics, definitions*, Std. 53

[100] *Regímenes de neutro en Baja Tensión. Dossier*, Hager. [Online]. Available: https://www.hager.es/files/download/0/.../regimen_neutro_dossier.pdf 56

[101] *Esquemas de conexión a tierra.*, Schneider. [Online]. Available: www.schneider-electric.com/resources/sites/schneider.../ECT.pdf 56

[102] N. Jayawarna, N. Jenkins, M. Barnes, M. Lorentzou, S. Papthanassiou, and N. Hatziagyriou, "Safety analysis of a microgrid," in *International Conference on Future Power Systems*, Nov 2005, pp. 7 pp.–7. 56, 57

[103] *Real Decreto 1699/2011, de 18 de noviembre, por el que se regula la conexión a red de instalaciones de producción de energía eléctrica de pequeña potencia*, Ministerio de Indistria, Tusrismo y comercio. Std. 57

[104] *IEC 608070-5-101. Telecontrol equipment 608070-5-101. Transmission protocols. Companion standard for basic telecontrol tasks*, IEC Std. 62

[105] *IEC 608070-5-104. Telecontrol equipment and systems. Transmission protocols. Network access for IEC-60870-5-101 using standard transport profiles*, IEC Std. 62

[106] *IEC 61850: Power Utility Automation*, Std. 62

[107] *IEC 62056: Data exchange for meter reading, tariff and load control*, Std. 62

[108] J. Dannehl, C. Wessels, and F. Fuchs, "Limitations of Voltage-Oriented PI Current Control of Grid-Connected PWM Rectifiers With

LCL Filters," *Power Electronics, IEEE*, vol. 56, issue: 2, pp. 380 – 388, 2009. 68, 71

[109] H. Cha and T.-K. Vu, "Comparative Analysis of Low-pass Output Filter for Single-phase Grid-connected Photovoltaic Inverter," in *Applied Power Electronics Conference and Exposition (APEC)*, 2010. 68

[110] E. Bueno, "Optimización del comportamiento de un convertidor de tres niveles NPC conectado a la red eléctrica," Ph.D. dissertation, Universidad de Alcalá. Escuela Politécnica Superior. Departamento de electrónica, 2005. 68, 70, 392

[111] T. Green and M. Prodanovic, "Control of inverter-based micro-grids," *Electric Power Systems Research, Distributed Generation*, vol. Volume 77, Issue 9, pp. 1204 – 1213, 2007. 70

[112] N. Kroutikova, C. Hernandez-Aramburo, and T. Green, "State-space model of grid-connected inverters under current control mode," *Electric Power Applications, IET*, vol. 1, no. 3, pp. 329–338, May 2007. 70

[113] M. Sowjanya and B. Babu, "Comparative analysis of LCL filter with active and passive damping methods for grid-interactive inverter system," in *Students' Technology Symposium (TechSym), IEEE*, Feb 2014, pp. 350–355. 70

[114] W. Wu, Y. He, T. Tang, and F. Blaabjerg, "A New Design Method for the Passive Damped LCL and LLCL Filter-Based Single-Phase Grid-Tied Inverter," *IEEE Transactions on Industrial Electronics*, vol. 60, no. 10, pp. 4339–4350, Oct 2013. 70

[115] A. Balasubramanian and V. John, "Analysis and design of split-capacitor resistiveinductive passive damping for LCL filters in grid-connected inverters," *Power Electronics, IET*, vol. 6, no. 9, pp. 1822–1832, November 2013. 70

[116] C. Yu, X. Zhang, F. Liu, H. Xu, C. Qiao, Z. Shao, W. Zhao, and H. Ni, "A general active damping method based on capacitor voltage detection for grid-connected inverter," in *ECCE Asia Downunder (ECCE Asia), IEEE*, June 2013, pp. 829–835. 70

[117] C. Bao, X. Ruan, X. Wang, W. Li, D. Pan, and K. Weng, "Step-by-Step Controller Design for LCL-Type Grid-Connected Inverter with

Capacitor Current-Feedback Active-Damping," *IEEE Transactions on Power Electronics*, vol. 29, no. 3, pp. 1239–1253, March 2014. 70

[118] J. He, Y. W. Li, D. Bosnjak, and B. Harris, "Investigation and Active Damping of Multiple Resonances in a Parallel-Inverter-Based Microgrid," *IEEE Transactions on Power Electronics*, vol. 28, no. 1, pp. 234–246, Jan 2013. 70

[119] T. Abeyasekera, C. Johnson, D. Atkinson, and M. Armstrong, "Suppression of Line Voltage Related Distortion in Current Controlled Grid Connected Inverters," *Power Electronics, IEEE*, vol. 20, Issue: 6, pp. 1393 –1401, 2005. 71

[120] M. Lisserre, F. Blaabjerg, and S. Hansen, "Design and control of an LCL-filter-based three-phase active," *Industry Applications Conference, IAS, IEEE*, vol. 1, pp. 299 – 307, 2001. 71, 312

[121] M. Lisserre, F. Blaabjerg, and A. Dell'Aquila, *Step-by-step design procedure for a grid-connected three-phase PWM voltage source converter.* Taylor & Francis, 2004. 71

[122] S.-K. Chung, "A phase tracking system for three phase utility interface inverters," *IEEE Transactions on Power Electronics*, vol. 15, no. 3, pp. 431–438, May 2000. 72

[123] P. Rodriguez, J. Pou, J. Bergas, I. Candela, R. Burgos, and D. Boroyevich, "Double Synchronous Reference Frame PLL for Power Converters Control," in *Power Electronics Specialists Conference, PESC, IEEE*, June 2005, pp. 1415–1421. 72

[124] A. Kulkarni and V. John, "A novel design method for SOGI-PLL for minimum settling time and low unit vector distortion," in *Industrial Electronics Society, IECO, IEEE*, Nov 2013, pp. 274–279. 72, 133

[125] V. Blahnik, T. Kosan, and J. Talla, "Control of single-phase AC/DC converter based on SOGI-PLL voltage synchronization," in *16th International Conference on Mechatronics - Mechatronika (ME)*, Dec 2014, pp. 652–655. 72

[126] S. Silva, B. Lopes, B. Filho, R. Campana, and W. Bosventura, "Performance evaluation of PLL algorithms for single-phase grid-connected systems," in *Industry Applications Conference, IAS, IEEE*, vol. 4, Oct 2004, pp. 2259–2263 vol.4. 72

[127] J. Kim, J. Lee, and K. Nam, "Inverter-Based Local AC Bus Voltage Control Utilizing Two DOF Control," *IEEE Transactions on Power Electronics*, vol. 23, no. 3, pp. 1288–1298, May 2008. 75

[128] Q. Lei, F. Z. Peng, and S. Yang, "Multiloop control method for high-performance microgrid inverter through load voltage and current decoupling with only output voltage feedback," *IEEE Transactions on Power Electronics*, vol. 26, no. 3, pp. 953–960, March 2011. 75

[129] L. Su, G. Li, and Z. Jin, "Modeling, control and testing of a voltage-source-inverter-based microgrid," in *4th International Conference on Electric Utility Deregulation and Restructuring and Power Technologies (DRPT)*, July 2011, pp. 724–729. 75

[130] J. Guerrero, J. Vasquez, and R. Teodorescu, "Hierarchical control of droop controlled DC and AC microgrids," in *Industrial Electronics, IECON, IEEE*, 2009. 75

[131] C. Hongbing, Z. Xing, L. Shengyong, and Y. Shuying, "Research on control strategies for distributed inverters in low voltage micro-grids," in *International Symposium on Power Electronics for Distributed Generation Systems (PEDG), IEEE*, June 2010, pp. 748–752. 75

[132] C. Wu, H. Liao, Z. Yang, Y. Wang, and H. Xu, "Voltage and frequency control of inverters connected in parallel forming a micro-grid," in *International Conference on Power System Technology (POWERCON),*, Oct 2010, pp. 1–6. 75

[133] C. Rowe, T. Summers, R. Betz, and T. Moore, "Implementing PCC voltage estimation utilising cascaded PI controllers in the dq rotating reference frame for microgrid inverter control," in *Energy Conversion Congress and Exposition (ECCE), IEEE*, Sept 2013, pp. 1026–1032. 75, 128

[134] E. Coelho, P. Cortizo, and P. Garcia, "Small signal stability for single phase inverter connected to stiff AC system," in *Industry Applications Conference, IAS, IEEE*, 1999. 78, 84

[135] ——, "Small signal stability for parallel connected inverters in stand-alone AC supply systems," in *Industry Applications Conference, IAS, IEEE*, 2000. 78, 84

[136] P. Kundur, *Power System Stability and Control.* McGraw-Hill, 1994. 81

[137] V. Venkatasubramanian, H. Schattler, and J. Zaborszky, "Fast time-varying phasor analysis in the balanced three-phase large electric power system," *IEEE Transactions on Automatic Control*, vol. 40, no. 11, pp. 1975–1982, Nov 1995. 81, 399

[138] M. Hannan, A. Mohamed, A. Hussain, and M. AI-Dabbagh, "Power quality analysis of STATCOM using dynamic phasor modeling," *Electric Power Systems Research*, vol. 79, no. 6, pp. 993 – 999, 2009. 81, 399

[139] M. Tao Yang, "Development of Dynamic Phasors for the Modelling of Aircraft Electrical Power Systems," Ph.D. dissertation, University of Nottingham, 2003. 81, 399

[140] T. Yang, S. Bozhko, and G. Asher, "Active front-end rectifier modelling using dynamic phasors for more-electric aircraft applications," *Electrical Systems in Transportation, IET*, vol. 5, no. 2, pp. 77–87, 2015. 81, 399

[141] S. Bala, "Integration of single-phase microgrids," Ph.D. dissertation, University of Wisconsin-Madison, 2008. 83

[142] L. Wang, X. Guo, H. Gu, W. Wu, and J. Guerrero, "Precise modeling based on dynamic phasors for droop-controlled parallel-connected inverters," in *IEEE International Symposium on Industrial Electronics (ISIE)*, May 2012, pp. 475–480. 85, 399

[143] X. Guo, Z. Lu, B. Wang, X. Sun, L. Wang, and J. Guerrero, "Dynamic Phasors-Based Modeling and Stability Analysis of Droop-Controlled Inverters for Microgrid Applications," *IEEE Transactions on Smart Grid*, vol. 5, no. 6, pp. 2980–2987, Nov 2014. 85, 399

[144] H. Rivas and J. Bergas, "Frequency Determination in a Single-Phase Voltage Signal using Adaptative Notch Filters," in *9th International Conference on Electrical Power Quality and Utilisation, EPQU*, Oct 2007, pp. 1–7. 89

[145] *ITI (CBEMA) Curve application note*, 2000. 90

[146] S. Elphick and V. Smith, "The 230 V CBEMA curve; Preliminary studies," in *Universities Power Engineering Conference (AUPEC)*, 2010, pp. 1–6. 91

[147] J. Dixit and A. Yadav, *Electrical Power Quality*, S. Dixit, Ed. University Science Press, 2010. 91

[148] J. C. Quesada Lacayo, "Medición y reglamentación de la calidad de la onda de tensión en el Sistema Eléctrico Nacional," Master's thesis, Universidad de Costa Rica Facultad de Ingeniería Escuela de Ingeniería Eléctrica, July 2005. 92

[149] E. Oliva, *Transformadores de potencia, de medida y de proteccion*, ser. Textos monográficos de electrotecnia. Marcombo, 1978. [Online]. Available: http://books.google.es/books?id=ym2uPQAACAAJ 101, 111, 119

[150] F. Corcoles, L. Sainz, J. Pedra, J. Sanchez-Nayarro, and M. Salichs, "Three-phase transformer modelling for unbalanced conditions, Part 1: core modelling and introductory examples," *Electric Power Applications, IET*, vol. 2, no. 2, pp. 99–112, March 2008. 101

[151] F. Corcoles, L. Sainz, J. Pedra, J. Sanchez-Navarro, and M. Salichs, "Three-phase transformer modelling for unbalanced conditions Part II: general formulation," *Electric Power Applications, IET*, vol. 3, no. 1, pp. 19–39, January 2009. 101

[152] M. A. Pozueta-Rodríguez, "Transformadores," in *Electrotecnia para ingenieros no especialistas.* Universidad de Cantabria. Departamento de ingenieria electrica y energética, 2012. [Online]. Available: http://personales.unican.es/rodrigma/primer/publicaciones.htm 101

[153] Transformadores trifásicos y bancos. [Online]. Available: referencias111.wikispaces.com/file/view/05CONVERSION3.pdf 105, 108

[154] R. Del Vecchio, B. Poulin, P. Feghali, D. M. S., and R. Ahuja, *Transformer Design Principles - With Application to Core-Form Power Transformers.* Gordon and Breach Science Publishers, 2001. 105

[155] M. R. Dolatian and A. Jalilian, "Voltage sag effect on three phase five leg transformers." World Academy of Science, Engineering and Technology, 2007. 108

[156] K. Ogata, *Sistemas de Control en Tiempo Discreto.* Pearson Education S.A, 1996. 123, 131

[157] ——, *Ingeniería de control moderno.* Pearson Education S.A, 2010. 123, 152

[158] A. Isidori, *Nonlinear Control Systems*, ser. Communications and Control Engineering. Springer, 1995, no. v. 1. 123

[159] R. Matusu, "Application of fractional order calculus to control theory," in *International journal of mathematical models and methods in applied sciences*, vol. 5, 2011. 123

[160] D. Zmood, D. Holmes, and G. Bode, "Frequency-domain analysis of three-phase linear current regulators," *IEEE Transactions on Industry Applications*, vol. 37, no. 2, pp. 601–610, Mar 2001. 123, 134, 137

[161] E. Sánchez-Sánchez, D. Heredero-Peris, and D. Montesinos-Miracle, "Stability analysis of current and voltage resonant controllers for voltage source converters," in *Power Electronics and Applications (EPE'15 ECCE-Europe), 2015 17th European Conference on*, Sept 2015, pp. 1–10. 124

[162] D. Heredero-Peris, E. Sámchez-Sánchez, C. Chillón-Antón, D. Montesinos-Miracle, and S. Galceran-Arellano, "A novel fractional proportional-resonant current controller for Voltage Source Converters," in *18th European Conference on Power Electronics and Applications (EPE-ECCE Europe)*, Aug 2016, pp. 1–10. 124

[163] C. Fortescue, "Method of Symmetrical Coordinates Applied to the Solution of Polyphase Networks," *Transactions AIEE*, vol. 37, 1918. 125, 387

[164] J. Bergas, "Control del motor d'inducció considerant els límits del convertidor," Ph.D. dissertation, Universitat Politècnica de Catalunya, 2000. 127, 275

[165] X. Wang, F. Blaabjerg, Z. Chen, and J. Guerrero, "A centralized control architecture for harmonic voltage suppression in islanded microgrids," in *37th Annual Conference on IEEE Industrial Electronics Society, IECON*, Nov 2011, pp. 3070–3075. 127

[166] B. Crowhurst, E. El-Saadany, L. El Chaar, and L. Lamont, "Single-phase grid-tie inverter control using DQ transform for active and reactive load power compensation," in *IEEE International Conference on Power and Energy (PECon)*, Nov 2010, pp. 489–494. 128

[167] A. Lorduy, A. Lazaro, A. Barrado, C. Fernandez, I. Quesada, and C. Lucena, "Simplified Synchronous Reference Frame Control of the three phase grid connected inverter," in *Applied Power Electronics Conference and Exposition (APEC), IEEE*, Feb 2010, pp. 1026–1033. 128

[168] N. Ninad and L. Lopes, "Per-phase vector (dq) controlled three-phase grid-forming inverter for stand-alone systems," in *IEEE International Symposium on Industrial Electronics (ISIE)*, June 2011, pp. 1626–1631. 128

[169] T. Huang, X. Shi, Y. Sun, and D. Wang, "Three-phase photovoltaic grid-connected inverter based on feedforward decoupling control," in *International Conference on Materials for Renewable Energy and Environment (ICMREE)*, vol. 2, Aug 2013, pp. 476–480. 129

[170] B. Bahrani, A. Rufer, and S. Kenzelmann, "Multivariable-PI-based DQ Current Control of Voltage Source Converters with Superior Axes Decoupling Capability," *Industry Applications, IEEE Transactions on Power Electronics*, vol. 58, Issue: 7, pp. 3016–3026, 2011. 129

[171] W. Hu, W. J. Cai, and G. Xiao, "Relative gain array for MIMO processes containing integrators and/or differentiators," in *Control Automation Robotics Vision (ICARCV), 2010 11th International Conference on*, Dec 2010, pp. 231–235. 131

[172] D. Heredero-Peris, M. Capó-Lliteras, C. Miguel-Espinar, T. Lledó-Ponsati, and Montesinos-Miracle, "Development and implementation of a dynamic PV emulator with HMI interface for high power inverters," in *16th European Conference on Power Electronics and Applications (EPE-ECCE Europe)*, Aug 2014, pp. 1–10. 131, 218

[173] B. Bahrani, A. Rufer, S. Kenzelmann, and L. Lopes, "Vector Control of Single-Phase Voltage-Source Converters Based on Fictive-Axis Emulation," *Industry Applications, IEEE Transactions on Power Electronics*, vol. 47 , Issue: 2, pp. 831– 840, 2011. 133

[174] B. Giampaolo, D. Barater, L. Tarisciotti, and P. Zanchetta, "High-dynamic single-phase Hilbert-based PLL for improved phase-jump ride-through in grid-connected inverters," in *Energy Conversion Congress and Exposition (ECCE), 2014 IEEE*, Sept 2014, pp. 4932–4939. 133

[175] C. Lascu, L. Asiminoaei, I. Boldea, and F. Blaabjerg, "Frequency Response Analysis of Current Controllers for Selective Harmonic Compensation in Active Power Filters," *IEEE Trans. Ind. Electron.*, vol. 56, no. 2, pp. 337–347, 2009. 134, 158

[176] S. Golestan, M. Monfared, J. M. Guerrero, and M. Joorabian, "A D-Q synchronous frame controller for single-phase inverters," in *Power Electronics, Drive Systems and Technologies Conference (PEDSTC), 2011 2nd*, Feb 2011, pp. 317–323. 134

[177] A. G. Yepes, F. D. Freijedo, J. Doval-Gandoy, O. López, J. Malvar, and P. Fernandez-Comesaña, "Effects of discretization methods on the performance of resonant controllers," *IEEE Trans. Power Electron.*, vol. 25, no. 7, pp. 1692–1712, 2010. 138, 142, 156, 162

[178] J. Eloy-García, J. M. Guerrero, and J. C. Vasquez, "Grid simulator for power quality assessment of micro-grids," *IET Power Electron.*, vol. 6, no. 4, pp. 700–709, 2013. 138

[179] S. Fukuda and T. Yoda, "A novel current-tracking method for active filters based on a sinusoidal internal model," *IEEE Trans. Ind. Appl.*, vol. 37, no. 3, pp. 888–895, 2001. 138

[180] X. Yuan, W. Merk, H. Stemmler, and J. Allmeling, "Stationary-frame generalized integrators for current control of active power filters with zero steady-state error for current harmonics of concern under unbalanced and distorted operating conditions," *IEEE Trans. Ind. Appl.*, vol. 38, no. 2, pp. 523–532, 2002. 138, 139

[181] D. N. Zmood and D. G. Holmes, "Stationary frame current regulation of PWM inverters with zero steady-state error," *IEEE Trans. Power Electron.*, vol. 18, no. 3, pp. 814–822, 2003. 138

[182] A. G. Yepes, F. D. Freijedo, O. López, and J. Doval-Gandoy, "High-performance digital resonant controllers implemented with two integrators," *IEEE Trans. Power Electron.*, vol. 26, no. 2, pp. 563–576, 2011. 139

[183] P. Rodríguez, R. Teodorescu, I. Candela, A. V. Timbus, M. Liserre, and F. Blaabjerg, "New positive-sequence voltage detector for grid synchronization of power converters under faulty grid conditions," in *PESC Rec. - IEEE Annu. Power Electron. Spec. Conf.*, 2006. 139

[184] F. Wang, M. C. Benhabib, J. L. Duarte, and M. a. M. Hendrix, "Sequence-Decoupled Resonant Controller for Three-phase Grid-connected Inverters," in *APEC, IEEE*, 2009, pp. 121–127. 141

[185] C. Lascu, L. Asiminoaei, I. Boldea, and F. Blaabjerg, "High performance current controller for selective harmonic compensation in active power filters," *IEEE Trans. Power Electron.*, vol. 22, no. 5, pp. 1826–1835, 2007. 141

[186] R. Bojoi, G. Griva, M. Guerriero, F. Farina, F. Profumo, and V. Bostan, "Improved current control strategy for power conditioners using sinusoidal signal integrators in synchronous reference frame," *PESC Rec. - IEEE Annu. Power Electron. Spec. Conf.*, vol. 6, no. 6, pp. 4623–4629, 2004. 141

[187] A. G. Yepes, F. D. Freijedo, J. Doval-Gandoy, O. Lopez, J. Malvar, and P. Fernandez-Comesaña, "On the discrete-time implementation of resonant controllers for active power filters," *IECON Proc. (Industrial Electron. Conf.*, no. 1, pp. 3686–3691, 2009. 142

[188] J. G. Proakis and D. G. Manolakis, *Digital Signal Processing*, 4th ed. Pearson Education Inc., Prentice Hall, 2007. 143

[189] M. J. Newman and D. G. Holmes, "Delta operator digital filters for high performance inverter applications," *IEEE Trans. Power Electron.*, vol. 18, no. 1 II, pp. 447–454, 2003. 143

[190] D. Sera, T. Kerekes, M. Lungeanu, P. Nakhost, R. Teodorescu, G. K. Andersen, and M. Liserre, "Low-cost digital implementation of proportional-resonant current controllers for PV inverter applications using delta operator," *IECON, IEEE*, vol. 2005, pp. 2517–2522, 2005. 143

[191] R. Teodorescu, F. Blaabjerg, U. Borup, and M. Liserre, "A new control structure for grid-connected LCL PV inverters with zero steady-state error and selective harmonic compensation," *IEEE Appl. Power Electron. Conf. Expo APEC*, vol. 1, no. C, pp. 580–586, 2004. 158

[192] A. G. Yepes, F. D. Freijedo, O. López, and J. Doval-Gandoy, "Analysis and design of resonant current controllers for voltage-source converters by means of nyquist diagrams and sensitivity function," *IEEE Trans. Ind. Electron.*, vol. 58, no. 11, pp. 5231–5250, 2011. 158

[193] M. S. Tavazoei and M. Haeri, "A note on the stability of fractional order systems," *Mathematics and Computers in Simulation*, vol. 79, no. 5, pp. 1566 – 1576, 2009. 167

[194] A. Radwan, A. Soliman, A. Elwakil, and A. Sedeek, "On the stability of linear systems with fractional-order elements ," *Chaos, Solitons & Fractals*, vol. 40, no. 5, pp. 2317 – 2328, 2009. 167

[195] J. Sabatier, C. Farges, and J.-C. Trigeassou, "A stability test for non-commensurate fractional order systems ," *Systems & Control Letters*, vol. 62, no. 9, pp. 739 – 746, 2013. 167

[196] Y. Q. Chen, I. Petras, and D. Xue, "Fractional order control - A tutorial," in *American Control Conference (ACC)*, June 2009, pp. 1397–1411. 167, 185, 186

[197] I. Podlubny, *Fractional Differential Equations*, N. York, Ed. Academic Press, 1999. 169

[198] I. Petras, "Fractional Order feedback control of a DC motor," *Journal of Electrical Engineering*, vol. 60, no. 3, pp. 117–128, 2009. 169

[199] I. Podlubny, B. M. Petras, I., P. Vinagre, Oleary, and L. Dorcak, "Analogue Realizations of Fractional-Order Controllers," *Kluwer Academic Publishers*, vol. 29, pp. 281–296, 2002. 171

[200] J. C. Bancroft, "Continued fraction expansion of the square-root operator," CREWES Research Report, Tech. Rep., 2004. 174

[201] A. H. V. F. BM Vinagre, I Podlubny, "Some approximations of fractional order operators used in control theory and applications," *Fractional calculus and applied analysis*, vol. 3, no. 3, pp. 231–248, 2000. 176, 179, 185, 191

[202] G. Maione, "Discretizing fractional order operators approximated by Thiele continued fractions," in *ENOC*, Rome, July 2011. 176

[203] P. Mata de Oliveira Valério-Duarte, *Ninteger v. 2.3. Fractional control toolbox for MatLab*, Universidad Técnica de Lisboa. Instituto Superior Técnico, 2005. 176

[204] A. Oustaloup, F. Levron, B. Mathieu, and F. Nanot, "Frequency-band complex noninteger differentiator: characterization and synthesis," *Circuits and Systems I: Fundamental Theory and Applications, IEEE Transactions on*, vol. 47, no. 1, pp. 25–39, Jan 2000. 179

[205] D. Xue, C. Zhao, and Y. Q. Chen, "A Modified Approximation Method of Fractional Order System," in *IEEE International Conference on Mechatronics and Automation*, June 2006, pp. 1043–1048. 179

[206] A. Charef, H. Sun, Y. Tsao, and B. Onaral, "Fractal system as represented by singularity function," *IEEE Transactions on Automatic Control*, vol. 37, no. 9, pp. 1465–1470, Sep 1992. 179

[207] B. M. V. a. YangQuan Chen, "Using Continued Fraction Expansion to Discretize Fractional Order Derivatives," *Special Issue on Fractional Derivatives and Their Applications (FDTA), Nonlinear Dynamic*, 2008. 185, 186, 189

[208] R. Gorenflo, "Fractional Calculus: Some Numerical Methods,," in *CISM. Lecture Notes*, Udine, Italy., 1996. 185

[209] M. A. Al-Alaoui, "Al-Alaoui Operator and the α-Approximation for Discretization of Analog Systems," *Electrical Energy*, vol. 19, no. 1, 2006. 186, 187, 191

[210] M. Al-Alaoui, "Novel digital integrator and differentiator," *Electronics Letters*, vol. 29, no. 4, pp. 376–378, Feb 1993. 187

[211] *IEC 62040-3. Uninterrumpible power system. Part 3: Method of specifying the performance and test requirements*, Std., 2001. 199, 202

[212] D. Heredero-Peris, C. Chillón-Antón, M. Pagès-Giménez, G. Gross, and D. Montesinos-Miracle, "Grid-connected to/from off-grid transference for micro-grid inverters," in *PCIM*, 2013. 207, 209

[213] D. Heredero-Peris, C. Chillón-Antón, M. Pages-Gimenez, G. Gross, and D. Montesinos-Miracle, "Implementation of grid-connected to/from off-grid transference for micro-grid inverters," in *Industrial Electronics Society, IECON, IEEE*, Nov 2013, pp. 840–845. 207, 209

[214] D. Heredero-Peris, M. Pagès-Giménez, G. Gross, and D. Montesinos-Miracle, "Permanent execution of MPPT algorithm for PV systems with energy storage," in *PEDG, IEEE*, 2015. 208

[215] R. Carreras-Margalef, E. Galvez-Moreno, D. Heredero-Peris, G. Gross, D. Montesinos-Miracle, M. Pagès-Giménez, and M. Torne-Pibernat, "Equipo fotovoltaico y procedimiento para controlar dicho equipo fotovoltaico," Spain Patent ES-2 421 857, 2012. 208

[216] S. Narendiran, "Grid tie inverter and MPPT - A review," in *International Conference on Circuits, Power and Computing Technologies (ICCPCT)*, March 2013, pp. 564–567. 232

[217] B.-Y. Chen and Y.-S. Lai, "New Digital-Controlled Technique for Battery Charger With Constant Current and Voltage Control Without Current Feedback," *IEEE Transactions on Industrial Electronics*, vol. 59, no. 3, pp. 1545–1553, March 2012. 267

[218] C.-L. Nguyen and H.-H. Lee, "AC voltage sensorless control of battery charger system in electric vehicle applications," in *Conference on Power Energy, IPEC*, Dec 2012, pp. 515–520. 267

[219] W. Lee, B.-M. Han, and H. Cha, "Battery ripple current reduction in a three-phase interleaved dc-dc converter for 5kW battery charger," in *Energy Conversion Congress and Exposition (ECCE), IEEE*, Sept 2011, pp. 3535–3540. 267

[220] C. Ho, H. Breuninger, S. Pettersson, G. Escobar, L. Serpa, and A. Coccia, "Practical Design and Implementation Procedure of an Interleaved Boost Converter Using SiC Diodes for PV Applications," *IEEE Transactions on Power Electronics*, vol. 27, no. 6, pp. 2835–2845, June 2012. 267

[221] W. Martinez and C. Cortes, "High power density interleaved DC-DC converter for a high performance electric vehicle," in *Workshop on Power Electronics and Power Quality Applications (PEPQA)*, July 2013, pp. 1–6. 267

[222] T. Hegarty. (2007, 11) Benefits of multiphasing buck converters - Part 1. EE Times. 267

[223] A. Khosroshahi, M. Abapour, and M. Sabahi, "Reliability Evaluation of Conventional and Interleaved DC-DC Boost Converters," *IEEE Transactions on Power Electronics*, vol. 30, no. 10, pp. 5821–5828, Oct 2015. 268

[224] P. Enjeti and B. Xie, "A new real time space vector PWM strategy for high performance converters," *Industry Applications Society Annual Meeting, IEEE*, no. i, pp. 1018–1024, 1992. 269

[225] A. Boglietti, G. Griva, M. Pastorelli, F. Profumo, and T. Adam, "Different PWM modulation techniques indexes performance evalu-

ation," in *nternational Symposium on Industrial Electronics, ISIE, IEEE*, 1993, pp. 193–199. 269, 273

[226] A. Kouzou, M. O. Mahmoudi, and M. S. Boucherit, "A New 3D-SVPWM Algorithm for Four-Leg inverters," *Electric Machines and Drives Conference, IEMDC, IEEE International*, pp. 1674–1681, 2009. 269, 281, 283

[227] S. Buso and P. Mattavelli, *Digital Control in Power Electronics.* Morgan & Calypool, 2006. 270, 275, 289

[228] J. Jose, G. Goyal, and M. Aware, "Improved inverter utilisation using third harmonic injection," in *Joint International Conference on Power Electronics, Drives and Energy Systems (PEDES)*, Dec 2010, pp. 1–6. 273

[229] M. Villalva, "3-D space vector PWM for three-leg four-wire voltage source inverters," in *Power Electronics Specialists Conference, PESC, IEEE*, vol. 5, June 2004, pp. 3946–3951 Vol.5. 275

[230] M.-A. Perales, L. Terrón, J.-A. Sánchez, A. De La Torre, J. M. Carrasco, and L. G. Franquelo, "New controllability criteria for 3-phase 4-wire inverters applied to shunt active power filters," *IECON Proceedings (Industrial Electronics Conference)*, vol. 1, pp. 638–643, 2002. 275

[231] H. Akagi, Y. Tsukamoto, and a. Nabae, "Analysis and design of an active power filter using quad-series voltage source PWM converters," *IEEE Transactions on Industry Applications*, vol. 26, no. 1, pp. 93–98, 1990. 275

[232] M. M. Kouzou A and B. M.S, *The Space Vector Modulation PWM Control Methods Applied on Four Leg Inverters, Electric Machines and Drives*, M. Chomat, Ed. InTech, 2011. 276

[233] R. Zhang, D. Boroyevich, V. Prasad, H.-C. Mao, F. Lee, and S. Dubovsky, "A three-phase inverter with a neutral leg with space vector modulation," *Applied Power Electronics Conference, APEC*, vol. 2, no. 1, pp. 857–863, 1997. 276

[234] V. Prasad, D. Borojevic, and R. Zhang, "Analysis and comparison of space vector modulation schemes for a four-leg voltage source inverter," *Proceedings of APEC 97 - Applied Power Electronics Conference*, vol. 2, pp. 864–871, 1997. 276

[235] S. M. Ali and M. P. Kazmierkowski, "Current regulation of four-leg PWM-VSI," *Industrial Electronics Society, IECON, IEEE*, pp. 1853–1858, 1998. 279

[236] P. Verdelho, "A Current Control System Based in $\alpha\beta 0$ variables for a four-leg PWM voltage converter," *Industrial Electronics Society, IECON, IEEE*, pp. 1847–1852, 1998. 279

[237] (2013) Digital Motor Control. Software Library: Target Independent Math Blocks. Texas Instruments, Inc. 290

[238] J. Kim, J. Guerrero, P. Rodriguez, R. Teodorescu, and K. Nam, "Mode Adaptive Droop Control With Virtual Output Impedances for an Inverter-Based Flexible AC Microgrid," *IEEE Transactions on Power Electronics*, vol. 26, no. 3, pp. 689–701, March 2011. 313

[239] A. Gómez-Yepes, "Digital Resonant current controllers for voltage source converters," Ph.D. dissertation, Universidad de Vigo, 2011. 320

[240] C. Wessels, J. Dannehl, and F. Fuchs, "Active damping of LCL-filter resonance based on virtual resistor for PWM rectifiers; stability analysis with different filter parameters," in *Power Electronics Specialists Conference, PESC, IEEE*, June 2008, pp. 3532–3538. 322, 323

[241] "Internal Model Control," University of Newcastle Upon Tyne. Chemical and Process Engineering., Tech. Rep., 2002. 341

[242] G. Paap, "Symmetrical components in the time domain and their application to power network calculations," *IEEE Transactions on Power Systems*, vol. 15, no. 2, pp. 522–528, May 2000. 389, 390

[243] R. Lee, P. Pillay, and R. Harley, "D-Q Reference Frames for the Simulation of Induction Motors," *Electric Power Systems Research*, 1985. 395